

IEEE 1977 MECHANICAL ENGINEERING IN RADAR



**DISTRIBUTION STATEMENT A**

Approved for public release;  
Distribution Unlimited

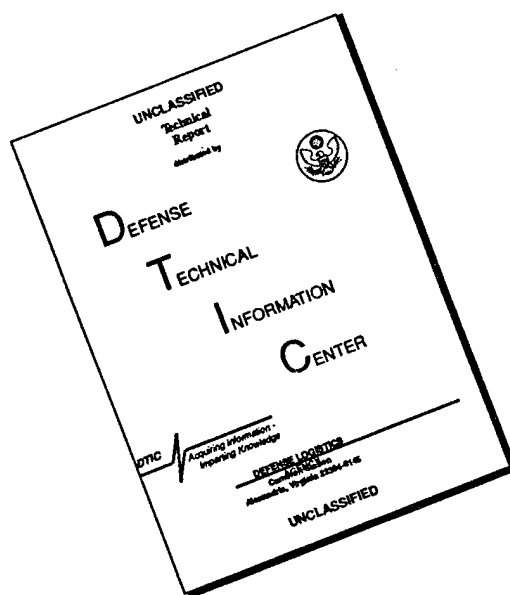
19951226 026

DEPARTMENT OF DEFENSE  
PLASTICS TECHNICAL EVALUATION CENTER  
ARRADCON, DOVER, N. J. 07801

HYDRO QUALITY ENGINEERING

PL-34863-  
34866

# DISCLAIMER NOTICE



THIS DOCUMENT IS BEST QUALITY AVAILABLE. THE COPY FURNISHED TO DTIC CONTAINED A SIGNIFICANT NUMBER OF PAGES WHICH DO NOT REPRODUCE LEGIBLY.

-- 1 OF 1

\*\*\*DTIC DOES NOT HAVE THIS ITEM\*\*\*

-- 1 - AD NUMBER: D429465  
-- 5 - CORPORATE AUTHOR: INSTITUTE OF ELECTRICAL AND ELECTRONICS ENGINEERS  
-- INC NEW YORK  
-- 6 - UNCLASSIFIED TITLE: THE RECORD OF THE IEEE 1977 MECHANICAL  
-- ENGINEERING IN RADAR SYMPOSIUM.  
--11 - REPORT DATE: NOV 08, 1977  
--12 - PAGINATION: 261P  
--14 - REPORT NUMBER: IEEE PUB 77CH1250-OAES  
--20 - REPORT CLASSIFICATION: UNCLASSIFIED  
-21 - SUPPLEMENTARY NOTE: PROCEEDINGS: 'THE RECORD OF THE IEEE 1977  
-- MECHANICAL ENGINEERING IN RADAR SYMPOSIUM', 8-10 NOV 77, ARLINGTON,  
-- VA. SPONSORED BY AES SOCIETY IEEE, WASHINGTON SECTION IEEE, AND  
-- NAVAL RESEARCH LAB. (SEE PL-34864 - PL-34866).  
--22 - LIMITATIONS (ALPHA): APPROVED FOR PUBLIC RELEASE; DISTRIBUTION  
-- UNLIMITED. AVAILABILITY: IEEE AEROSPACE AND ELECTRONICS SYSTEMS  
-- SOCIETY, 345 E. 47TH ST., N.Y., N.Y. 10017. IEEE PUBLICATION 77CH  
-- 1250-0 AES.  
--33 - LIMITATION CODES: 1 24

-----  
-- END OF DISPLAY LIST  
-- ((ENTER NEXT COMMAND))

Alt-Z FOR HELP3 ANSI 3 HDX 3 3 LOG CLOSED 3 PRINT OFF 3 PARITY

DEPARTMENT OF DEFENSE  
PLASTICS TECHNICAL EVALUATION CENTER  
ARRADCOM, DOVER, N. J. 07801

PL-34863  
→ 34866



**The Record of the  
IEEE  
1977  
MECHANICAL  
ENGINEERING IN  
RADAR  
SYMPOSIUM**



**Held at  
Sheraton National Hotel  
Arlington, Virginia  
November 8-10, 1977**

**Sponsored by:  
AES Society IEEE  
Washington Section IEEE  
Naval Research Laboratory**

**DTIC QUALITY INSPECTED 3**

Conference Committee	<b>v</b>
Table of Contents	<b>viii</b>
Author Index	<b>x</b>
Papers Start on Page	<b>1</b>
Authors Biographies Start on Page	<b>245</b>

IEEE Publication 77CH 1250-0 AES

## **IEEE AEROSPACE AND ELECTRONIC SYSTEMS SOCIETY**

The IEEE Aerospace and Electronic Systems Society is an organization, within the framework of the IEEE, of members with a similarity of professional interests. All members of the IEEE are eligible for membership in the Society, and will receive the TRANSACTIONS and NEWSLETTER of the group upon payment of the annual Society membership fee of \$5.00. For information on joining write to IEEE.

The Mechanical Engineering in Radar Symposium Record is a publication of the IEEE Aerospace and Electronic Systems Society and is published in conformance with and pursuant to the policies of the Society.

The Record is exempt from the requirement for individual export license under the terms of Title 22, Subchapter M, Article 125.30-a-2 of the Regulations of the U.S. Department of State, as amended 1 March 1960.

## **PUBLISHED BY THE IEEE AEROSPACE AND ELECTRONIC SYSTEMS SOCIETY**

THE INSTITUTE OF ELECTRICAL AND ELECTRONICS ENGINEERS, INC.  
345 East 47th Street, New York, New York 10017

Responsibility for the contents rests upon the authors, and not upon the IEEE, the Society, or its members. Individual copies may be purchased from the IEEE Service Center, 445 Hoes Lane, Piscataway, NJ 08854. Reference Catalog Number 77CH 1250-0 AES. Abstracting is permitted with mention of source. All rights, including translation, are reserved by the IEEE. Requests for republication permission should be addressed to Director of Publications, IEEE, 345 East 47th Street, New York, N.Y. 10017. Copyright © 1977 by the Institute of Electrical and Electronics Engineers, Inc. Printed in the U.S.A.

# Forword

The merging of two apparently unrelated technical disciplines such as electrical and mechanical engineering would seem to be exceedingly complex. And yet, this merger successfully occurs over the gamut of aerospace equipments wherever electronic systems of any type are employed. The fact that it occurs so smoothly and successfully is certainly a tribute to the abilities of the individual mechanical and electrical engineers to communicate with each other, to endeavor to understand the other's technology, and to work together in an atmosphere of mutual respect and enthusiasm. This Symposium, MERS-77, has been designed to facilitate the understanding of the mechanical engineering technology by the electrical engineering community, and to create a forum by which radar mechanical engineers can meet and openly discuss solutions to intricate design problems. The Symposium has been made possible through the initiative and the guidance of the Radar Systems Panel of the IEEE's Aerospace Electronic Systems Society, through the dedicated efforts of a number of key people in its planning and organization, and through the contributions from the authors of the many fine papers that comprise these Proceedings.

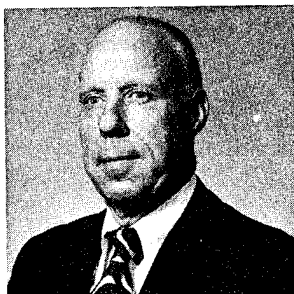


A handwritten signature in dark ink, which appears to read "Harry C. Moses". The signature is stylized with a large, sweeping initial 'H'.

Harry C. Moses  
Symposium Chairman

# Symposium Committee

## General Chairman



Harry C. Moses

## Deputy Chairman



Richard D. Roche

## Publications



John D. Bailey

## Arrangements Chairman



William J. Kanewski

## Publicity



Leonard J. Hayes

## Treasurer



Cramer Bacque

## Activities



James V. Smith



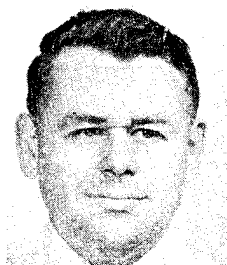
Lionel I. Moskowitz

## Registration



James A. Kalitta

## Technical Programs Chairman



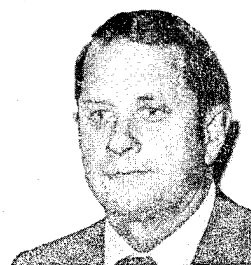
William R. Fanning

## Paper Review



Angelo Colao

## Paper Review



Carroll Phillips

## Advisory Board



H. Alen Ecker



David K. Barton



Merrill I. Skolnik

# Session Chairmen

## Systems Concepts



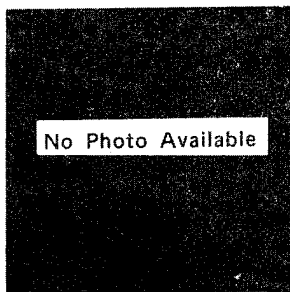
Robert M. Goodman, Jr.

## Impact of System Requirements on Packaging Design



Eugene H. Stomblor

## Structural Design



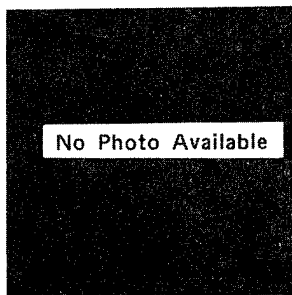
Walter J. Noble

## Thermal Control



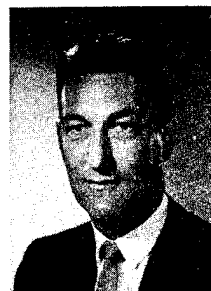
Irving D. Kruger

## Antenna Positioning and Control



Samuel F. Hutchins

## Environment and Materials



Orison Wade

# Table of Contents

## SYSTEM CONCEPTS SESSION

Mechanical Design and Performance Studies for the GWS.25 Surveillance and Tracker System, A. T. Humphrey, GEC-Marconi Electronics Limited, Great Baddow Research Laboratories .....	1
Deployment Flexible Mechanical Design for a Mobil-3D Radar Antenna, M. Sugie, M. Kawai, M. Wakabayashi, and Y. Katou, Nippon Electronic Company .....	7
The Control Tolerances In An Array Antenna, W. R. Fanning, G. N. Tsandoulas, and M. A. Nader, M.I.T. Lincoln Laboratory .....	236
The Viking Radar Systems—Design for Space Programs, H. G. Frankland and N. Sawyer, Teledyne Ryan Aeronautical .....	13
Mechanical Design and Integration of Phased Arrays—Naval Systems Command-AEGIS Program, R. F. DiFelice and J. Drenik, RCA Corporation .....	230
Mechanical Engineering Considerations in the Design and Fabrication of Large Phased Array Radars, J. T. Mead, P. W. Thiessen, and W. R. Anderson, Raytheon Company .....	
The Ku Band Integrated Radar/Communications Subsystem for the Shuttle, L. C. Parode, Hughes Space & Communications Group .....	21
Military Lightweight L-Band Shipboard Surveillance Radar Antenna, P. D'Offizi and E. M. Natargiacomo, Selenia Industrie Elettroniche Associate Spa .....	
General Purpose Multichannel Small Size Commutator Type SlipRing Assembly Suitable for Low Frequency Currents, P. D'Offizi and E. M. Natargiacomo, Selenia Industrie Elettroniche Associate Spa .....	
Mechanical Reliability Considerations in a Minimally Attended Radar (MAR) System, T. P. Kabaservice and Lt. Col. R. E. Brandau, The MITRE Corp .....	27
Implementation of Wind Performance Studies for Large Antenna Structures, R. Levy and M. S. Katow, Jet Propulsion Laboratory, California Inst. of Tech ..	34
AN/TPS-59,A Unique Tactical Radar, L. E. Bertz and L. J. Hayes, Genreal Electric Corp. ....	
CN Tower Microwave Radome, M. B. Punnett, Birdair Structures .....	40
Developments in Ground Mounted Air Supported Radomes, M. B. Punnett, Birdair Structures .....	
Synergized Design Approach to Antenna Systems, L. E. Rhoades and A. B. Rohwer, Electronic Space Systems Corp. ....	46
Structural Design Improvements of ESSCO Radomes and Antennas, J. B. Sangiolo and A. B. Rohwer, Electronic Space Systems Corp. ....	

## IMPACT OF SYSTEM REQUIREMENTS ON PACKAGING DESIGN SESSION

The Mechanical Engineer's Role in Military Electronics, J. Karpuk and C. Levine, Raytheon Co. ....	52
Lightweight Antennas for a Guidance System for Tactical Military Usage, E. Kolb, Bendix Communications Div. ....	
Design and Fabrication of a Lightweight Radome for Use with the Hemispheric Coverage Antenna, M. Costagliola and R. C. Berg, Sperry Gyroscope Div. ...	58
An Extremely Lightweight Fuselage-Integrated Phased Array for Airborne Applications, J. S. Yee and W. J. Furlong, The Boeing Aerospace Co. ....	
Challenges in Interconnection—A Phased Array Radar Antenna, P. J. Walsh and J. A. Henderson, Westinghouse Electric Corp. ....	62
High Voltage Packaging Problems for Airborne Systems, W. G. Dunbar, The Boeing Aerospace Co. ....	66
An Improved Maintainability Concept For Advanced Radar Systems, W. Garner, Westinghouse Electric Corp. ....	242

Crystal Oscillator Vibration Isolation for Airborne Radar Applications, H. Rossman and J. Chino, Westinghouse Electric Corp. ....	72
---	----

## STRUCTURAL DESIGN SESSION

On the Design of Self-Deploying, Extremely Large Parabolic Antennas and Arrays, A. A. Woods, Jr., Lockheed Missiles & Space Co. ....	75
Deployed Antenna Surfaces, W. A. Wade, Lockheed Missiles & Space Co. ....	
Antenna to IMU Mounting for SAR Motion Compensation, L. C. Miller, and V. M. Foxwell, Westinghouse Electric Corp. ....	80
Development of a Pointing Bias Model for a 40-foot Diameter Radar Antenna, J. Antebi, R. Luft, and H. Simpson, Simpson Gumpertz & Heger, Inc .....	224
Antenna/Mast Requirements for Low Altitude Aircraft Detection System, D. Zona and R. W. Milligan, Sanders Associates .....	85
Conceptual Studies for Unmanned Hardened Radar Facilities, R. W. Luft, J. Antebi, and H. Simpson, Simpson, Gumpertz and Heger, Inc. ....	216
Reliability of Unmanned Radar Facilities, J. Antebi, and R. Luft, Simpson Gumpertz & Heger, Inc. ....	
Evaluating Computed Distortions of Parabolic Reflectors, M. S. Katow and R. Levy, Jet Propulsion Laboratory, Calif. Institute of Technology .....	91
Antenna Bias Rigging for Performance Objective, M. S. Katow and R. Levy, Jet Propulsion Laboratory, Calif. Institute of Technology .....	94
Design of Hardened Radar Structures, R. L. Mann, General Electric Co. ....	98
Low-Cost Approach to Large Surveillance Antenna Pedestal, E. C. Hawkins, Bendix Communications Div. ....	104
The E-3A Radome Structural Damage Tolerance and Repair, C. T. Ray, Jr., The Boeing Aerospace Co. ....	

## THERMAL CONTROL SESSION

Thermal Design of Airborne Radars—Present and Future, F. Altoz, Westinghouse Electric Corp. ....	110
Ebullient Cooling for an Active Radar Seeker, Q. Sutton, L. Battin, and V. P. Duffy, Motorola, Inc. ...	
Heat Pipe Applications to Control Electronic Temperature in Radars, K. S. Sekhon, Hughes Aircraft Co. ...	114
Temperature Control of Highly Sensitive Electronic Devices, H. Rossman and J. Chino, Westinghouse Electric Corp. ....	120
Thermoelectrics in Radar Systems, D. Ash, ELTA Electronics Industries, Ltd. ....	
A Heat Pipe Application to a Radar TX Cabinet, U. Corsi and G. Malagoli, Selenia Industrie Elettroniche Associate Spa. ....	124
Shipborne Radar Cabinets Designed and Tested According to MIL Spec. 1640, U. Corsi and G. Malagoli, Selenia Industrie Elettroniche Associate Spa. ...	
Controlling Temperatures in Phased Array Antennas, R. F. Porter, Westinghouse Electric Corp. ....	128
OPENCE (OPTimum perform ENCE) Heat Sink Design Procedure, M. Tadmer and H. Frenkel, ELTA Electronics Industries, Ltd. ....	132

## ANTENNA POSITIONING AND CONTROL SESSION

E-3A Antenna Pedestal Turntable, C. M. Fritz, Keystone Engineering Co. ....	136
Shock Mounts for Shipboard Radar Pedestals and Stable Platforms, L. Fuss, D. Hoecht, and R. P. Staley, Scientific-Atlantic, Inc. ....	145
Radar Azimuth Bearings—Design, Selection and Application, T. A. Bushar, Keene Corp. ....	151

Slip Ring Assemblies for Radar Antennas, H. C. Walker, S. R. Cole, and S. L. Brady, Litton Poly Scientific .....	157	Battle Damage Survivability for Consideration in the Design of Radars, M. L. Salive, W. R. Coggins, H. L. Wolk, and S. L. Wang, David Taylor Naval Ship ..	188
Radar Antenna Stabilization on Naval Ships by a Tilted Axis Configuration, W. Delaney and R. Wilson, Admiralty Surface Weapons Establishment .....	163	Custer Horn—A Novel Application of Fiberglass Structural Composites, W. B. Hebenstreit and T. Ryan, Structofab, Inc. .... PL-34864	194
Static Mass Balancing with a Torsion Spring and Four-Bar Linkage, W. Harmening, RCA .....	169	Use of Advanced Composites in Design of Lightweight AEGIS Tracking Antennas, J. N. Arnold and K. L. Johnson, Raytheon Company .....	
Impact Loads on Radar Director-Geared Systems, K. Redmond, Lockheed Electronics Co. ....	173	Composite Structures for Naval Pointing Systems, D. C. Brecht, General Electric Corp. PL-34965	201
High Accuracy Hydraulic Motors for Radar Antennas, C. Ekenberg and P. Strom, Philips Elektronikindustrier AB .....	177	Development of a Fiber-Reinforced Composite Design Concept for Large, Mechanically-Scanning, Planar Slot Arrays, J. W. Small, ITT Gilfillan PL-34966	204
The Design of a Stable Platform for a Radar Scanner on a Naval Vessel, M. H. Brown, The Plessey Company, Ltd. ....		Corrosion Protection for Shipboard-Mounted Antennas, A. W. Kline, Lockheed Electronics Co. ....	210
		The Manufacturing of Airborne Cassegrain Antennas, J. Shalit, ELTA Electronics Industries, Ltd. ....	214
<b>ENVIRONMENT AND MATERIALS SESSION</b>			
Advanced Composite Antenna Development, J. H. Heathman and R. S. Wilson, General Dynamics/Convair Div. ....	182	Biographies .....	245



# AUTHOR INDEX

Altoz, F., 110  
Antebi, J., 216,224

Berg, R. C., 58  
Bertz, L. E., 34  
Brady, S. L., 157  
Brecht, D. C., 201  
Bushar, T. A., 151

Chino, J., 72, 120  
Coggins, W. R., 188  
Cole, S. R., 157  
Corsi, U., 124  
Costagliola, M., 58

Delaney, W., 163  
DiFelice, R. F., 230  
Drenik, J., 230  
Dunbar, W. G., 66

Ekenberg, C., 177

Foxwell, V. M., 80  
Frankland, H. G., 13  
Frenkel, H., 132  
Fritz, C. M., 136  
Fuss, L., 145

Garner, W., 242

Harmening, W., 169

\*

Hawkins, E. C., 104  
Hayes, L. J., 34  
Heathman, J. H., 182  
Hebenstreit, W. B., 194  
Henderson, J. A., 62  
Hoecht, D., 145  
Humphrey, A. T., 1

Karpuk, J., 52  
Katov, Y., 7  
Katow, M.S., 27, 91  
Kawai, M., 7  
Kline, A. W., 210

Levine, C., 52  
Levy, R., 27, 94  
Luft, R. W., 216,224

Malagoli, G., 124  
Mann, R. L., 98  
Miller, L. C., 80  
Milligan, R. W., 85

Nader, M. A., 236

Redmond, K., 173  
Rohwer, R. B., 46  
Rossman, H., 72, 120

Parode, L. C., 21  
Porter, R. F., 128  
Punnett, M. B., 40

Ryan, T., 194

Salive, M. L., 188  
Sangiolo, J. B., 46  
Sawyer, N., 13  
Sekhon, K. S., 114  
Shalit, J., 214  
Simpson, H., 216,224  
Small, J. W., 204  
Staley, R. P., 145  
Strom, P., 177  
Sugie, M., 7

Tadmer, M., 132  
Tsandenlas, G. N., 236

Wakabayashi, M., 7  
Walker, H. C., 157  
Walsh, P. J., 62  
Wang, S. L., 188  
Wilson, R., 163  
Wilson, R. S., 182  
Wolk, H. L., 188  
Woods, Jr., A. A., 75

Zona, D., 85

# MECHANICAL DESIGN AND PERFORMANCE STUDIES FOR THE GWS.25 SURVEILLANCE AND TRACKER SYSTEM

A. T. HUMPHREY.

G.E.C. MARCONI ELECTRONICS LIMITED,  
GREAT BADDOW RESEARCH LABORATORIES, CHELMSFORD, ESSEX, U.K.

## ABSTRACT

The GWS.25 radar system currently in the final stages of environmental and sea going trials provides an effective addition to the weapon system used by the British Navy. The development programme necessary to produce the hardware demanded considerable technological resource and the paper attempts to highlight some of the features of the design and environmental test programme and the problems met during the various design stages. Constraints imposed by spatial, mass and mechanistic requirements necessitate the development of novel structural configurations. Thus the utilisation of finite element programs provide the only meaningful basis for mechanical performance studies. It is inevitable that hardware testing will highlight areas where improvements in the design need to be effected. Governmental and Company test facilities provide the medium for assessing the acceptability of the final design configuration.

## 1. INTRODUCTION

This paper discusses the mechanical design of the GWS.25 point defence radar shortly to be installed on a range of frigates and destroyers. Operational aspects are briefly reviewed in order to provide an over-view of the system. A description is included of the development programme for the surveillance and tracking radar that includes various features of the design and analysis together with details of environmental tests. Modifications were introduced at a number of stages throughout the programme based on the results of various theoretical or experimental studies. A redesign of one of the major fabrications was necessary to comply with ship fitting requirements. This resulted in problems in maintaining mount stiffness and tests on a full scale prototype were devised to confirm the results of the theoretical studies.

## 2. GWS.25 SYSTEM

GWS.25 is a fully automatic anti-missile naval defence system. The radar will deal with almost any attack profile tracking a large number

of targets simultaneously. All weather operation and the ability to function at high clutter levels permits the effective neutralisation of fast targets having small echoing areas. To achieve this performance adaptive pulse doppler radars are used each having its own data handling system. Surveillance equipment locates, resolves velocity and range and range ambiguities, track initiates, completes threat evaluation, takes engagement decision and performs attack allocation by assigning a tracker with its associated weapon complex. Direction to the Seawolf missile is given in the form of command to line of sight signals and tracking is achieved differentially. On receipt of allocation data from the surveillance the tracker performs a swift elevation search, acquires the target, computes missile/target intercept optimisation and dispatches Seawolf missiles singly or in salvo form. Impact or proximity fuses are utilised.

The loading and environmental specification for the equipment above decks is summarised as follows:-

Shock 30 g up 20 g down, 12 g horizontal.  
Vibration  $\pm 1$  mm at 2 Hz  $\pm 0.2$  mm at 33 Hz.  
Temperature, operational  $-10^{\circ}\text{C}$  to  $+50^{\circ}\text{C}$ .  
Ice, snow, rain as DEF.133.  
Wind, survival 120 knots.  
Wind, operational 70 knots.

## 3. SURVEILLANCE SYSTEM

### 3.1 Mechanical Design

The overall mechanical configuration of the surveillance system is shown in Fig. 3.1. The antenna is bolted to the centre spindle which is supported via a pair of preloaded taper roller bearings. A spur gear attached to the spindle and driven by a pinion provides a reduction by 3.37 : 1. A three phase, 60 cycle, 2.5 HP motor running at a nominal speed of 1800

RPM drives the pinion via a lightweight spur gear box with a reduction ratio of 16.63 : 1. A section of the turning gear is shown in Fig. 3.2. Forward prediction requirements necessitate that the speed fluctuation is minimal.

The gear case is supported by the fabricated steel yoke via an intermediate gymbal frame. Motion is imparted to the gymbal by recirculating ball screw jacks. A servo controlled 50 volt DC motor operating the jacks drives the ball screw nut via a single spur gear reduction of 3 : 1. The lead screw pitch is 0.5 inches. Buffer stops limit the over travel. A section of the actuator is shown in Fig. 3.3. The power requirements necessitate the supply of an RMS torque of 3 lbs.ft. and peak operating torque of 4 lbs.ft., together with a peak starting torque of 8 lbs.ft. The motor must ensure the unit is capable of following SHM in the pitch and roll directions with periodic times of 8 and 11 seconds respectively and modified SHM with a periodic time of 11 seconds.

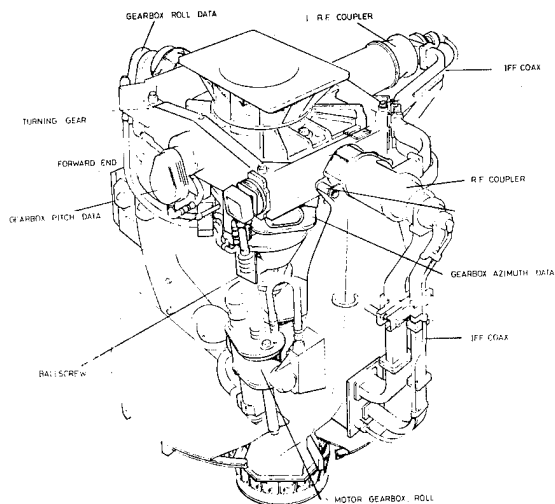


Fig. 3.1 - Mechanical Configuration Surveillance

The gymbal is supported about both axes via preloaded pairs of taper roller bearings. Thus the gearcase, gymbal and yoke assemblage interacts structurally as rotational reactions may be transmitted through the bearing pair.

The three phases of prototype hardware development are referred to as X, Y and Z. The Y model incorporated considerable modification both as a result of an updated design requirement, and also to eliminate problems that arose during system and environmental tests. Modifications incorporated into the Z model were essentially of a detailed nature and arose from the need to correct structural faults highlighted during laboratory shock and vibration trials.

The X model is shown in Fig. 3.4 undergoing system trials. It can be seen that the interface between the support yoke and mast is relative-

ly large. A ship fitting requirement to raise the aerial created a severe design problem as the area available for the interface was considerably reduced. Further the design modification

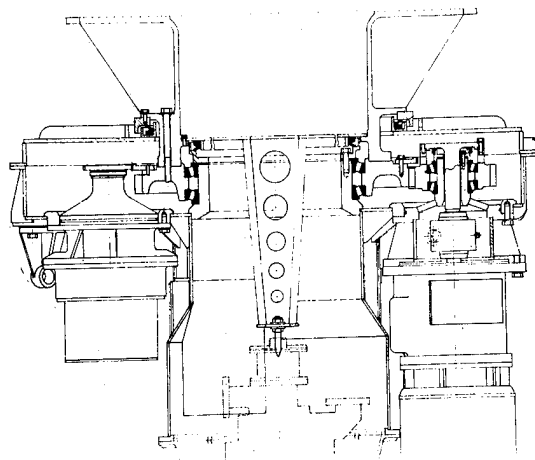


Fig. 3.2 - Turning Gear - Surveillance.

resulted in an increased weight of approximately 500 lbs and thus there was an incentive to review the weight and stiffness of all elements in the structure. Particular emphasis was placed on ensuring that the weight distribution was symmetrically disposed about training and elevation axes to eliminate out of balance moments induced by the ship motion.

The Y model incorporated major modifications as follows:-

1. Modified yoke geometry.
2. The utilisation of preloaded taper roller bearing pairs to mount the gymbal frame.
3. Modified jack support structures.
4. The utilisation of a pair of preloaded taper roller bearings in the turning gear to replace the original cross roll bearing.

### 3.2 Stress and Vibration Analysis

The yoke, gymbal frame and gear case are interconnected hyperstatically by virtue of the arrangement of double taper roller bearing cells on the roll and pitch axes. Bandwidth limitations ( $UBW = 210$ ) precluded the analysis of a model in which all three structural subassemblies could be assessed simultaneously. A model was devised however, in which the yoke, gymbal and ballscrew were incorporated and in which the flexibility of the central gear case was simulated by springs based on an assessment of the gear case characteristics using a separate three dimensional model. The gymbal frame and ballscrews incorporated were modelled as an assembly of line elements and the yoke as an assembly of shell elements. The complete model consisted of 350 grid points and 600 elements. A view of the

scheme is shown in Fig. 3.5 together with a detailed view of an idealisation devised for checking the distribution of stress in the base flange.

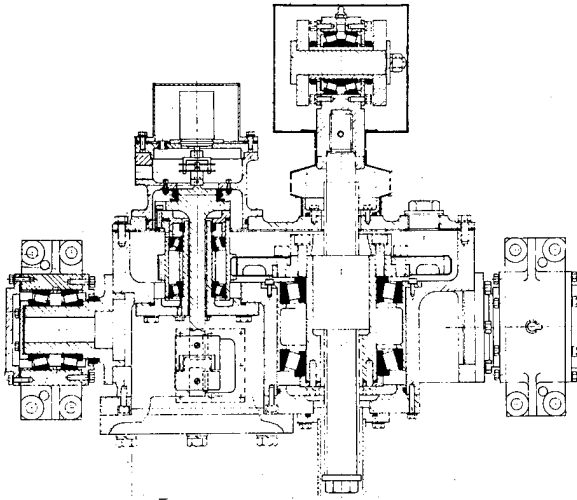


Fig. 3.3 - Roll and Pitch Actuator

Loading cases were devised to simulate three shock and two aerodynamic conditions. Structural and non structural mass components were allocated to the relevant grid points and assembled as a series of static loading cases. Whilst this approach is simplistic, software to treat the loading systems dynamically had not been developed in house at that time and propriety programs were not demonstrably cost effective. Peak stresses were calculated to occur at the base of the fabrication in the radial gusset material and amounted to 9.5 tons/sq.inch for horizontal shock loads. Results from the more detailed model of the flange region resulted in average element centroidal stresses in the gussets of 11 tons/sq. inch. This may be compared with peak measured stresses of 13.0 tons/sq.inch.

Comparatively simplified line element models were devised for the initial vibrational analysis studies and thus some approximations were inherent in modelling fabricated segments. Vibrational and response studies using slightly more refined models permitted a higher level of confidence in the solutions. Dynamic analysis can be extremely costly and budgetary constraints preclude the incorporation of high levels of refinement comparable to that incorporated for stress analysis studies. One of the models used for assessment of the dynamic characteristics is shown in Fig. 3.6. The assembly shown exhibits a frequency of 13 Hz. When constrained at the base of the yoke the frequency for a similar mode was calculated as 17 Hz. It is inevitable therefore that results obtained from vibrational tests require some interpretation.

### 3.3 Structural, Resonance and Shock Tests

Tests were completed on the Y model yoke fabrication to confirm the calculated displace-

ments and stress levels throughout the structure. The pedestal fabrication was mounted on to a base plate forming part of an integral test frame. A test load of 22 tons was applied to the top of the yoke by a hydraulic jack. A set of 25 electrical resistance strain gauge rosettes were attached to the welds and vertical and horizontal faces of the flange. Three of the flange bolts were also fitted with strain gauges in order to monitor the tightening tension and tension induced during the load tests.

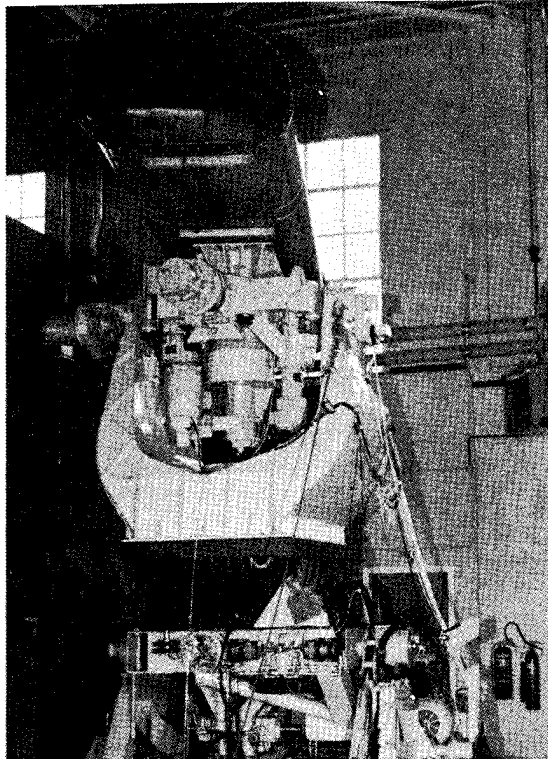


Fig. 3.4 - X Model Servo Tests

The results plotted for deflection at the point of application of the load was reasonably linear although a departure from linearity started to occur at 20 tons. The measured displacements of 0.25 inches were comparable to the theoretical predictions. Peak stresses were found to occur in the stiffening webs separating the attachment bolts and maximum values calculated to be 13.0 tons/sq.inch. These stress levels were in fact predicted with some precision by the finite element models. Some yielding began to occur at 20 tons, however, the full load of 22 tons was held for a number of minutes prior to load removal. A tightening tension of 13 tons was induced in the bolts. During the test the tension for the bolts in the load plane increased to 15 tons whilst the load in that at 90° decreased by 1.0 ton. Thus it was apparent that some bolt extension had occurred. The original pre-tension was re-established within a few percent when the load was removed.

A resonant search and functional test was

performed in the fore and aft, transverse and vertical directions over the frequency range 2 to 30 Hz. Two orthogonal aerial locations were employed for each test. Q factors greater than 3 on the structure and greater than 10 on the antenna envelope were monitored in the 8 - 10 Hz frequency band. Evidence of a 9 Hz resonance is present in all traces and points to a characteristic that is a function of the complete system

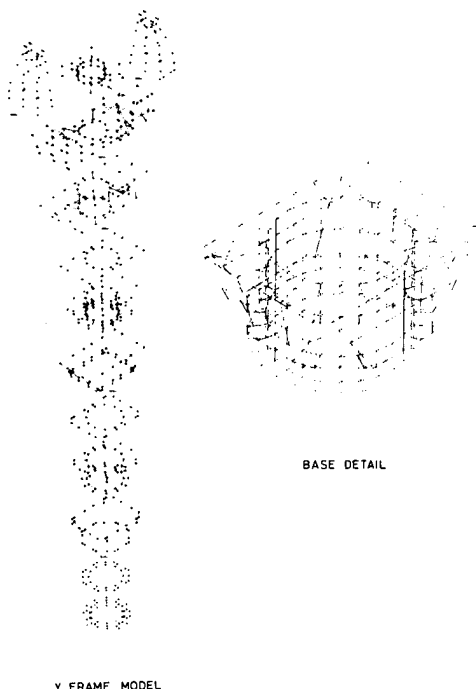


Fig. 3.5 - Finite Element Model - Yoke

including the table. The antenna envelope exhibits a resonant frequency in the 28 to 30 Hz band. Theoretical predictions for the equipment mounted on the table indicates the lowest frequency occurs at 11 Hz. The table highlighted structural weaknesses in some aluminium cast support brackets within the antenna envelope that necessitated a redesign.

The accelerations from a vertical shock test are shown in Fig. 3.7, no structural damage was sustained during the series of tests.

### 3.4 Aerodynamic Tests

Static yawing moments measured on both scale model and full size prototype are compared in Fig. 3.8. Dynamic yawing moments obtained from measurements on a scale model are also shown. The curves are based on a wind speed of 70 knots, the dynamic yawing moment was measured at 30 RPM.

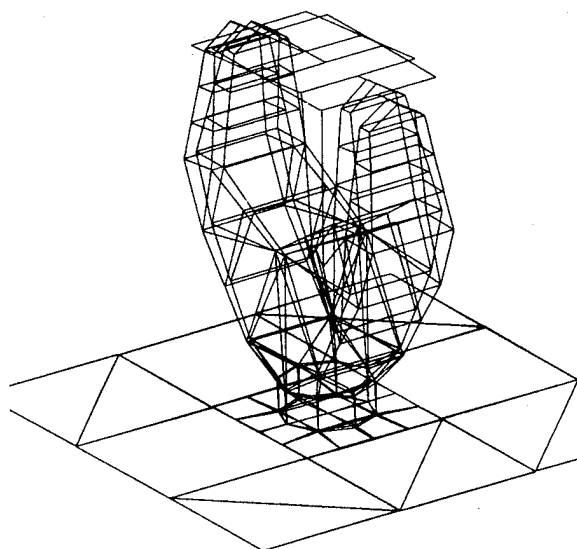


Fig. 3.6 - Finite Element Model - Yoke Dynamics

## 4. TRACKER SYSTEM

### 4.1 Mechanical Design

The overall mechanical configuration is shown in Fig. 4.1. The antennas are attached to a tubular steel shaft which in turn is located via preloaded taper roller bearings in a fabricated steel pedestal. A spur gear is attached to the shaft and meshes with the output pinion in the elevation gearbox. The fabrication layout and gear box design is shown in Fig. 4.2.

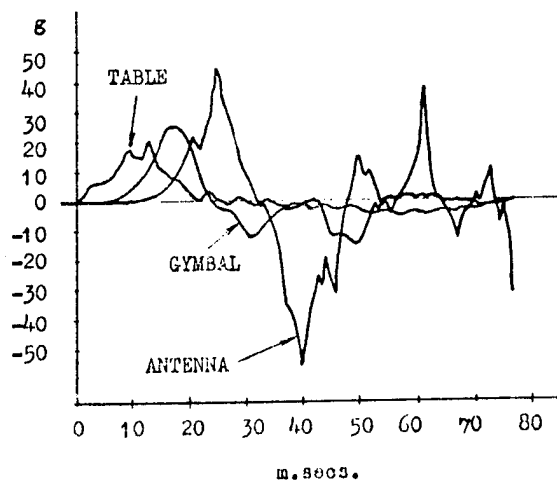


Fig. 3.7 - Shock Tests - Acceleration Levels

The overall gear ratio is 70.8 : 1. A 4.7 HP motor running at 1800 RPM and driving through a hydraulic motor provides the necessary rates of elevation, velocity and acceleration. The pedestal is bolted to a drive gear which in turn is supported via a pair of preloaded taper roller bearings. Details of the gear case fabrication and gearbox design are shown in

Fig. 4.3. The overall training axis gear ratio is 88.5 : 1.

The major enhancements introduced into the Y model consisted of:-

1. Replacement of training axis cross roll bearing by two pre-loaded taper roller bearings.
2. Stiffening of pyramid and cabin grid to increase rotational stiffness.
3. Repackaging of electronics behind main antenna to improve thermal performance.

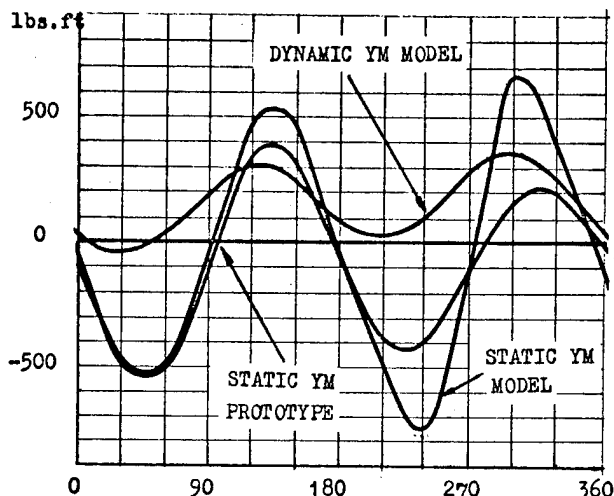


Fig. 3.8 - Static and Dynamic Yawing Moment

The direction of cable spiral and tension were found to be of particular importance in minimising cable fatigue failures.

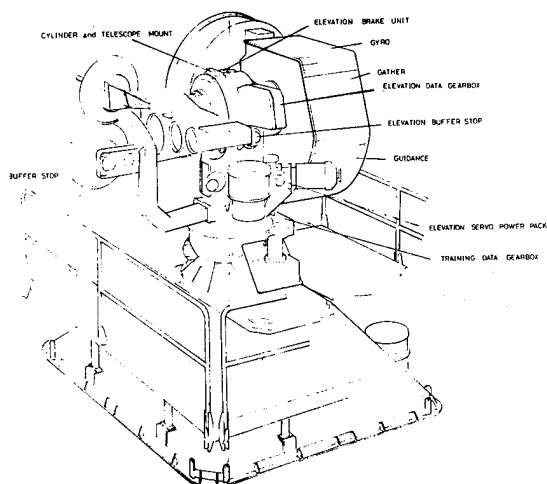


Fig. 4.1 - Tracker System

## 4.2 Stress Analysis

A structural model of the cabin, transition cone and training axis gear box was devised as an assembly of 350 grid points interconnected by line and shell elements. An exploded view of the idealisation scheme is shown in Fig. 4.4. Whilst there is inevitably some interaction between the pedestal and the training axis gear-box fabrication the effect was not introduced. Reference to the computer solution indicated that the deformation of the bearing ring was small and thus the pedestal could be reasonably considered in isolation.

It was apparent following the analysis that the stress levels in the cabin roof structure and localised segments of the cone were excessive under the 12g horizontal and 30 g vertical shock loads and stresses in excess of yield were calculated. Deformation of the cabin roof was influential in inducing localised stresses into the transition cone and necessitated the introduction of additional stiffening. Recommendations were made regarding minimum sizes for the cabin roof grid in order to limit deformations and stresses to acceptable levels.

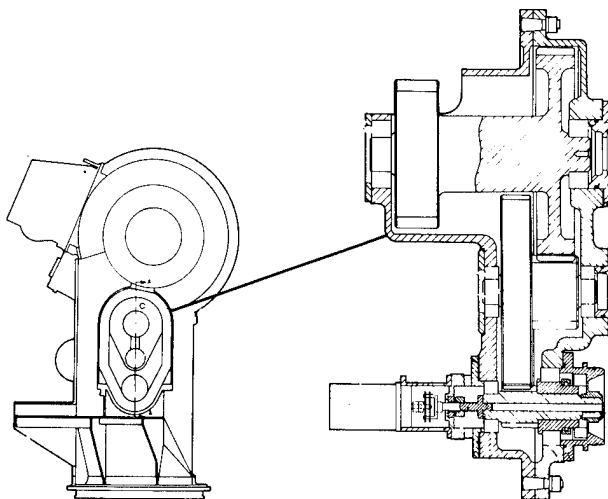


Fig. 4.2 - Pedestal and Elevation Gearbox

## 5. SHOCK AND VIBRATION TEST EQUIPMENT

The shock machine has a loading capacity of 8 tons including any fixtures and is capable of generating a maximum deceleration of 15 g horizontally or 40 g vertically. The deceleration shock pulse is basically of sinusoidal form with no rebound. The maximum impact velocities which can be produced at 12 ft/sec. vertically and 7 ft./sec. horizontally, with a shock pulse duration of between 15 and 30 ms. according to the velocity and peak g condition selected.

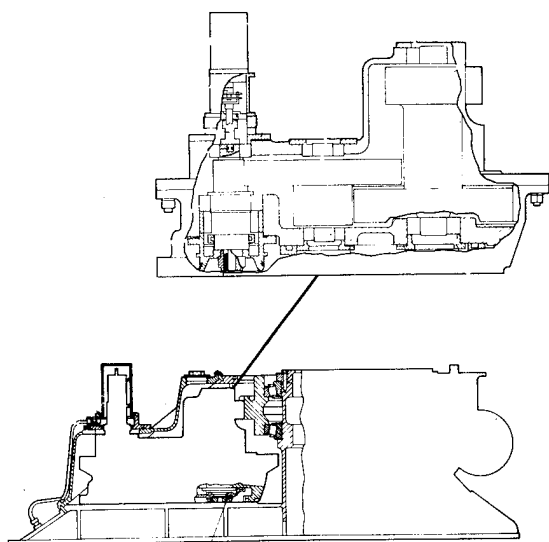


Fig. 4.3 - Training Axis Gearcase and Gearbox.

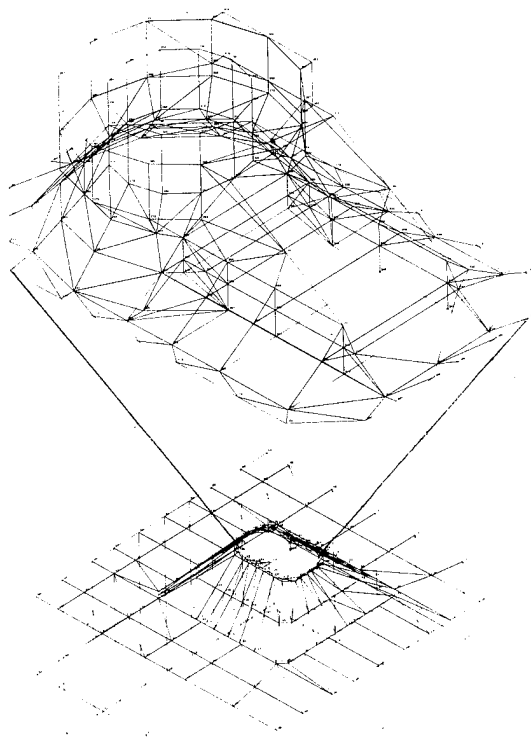


Fig. 4.4 - Finite Element Model Gearcase and Cone.

The vibration table is capable of exciting a load of 6 tons in both the horizontal and vertical planes. The range of operation is from  $\pm 9$ mm at 2 Hz to  $\pm 0.25$  mm at 35 Hz. The table is activated by servo controlled hydraulic rams. The four channel servo control can provide either automatic frequency scanning or manual control as required.

## 6. APPLICATIONS PROGRAMS

A range of finite element programs have been devised within the Marconi Research Laboratory under the general title MARSTRAN. These programs have been devised specifically for the analysis of space frames, fabrications and axis-symmetric structural forms. A subset, FIESTA, has been used extensively for stress analysis studies, and DYNAM for the earlier vibrational analysis studies using line element models. FIESTA has a range of elements which include line membrane and shell elements. The program is divided into basic subsets for ease of usage and economy. Prepared proformas and compact documentation enables intermittent users to utilise the program effectively. A real time graphics facility using the Marconi Myriad computer provides a data validation facility.

NASTRAN currently provides an in house capability that is used for the larger stress and vibrational studies.

**ACKNOWLEDGEMENTS** - The author acknowledges with thanks the material supplied by Mr. G. Cross, Assistant Engineering Manager, Mr. M. Healey, Chief of Mechanical Engineering, Mr. J. Brazen-dale, Chief of Environmental Test, Mr. D. Rainbird, Chief of Control Section and Mr. M. D. Churchlow, Aerodynamicist. The author also wishes to express his gratitude to Mrs. Sheila Pile for typing the drafts and to Mr. V. Tate, Chief of the Photographic Section.

The author wishes to thank the Technical Directorate for permission to publish this paper.

# DEPLOYMENT FLEXIBLE MECHANICAL DESIGN FOR A MOBILE-3D RADAR ANTENNA

MITSURU SUGIE    MASARU KAWAI    MATSUKICHI WAKABAYASHI    YASUO KATOU

Nippon Electric Co., Ltd.  
Fuchu, Tokyo 183, Japan

## ABSTRACT

In designing a novel phase-frequency scanned phased array antenna, a planar array, constructed in two parts for opening and folding was developed. This was a means of providing this antenna with flexible mobility by helicopter, truck etc. Also deployability within an hour without using loading equipment at any site was assured. Moreover, a shock-absorber was developed to reduce the weight of the planar array while making it shock-resistant. Details of the mechanical design during these developments are described, as well as details in finalizing the design on the basis of data obtained from strength and deployment tests performed on a mock-up planar array.

## INTRODUCTION

This mobile-3D radar system has been developed and manufactured in Japan as the first operational phased array radar system.<sup>1)</sup> Two systems are now used in the field.

The system, as shown in Figure 1, consists of antenna, transmitter-receiver, signal processor and command control operation center. Each sub-system is mechanically designed to have a flexible mobility (by truck, helicopter, medium-size cargo plane) and to be deployed and operated within an hour upon arrival at the point of deployment.

The authors attempt to focus their attention upon the novel phase-frequency scanned phased array antenna sub-system.<sup>2)</sup> This array is the most important portion of the entire system design, incorporating a wide variety of ingenious design concepts.

## MAJOR ANTENNA SUB-SYSTEM FEATURES

The most salient feature of this antenna lies in the fact that it is a phase-frequency scanning 3-D radar antenna operated in the S-Band.

The RF circuitry configuration is shown in Figure 2.

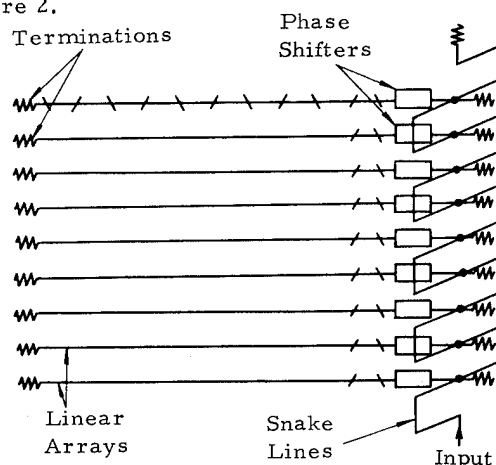


Fig. 2 THE RF CIRCUITRY

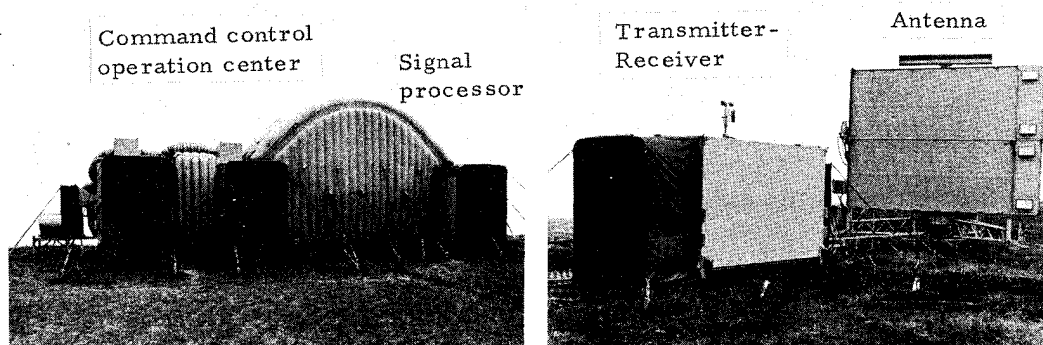


Fig. 1 MOBILE-3D RADAR SYSTEM



Frequency scanning is performed by transmission of a series of sequential sub-pulses, conveyed along the snake line, which results in a series of beams sequential in elevation, separated approximately 1 degree from each other.

Furthermore, these sequential beams are subjected to phase scan in a group to acquire steering for up to 24 degrees or more in elevation. This is done by means of the programmed control of the 4-bit non-reciprocal ferrite phase shifters, developed specifically for this project.<sup>3)</sup>

It is worthy of special note that the methodology described above enables making beneficial use of frequency scanning technique and phase scanning features, minimizing required frequency bandwidth and scanning time.

The major mechanical features of this antenna, necessary to realize required electronic configuration and to satisfy operational requirements for mobility and deployability, are summarized as follows:

- o The planar array is divided into two parts for folding, facilitating mobility.
- o The divided planar array is easily opened or closed by a manual hydraulic pump for simple deployment and transportation.
- o Light weight is gained by constructing the planar array thin aluminum alloy plates and supporting pipes.
- o The planar array is pin-joint coupled with the pedestal for folding down without separating them, resulting in a reduction in the time needed for deployment.
- o Small dimension light weight pedestal is made possible by using a small cam-follower bearing rotation system and a 400 Hz planetary geared motor to match airplane power supplies.
- o Three leveling legs are extended or retracted by a manual hydraulic unit. Three supporting legs are easily removable from the pedestal for manual loading and unloading onto or from a truck without using a crane, and for deployment on uneven ground.

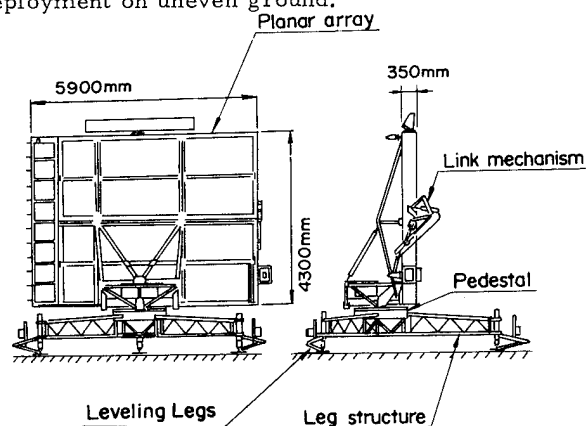


Fig. 3 ANTENNA SUB-SYSTEM

The antenna sub-system is shown in Figure 3.

#### DESIGN CRITERIA

The antenna sub-system had to be mechanically designed to meet the diverse requirements shown in Table-1 for assuring satisfactory performance.

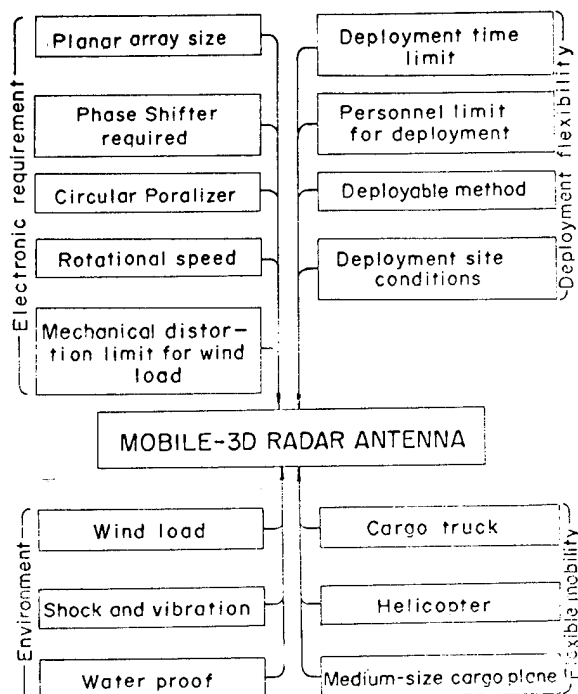


Table-1 ANTENNA MECHANICAL REQUIREMENTS

Design criteria details, satisfying the various requirements shown in Table-1, are as follows:

#### Electronic Performance:

- o Minimum planar array size is 4250 mm x 5200 mm.
- o The plane tolerance for the planar array, composed of 64 linear arrays with 77 baffle plates assembled on a plane, is less than 1.5 mm.
- o Easy accessibility for maintenance is necessary to the high density mounted planar array because of 64 phase shifters coupled with flanges on the input side of the linear arrays, as well as with the snake line waveguide.
- o For maintaining reliability in adverse ambient conditions (particularly rain, wind, sand, dust), the planar array, phase-shifters and electronic components have to be enclosed with a flat-plate radome and a frame which also adds strength reinforcement.

A complete cooling function should be provided for phase shifter heat dissipation.

- o The pedestal requires in addition to the drive mechanism, angle data generator, slip ring

rotary joint and cooling function as well as a heater for removing humidity. Its construction should be water-proof and dust-proof. It should be designed for good accessibility.

#### Flexible Mobility:

- o To be transported by cargo truck, the dimensions of the antenna sub-system under transport should be 2200mm high x 2150mm wide x 5900mm long. The weight should be less than 2500 kg or less. It should have sufficient strength to resist vibration and shock during transportation (Maximum 2.6 Gravities 2 to 100 cps).

- o For helicopter transport, the total weight of the antenna sub-system, including the support tray should be less than 2200 kg. It should have sufficient strength to resist shock (about 20 gravities) on landing, under the worst conditions.

- o Sufficient strength to resist a shock of about 5 gravities from every direction during transport via a medium-size cargo plane. (Loading dimensions are about the same as those for trucking).

#### Deployment Flexibility:

- o The planar array should be constructed for easy folding and unfolding in a short period of time.

- o The leg structure and leveling leg should weight 70 kg or less, to allow it to be coupled to the pedestal manually.

#### DETAILED PLANAR ARRAY DESIGN

To meet electronic performance requirements, the planar array should be a lattice-like combination of 64 linear arrays (a 60 mm x 30 mm x 5200 mm waveguide) with 77 baffle plates (50 mm x 30 mm x 4200 mm rectangular pipe) involving firm connections at 4928 contact points. (Figure 4). These sizes and numbers are determined mainly by the factors of controlling mutual coupling and impedance matching of the slot radiators which result the superior radiation characteristics.

Consequently, the lattice-shaped planar array itself serves as a mechanical reinforcement, giving more strength.

This instigates a great difference from the curved reflector (usually formed with perforated plates) of the ARSR antenna, for example, which requires a backup structure for maintaining the curved surface, without contributing by itself to the mechanical strength.

Nonetheless, the following problems had to be resolved. For reducing weight and maintaining tightly restricted dimensional tolerances, it was decided to manufacture the planar array by dip brazing waveguides of aluminum 1 mm in

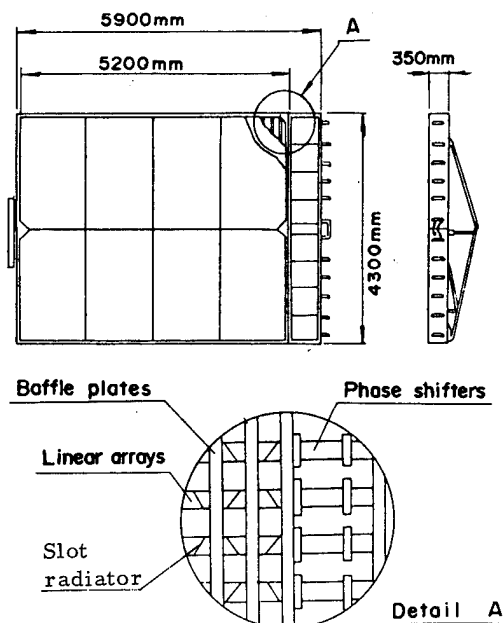


Fig. 4 PLANAR ARRAY

plate thickness. However, the yield strength of the dip brazed aluminum material declined to the order of 1/6 as shown in Figure 5.

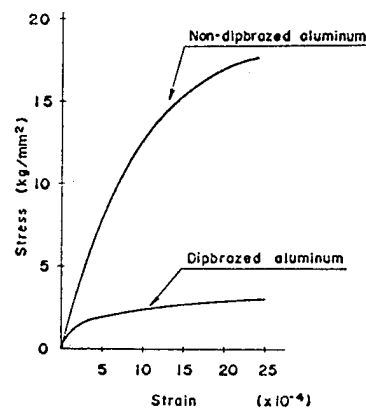
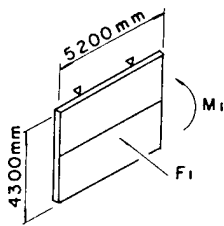


Fig. 5 STRESS-STRAIN DIAGRAM OF ALUMINUM WAVE GUIDE FOR PLANAR ARRAY

This means that the planar array itself requires a considerable reinforcement of its strength when utilizing a planar array of waveguides, which is easily deformable, as a structure for reinforcing the strength.

Table-2 compares the strength of the planar array itself with external forces.

For resolving the above problem, it was decided to enclose the planar array with a frame of thin aluminum alloy plates, and to provide the back of the planar array with a backup structure reduced to the minimum required, by taking into account the dimensional restrictions (2.15



	Load	External forces	Strength of the planar array
F <sub>1</sub>	Wind	1540kg	510kg
M <sub>1</sub>	Bending at folding	664kg-m	390kg-m

Table-2 STRENGTH OF THE PLANAR ARRAY

meters x 5.9 meters during transport) and the weight restriction (target: less than 1200 kg). (Figure 4).

The concept regarding the mechanical strength is as follows:

The wind load is received by the baffle plates of the planar array, and conveyed via the frame to the rear support.

Opening and folding bending load ( $M_1$ ) is borne by the planar array itself.

Figures 6 and 7 illustrate the construction concept of the planar array and its flexibility under a load.

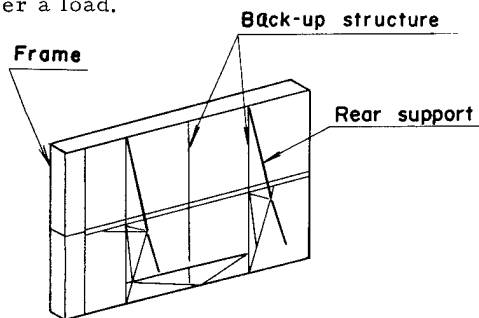


Fig. 6 PLANAR ARRAY'S CONSTRUCTION

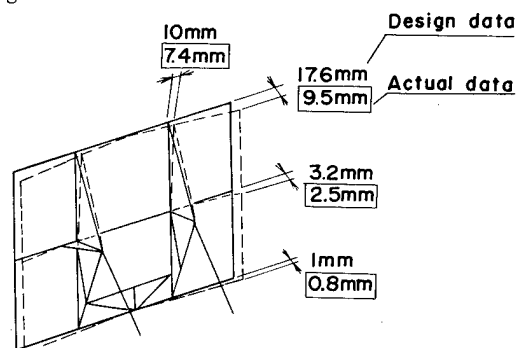


Fig. 7 PLANAR ARRAY FLEXIBILITY UNDER THE WIND LOAD

The next problem to be resolved is the design requirement to give a sufficient resistance to the antenna to withstand a 20 gravity shock if it is dropped at the time of transport by a helicopter.

Designing the antenna just to resist the 20 gravity shock would increase the weight of the

planar array to about 2000 kg (calculated value). This would make the overall weight of the antenna, including the pedestal, etc. 3000 kg, making it infeasible to carry it by a helicopter. To resolve this problem, it was decided to use a shock-absorber to damp the shock to less than 5 gravities only during of helicopter transportation.

Consequently, it was decided to design the planar array to have sufficient strength to resist the 5 gravity shock, and, at the same time, to develop a light weight shock absorber system with small dimensions (target: four component absorbers weighing less than 80 kg).

Figure 8 illustrates transporting the antenna sub-system by helicopter.

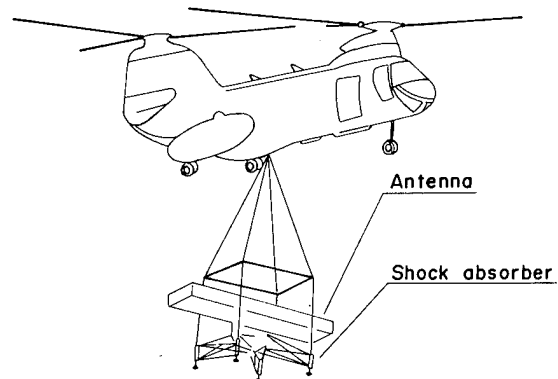
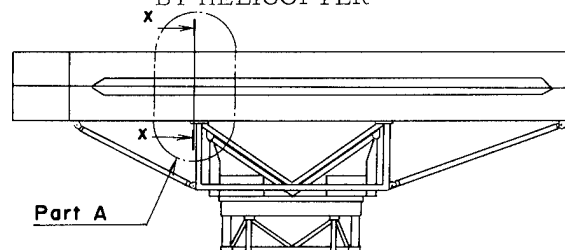


Fig. 8 TRANSPORTING THE ANTENNA BY HELICOPTER



Formula of the thin plate.

$$\sigma_k = \frac{kE\pi^2}{12(1-\nu^2)} \left(\frac{h}{b}\right)^2$$

$\sigma_k$  : Buckling stress

E : Young's modulus

$\nu$  : Poisson's ratio

k : Constant

h : Thickness

View x-x

Fig. 9 CONSIDERATION OF THE TEST RESULT BUCKLING LOADED

To perfect the design reliability of the planar array and shock absorber, pilot manufacture, testing, and feedback of the results to the design were repeatedly performed.

The drop shock test, performed on the first pilot-manufactured planar array and shock absorber, resulted in a damaged planar array, but enabled us to obtain the following design data:

The frame is susceptible to a buckling load. (Figure 9 part A). The plate thickness of the frame of part A should be increased by 33% and adding ribs.

The shock absorber (initially test manufactured air ride type) had a poor damping characteristic and could only damp the 20 gravity shock to 7 gravities. Therefore, the shock absorber type was changed an oil strut type was developed.

The dimensions and characteristics of the final successfully developed light-weight, small-sized oil strut shock absorber are shown in Figure 10 and Figure 11.

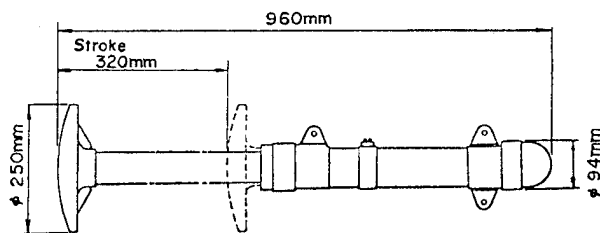


Fig. 10 OIL STRUT SHOCK ABSORBER

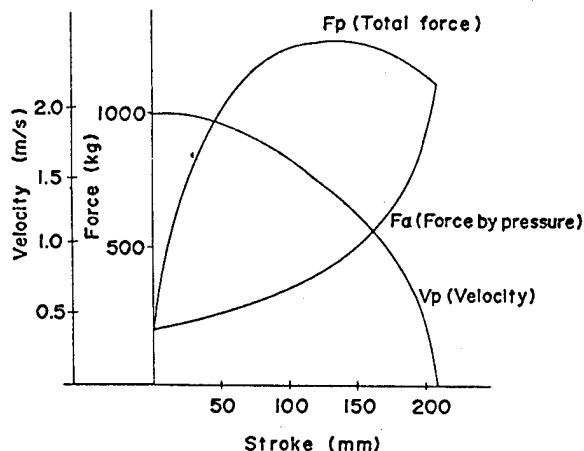


Fig. 11 OIL STRUT SHOCK ABSORBER CHARACTERISTICS

The second pilot-manufactured planar array and the oil strut shock absorber successfully passed the shock test.

The deflection data obtained by the wind load test of the planar array are shown in Figure 7.

The oil strut shock absorber showed a completely acceptable shock damping performance of

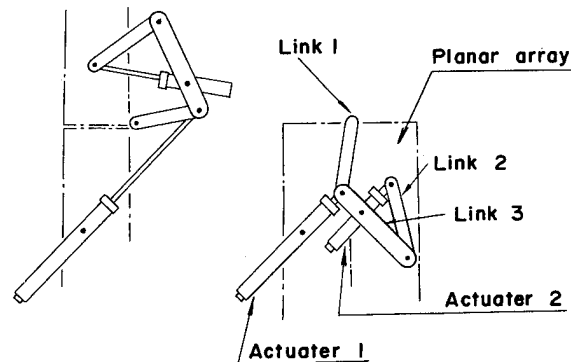
20 to 2.8 gravities.

#### DEPLOYABILITY EVALUATION ON THE MOCK-UP

The part of the deployment mechanism which required the most ingenious work was the means of folding and unfolding the planar array.

In the design approach stage, the use of gear mechanism and manual winch was tested on smaller models. However, this method proved unfeasible because of the restricted deployment time, limited manual force, and restrictions in reliability, safety and weight.

The finally developed method involved a mechanism for folding and unfolding, composed of two actuators and three links. (Figure 12)



Unfolding

Folding

Fig. 12 LINK MECHANISM

Deployability was tested on a full size mock-up, shown in Figure 13. The procedure, from unloading from a truck to final set-up, is shown in Figure 14.

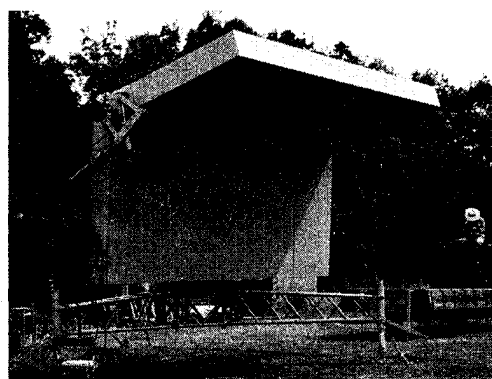


Fig. 13 ANTENNA FULL SIZE MOCK-UP

The results of the test on the mock-up confirmed that the antenna sub-system can be deployed in about 30 minutes.

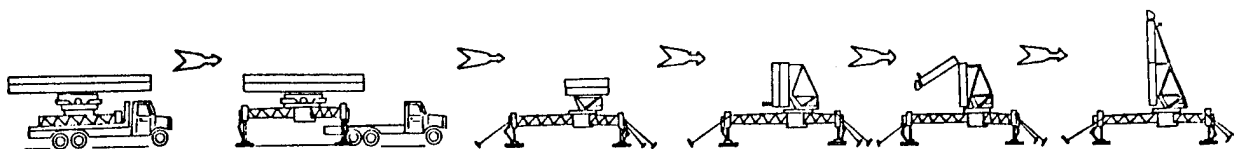


Fig. 14 PROCEDURE OF THE ANTENNA SET-UP

### DEMONSTRATED FLEXIBLE DEPLOYABILITY AND MOBILITY

The completed antenna sub-system was subjected to wind load tests, running vibration tests, drop shock tests, truckability tests, helicopter suspended transportability tests, medium-size plane air transportability tests, deployability tests, truck loading and unloading tests as well as electronic performance tests.

During transportability tests involving suspension by a helicopter (Figure 15), the antenna was dropped from a height of about 50 cm above the ground on a concrete-covered surface, but the planar array remained intact.



Fig. 15 DEMONSTRATED MOBILITY BY HELICOPTER

For air transport by a medium-sized cargo plane, a complete test was performed covering all steps from storing in the cargo room, trans-

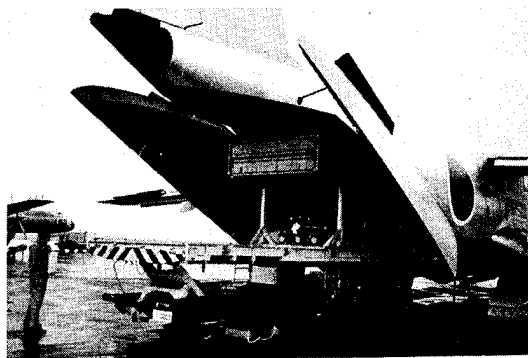


Fig. 16 DEMONSTRATED MOBILITY BY CARGO PLANE

port to the deployment site, and deployment through operation as a radar system.

Figure 16 illustrates loading the system into the airplane.

### CONCLUSION

The successful completion of the mechanical design and manufacture of this antenna has enabled realizing a fully operational mobile-3D radar system.

Moreover, the mechanical design, with various ingenious concepts, has established various invaluable design data for developing similar systems requiring more rigorous design conditions.

### ACKNOWLEDGEMENT

The authors wish to express their sincere appreciation for generous supports and encouragements offered during the course of this development by the personnel of Japan Air Self-Defense Force.

### REFERENCES

- 1) R. Toyoda, I. Matsukasa "Consise Three Dimensional Surveillance Radar" IEEE Inf. Radar Conf. P48 1975.
- 2) M. Sugie, K. Fukumoto, Y. Hashimoto "A Novel Phase-Frequency Scanned Planner Phased Array Antenna" International Symposium on Antenna and Propagation 2-IC, 1 (Sept. 1971)
- 3) N. Ogasawara, M. Sugie, J. Aiba "High Power Latching Phase Shifter for S, C-Band" International Conference on Ferrites 8B4.3 (July 1970)

## THE VIKING RADAR SYSTEMS -- DESIGN FOR SPACE PROGRAMS

H. G. FRANKLAND AND N. J. SAWYER

Teledyne Ryan Electronics  
2701 Harbor Drive  
San Diego, California 92112

### ABSTRACT

This paper discusses the general principles involved in preparing the mechanical designs of sophisticated electronic systems for space use and how by careful consideration of all design, test and mission parameters, successful missions can be accomplished.

- By creating useful design standards
- By care in selecting the correct materials
- By standardization of hardware
- By specific design for heat sterilization
- By simplicity of design<sup>1</sup>

### INTRODUCTION

Space programs set limitations on many aspects of the equipment design.

- To enable the equipment to perform correctly
- To keep weight to a minimum
- To reduce the proportions of organic materials
- To sterilize against contamination "bugs"

Applications of these principles to the Viking Radar Systems are explained together with specific examples of the detail design of the Landing Radar system, and Radar Altimeter Electronics (RAE). The Lander staging and dynamics is depicted in Figure 1.

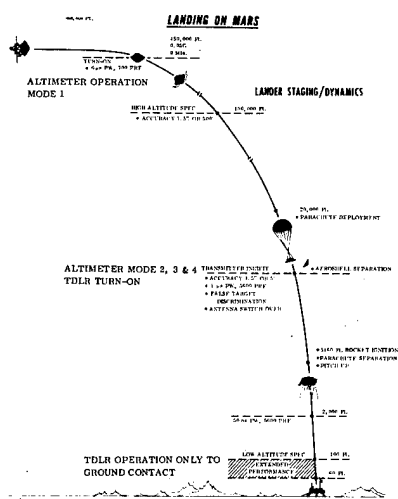


Figure 1. Lander staging and dynamics.

### TERMINAL DESCENT LANDING RADAR (TDLR)

The TDLR is a 4-beam CW Doppler Velocity Sensor using four slotted phased array antennas. The Solid State Transmitters have Impatt diodes operating at frequencies around 13.3 GHz. One of the four beams is redundant.

In the Viking landing sequence, the aeroshell is jettisoned at 22,000 feet to start parachute descent and the TDLR is turned on. At 17,000 feet the radar acquires and is locked on to the surface of Mars, at a spacecraft velocity of 450 fps. Parachute descent continues to about 5000 feet, the spacecraft engines are turned on and the parachute released. The spacecraft is aligned to the velocity vector using the radar data. At 200 feet and 100 fps the radar is commanded to low mode. Touchdown occurred when the Lander velocity was 5 fps. The layout of the TDLR system built by Teledyne Ryan Aeronautical Co., San Diego, for the Viking Mars Soft Landing Vehicle is shown in Figure 2.

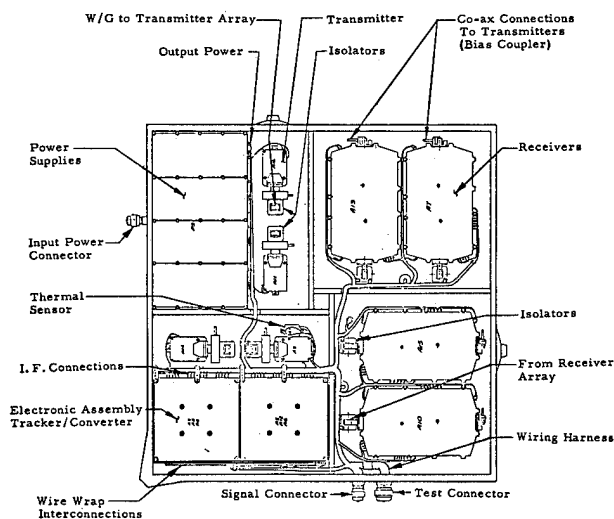


Figure 2. Viking TDLR top assembly arrangement.

### MATERIAL SELECTION

**Metals** - Zinc, tin and cadmium are poor performers in space and must be avoided. The preferred metals are aluminum alloys - low copper content, magnesium

alloy, corrosion resistant steel, titanium, beryllium and copper alloys. Great care was taken in design to avoid juxtaposition of metals having a high potential difference so that electrolytic corrosion could be minimized. Magnesium alloys chosen for weight savings were plated with other metals so as to prevent direct contact with the more noble metals.

**Organics** - In all space programs where landing on another heavenly body is required, it is essential to keep non metals to a minimum. When scientific experiments are involved which analyze matter, it is essential to contain the organic material within the Landing Vehicle equipment so that it is not spilled onto the surface and scooped up by the analyzer. On the external surfaces of the Radar systems, especially the externally mounted TDLR, only thin bond lines of epoxy were allowed.

Selection of organic materials is based not only on their ability to do the job under normal earth conditions, but also in hard vacuum. Many organics simply outgass away when subjected to the temperatures and pressures of a space environment. Thermo-gravimetric analysis (TGA) screened out all materials with a weight loss of more than 2% - most materials selected had a weight loss of less than 1%. Screening consists of TGA and  $5 \times 10^{-6}$  Torr and up to 200°C for a weight loss of  $\leq 1\%$ . The radome which consisted of a thin membrane of teflon sheet etched and bonded to the face of the arrays was not considered to be organic.

#### PROCESSES

Often materials may be allowed for use in space but their application may render them unsatisfactory. For this reason, strict check verification and control of processes is needed. Documents must define the materials, tools, equipment and consumable (cleaning) materials which are used in the production of the end item.

In-process checks required the operator to have a quality control representative at the various stages of structural bonding and electrical assembly work.

#### STERILIZATION

Landing material on another planet could involve planting earth microbes on its surface if the spacecraft is not biologically sterilized. Early requirements of the space landing programs involved sterilization with ethelene oxide and baking at high temperatures. Tests showed that baking only at temperatures of 265°F for long periods of time was adequate to eliminate bacteria.

Equipment must not only be designed to survive hostile atmospheres but also for heat compatibility. Loads not normal to structural elements due to differential expansion of the different metals have to be taken into consideration in structural design.

Check points after heat sterilization cycle tests were loosening of hardware - attachment screws; flaking

or cracking of epoxy bond fillets; change of electronic performance characteristics due to stress.

#### TDLR BASIC STRUCTURE

The form factor and arrangement of the elements in the mechanical design of the TDLR was dictated to a large extent by the type of antennas needed and their location on the Viking spacecraft. Phased array transmitting and receiving antennas were used, each element having slots for a two-beam arrangement in the four-beam system. All arrays were built from aluminum alloy sheets suitably milled for the radiating surfaces, back planes and aluminum alloy dividers and feeders, all dip brazed together. The process was developed by Teledyne Ryan. The radar had to be mounted on the underside of the spacecraft basic structure. Radiating and receiving surfaces were co-planar within the limits of boresighting adjustments. Figure 3 shows the arrangement of the arrays.

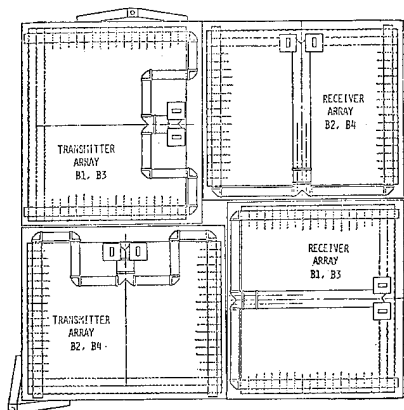


Figure 3. Antenna Assembly.

A large plan form area enabled the electronic modules in the system to be positioned in planar form. Attachment to the spaceframe structure had to be a 3-point mounting, although a 4-point attachment would have made the radar structure much easier to design. The basic envelope is shown in Figure 4. The three attachment brackets were made from 6061-T6 aluminum alloy, they are held to the structural walls by fasteners and by bonding.

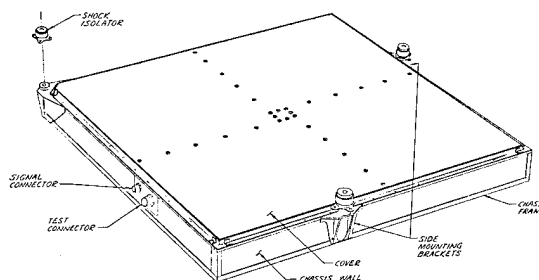


Figure 4. Viking Terminal Descent Landing Radar.

A lightweight structure was necessary to form a mounting frame for the four antenna arrays, provide structure for spaceframe mounting, have a base for attachment of all electronic modules, provide EMI shielding, and provide heat conduction.

The build-up of the basic structure was as shown in Figures 5 and 6. The side walls and center dividers were made from a combination of nickel plated magnesium alloy skins with a bonded aluminum alloy honeycomb core. Welded magnesium frames made from channel sections formed the top and bottom caps to close off the honeycomb cores to the side and center walls. Magnesium angles were used for the vertical joints to complete the structural frame. Divider walls were located in the gaps between the four arrays. These provided the necessary stiffness for the structure. They were also used as EMI shielding between transmitters and receivers.

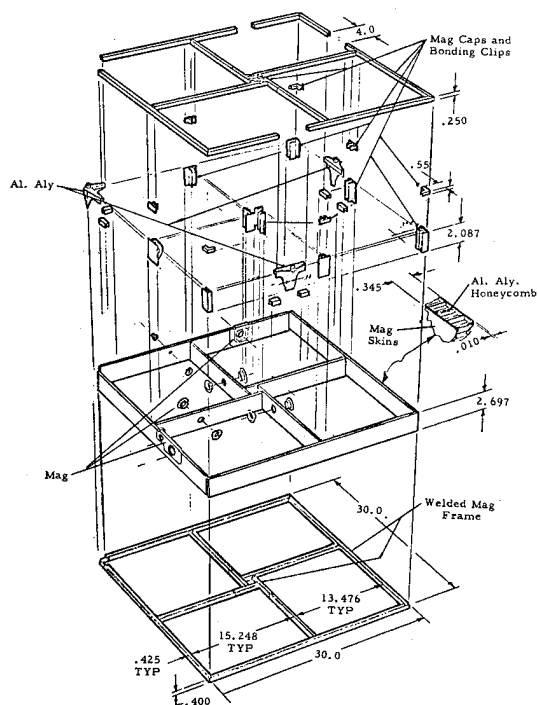


Figure 5. Chassis Structure.

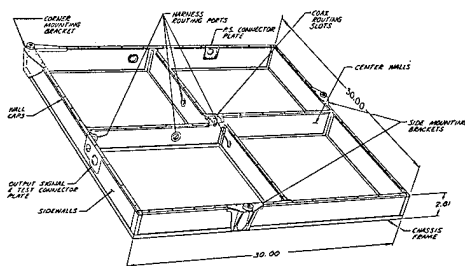


Figure 6. Viking TDLR Chassis Assembly.

## COVER

It was necessary to close the box completely with a cover which would provide stiffness to the chassis structure and whose edges would provide an EMI seal. This called for a stiff panel of sandwich construction. Even with this form, a panel made from aluminum alloy skins of sufficient thickness to provide the necessary stiffness, was too heavy. In spite of the large cost, it was decided that reduced weight was important enough to use beryllium skins with an aluminum honeycomb core build-up. The skins were etched down to .008 inch thick top and bottom, plated and bonded to the honeycomb interior and attachment reinforcements.

## FUNCTIONAL ARRANGEMENT

The separable functional modules were four solid state transmitters, four receivers with preamplifiers, four independent power supplies, and one electronic assembly consisting of four tracker boards and two converter boards.

The functional modules had to be located and mounted with special reference to waveguide hook-up to antennas, cooling requirements, vibration displacement (proximity to mounting points) and EMI isolation, especially between transmitter units and receivers. Figure 2 shows the final arrangement of compartments.

This arrangement gave excellent shielding and low resistance chassis grounding properties. A description of each of the modules follows.

## TRANSMITTER UNITS (FIGURE 7)

The heart of the solid state transmitter was the Impatt diode. Due to its high power dissipation and the need to conduct heat to the chassis, the diode had to be mounted and soldered into a copper plug, which then was press fitted into the transmitter housing. The housing accommodated the current regulator circuit which fed controlled power by short leads to the Impatt diode. For weight reduction, these housings were made from hogged out magnesium alloy with nickel plating, copper flash and gold plating finish.

Low coefficient of thermal expansion invar microwave cavities had the accurately machined low tolerance iris and microwave tube outputs. These had to be assembled over the diode plug using pre heat conditioning and bolt torquing figures which were determined for the specially designed "necked" bolts used for the attachment. These provided compensation for differential expansion between the magnesium, invar and copper.

Output from the cavity was fed through a bias coupler made from standard Ku-band waveguide and flanges dip brazed together. The bias feed to the receiver was accomplished by designing a special waveguide to semi rigid coaxial cable transition piece to take RF energy through coax to stripline boards.



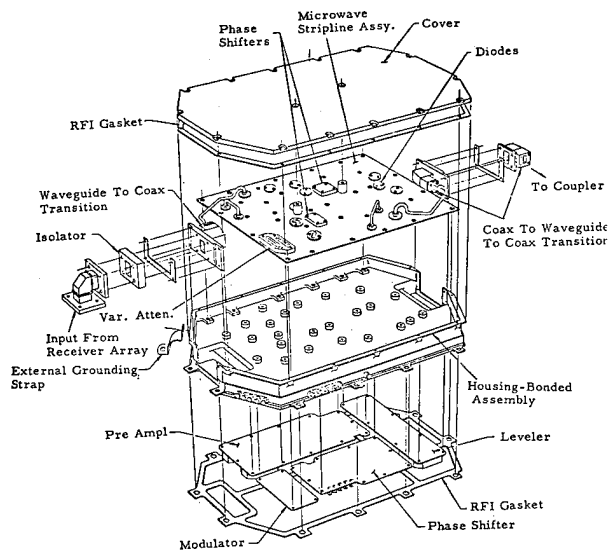


Figure 7. Viking TDLR Receiver Assembly.

#### RECEIVERS (FIGURE 8)

The receivers consisted of a stripline RF board and four circuit boards. Complete shielding of all functions by total enclosure was an essential feature. Because the gain in the preamplifier was so high it was very important to keep vibration excursions to a minimum, especially in the first stage. This was an important feature also in the mechanical arrangement of the stripline board. The illustration shows that the boards were attached to the housing, not only around the periphery, but also by 24 spacers built into the housing. The "egg crate" divisions in the housing shields each of the four electronic functions from each other.

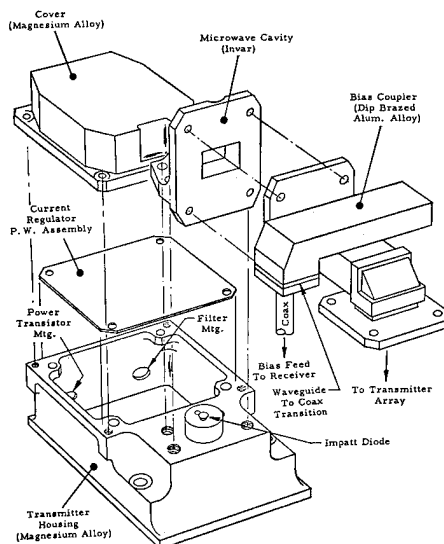


Figure 8. Viking TDLR Transmitter Assembly.

The housing and its cover were made from hogged-out magnesium alloy, nickel plated with a copper flash and then gold plated. This plating was needed for low resistance contact between the RF gaskets on the cover and mounting faces.

It was decided not to have any friction connections anywhere within the radar. To do this for RF connections, the disconnect points in the RF leads had to be made by waveguide and not in the coaxial connections. This was accomplished by making transition from the coaxial connections in and out of the stripline board to waveguide parts for connections to the receiver antenna and the run to the bias connections on the transmitters.

#### POWER SUPPLIES (FIGURE 9)

It was decided to provide one power supply for each of the four beams. The radar can perform correctly on three beams, one of the power supplies could fail and correct performance would still be assured.

Most power supplies require an awkwardly shaped hook-up harness to make the intraconnections between the stages. This design had only a few bus connections between the high dissipating parts and the printed circuit boards. All magnetics, power transistor diodes, and filters were attached to a stiffened plate which served as a mechanical mounting and heat conductor. Printed circuit boards containing the smaller low dissipators, such as regulating circuits, were designed for attachment to each side of the mounting plate. The DC to DC input regulator on the underside of the mounting plate was completely shielded when the assemblies were installed in the four partition mounting frame, leaving only the "clean" output regulators exposed.

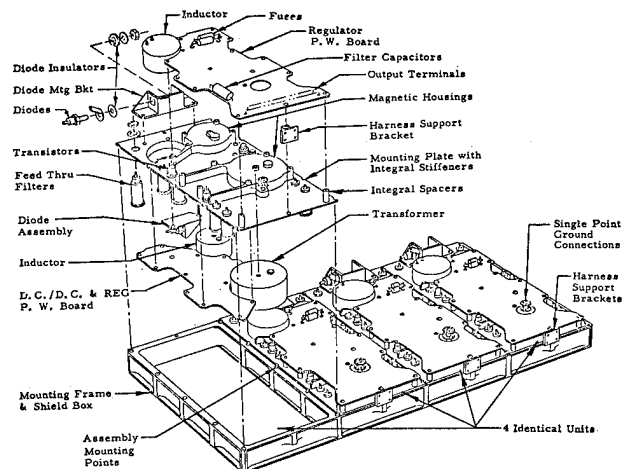


Figure 9. Power Supply.

## PRINTED WIRING BOARDS FOR THE ELECTRONIC ASSEMBLIES - TRACKERS AND CONVERTERS

**Part Mounting** - There was evidence from research in the Lunar Module program that solder joints would be more likely to survive heat compatibility tests if planar printed wiring boards were used. To achieve this, multilayer boards of up to 10 layers were used in the Viking program. Figure 10 shows the arrangement of the electronics assembly. Note the high reliability split pin wire wrap method of intraconnecting.<sup>2,3</sup> This was adapted to insure that no "friction" connections existed anywhere in this radar. In all cases, solder joints are readily visible on both sides of the boards. Potentiometers have poor reliability; the factory adjust method of tuning by changing resistor values was adopted and only fixed resistors were used.

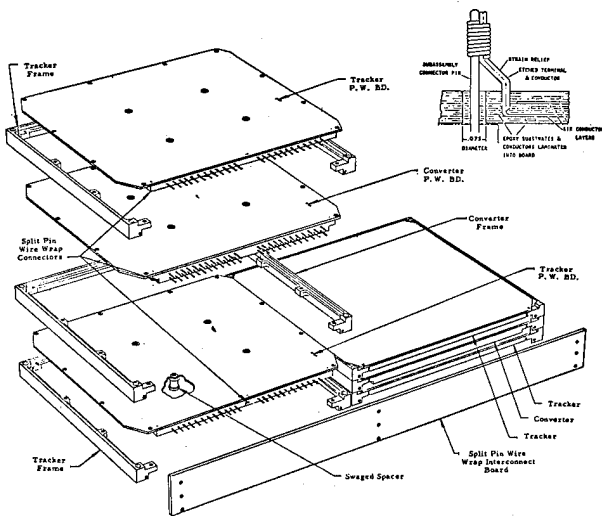


Figure 10. Electronic Assembly

**Solder Joints** - "Solder joint cracking" was a very real problem. Much research and many papers have been written on this subject. An over-stressed solder joint is not easy to detect visually.

The mounting and connecting methods are those which were adopted to obviate stressing solder joints to failure by thermal cycling, during temperature testing, heat sterilization and the mission.

Tests basically confirmed that the TDLR mechanical design was very adequate. The two successful missions proved it.

## VIKING RADAR ALTIMETER

The Viking Radar Altimeter is a solid state non-coherent pulse radar operating at 1 GHz. The transmitter generates a short pulse of 1 GHz energy which is directed to the ground via one of two antennas. A fraction of this pulse is scattered off the ground and returns to the same antenna and is processed by the receiver.

Some specifics of this operation are depicted in Figure 1. In Mode 1, which is used for altitudes from 800,000 feet to 20,000 feet during the aeroshell braking portion of the flight, the transmitter generates a 140 watt 6 microsecond pulse 700 times per second. After the vehicle senses 20,000 foot altitude the aeroshell is jettisoned and a parachute deployed. The TDLR becomes operational at this point. The Altimeter data continues to be processed down to 100 feet.

**Radar Altimeter Electronics (RAE)** - The RAE consists of a rectangular assembly 9.18" long x 8.81" wide x 5.77" high, excluding connectors. The design utilizes magnesium and aluminum throughout and weighs 9.3 lbs. Multi-utilization of mass allows structural, thermal and shielding requirements to be integrated in the design. Titanium fasteners were used throughout. The arrangement of the functional subassemblies allowed for direct path heat sinking to the chassis. The RAE is accessible for tests with top cover removed as shown in Figure 11.

The separable, pluggable and interchangeable subassemblies consist of a Digital filter, Tracker, two Intermediate frequency units, a Duplexer receiver, Solid state transmitter, and Power supply. These units are all the same height and width. The Power supply is the only internally mounted exception - it occupies the complete end of the altimeter. The externally mounted Antenna Switch is a fail safe redundant microwave device to switch energy from either of two redundant Altimeters to the desired antenna (aeroshell antenna for mode 1 and Lander Antenna for modes 2, 3 and 4). Microwave Integrated Circuits (MIC's) were used extensively in the Solid State Transmitter (SSX) Duplexer Receiver and Antenna Switch.

The two separable side plates (top and bottom cover and front panel) provide an isothermal design and structural support. Both side plates extend far enough on the sides of the power supply converter to provide an adequate thermal transfer of the overlap area and structural mounting. The RAE has an 8.0" x 8.0" mounting pattern. An input power connector is integral with the power supply. Utilizing the power supply converter module as the altimeter end structure exposed the maximum surface area for cooling during operation and bench test.

At the opposite end of the unit, the front panel mounts the signal and test connectors. The antenna switch is mounted below the test signal connector and can be mounted on either RAE with external RF connections. Figure 12 shows a cross section of the RAE.

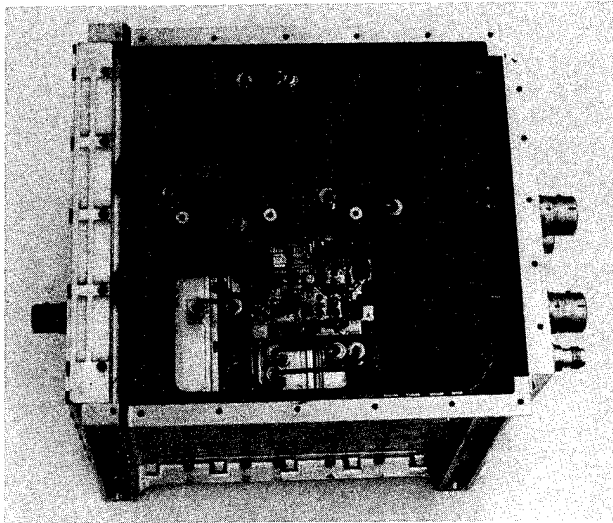


Figure 11. RAE with cover removed showing interconnect matrix connecting subassemblies.

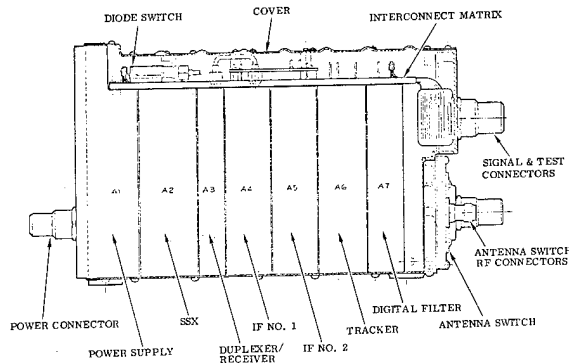


Figure 12. Section view of RAE subassemblies.

All internal interconnections are made by interconnect matrix assembly utilizing split-pin multilayer wire wrap and integral flexible wiring.

The estimated weight of organics used in the RAE was 0.846 lbs/RAE and with antenna switch of 1.6 lbs/system. The RAE's were sealed with RTV 566.

The Power Supply Converter components are packaged within a machined 6061-T6 aluminum alloy chassis. The Converter chassis has one compartment. The converter circuit components are packaged on a standard printed wiring board and located in the outboard compartment. The Preregulator input filter and rectifier filter circuits are packaged on a circuit board and located in the inboard compartment. Access to the circuit boards is accomplished by the removal of two shield/covers on each side of the module. The larger components are mounted directly to the chassis. The size of the circuit boards, along with the inherent stiffness of the chassis with its compartment-like construction, resulted in a rigid assembly with excellent vibration and thermal characteristics.

Electrical connections are made through a split pin wire wrap connector located in a recess at the top of

the module above the preregulator section. RF shielding was implemented by the use of a wire wrap interconnection circuit board which is located outside of the main two compartments. All electrical connections to the regulator module are made through feed-thru capacitors located in the wall of the chassis. Conducted interference on the input lines has been reduced by the use of L.C. line filters located in the wall of a small compartment directly behind the input connector and apart from the rest of the Power supply components.

The Power supply converter module has an internal heat dissipation of 14 watts. The major heat dissipators have been mounted directly to the chassis.

#### MICROWAVE INTEGRATED CIRCUIT SUBASSEMBLIES

The many advantages of microstrip resulted in this technique being selected for the 1 GHz altimeters. All Viking Lander equipment had to withstand the rigors of sterilization baking at 125°C - 8 cycles for 300 hrs. Teledyne Ryan's Electronic and Space Systems developed the interconnecting techniques for microstrip elements used in the SSX, Duplexer Receiver, and Antenna Switch on the altimeters.

In the transmitter section, the layout of the microstrip circuits was critical since a high degree of isolation was required between some circuits. In many cases complete shielding was necessary with interconnecting feed-throughs. In the Local Oscillator section, hybrid MIC's were packaged utilizing discrete and chip components within individual compartments. The launch geometry required special jumpers, such as coax to substrate and substrate to substrate jumpers.

During thermal cycling, the differential motion between the connector and the substrate is accommodated by the flexing of the jumper strain relief. Throughout the sterilization temperature range, a differential motion of 1 to 2 mils between the alumina substrate and magnesium/aluminum housing must be accommodated without straining the jumper solder joints<sup>5</sup>.

The RF circuits on the SSX and Local Oscillator (L/O) are packaged within a machined HK31 magnesium alloy chassis - the SSX on one side with the L/O on the opposite side. The chassis contains MIC's mounted on alumina substrates and epoxy fiberglass boards and conventional PC board.

The MIC compartments are RF isolated and all electrical connections are made through feed-through capacitors of coaxial connections. The MIC area is divided up into four sections on the SSX side and is sealed with an integral cover.

The MIC's used were constructed using an alumina substrate .025" thick and a maximum of 2" in length. One side utilized a copper ground plane while conductive copper paths were photo etched on the

opposite side. The width, length, shape and arrangement of the conductors form many of the capacitive inductive and coupling functions of the circuits. Other discrete components in chip form are soldered onto the conductors where required. The substrates are soldered on the ground plane side to Kovar support plates. Electrical connections between substrates are accomplished by Kovar jumpers and small metal corrugated ground strips the same width as the conductors<sup>5</sup>. The inputs and outputs to the MIC's are mated with standard semi-rigid 50 ohm coax transmission line. The small size of the circuit component and the mounting arrangement of the substrates of the MIC's provide excellent thermal and vibration characteristics. Figure 13 shows a closeup of L/O MIC's.

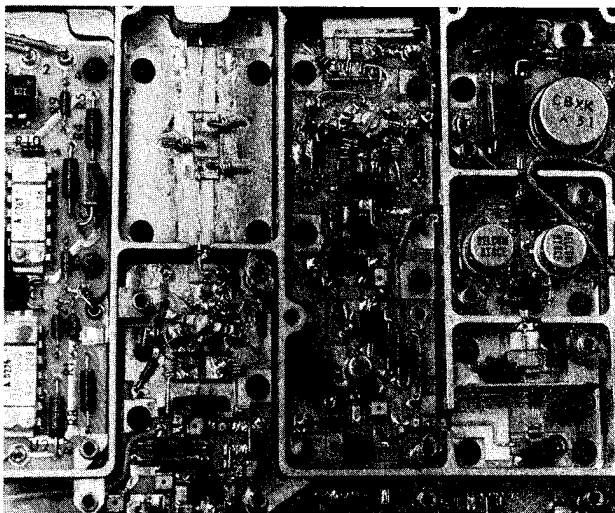


Figure 13. MIC component mounting within L/O subassembly compartments.

The remaining electronic components are mounted in a conventional manner on printed wiring board. The basic module chassis design and its attachment to the altimeter structure can be seen in Figure 14.

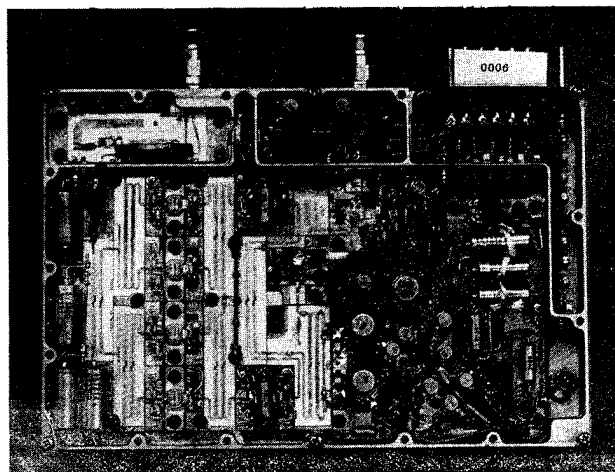


Figure 14. Transmitter side of SSX/LO subassembly.

The Duplexer/Receiver components are packaged within a double-sided machined HK31A magnesium alloy chassis. A circulator with RF connection, MIC boards, filters and PC board mounted components are arranged similar to L/O. Shield covers provide easy access. The circulator, filter and thermal sensor are mounted directly to the module chassis. The remaining electronic components are mounted on compartmented printed circuit boards with split pin and RF connections located on the top of the unit. All electrical connections are made via feed-thru capacitors.

The fail safe Antenna Switch consists of a machined Kovar planar chassis mounting the interconnecting RF connectors for both RAE's and both antennas. Internally mounted are three MIC's approximately 2 x 2" jumpered together and terminated externally to RF connectors with 90° address. The switch was mounted with a gasket on the front of RAE for the Viking missions and can be seen in Figure 12. Exhaust apertures in the front chassis allow for pump down.

#### TRACKER AND DIGITAL FILTER SUBASSEMBLIES

The Tracker and digital filter contain the circuits and components, tracker, false target-bit and digital filter function of the altimeter.

The tracker consists of two multilayer PC boards mounted back to back on magnesium frame. Tracker PC boards 1 and 2 have six and seven layers respectively. System connections are made through two split pin wire wrap connectors at the top of the mounting frame - additional shielding is provided by a shield cover over the tracker 2 PC board compartment. RF connections are made through coax connector mounted in the split pin connector.

The Digital Filter board consists of two multilayer boards joined by flexible jumpers and mounted to a magnesium alloy frame. High density was achieved with this technique as approximate 130 TO-87 type IC's and 78 discretes were packaged on two 10 layer boards 6.5" wide x 4.0" high as shown in Figure 15.

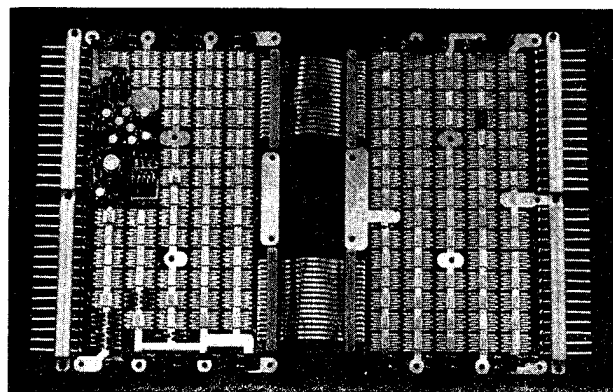


Figure 15. Digital Filter boards before mounting in subassembly frame.

The IF subassemblies were compartmented similar to L/O layout with discrete wire jumpers between compartments. These can be seen in Figure 16.

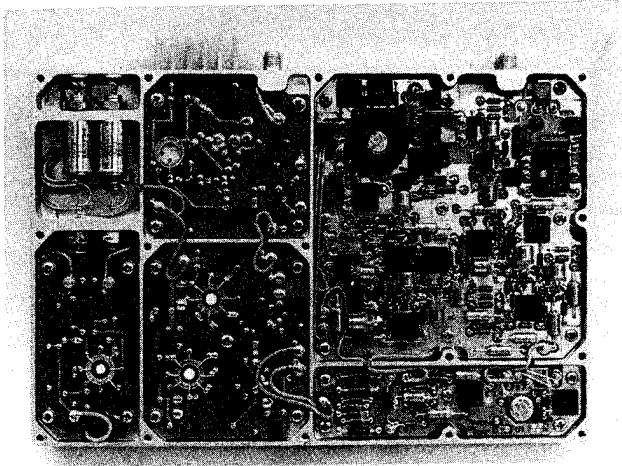


Figure 16. IF subassembly with cover removed.

#### INTERCONNECT MATRIX

The split-pin interconnect matrix and flexible wiring shown in Figure 17 provided a controlled electronic interconnection between subassemblies. The split-pin wire wrapping technique provides gas-tight electrical connections to the integral flexible wiring while maintaining separable, maintainable subassemblies. The individual subassemblies have laminated split-pin wire wrap connectors designed to interface with the matrix. The split-pin wire wrapping method of interconnecting subassemblies has been used extensively on the Polaris, Apollo and Poseidon systems<sup>4</sup>.

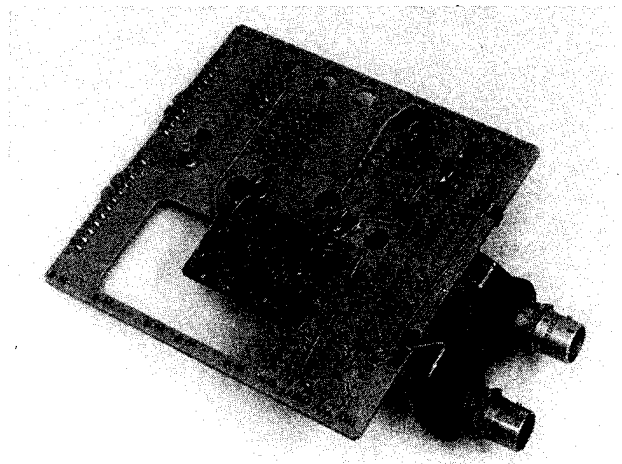


Figure 17. Interconnect matrix with integral split-pin terminals and piggyback growth board.

There are no electrical or mechanical junctions anywhere within the board. All these functions have been accommodated in the design; ground planes, vertical and horizontal shields, sensitive signal lines, heavy

current carrying conductors, and flexible wiring guards. The flexible portion contains all conductors that exit from the rigid board - these terminate with integral etched eyelets<sup>6</sup>.

A high degree of reliability can be predicted for this packaging arrangement<sup>4</sup>. Approximately 365 junctions are integrated within the matrix, with 208 interconnections between subassembly split pins. Less than 50 stud type solder joints are made to the signal and test connectors.

#### MECHANICAL AND THERMAL ANALYSIS

The RAE was analyzed for a realistic environment load of  $\pm 100$  g's in the assemblies critical direction with all stress concentration factors being considered. Resonant survey revealed a  $F_n$  for the modules to be approximately twice the chassis  $F_n$ . Fatigue stress levels were kept below the yield point for 6061-T6. Computer programs were used extensively for dynamic analysis - resonant frequencies and transmissibility calculations were made using these programs. Thermal stress programs were utilized for calculating stress versus temperature. Refined analysis along with weight calculations were made to insure no structural or functional part inadequacies. Design refinements were made as the design progressed when deficient items were revealed. The analysis was made down to the electronic part level to insure all margins were above 100%.

The thermal analysis was performed concurrently with Product Design and the thermal model was upgraded continuously to the point of hardware fabrication. Actual power dissipation measured in thermal vacuum test was 23 watts, showing a 40% safety margin for the design.

At hot mission touchdown, the hottest point of the unit was a diode junction in the power supply and the coldest biologically contaminated point was on Tracker board No. 1.

During both landings the active RAE locked on to ground return on the first sweep after turn-on and performed flawlessly to touchdown.

#### REFERENCES

1. "Design for Quality: A Designers Notebook for Electronic Systems", by H. G. Frankland and Mary Jane Hyde, *Quality Progress*, June 1975
2. "Final Report for LM Landing Radar Solder Joint Research Program", by H. G. Frankland and N. J. Sawyer, Report No. 53969-55, Teledyne Ryan Aeronautical, April 1969
3. "Solder Joints I, II and III", by H. G. Frankland, N. J. Sawyer and I. Sanderson, *Insulation/Circuits*, January/February/March 1971
4. "Split Pin Multilayer Interconnections", by H. G. Frankland and N. J. Sawyer, *Electronic Packaging and Production*, June 1967
5. "Interconnecting Microwave Integrated Circuits in High Temperature Applications, Parts 1 and 2", by N. J. Sawyer, D. C. Wells and H. G. Frankland, *Insulation/Circuits*, March/April 1975
6. "Split Pin Wire Wrapping and Flexible Wiring", by N. J. Sawyer, *Insulation/Circuits*, July 1974

# KU BAND INTEGRATED RADAR/COMMUNICATIONS SUBSYSTEM FOR THE SHUTTLE

Lowell C. Parode

Space & Communications Group  
Hughes Aircraft Company  
Box 92919  
Los Angeles, California 90009

## ABSTRACT

The Ku Band Subsystem for the Space Shuttle Orbiter must operate as rendezvous radar and provide two way communications with the ground. A discussion of accomplishing these objectives while meeting the additional requirements of minimum weight, limited stowage volume, and adequate cooling is presented.

## KU BAND SUBSYSTEM FOR THE SHUTTLE

The Ku Band Subsystem for NASAs Space Shuttle Orbiter operates as a radar during rendezvous with other space vehicles, and provides two way communications with the ground through the Tracking and Data Relay Satellite System (TDRSS). The subsystem must meet its requirements despite severe weight and stowage volume limitations.

In the communications mode, the subsystem searches for and acquires the TDRSS anywhere within 20 degrees of the designation given by the Orbiter. The subsystem then tracks the target anywhere within the unobscured volume. As shown in Table 1, the subsystem receives data at 216 kbps and transmits data at up to 50 Mbps. To achieve the required bit error rate (BER) of  $10^{-6}$ , at the  $0.2 \times 10^{-12} \text{ W/m}^2$  provided by the TDRSS, the ratio of antenna gain to receiver noise temperature must be 4.8 dB/°K. To provide the required  $3 \times 10^{-12} \text{ W/m}^2$  at TDRSS, the effective isotropic radiated power (EIRP), that is, the product of the effective antenna gain and the transmitter output must be greater than 48.8 dB above 1 W.

In the radar mode, the subsystem searches for, detects, and acquires targets within 30 degrees of the designation given by the Orbiter. The subsystem then tracks the target to provide the Orbiter with range, velocity, angle, and inertial angle rates. Table 2 details the requirements for this mode. The detection range and range accuracy requirements could be met by a simple, non-

TABLE 1. COMMUNICATIONS REQUIREMENTS

SEARCH AND ACQUISITION VOLUME	±20 DEGREES
TRACKING LIMITS	ORBITER OBSCURATION
FORWARD LINK	
DATA RATE	216 KBPS
SIGNAL POWER DENSITY FROM TDRSS	$0.2 \times 10^{-12} \text{ W/M}^2$
BIT ERROR RATE	ONE ERROR IN ONE MILLION BITS
GAIN/NOISE TEMPERATURE	4.8 DB/°K
RETURN LINK	
DATA RATE	UP TO 50 MBPS
SIGNAL POWER DENSITY AT TDRSS	$3 \times 10^{-12} \text{ W/M}^2$
EFFECTIVE ISOTROPIC RADIATED POWER	>48.8 DB ABOVE 1 W

TABLE 2. RADAR REQUIREMENTS - NONCOOPERATING TARGET

SEARCH AND ACQUISITION VOLUME	±30 DEGREES, 100 FEET TO 12 MILES
TRACK LIMITS	ORBITER OBSCURATION, 100 FEET TO 12 MILES
RANGE ACCURACY (3σ)	80 FEET OR 1 PERCENT
VELOCITY ACCURACY (3σ)	1 FPS
ANGLE ACCURACY (3σ)	8 MR
ANGLE RATE ACCURACY (3σ)	0.14 MR/SEC

coherent pulsed radar, but the velocity accuracy requirement dictates the use of doppler measurement techniques. The specification of 0.14 deg/sec (3σ) angle rate accuracy is the most difficult requirement to meet.

The subsystem performance requirements translate into the functional requirements shown in Table 3. The transmitter uses a traveling wave tube (TWT) with an average output power greater than 50 W. The receiver uses a microwave amplifier with a noise figure of less than 5 dB. Most important, it is possible to make use of a parabolic antenna with a 3 foot diameter.

In the communications mode, the Ku band equipment receives at 13.8 GHz and transmits at 15.0 GHz. To simplify the

receiver, and because a wide band transmitter is feasible, the radar is operated near the communications receive frequency. Table 4 lists the characteristics to be demonstrated by the traveling wave tube employed. The helix TWT easily meets the bandwidth requirement, also providing a comfortable margin for the bandwidth required to handle 100 Mbps of convolutionally encoded data. The TWT is provided with a two stage collector. This characteristic means a higher tube efficiency resulting in a lower power consumption and a significantly minimized thermal management problem. More important, it means that low level RF drive modulation can be employed in the pulsed (radar) mode without suffering unmanageable increases in dissipation. The TWT is expected to weigh less than 6 pounds.

As shown in Table 5, the low noise microwave amplifier provides a 1550°K system noise temperature, including the effects of antenna noise, waveguide losses, and the

TABLE 3. FUNCTIONAL REQUIREMENTS

TRANSMITTER TUBE AVERAGE POWER	>50 WATTS
RECEIVER NOISE FIGURE	<5 DB
ANTENNA DIAMETER	3 FEET

TABLE 4. TRAVELING WAVE TUBE CHARACTERISTICS

BANDWIDTH	13.8 TO 15.1 GHZ
EFFICIENCY	43 PERCENT
COLLECTOR STAGES	2
WEIGHT	<6 POUNDS

downconverter noise contribution. To accommodate the variation in signal strength with target size and range, the receiver provides a dynamic range of 110 dB. In the communications mode, a predetection bandwidth of 8 MHz is provided to pass 90 percent of the energy of the 3 MHz spread spectrum modulation on the forward link. In the radar mode, a 10 MHz bandwidth is required to pass the 122 ns pulse used at the shortest ranges. Because the radar uses frequency hopping, the receiver RF bandwidth is 300 MHz.

The principal constraints on the subsystem are the size and weight limits of the antenna assembly. The antenna is stowed in the space between the payload outer contour and the payload bay door inner contour as shown in Figure 1. After the payload doors are opened, the antenna assembly is deployed by rotating the mounting boom with a deployment mechanism. To keep the mechanism within feasible limits, the weight of the deployed assembly must be kept to less than 160 pounds. The microwave assembly contains both the transmitter and the microwave receiver and is mounted on the deployed assembly to minimize the losses in waveguide runs. Figure 2 shows the assembly in its deployed configuration. The microwave

TABLE 5. RECEIVER CHARACTERISTICS

EFFECTIVE SYSTEM NOISE	1550 °K
DYNAMIC RANGE	120 DB
RF BANDWIDTH	300 MHZ
IF BANDWIDTH	
COMMUNICATIONS	8 MHZ
RADAR	10 MHZ

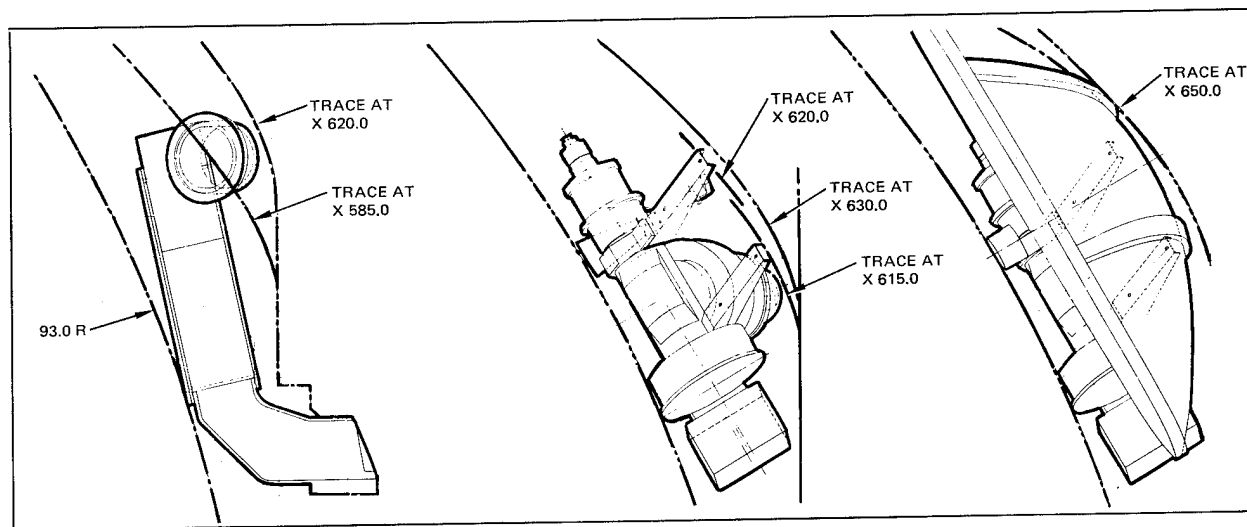


FIGURE 1. STOWED ANTENNA - PAYLOAD BAY DOORS CLOSED

assembly is sealed in a rectangular box supported at the forward end by a canted pedestal bolted to the deployment mechanism. The antenna is moved by the gimbals bolted to the top rear of the microwave assembly.

The antenna is edge mounted to save weight. Figure 3 shows that as the arms of a conventional yoke are shortened, the total weight of antenna and gimbals still remains the same. The weight saved by the lighter yoke is offset by the larger, heavier motors required to drive the increasing moment of inertia of the antenna. However, as the yoke arms approach their minimum length, the yoke weight drops sharply and also reduces the outer axis motor size and weight. The antenna drives are sized for a zero g field. Counterbalances are required for testing in a 1 g field.

The antenna characteristics are shown in Table 6. Circular polarization is required

for compatibility with TDRSS, but linear polarization is preferred for radar. Several antenna configurations, such as Cassegrain feed and planar array, were considered, but the front feed parabola was selected because low sidelobe levels can be achieved and the antenna polarization can be switched with a simple waveguide phase shifter. The diameter, 36 inches, is the largest that will fit. The focal length, 0.292 D, is shortened to fit the stowage volume. The small f/D ratio reduces the gain slightly, but the communications transmit gain is still 39.4 dB and the communications receive gain is 38.9 dB. With the 50 W transmitter, an EIRP of 52.8 dBW provides a 4.0 dB margin over the required value shown in Table 1. Similarly, the receive G/T of 6.4 dB/°K provides a 1.8 dB margin over the requirement of Table 1. Finally, the front fed parabola provides low sidelobe levels because the aperture blockage is small and the distribution taper can be well controlled.

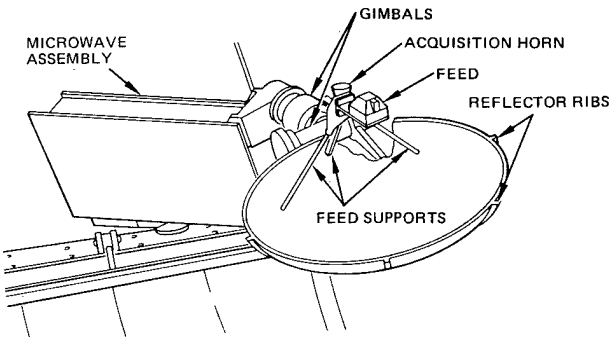


FIGURE 2. DEPLOYED ASSEMBLY

TABLE 6. ANTENNA CHARACTERISTICS

POLARIZATION (COMMUNICATIONS/ RADAR)	CIRCULAR/LINEAR
DIAMETER (D)	36 INCHES
FOCAL LENGTH	0.292 D
GAIN (TRANSMIT/RECEIVE)	39.4 DB/38.9 DB
FIRST SIDELOBE	-22 DB

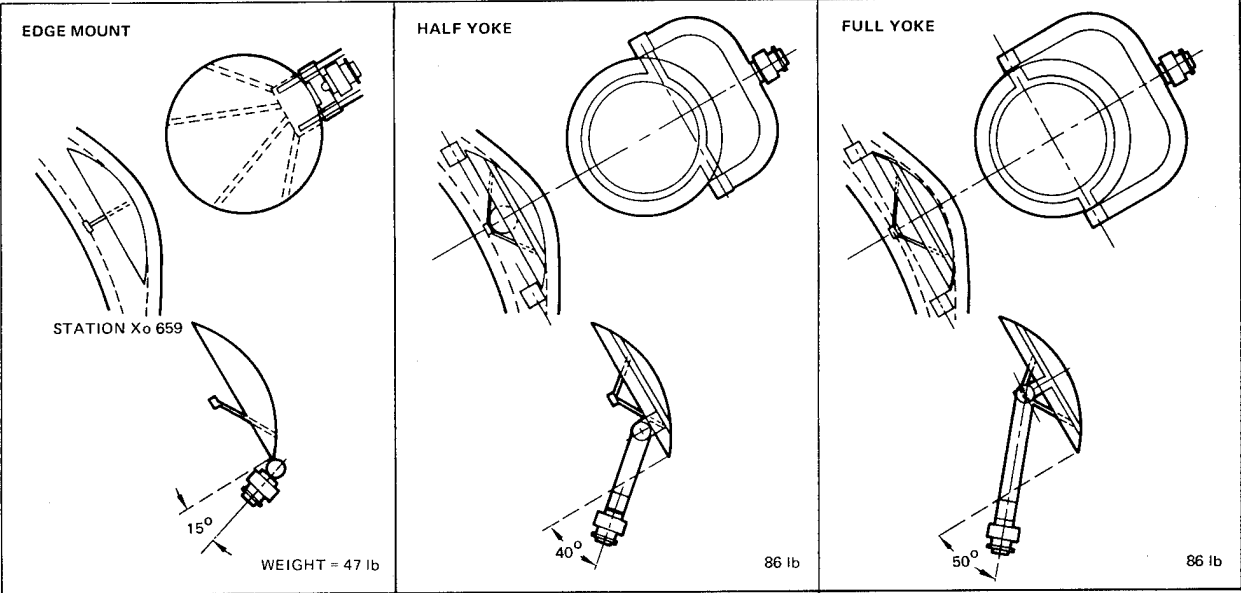


FIGURE 3. WEIGHT VERSUS ANTENNA UNBALANCE



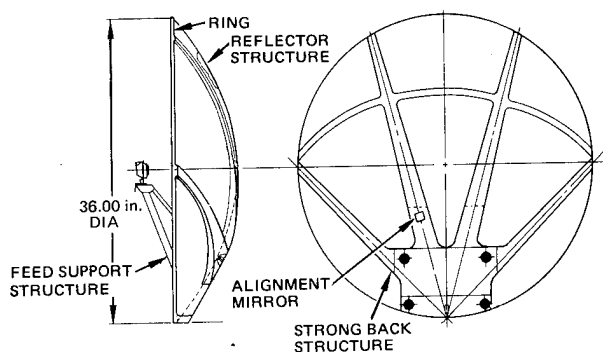


FIGURE 4. ANTENNA REFLECTOR

The antenna reflector is the dominant load for the servo motors. Consequently, it is essential to keep the reflector weight to a minimum. A graphite-epoxy laminate of 0.016 inch thickness weighs just 2.95 pounds. Servo drive loads are distributed from the gimbal assembly to the reflector by four graphite ribs that radiate across the back of the reflector as shown in Figure 4. The entire antenna assembly, including reflector, ribs, feed, and feed supports, weighs less than 6 pounds. In addition to its light weight, the graphite-epoxy provides excellent dimensional stability over the operating temperature range of  $-250$  to  $+250^{\circ}\text{F}$ . While graphite reflects microwaves as well as aluminum, it does not reflect visible energy very well, thus minimizing the thermal problem when the sun's rays will focus on the feed.

The gimbal assembly is shown in cross section in Figure 5. The inner gimbal axis is just long enough to hold the torque motor, the microwave rotary joint, the digital shaft angle encoder, and the cable wrap. The inner gimbal is supported at the end of the outer gimbal axis, which also has a motor, rotary joint, angle encoder, and cable wrap. Inertial stability is provided by two rate-integrating gyros that sense inertial rates about the two gimbal axes. The gyros are mounted to the antenna support arms so as to sense directly the antenna motion. The gimbals are also provided with a locking mechanism so that the antenna can be locked at the stow gimbal angles before the deployed assembly is returned to the stowed position.

The antenna is inertially stabilized by closing the output of the gyros back to the torque motors. The antenna is moved by sending precession signals to the gyros. To move the antenna to a designated angle in Orbiter coordinates, a microprocessor transforms the commands into antenna coordinates. The command coordinates are compared with the shaft angles from the shaft angle encoders to provide error signals. The error signals are shaped and

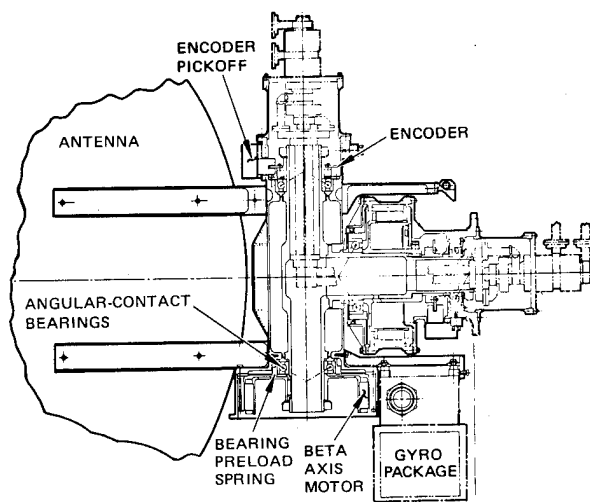


FIGURE 5. GIMBAL ASSEMBLY CROSS SECTION

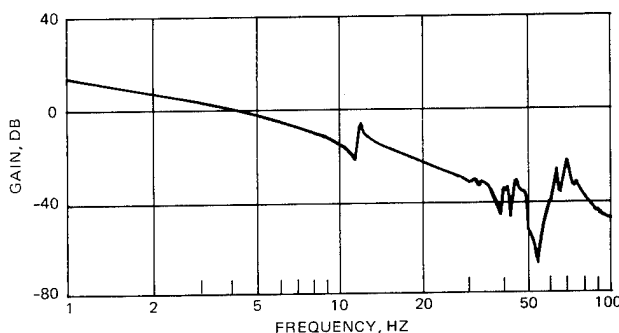


FIGURE 6. SERVO OPEN LOOP GAIN

then precess the gyros until the antenna reaches the commanded position. To track, angle error signals from either the radar signal processor or the communications angle tracking circuits are selected to precess the gyros. In search, the microprocessor calculates rate commands which precess the gyros to create a spiral search pattern. Whether manually directed by the Orbiter crew or automatically controlled by internal events, the antenna is supervised by the microprocessor.

The most difficult servo problem involves the structure of the deployed assembly and the structure of the Orbiter itself. Figure 6 is the open loop transfer function of the antenna servo in a high gain state. The gain peak at 12 Hz is caused by the structural resonance of the deployed assembly and its mounting. It is necessary to stiffen both the deployed assembly and the Orbiter structures to move the resonance out of the servo pass-band. A computer model of the structure is shown in Figure 7. Analysis of the model shows a low frequency resonance below 10 Hz

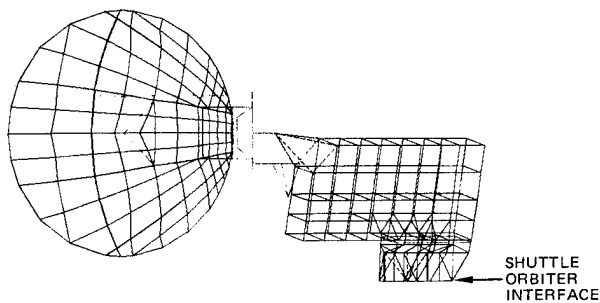


FIGURE 7. COMPUTER MODEL - STRUCTURE

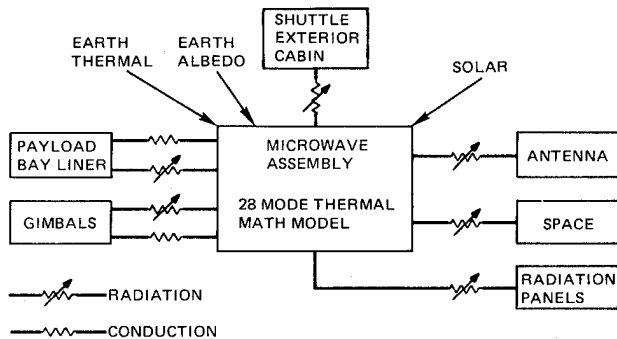


FIGURE 8. DEPLOYED ASSEMBLY - THERMAL ENVIRONMENT

and several more in the vicinity of 20 Hz. As the structure was stiffened, the low frequency resonance moved up, but the lowest resonant frequency remained below 20 Hz. The Orbiter structure limited the attainable stiffness and has to be stiffened by carrying torsion loads from the deployment mechanism mounting to the bulkhead.

The microwave assembly is shown in Figure 8. Total dissipation in this unit is about 210 W which must be radiated to space without overheating any of the electronics within. As shown in Figure 8, the thermal environment is quite complicated. Direct solar energy is a major source of heat, but there are numerous other sources, including sunlight reflecting off the cabin, off the radiator panel, and off the earth (albedo). In addition, the cabin, the radiator panel, the payload bay, and the earth are sources of IR energy. A computer model of the thermal environment shown in Figure 9 takes 154 nodes and 990 coefficients to account for all sources and sinks of thermal energy. The transmitter temperature variation is shown in Figure 10. As a result of the analysis, the entire assembly was covered with a silvered teflon to help reduce solar heat loads. Extending the thermal radiator by 6 inches could drop the unit temperature about 10°F, but such extension was rejected because it adds considerable weight. Finally, a concerted effort is being made to reduce dissipation within the unit.

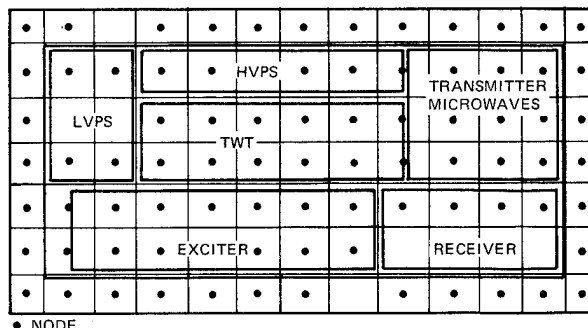


FIGURE 9. COMPUTER MODEL - THERMAL ENVIRONMENT

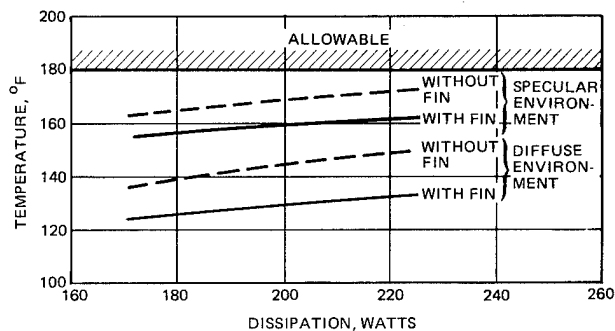


FIGURE 10. TRANSMITTER TEMPERATURE VARIATION

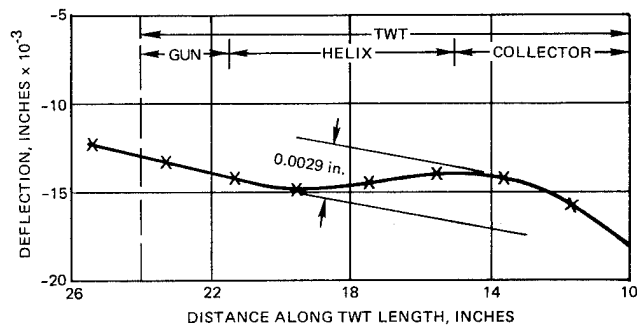


FIGURE 11. TWT DEFLECTION VERSUS STRUCTURAL LOAD

The TWT is a major source of heat in the microwave assembly and is mounted directly to the baseplate. The baseplate is 0.25 inch thick to spread the heat from the TWT. To take advantage of the strength of the baseplate, it is made an integral part of the deployed assembly's load-bearing structure. However, the presence of loads in the baseplate causes deflections which could be transmitted to the TWT. Since deflection of the TWT could affect the electron ballistics, it is calculated, and the results are shown in Figure 11. The TWT will tolerate 0.005 inch deflection. Pressurization of the microwave assembly proves to be the largest contributor to deflections.

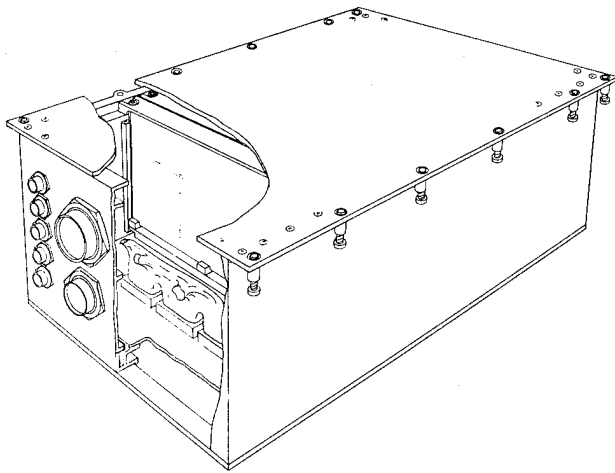


FIGURE 12. AVIONICS BAY UNIT

The electronics not required in the deployed assembly are located in four units within the avionics bay. A typical unit is shown in Figure 12. The units are sealed, purged, and then back filled with nitrogen to meet flammability and outgassing requirements. The units must be pressure tested in a 36 psia ambient since the Orbiter cabin is pressurized as part of its normal checkout. To meet the stresses imposed by the pressure test, the dip-brazed structure shown in Figure 13 is used in the sidewalls and covers. This lightweight hollow structure is about 10 percent lighter than the tape-milled structure it replaces, saving about 8 pounds of the system weight.

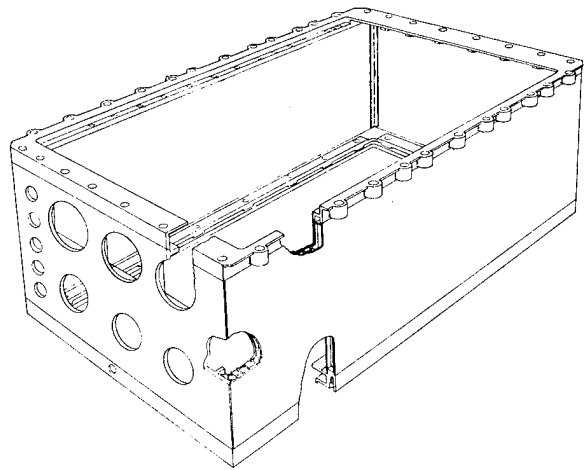


FIGURE 13. DIP — BRAZED STRUCTURE

Key requirements of the Ku band subsystem relate to performance: kilobits or megabits of data transferred with minimum error, and the acquisition and tracking of a target at some range. None of the requirements are difficult to achieve until the restraints on weight, cooling, and stowage are imposed. Then solutions are heavily dependent on the mechanical design of the subsystem. In particular, the achievement of a lightweight antenna assembly employing an extremely light reflector greatly simplifies the accomplishment of the subsystem requirements.

IMPLEMENTATION OF WIND PERFORMANCE STUDIES  
FOR  
LARGE ANTENNA STRUCTURES<sup>1</sup>

ROY LEVY and M. SMOOT KATOW

Jet Propulsion Laboratory  
Pasadena, Calif. 91103

ABSTRACT

Structural design procedures are described for a large antenna system to meet performance requirements under gravity and wind loading. A computational method is shown for the evaluation of performance in response to wind loading. Cumulative probability distribution curves for wind loading gain reductions for 100-m-diameter antennas are developed to compare a relatively heavy baseline reflector backup structure with two lighter-weight structures; all have equivalent, acceptable performance for gravity loading.

INTRODUCTION

Design studies for large paraboloidal antenna structures are useful to derive cost and performance tradeoffs associated with a number of configuration alternatives. Both cost and performance can be characterized by any of a number of quantitative measures, while configuration alternatives also are conceptually limitless. Consequently, to expedite timely completion of any study, some restrictions on the scope are essential. Nevertheless, within a framework of practical and reasonable restrictions, it is feasible to develop significant parametric study information for a comprehensive range of antenna structure designs within a given diameter class.

Within the context of the present discussion, cost will be measured by the structure weight. It is well known that weight is an imperfect measure of structure cost when a wide variety of configurations with diverse fabrication, material, and installation requirements are contemplated. However, when alternative configurations are similar in concept, structure weight is a convenient and acceptable cost measure. Performance will be measured by the antenna radio frequency (RF) gain reduction, which depends upon the structural deformations caused by gravity and wind loading.

Gravity loading, which is always present on antenna structures, is deterministic and well understood. Wind loading is statistical, and the

assessment of related response is more complex. Depending upon the location, wind can have a significant effect upon performance. Other loadings such as thermal, shock, and earthquake are primarily stochastic, difficult to quantify, and of relatively short duration. These loadings can be treated as constraints on the design to maintain structure integrity and survivability but are not included for evaluation of operating performance.

Configuration studies will be limited to be within one particular reflector class: The traditional structural format of radial rib trusses braced by circumferential hoop ring trusses. Within this format class, nevertheless, there are many possible variations of the geometrical arrangement, such as proportions, numbers and spacing of trusses, and the configuration of the external supporting structures. Several of these variations were examined early in the present study but, for brevity, the designs to be described here will include only the preferential geometry as previously developed.

Here the emphasis will be placed upon the relationships between weight and performance for wind loading. The calculational procedure and results obtained will be described for a proposed 100-m-diameter antenna reflector system illustrated in Fig. 1. This system is intended to operate at the X-band frequency of 8.5 GHz. Cumulative probability distribution curves of gain reduction for wind loading will be shown for three alternative reflector designs for this system. These designs have the same geometry and differ only in the cross sectional areas of the bars chosen for the reflector backup structure. They represent a baseline design and two lighter variations with weight reductions of up to 30%. All three designs are constrained to have equivalent performance in the absence of wind loading. The maximum gain reduction due to gravity loading is less than 10% of the total gain reduction from all sources. Those consist of manufacturing and surface alignment errors and subreflector and quadripod blockage.

<sup>1</sup>This paper presents the results of one phase of research carried out at the Jet Propulsion Laboratory, California Institute of Technology, under NASA Contract NAS 7-100, sponsored by the National Aeronautics and Space Administration.

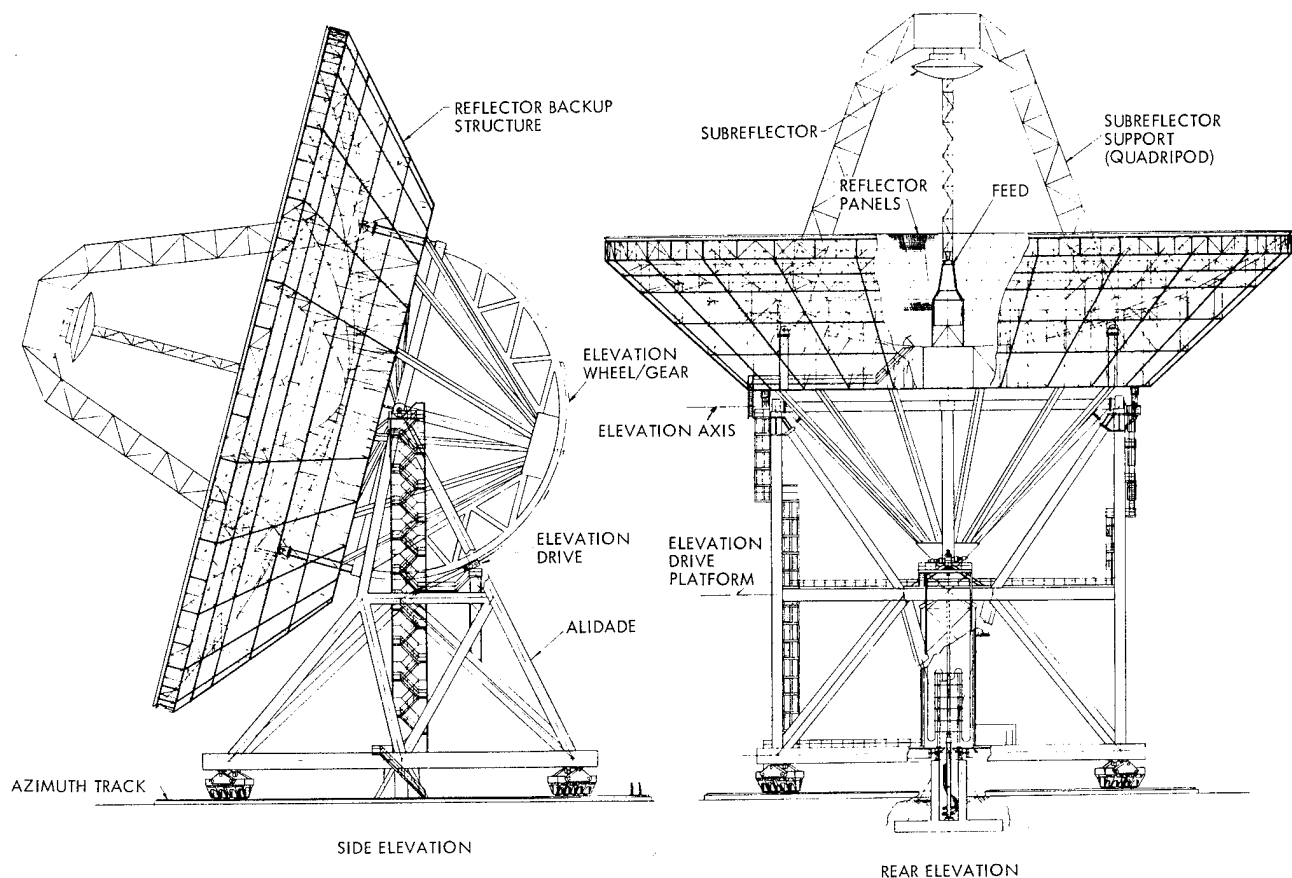


Figure 1. Configuration of 100-m-diameter antenna system

#### SOURCES OF GAIN REDUCTION

Table 1 is a summary of the sources of gain reduction that have been considered for gravity or wind loading. Two categories are identified: the deformation-type category includes pathlength phase errors of the radiofrequency (RF) beam; the beam-deformation-type category covers pointing misalignment losses of the main beam with respect to the target.

Referring to the table, backup structure contribution is computed with respect to the paraboloid that best fits the deflected surface. Surface panel contributions are also considered with respect to a best-fitting surface. The subreflector offsets are the axial and lateral mismatches of the subreflector position from the focal point of the best-fitting paraboloid. For computational purposes, these offsets can be converted to equivalent additional backup structure deformations (Ref. 1). For gravity loading, which is repeatable and calibratable, the subreflector can be repositioned to the actual focal point, and thus the offsets produce no gain reduction. Subreflector surface deflections are another source of deformation-type losses. However, these will be disregarded because appropriate design can make them small.

The wind speeds are represented by the conventional model of a slowly varying, quasi-steady component and a superimposed gust turbulence. Beam deviation error that results from the steady component of the wind speed is corrected by a programmed pattern search that removes these low-frequency pointing errors. We make a conservative assumption, however, that the pattern search is too slow to overcome the gust effects, so that gust loading always produces gain reductions through beam deviations. The pointing errors from gravity loading can be overcome by calibration that compensates the input command signal. The servo loop error occurs because the servo system is not fully effective in compensating for the higher-frequency components of the gust disturbance torque.

#### REFLECTOR DESIGN SYNTHESIS

The baseline reflector backup structure design was developed by an evolutionary process. Although the JPL-IDEAS computer program (Ref. 2) was used as a pivotal design tool to perform analysis and optimization of member cross-sectional area selection, no software was available to optimize the geometrical proportions for this structure. Consequently these proportions were developed from a sequence of trial variations of

Table 1. Gravity and wind loading contributions to gain reduction

Source	Gravity loading <sup>a</sup>	Wind loading	
		Steady wind	Gust wind
A. Deformation type			
Backup structure deflection	Contr	Contr	Contr
Surface panel deflection	Contr	Contr	Contr
Subreflector offsets	Comp	Contr	Contr
B. Beam deviation type			
Backup structure pointing error	Calib	Corr	Contr
Alidade pointing error	Calib	Corr	Contr
Servo loop error	None	None	Contr

<sup>a</sup>Contr - Contributes to gain reduction  
Comp - Compensated by subreflector repositioning  
Calib - Calibration used to modify the commanded position  
Corr - Corrected by programmed pattern search

the geometry. The variations were tested by analysis and member area redesign within the IDEAS program to assess their ultimate potential.

The ordinarily laborious and time-consuming task of preparing the extensive data card sets required for structural computer analysis was expedited by a program that automatically generated these cards for each variation. This program supplies almost all of the card images needed to describe reflector backup structures of the conventional radial rib truss and circumferential hoop type of construction. The sequence of trial geometry generation and subsequent testing entails generation and processing of an extensive data bank; nevertheless, it is executed rapidly. Furthermore, only a limited amount of effort by the engineer is needed. His participation is required primarily for decision-making to guide the operations and to select from among the many options available to him, with only a small requirement for time to be spent on clerical tasks.

The root mean square (rms) pathlength deviation of the reflector surface from the best-fitting paraboloid was selected as the performance measure for design evaluation. The goal was to achieve a reasonable balance between response to gravity loading and response to wind loading. For the gravity loading, the objective response was the average of the rms values over the elevation angle range weighted by tracking mission

probabilities (Ref. 3) associated with the elevation angles. A criterion wind-loading case was established to represent the condition of the antenna at the 60-deg elevation angle with a rear wind at an arbitrary reference speed of 13.4 m/sec (30 mph). Previous experience with similar antennas indicated that this wind orientation was likely to be the most severe. During all of the redesign iterations, member area selections were subjected to constraints on stress and buckling for the gravity loading, for the criterion wind loading, and for additional wind loadings that represented the most severe operational wind (31.3 m/sec) and the survival wind (44.7 m/sec).

The geometry evolved for the baseline design resulted in a nearly homologous response (Ref. 4) for gravity loading and a very good surface rms (0.69 mm) for the criterion wind loading. Two lighter-weight variations of the basic design were developed by permitting a degeneration of performance for the criterion wind loading but at the same time retaining the stress and buckling constraints for all loads and by invoking a new constraint that maintained the performance for the gravity loading. The weight of the backup structure and counterweight for the baseline design was 1210 tons, and the lighter designs produced reductions of 200 and 335 tons with the wind criterion loading rms values of 0.86 mm and 0.93 mm respectively.

The alidade comprises a much less complex analytical model than the reflector. The few data cards required for analysis and redesign were hand-generated. The final geometry also entailed evolutionary proportioning to achieve a favorable arrangement. Analysis and member redesign were performed by the IDEAS program using an option invoked to maximize stiffness with respect to pointing accuracy for wind loading. Only one alidade design was developed, and this is used to support all three of the backup structures.

The alidade model was eventually converted for analysis by the NASTRAN program (Ref. 5). This was done for the convenience of having a direct output of specific internal rotation angles related to the servo loop wind gust error. The NASTRAN program analysis included the bending stiffness of the alidade bars, which is presently not possible within the IDEAS program. Nevertheless, responses from the two programs agreed closely, indicating that the bending rigidity is not significant.

#### COMPUTATIONAL MODEL FOR WIND LOADING GAIN REDUCTION

A multidimensional four-component statistical model was used for computation of gain reduction due to wind loading. The four random components were (1) V, the mean wind speed; (2) v, a superimposed gust turbulence; (3) AZ, the azimuth of the wind relative to the antenna pointing direction; (4) EL, the elevation of the antenna relative to the horizon.

The mean speed has slow variations that comprise periodic components measured by hours or days. Statistics of the mean speed obtained for the same site (Goldstone, California) as the proposed 100-m antenna have been tabulated in Ref. 6.

The gust speed was described by the conventional model, which represents the gusts as gaussian, with zero mean and standard deviation  $\sigma_v$  proportional to the mean speed; e.g.,

$$\sigma_v = CV \quad (1)$$

The tabulated mean speeds are based upon observations at a 46-m (150-ft) height above ground. For convenience, the mean speeds here are also considered at the same height. Estimating the surface drag coefficient at 0.006 for the proposed terrain and using the computed power law coefficient for speed variations with height equal to 0.1405 (Ref. 6), we find  $C = 0.1533$ .

Gusts are the dynamic component of the wind speed. Spectral decompositions according to conventional models (Refs. 7, 8) show that the predominant fluctuations are characterized by periods in the order of several seconds to minutes. The natural frequency of the antenna-reflector system of Fig. 1 will be at least 1 Hz for the slowest natural mode. The response of such a system to both the mean speed and the gust speed is essentially the same as for static load application. Consequently the structural response can be computed as a static response to total wind loading  $V$  where

$$\underline{V} = V + v \quad (2)$$

Wind tunnel test data on antenna reflector and alidade components (Refs. 9, 10) were used to convert from wind speeds to pressure loadings on the proposed reflector and alidade structures. Wind tunnel tests are a logical and reasonable basis for deriving the pressures and forces for the mean components of the wind speeds. Nevertheless, it is recognized that using the same type of conversion for gust effects is a major assumption and simplification of this model. The gust speeds actually have a three-dimensional spatial correlation for which theoretical models require further development. A possible approach to providing a better estimate of the gust loading is available through computer simulation (Ref. 11). However, it was estimated that the application of this approach would have entailed a major additional computational effort and also more wind tunnel test data than is currently available. Nevertheless, despite the simplified representation for gust loading, the present work employs the same formulation to compare alternative designs and should furnish a reasonable basis for comparison.

The distribution of wind azimuths relative to the antenna was also simplified in this model by assuming a uniform distribution in the range of azimuths from 0 to 360 deg. Because of symmetry, only half of this range is considered in the calculations. Had statistics been available to describe the distribution of wind azimuths at the proposed site, it would have been possible to determine a more accurate distribution of relative wind azimuths in conjunction with analysis of the statistics of proposed antenna targets. The related uncertainty in the assumption of uniform relative azimuths does not appear to be sufficient to undertake the additional computational complexity.

The distribution of antenna elevations was considered for elevations in the range of 0 to 90 degrees. Probability densities of the elevation angles were available from analysis of composite statistics of planetary tracking missions (Ref. 3).

For computational purposes, discretization of the four random components into specific class marks and class intervals was as follows:

1. Mean speed,  $V$ ; 0 to 22.35 m/sec (50 mph) at intervals of 2.235 m/sec (5.0 mph). 10 terms.
2. Gust speed,  $v$ ; -4 to +4 standard deviations. 19 terms unevenly spaced with finest resolution in the vicinity of 0 standard deviations.
3. Relative azimuth,  $AZ$ ; 0, 30, 60, 90, 120, 150, 180 deg. 7 terms.
4. Antenna elevation,  $E1$ ; 0, 30, 60, 90 deg. 4 terms.

The computational results are represented by cumulative probability distributions of gain reduction. The distributions cover the range of 0 to 4 decibels (dB) at 100 discrete increments of 0.04 dB. Conditional distributions ( $10 \times 7 \times 4 = 280$ ) were developed for each combination of mean speed (including the related gust probability), azimuth, and elevation angle. The final distributions were the composite of the conditional distributions weighted by the probability associated with the mean speed, azimuth, and elevation class marks. This very simple method of combining the conditional distributions is permissible from the assumption of independence of wind speed, azimuth, and elevation angles.

#### COMPUTATION OF GAIN REDUCTION DISTRIBUTION

The computational method used to compute a typical gain reduction conditional probability distribution will be described here. Each of these distributions represents the random effects of wind gusts and is conditioned upon specific values of mean wind speed, wind azimuth, and antenna elevation.

With reference to gain reduction categories A and B of Table 1, the wind pressures, and consequently the forces, are proportional to the square of the wind speed. The deformations and deviations (pointing angle errors) are proportional to the forces. Gain reductions for category A are proportional to the squares of the deformation. Gain reductions for category B are proportional to the squares of the differences in deviations for the total wind speed minus the deviations for the mean wind. Consequently the gain reductions for these two categories can be represented as

$$G_A = G_R (V/V_0)^4 \quad (3)$$

$$G_B = G_P (V^2 - V_0^2)^2 / V_0^4 \quad (4)$$

in which

$G_A, G_B$  = category A, B, gain reduction

$V_0$  = reference mean wind speed

$V$  = total (mean + gust) speed

$V$  = mean speed

$G_R$  = category A gain reduction at reference speed

$G_P$  = category B gain reduction computed for  $V_0$  and not allowing correction for the mean speed. Thus  $G_P$  is equivalent to a "blind pointing" loss for  $V_0$ .

To obtain a convenient computational formula, the gust speed  $v$  is replaced by a standardized normal variate  $Z$  such that

$$Z = v/\sigma_v \quad (5)$$

Then from Eq. 1

$$v = CZV \quad (6)$$

and from Eq. 2

$$\underline{V} = V(1 + CZ) \quad (7)$$

From these relationships, Eqs. 3 and 4 can be combined so that the total gain reduction  $G_T$ , which is the sum of  $G_A$  and  $G_B$ , can be expressed as

$$G_T = (G_R f_R + G_P f_P) \cdot (V/V_0)^4 \quad (8)$$

where

$$f_R = 1 + 4 CZ + 6(CZ)^2 + 4(CZ)^3 + (CZ)^4 \quad (9)$$

$$f_P = 4(CZ)^2 + 4(CZ)^3 + (CZ)^4 \quad (10)$$

The conditional distribution for gain reduction,  $F(G_T)$ , can then be obtained from Eq. 8, using the relationships of Eqs. 9 and 10. Although the procedure is automated within a digital computer program, equivalent operations can be illustrated graphically with respect to Fig. 2 as follows:

- ① Compute  $G_T$  for a set of values of  $Z$  in the range  $(-4, +4)$  and plot  $G_T$  vs  $Z$ , as in Fig. 2a.
- ② At a selected value of gain reduction  $G_{Ti}$ , find the intersections of  $G_{Ti}$  with the curve in ①.
- ③④ Project the intersections down to the curve in Fig. 2b. This curve is constructed to be the standard normal cumulative probability distribution of  $Z$ . Read the ordinates where the projections intersect the curve.
- ⑤ The value of the distribution of gain reduction at  $G_{Ti}$  is the difference in the ordinates read from the curve of Fig. 2b.

#### COMPUTATIONAL PROCEDURE

Figure 3 contains a schematic diagram of the complete computational procedures used to derive

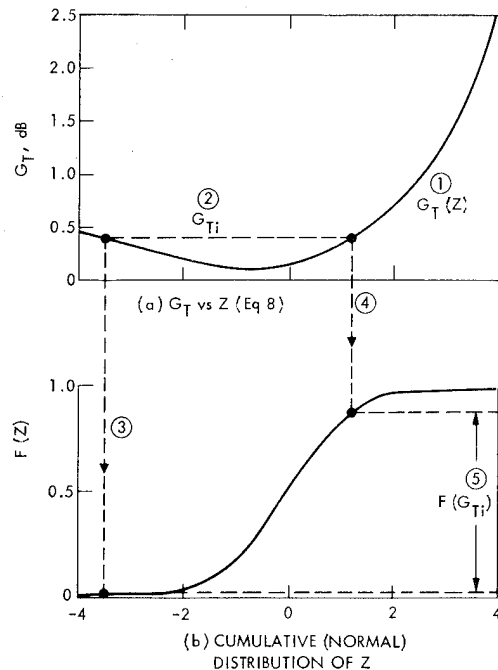


Figure 2. Development of cumulative distribution of  $G_T$



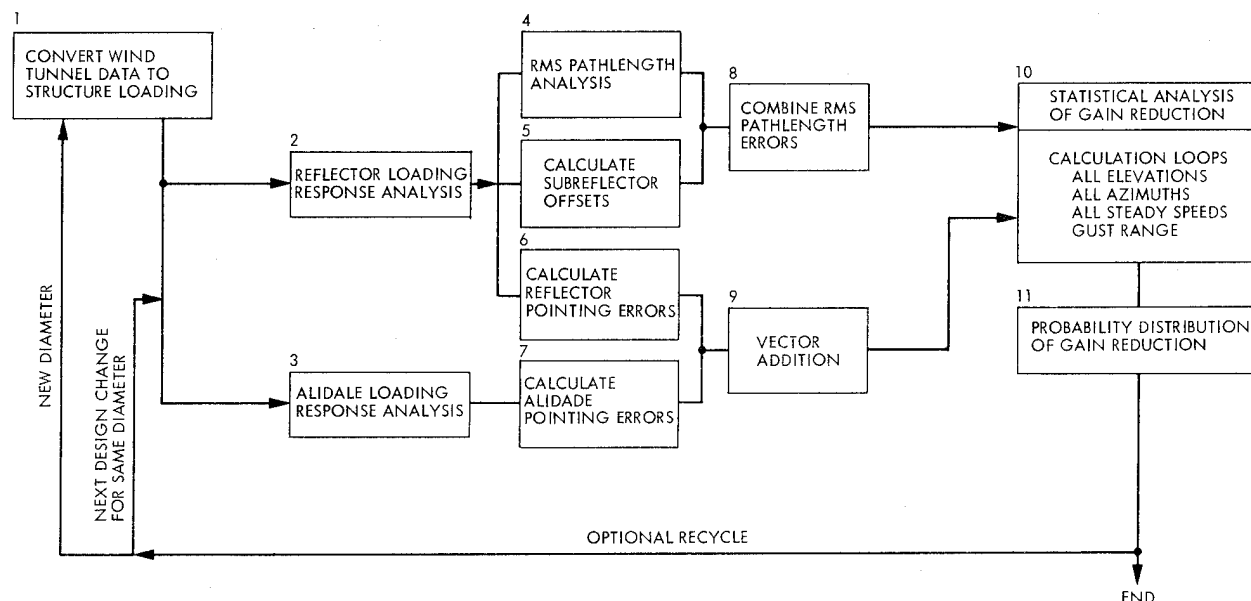


Figure 3. Computational procedure

the gain reduction distribution for wind loading. The following notes apply to the labeled blocks of the figure:

**Block 1.** Wind tunnel pressure distribution data for specific relative wind attitudes with respect to the antenna are converted to the force data required as input for reflector analysis. The forces are represented by the three Cartesian coordinates at each node and are derived from the interpolated wind pressures, the surface area tributary to the node, and the components of the unit vector normal to the surface. Development of force data, except for the interpolation, is automated. Wind loading on the structural members of the alidade is also developed from wind tunnel data. For both reflector and alidade, sets of loads are developed to correspond with the discretization of wind azimuth and antenna elevation.

**Block 2.** The reflector is analyzed by the IDEAS program to supply the responses to the wind loadings. The program is used here for analysis only, by specifying no redesign cycles.

**Block 3.** The alidade is analyzed by the NASTRAN program to find the response for the wind loadings. Wind reactions of the reflector on the alidade are included.

**Block 4.** Computation of pathlength deviations from the best-fitting paraboloid are automated within IDEAS.

**Block 5.** Gain reductions for subreflector offsets are calculated by hand, using results from the reflector analysis.

**Block 6.** Reflector contributions to the pointing errors are automated within a separate

computer program. Results are assembled within a matrix (4 elevations X 7 azimuths).

**Block 7.** Alidade contributions to pointing error and to servo loop are hand-computed (presently) and assembled within matrices.

**Block 8.** The category A (deformation-type) gain reductions are combined by hand calculation. These individual  $G_R$  terms (Eq. 3) are assembled within a matrix.

**Block 9.** A computer program derives a matrix containing the  $G_p$  terms (Eq. 4). In the preceding blocks, the alidade and reflector pointing deviations have been computed with separate components for the elevation and cross-elevation axes. Vector addition is required to combine the separate components.

**Block 10.** The  $G_R$  and  $G_p$  matrices are input. A computer program develops conditional distributions for gain loss, described previously, for all 280 combinations of mean wind speed, wind azimuth, and antenna elevation.

**Block 11.** The computer program of Block 10 applies probability weighting factors for mean speed, wind azimuth, and antenna elevation to the conditional distributions and assembles the composite distribution of gain reduction for wind loading.

## RESULTS AND CONCLUSIONS

Figure 4 shows the distribution of gain reduction for wind loading for the baseline 100-m antenna system and the two alternative designs with lighter reflector backup structures. As

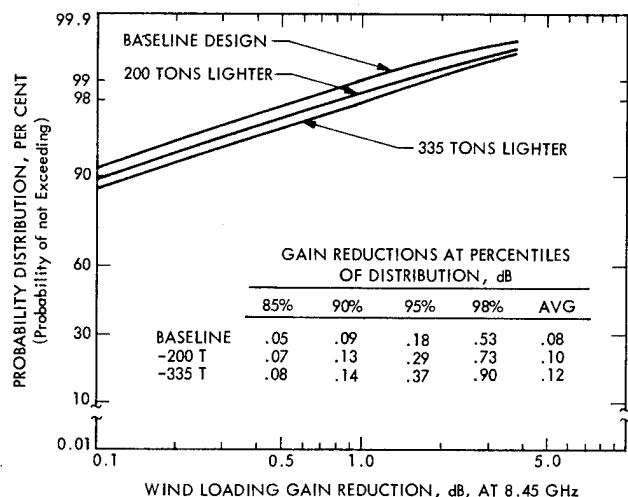


Figure 4. Gain reductions for 100-m design variations

stated previously, all designs provide equivalent high performance for gravity loading.

For ready reference, Fig. 4 tabulates reductions at a few selected percentiles of the distribution. It can be noted, for example, that the reduction in weight of 335 tons for the lightest structure is achieved with a reduction in performance of 0.37 dB (8% loss in efficiency) at the 98th percentile, and with much smaller reductions at lower percentiles. On the average, the table shows this design to be only 0.04 dB worse than the baseline.

Whether or not the lightest design shown, or possibly a design lighter than any of these, will be adopted must be considered in view of the performance requirements for the entire system. Tracking mission requirements and desired reliability in conjunction with other sources of gain reduction must be integrated within this type of evaluation.

#### REFERENCES

1. Katow, M. S., "Evaluating Computed Distortions of Parabolic Reflectors," Mechanical Engineering in Radar Symposium, Nov. 8-10, 1977, Washington D.C. (this symposium).
2. Levy, R., "Computer-Aided Design of Antenna Structures and Components," Computers and Structures, Vol. 6, pp. 419-428, Pergamon Press, 1976.
3. Levy, R., "Antenna Bias Rigging for Performance Objective," Mechanical Engineering in Radar Symposium, Nov. 8-10, 1977, Washington D.C. (this symposium).
4. Von Hoerner, S. "Homologous Deformations of Tilttable Telescopes," J. Struct. Div., Proc. ASCE 93(ST-5), Proc. Paper 5529, pp. 461-485.
5. The NASTRAN User's Manual, NASA SP-222(01), C. W. McCormick, editor, May 1973.
6. Levy, R., and McGinness, H., Wind Power Prediction Models, JPL TM 33-802 Jet Propulsion Laboratory, Pasadena, California, Nov. 1976.
7. Davenport, A. G., "The Spectrum of Horizontal Gustiness Near the Ground in High Winds," Quarterly Journal of the Royal Meteorological Society, London, Vol. 87, Aug. 1961, pp. 194-211.
8. Hino, M., "Spectrum of Gusty Wind," Proceedings of the Third Conference on Wind Effects on Buildings and Structures, Tokyo, Japan, Sept. 6-11, 1971, pp. 69-78.
9. Fox, N. L., Load Distributions on the Surface of Paraboloidal Reflector Antennas, Internal Memorandum JPL-CP 4, Jet Propulsion Laboratory, Pasadena, California, July 1962 (JPL internal document).
10. Blaylock, R. B., Aerodynamic Coefficients for A Model of A Paraboloidal-Reflector, Internal Memorandum JPL-CP6, Jet Propulsion Laboratory, Pasadena, California, May 1964 (JPL internal document).
11. Shinozuka, M. S., and Levy, R., "Digital Generation of Alongwind Velocity Field," J. Engineering Mechanics Div., Proc. ASCE 103 (EM-4), Proc. Paper 13159, Aug. 1977, pp. 689-700.

## AN/TPS-59 - A UNIQUE TACTICAL RADAR

L. E. BERTZ & L. J. HAYES

General Electric Company  
Electronic Systems Division  
Court Street Plant  
Syracuse, N. Y. 13221

### ABSTRACT

The AN/TPS-59 is a recently developed 3-D tactical radar that has unique and advanced state-of-the-art features. This paper presents a brief system overview along with pertinent mechanical design constraints and features. Significant events in the development of the AN/TPS-59 radar are discussed and spin-off system configurations are described.

### INTRODUCTION

In June 1972, the Electronic Systems Division of the General Electric Company was awarded a contract by the Naval Electronic Systems Command to build an Engineering Development Model (EDM) of the AN/TPS-59 long-range, 3-D, L-band, air defense radar for the U. S. Marine Corps. This first system, shown in figure 1, was delivered for service test in mid-1976.

The AN/TPS-59 is unique in many ways. Its RF electronics, including the transmitter, are totally solid-state. Performance, notably in the areas of detectability in clutter, low-angle height finding, reliability, and maintainability is substantially better than that of any other tactical radar. Innovative mechanical design features enable the radar to meet stringent environment, mobility, and light-weight requirements.

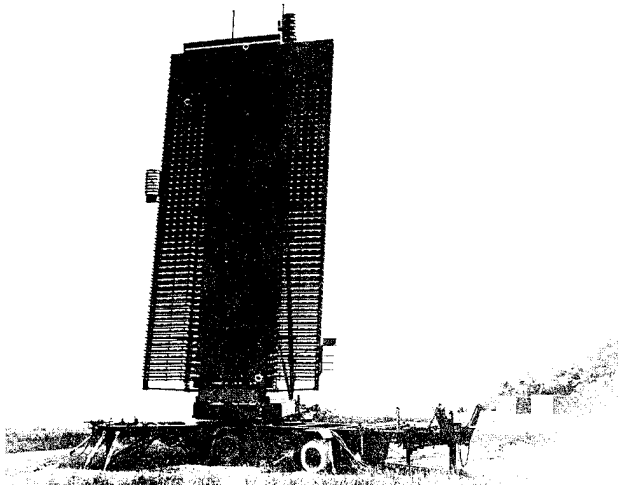


Figure 1. AN/TPS-59 Radar System

### MISSION

The primary mission of the AN/TPS-59 is to provide long-range surveillance of a tactical air space.

In addition the radar's detectability, tricoordinate accuracy, and console readouts and controls fulfill the requirements for autonomous support of a ground control intercept mission. Its high data rate capability supports the third mission of air traffic control.

The radar is designed to detect 500 targets per 10-second scan. The target model contains 1-m<sup>2</sup> scan-to-scan fluctuating targets flying at speeds up to Mach 4. The anti-clutter capability of the radar allows maintenance of full detectability against a simultaneous weather and ground clutter threat.

### PERFORMANCE

Table 1 lists salient performance characteristics of the AN/TPS-59.

TABLE 1  
PERFORMANCE SUMMARY

Parameter	Performance Level	Notes
Frequency	1215-1400 MHz	With pulse-to-pulse frequency agility
Surveillance	360° azimuth 6-540 km range 0-19° elevation 10,000 ft altitude	Elevation coverage may be shifted electronically in 0.25° steps
Frame Time	10 or 5 seconds	
Detectability	P <sub>D</sub> = 0.9 within 360 km = 0.7 from 360-450 km FAR = 5 per scan	Against a 1-m <sup>2</sup> fluctuating target
Resolution	Range = 61 m Azimuth = 3.2° Elevation = 1.6°	
Accuracy	Range = 24 m Azimuth = 3 mrad Elevation = 1.7 mrad	The approximately 17 to 1 beamsplitting is achieved with monopulse processing
Reliability	MTBF = 1000 hours	Calculation excludes IFF, prime power generation and shelter air conditioning and assumes a 600 hour preventive maintenance cycle
Maintainability	MTTR = 40 minutes	Maintenance performed by a two-man team
Weight	System = 13,600 kg Max Package = 2900 kg	
Prime Power Utilization	89 kW	Includes 23 kW for shelter air conditioning

### COMPONENT IDENTIFICATION

The AN/TPS-59 consists of a self-erecting antenna assembly and two equipment shelters.

The antenna assembly is transported on three single-axle trailers which are joined together in a Y-configuration to form a stable base during system operation. The solid-state transmitter and receiver equipment is antenna mounted above the azimuth bearing. A separate IFF trough antenna and three auxiliary sub-arrays are mounted on the main array structure.

The processing and display equipment is housed in two standard S-280 military shelters. The Radar Control Shelter, shown in figure 2, accommodates the two position display console and the data processing subsystem, which includes an AN/UYK-7 Computer. The Signal Processor Shelter houses a waveform generator/pre-processor cabinet and a three-bay digital processor cabinet.

Separately packaged prime power generators and shelter air conditioning units complete the system configuration.

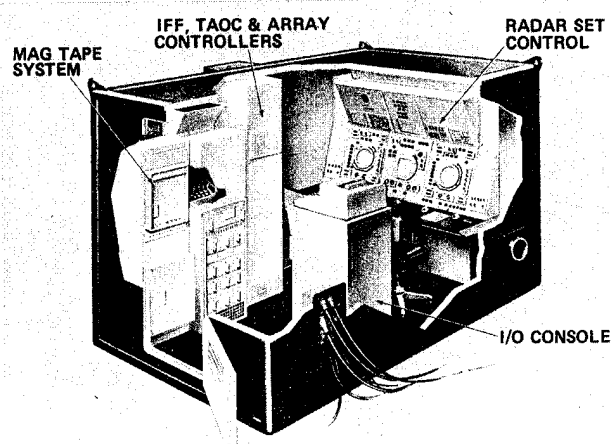


Figure 2. Radar Control Shelter

#### MECHANICAL DESIGN CONSTRAINTS

The AN/TPS-59 is designed to meet the general Navy specification for electronic equipment MIL-E-16400, except as modified in the ELEX-R-50 procurement specification.

The specified environmental conditions given in Table 2 had a significant impact on the design of the system.

TABLE 2  
ENVIRONMENTAL CONDITIONS

Temperature - Operation -54°C to +50°C Storage - 62°C to +75°C	
Relative Humidity - Operation and Storage 0-95%	
Wind - Normal Operation (Non-degraded)	0-50 knots
Operation (degraded)	50-75 knots
Survival (Non-Operating lowered)	75-100 Knots
Transport	0-120 knots
Wind and Ice - Operation (degraded)	75 knots and 3.5 PSF ice
Survival/Transport	100/120 knots and 3.5 PSF ice
Altitude - Operation	0-10,000 ft.
Air transport	0-45,000 ft.
Sand and Dust - Particle size 10 to 150 microns	
Shock and Vibration - As encountered during transport and service.	

The mobility specifications greatly influenced the mechanical design and system configuration. Requirements for transport by helicopter, 2-1/2-ton truck, C-130 aircraft, rail and ship dictated transport package size and weight. System assembly within one hour and disassembly in one-half hour combined with the requirement for self-erecting provisions to pose a formidable mechanical design constraint.

Stringent reliability and maintainability requirements, including the 1000-hour MTBF and 40-minute MTTR, necessitate fault locating and built-in-test features as well as modular packaging for the AN/TPS-59.

#### MECHANICAL DESIGN FEATURES

Although the packaging of AN/TPS-59 shelter-housed equipment reflects many state-of-the-art innovations, the antenna design incorporates more unique mechanical design features. This paper limits itself to description of antenna features.

##### Overall Antenna Design

The AN/TPS-59 antenna array, shown in figure 3, measures 9.1 m (30 ft) high by 4.7 m (15.5 ft) wide. When operational, the bottom of the array stands 2.1 m (7 ft) above ground level.

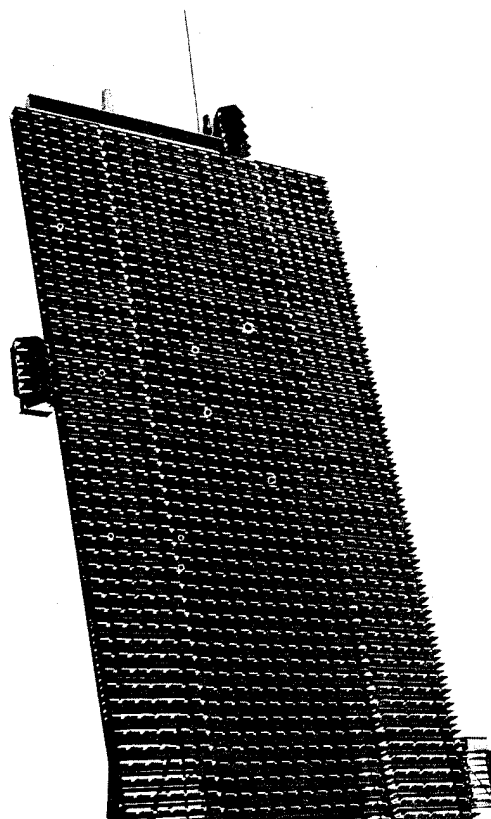


Figure 3. Antenna Array

The array is composed of 54 identical row feed assemblies and associated row electronics and transmitter power supply units. The row electronics, or transceiver unit, consists of the solid-state transmitter, receiver preamplifier, phase shifters, duplexer, and logic control. It is housed in a single package directly

behind the center section of each feed assembly. Row power supplies are individually packaged and mounted on alternate sides of the transceiver units. The vertical, or row-to-row, signal distribution, is accomplished by three stripline column feeds.

The RF exciter, final receiver, and array control circuitry are located in enclosures on the rotating support platform below the array.

Figure 4 shows the antenna array block diagram. Figure 5 identifies the major electronic components via a rear view of the array.

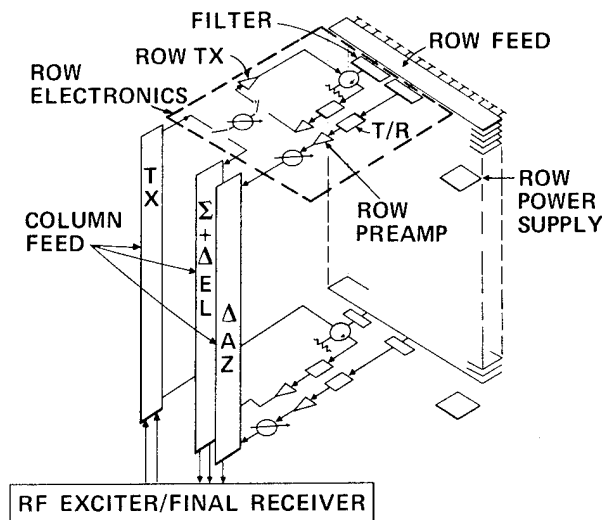


Figure 4. Antenna Array Block Diagram

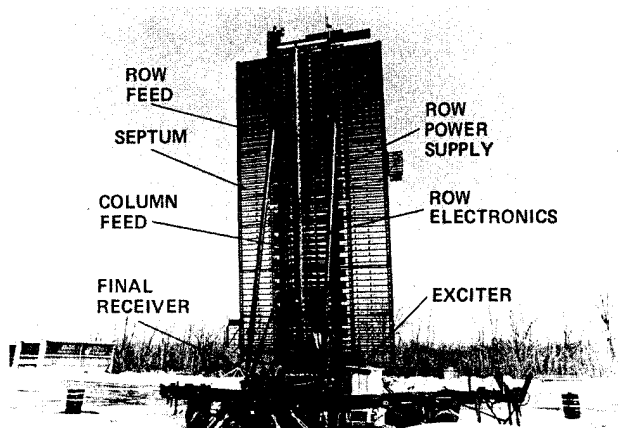


Figure 5. Rear View of Antenna

The physical proximity between row transmitter output and radiating elements, and between receiving elements and row preamplifiers, minimizes losses and system noise temperature. This translates to a 50 percent or more reduction in required prime power relative to a more conventional tube radar performing a comparable mission.

The main array is divided into two sections for transport, with 26 and 28 row feed and electronic assemblies in the lower and upper sections, respectively.

Each row feed assembly is made up of a stripline row feed network and a ground plane septum. The assembly is segmented into a 2.4-m (8-ft) center section

and two 1.1-m (3.75-ft) outboard wing sections, as shown in figure 6. An RF hinge permits the wings to fold without breaking an RF connection. Groups of 8 or 10 wing sections are structurally joined on the array to facilitate rapid folding and nesting of the wings into the fixed center sections for transport. Telescoping tubes support the extended wing assemblies during operation.

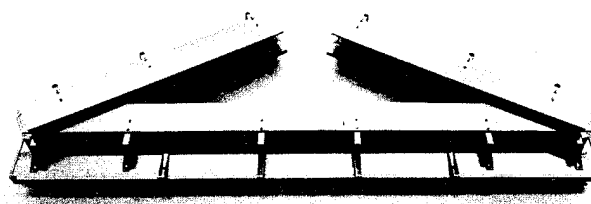


Figure 6. Row Feed with Ground Plane Septa

The array construction has an openness not found in conventional L-band or higher-frequency antennas. The 2.5-cm (1-in.)-thick row feed networks are spaced on 16.8-cm (6.6-in.) centers. The intermediately spaced septa, each measuring 0.6 cm (0.25 in.) thick, provide an electrically solid-surface ground plane that is mechanically open for minimum wind resistance. The array openness also provides for natural anti-icing.

Wind tunnel testing at the Cornell Aeronautical Laboratory on a 1/10 scale model showed a 40 percent reduction in wind forces for the AN/TPS-59 antenna as compared to a solid-surface array. Forces and moment coefficients derived from the wind tunnel test were used in subsequent structural analysis of the antenna.

Exposure of the AN/TPS-59 EDM to upper New York State winters has further demonstrated the effectiveness of the open array configuration. Minimum deflection was measured under high winds, and snow and ice build-up was minimal.

#### Row Feed

Figure 7 shows a partially folded row feed network and center-section stripline circuit board. The row feed is a lightweight single-layer stripline circuit etched on teflon glass and centered between ground planes by dielectric foam. Structural rigidity and light weight were achieved using balsa-core aluminum and crushed honeycomb ground plane panels. The assembly is sealed with RTV sealant and the 24 stripline dipoles in each row feed are protected from physical and environmental damage by Lexan plastic covers.

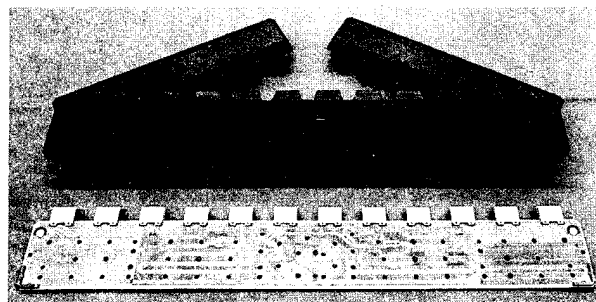


Figure 7. Row Feed Network

## Row Electronics

Each of the 54 row transceivers are identical with the unit shown in figure 8. The upper level, photographed with top panel removed, houses all of the low-power RF circuitry. The lower level accommodates 22 RF power modules, which are mounted on the upper surface of three bottom covers. The power modules slide into place between rails and are held against the heat sink cover with springs. The module design prohibits backward or upside-down installation. Leaf spring contact to each module and weather seal are accomplished when a cover is closed. Cover travel is limited to prohibit foreign materials or fingers from damaging the module contact area. Two quick-disconnect latches secure each cover and facilitate on-array power module replacement.

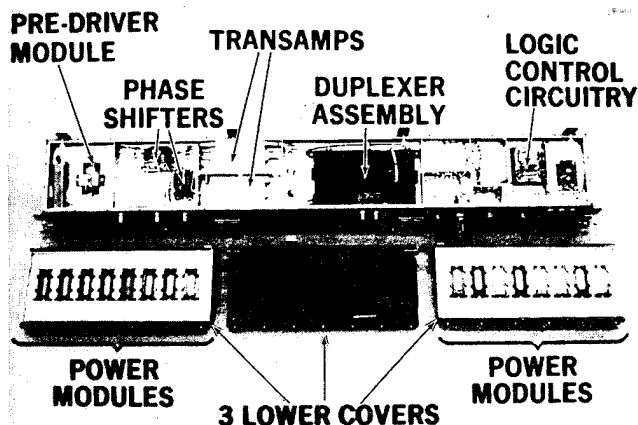


Figure 8. Row Electronics Assembly

Transceiver waste heat is removed from the aluminum finned covers via forced convection. Duplex fan units are located on both sides of the array transceivers, as shown in figure 5. Each fan draws air from the center and cools one-half of two transceivers. The exhausted air is then used to cool the row power supplies, which are mounted outboard of the fan units and array support channels. The power supplies have a finned area which protrudes through an opening in the support channel into the fan air stream. Heat conduction into the aluminum channels aids in power supply cooling.

A row power supply unit provides regulated 28 V at 120 A to each row transmitter. Its efficiency from the 400-Hz input to the dc output is 75 percent. The 12.7-kg (28-lb) row power supply, shown in figure 9, reflects efficient high-density packaging. The low-level dc voltage associated with the solid-state transmitter enhances AN/TPS-59 maintenance safety.

## Array Support Structure

Support for the array electronics is provided by a composite beam structure consisting of two 12-in. 7075T6 aluminum channels spaced by cross-tubes and flanges. The row feed networks are secured to each channel and flanged on the ends with vertical stringers. Six vertical angles also tie into each row feed network and provide the mounting members for the row electronics. All structural connections are bolted.

A quick-disconnect clamp was designed for the upper-to-lower array section splice. A V-bar clamp with spring-loaded bolts was chosen to resist a moment

load in excess of 250 in.-kips. Analysis and testing of the stainless steel clamp showed adequate safety margin under maximum load.

Access to the row electronics units on the array is accomplished with a service lift, which stores for transport on the lower array section. The 227-kg (500-lb) capacity lift is permanently attached to the main support channels and it facilitates personnel travel up or down the back of the erected array in less than 5 minutes.

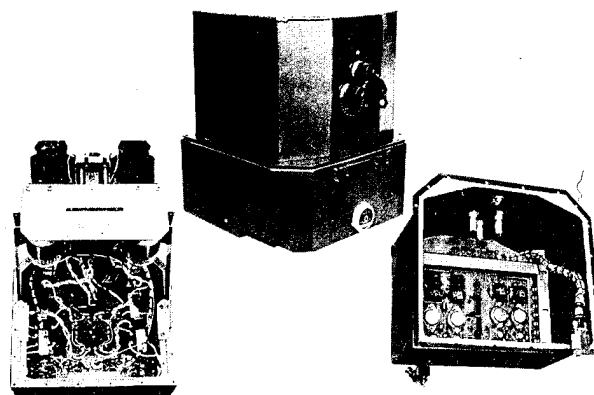


Figure 9. Row Power Supply

## Erection Mechanism

The antenna is raised to its operational position above the azimuth platform via dual telescoping ball-screws. The ballscrews are trunion mounted to the platform and are driven by a double-ended electric motor/gear box unit. Travel time is approximately 5 minutes. The erection mechanism is equipped with a brake and a hand crank is provided for fine positioning and emergency lowering. The ballscrews can raise or lower the antenna in 50- or 75-knot winds, respectively.

Two aluminum backstay members along with the ballscrews support the erected array. The backstays are sectioned into three 2.4-m (8-ft) lengths. Two of the three sections are joined and utilized as a load spreader-bar for helicopter lift of an array section trailer. Figure 10 shows the backstay and nesting of the array feeds for transport.



Figure 10. Transport Configuration

## Azimuth Platform and Drive

The azimuth platform, shown in previously referenced figure 5, supports the antenna and platform electronic enclosures. The aluminum platform is rotated at 6 or 12 rpm by a drive system consisting of a

5-HP 6000/12000-rpm motor, a 100:1 gear box, and a 10:1 pinion-to-bull gear. Platform loads are transmitted through a 1-m (40-in.) diameter X-roller bearing to a rigid structural base formed by the three joined trailers. Locking pins secure the antenna and a hand crank is provided for unpowered azimuth positioning.

An RF rotary joint is provided for IFF signal transfer, and a slipping assembly in the azimuth platform accommodates all other signal and power transfer to the rotating antenna assembly. An azimuth encoder provides position data.

Antenna deflection measurements are made with a tilt sensor located on the azimuth platform at the center of rotation. The sensor is an electromagnetic pendulous vertical sensor with a time constant of 50 milliseconds. The output is fed continuously to the system computer for real-time correction of height accuracy.

#### Platform Electronics

The three platform electronic enclosures shown in figure 5 house the exciter, receiver, and antenna control circuitry. The enclosures are shock mounted and weather tight. The inside ambients are controlled via thermostatically controlled heaters and cooling fans with air-to-air heat exchanger. Insulation and solar reflecting paint aid in environment control.

#### Trailers

Three single-axle trailers, meeting military running gear requirements, are used for antenna transport. Two trailers each carry an array section, and the third has the azimuth platform and drive as an integral assembly. Ancillary equipment items are attached to the trailers.

When joined together in a Y-configuration, the trailers form a stable base for antenna operation. Rugged guides provide alignment during trailer assembly, and the trailers are secured together via three swing bolts per joint, two joints per trailer.

The antenna/trailer assembly is leveled on three legs with hydraulic jacks. A spirit level is used for initial set-up followed by use of the tilt sensor for fine leveling. Remote control of the three hydraulic cylinders facilitates rapid leveling.

After leveling, jam nuts are tightened on the support legs, and ground anchors are installed for high-wind overturning resistance.

Incorporation of dedicated trailers for the AN/TPS-59 results in minimum array segmenting, ease of assembly, enhanced mobility, and inherent shock and vibration isolation.

#### Erection Sequence

The design of the AN/TPS-59 facilitates assembly in one hour and disassembly in one-half hour. Figure 11 illustrates the sequence of events for antenna assembly. Self-erecting provisions and mechanical aids have eliminated the time-consuming "bull-work" normally associated with assembly of large tactical radars.

#### Structural Analysis

All structural members, splices, and joints were analyzed using the SOLID SAP finite element computer program. Backstay positioning and array

deflection modes were optimized for minimum RF side-lobe perturbation and boresight shift. A combined deflection budget of 0.1 degree or less was met in the structural design. The main structural members were sized for stiffness and minimum deflection.

Natural frequency and vibration mode shapes were determined with the SAMIS dynamic analysis computer program. The predicted natural frequency for the array is 7 Hz and for the trailer base is 1.3 Hz. A rotational exciting frequency of 0.2 to 0.4 Hz was calculated.

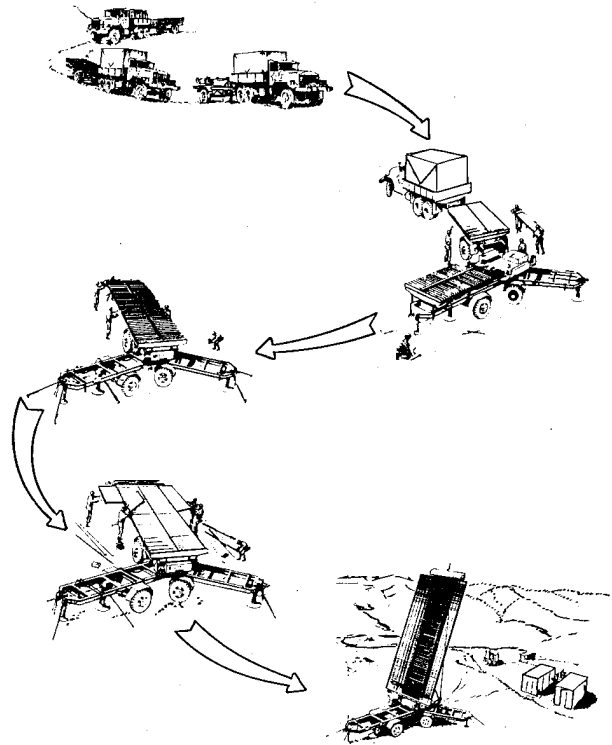


Figure 11. AN/TPS-59 Erection Sequence

#### Reliability and Maintainability

The high reliability of the AN/TPS-59 results from the use of high-reliability components, computer-aided diagnostics, and inherent redundancy. In fact, the system will achieve full performance even when its sensitivity falls 2 dB below the design condition.

Maintenance of the system is simplified by the automatic on-line performance monitoring (PM) and off-line fault location (FL) procedures. The PM process operates continuously, under computer control, using status messages and special loop tests scheduled between operational pulse repetition periods to evaluate all aspects of performance. A total of 469 special PM tests are run at a 6 percent duty factor to provide a thorough assessment of performance every 30 seconds. The performance state of the system is indicated on the Status Display in the Radar Control Shelter.

Having determined via computer diagnostics that sufficient degradation exists to warrant a shutdown for repair, the FL program is run after input to the computer from magnetic tape. It performs a large number

of internal loop tests which indicate the equipment area in which a fault occurred. Hard-copy output is provided on the teletype/printer.

Generally the faulted component is removed for bench repair. However, when a particular row transmitter is identified as a fault area, power module fault isolation is performed by maintenance personnel on the array service lift using a special power module tester. Having determined which module is defective, the particular cover is unlatched and the module is replaced with a simple tool.

Reliability and maintainability of the AN/TPS-59 are enhanced by the modular quality of the system.

#### SIGNIFICANT EVENTS

The AN/TPS-59 has been undergoing exposed field testing since the beginning of 1975 in the harsh central New York State environment and more recently in the heat and sea coast environment of southern California. It has experienced temperature extremes of  $-39^{\circ}\text{C}$  ( $-22^{\circ}\text{F}$ ) to  $+35^{\circ}\text{C}$  ( $+95^{\circ}\text{F}$ ), a good deal of rain (132 cm per year), heavy snow (305 cm per year), a severe ice storm, and a near miss (or slight hit) by lightning.

During this interval the radar has successfully performed pattern, EMI, and noise tests. Its detectability, in the clear and in clutter, are substantiated by more than 30 hours of controlled flight testing. Its reliability, maintainability, and availability have been substantiated by formal tests and by more than 18 months of 12-hour-per-day operation, during which only one scheduled test had to be postponed because of a radar failure.

Actual experience clearly indicates that the AN/TPS-59 meets electrical and mechanical requirements and degrades gradually and not catastrophically.

#### SPIN-OFF CONFIGURATIONS

The technology base and inherent modularity of the AN/TPS-59 has led to the design of a family of solid-state radars.

Figure 12 is an artist's concept of the GE 592 Air Defense Radar System. This system, based upon AN/TPS-59 technology, has been developed by General Electric for fixed installation applications. The first of these radars is now being produced for the Belgian Air Force. Since mobility is not required, the system utilizes a 7.3-m (24-ft) square array. It has 44 rows

instead of 54, and the row feed networks are 50 percent larger than their AN/TPS-59 counterparts; however, the row transceivers are in essence the same as employed on the AN/TPS-59.

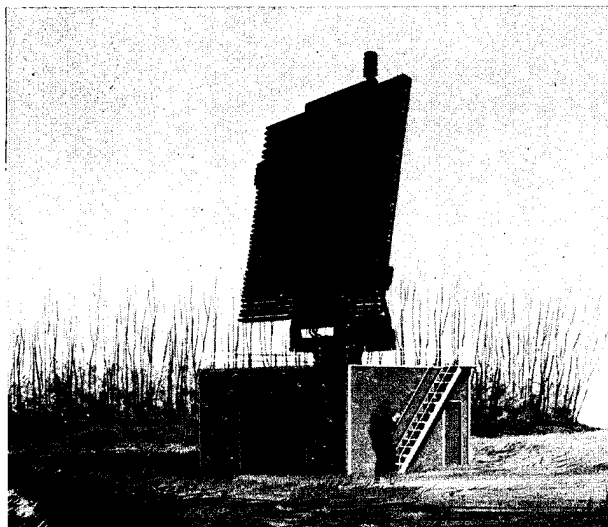


Figure 12. GE 592 Fixed-Site Radar

Figure 13 shows a short-range 3-D mobile radar concept. A single antenna trailer supports the 4.3-m (14-ft)-high by 4.9-m (16-ft)-wide array. The system uses 24 row feed networks and transceivers similar to those incorporated on the AN/TPS-59.

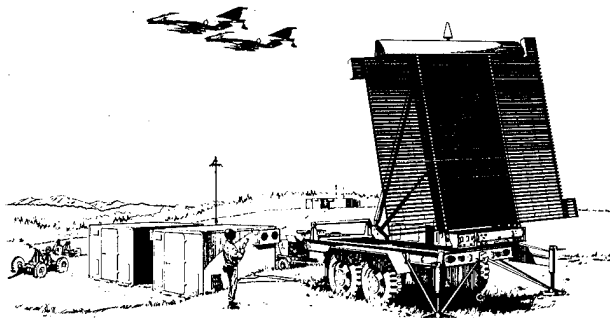


Figure 13. Short-Range Mobile Radar



## DEVELOPMENTS IN GROUND MOUNTED AIR SUPPORTED RADOMES

MILTON B. PUNNETT

Birdair Structures, Inc.  
2015 Walden Avenue  
Buffalo, New York 14225

### ABSTRACT

A review of some of the developments in air supported radomes which may be of interest for new designs. Variations in geometry and material are reviewed. Long term exposure results and electrical performance of Hypalon, vinyl, and Teflon coated materials are presented. Guidelines for reliable pressurization systems and methods of installation are outlined. The paper concludes with several examples of air supported radomes, varying from an 8 ft., highly portable, military unit to the 138 ft. diameter torus installed on the CN Tower.

### INTRODUCTION

Since the introduction of the first (AN/CPS 6B) air supported radome in 1948, many variations in geometry, materials, pressurization systems, and functional uses have been developed. Some of these variations were actually forecast in the "textbook" of radome engineering, "Design Manual for Spherical Air Supported Radomes," prepared by Walter W. Bird at Cornell Aeronautical Laboratory in 1956. However, others, such as a hybrid single/dual wall radome or the new Teflon coatings, were not even in the conceptual stage at that time. Surprisingly, the 50's marked the end of significant Government research funding directly in this field and most of the work reported in this paper has been developed to meet the real needs of actual applications. This report is intended to review these developments, to present some actual long term results, and to assist the radar designer in evaluating the potential use of a radome.

### GEOMETRY

The simple spherical shape is still the most prevalent for radomes. See Fig. (1). Based upon actual experience, a general rule has evolved that the height/diameter ratio for a single ply radome should not exceed .75 for stability in high winds; if the radome has a two ply fabric with a 45° diagonal bias to give shear restraint, the maximum height/diameter ratio is 0.85.

Frequently, the radome shape is modified to a prolate spheroid. Extremely prolate shapes should be carefully considered in the design analysis, but special radomes have been built where the height exceeded the diameter at the

equator ( $h/D > 1$ ). See Fig. (2). Generally, the prolate spheroid is selected to best match an antenna dish or array on a pedestal mount. Slightly prolate shapes are now common enough that computer generated patterning is available and the prolate, egg-shaped, radome can be fabricated as easily as a perfect sphere.

Conventional radome designs truncate the sphere horizontally at some base cutoff. This is not always the case. A 1/4 sphere segment radome has proved successful and shown that there are variations possible even with the sphere. Basically these consist of taking a "pie" cut from a spherical shape.

Toroidal, or doughnut-shaped radomes present another alternative. The usual radome application involves using only the outer portion of the toroidal ring and clamping at both the top and bottom. This then results in a stable shape with the vertical cross-section limited to a circular arc. The basic approach in such a design is to carry all stress loads vertically between the two clamps. This is achieved by using a low fill modulus fabric and patterning with the warp running vertical. Although it is conceivable to design a toroid where the vertical cross section is not a constant radius, such a design would inherently lack stability. An interesting point with the clamped toroid is that by stressing vertically there is very little tendency for a tear or cut across the generally weaker fill fabric direction to propagate. Ideally it would be possible to heavily unbalance the warp to fill threads to optimize the design for the minimum amount of material and resultant membrane thickness or mass.

The geometries mentioned are all single wall configurations. As such, they share the high efficiency of a stressed skin design. That is, the designer gets the most structure for the minimum amount of mass and RF blockage. In such designs the basic stress equation is:

$$P = \frac{N_{\theta}}{R_{\theta}} + \frac{N_{\phi}}{R_{\phi}}$$

where P = differential pressure (PSI)

N = stress (lb./in.)

R = radius of curvature (in.)

$\theta, \phi$  are mutually perpendicular directions of stress

Under aerodynamic loading the pressure varies over the surface of the radome. This results in changing stresses and curvature radii. The

basic equation is still true, but the analysis becomes much more difficult. In 1966 Natick Laboratories (U.S. Army) published a design manual for air supported structures which was to extend the CAL work beyond spherical radomes. A subsequent Natick report of large scale wind tunnel testing in 1975 cast some doubt upon the routine use of their original data. Consequently, it is still necessary to analyze any but the simplest or less critical designs. Fortunately, wind tunnel data has been accumulated since the original work at CAL, and it is often possible to either find directly applicable pressure coefficients for a given configuration or a sufficiently similar geometry to allow extrapolation. In the most critical case (such as the CN Tower), wind tunnel tests may be run fairly easily. Radomes have been tested at the wind tunnel facilities of Calspan, University of Western Ontario, University of Maryland, and MIT, to mention a few.

## MATERIALS

Perhaps the most significant development in air supported structures has centered on materials. Neoprene-coated nylon remains a common material, but now has several alternative exterior surfaces. These include (1) 1-3 mil Hypalon coatings, (2) a laminated PVF (Tedlar) film approximately 1 mil thick, (3) a surface coating of silicon base rubber compound, (4) a laminated TFE (Teflon) film approximately 1 mil thick, (5) a high gloss urethane paint finish. Of these the Hypalon is common and the Tedlar is being used on a production military air structure. The others have been experimentally produced, but to our knowledge have not been put into any operating system.

During the 60's, Hypalon-coated Dacron was introduced as an improved radome material. Two significant advantages were advanced: (1) better electrical properties and (2) longer life. The electrical properties as shown in Fig. 3 are general knowledge. Exposure samples were prepared with the Telstar series of 120 ft. to 210 ft. diameter, two ply radomes. These samples have been exposed at the actual sites since 1962. Originally laboratory tests were run every year, but as time elapsed it has become apparent that the radomes are going to outlast the supply of samples. Typical results are shown in Table 1 for a 12-year period. This data is from a 210 ft. radome site on the French coast; it has seen winds > 100 mph that destroyed adjacent office buildings. Structural properties continue to exceed the original specifications with the exception of a drop off in coating adhesion during the first few years. Thus, Hypalon/Dacron has proven itself to have the superior life characteristics originally envisioned. Unfortunately, it also is more costly than neoprene-nylon and the tradeoff has become very close.

Tedlar is frequently used as a surfacing material for MSF radomes. It is also available on air supported structures. Although it has excellent weathering characteristics, one of the originally noted benefits, a hydrophobic (anti-wetting) surface, has been found to diminish with aging. Tedlar samples on the weather rack in Buffalo, N.Y. lost the hydrophobic characteristic in less than

one year. However, a polymerizing silicon solution can be wiped on (at 3-6 month intervals) to maintain a hydrophobic action. This same solution may also be used on other surfaces such as the Hypalon.

A material limited to single ply designs, polyvinyl coated nylon or Dacron, has proven very cost effective. Electrical properties are good (see Fig. 4) and cost among the lowest.

Frequently used in commercial air structures, vinyl-coated fabrics have had considerable development. Unfortunately, the plasticizers tend to bloom out after several years' exposure, leaving a brittle film. This in turn results in high water absorption and eventually physical degradation of the base fabric. Many vinyl radomes now have a urethane paint top coat to retain the plasticizer with a significant improvement in life. Unfortunately, all urethane paints do not provide such protection and it is extremely critical that the compound selected is suitable.

Perhaps the most significant new material is Teflon-coated fiberglass. Although developed principally for architectural applications, it combines superior electrical properties with physical performance never before available. Classed as incombustible, it has an indicated life of more than 20 years, based upon limited outdoor exposure tests and 6000-hour weatherometer tests. Its surface is inherently hydrophobic and resists adherence of ice and dirt. A special "Beta" glass yarn is woven into the structural base fabric. The coating is a combination of TFE and FEP fluorocarbon resins fused to the fabric. The latter permits a high temperature thermal weld to be used in the fabrication. Table 2 presents a summary of physical properties available in existing materials. Table 3 presents detailed microwave dielectric measurements on the 28 oz./yd.<sup>2</sup> radome material. In these tests each specimen was laid on the floor inside a rectangular cavity. Resonant frequency and 10 db bandwidth frequencies were measured with and without the specimen. These six frequencies, the specimen and cavity dimensions were entered into calculations of dielectric constant and dissipation factor as described in ASTM-2520 (Method B). It should be observed that these results are not inherent; special care must be used in the manufacture. For example, an earlier Teflon/fiberglass had shown a dielectric constant of 2.25 and dissipation factor of 0.0019 when dry. After 24 hours water immersion, the specimen gained 0.7-0.96% in weight, the dielectric was then 3.01 and the dissipation factor increased to 0.124 (as contrasted to  $\epsilon = 2.1$  and dissipation factor = 0.005 for the acceptable material when wet).

A critical point in the design of inflatable radomes is the need to use a two ply, bias reinforced fabric construction to obtain maximum tear and shear strength. Two ply, Teflon-coated fabrics are not available. A loom developed by Dow Weave has promise; it weaves on a triaxial, 60° grid, rather than the conventional 90° square pattern. The result is a high tear resistance in a single ply.

Experimental coating is now being done on high tenacity Aramids, such as Kevlar, having strength to density ratios two to three times

that of glass or steel. Kevlar's high cost is rather prohibitive, but it has potential on very special applications.

### PRESSURIZATION

An air supported radome depends upon the pressurization system for its shape and rigidity. In actual experience, radomes have been deflated and later re-inflated without difficulty if they have not been ripped or snagged on the antenna. However, under high winds a deflated radome acts as a sail and damage is very likely to occur. Over a period of many years certain basic principles have been established which, if adhered to, will provide a reliable system. These include: 1) Continuous blower operation. In contrast with the cyclic operation utilized in early systems, it has been demonstrated that continuous blower operation provides greater reliability than a start-stop system. 2) Size blower motors to be non-overloaded under any and all conditions. 3) Select blowers which provide a maximum pressure equal to the desired inflation pressure with a flat performance curve. The blower itself then provides a simple and reliable means of pressure control. Generally the blower is a backward curve or airfoil blade centrifugal. 4) Use multiple blowers, parallel installed with reverse flow check valves. This provides a redundant system that insures against mechanical failure of a single blower. 5) Provide a reliable source of power to the inflation system. Generally a critical radar system already has an emergency power source which can be utilized for the radome as well. In fact, as power outages become more common, it is rather shortsighted to design any radar facility without a backup power source. 6) Provide a system with several pressure levels if there are severe wind requirements. This permits the radome to operate at low pressures (lightly stressed) during the majority of the time.

The Telstar radomes built in the early 60's followed these precepts. There have been no instances of a pressurization failure and all station managers have noted how trouble-free the systems function. The only reported replacement items have been panel lites, the light source in the solid state anemometer meter relay, and occasional fan belt deterioration.

Tests conducted on the 160 ft. dia. radome in Raisting, W. Germany indicated that with all blowers off, the pressure dropped from a peak of 5" H<sub>2</sub>O to 1.5" H<sub>2</sub>O (normal Stage 1) in 10 minutes time. Approximately 18 minutes were required until buckling was initiated (in a 5 mph wind). The radome had sagged about 2 ft. after 50 minutes. On reactivating the blowers, it took 2 minutes to return to Stage 1 levels. During normal operation the airflow was 1700 cfm.

### INSTALLATION

One of the significant advantages of an air inflated radome is the ease and quickness of erection. This is especially significant under critical weather conditions at exposed sites or at high labor cost areas. The two most common methods are: 1) Spread out the radome envelope within

the base area sufficient to attach the base to the clamp ring, turn on the pressurization blowers, inflate into position. Recently a 200 ft. dia. radome was erected in this manner, using the blowers to assist in spreading the fabric. With a 10 man crew of unskilled workers (to unfold fabric), it was uncrated, spread out, and inflated in less than 3 days. This contrasts to 2 weeks which was previously required on the large Telstar radomes. 2) Using a temporary lift ring placed inside the radome crown, lift the radome with a crane, allowing the sides to drape down. Spread out the base edge to the clamp ring, attach, and inflate. Typically a 50 ft. radome can be installed in about one to two hours. While the radome is draped from the crane, wind conditions are critical, but the short duration makes it feasible to make an accurate forecast.

The installation of the CN Tower radome presented an unusual problem due to both the torus geometry and the 1300 ft. elevation. Shown in Fig. 8, the radome was pleated at the factory, attached temporarily to an existing monorail ring, and unfurled around the tower much like a shower curtain. This installation took about half of one day (much to the surprise of the tower engineers).

Of course, the times mentioned do not include the prior installation of the base ring and blowers, but these items are much less weather sensitive and usually are done concurrent with other site work.

### ACTUAL RADOMES

Fig. 1 illustrates a typical 57 ft. dia., two ply neoprene-coated nylon radome. This particular test facility installation is entirely non-metallic, including a large airlock for the entry of space vehicles. The pressurization equipment and electronic gear are mounted below ground. The radome envelope is 0.054" thick, including the Hypalon top coat. It has an anti-wetting treatment. The envelope had a measured  $\epsilon = 3.57$  and loss tan. = 0.031 at 9.375 GHz.

Fig. 2 illustrates a small vinyl-nylon radome made to an oblate shape due to internal antenna subreflections. The lower base section below the ring is also air inflated and protects separate antennas.

Fig. 5 illustrates a 70 ft. dia., 1/4 sphere segment radome fabricated of 0.010" thick Teflon fiberglass. The radome is used for precise final tests of communication satellites and clamps to the wall of a clean room assembly building. A large door allows entry from the clean room which is slightly pressurized; however, the radome is normally held at a higher pressure to minimize any movement in the skin which might affect RF measurements. The mating site is now protected with a window of similar material after it was found that wind gusts had a significant effect upon the test facility antennas.

An unusual example, Fig. 6, is a special 8' dia. radome which attaches directly to the antenna yoke. This is similar to the Nike tracking radomes. The radome rotates in azimuth with the antenna, but antenna elevation is independent inside the radome. Fiberglass hoops support the radome when the blower is off. The radome is

removed and stowed in a duffle bag for transport. It may be installed in approx. 10 min. and removed in 2 min. The material is a neoprene-nylon, having a thickness of 0.018" and a tensile strength of 225 x 210 lb./in. It has a Hypalon exterior top coat with an anti-wetting treatment.

Fig. 7 illustrates a hybrid radome combining both single wall and dual wall construction. The single wall "curtain" may be raised to allow entry of the test antennas or to make extremely critical tests. Several of these radomes are in use. The trend now is to improve upon the performance thru the window and reduce reflections even further. Thus, although a 0.023" vinyl-nylon window has been commonly used, it may show a "ripple" of  $\pm 0.05$  db in making a detail antenna scan. By substituting a 0.010" or less uncoated Dacron, it is possible to get unmeasurable effects. Unfortunately, such a material deteriorates under continual UV exposure and has insufficient strength for the 100 mph design loads. Consequently a double curtain is used. The heavier curtain carries high loads and is opened during critical RF tests. The lighter window is made replaceable. We are still striving for an optimum single skin material.

Figs. 10 and 11 show the unique toroidal CN Tower radome located below the skypod. 138 ft. in dia. x 26 ft. high, it provides complete protection, will allow future changes with uninterrupted viewing, and has a smooth exterior to prevent snow and ice accumulation. Radome material is a Beta glass yarn woven to 16 oz./sq. yd., coated with Teflon to a total weight of 47 oz./sq. yd. and having a thickness of 0.038". Strip tensile strength is 935 x 870 lb./in. After repeated folding it is still 700 x 815 lb./in. Excellent resistance to weathering; water absorption less than 0.1% after 24 hrs. immersion. Based upon wind tunnel measurements the peak loads in the envelope reach 100 lb./in. at a yaw angle

of 150° with 110 mph winds. Under normal inflation the skin is only stressed to 20 lb./in. One of three pressure levels is automatically selected in accordance with ambient wind, Ref. Fig. 9. Stage 3 develops 15" H<sub>2</sub>O static pressure, but negative aerodynamic coefficients at the intake (in the upper skypod) reduce the level to 10" H<sub>2</sub>O at 120 mph gradient mean wind speed.

### CONCLUSION

The data and various examples should point out both the reliability of a properly designed air supported radome and some of the variations possible. Further details are available by consulting the references or contacting Birdair Structures. The majority of radomes are designed for their specific application using existing materials. However, the cases where a new and untried material is developed or a unique geometry designed are what have advanced the state of the art.

### REFERENCES

- 1) "Design Manual for Spherical Air Supported Radomes," W. Bird & M. Kamrass, CAL Report No. UB-909-D-2.
- 2) "CN Tower Microwave Radome," M. Punnett, I.E.E.E. International Conference, Sept. 1975, Paper No. 75083.
- 3) "Design Guide for Air Supported Radomes," M. Punnett, Birdair Structures Technical Bulletin ER71-3.
- 4) "Utilization of Hydrophobic Materials for Air Inflated Radomes," M. Punnett, J. Coated Fibron Materials Jan. 1972.
- 5) "Large Air Supported Radomes for Satellite Communications Ground Stations," W. Bird, OSU-RTP Symposium of Electromagnetic Windows, June 1964.
- 6) "Design Manual for Ground Mounted Air Supported Structures," U.S. Army Natick Lab. Technical Report No. 67-35-ME.

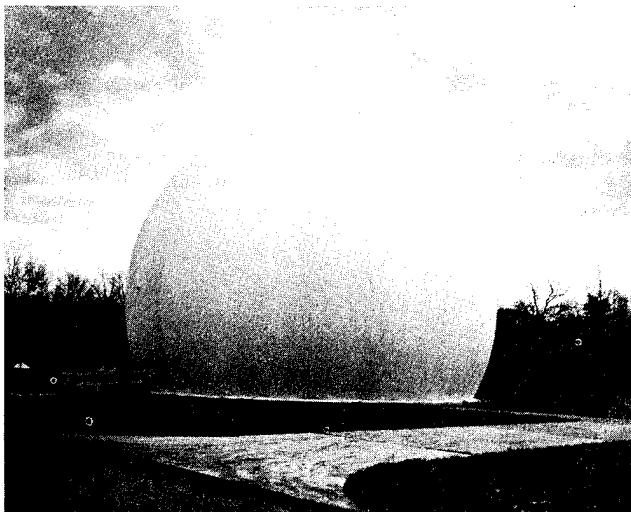


FIG. NO. 1 66' DIA. RADOME

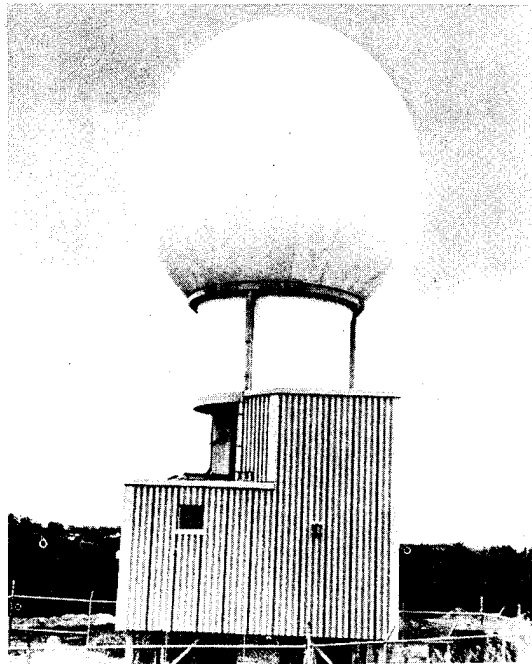


FIG. NO. 2 PROLATE SPHERE  
OR ELLIPSOID RADOME

TABLE I  
EXPOSURE RESULTS 2 PLY HYPALON/DACRON (2D17H70)  
Pleumeur-Bodou, France

YEARS EXPOSED	0	1	2	3	4	6	7	10	11	12
TENSILE $\sigma$ (LB/IN) F	1117	1135	1125	1125	1250	1170	1125	1175	1130	1215
TEAR (LB) V	1005	993	1062	1025	980	1090	985	--	1110	1053
H <sub>2</sub> O ABSORP. (%)	445	--	--	400	400	--	500*	--	420	438
PLY ADHES. (LB./IN)	--	38	34	19.5	25	21	23	0.27	--	--
COAT. ADHES. (LB/IN)	23	--	22	21.5	28	16	24	15	--	13

TABLE II  
MEASURED FABRIC PROPERTIES, TEFLON/FIBERGLAS

	G18T45	G13-5T38	G6T10
Fabric Wt., oz./sq. yd.	48	39	15
Total Coated	18	12	6
Base Fabric			
Strip Tensile Strength, lb./in.			
Warp	1000	850	400
Fill	900	700	300
Trapezoidal Tear, lb.			
Warp	80	50	17
Fill	100	65	15

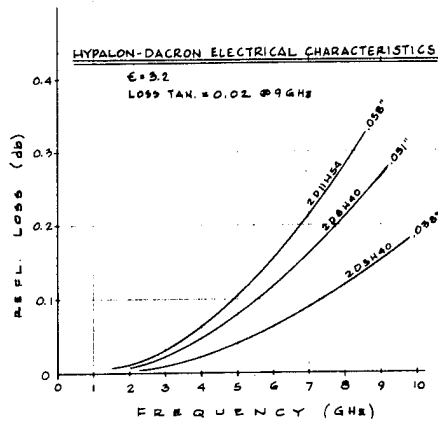


FIG. NO. 3

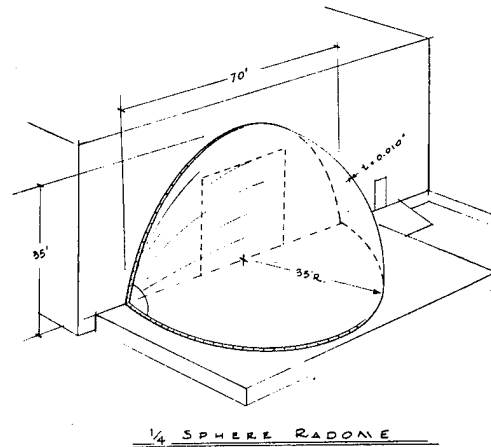


FIG. NO. 5

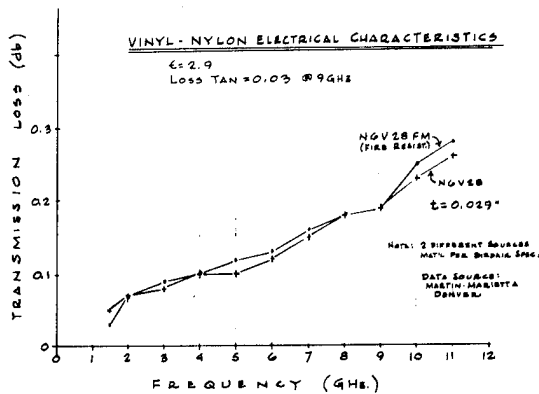


FIG. NO. 4

TABLE III  
Microwave Dielectric Measurements

Specimen No.	Frequency Gigahertz	Dielectric Constant	Dissipation Factor
1, dry	10.036	1.96	0.0015
2, dry	10.028	2.02	.0023
1, dry	8.654	1.95	.0010
2, dry	8.647	2.01	.0018
1, wet	10.033	2.00	.0046
2, wet	10.024	2.06	.0043
1, wet	8.646	2.05	.0038
2, wet	8.643	2.06	.0040

Matl.: G12T28,  $t = 0.028$ ", wt = 27.4 oz./sq. yd.  
Wet: After 48 hrs. immersion in water at 23C.

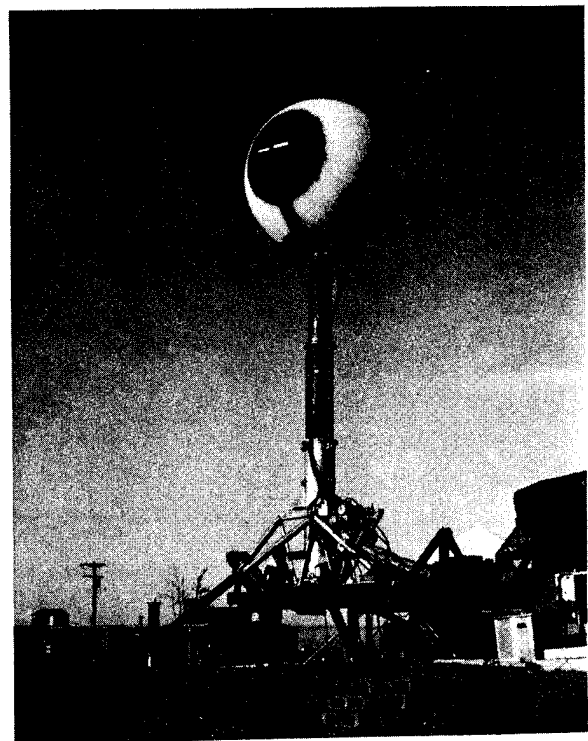


FIG. NO. 6 PORTABLE RADOME

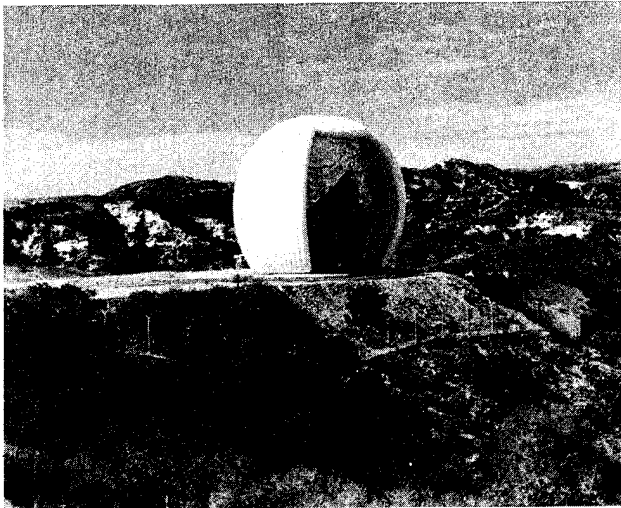


FIG. NO. 7 DUAL/SINGLE WALL RADOME



FIG. NO. 10 CN TOWER



FIG. NO. 8 CN TOWER RADOME INSTALLATION

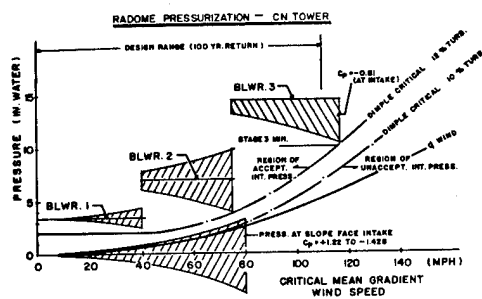


FIG. NO. 9  
RADOME PRESSURIZATION  
VS. GRADIENT MEAN WIND SPEED

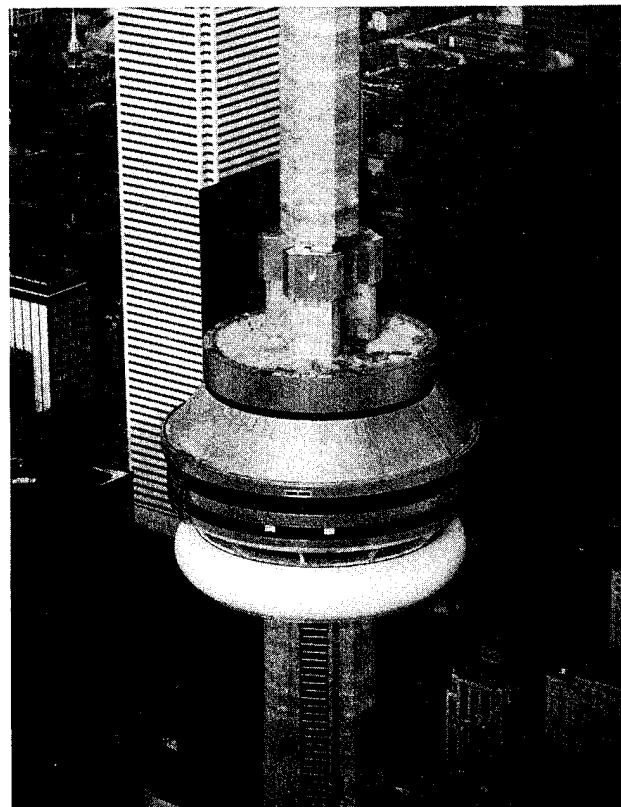


FIG. NO. 11  
CN TOWER SKYPOD WITH MICROWAVE RADOME

Photo Credits: NASA, Raytheon, Sierra Research, TRW, CN Foundation, Robertson

# STRUCTURAL DESIGN IMPROVEMENTS OF ESSCO RADOMES AND ANTENNAS

JOSEPH B. SANGIOLO and ALAN B. ROHWER

Electronic Space Systems Corporation  
Old Powder Mill Road  
Concord, Massachusetts 01742

## ABSTRACT

Over the past decade, the ESSCO Metal Space Frame Radome has continually evolved. Design techniques, materials selection and manufacturing innovations have contributed to a state-of-the-art product.

The report elicits the structural design improvements, as well as the Manufacturing and Quality Control improvements which have been introduced, making the ESSCO radome a structurally superior, reliable product requiring little, if any, maintenance. ESSCO has taken advantage of the controlled environment produced by the radomes in the design of the reflector backstructure, antenna pedestal and antenna servo system. The new ESSCO box-beam backstructure is detailed. The numerically controlled coordinate measuring machine which has enabled ESSCO to demonstrate its state-of-the-art reflector surface accuracy is discussed.

Preliminary field results from the performance of ESSCO radio telescopes are already verifying a surface accuracy of better than 0.13 r.m.s. and no loss due to tracking inaccuracies.

or

$$\sqrt{3} P + \sigma_m t_m a = N a \quad (1)$$

where  $\sigma_m$  is the membrane stress in lbs/in<sup>2</sup>

$t_m$  is the thickness of the skin

$P$  is the load in the beam

$N$  is the direct stress in lbs/in.

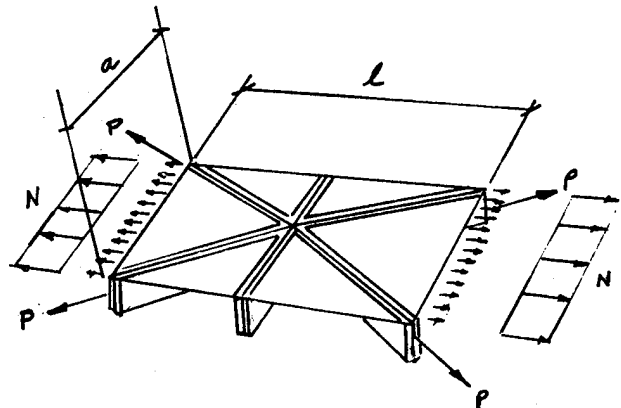


Figure 1 - Typical Structural Element

From Figure 1, we see that the load applied to a typical element of radome surface structure involves the transfer of load through a joint. Whenever there is a connection, there is the potential of additional deflection above that which occurs from the stretching of the skin and the frame. This is illustrated in Figure 2. Using equation (1) and the relationship of the stiffness of the components of the structural element of Figure 2, the following expression has been derived.

$$\sigma_m = \frac{\bar{N} q \left( \frac{R}{t_m} \right)}{\frac{\sqrt{3}}{2} \left( \frac{E}{E_m} \right) \left( \frac{A}{L t_m} \right) + 1} \quad (2)$$

where  $A$  is the cross sectional area of the beam  
 $E$  is the elastic modulus of the beam  
 $L$  is the average length of the beam in the framework

## RADOME DESIGN IMPROVEMENTS

The distribution of wind pressure to membrane stresses on a spherical structure is independent of size or design details. The magnitude of these stresses varies widely over the surface of the structure. The actual values of these stresses are calculated by means of standard shell analysis.

This is as far as we can go in viewing the radome as a uniform continuous shell. From here on, we must consider a more specialized representation -- the space frame, which approximates the surface of the shell with a triangular network of beams. Figure 1 illustrates a space frame representation of a typical shell element. For clarity of our exposition, only one component of direct load is shown along with the forces in the beams and skin covering the frame. In order for the element to be in static equilibrium, the beam (with proper components taken) and skin force components must add up to the direct stress. This can be expressed as a formula:

$$2 \times \frac{\sqrt{3}}{2} P + \sigma_m t_m a = N a$$

$E_m$  is the elastic modulus of the skin  
 $t_m$  is the thickness of the skin  
 $K_J$  is the stiffness of the joint  
 $R$  is the radius of the radome  
 $q$  is the dynamic pressure  
 $N$  is a stress resultant coefficient

Consider now the content of this equation. We note first of all that  $N$  is a coefficient which is invariant with size of the radome and is a function only of overall radome geometry, and  $q$  is a function only of the wind speed and air density. All of the remaining terms are functions of the properties of the radome structure. When we look at the denominator, we come to the following conclusions:

For a given  $E$ ,  $L$ ,  $t_m$ ,  $A$  which are generally governed by other considerations:

- (1) Increasing the joint stiffness will decrease the stress in the skin.
- (2) Decreasing the membrane modulus will decrease the stress in the skin.

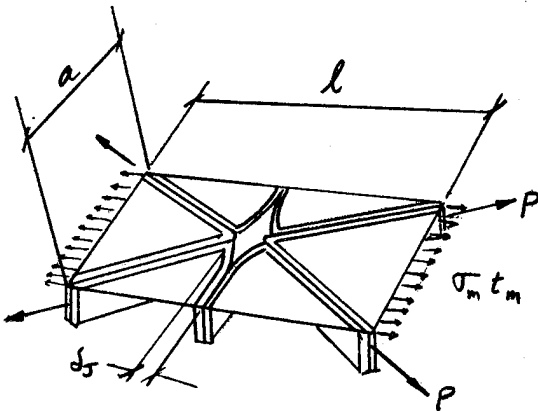


Figure 2 - Deformed Structural Element

For the latest ESSCO designs, the joint stiffness has significantly increased from the earlier designs. In addition, there has been a substantial decrease in the skin modulus. These two steps have markedly decreased the skin stresses which are transferred through the joints (indirect skin stresses).

For the current ESSCO design which uses ESSCOLAM 6 for the skin, the stiffness is lower than that for fiberglass. To compensate, the beam is made wider (to increase the stiffness) and, with a wider beam, there is the side benefit that the area for the adhesive bonding of the skin to the beams is also increased -- thus, increasing the structural capacity for this element.

It must be remembered that the motivation for a narrow, compact beam is the electromagnetic performance of the radome. The thickness of the beam cannot be increased drastically without a severe penalty in the radome performance. What has been accomplished in this trade-off of a slightly increased beam width is a better balance between structural reliability and electromagnetic performance.

Consider now the direct stresses in the skin

due to the wind pressure loads. The maximum skin stress (for both material strength and attachment to the beams) is:

$$\sigma_m t_m = 0.238 (E_m t_m)^{1/3} (C_p q L)^{2/3} \quad (3)$$

where  $C_p$  is a local wind pressure coefficient.

From equation (3), it is seen again that the direct membrane stress decreases as the modulus decreases.

To illustrate the effect of the two major improvements, the old and new designs are compared for a typical 110-foot radome. For the old design, we have:

$$\text{Joint stiffness: } K_J = .073 \times 10^6$$

$$\text{Membrane modulus: } E_m = 2 \times 10^6$$

For the new design, we have:

$$\text{Joint stiffness: } K_J = 10^6$$

$$\text{Membrane modulus: } E_m = 0.5 \times 10^6$$

Under these conditions, the indirect membrane stress (equation 2) decreases from 145 lbs/inch for the old design to 5 lbs/inch for the present design, and the direct membrane stress (equation 3) decreases from 188 lbs/inch for the old design to 119 lbs/inch for the present design. Thus, the total stress on the membrane is reduced from 333 lbs/inch to 124 lbs/inch.

The skin of the radome provides lateral stability against beam buckling as well as its direct and obvious function of absorbing the direct wind pressures. For modern high performance radome design, it is necessary that the skin be intact for full structural capability. It is therefore, necessary to assure high reliability of this structural element.

As we have shown, the improved ESSCO design (first major implementation in 1969) resulted in nearly a three-fold reduction of stress in this vital element.

Furthermore, a superior membrane (ESSCOLAM 6) has been developed and increased controls in the fabrication of the membrane have been implemented.

A most important characteristic of ESSCOLAM 6 is its crack resistance. It is difficult to quantify this advantage. However, it is best illustrated by performing a simple test using a piece of fiberglass membrane and a piece of ESSCOLAM 6. Fold each sample through an angle of 180°. The fiberglass laminate will crack in two pieces before it reaches 180°. The ESSCOLAM 6 sample will remain intact through several reverse bends. This is admittedly a more severe test than actual usage because the membrane fluctuation angle is very small. It is indicative of an accelerated life test simulating the flexing of membranes over many thousands of cycles. Actual flexural fatigue tests have been performed on ESSCOLAM 6 material under load simulating the maximum excursion likely under severe wind conditions. After 5,000,000 cycles of 50 mph wind loading, no evidence of cracking was observed.



## TYPICAL RADOME MANUFACTURING IMPROVEMENTS

The entire radome manufacturing process is continually being refined towards an end goal of zero defects. Some improvements that have been introduced in the membrane fabrication and membrane/beam bonding are described below.

The membrane fabrication process now includes Quality Control testing as follows:

- (1) Daily membrane samples are taken from each production lot and subjected to tensile testing, interlaminar strength testing, and Tedlar adhesion testing to ascertain that the required material properties are achieved.
- (2) The entire bond area of each membrane is subjected to 100% testing to verify that the required interlaminar strength and Tedlar adhesive strength are achieved.
- (3) The development of ESSCOLAM 6, which utilizes Tedlar on both inside and outside surfaces, eliminates the need to apply wax to the separating cauls used in the fabrication of the membranes. This wax was baked in during the curing process of the membranes and had to be removed prior to bonding. Since no wax is now present in the bonding area, another possible human error is eliminated from the bonding process.

The following precautions are included in the bonding process to increase reliability.

- (1) The bonding groove in the aluminum frame is sandblasted the same day the frame is bonded. If more than 8 hours elapse before the cleaned frame is bonded, the frame is sandblasted again.
- (2) Permanent inspection lines are marked on the membranes prior to bonding. If these lines are visible after bonding, it is an indication that the membrane engagement is not adequate. Panels are 100% inspected after bonding. Thus, the possibility of insufficient bond area is eliminated.
- (3) Small samples from each resin mix are collected by Quality Control and each mix is inspected the following day to ascertain that it has cured.
- (4) Daily sample membrane/beam specimens are bonded during production. These samples are tested to ascertain that the process is yielding the required bond strength.

A similar program of increased controls and testing has been implemented in the welding and other manufacturing processes.

The combination and utilization of non-corrosive 6061-T6 aluminum frames, coupled with ESSCOLAM 6 membranes, satisfies all the environmental conditions imposed on radomes. Further, this combination, when added to the highly controlled production processes, results in a Metal Space Frame Radome product line with high reliability and a genuine trouble-free and maintenance-free service life.

## ELECTROMAGNETIC PERFORMANCE

The electromagnetic performance of a radome is directly dependent upon the amount and distribution of the structural material of which it is composed. For a radome to exhibit excellent electromagnetic performance, it must be efficiently designed so as to use a minimum amount of structural material arranged in such a way as to be completely consistent with the structural integrity required. In addition, other constraints, both physical and electromagnetic, must also be balanced. For example, the panel size cannot be so large as to increase the bore-sight shift performance, create variability in the transmission and sidelobe efficiency as a function of angle, or be difficult to handle, transport and install. On the other hand, the panels cannot be so small as to increase the amount of material necessary for mechanical and structural design, thereby lowering the electromagnetic efficiency and increasing costs.

The radome panel size determinations and randomization of the individually small cross-sectional metal structural beams, have been thoroughly accomplished. The ESSCO radome geometrical subdivisions of the sphere have been especially designed for high performance at all frequencies for various size radomes. Each geometrical subdivision used by ESSCO is a modified trapezoidal hexacontrahedron configuration, optimized for the physical size radome to be employed.

The transmission efficiency of the ESSCO Metal Space Frame Radome is based upon extensive model measurements and full scale field tests. Membrane losses are based on measurements of the dielectric properties of ESSCOLAM 6 and computer analysis of the exact technical formulations governing the transmission, reflection and absorption coefficients.

The transmission loss characteristics of the radome exhibits a very broadband capability. The low-frequency limit is determined by the average size panel opening of the metal framework which varies with radome size. The high frequency loss is dependent on the amount of metal framework present and the thickness of the laminate membrane. Typically, for a 55-foot diameter radome, the transmission loss will be about 1/2 dB over a frequency range of from 0.20 GHz to 6 GHz. Less than 1.0 dB loss can be expected over a frequency range of .16 to 20 GHz. The loss due to the membrane is a direct function of its thickness, uniformity, dielectric constant, and loss tangent. At very high frequencies, resonant peaks are present which permit low-loss operation over narrow bands. For example, less than 1.0 dB transmission loss due to the radome has been measured at a frequency of 96 GHz, using a .033-inch thick membrane material in the radome.

Other electromagnetic characteristics of the Metal Space Frame Radome have been thoroughly investigated. The values stated below may vary

slightly, depending on the particular features of the enclosed antenna system; however, they may be considered typical for a 55-foot diameter radome.

Boresight Error - less than 0.1 milliradian peak (.0057 degree).

Sidelobe Perturbation - approximately 1.0 dB change at a -25 dB power level providing the antenna has a gain of 35 dB or greater.

Noise Temperature - less than 5°K increase at frequencies up to 8.0 GHz.

Beam Width - negligible change.

The minor effects caused by the radome must be equated with the major beneficial effects obtained by operating an antenna system in the controlled environment provided by the radome.

#### ANTENNA REFLECTOR DESIGN

By taking advantage of the radome technology developed by ESSCO and by fully utilizing the advantages of the enclosed radome environment, we have designed antenna systems with both the high reflecting surface accuracies and pointing and tracking accuracies necessary for operation at millimeter wavelengths.

Gain limitations of the antenna reflector at short wavelengths are governed by the surface tolerance. Reflector design, therefore, revolves around producing a reflector of high surface accuracy and in maintaining that surface accuracy at all elevation orientations of the antenna.

The radome environment greatly simplifies the structural design problem by eliminating both wind-induced and thermal-induced structural loads. Given this fact, the backstructure design resolves into structural limitations due to gravity deflections at various elevation orientations, and into thermal gradients within the radome. Thermal gradients result solely from stratification of the air mass inside the radome. Elimination of thermal gradients, therefore, can be accomplished by providing sufficient circulation. Evaluation of reflector gravity deflection is accomplished during the design phase through use of the STRUDL finite-element structural analysis computer program. Deflection output files from this program are then manipulated and evaluated to provide best-fitted r.m.s. deviations from the theoretical reflector parabola.

Following the evaluation of an earlier welded-angle truss design, ESSCO has developed a reflector backstructure consisting of riveted and bonded aluminum box-beam radial ribs and circumferential intercostals. Box-beam construction for the reflector backstructure has resulted in a number of design advantages. The box beams produce a lightweight structure with large cross-sectional moments of inertia. In addition, as particularly opposed to the welded truss, the final assembled structure is free of internal stresses and is simple to model on the computer. This second point is of concern in this application where the final deflection

characteristics of the structure are of such importance. Finally, the aircraft-style construction used to produce the box-beams is one readily adaptable to producing structural members with the desired sectional properties. In this case, inertias of individual ribs can be varied while maintaining a single set of production tooling merely by changing the thickness of the sheet stock used in rib walls. Ribs and intercostals are sized for ship-borne containerized shipment, and the final assembly of parts completed by riveting in the field.

Recognizing that an antenna reflector can be no more accurate than the inherent r.m.s. reflector surface tolerance, ESSCO has spent much time developing its fabrication techniques for reflector panels. Our antenna surfaces are lightweight panels consisting of a sheet aluminum reflecting surface with a bonded backstructure of rolled-formed aluminum channel. The reflector surface contour is produced on a male mold where the panel surface replicates the surface of the mold. To date, ESSCO has produced antenna panels with r.m.s. surface deviations of .0015 inch (.039 mm) using this technique, and it is believed that accuracies greater than this can be achieved.

Verification of surface accuracies for the reflector panels is itself a demanding task. This is accomplished using a numerically-controlled X-Y-Z Coordinate Measuring Machine with a measurement capability of 15 ft. (457 cm) x 6 ft (183 cm) x 2 ft (61 cm). This machine is directly coupled to an on-line computer which does the required data recording and coordinate conversion. The computer processes the coordinate machine measured values and converts them into local surface deviations from the theoretical parabola as measured along the final antenna focal axis. When combined as an r.m.s. value with the deviations for an entire complement of reflector panels, these numbers become a measure of the final antenna's performance. Determination of the final antenna surface tolerance is widely recognized to be a statistical summation of a) the as-manufactured antenna panel r.m.s. surface errors; b) the r.m.s. errors due to setting the antenna panels on their supporting structure; and c) the r.m.s. errors induced by gravity and environmental structural loads as the antenna is moved from the initial setting condition.

During the design phase, the antenna performance is predicted using the outputs from the structural analysis and known panel measurements. The structural characteristics for the finished reflector are measured in the field using a theodolite to measure the positions of targets located on the reflector surface. These targets are measured at two antenna orientations and the deflection characteristics deduced from the differences between target measurements at these elevation angles.

The antenna surface panels must be properly located on the antenna backstructure to produce the desired overall reflector surface. Panels are traditionally positioned utilizing very ac-

curate strap gauges for radial distance location and precision theodolites to determine angular location. A limiting precision with the best operator and theodolite is about 1-2 arc-sec. which translates into an effective r.m.s. error of about 0.06 mm (without any weighting functions being applied) for the 13.7 meter size reflector and, of course, is better for the inner panels than the outer panels because of the ability to visually resolve the panel target cross hair at the shorter distances. Our latest installation, the University of Massachusetts telescope, has a reflector surface tolerance of less than 0.13 mm r.m.s. with an aggregate panel accuracy of 0.06 mm r.m.s., and until experiments beyond several hundred GHz are conducted, setting the panels with the theodolite has been deemed satisfactory. It is expected that radiometric measurements, now in process, will determine how much less than 0.13 mm r.m.s. the antenna actually exhibits.

It is clear, however, that more precise procedures for setting the panels are necessary if backstructure and panel design and fabrication research are to be fully utilized. ESSCO is continuing to investigate more precise setting techniques so that they may be utilized in the future, and the enclosed environment provided by the radome is very helpful in this activity. It is noteworthy, however, to understand that the inherent capability of a millimeter wave antenna lies in its pointing/tracking accuracy and panel surface tolerance since technological advances in setting tolerance are rapidly being developed.

#### PEDESTAL AND SERVO SYSTEM DESIGN

The radome-enclosed environment has significant impact on the design of antenna pedestals with high pointing accuracy. The elimination of wind induced torques and thermal effects precludes the need for designing these components to survive and actively resist these wind and thermal loads. By reducing the drive and survival torque loads, we are able to significantly decrease the size and strength requirements for the drive components and to concentrate on the precision which yields the high pointing accuracy required. This design utilizes a basic yoke on king post configuration which has inherent advantages both in the pointing accuracy obtainable and in the accessibility of the Cassegrain focus of the antenna.

The controlled radome environment also greatly simplifies the design of the antenna servo system. Through the use of the highly stiff yoke on king post design and a biased multi-motor drive system, we are able to obtain fine pointing and tracking accuracy. The multi-motor drive system allows the pedestal gear train backlash to be eliminated by electrically biasing the motors against one another. This effectively removes the major drive system non-linearity and allows a Type II servo position loop to be used which provides precise position error sensing and thus excellent pointing and tracking accuracies.

Achieving accurate position feedback information is accomplished by using a 22 bit

(binary plus sign) position indicating system that centers around the selection of a multi-pole inductosyn as the position transducer. The inductosyn is a 512 pole device that has an inherent accuracy of 1 - 1.5 arc seconds peak with an r.m.s. repeatability of less than 1 arc second. The analog output of the inductosyn and an integrally mounted 1:1 synchro resolver (coarse transducer) is digitized over 22 bits into a natural binary plus sign format. This binary word, for each axis of the pedestal, is used as the position feedback signal for computer control of the antenna. The stability of the binary word from field and laboratory testing has been measured down to the 22nd bit (.31 arc seconds) denoting that the noise level of the analog/digital readout electronics is less than .31 arc seconds. Thus, the repeatability of the readout system is dependent upon the inductosyn transducer and is less than 1 arc second r.m.s.

#### RADIOMETRIC PERFORMANCE

Until recently, information from customers based on their scientific observations has been slow in coming for frequencies above K band. The primary reason is that the development of high frequency, low-noise front ends has been a slow and very expensive process and, as a result, observations with the earlier radio telescopes have been done, in the main, at K band. There have been periods, however, when higher frequency equipment has become available and observations have been performed with the 13.7 meter radio telescope at Sao Paulo, Brazil at 85 GHz and with the same size radio telescope at Helsinki, Finland at 80 GHz. Data that we have received in the past has confirmed our physical measurements with-in the accuracies possible at K-band, but precise confirmation of the measured results for our latest radio telescopes can only be made at frequencies in the order of 100 GHz and above.

We are pleased to have recently received verbal reports of observations made at 110 GHz with the 20.1 meter radio telescope at Onsala, Sweden. Preliminary data verifies our measured results for both reflector surface tolerance and tracking accuracy and gives us confidence in our fabrication and alignment techniques. In fact, this preliminary information shows that the antenna may be better than our original measurements indicated.

In addition, the radio astronomy group at the University of Massachusetts has just begun to make observations with an uncooled mixer front end at frequencies in the area of 100 GHz and their initial results look very promising. Data that has been collected at 82 GHz points to an excellent beam efficiency, indicating that the reflector surface tolerance is better than the 0.13 mm r.m.s. Also, they have not been able to discern any losses due to tracking inaccuracies. The next step will be to make observations at 115 GHz and these results will allow us to further verify our system characteristics.

It is premature, at this time, for ESSCO to publish detailed results of the very recent

observations that have begun at University of Massachusetts and in Sweden, but we anticipate that complete data will be available in the near future. We are keeping a close watch on all six radio telescope sites and will be updating the information as more data becomes available.

All of ESSCO's radio telescope designs are produced under a configuration management control system such that updating is readily accomplished. For example, our pointing/tracking accuracy is built into all telescopes allowing 1 mm or less operation. Thus, as we are able to make reflector surface panels significantly more accurate, we can resurface our telescopes for higher frequency performance.

# THE MECHANICAL ENGINEER'S ROLE IN MILITARY ELECTRONICS

JOHN P. KARPUK and CHARLES LEVINE

MECHANICAL ENGINEERING DEPARTMENT  
EQUIPMENT DIVISION  
RAYTHEON COMPANY  
Wayland, Mass. 01778

## ABSTRACT

The paper discusses and illustrates equipment designed for radar applications, such as surveillance, land based and shipboard, air traffic control and early warning functions.

It highlights some of the examples of innovativeness demonstrated by mechanical engineers in the role of packaging equipment for military use in configurations such as:

- Shipboard equipment — above and below decks.
- Tactical-mobile-deployable systems.
- Fixed site — construction of a giant radar phased array.

Special attention is focused upon the design and cooling of equipment enclosures.

## INTRODUCTION

Customer specifications establish the performance and functional requirements for electronic equipment. The equipment enclosures must maintain the integrity of the equipment under all environmental conditions. They must support and protect the equipment under the most adverse shock and vibration conditions; seal out dirt and moisture; attenuate electromagnetic interference, provide for dissipating component generated heat and insure the reliability and maintainability of the equipment contained within.

Depending upon the type of service, an enclosure may be in the form of a pressure tight weldment, cabinet, shelter or building.

For the purpose of service classifications, equipment enclosures may be divided into the following configurations:

- Operational shipboard equipment:

- above decks; spray-tight pedestals and junction boxes

- below decks; drip-proof cabinets

- Ancillary/test equipment: drip-proof cabinets
- Transportable equipment: shelters and enclosures
- Fixed site: buildings, EMP and RFI secure

## SHIPBOARD "ABOVE DECKS" EQUIPMENT

An example of "above decks" equipment is the lightweight roll/pitch stabilized search antenna shown in Figure 1. It is track-while-scan radar, data processing and weapon direction system for quick reaction target acquisition commensurate with small ship installation.

In addition to providing the equipment with protection from the environment, the mechanical engineer had to assure the required accuracy of the system.

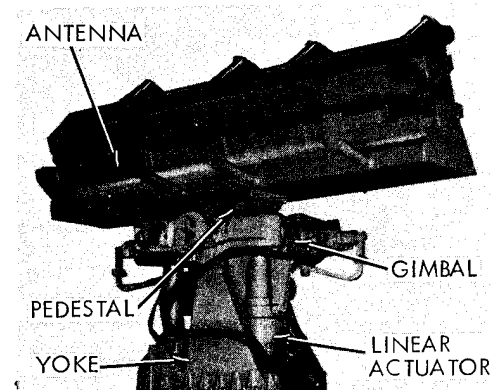


Figure 1. Lightweight Stabilized Antenna

Stabilization accuracy objectives require structural stiffness exceeding normal design requirements. Wind loading and array weights must be kept at practical limits to reduce drag and stabilization torque requirements to

achieve a weight objective of 1000 lb, which is compatible with small ship installation requirements. The platform must withstand MIL-S-901 shock and 6 psi nuclear air blast, as well as a 100-knot wind, without structural failure. It must be operable at wind loads to 75 knots.

The gimbal is a box beam casting of A356-T6 aluminum, while the pedestal and yoke are weldments of 6061-T6 aluminum. The pitch and roll stub shafts are high strength steel having a yield stress of 160,000 psi.

The 15-30 RPM azimuth drive is obtained by reducing the output of the two-speed azimuth motor in two stages. The first reduction is through a Spiroid right angle gear drive and the second is by spur gears, a pinion driving an internal gear. The combined efficiency of the gear train is 88 percent.

In the early stages of the stable platform design, the low production quantity and stringent engineering requirements resulted in little or no interest from linear actuator vendors. An "in-house" design was therefore initiated using spur gears, a flange mounted D.C. servo motor and ball screw. The spur gear system was discarded when calculations indicated that the weight of the gear box would be excessive. A helical spur gear drive concept was investigated and also abandoned because of its inability to accept the shock loading. The present design using D.C. torque motor directly in line coupled to a ball screw shaft eliminating gears and a cantilevered motor. Over-travel stops are integral with the assembly. The actuator also includes a tachometer and a failsafe electro-magnetic brake.

The antenna is constructed of expanded aluminum alloy-honeycomb with internal bulkheads. Compared to an aluminum alloy skin structure this results in a 30% saving in weight, increased stiffness and reflector strength.

#### EQUIPMENT ENCLOSURES FOR USE BELOW DECKS

Through the use of standard design elements, a shipboard cabinet (Figure 2) was developed for "below decks" equipment such as:

- Transmitters
- Receivers
- Data/signal processors
- Test equipment
- Junction boxes
- Power distribution/control

The cabinet illustrated in Figure 2 is a free-standing,

hard-mounted weldment aluminum composite design with a removable front door. The weight of a 24-inch x 24-inch x 72-inch enclosure is approximately 250 pounds.

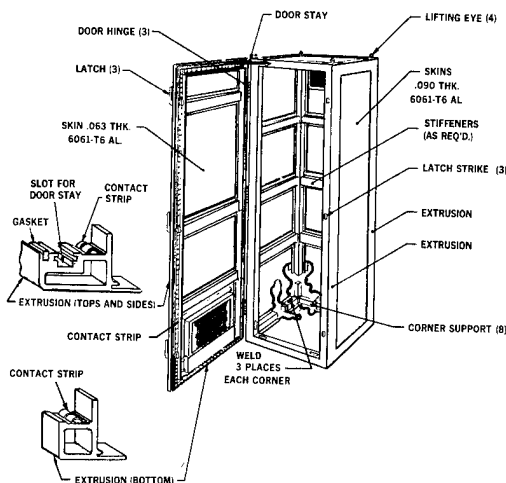


Figure 2. Standard Cabinet Design Elements

The door is a non-structural member since the cabinet design does not require the door for structural rigidity. It is attached by three individual hinges and secured by quick-release latches. RFI shielding (62dB at 12 GHz) is provided by spring finger contacts and a compression gasket effects a moisture barrier. Air intake openings have RFI/drip-proof filters.

A door stay provides positive lock with the door open in a 90° to 120° position.

The extrusions include a slot along the outside edges into which the skin of the cabinet is inserted (Figure 2). Additional internal hat-shaped stiffeners are added as required to the rear and sides to provide structural integrity or component mounting surfaces. The entire assembly is then welded to form an integral five sided cabinet. The door is constructed in a similar manner.

The NASTRAN general purpose structural analysis computer program is used for determining stresses under static and dynamic loading environments. The actual structural support assembly is simulated by a mathematical model of finite element. Elastic members connect the grid points which define the geometry of the structure where loads, weights, displacements and restraints can be specified.

#### COOLING OF CABINET EQUIPMENT

Since electronics equipment must be properly cooled to operate efficiently and reliably, effective cooling of design involves several considerations:

- The maximum component temperatures desired for reliable operation.

- The minimum air flow rate required to produce the desired maximum component temperatures.
- Assurance that packaging design minimizes pressure drop by avoiding restrictions to air flow, such as excessive turning of the air, sudden changes in flow cross-section, or dust filters which are either thicker or of finer mesh than required to meet the dust conditions referenced in the specifications.
- Assurance that the equipment is effectively cooled in the maintenance as well as in the operating mode.
- Selection of fans which will supply the volume of air flow required against the anticipated head.

A practical application of considerations discussed previously is shown in the cabinet cooling plan in Figure 3. It uses forced convection filtered air for a signal processing unit dissipating approximately 2.5 kW of power.

- Inlet air pressure drop is minimized by using a large cross-section filter to reduce air velocities.
- The air flow is split into two separate paths (power supplies and card basket) to minimize the flow rate and resulting pressure drop through any portion of the cabinet.

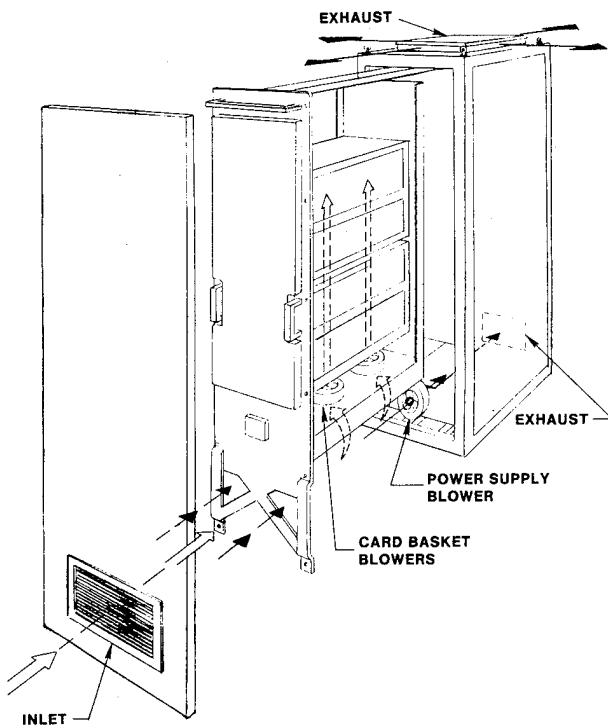


Figure 3. Cabinet Cooling

Air flow through the power supply area is straight through, with no turns and minimum changes in cross-section; therefore, pressure drop is minimized.

Air flow through the card basket area is upward and is augmented by the natural convection tendency for heated air to rise. Again, the flow is straight through with minimal turning and changing of cross-section.

The exhaust opening for the card basket cooling air is in the cabinet top rather than at the top of a side wall. This assures that no dead air space with stratified hot air will occur near any electrical or electronic parts.

There are instances where forced-convection cooling is not practical, such as where an accelerated humidity test is imposed upon individual components. This is accomplished by a continuous exposure of the equipment to an environment usually equal to or greater than 90% R.H. with the ambient temperature cycled during this test to further accelerate humidity effects. Problems are encountered with the resulting moisture or condensation. Among these are:

- Printed circuit boards:
  - Low voltage flashover
  - High frequency circuit instability
  - High impedance circuit failure
- Accelerated corrosion at dissimilar metals interface
- High voltage circuit flashover

After trying methods of protection from moisture such as assembly orientation, drip shields, drain holes, heaters, and baffles, it becomes apparent that these methods do not always afford adequate protection from water vapor penetration. Even the best conformal coatings for printed circuit boards such as vacuum deposited paraxylene, particularly in high frequency circuits, is not completely satisfactory. Complete protection from external moisture can only be accomplished by eliminating the need of outside air for cooling.

Since it is not practical or economical to provide hermetically sealed enclosures for large electronic components, an effectively sealed cabinet with a closed loop cooling system is used to solve the problem.

Closed loop cooling systems using sealed cabinets with built-in air-to-liquid heat exchangers offer advantages over the open loop forced air circulation system. Since no external air is drawn into the cabinet, contaminants such as dust and moisture cannot enter the circuitry areas. The use of the closed cabinet offers other advantages:

- No internal condensation can occur even when room air conditioners have failed.
- Since there are no air intake or outlet openings, the need for air dust filters and expensive RFI/drip-proof filters is eliminated.

Air-to-liquid heat exchangers have proven most practical with high heat density components requiring water cooling, such as those used in high power transmitters.

## TRANSPORTABLE SYSTEMS

The AN/TPN-19 (Figure 4), developed for the U.S. Air Force, is "the most modern transportable and capable Terminal Air Traffic Control and Landing System available for use in this decade."

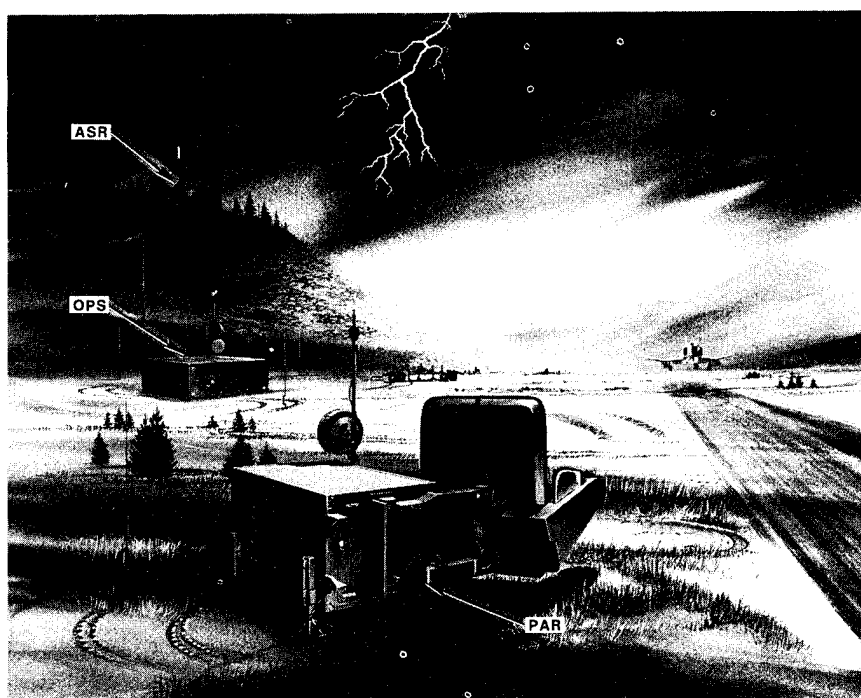


Figure 4. Artistic Concept of Typical AN/TPN-19 Deployment

The design engineer's capabilities and innovativeness are demonstrated in this unique system's compatibility with specification, the various modes of transportation and mobility as well as rapid erection and deployment, and operational flexibility for tactical and fixed site requirements under world-wide climatic conditions. These requirements demand minimum weight with high structural integrity.

The system consists of three or four shelters depending upon the existing operational requirements.

- Airport Surveillance Radar (ASR)

- Precision Approach Radar (PAR)
- Operations Central (OPS), GCA Configuration
- Additional Operations Central, RAPCON Configuration

The ASR and PAR antennas are designed to be retracted and stowed within their respective shelter during transport. Both antennas are designed to operate under wind loads up to 65 knots with ice, plus survival at 130 knots without ice.

The ASR antenna shown in Figure 5 consists of a spur gear train and electrical components mounted on an antenna drive assembly. Continuous rotation at 15 RPM

is provided by a motor driven torque tube at the base of an antenna drive. The drive assembly also serves as an erection mechanism (a four bar linkage) which permits the pedestal and microwave antenna and components to be stowed for transport or erected during deployment. The reflector consists of three sections: a center structure and two tip sections. The microwave components, the coupler network, waveguide runs (12) and the 12 individual horns are dipped brazed aluminum assemblies. Each horn assembly has an integral polarizer driven in tandem with the others by a gearhead motor and linkage assembly to select either linear or circular polarization.



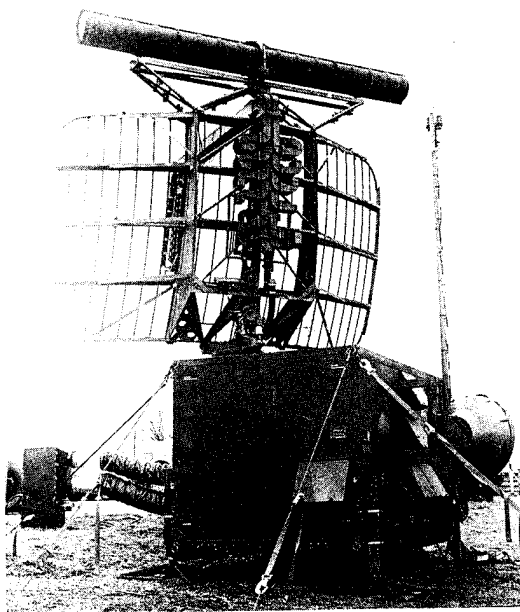


Figure 5. An ASR Antenna

The PAR Antenna group shown in Figure 6 consists of a limited scan computer-controlled phased array, X-band Precision Approach Radar. The use of only 824 elements with a large reflector (an effective cost and weight trade-off) achieves a beam sharpness normally requiring 8000 elements in a standard phased array. The group pivots from a structure called a support drive, which is sufficiently stiff to insure the aiming accuracy of the antenna group. The general approach is to remove all moment reactions and impose only shear loads on the shelter floor, ceiling and sidewalls. This is accomplished by an upper and lower box section beam connected to the shelter and the reflector support with an interstitial support.

The drive power for the array and support is provided by an integral D.C. drive motor/brake coupled to a composite spur-to-planetary-to-cone drive which provides an overall speed reduction of approximately 80,000 to 1.

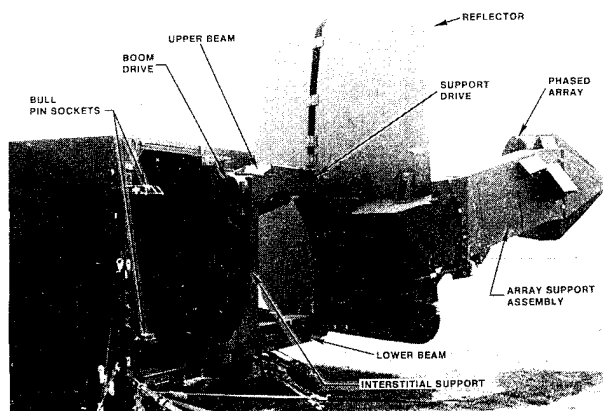


Figure 6. PAR Antenna Group

The Phased Array Support Assembly contains the electronic assemblies, microwave receiver components and horn and environmental controller and the phased array.

In selecting alternate runway coverage, the Support Drive and Antenna Group are driven 90° to either side of a center axis (roadside or curbside). During this operation, interlocks and logic circuits assure that the Antenna Group is maintained within 5° of center to prevent component collision with the shelter. When this group reaches either limit the drive power is shut off by limit switches and the array is secured by an electrically actuated bull pin inserted into a socket housed in castings at the top and bottom of either side of the shelter.

In the transport stow position, the reflector is removed and the antenna boom folds against the reflector support. This package (including beams and drives) is stowed within the shelter on a set of internal stow assist tracks and secured to the shelter. The reflector is separated into three parts and stows on a pallet.

## FIXED SITE INSTALLATIONS

Our mechanical engineers recently became involved in the design, installation and support of a military fixed site.

A technically sophisticated component of the U.S. military intelligence data gathering system, known as Cobra Dane, was installed in Shemya, Alaska. It is designed to monitor Soviet ballistic missile development flights as authorized under the ABM treaties resulting from the SALT talks. This giant radar, one of the worlds largest, is housed in a six-level, 57,000 square foot building as illustrated in Figure 7.

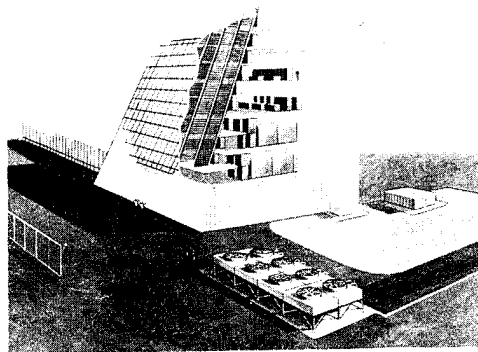


Figure 7. Artist Concept of Cobra Dane Site

The radar uses a phased array antenna consisting of approximately 35,000 state-of-the-art elements that are precisely spaced with respect to one another on a 94-foot diameter formed by 180 flat aluminum plates.

In the interests of economy, performance and the

more technically complex problems associated with them, the Cobra Dane Phased Array Antenna was designed to operate without a weather radome.

The engineers were concerned with three major potential problems; the erosion of the face of the elements by windborne particles, corrosion of the aluminum array plates and the ice build-up on the face of the elements. Potential corrosion of the plate was avoided by specifying a special melt of aluminum which is equivalent to 6061 wrought alloy with its good corrosion resistance.

Building a phased array radar on an island like Shemya required initial extensive testing to verify that designs would be able to meet the technical, environmental and schedule requirements. The tests ranged in complexity from simple breadboard evaluations to an exhaustive installation test to verify the installation technique. Also included were a full scale wooden mock-up of part of the building, and a complete simulation of the Shemya winter weather to predict whether ice would form on the array. The elements are protected with a coating of non-corrosive room temperature vulcanizing (RTV) silicone compound on the face. "Test before ship," philosophy was effective in proving the designs would work before hardware was shipped to the island and was the key to the successful array installation.

After the building steel was erected at the site, preliminary alignment of the array mounting structure was performed. Each of the 180 array plates are supported by four jackscrews, each of which had to be adjusted in the "X" and "Y" planes prior to the installation of the array plates.

After the X and Y axis alignment of the 720 jackscrews, the array element face flatness adjustment (Z axis) was performed (Figure 8). Alignment tooling consisted of a commercially available construction type laser optical positioning system. The laser was mounted to the building and, by use of a set of laser detectors, as shown in Figure 8, each of the 720 jackscrews was adjusted so they lay in a plane flat to  $\pm 0.12$  inches.



Figure 8. Adjustment of Jack Screws

Nature added a small parameter of her own into the planning, an earthquake measuring 7.5 on the Richter scale. The array alignment survived the shock.

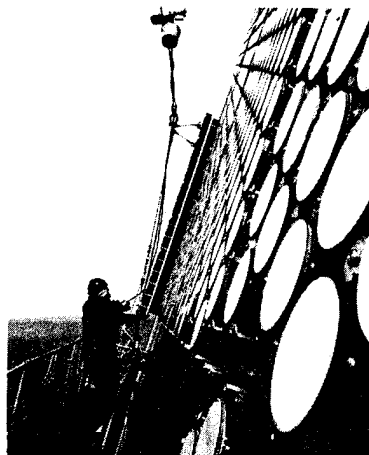


Figure 9. Typical Array Plate/Element Installation

Imagine 100,000 pounds of aluminum, precision machined into 180 ping pong table size plates, covering one whole wall of a twelve-story building, supporting approximately 35,000 radar elements, whose faces must form a plane flat to within  $\pm 0.12$  inch.

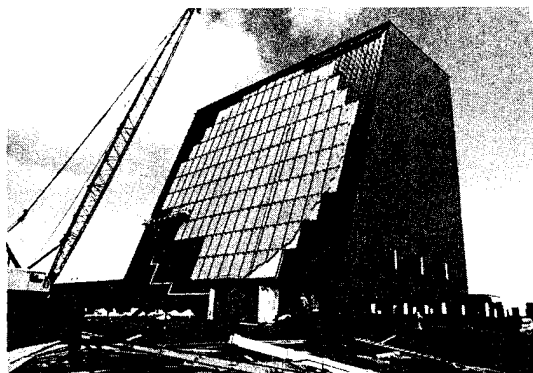


Figure 10. Array Face Near Completion

The Mechanical Engineering Group worked closely with the construction contractor to develop a procedure that would allow for a speedy and safe installation of the array.

Special lifting equipment and installation tools were designed by the mechanical engineers to aid in the installation in the tricky Shemya weather.

After plate installation and weather and R.F. caulking were completed, the flatness of the array was rechecked and verified to be well within the requirements.

# DESIGN AND FABRICATION OF A LIGHTWEIGHT RADOME FOR USE WITH THE HEMISPHERIC COVERAGE ANTENNA

by

Michael Costagliola  
Research Section Head  
Sperry Gyroscope Division, Sperry Rand  
Great Neck, New York 11020

and

Roy C. Berg  
Vice President for Engineering  
Lunn Industries, Inc.  
Wyandanch, New York 11798

## ABSTRACT

This paper describes design and fabrication of a unique dielectric radome which not only provides environmental protection but accurately locates 25,000 passive phase delay modules on its surface. The radome is 113" in diameter, 99" high and incorporates 106 circular lands on the inside skin to provide channels for location of the modules. A novel tooling concept was developed, using an inexpensive "breakaway" plaster mold to produce the dome. The final part met all dimensional requirements and weighed only 330 pounds.

## INTRODUCTION

The subject of this paper is the radome built for the Hemispheric Coverage Antenna being developed by the Sperry Gyroscope Company for the U.S. Army (Miradcom, Huntsville, Ala.), under Contract No. DAAH01-74-C0334. The "Dome Antenna" used in this system is a Sperry development which is described in the references (1,2,3).

The principle of the Dome Antenna is illustrated in Figure 1. A planar phased array at the base of the dome generates a radar beam which is deflected and focused by a passive lens. The passive lens consists of a dielectric radome which supports 25,000 electrical modules which completely cover the interior surface.

The design problem was to provide a light weight radome of the required shape, with means to accurately locate and attach the electrical modules.

## DESIGN CONCEPT

Many alternates were evaluated in the study phase, resulting in the final concept shown in Figure 2. The modules are in a rectangular configuration allowing them to be placed in horizontal rows. The vertical location of module rows is established by "lands" or circular ribs, molded integrally with the radome. Azimuth location of the modules is established by measurement from four accurately located scribe lines on the inside of the dome.

As only one prototype dome was to be built, it was felt that inexpensive plaster tooling would be adequate. The question of meeting the required tolerances was resolved through a series of conferences with prospective radome suppliers.

## RADOME DESIGN

The size of the dome was limited by transportation requirements, (113 inches in diameter and 99 inches high). The shape was determined by computer antenna design studies which optimized the electrical characteristics. Figure 3 shows a section through the dome with the characteristic dimensions. Because of the arbitrary dome contour, the "pitch", or chordal distance between lands, is non-uniform.

The radome structure is the conventional type, consisting of two fiberglass skins separated by a NOMEX honeycomb core, with a solid fiberglass flange. The structural design was thoroughly analyzed to minimize the dome weight, consistent with strength and rigidity requirements. A sample panel was built for structural tests and to check the microwave transmission characteristics.

A specification was prepared incorporating the usual radome requirements for materials and workmanship, as well as the unique requirements for this design. These were mostly concerned with the land accuracy requirements and the criteria for acceptance. In view of the difficulty in measuring the final part, it was decided that the vendor's tooling would be inspected by Sperry at each step, before approving the next step. This would give assurance that the final part would meet the functional requirements.

The drawings and specifications were submitted to candidate vendors with a request for quote. In addition, visits were made to the prospective vendor's plants to inspect their facilities for suitability. The successful bidder was Lunn Industries, Inc., who received a contract for the tooling and fabrication of the dome.

## FABRICATION CONCEPT

The plan adopted for manufacture was fabricating an accurate male mold which would be the counterpart of the desired inside surface of the dome. First, a plaster mold was to be generated to the contour, and then "land grooves" were to be cut into the surface, to produce the lands in the molded part. This meant that the molded part could not be pulled off the mold without breaking the plaster, since the lands "key" the part to the mold.

The solution to this problem is shown in Figure 4. An inner mold was built, about 1/4" inside the final contour. An outer "breakaway" plaster shell was shaped over this mold, and the land grooves were cut into the outer shell. A mold release compound was used between the two molds to insure separation. The plan was to remove the dome from the inner mold, with the "breakaway" plaster attached, and then to remove the plaster from the inside of the part.

## TOOLING

The contour for a master (male) template was generated on a two axis numerically controlled machine. From this male template, female screeding and check templates were fabricated. The mold was built on a 10' diameter turntable (see Figure 4). To achieve the desired accuracy, the turntable was completely re-worked and adjusted until the runout was within acceptable limits.

The inner mold was built over a steel skeleton covered with wire cloth. The plaster was swept to a contour 1/4" inside the final contour. It was sealed with epoxy paint and coated with mold release. (See Figure 5.) The "breakaway" plaster mold was formed over the inner mold and swept to the final contour. After curing and checking for contour, the land grooves were cut in the plaster.

The cutting tool was 0.58" diameter and was driven by an air router. The cutter support block was attached to a stationary aluminum template which had scribe lines for each land location. The advance of the tool into the surface was measured directly from the mold surface with a dial indicator. Each groove was cut with a single rotation of the turntable.

The mold surface was coated with epoxy paint and the land grooves checked for final dimensional accuracy. A height gage was used to check vertical locations and runout of grooves up to a height of 40" above the base. Above this level, checks were made of land pitch using modified Mueller gage. Several hundred measurements were taken, with a maximum discrepancy of 0.017" in pitch, compared with an allowable tolerance of 0.020". Figure 6 shows the finished mold.

Tests of the molding technique indicated that the land grooves required modification in the areas of high curvature, because the angle between adjacent land grooves caused the plaster to lock into the grooves. The grooves were modified to a trapezoidal shape by using a splining epoxy resin to fill the lower corner of the grooves.

## FABRICATION

A high temperature polyester resin was used for the layup. To meet the peel test requirement for bonding the honeycomb core to the skin, an epoxy resin was used for the bonding ply.

The first step was to apply the mold release, after which the grooves were filled with a mixture of resin, vitro strand, fumed silica, and 1/8" chopped glass fibers. The inner plies were applied directly over the filled grooves and cured. The honeycomb core was installed against an epoxy adhesive ply, vacuum bagged and cured. The core fabrication was accomplished in two steps. Figure 7 shows the dome after the first stage of core construction.

The outer skin with epoxy and polyester plies were laid up over the core, vacuum bagged and cured for 6 hours at 300°F. The jack screws under the flange (see Figure 4) were used to lift the dome, with breakaway plaster attached, about two inches above the inner mold. The dome was then hoisted off the mold and the plaster chipped from the inside.

Figure 8 shows the completed dome. Numerous dimensional checks were made to ensure that the dome was within tolerance. These showed that all accuracy requirements were met. The finished weight was 330 pounds.

## SUMMARY

The feasibility of fabricating a highly accurate, light weight radome of complex design using inexpensive tooling has been demonstrated with the successful fabrication of the dome for the Hemispheric Coverage Antenna. The novel tooling concepts employed have significantly advanced the state of the art.

## REFERENCES

- (1) "Dome Radar - A New Phased Array System" by P. M. Liebman, L. Schwartzman and A. E. Hylas. I. E. E. E. International Radar Conference Proceedings page 349 (1975)
- (2) "Phased-Array Antenna Advances Detailed" by Philip J. Klass Aviation Week, May 5, 1975
- (3) "The Sperry Dome Radar" by L. Schwartzman and P. M. Liebman Tri-Service Radar Symposium July 6-8, 1976 (Unclassified)

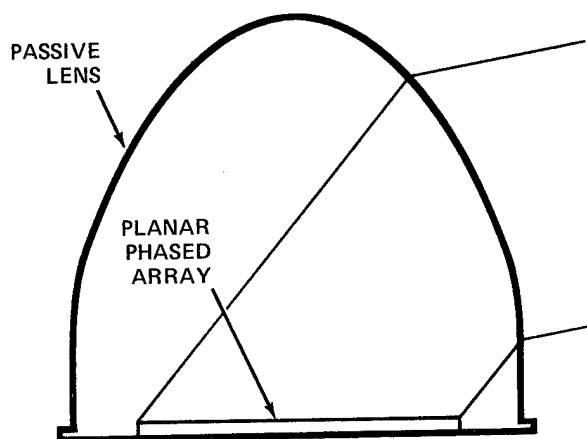


Figure 1. Dome Antenna Concept

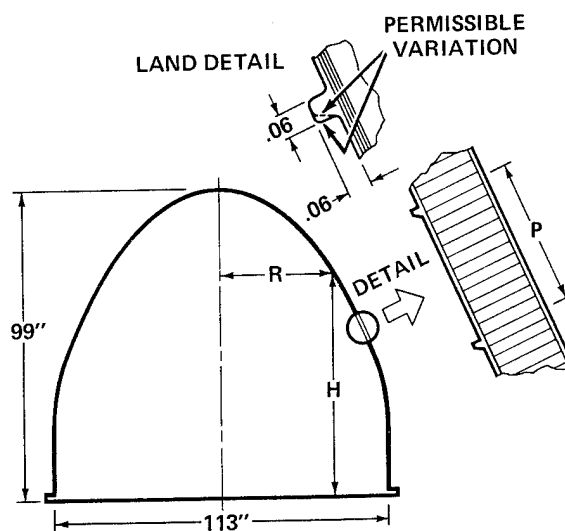


Figure 3. Section Through Dome

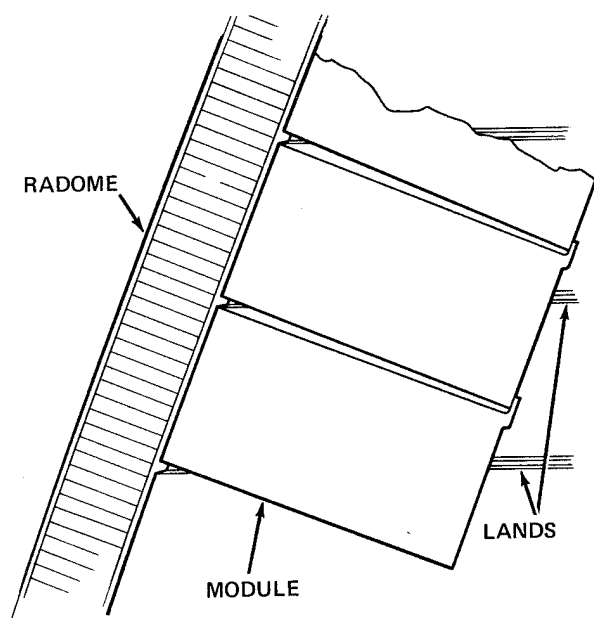


Figure 2. Lens Construction for Hemispheric Coverage Antenna

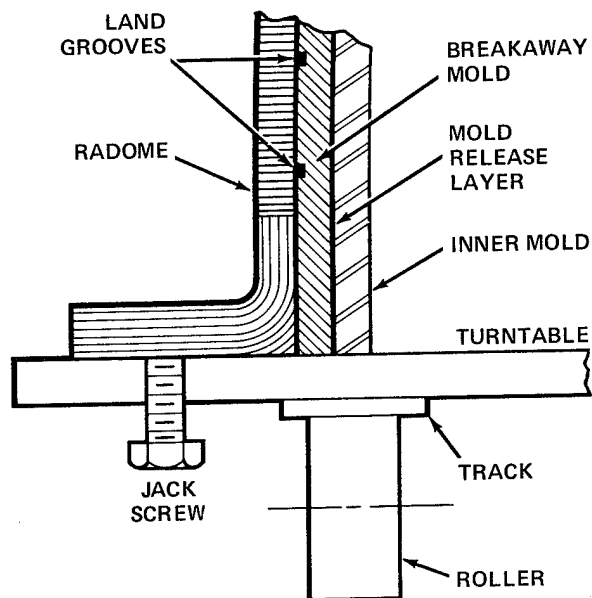


Figure 4. Mold Construction

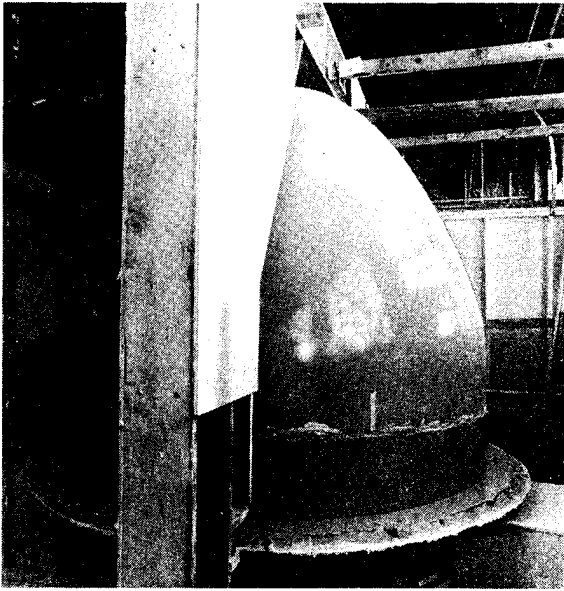


Figure 5. Inner Mold

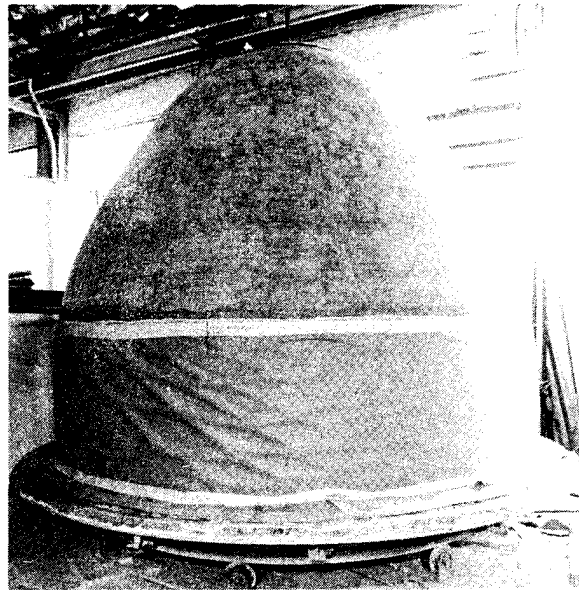


Figure 7. Applying Core

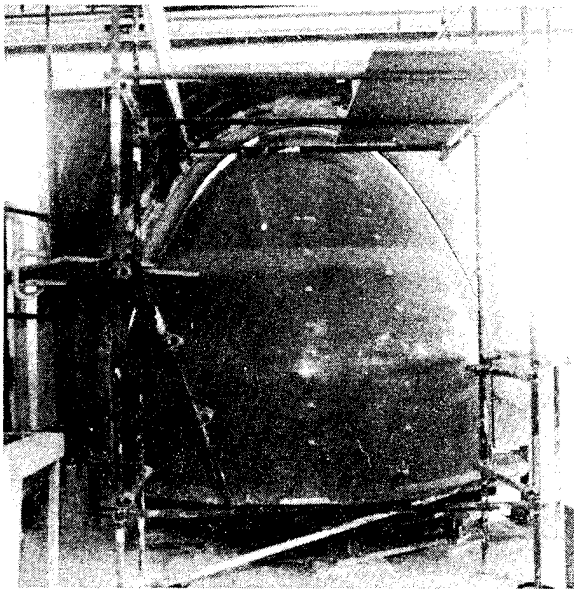


Figure 6. Completed Mold

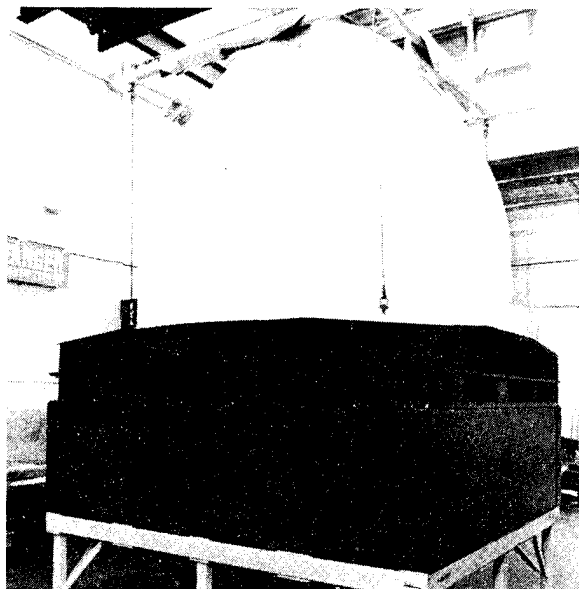


Figure 8. Completed Dome

## CHALLENGES IN INTERCONNECTION A PHASED-ARRAY RADAR

P. J. WALSH  
J. A. HENDERSON

Systems Development Division  
Westinghouse Electric Corporation  
Baltimore, Maryland

### ABSTRACT

A means of interconnecting a phased array radar antenna for a new airborne radar is presented. Nearly 2000 phase shifters are to be individually controlled requiring that 6 connections be made to each of them. These connections are made through a 14 layer multilayer printed wiring board. The latest technology available for making the PWB and external cabling is described.

### INTRODUCTION

A solid-state, phased array radar antenna presents an unusual opportunity for the development of new techniques for multiple high-density control interconnections. Such a system has recently been demonstrated for a new airborne radar system employing almost 2000 individually controlled phase shifter control assemblies (PSCA). The complex interconnection requirements and techniques employed to meet them are described in this paper. While the technologies are not new, their application has been extended to new areas.

### REQUIREMENTS

The antenna configuration for this radar is physically fixed in position. It is an electronically agile array. The beam is shaped and directed by the changing of phase of the almost 2000 ferrite phase shifters individually to provide the required results. It was necessary, therefore, that each phase shifter be independently set for phase. Also, different polarizations were required to enhance the radar beams for different conditions, and polarization had to be set for the phase shifters as a total group. An optimization of this established that the location of some of the control electronics for each phase shifter be individually assigned to that unit. Further studies led to the design of those electronic drivers in a package which mounted directly onto each phase shifter, providing for the individually testable phase shifter control assemblies. Driver design was accomplished in such a way that the only power requirements were +15 VDC and ground.

With this resolved, control of the individual drivers (and thus the phase settings) could be established through an x-y grid coordinate system that permitted each individual PSCA to be addressed separately. This was all coordinated electronically in a Beam Controller, an electronic subassembly located remotely from the antenna.

The approach taken (Figure I) included a driver "substrate" on the PSCA, pluggable into a multilayer PWB assembly. The PWB provided power, ground, and polarization circuitry to all PSCAs as well as the x-y addressing system. Flexible coaxial cable was used to provide the data and load instructions from the Beam Controller, and a power distribution and bus network provided power to the PWB. The entire system was designed to meet the EMI environment typically found in a military aircraft.

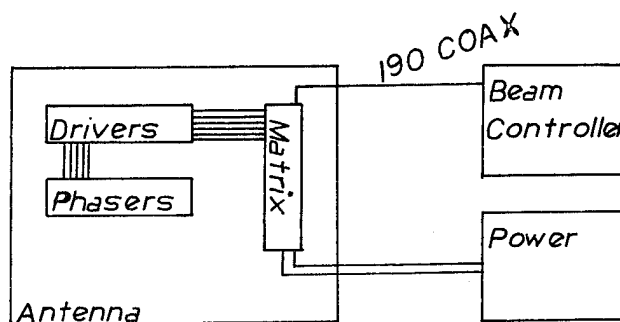


Figure I BLOCK DIAG OF SYSTEM

### DESIGN DETAILS

The block diagram of Figure I can be redefined in terms of interfaces and carriers. As an example, consider two electronic packages to be electrically interconnected, and let the connection be a cable. The diagram of this is shown in Figure II. The interfaces are the points where the cable engages each of the packages, and the carrier is the cable which carries the signals (or power) between the interfaces. Conversely, consider those points where carriers engage each other as interfaces. Thus, in an interconnection system where coaxial

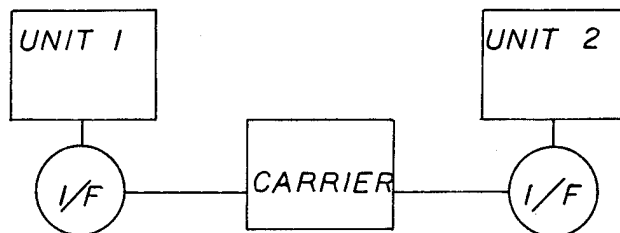


Figure II INTERFACES AND CARRIERS

cable changes to twisted pair, the point of change is an interface.

In the phased array antenna under consideration, the block diagram of Figure I becomes that shown in Figure III.

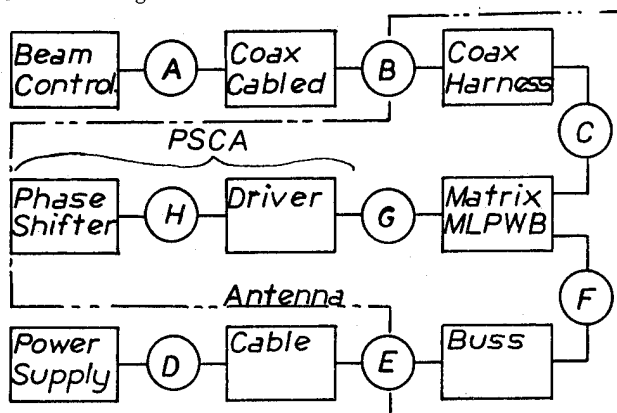


Figure III PHASED ARRAY ANTENNA  
INTERCONNECTIONS IN TERMS OF  
INTERFACES AND CARRIERS

#### BEAM CONTROLLER

The data and load/enable signals originate at the Beam Controller. There is one data signal for each "row" of PCMs in the antenna, and one load/enable signal for each column. With return lines required for each one to facilitate system self-test, the total number of signal lines required is 190, namely, 88 data and 102 load/enable. The beam controller also is the termination point for all coaxial cable shields.

#### COAXIAL CABLE INTERFACES - A and B

Due to the large number of interconnections required and the very limited area for them, a multiple contact coaxial connector of high density was selected. Each connector carried 51 coaxial contacts in a circular connector of shell size 24. The connectors (RAYCHEM RD-1) utilize contacts with solder preforms and heat shrinkable insulating sleeves to terminate the center and outer contacts to their leads in one controlled step. The connectors at Interface B included provision for EMI and pressure seals.

#### CABLING (COAX)-EXTERNAL

Because of the EMI environments external to the Beam Controller and the Antenna casing, it was determined that an additional shield for these coaxial lines was necessary. There were four cabled groups of coaxial wires formed for this carrier. Each one was composed of 51 95 ohm coaxial lines and one filler. The cables were formed into a very flexible contrahelically twisted cable.

#### CABLING (COAX)-INTERNAL

The cabling inside of the antenna from the antenna wall to the distribution board was made of

groups of six coaxial lines. These groupings were formed as a flat, woven cable to facilitate passing between the rf waveguides, which were spaced only 0.70 inches apart. This grouping of six lines was also convenient for the distribution of the input lines around the periphery of the PWB matrix plate. Because of the necessity to form the matrix plate in four quadrants, as will be discussed later, it was necessary to use an additional 95 coaxial lines, grouped as woven cables and interlaced with the groups of input lines. These were to tie the rows and columns in each of the quadrants together. As can be seen in Figure IV, even though the cabling within the antenna was complex, the woven cable groupings enabled an orderly cabling arrangement.

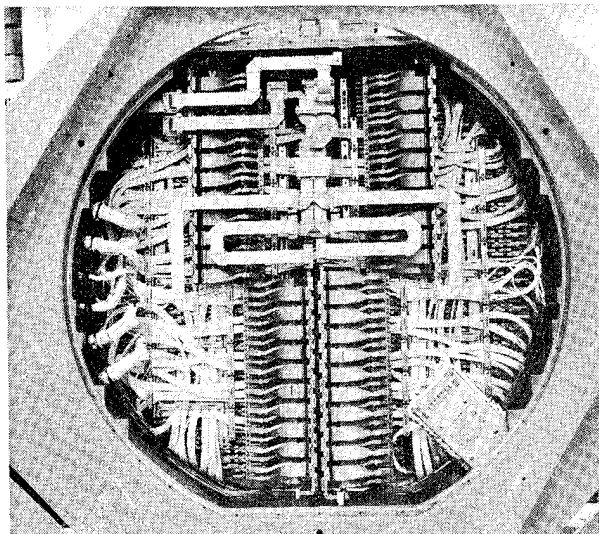


Figure IV PHASED ARRAY ANTENNA  
RF, POWER, AND SIGNAL DISTRIBUTION

#### INTERFACE C-COAXIAL WIRING TO MATRIX PWB

At this interface, the signal coax and shields were terminated to the multilayer PWBs used as the distribution matrix. This was done through the use of a pin and solder preform in an insulating heat-shrinkable sleeve for each center conductor. A separate pin was then used to terminate the shields as a group. The seven pins were positioned on .100 centers and soldered into plated-through holes on the multilayer matrix board. This termination technique provided for a minimum disturbance to characteristic impedance at this interface.

#### POWER SUPPLY SYSTEM

The power supply assembly consisted of two power supplies driving one +15 volt power bus. This bus was interconnected to the output interface by 19 AWG #12 wires, 9 of which were used for +15 VDC, and 10 for power return. MIL-C-38999 connectors were used at the power supply and antenna.

The distribution of power and ground to the matrix quadrants inside the antenna was accomplished by first converting from the #12 wires to a unique



distribution bus system (Figure V), which inserted the 75 ampere current into the matrix boards through many power tabs. Provision was also made for attaching energy storage capacitors if

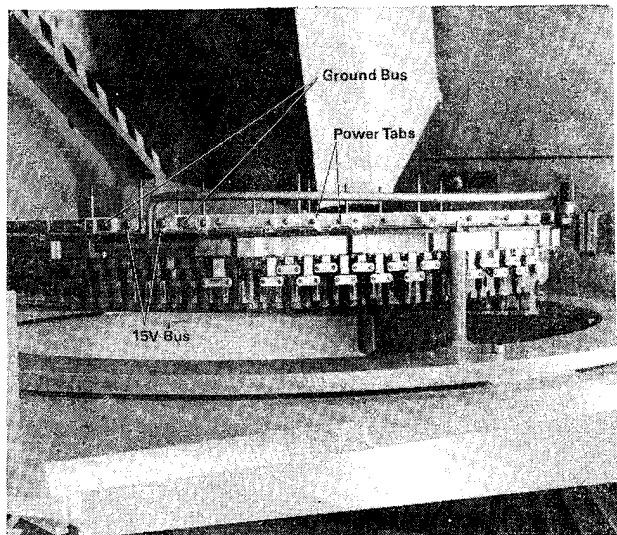


Figure V POWER BUS ASSEMBLY

future growth should require them.

#### MULTILAYER PWB (MATRIX)

The distribution matrix was formed of four 14 layer multilayer epoxy glass printed wiring boards. Many of these layers were ground planes, to enhance the stripline configuration used for the data and load/enable signals. Additional layers were used for carrying the polarization network and +15 volt power.

Four boards similar to that in Figure VI were required due to the 36 inch diameter of the total matrix and the uncertainties involved in controlling close tolerance dimensions on epoxy-glass

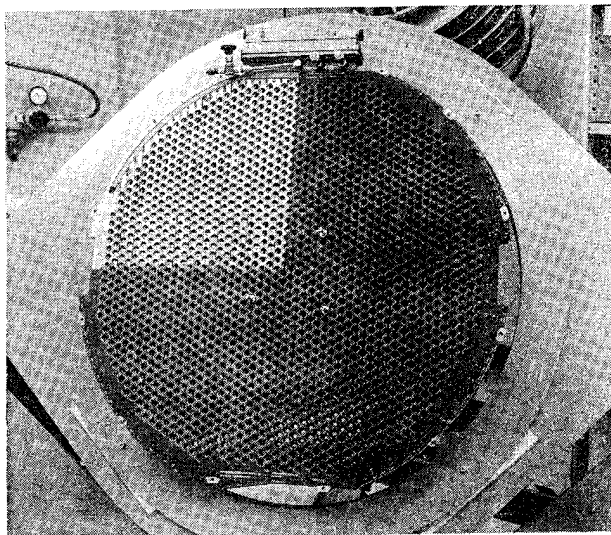


Figure VI MATRIX MANIFOLD ASSEMBLY

boards (over 11,000 connections had to be held to tolerances of a few mils). To facilitate the electrical engagement of the phase shifters, the boards had to be held flat. This was accomplished by preventing warpage during fabrication through the careful balancing of copper planes about the board center plane, and by multipoint attachment of the boards to the rf distribution assembly.

#### INTERFACE G

The interfaces of phase shifter control assemblies consisted of six pins (.019 dia) and mating sockets in the matrix board, and the tapered rf interface of the phase shifter into the rf assembly. Pluggable interfaces were required to meet antenna ease of assembly requirements. Close tolerancing was needed between the tapered rf interfaces and the pin/socket interfaces to allow complete seating of all of the tapers and still be within electrical engagement of the pins.

#### PHASE-SHIFTER DRIVER

This electronic package consists of several components mounted on a "substrate" of flexible printed wiring (FPW). (See Figure VII.) Soldered to the six pins, the FPW distributed the data, load/enable, polarization, power, and ground to the electronics and to the phase shifter, as well

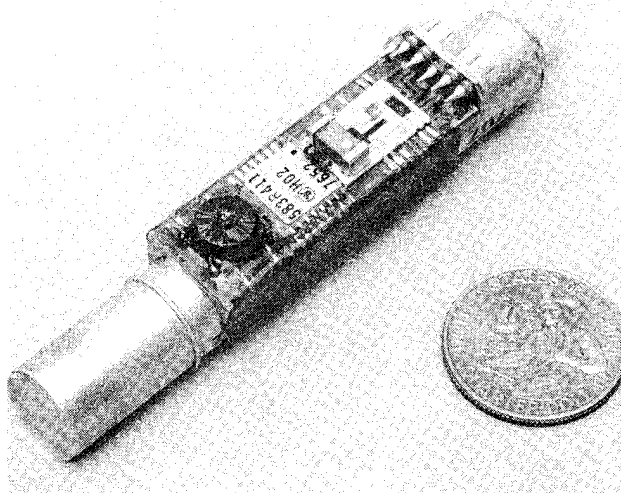


Figure VII PHASE SHIFTER CONTROL ASSEMBLY FOR PHASED ARRAY ANTENNA

as providing additional electrical interconnections to the driver. The FPW was bonded to the aluminum saddle with thermally conductive epoxy. Thermal stability for these assemblies is maintained through the phase shifter body to the rf manifold assembly.

#### INTERFACE H-PHASE SHIFTER

To provide this required interconnection in the very small available space, the phase shifters were required to provide their input lines on

flexible printed wiring, which was directly soldered to the driver FPW at a specified interface point. This required only five interconnections, which could be easily soldered in the FPW/FPW interface, and then insulated for protection.

#### ASSEMBLIES

Many of the initial concepts of this interconnection assembly were proven or modified with the fabrication and test of a 100 element array of this antenna. The lessons and demonstrations gained from the 100 element array were used to full advantage in design and fabrication of the full-size antenna, which is now being tested on the Westinghouse antenna test range in Baltimore, Maryland.

#### SUMMARY

The complex interconnection requirements of nearly 2000 phase control modules remotely controlled by a Beam Controller have been described. The heart of this technique has been the ability to column/row address each PCM through a stripline multilayer PWB matrix assembly. The large number of coaxial lines needed have been successfully applied through the use of many state-of-the-art technologies, including the heat-shrinkable devices, multiple pin coaxial connectors. Flexible printed wiring has also been used as substrate material. In short, a significant improvement in systems capability has been achieved through the careful application of modern electro-mechanical design technologies.

## HIGH-VOLTAGE PACKAGING PROBLEMS FOR AIRBORNE SYSTEMS

W. G. DUNBAR

Boeing Aerospace Company  
Seattle, Washington 98124

### ABSTRACT

Methods are presented for packaging high-density, high-voltage, high-power parts and modules. Example designs are shown for several mechanical conditions that involve high-voltage gradients through or across the surface of insulating materials. References are given for test specifications for materials, parts, components, and systems to alleviate packaging problems in airborne systems.

### INTRODUCTION

Electrical and mechanical packaging of high-density, high-voltage, high-power components within imposed volume and weight constraints becomes an exceedingly difficult task because of the potential corona onset and voltage breakdown. Therefore, it is not surprising that problems have occurred.

The voltage stress between RF electrodes in a radar circuit can be much higher than indicated by the supply voltage because of resonances and impedance mismatches. Also, the voltage gradient of insulation can be unexpectedly high because of dielectric mismatches and stress-concentrating geometry. In packaging high-voltage circuitry in restricted volume, close attention must be given to voltage gradients, the shape of the conducting surfaces, and the insulation system. It is essential to avoid small-curvature radii and sharp corners. High field concentrations can raise the local voltage gradients and produce corona, which in time will erode the insulation and cause voltage breakdown. Other high-voltage packaging annoyances that go unnoticed in lower voltage systems include collection of debris, flexing of wiring, lack of manufacturing cleanliness, and improper testing and overtesting of materials, components, and systems.

Examples of designs that produce these problems are shown and discussed in this paper. In addition, application of potting materials to large surfaces is discussed—specifically, the length-to-thickness ratio and thermal expansion of materials and the use of fillers next to small-radii wires and conductors.

Preferred tests, test equipment, and test voltages are known for the high-voltage, high-power systems. Large power system, communication, and radar manufacturers have built terrestrial equipment with high-voltage amplifiers, modulators, pulse-forming networks, generators, transformers, and switch gear. Much of this equipment is designed with insulation voltage gradients of 5V to 15V per mil (200V to 600V per millimeter) average. These equipments are designed to operate trouble free for 20 years or more. Equipment designed for a shorter lifetime (e.g., 1 month to a year) still has fairly low voltage gradients of 300V to 900V per millimeter. But for aerospace equipment, these same units must be designed with stresses between 2,000V and 4,000V per millimeter. Some have been designed with stresses to 6,000V per millimeter and operated successfully.

This paper examines some of the problem areas and describes how they can be overcome by the designer. The design of airborne electrical insulation is a professional activity based on an extensive theoretical background supplemented by some very

costly experience, mostly accumulated in the past 20 years. From this background and experience a few guides are extracted that are pertinent to the designer of airborne radars.

### ELECTRIC FIELDS

As the high-voltage portions of an airborne radar are resolved into small circuits and parts, ultimately unit pieces of conducting surfaces are obtained, called electrodes. These electrodes are at different voltages and are separated by an electrical insulation. Electrode configurations fall into three general categories: (1) points, which include sharp corners, sharp bends in wire filaments, and projections from a surface, such as a solder draw; (2) curved surfaces such as long spaced wires, round wires close to a ground plane, corona balls, and coaxial cables; and (3) parallel plates.

The space between and surrounding two or more electrodes is regarded as the electric field. Every point within this space has a definite potential that is related to its physical position in the field. The negative gradient of voltage at any point is a vector that is defined as the electric field strength  $E$  at this point. This gradient can be conceived as a force tending to displace a positive charge in the direction of the vector toward the negative electrode. A plot of the field for a sphere and a flat ground plane is shown in figure 1. The field lines emanate perpendicularly from the negative electrode and terminate perpendicularly on the positive electrode. The equal potential lines are perpendicular to the field lines.

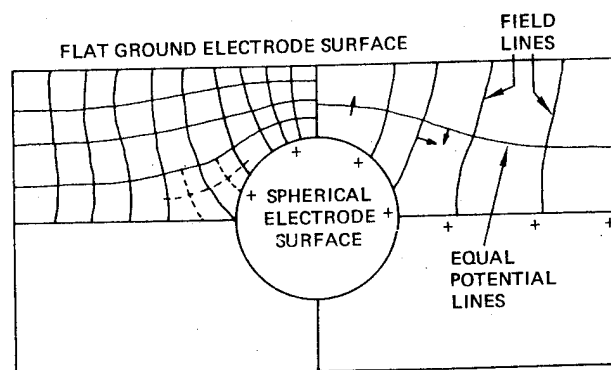
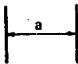

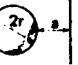
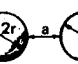









Figure 1. Freehand Field Mapping by Curvilinear Squares Method

Electric field theory is explained in texts on electricity, magnetism, fields, and waves (refs. 1, 2, 3). Table 1 shows methods used in predicting the field configuration.

For electrodes of any given shape, the variation in potential, as a function of the distance from one electrode to the other electrode, can be calculated by solving the differential equations for the electrostatic field. For parallel plates, concentric spheres,

**Table 1. Maximum Field Strength  $E$  With a Potential Difference  $V$  Between the Electrodes, for Different Electrode Configurations**

Configuration		Formula for $E$
Two parallel plane plates		$V/a$
Two concentric spheres		$V/a [(r+a)/r]$
Sphere and plane plate		$0.9 V/a [(r+a)/r]$
Two spheres at distance $a$ from each other		$0.9 V/a [(r+a/2)/r]$
Two coaxial cylinders		$V/[2.3r \lg [(r+a)/r]]$
Cylinder parallel to plane plate		$0.9 V/[2.3r \lg [(r+a)/r]]$
Two parallel cylinders		$(0.9 V/2)/[2.3r \lg [(r+a/2)/r]]$
Two perpendicular cylinders		$(0.9 V/2)/[2.3r \lg [(r+a/2)/r]]$
Hemisphere on one of two parallel plane plates		$3 V/a; (a \gg r)$
Semicylinder on one of two parallel plane plates		$2 V/a; (a \gg r)$
Two dielectrics between plane plates $\epsilon_1$ and $\epsilon_2$		$V\epsilon_1/(a_1\epsilon_2 + a_2\epsilon_1)$

parallel cylinders, and a sphere gap, the equations for the field strength are:

a. Parallel plates:  $E_x = \partial\phi/\partial x = -A = V/S$ , volts/centimeter (1)

b. Concentric spheres:  $E_x = (V/x^2)[(r_1 r_2)/(r_2 - r_1)]$  (2)

c. Parallel cylinders:  $E_m = (V/2r)[1/\cosh^{-1}[(S/2 - r)/r]]$  (3)

d. Sphere gap:  $E_m = \frac{V(1+x)^2}{2r(1-x)} \sum_{n=0}^{\infty} x^n \left[ \frac{1-x^{2n+1}}{(1+x^{2n+1})^2} \right]$  (4)

$$\text{or: } E_m = \frac{V}{2r} \left[ 1 + \frac{(1+x)^3}{1-x} \left[ x \frac{1-x^3}{(1+x^3)^2} + x^2 \left( \frac{1-x^5}{(1+x^5)^2} \right) + x^3 \left( \frac{1+x^7}{(1+x^7)^2} \right) + \dots \right] \right] \quad (5)$$

where:  $E_x$  = voltage gradient at distance  $x$  between electrodes, volts/centimeter  
 $E_m$  = maximum voltage gradient at surface of smaller electrode, volts/centimeter  
 $\phi$  = potential at the electrode, volts  
 $x$  = distance from the reference electrode, centimeters  
 $A$  = constant  
 $V$  = volts  
 $S$  = spacing between electrodes, centimeters  
 $r_1$  = inner sphere (outside) radius, centimeters  
 $r_2$  = outer sphere (inside) radius, centimeters  
 $r$  = radius of sphere or cylinder, centimeters

**Empirical Field Equations.** An empirical field equation or formula is the shortened, simplified form of a rigorous equation. Rigorous equations, manageable with electronic calculators, are still difficult to use in everyday design work, especially if the design has to be assembled piecewise. Often the equation for the exact required electrode shape is not readily available to the designer. To derive or compute a rigorous equation is costly and time-consuming, so it is usually more advantageous to use time-proven empirical equations. Furthermore, the maximum stress is often the only value needed in a design, and the plotting of the complete field using a rigorous equation is not necessary. Empirical equations for the maximum field stresses at the smaller electrodes, for several electrode configurations, are given in table 1 (ref. 4). Electrical stresses calculated with these equations are within 10% of values obtained with rigorous equations.

**Utilization Factor.** The utilization or efficiency factor is defined as the ratio of the field stress between parallel plates to the maximum field stress at the smaller electrode of a nonuniform configuration with identical spacing. The utilization factor is numerically equal to the required voltage derating. In equation form:

$$n = E/E_m < 1 \quad (6)$$

where:  $n$  = utilization factor  
 $E$  = voltage stress between parallel plates spaced a unit apart, kilovolts/centimeter  
 $E_m$  = maximum voltage stress between two conductors spaced a unit apart, kilovolts/centimeter  
 $a$  = spacing, centimeters

Figure 2 plots the utilization factors as functions of electrode spacing for several electrode geometries commonly used in electrical/electronic designs. The utilization factor, which provides a way of quickly estimating the sparkover or breakdown voltage of a configuration, can also be used for estimating the minimum electrode radius for a given spacing when the electrical stress capability of the dielectric is known.

## DESIGN IDEAS THAT HAVE WORKED IN HIGH-VOLTAGE EQUIPMENT

Examples of designs used to increase field stress in high-voltage equipment are described in the following paragraphs.

**Terminal Boards and Supports.** Composite and laminated insulation is used for terminal boards and for supports that separate the coils and wiring from the cores, structure, and containers. A terminal board for high potential should be made from qualified

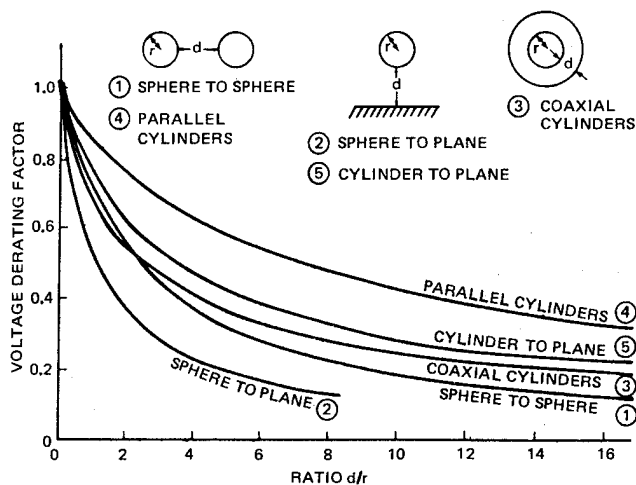


Figure 2. Utilization Factor for Various Electrode Configurations

insulation. The board may be flat, if the voltage is less than 20 kV, provided the electrical stress is:

- Less than 10 V/mil for long life (10 to 30 years)
  - Less than 10 to 25 V/mil for short life (1 month to 1 year)
- With treated boards in a dry, clean atmosphere of pure gas these values can be increased threefold.

Terminal boards operating at voltages greater than 20 kV should be contoured to increase the creepage paths. Three basic methods of contouring (shown in fig. 3) are:

- Cutting slots (gas-filled regions) between the terminals
- Building barrier strips between the terminals
- Mounting the terminals on insulated standoffs

A combination of the three methods may be necessary for voltages greater than 100 kV.

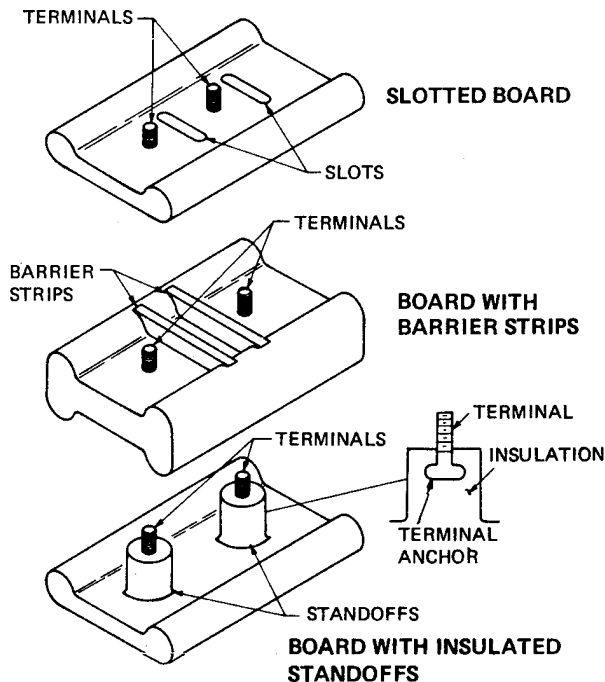


Figure 3. Terminal Boards

The slots in a slotted board form creepage paths as well as flashover barriers on both sides of the board. A board with barriers is the most difficult to design. The barriers must be built on both sides of the board, and the board has to be made from materials that will not form creepage paths under the barriers or, in laminated boards, through the board laminates. The barriers must not interfere with the terminals or the wiring.

Insulated standoffs are a form of the barrier strips. They are difficult to design because they must withstand the forces applied by the terminals, and the terminal anchor must be embedded in the top surface of the standoff. The anchor must be contoured for minimum electrical stress.

**High-Voltage Leads.** Leads between high-voltage parts should be made of round, smooth-surfaced, polished metal tubing. Steel and nickel-plated metals are preferred, but softer metals often are used because they are easier to fabricate. The radius of curvature on all bends should be at least 2.5 times the conductor diameter to avoid flattening or crushing the tube at the bend. The ends of the tubes should be flattened as little as possible, but this becomes difficult for pieces other than straight sections. When the end of the tubing is flattened, the corona-suppression shield should extend over the edges and the flattened end of the tubing, as shown in figure 4. Ample space must be provided between the inside surface of the insulator and the metal tube. A safe design would be based on the assumption that the full voltage stress exists on the top edge of the bushing.

Hollow tubing must be vented. Vent holes should be drilled through one wall of the tubing at both ends. The vent hole should face the corona shield.

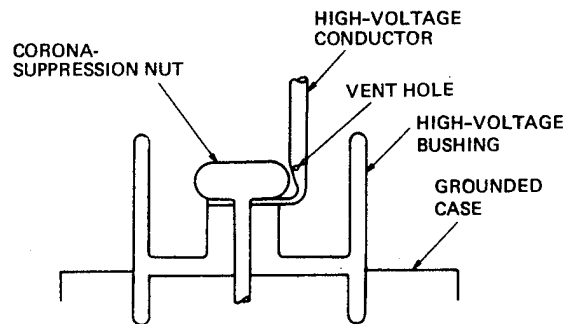


Figure 4. High-Voltage Lead and Bushing

**Special Design Features.** High-voltage flexible-lead terminations should be designed to eliminate pressure points on the terminal board (fig. 5); pressure points will cause delamination, which enhances internal tracking. The terminal should be protected with a corona ball or shield.

Other insulation techniques include either burnishing or enameling over the knots in ties to prevent the feathered ends from becoming points from which corona discharges will emanate (fig. 6).

Small pieces of insulation must be cleaned out of transformer cases; otherwise "chips" may lodge in the field between a coil and metal and cause corona, which ruins the gas or oil insulation. Wire terminations should be designed and installed so the field approaches that of a parallel-plate configuration without point discontinuities.

**Standoffs and Boards.** For high-density packaging, high-voltage parts are separated by either laying them out on the surface of a board or placing them on standoffs. A few critical problem areas are board delamination, joints, cleanliness, surface coating, and edges.

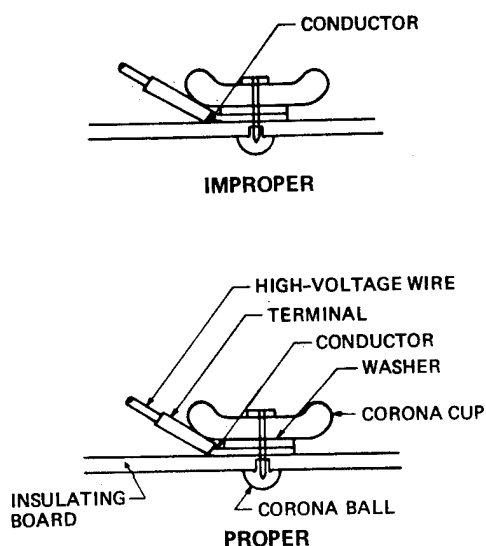


Figure 5. High-Voltage Terminals

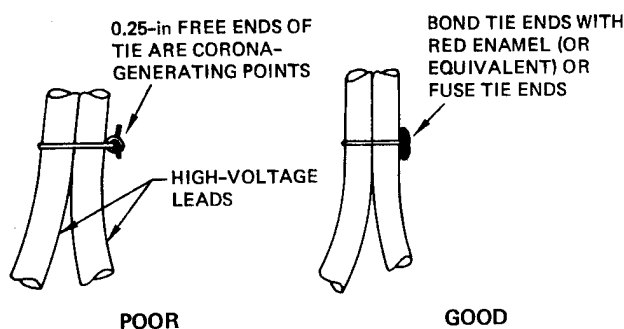


Figure 6. High-Voltage Ties

**Board Delamination.** Boards used to separate high-voltage parts from grounds must serve a dual purpose: structural and mechanical. Fiberglass usually is the major composite of boards, with epoxy or other material used for the filler. When the board is made in large, thick sections, the filler material occasionally does not completely penetrate the fiber. Thus, the board has large internal voids that are difficult to detect. (One scanning method is described in reference 5.) Once a board or rod is found with this type of fault, it is best to have all boards scanned for defects; otherwise, application of a high potential will initiate internal tracking and failure. These types of failures usually are discovered in the field after many hours of service.

**Joints.** Screws frequently are used to join a metal plate to the end of a rod or standoff. This is strictly unacceptable in high-voltage designs because the screw is always accompanied by a hole that is deeper than the screw; thus, a void exists at the bottom of the screw and the screw will attain a potential causing a very high field gradient at the point of the screw and along the threads. This will cause a high-voltage gradient across the air gap. Then partial discharges will enhance treeing through the standoff, resulting in arcing. Bonding within a loose-fitting clamp is best. A tight-fitting clamp is unwise because if the clamp is tightened enough to secure the standoff in place, it will cause the standoff to delaminate, and again tracking will occur. (See figure 7.)

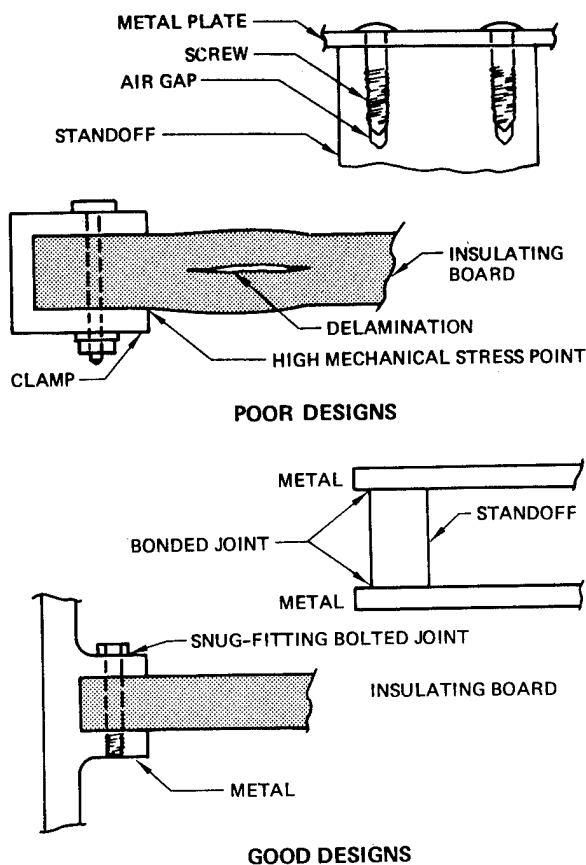


Figure 7. Board Standoff Clamping

**Cleanliness and Surface Coatings.** Prior to coating the surface of a board or joint, before or after assembly, it must be thoroughly cleaned of oils, greases, dirt, foreign objects, cleaning salts, and acid deposits. Large boards often require two or more cleaning processes (ref. 6). Following cleaning, the board should be taken to the area where the coating is applied. During transportation the board should not be touched with bare hands or contaminated objects. The coating must be placed on the board in a dust/lint-free compartment. Likewise, during installation into the final assembly, the board must be handled so as not to contaminate the surface.

**Edges.** A large board often has cutouts, holes, slots, and indentations. Remember, all edges are to be smooth and rounded. A sharp edge on an insulating board is equal to a sharp edge on a metal sheet.

**Taps and Plates.** A high-voltage rectifier normally is assembled from a series of connected diodes. Occasionally, a voltage tap is required at the center of the diode string. This tap should be made of material having the same diameter as the diode surface and thick enough for attachment of a round tubular connection. Soldered joints should not be used because most solder electrodes have lower breakdown potentials than metals such as steel, nickel, brass, copper, and aluminum.

A potential shaping surface within a stack of series-connected diodes can be a thin plate of metal provided with a large-radius edge, as shown in figure 8. This curved edge suppresses corona.

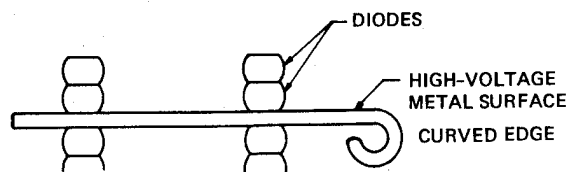


Figure 8. Curved Edge on High-Voltage Plate

#### THERMAL SHOCK RESISTANCE AND ADHESION TESTS

A special test cell has been designed to evaluate thermal shock resistance and adhesion concurrently. The coaxial configuration is made of two thin-wall aluminum tubes, each 4 in long. The inner tube has a 1-in diameter and the outer tube a 2-in diameter. These are physically spaced by placing the tubes in the assigned grooves of an aluminum base plate as shown in figure 9. The filled cell can be removed from the base plate after encapsulation for testing and inspection. Web length-to-thickness ratios can be varied by changing the height of potting.

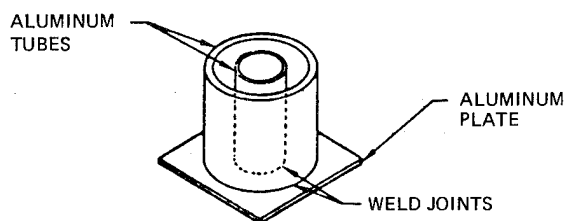


Figure 9. Adhesion, Thermal Shock Resistance Test Cell

Each potting material can be evaluated in this cell by subjecting the potted coaxial configuration to thermal shock by temperature cycling. The material will be inspected for adhesion to the aluminum surfaces after thermal cycling by visual inspection or by cross-sectioning techniques. Clear materials will be inspected for cracking and crazing using a high-intensity polarized light source. Any cracking, crazing, or disbonding of the material would constitute a failure of the material, and it should be eliminated from further consideration.

A material usually is evaluated by placing a small sample in a shallow, thin-wall aluminum dish. The sample is thermally cycled and then inspected for cracking, crazing, and adhesion. Unfortunately, the aluminum dish does not simulate a real potting situation.

#### POSSIBLE PROBLEM AREAS AND SUGGESTED SOLUTIONS

High-voltage systems are plagued with annoyances that are unnoticed in low-voltage systems. Some of the more subtle annoyances are described in the following paragraphs.

**Debris.** Small dielectric flakes or chips lodged or lying on the surface or edge of a coil will align themselves with the electric field. They will be charged to the same potential as the surface to which they are attached, acting as a point on the surface. This will decrease the utilization factor of the gas or oil and cause excessive corona and eventual breakdown. Inspections and thorough cleaning with high-pressure air will eliminate this problem.

**Mechanical Stress.** Terminations should be designed to minimize mechanical stress points on the insulating boards. This can be accomplished by molding the terminal in a solid insulating material that is attached to the board or by placing metal spacers with flanges through the board. The metal spacers not only reduce the mechanical stress but also increase the surface utilization factor between the flange edges.

**Flexible Wiring.** High-voltage, extra-flexible wiring is acceptable in some limited cases. It should be used only as a last resort. When used, it should be guided from terminal to terminal to eliminate the probability of the wire insulation intermittently touching other surfaces containing higher or lower voltage circuits.

**Manufacturing Cleanliness.** No one can overstress the need for manufacturing cleanliness. Gloved hands should be mandatory when papers, films, and other cleaned surfaces are handled. Slight amounts of oils or acids can cause an improper bond or encapsulation. Any paper, cloth, film, or other dielectric material is suspect and should be inspected by material, shop fabrication, or engineering personnel. Smoke-emitting objects in materials fabrication shops may contaminate the dielectric.

**Mold Release Agents.** Silicone products may contaminate certain epoxies, urethanes, and other insulating materials. Compatibility and contamination of materials for bonding purposes should be investigated prior to fabrication. When there is an incompatibility, precautions must be taken to avoid contamination.

**Similarity.** Materials and designs too often are used because they have similar characteristics. Similarity ends at the last pour of a batch, the last section of the roll, and the last fabricated part by a skilled craftsman.

**Testing.** Flaws in outer surfaces and between a single conductor and a surface can be visually inspected. When a coil, circuit, or multiple-conductor assembly is tested, the test must include the detection of imperfections between coil layers, circuit parts, and assembly layers. This implies that the total assembly must be energized in such a way that all overstressed electrical parts will be detected. An overvoltage test and/or overfrequency test are two methods for testing.

**Environment and Life.** Most high-voltage circuits and parts will be installed in enclosed pressurized containers. This reduces the probability of thermal shock, but not temperature extremes. Testing an insulation in a small dish is inadequate. Fabricated parts and circuits should be assembled per specification inside the container and tested through the temperature extremes with all circuits normally energized. Five to nine cycles are recommended. Pre-environmental tests and post-environmental tests should include corona, dissipation factor, insulation resistivity, and a visual inspection for breaks, tears, and deformation. Any significant changes in appearance or electrical characteristics are reason for further testing and/or modification prior to qualification and life testing.

**Tabs.** Small tabs often are placed on wires and parts for identification and installation purposes. When these coils and circuits are encapsulated, film-tape tabs such as Mylar adhesive may cause built-in gas pockets or voids. These voids may initiate partial discharges and eventual voltage breakdown. If tabs are required, make them of porous materials that are compatible and easily wetted with the encapsulant.

**Spacers.** Spacers between two energized encapsulated units must be nearly void-free and have smooth or rounded surfaces to reduce tracking susceptibility across the spacer surface. The two dielectrics will reduce the stress across the spacer and the available charging current but they will not eliminate the problem. The spacer surface should be designed as though the voltage at the dielectric surfaces was from base electrodes not dielectrics.

**Coatings.** Coated metal surfaces have higher breakdown voltage characteristics than uncoated surfaces, provided the correct coating material is applied. Some coatings do not bond well, flake, and reduce the electrical stress capability of the two electrodes.

Others may have pin holes and voids or blisters that also cause flaking. Coatings must be evaluated with proper materials under identical environmental and electrical stress conditions to be fully qualified.

**Determining Corona Limitation Voltage.** The corona initiation voltage (CIV) of an electrical apparatus can be determined when the design parameters and the applicable Paschen-law curve are known. The Paschen curve used depends on the type of gas the corona would occur in, the temperature of the gas, and the configuration of the electrodes. Figure 10 compares Paschen curves for different gases. The most common gas is air, of course. If the temperature exceeds 500°F, special Paschen curves must be used. Several curves for insulated and noninsulated wires are given in reference 7.

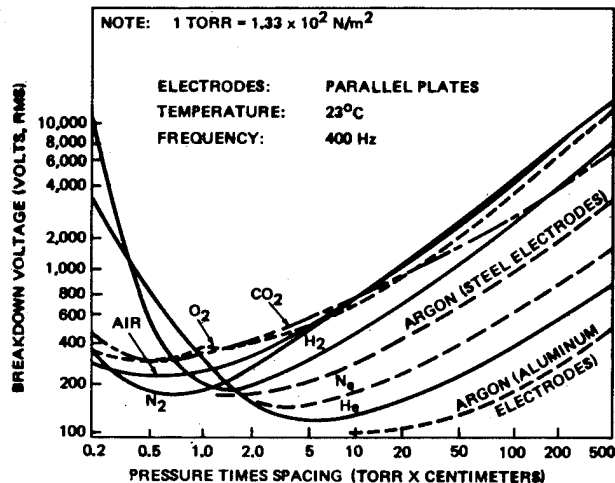


Figure 10. Paschen-Curve Comparison for Different Gases

## SUMMARY

Properly designed electrical insulation is essential for the successful operation of high-voltage, high-power, densely packaged airborne systems. All parameters affecting voltage stress and insulation life must be included in the design, development, and test program. Special attention must be given to mechanical attachment of parts, large-board delamination, and the electrical field stresses imposed by nonuniformly constructed electrodes. Corona shields must be applied to all sharp electrodes to lower field stresses. Above all, manufacturing and assembly must be in clean rooms by personnel certified for clean-room procedures.

## REFERENCES

1. W. R. Smythe, *Static and Dynamic Electricity*, McGraw-Hill, New York, 1968
2. J. D. Stratton, *Electromagnetic Theory*, McGraw-Hill, New York, 1941
3. E. W. Greenfield, *Introduction to Dielectric Theory and Measurements*, College of Engineering, Washington State University, Pullman, Washington, 1972
4. A. Bowers and P. G. Cath, "The Maximum Electrical Field Strength for Several Simple Electrode Configurations," *Philips Technical Review*, No. 6, 1941, p. 270
5. S. J. Klima and T. J. Riley, "Ultrasonic Evaluation of High-Voltage Circuit Boards," *Power Electronic Specialists Conference 1976 Record*, 76CH1084-3AES, pp. 128-135
6. C. J. Tautcher, *The Contamination of Printed Wiring Boards and Assemblies*, Omega Scientific Services, Bothell, Washington, 1976
7. W. G. Dunbar, "Corona Testing of Supersonic Airplane High-Temperature Wire," *Eighth Electrical Insulation Conference*, No. 68C6-EI-73, December 1968



# CRYSTAL OSCILLATOR VIBRATION ISOLATION FOR AIRBORNE RADAR APPLICATIONS

HERMAN ROSSMAN  
JOHN J. CHINO

Systems Development Division  
Westinghouse Electric Corporation  
Baltimore, Maryland 21203

## ABSTRACT

This paper deals with a method for determining a vibration isolation system capable of attenuating airborne induced vibration imparted to the stable crystal oscillators used in airborne radars. Suitable isolation is achieved when maximum permissible vibration levels, based on system noise limits, have not been exceeded.

Included in this paper is a procedure for calculating the response of multi-stage (or single stage) vibration isolation systems. Foremost, the procedure considers the "real world" effects introduced by complex, nonhomogeneous structures. Essentially, the approach depends on assuming a reasonable value for the occurrence of the first major structural resonance (not the isolators) and the ensuing selection of a damping ratio ( $\zeta$ ).

## INTRODUCTION

The stalo is comprised primarily of crystal oscillators. In Doppler radar application of crystal oscillators, vibration can cause frequency modulation (FM) of the resonator section. The incidental FM caused by motion can produce noise sideband levels sufficiently high so that the desired system targets are masked.

A Westinghouse designed stalo system which successfully employed three stages of vibration isolation will be discussed. Verification between the computed and actual vibration results will be given.

## DESCRIPTION OF CALCULATION PROCEDURE

The procedure is accomplished in three parts:

1. Determination of the permissible vibration limits, based on crystal sensitivity.
2. Select a "best guess" estimate of the isolation system necessary to meet requirements of (1) above. Develop a theoretical mechanical model of the system and determine the transmissibility using a 1.0 g sinusoidal input. For the solution described in this paper an electro-mechanical equivalent was developed (see Figures 1 and 2).

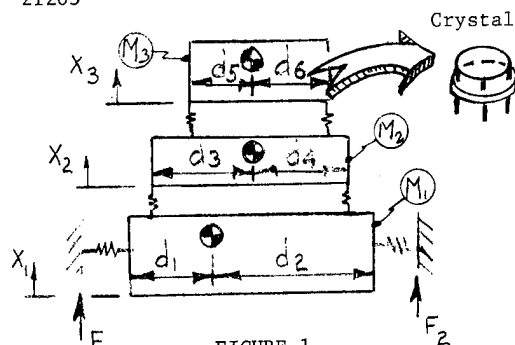


FIGURE 1

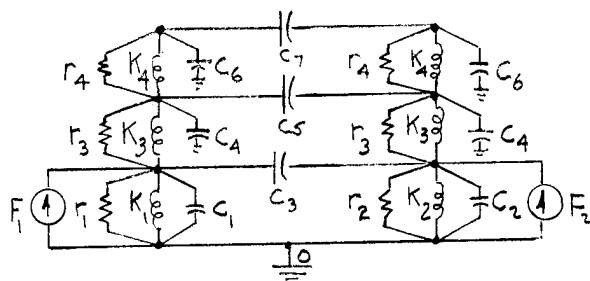


FIGURE 2

3. Calculate the correlated random-sinusoidal  $g_{\text{peak}}$  response by employing the following equation:

$$g_{\text{peak}} = 3\sigma = 3\sqrt{S_i H^2 \Delta f} \quad (1a)$$

as modified under the development of the empirical curve section of this paper.  $S_i$  is the random vibration input,  $H$  is the transmissibility, and  $\Delta f$  is the incremental frequency bandwidth of vibration.

## ANALYSIS

Permissible Level: In airborne radar systems, the required phase noise spectral density  $\mathcal{L}(f)$  is the ratio of phase noise power at each sideband frequency ( $f$ ) to the total signal power, as observed in a unit bandwidth. At frequencies where mechanical vibrations might cause unwanted phase noise, a typical requirement is:

$$\mathcal{L}(f) = \mathcal{L}_0 \left[ \left( \frac{f_0}{f} \right)^3 + \left( \frac{f}{f_0} \right) \right] \quad (2)$$

where  $\mathcal{L}_0$  is the phase noise at intercept frequencies  $f_0$ . Since the quartz crystal has a

a known acceleration sensitivity,  $\eta$ , the permissible vibration levels at the crystal are easily calculated.

$\mathcal{L}(f)$  is related to frequency deviation  $\Delta F$ , and modulation rate,  $f$ , as:

$$\mathcal{L}(f) = \frac{\Delta F^2(f)}{2f^2} \quad (3)$$

$\Delta F$  is related to crystal sensitivity  $\eta$  and microwave frequency  $F_x$  as:

$$\overline{\Delta F^2}(f) = \eta^2 F_x^2 \overline{a^2}(f) \quad (4)$$

Combining 2, 3, and 4 results in a typical permissible crystal acceleration:

$$\overline{a^2} = \frac{2\mathcal{L}_0}{\eta^2} \left( \frac{f_0}{F_x} \right)^2 \left( \frac{f_0}{f} + \frac{f}{f_0} \right) \quad \text{Ref. 1} \quad (5)$$

For example:

$$F_x = 10 \times 10^9 \text{ Hz (X band)}$$

$$\mathcal{L}_0 = -110 \text{ dB/Hz} = 1 \times 10^{-11} / \text{Hz}$$

$$\eta = 1 \times 10^{-9} / \text{g} \quad (\text{Ref. 2})$$

$$f_0 = 2000 \text{ Hz}$$

Then

$$\overline{a^2} = 8 \times 10^{-7} \left( \frac{2000}{f} + \frac{f}{2000} \right) \text{ g}^2 / \text{Hz}$$

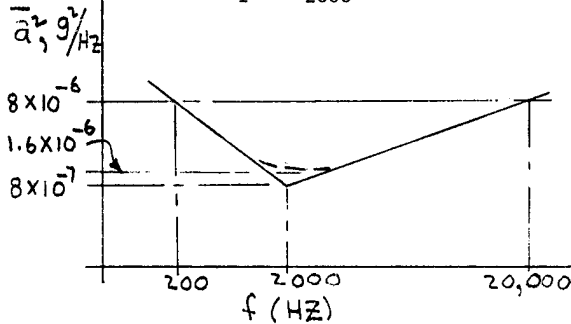


FIGURE 3

Electro-mechanical Model: The circuit shown in Figure 2 describes the electro-mechanical model used to analyze the system shown in Figure 1. (This system was expanded from a single stage system described in Reference 3.)

The element  $c_3$  ties nodes 1 and 2 such that if  $d_1 \neq d_2$  the model will yield both translational and rotational motion. The various circuit elements can be calculated by using the following expressions:

$$(\text{Spring Constant}) K = \frac{P}{X} \quad (6)$$

$$(\text{Damping Constant}) r = 2\sqrt{\frac{KM}{386}} \quad (7)$$

For  $c_1$ , and similarly for  $c_2$ ,  $c_4$ , and  $c_6$ :

$$c_1 = \frac{[2k^2 + (d_1 \text{ or } d_2)^2 - d_1 d_2] M}{(d_1 + d_2)^2} \quad (8a)$$

where the  $(d_1 \text{ or } d_2)$  term is the distance from the isolator to the center of gravity, and the radius of gyration

$$k^2 = \frac{I}{M} \quad (9)$$

and for  $c_3$ , and similarly for  $c_5$  and  $c_7$ :

$$c_3 = \frac{(d_1 d_2 - k^2) M}{(d_1 + d_2)^2} \quad (10)$$

For the system described in this report  $d_1 \neq d_2$ ,  $d_3 = d_4$ , and  $d_5 = d_6$ . Thus, for the cases where the distance from the center of gravity to the isolators on the various stages are equal, equation (8a) becomes:

$$c = \frac{2k^2 M}{d^2} \quad (8b)$$

The response for a 1.0 g sinusoidal input is plotted in Figure 4.

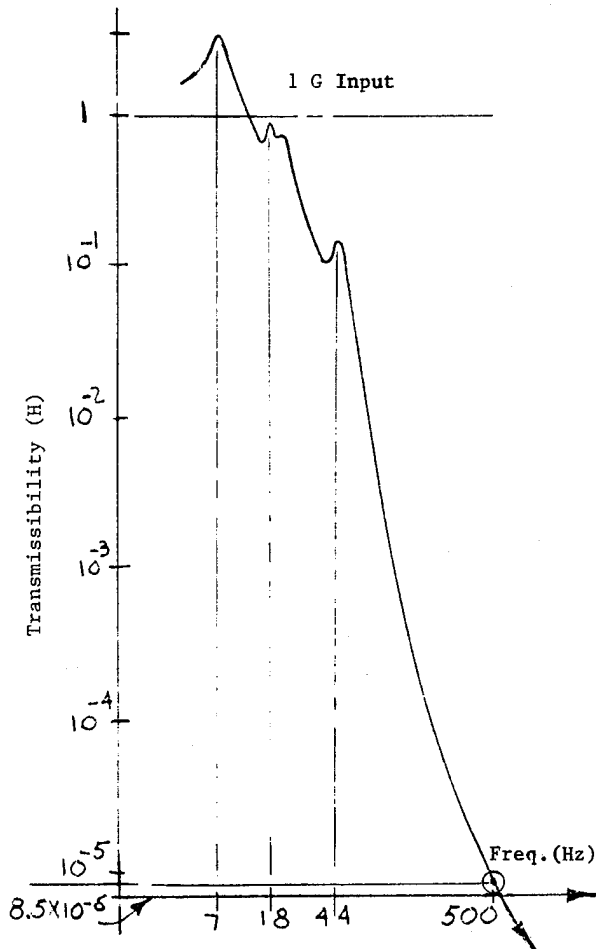


FIGURE 4

**Developing an Empirical Curve:** Generally, calculations of the response of an isolation system are initiated by assuming that the masses are homogeneous and exhibit no frequencies in the domain of excitation. Reality, however, tells us that in a real system there are numerous frequencies and associated harmonics. Consequently, the theoretical response, which only considers the isolation system, differs somewhat from that of the tested model. For the most part, the most significant departure from the theoretical response occurs at the first major structural frequency and thereafter.

Complicated and expensive computer programs do exist which could be employed in arriving at the solution. However, even here the results depend largely on assumptions so that the result is still only as good as the input information. The approach described in the ensuing discussion will offer the engineer a simple method of achieving good accuracy by combining theory with empirical design techniques.

It can be seen from the table below that different types of structures are characterized by having various values of  $\zeta$  where:

$$T = \frac{1}{2\zeta} \quad (11)$$

Typical Values of Damping for Different Methods of Construction

Method of Construction	Damping Ratio, $\zeta$
One-piece Unit	0.01
Welded Assembly	0.02
Riveted Assembly	0.04
Bolted Assembly	0.05

(Ref. 4)

TABLE I

The stalo system indicated earlier employed various types of construction techniques including castings, welded elements, bolted and riveted structures, etc. For purposes of this analysis, based upon prior experience, a value of  $\zeta = .02$  was selected. Using this value we obtain  $T = 25$ . Further, it was assumed that the first major structural frequency occurs at 150 Hz (based on experience with similar systems) and is followed by an infinite number of structural frequencies and harmonics. Equation (1a) will now be modified to read:

$$g_{\text{peak}} \Big|_{150 \rightarrow 2000 \text{ Hz}} = 3\zeta = 3 \sqrt{s_i \left[ \frac{H(T)}{H} \right]^2 \Delta f} \quad (1b)$$

where  $\Delta f$  is assumed to equal 1 Hz. For frequencies  $< 150$  Hz equation (1a) is used.

#### SAMPLE CALCULATION

At  $f = 500$  Hz, with a random vibration input level  $s_i = 1.4 \times 10^{-3} \text{ g}^2/\text{Hz}$  and  $H = 8.5 \times 10^{-6}$  (from Figure 4), we obtain from equation (1b):

$$g_{\text{peak}} = 3 \sqrt{(1.4 \times 10^{-3}) \left[ (8.5 \times 10^{-6}) (25) \right]^2} \quad (1)$$

$$g_{\text{peak}} = 2.39 \times 10^{-5} \text{ g}$$

This procedure is repeated for all frequencies up to 2000 Hz. For values of frequency  $< 150$  Hz, equation (1a) is used. See plot in Figure 5.

#### VERIFICATION OF ANALYSIS

From Figure 5, it is evident that the computations agree favorably with the test results up to approximately 500 Hz. The primary source of discrepancy between the calculated and the test results, for values of frequency  $> 500$  Hz, is due to the high noise floor associated with the vibration test equipment. Additional disparities also occur since  $\zeta$  varies with each structural element; further, resonances are not actually present at each discrete frequency.

The foregoing analytical approaches have been utilized for analyzing three additional vibration systems - both single and a two-stage systems. In each case, the results of these analytical approaches agreed very favorably with the actual test data.

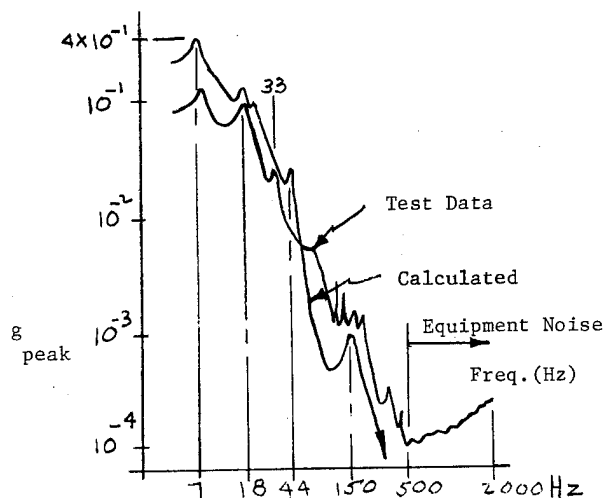


FIGURE 5

#### REFERENCES

1. F. W. Hopwood, Fellow Engineer, Westinghouse Electric Corporation, Personal Correspondence.
2. Vibration Characteristics of Crystal Oscillators by Gilbert F. Johnson, Proceedings of the 21st Annual Symposium on Frequency Control.
3. W. A. Lynch and J. G. Truxal, "Introductory System Analysis." (McGraw-Hill Book Company, Inc.).
4. C. M. Harris and C. E. Crede, "Shock and Vibration Handbook", Volume 3 (McGraw-Hill Book Company, Inc.).

## ON THE DESIGN OF SELF-DEPLOYING, EXTREMELY LARGE PARABOLIC ANTENNAS AND ARRAYS

Arthur A. Woods, Jr., and William D. Wade  
Lockheed Missiles & Space Company, Inc.  
Box 504 Sunnyvale, CA 94086

### ABSTRACT

A design solution for a large aperture space antenna is presented. This solution is a self-deployable antenna within state-of-the-art technology. This design is being proven in independent research and development work conducted at Lockheed Missiles & Space Company, Inc., (LMSC). The antenna described in this paper is compatible with Space Shuttle and usable at sizes up to 2000 feet in diameter for parabolic antennas and phased arrays. The availability of an antenna of this size removes a significant technology development activity, space assembly and manufacturing, as a stumbling block for space systems requiring extremely large aperture antennas.

### INTRODUCTION

NASA, specifically Goddard Langley and JPL, have announced their plans to place parabolic and/or array antennas in space for use as public services platforms and solar power transmission, radio astronomy and communications. These missions require phased arrays and parabolic reflectors with apertures of up to 10,000 feet. The majority of missions identified, however, will be possible using apertures of less than 2000 feet. The design solution advocated by some authors is the fabrication of structures in space. This solution unfortunately requires the development of technology to build and assemble parts in a space environment. It is this technology which paces performance of the proposed missions.

Lockheed Missiles & Space Company has been involved in a program to develop an alternative, near-term solution for large aperture antennas. This program was built on the successful wrap-rib antenna design concept. Through the application of new materials and design improvements the wrap-rib structure can now be extended to support antennas of up to 2000 feet in diameter. These designs can be packaged for ascent on the Space Transportation System and are self-deploying in space. Application of this design to both parabolic reflectors and phased arrays is discussed here. Design and performance parametric data, materials for use with the reflective and array surfaces, descriptions of hardware, and projections to the large sizes are provided.

### DESIGN CONCEPT

The wrap-rib surface support design concept consists of a number (variable) of radial ribs or beams which are cantilevered from a central hub structure. Each of the ribs is attached to this hub through hinges. This radial spoke system provides the mounting for the antenna structure. Arrays are formed by mounting a membrane with elements on the front edge of the ribs

and, if required, a ground plane on the back edge. For parabolic or other curved reflectors the ribs are formed in the required shape and reflective pie shaped gores are attached between the ribs. An overview of the deployed system is presented in Figure 1.

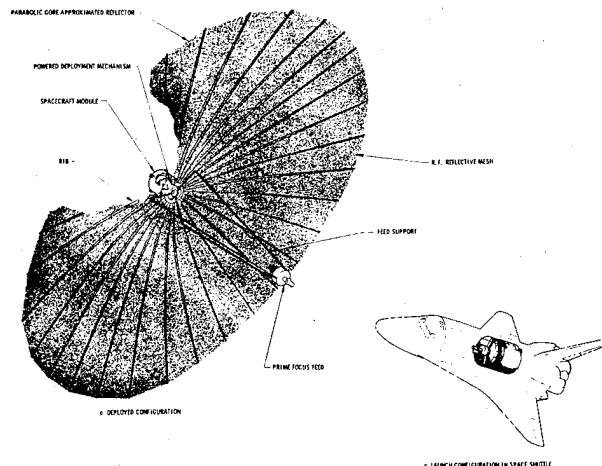
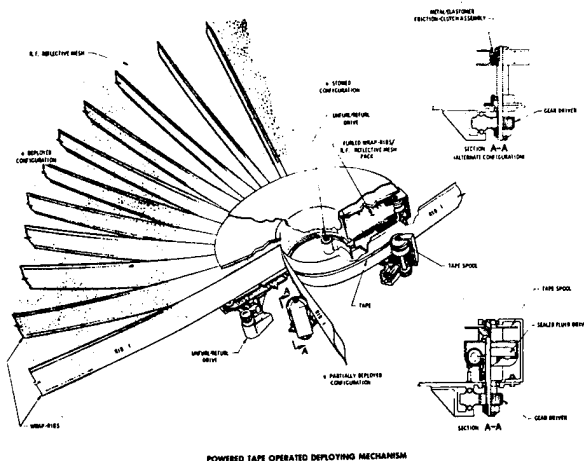


Figure 1 Deployed System

The rib cross section and material are chosen to permit the elastic buckling of the ribs. This is to allow the ribs to be wrapped around the hub structure in the ascent or stowed package configuration.

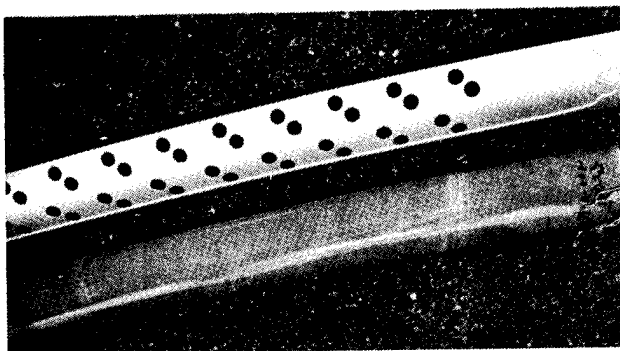
In the stowing process the ribs and attached surface are rotated about the rib hinges until the ribs are tangent to the hub. After this rotation the ribs are pulled around the hub and wrapped up. The elastic buckling of each rib accommodates this action. The surface material is allowed to form a package between the ribs. Details of the stowed package are shown in Figure 2.

The elastic energy stored in the wrapped ribs is sufficient to accomplish deployment of relatively small (less than 75 feet) diameter systems. In this case, the stowed package is contained by a series of hinged doors which are held in place by a restraining cable. Deployment occurs when the cable is severed. For the larger diameters with which we are concerned the surface loads and momentum exchange with the spacecraft will not allow this free deployment. A deployment restraint system has been incorporated in the design to control this sudden release of strain energy. This mechanism is discussed later in this paper.



**Figure 2 Stowed Package/Tape Drive Mechanism**

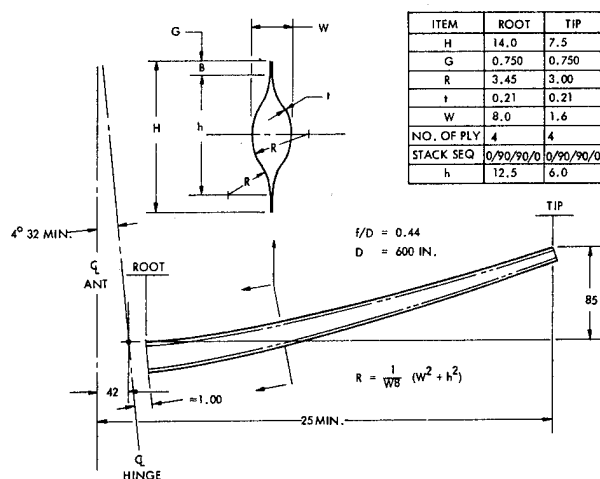
**Rib Design.** Previously the ribs have been fabricated from aluminum. The crosssection was semilenticular (C-shaped) with chemically etched radial stiffness. (See Figure 3.) This design was limited in size by the high thermal coefficients of expansion and the density of the metal. The density limited the available diameter by weight and the thermal coefficient of expansion limited the antenna frequency due to excessive orbit surface distortions even with optimized thermal control systems.



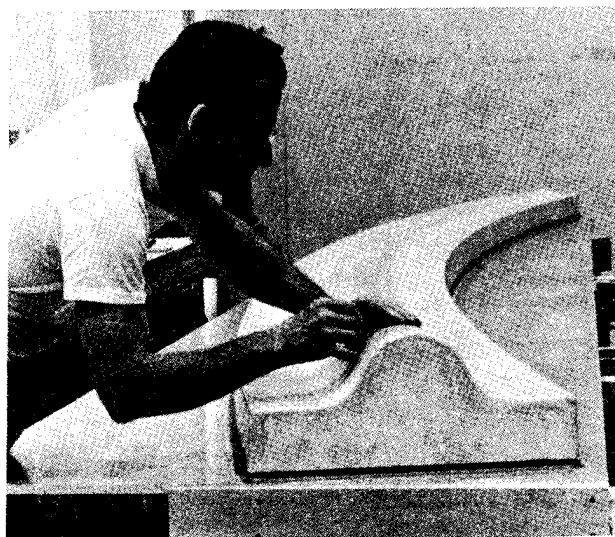
**Figure 3** ATS Rib

To remove these constraints, LMSC investigated the use of composites for the rib application. After several years of development, it was determined that graphite epoxy ribs can be fabricated and can perform to the requirements. Ribs have now been fabricated to replace the semilenticular design and are even being fabricated in a full lenticular cross section.

The design details for a 23.5 foot long graphite epoxy lenticular rib are presented in Figure 4. The tooling for fabrication of ribs which will be incorporated in a development reflector being built this year on independent development funds is shown in Figure 5.



**Figure 4 Stiff Rib Configuration**



**Figure 5 Stiff Rib Tooling**

Central Hub Design. Several objectives were established for the controlled deployment of large reflectors.

1. The system should be mechanically simple
2. The system should restrain the release of energy as opposed to actively deploying the reflector
3. The system should be compatible with both curved and straight ribs
4. The system should allow the attachment of more than one membrane to the ribs
5. The system should be size independent

A design solution which satisfies the above objectives for a deployment restraint system was found. The solution uses a tape and pulley system. With this system, a metal tape is placed between each rib, the ribs and mesh are wrapped with the tape, and the tape, under tension,

keeps each rib wrapped around the hub. For deployment a motor drives a large gear which in turn rotates the tape take up reels. The ribs deploy as the tape is reeled up. A constantly slipping clutch is located in each tape reel drive to limit the tape tension and allow positional and speed variations from rib to rib and during reflector deployment. The design description of the system is presented in Figure 2. This deployment mechanism is being fabricated and will be included in the large aperture demonstration model. Because the function of the tape is to apply pressure to the rib, the system allows membranes to be wrapped between the tape and the rib thus permitting locating surface attachments anywhere on the rib. The design is also independent of diameter because larger diameters will only increase tape pulley diameter and operating time.

**Antenna Surfaces.** There are two basic sets of surface requirements, those for reflectors and those for arrays. The major difference is that the reflector surface must reflect while the array surface must be nonreflective and support antenna elements. The array may or may not require a ground plane. In general there are two types of meshes, those of metallic substrate which are inherently reflective and those with a nonmetallic substrate which are plated with a metal to reflect. This is not the case in one instance, that of carbon, because carbon will reflect. The remainder of this discussion will deal primarily with the reflective mesh characteristics because these are required for reflectors, array elements, and ground planes.

**Deployable Antenna Surfaces (Reflective Mesh).** The primary requirement for a reflective mesh is obviously that it reflect rf energy. The development of the theory that predicts the amount of reflected energy that can be expected with a particular grid material dates back to the late 1800's. Numerous iterations and refinements have been performed since to define more precisely the phenomena occurring. This theory is well developed at present for square or rectangular grid patterns such as those found in woven goods. Application of the theory to the more complex knitted geometries, however, is not as straightforward as might be hoped. Knitted meshes characteristically do not have continuous strands of reflective wires which run in two orthogonal directions. One must, therefore, rely on intimate contact of the knots to provide for electrical conduction in the course direction (perpendicular to the warp). For knitted wire such as that shown in Figure 6b, all that is required is that a certain minimum preload be applied to the mesh under worst-case thermal conditions. This minimum load is generally on the same order as that required to maintain the flatness of the panel under the same thermal conditions.

For knitted nonmetallics with a metallic plating, the solution is not as obvious. In this case, the plating itself must provide the continuity through the joint. This can create problems if the plating is fragile and susceptible to cracking for then in the ground environment, it develops a nonconductive surface oxide at the cracks. Another effect that has been observed with plated dielectrics is caused by the application of the thermal control overcoat that must be used to maintain an acceptable upper temperature limit. The metallic plating will exhibit optical properties representative of the particular metal used. This means the maximum temperature can be expected to be on the order of 350°F to 450°F depending on the

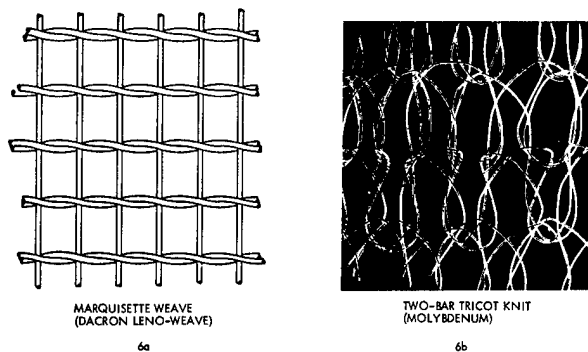


Figure 6 Typical Mesh Configurations

metal. These are well above the useful operating temperature of most nonmetallic substrates. Dacon polyester, for example, will exhibit dimensional shrinkage at temperature above the heat set temperature of 275°F and will char at about 350°F. Application of a thermal control material such as silicone or teflon over the metallic plating sufficiently increases the emittance of the surface to reduce the upper temperature to slightly below room temperature (~60°F) thereby providing adequate margins.

The problem that develops with application of the overcoat is that electrical insulation can occur at points of discontinuous plating, thereby, significantly reducing the transverse reflectivity of a knitted material. Solution of this problem has been found to reside in the viscosity control and application processes. Recent studies at LMSC indicate that with proper controls, this effect is not observed.

One other property of knitted materials that must be taken into account is the Poisson ratio. Some knitted configurations can exhibit Poisson ratios near unity. The effect on a curved panel, such as those found on a gored reflector, is to produce under adverse thermal conditions significant out of plane motion commonly referred to as pillow. Figure 7 illustrates this phenomenon.

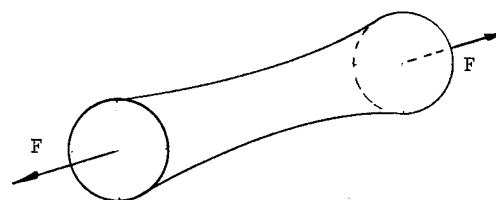


Figure 7 Poisson Effect Analogy

Consider a tube of mesh attached to load rings at the ends. When the force,  $F$ , is applied to the load rings, the tube will decrease in circumference at mid-length. The amount of motion produced is a function of the bi-axial or membrane stiffnesses and the Poisson ratios in each of the two orthogonal directions, the radius of curvature, and the load applied. This effect can readily be taken into account through appropriate tooling during fabrication and assembly. In general, the approach provides for a chordal preload during the cutting operation while allowing the radial direction to suck in, producing an effective compression strain in that direction.

With all the problems associated with knitted materials, it would seem there is little justification for their use. Woven materials, i.e., materials which are constructed of orthogonal fibers, typically exhibit a very high stiffness. The material illustrated in Figure 6a exhibits a stiffness approximately 800 times that shown in Figure 6b. The effect of this stiffness is to increase the thermally induced distortions in the reflector contour, particularly during an orbital eclipse period. This can most readily be seen by comparing the performance analyses of the ATS-6 30-foot reflector using the woven dacron and the knitted Chromel-R material shown in Figure 8.

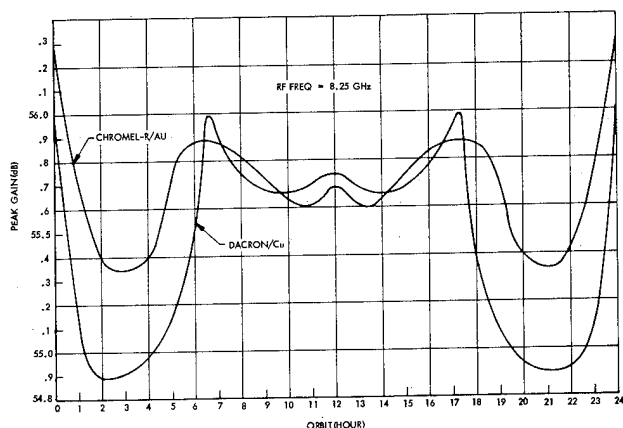


Figure 8 ATS-6, Chromel-R, and Dacron Performance

One property common to both knitted and woven materials not heretofore considered a big design driver is the optical transparency ( $\tau$ ). As apertures increase, however, the transparency and its effect on solar torques are becoming significant. These torques result in increased attitude control propellant weight requirements or increased torque compensation lower areas (paddles). Figure 9 illustrates the relationships between transparency and reflectivity that can be used by the systems analyst along with the detail design and analysis people to produce significant reductions in solar torques while having little or no effect on system gain.

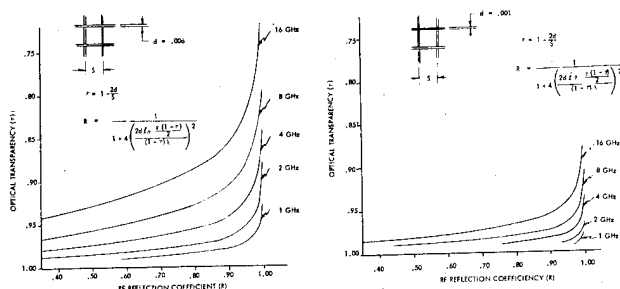


Figure 9 Transparency Versus Reflectivity

Another consideration is system weight and cost. Reduction in wire diameter has a strong influence on the amount of metallic coating used. The amount of gold one skin depth thick which is required for a 1000-foot reflector designed for operation at X-band using 6-mil diameter wire is 2500 pounds. When 1-mil wire is used, the amount of gold required is only 674 pounds. At current

gold prices that would mean a savings of approximately \$2.6 million plus shrinkage. This example is illustrative only. There would be great pressure to refrain from using gold and to use less politically and emotionally sensitive materials.

## PERFORMANCE CHARACTERISTICS

The significant performance characteristics of a wrap rib antenna system have been projected based on the data obtained during the development activity. These characteristics are

- Stowed dimensions versus deployed diameter
- Weight versus deployed diameter
- Deployed natural frequency versus deployed diameter
- Maximum diameter and gain versus operational frequency for a passively controlled surface parabolic reflector

As the data shows, Shuttle-compatible parabolic antenna systems are practical up to diameters of 900 to 1000 feet. Arrays of over 2000-feet in diameter are also projected. These systems projections are based on present technology and require no advancement in space extra-vehicular activity technology or manufacturing.

## HARDWARE BACKGROUND

Lockheed Missiles & Space Company is not new to the space deployable antenna field. This area of engineering has been recognized as a significant portion of spacecraft development since 1962 when LMSC fabricated a 3-foot deployable, parabolic antenna. Through the years larger self-deployable antennas have been fabricated. The worlds largest qualified self-deployable reflector being used on the ATS-6 mission was designed and fabricated at LMSC. This history of self-deployable antenna technology is shown in Figure 10. The first picture of a self-deployable antenna in space was taken from the Earth-Viewing Module (EVM) of the ATS-6 spacecraft.

The ATS-6 30-foot diameter parabolic reflector successfully operating in space is shown in Figure 11.

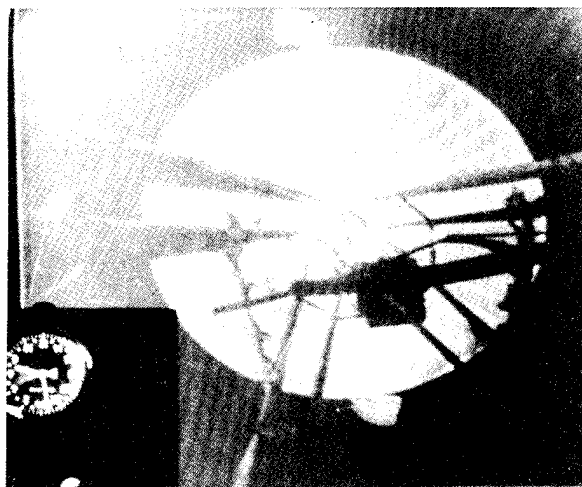
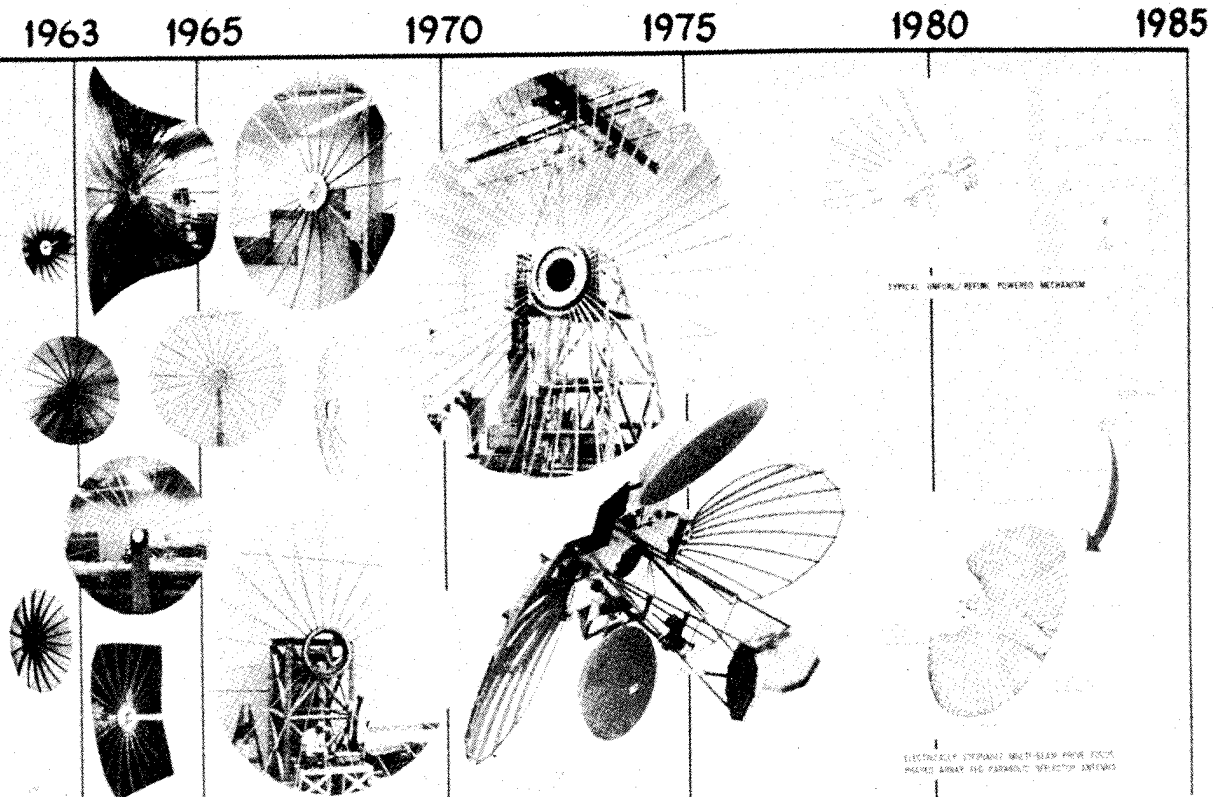


Figure 11 ATS-6 in Orbit



# ANTENNA TO IMU MOUNTING FOR SAR MOTION COMPENSATION

L.C. Miller  
V.M. Foxwell

Westinghouse Defense and Electronics Systems Center  
P.O. Box 746  
Baltimore, Maryland 21203

## ABSTRACT

Motion compensation for a synthetic aperture radar requires careful installation of the inertial navigation system (INS) used for sensing antenna motion. Limits on relative motion between the INS and antenna, and typical environments are presented. An approach for analyzing the differential motion is discussed and two example configurations are considered. It is demonstrated that the mounting problem is critical to good imaging performance but that acceptable performance can be achieved with reasonable designs.

## I. INTRODUCTION

The coherency requirement of synthetic aperture radar<sup>1,2</sup> (SAR) results in a need for compensation of antenna motion. This places restrictions on relative motion between the antenna and the inertial motion sensing used to measure its motion. To provide an integrated radar/navigation capability at minimum cost, it is desirable to obtain the motion measurements used for motion compensation from the on-board INS (inertial navigation system) used for aircraft navigation. It is therefore necessary to exercise great care in the installation design for the IMU (inertial measurement unit) which is the INS LRU (line replaceable unit) containing the basic inertial measurement instruments. The first installation consideration is selection of the IMU location relative to the antenna phase center. The IMU to antenna separation affects imaging performance by way of coupling of aircraft rotations into antenna to IMU relative translations, which must be corrected based on attitude measurements and the "lever arm" calculation<sup>3</sup>. Errors in the attitude data do not allow acceptable corrections when the antenna separation from the INS exceeds 3 feet. Limiting this separation is difficult because of the lack of space in the area adjacent to the antenna and the desirability of placing the IMU near the aircraft center of gravity. However, for large airplanes and bombers, in particular, forward space often is available and the use of the same INS for both motion compensation and navigation is the preferred alternative. This imposes special requirements on the mounting of the INS, which would normally not be encountered.

## II. REQUIREMENTS

The antenna to IMU mounting requirements are determined by the limits on allowable relative motion of the two, as established by the motion compensation requirements, and by the environment in which this relative motion must be limited.

### Allowable Relative Motion

Figure 1 defines the limit on sinusoidal motion of the antenna phase center relative to the IMU (inertial motion unit) for a synthetic aperture radar. The family of curves spans coherent integration times typically of interest. The low frequency portion of the curves are established by a

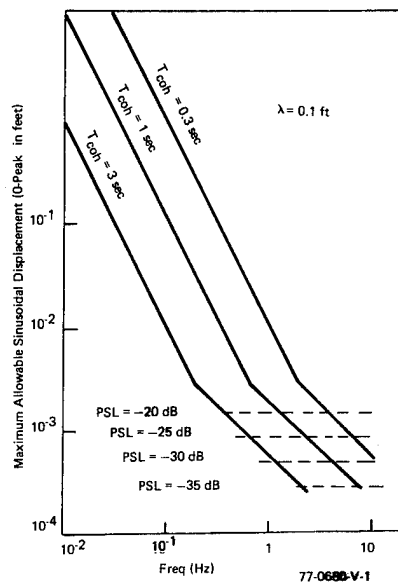


Figure 1. Limit On Uncompensated Displacement Error

limit on errors of constant acceleration during a coherent integration time which cause image defocusing. Low frequency sinusoidal errors have nearly constant values near their peaks. The quadratic phase error due to such acceleration errors acting over half of the coherent integration time is limited to  $\pi/4$  radians for these curves. This value is halved relative to the usual  $\pi/2$  limit because only a subsystem of the radar is being considered, and other subsystems also contribute to the total system error. The dashed portion of the curves apply at frequencies greater than that of their intercept with the solid lines. These high frequency limits are established by the limit on peak sidelobes which arise from sinusoidal phase errors that have more than one cycle during a coherent integration time. The short intermediate segments between the high and low frequency lines are limits established by image smearing due to sinusoidal errors having nearly one cycle per synthetic aperture. A discussion of limit functions such as those of figure 1 is presented in references 4 and 5.

In addition to the specified limit on the amplitude of sinusoidal errors, there is a limit on the total rms uncompensated displacement. The rms uncompensated displacement establishes the integrated sidelobe level (ISL) and is limited to

$$\sigma_a \leq \frac{\lambda}{4\pi} \sqrt{\text{ISL}} \quad \text{ISL} \leq 10^{-2}$$

For a typical integrated sidelobe limit of  $-26$  dB, the rms uncompensated displacement is limited to  $4 \times 10^{-4}$  feet at X-band.

For applications where doppler monopulse measurements are to be made and INS attitude data are used for beam stabilization, it is also necessary to limit angular motion of the IMU relative to the antenna. For a stabilization limit on rms rotational errors of  $\sigma_\theta$ , the pointing error power spectral density  $P_\theta(w)$  must be limited such that

$$\frac{1}{2\pi} \int_0^\omega P_\theta(w) \left( \frac{\sin \frac{wT}{2\pi}}{\frac{wT}{2\pi}} \right)^2 dw \leq \sigma_\theta^2$$

Where:

- $P_\theta(w)$  = power spectral density on  $\theta(w)$  in radians<sup>2</sup>/Hz
- $\theta(w)$  = misalignment of the IMU relative to the antenna
- $T$  = doppler monopulse measurement integration time

This error source is just one of many affecting antenna stabilization and a reasonable goal would be to limit its contribution to 20 percent of the total limit. For milliradian stabilization accuracy,  $\sigma_\theta$  might have a value as small as  $2.5 \times 10^{-4}$  and this value will be adopted for later examples.

### Environment

The allowable translation and rotations cannot be exceeded when the system is operating in the expected environment. The environment specification is usually in three parts: Sinusoidal Vibration Specification, Random Vibration Specification, and Power Spectral Densities (PSD's) that represents expected or actual motion under operational flight conditions. The PSD's are the most useful environmental information since they represent the actual effects of gusts, buffeting, etc.

A typical sine vibration environment which is applicable from 5 Hz to 100 Hz is presented as figure 2 and a similar random vibration environment which is applicable from 20 Hz to 2000 Hz is presented as figure 3. These specifications will be used in later examples. The sine

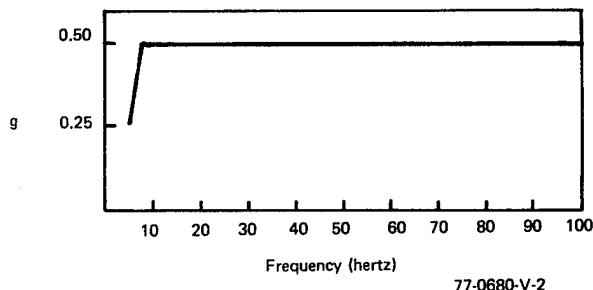


Figure 2. Sinusoidal Vibration Requirement

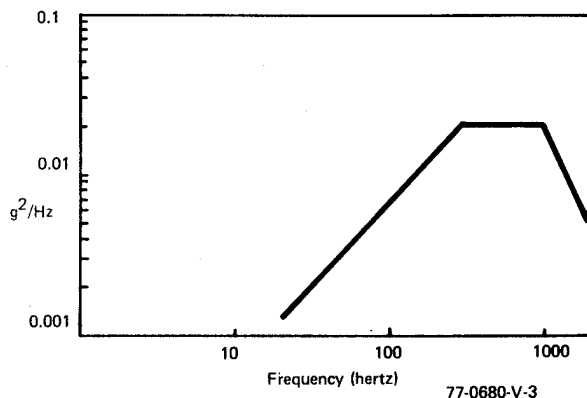


Figure 3. Random Vibration Environment

and random vibration environments are usually only given as translational environments, and the only rotary inputs are those provided by the gust data.

The significant components for the power spectral densities describing gust-induced motion are vertical translation and pitch rotation. These power spectral densities are derived from gust and complex structural models and cover the frequency region from below 0.25 Hz to above 10 Hz. Representative PSD's for vertical translation and pitch rotation were used in the example evaluations that follow. These PSD's are presented as figures 4 and 5.

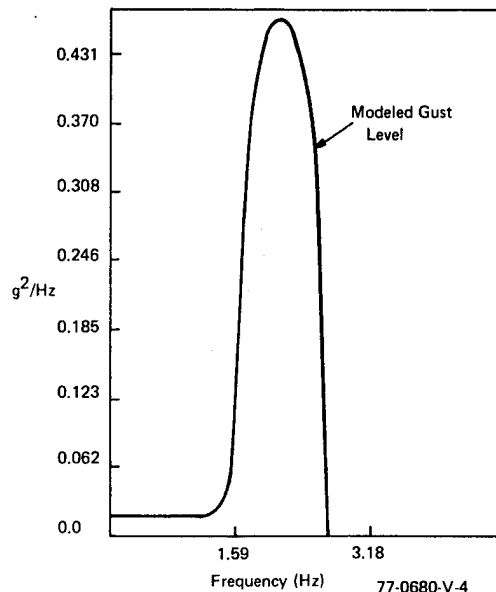


Figure 4. Vertical PSD Due To Turbulence

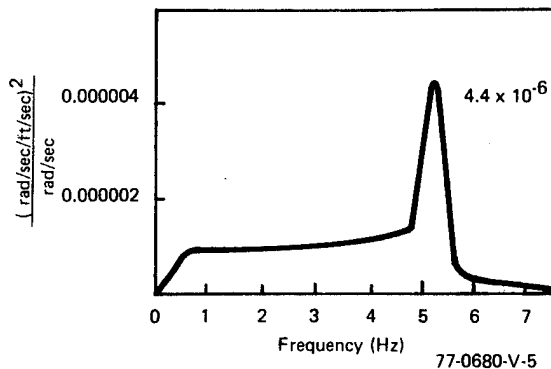


Figure 5. Pitch Rate Power Spectral Density at Radar Due to Turbulence

### III. ANALYTICAL APPROACH

The two antenna to IMU mounting concepts were modeled using a finite element computerized structural analysis program known as STARDYNE<sup>7</sup>. Using finite elements, the structure is considered as a geometric assemblage of individual structural components or elements. This assembly is defined by way of representative structural equations for computer analysis and the resulting matrix solutions describes the interrelationship of the elements in the structure. The computer model is verified by plotting the structural elements from grid point to grid point. Eigenvalues and eigenvectors are then obtained. Next, differential transfer functions between the antenna and IMU are obtained for

the selected degrees of freedom. The relative response for the given environment is obtained by operating on the transfer function for that degree of freedom by the respective environment. The results are then compared with the specification requirements. The relative response PSD's include three translations and three rotations, but one of each usually far exceeds the other two.

#### Structural Model of Isolated IMU Configuration

The first configuration is described as follows. The antenna is rigidly mounted to the bulkhead, and the IMU is mounted in the avionics bay on 40 Hz isolators. A model of this concept is presented by figure 6. To

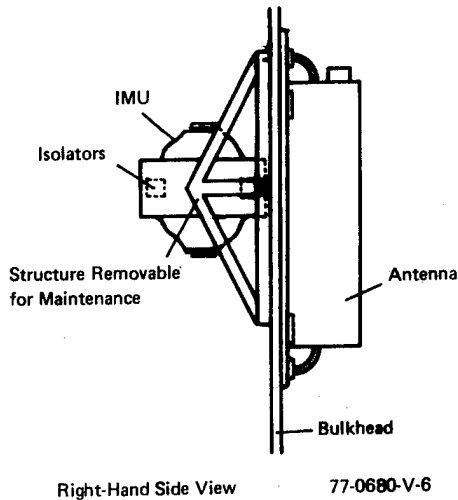


Figure 6. Isolated IMU

reflect a more realistic model, the dynamic and static center of gravity have been displaced by 0.5 inches in the x and y direction. A finite element structural model was developed using STARDYNE with the following assumptions:

- 0.5 inch eccentric CG in two axis (x and y)
- The antenna and the bulkhead are considered as rigid bodies
- The isolators have equal characteristics in all directions
- All attachments are considered rigid
- Structural damping is 4 percent
- Shock and vibration isolator damping is 15 percent
- The IMU is considered as a rigid body.

The IMU isolators for the model are supported by honeycomb beam/shear webs that are 1.5 inches deep with 0.040-inch thick skins. These beams are supported by a tubular truss designed to eliminate bending stresses and this is mounted to the rigid aircraft bulkhead. The antenna is modeled as a rigid structure. The rigid beams between the antenna and the IMU truss are considered as the rigid aircraft bulkhead. The dynamic characteristics and the rms motion response to the selected environments is presented in the following section.

From the eigenvalue solutions to the STARDYNE finite element mode, the frequency characteristics are as follows:

#### 1. Isolator Frequencies (Hz)

	x	y	z
a. Translation	37.5	37.4	39.6
b. Rotation	112.0	73.7	85.6

#### 2. Structural Modes (Hz)

The first structural mode is 395 Hz and this is beyond the range of interest.

The isolator frequencies are rigid body modes of the antenna/IMU assembly.

The weight of the IMU to bulkhead/antenna mounting structure is 13.6 pounds, but this does not include the isolators or attachments.

#### Structural Model of Antenna/IMU Assembly Configuration

The concept of a rigidly mounted IMU on a shock and vibration isolated antenna is presented with figure 7.

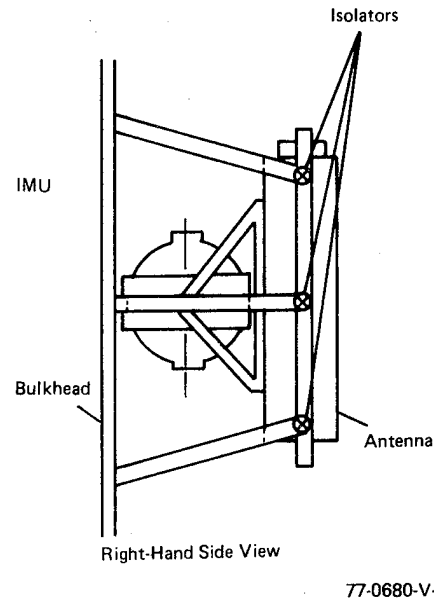


Figure 7. Antenna - IMU Mounting Configuration

Based on avionic experience and the shock and vibration sensitivity of the IMU, a 20-Hz isolation system for the antenna/IMU assembly is considered a good choice. This will produce acceptable motion and about the same environment to the IMU as the original 16-Hz isolation system (the weight of the antenna/IMU assembly is 410 pounds versus 67 pounds for the separate IMU). The isolators were located to balance the static and dynamic center of gravity to minimize rocking modes.

A finite element structural model was developed using STARDYNE with the following assumptions:

- 0.5 inch eccentric CG in two axis (x and y)
- The antenna is considered as a rigid body
- The isolators have equal characteristics in all directions
- All attachments are considered rigid
- Structural damping is 4 percent
- Shock and vibration isolator damping is 15 percent
- The rigidity of the IMU will not be considered in the finite element analysis
- The weight of the IMU is distributed equally to the four IMU mounting points.

The IMU for this model is supported by the same honeycomb beam/shear webs and tubular truss as was used with Concept No. 1. In Concept No. 1, the tubular truss was attached to the rigid A/C bulkhead, but with this concept it is attached to the antenna, assumed rigid, and the total assembly is isolated from the A/C. The shock and vibration isolator mountings were located so that the static and dynamic CG could be superimposed with the aid of the computer analysis. There are six isolators mounted in a CG plane of the antenna/IMU assembly as close as possible to the tubular attachment of the IMU mounting structure. The location of the isolators are then shifted

0.5 inches in x and y direction to account for manufacturing tolerances. The weight of the IMU (67 pounds) is shared equally at four grid points on the honeycomb beam/shear webs to avoid any stiffening effect from the IMU. The dynamic characteristics and the rms motion response to the selected environments are presented in the following section.

From the eigenvalue solutions to the STARDYNE finite element model, the frequency characteristics were determined as follows:

#### 1. Isolator Frequencies (Hz)

	x	y	z
a. Translation	19.5	19.5	19.5
b. Rotation	33.7	26.3	24.7

#### 2. Structural Modes (Hz)

- First cantilever mode of supports = 90.0
- Second cantilever mode of supports = 105.2
- Next mode = 263.0

The isolator frequencies are rigid body modes of the antenna/IMU assembly and the lowest structural mode is 90.0 Hz. The first and second cantilever modes of the supports are 90.0 and 105.2 Hz respectively, and the mode shape of the 90-Hz mode is presented by figure 8. If

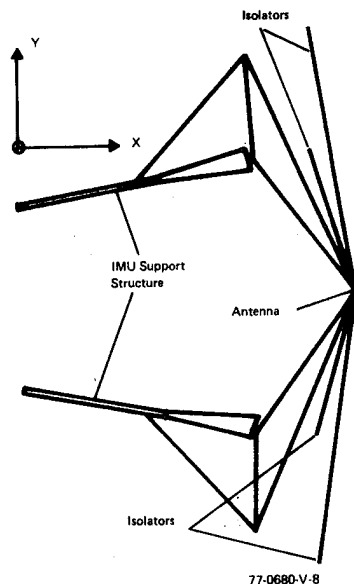


Figure 8. Isolated Assembly Finite Element Model  
First Cantilever Mode - 90.0 Hz

the rigidity of the IMU were included in the finite element mode, the 90.0-Hz mode would be eliminated and the 105.2-Hz mode would increase in frequency. Thus, it is conservative to assume that structural frequencies will be well above 100 Hz and likewise the response motion should be lower than those determined with this evaluation.

The weight of the IMU to antenna mounting structure is 13.6 pounds, but this does not include the isolators or attachments. This was the same structure used with Concept No. 1.

## IV. RESULTS

The differential motion was determined for cases where the previously defined example environments (sinusoid, random and PSD's) operate on the differential transfer functions defined for the structural

models. The resulting differential motion power spectral densities were then analyzed to measure dominant components or total integrated motion. The performance achievable with the two different mounting approaches is summarized in figures 9 and 10 and limit values suggested in the requirements section above are indicated in the figures.

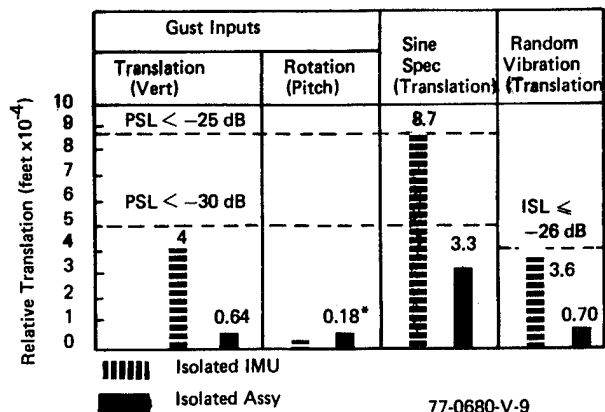


Figure 9. Relative Translation Motion  
Input

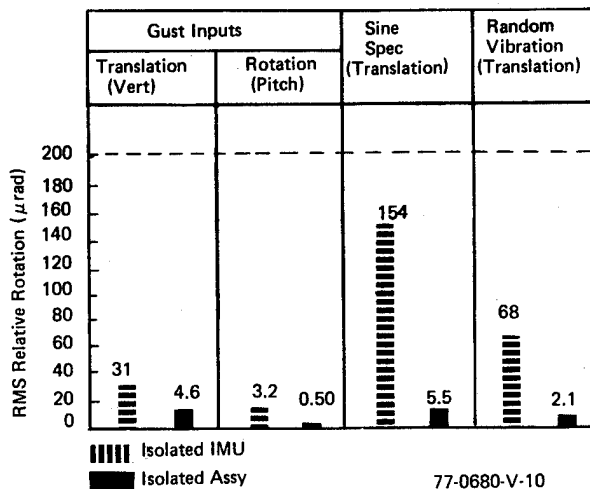


Figure 10. Relative Rotation Motion

Figure 9 presents the relative IMU to antenna translation for each of the specified motion environments. The dashed horizontal lines give the limit on the amplitude of sinusoidal relative translation for -25 dB and -30 dB peak sidelobes, and on the far right of the curve, the limit on rms relative translation is given for an integrated sidelobe level of -26 dB. The relative motions for the isolated IMU and isolated assembly configurations are given by the shaded and unshaded bars respectively. Each bar represents the error for the worst case axis (e.g., the first bar represents the z axis motion which exceeds the motion in the other two directions).

The largest motion component occurs for the isolated IMU configuration in the sine spec environment. This motion just meets the limit allowable for -25 dB PSL. The next largest motion is the translation due to translation inputs but this motion is less than the -30 dB PSL limit. Note the negligible translation due to the effect of gust induced rotations with the 1/2 inch CG to elastic center mismatch in the x and y directions. Finally, the random translation motion due to the random vibration environment is below the -26 dB integrated sidelobe limit.

The relative rotation motion is summarized in figure 10. The format

is similar to that of the figure described above and a subsystem spec of  $200\ \mu\text{rad}$  is indicated by the dashed horizontal line. The worst case relative motion again occurs for the sine spec environment and the subsystem spec is met.

The next largest rotation occurs for the random vibration environment, and this and all other errors are below the  $200\ \mu\text{rad}$  limit. The cross coupling of translation inputs to relative rotation inputs (due to CG to elastic center mismatch) is not the significant error that had been feared for the isolated IMU configuration.

## V. SUMMARY

The requirements for mounting an IMU for SAR motion compensation have been discussed, and the necessary information and an analytical approach for meeting these requirements have been identified. The primary environmental information for the evaluation is the aircraft motion in a gust environment, as described by power spectral densities. Unfortunately, such PSD's have not usually been available except for recent aircraft. Hopefully, this information will be more readily available in the future.

The specific examples presented have demonstrated that as expected, the sidelobe spec can be easily met (or even exceeded) in typical airborne environments with the IMU hardmounted to the antenna, and the assembly then isolated from the aircraft and placed forward of the bulkhead. In addition, it has been demonstrated that the sidelobe spec can be met with the IMU isolated from the antenna. This, then, allows separation of the antenna and IMU by an interposed bulkhead if the bulkhead and mounting structure are properly designed.

## VI. ACKNOWLEDGEMENT

The authors would like to acknowledge Mr. Dale Logan and Mr. Robert Bernhard for their contribution to the structural modeling.

The work reported in this paper was sponsored by the Air Force Avionics Laboratory (AFAL) under USAF Contract F33615-74-C-1040.

Publication of this paper does not constitute approval by the Air Force of the conclusions and recommendations contained herein.

## VII. REFERENCES

1. Cutrona, L.J., Vivian, W.E., Leith, E.N., and Hall, G.O., "A High Resolution Radar Combat-Surveillance System," *IRE Trans Mil Electronics* MIL-5 127-131.
2. Harger, R.O., *Synthetic Aperture Radar System Theory and Design* Academic Press, New York, 1970.
3. Farrell, J.L., Mims, J.H., and Sorrell, A., "Effects of Navigation Errors in Maneuvering SAR," *IEEE Transactions AES-9* (5) September 1973, pp. 758-776.
4. Liskow, C.L. and Therkelsen, E.B., "Motion Compensation for Synthetic Aperture Radars," Seventh Annual Tri-Service Radar Symposium, 1961.
5. Kirk, J.C. Jr., Motion Compensation for Synthetic Aperture Radar, *IEEE Transactions AES-11* (3) May 1975.
6. MIL-STD-810B.
7. STARDYNE - Static and Dynamic Structural Analysis Systems, MRI/STARDYNE 3, Developed by Mechanics Research Incorporated, available at CDC-6600 Data Centers.

## ANTENNA/MAST REQUIREMENTS FOR LOW ALTITUDE AIRCRAFT DETECTION SYSTEM

R. W. Milligan & D. J. Zona

SANDERS ASSOCIATES, INC.  
95 Canal Street  
Nashua, New Hampshire 03060

**ABSTRACT:** The paper describes the basic mechanical design philosophy of the LAADS mobile ground radar antenna system. Impact of specified operational as well as environmental requirements upon the physical development of the antenna system are outlined and their effect discussed. The selected methods of achieving the major antenna system functions, including automatic deployment, leveling, rotation, stow, and locking within the context of specified requirements are also detailed. A critique of the implemented antenna system after exposure to specified environmental testing and nine months of operational field service concludes the paper.

designed to provide 360 degree, all weather detection of low flying aircraft, classify target data, and display this information. The complete operation is automatic or can be manually overridden at any time by the radar operator.

The LAADS radar is made up of numerous subsystems; a principle one being the radar antenna assembly. This subsystem controls the operation of the radar antenna by providing the following physical functions: Automatic antenna deployment, leveling, and stow functions, rotating the antenna assembly (radar feed horn, reflector, and IFF horn) at an antenna scan rate of 30 rpm, and supplying antenna azimuth position data to the radar display.

**INTRODUCTION:** The mission of the Low Altitude Aircraft Detection System (LAADS) radar shown in Figure 1 is to acquire and identify aircraft targets within its

**DESIGN REQUIREMENTS:** The design specification required the radar system be housed in a modified S-280 shelter adapted for both ground and M36C vehicle operation. The specification dictated the radar antenna be supported by a self-erecting and leveling mast integrally assembled to the radar shelter. When vehicle installed and erected, the 5 X 8 ft. radar antenna must be 24 feet above ground level. When retracted and stowed, it must lie on the shelter roof with a maximum overall height not to exceed 14.5 feet. The antenna, when deployed, is required to maintain its axis of rotation level to within 1° of true vertical when subjected to a maximum vehicle inclination of 10°. Electric motor drive systems, with provisions for manual backup, were specified for mast erection and leveling requirements.

A fully automatic system capable of being operated by a single crew member including preparation for emplacement and march order conditions was specified. With the radar system properly installed on the M36C vehicle, the time allotted for system emplacement could not exceed seven minutes. March order configuration could not exceed five minutes.

The overall radar system was required to meet the general environmental conditions specified in MIL-STD-810 for wheeled vehicle electronic equipment. The conditions included temperature,

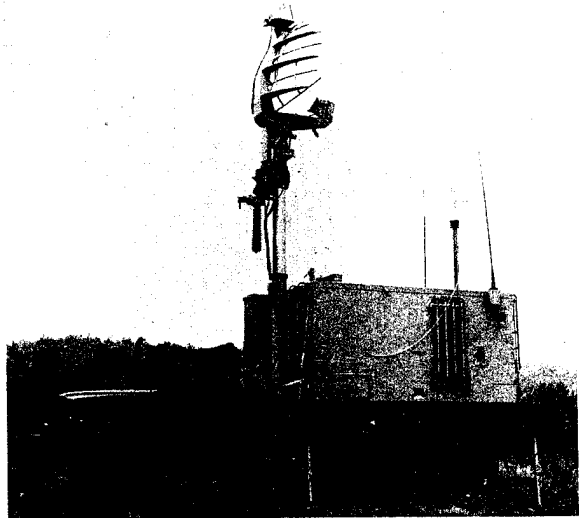


FIGURE 1

range and altitude limits and to display target data to the radar operator. The LAADS radar is a pulse doppler acquisition radar housed in a modified S-280 shelter. The shelter has been configured for both mobile M-36C vehicle or fixed ground installation. The radar system is

vibration, rain, sand and humidity. Specified conditions of major importance to the design of the Antenna System included:

1. Ice - Operation with accumulation of .50 inches of clear glaze ice.
2. Wind - In combination with ice condition: Operating, 50 knots; non-operating (stowed configuration), 70 knots.
3. Snow - Operating, 5#/sq.ft. accumulations; non-operating, (stowed configuration), 25#/sq.ft. accumulation.
4. Vehicle Transport Test - MIL-S-55286, 4" Bump Test, (stowed configuration).

**ANTENNA OPERATION:** Deployment of the LAADS antenna system from the stowed configuration is shown in Figures 2 and 3. Figure 2 illustrates the erection processes from march order configuration to operational deployment. Figure 3 depicts the antenna's leveling ability, capable

2. Pitch drive mechanism is activated disengaging the stow locking hook from the shelter tiedown structure. Disengagement of the locking hook allows the antenna assembly to be rotated from its horizontal stow position to the true vertical operating orientation.
3. As the pitch actuator rotates the antenna assembly through the 30° inclination angle with the shelter roof, both the elevation and roll drive mechanisms are energized, driving the telescoping mast assembly to its extended position and initiating roll corrective action as determined by the roll level pendulum potentiometer. Continued rotation of the antenna assembly through the 60° inclination angle activates the azimuth drive circuits. Antenna azimuth rotation is started at this time.
4. When the antenna assembly achieves

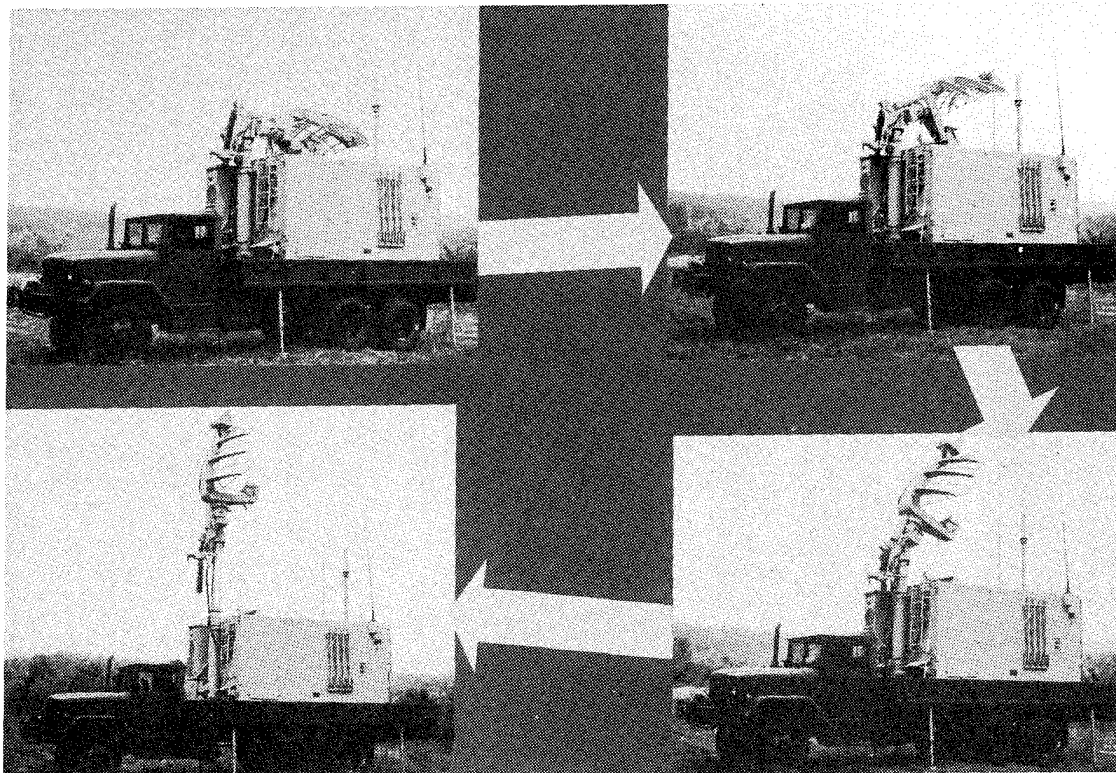


FIGURE 2

of maintaining the antenna assembly to within 1° of true vertical during system operation.

The sequence required to accomplish the illustrated deployment follows:

1. Power is applied to the antenna controller drive circuits.

5. The elevation drive actuator continues to extend the telescoping mast assembly until the upper limit

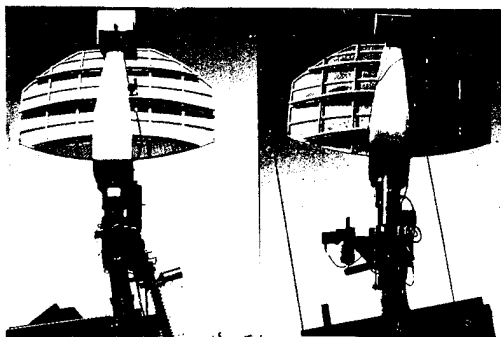


FIGURE 3

switch de-energizes the elevation drive circuits and applies the elevation locking brake.

Stowing of the antenna assembly follows the reverse sequence. As the pitch drive mechanism rotates the antenna assembly to its horizontal stow position, the antenna azimuth drive and roll drive circuits orientate the antenna in its correct stow position. Correct azimuth is assured by the azimuth stow sensor while correct roll orientation (antenna parallel to the shelter roof) is provided by the two photon-coupled interrupter modules located in the roll axis box. Final lock up of the antenna assembly to the shelter tiedown structure is completed when the pitch lock stow sensor de-energizes the pitch drive circuits and the pitch lock indicator is illuminated. The antenna assembly is then in march order configuration.

**ENVIRONMENTALLY INDUCED LOADS:** Aerodynamic loads for the antenna under simulated icing conditions were determined by means of wind tunnel tests on a 1/4 scale antenna model. The principle load component is associated with aerodynamic drag and the variation of drag coefficient with yaw angle is shown in Figure 4. As indicated, a peak drag coefficient of 2.1 was measured at a yaw angle of 52°. Also shown in the figure is the corresponding theoretical drag coefficient for the antenna for non-icing conditions. In this case, the peak drag coefficient is approximately 1.0 and occurs at zero degree yaw. It is apparent from the figure that iced antenna conditions would result in significantly greater mast loading as compared with "no ice" conditions.

In addition to steady state aerodynamic loads, antenna-mast configurations are susceptible to transient unsteady loading associated with Von Karman vortex phenomena. A quantitative assessment of such loading for the LAADS antenna was performed by Prof. Ham at M.I.T. under subcontract to Sanders. Principal results of Prof. Ham's study are as follows: Mesh Type antennas without ice are not subject to vortex shedding phenomena. Iced antenna configurations produce alternating vortices

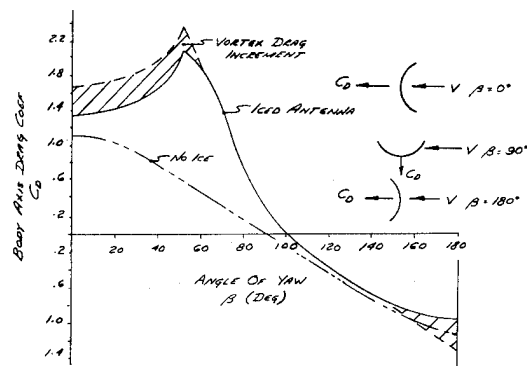


FIGURE 4

from the antenna sides which result in periodic drag and torsional loading on the antenna. The frequency of the loading is a function of Strouhal number with the drag loading frequency being twice the torsional frequency. For the LAADS antenna, the effect on drag coefficient of vortex shedding is shown by the dashed curve of Figure 4. At 50 knots, the vortex drag and torque loading frequency was approximately 4 Hz and 2 Hz, respectively. Loads induced by vortex shedding from cylindrical mast components were negligible compared with the antenna vortex loads.

Mast inertia load effects under transportation conditions were also considered. Based on limited test data for other mobile radar configurations, shelter vibrations on Munson Road test courses are in the order of 5 g's maximum. Peak accelerations due to shelter drop testing approached the 10 g level. For the LAADS design, a maximum value of 15 g's was assumed.

**SYSTEM CONFIGURATION:** Figure 1 illustrates the LAADS system installed on the M36C vehicle. Figure 5 defines the various antenna components, their configuration, and their physical location with respect to the radar shelter.

The mast assembly is made up of the following subassemblies (see Figure 5):

- Pedestal
- Pivot Box
- Pitch Actuator
- Roll Actuator
- Telescoping & Fixed Masts
- Elevation Actuator

The pedestal assembly provides the mounting surface, rotational drive and stow locking facility for the radar and IFF antenna. The antenna azimuth drive, a three-channel r.f. rotary coupler, and a synchro transmitter are included as part of the pedestal subassembly. The azimuth drive provides antenna rotation and the rotary coupler allows signal transfer between rotating and stationary transmission lines. The synchro transmitter provides relative antenna position information to the radar control



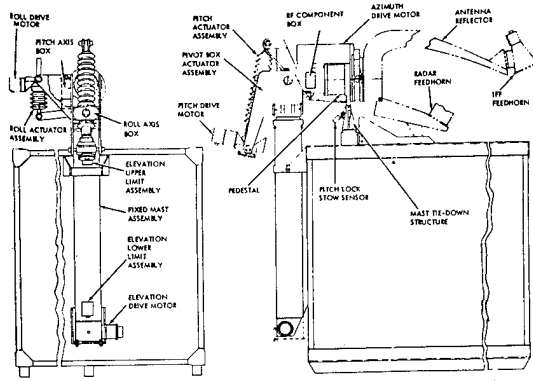


FIGURE 5

indicator.

The pivot box assembly provides the required structure for pitch and roll axis for erecting, leveling, and retracting the radar antenna assembly. The pivot box structure also provides the necessary mounting facilities for the pitch and roll actuator assemblies.

The pitch and roll actuator assemblies provide the motor drive mechanism required to accurately position the antenna assembly in either its deployed or stowed configuration.

The telescoping mast provides the mounting platform for the pivot box assembly. It also allows for the elevation and retraction of the antenna assembly. The fixed mast assembly provides structural support and guidance for the telescoping mast, and a mounting platform for the elevation drive motor. The elevation actuator provides for erecting and retracting the telescoping mast section within the structural support of the fixed mast.

**COMPONENT STRUCTURAL DESIGN:** Based on considerations of availability, strength, and ease of fabrication, 6061-T6 aluminum was selected as the material of construction. To obtain a minimum weight design consistent with fatigue strength requirements, sizing of structural components was based on maximum anticipated loads in conjunction with a safety factor of three (3.0). The safety factor evolved from fatigue considerations and was based on a design operational life of 10,000 hours, an allowable static stress of 35 ksi, and an assumed frequency of occurrence of maximum load corresponding to 5% of the total life.

As would be expected almost all mast components were designed to the 50 knot wind, iced antenna condition with the mast fully extended. The one significant exception was the pedestal tube which was designed to inertia loads corresponding to an iced antenna in a stowed configuration and transported over a Munson Road environment.

The fixed and telescoping mast components were fabricated from 6061-T6 extruded aluminum tubing. The fixed mast has a machined inside diameter of 9.25" and a .375" thick wall. The sliding mast has a machined outside diameter of 8.75" and a .375" thick wall. The sliding mast is radially constrained inside the fixed mast by two nylon bearings. The base plate of the sliding mast engages two longitudinal guide rails mounted on the inside surface of the fixed mast. These rails restrain rotational motions of the sliding mast section induced by antenna torsional loads. Vertical constraints on the sliding section is provided by a ball screw mounted at the base of the fixed mast. Final selection of wall thickness was based on a fatigue analysis which included the effects of vortex induced loads. Aerodynamic loads were based on climactic data which indicated that the average wind velocity during cold weather conditions is approximately 15 knots and that there would be a 99% probability that the wind velocity would not exceed 50 knots. The analysis showed that virtually all fatigue damage occurred when the resonant frequency of the mast coincided with the forcing frequency of the vortex loading. The .375" wall design resulted in a high value for mast bending frequency (4.2 Hz) which corresponded to the vortex forcing frequency in a 50 knot wind. Although the vortex loads are large at this velocity, the wind velocity distribution gave a low probability of occurrence and resulted in a low value for fatigue damage.

The mast section directly above the pivot box consists of two additional tubular components identified as RF tube (9.0" OD X 0.25" wall) and pedestal tube sections (11.0" OD X 0.375" wall). As noted above, the pedestal section was designed to inertia loads during ground transport. In the stowed configuration, the two structural supports for the assembly are both forward of the antenna base. As a result, the antenna under iced conditions behaves as a large cantilevered mass (343 lbs. with ice) which induces critical design bending moments at the pedestal/antenna joint. For the transport condition, the design loads were based on a peak inertia load of 5 g's and a safety factor of 3.0. For the RF tube, however, critical design loads were again associated with the deployed iced antenna subject to 50 knot winds. A distinguishing feature of the RF section is that the tube is slit in the vicinity of the pitch pivot to accommodate a 1.0 in. thick fin plate which provides the lever arm for stabilizing the antenna for pitching moments about the pivot. The fin plate is welded to the tube walls along two plate edges. A flanged adapter ring is welded to the top end of the RF tube and both

ends of the pedestal tube to accommodate a bolted connection at the RF/Pedestal and Pedestal/Antenna joint.

The antenna assembly is free to rotate in pitch and roll because of the pitch and roll pivot points located in the pivot box assembly. The pivot box is essentially a five-sided box structure welded from 6061-T6 plate stock 0.75 in. thick. The top of the box has an open end to accommodate the top section of the mast. Box side plates are extended in pitch and yaw planes to provide an offset location for jack actuators thereby obtaining a lever arm for jack forces about the mast pivots. The side extension plates also have pivot points for the jack support base and allow jack angular motions during mast articulation. Under antenna aerodynamic load, large vertical loads are generated at opposing jack pivot and mast pivot locations due to the stabilization of mast bending moments by the jack actuators. At the mast pivot locations, there are side loads in the plane of pitch and yaw due to aerodynamic drag and also side loads due to aerodynamic torsion. The structure is configured such that almost all loads are oriented in the plane of the plates. The two exceptions are drag load in the plane of pitch which is reacted at the forward lower pivot location perpendicular to the side of the box. In a similar manner, drag load in the plane of yaw is reacted at the top starboard pivot location. At these two locations, the box sides have ribbed flanges to provide additional reinforcement. Critical design load for the pivot box was based on the 50 knot wind, deployed iced antenna condition.

Design requirements for the pitch actuator jack system included a long stroke (28.5 in.) to accommodate the large (110°) angular excursion of the antenna from stow to maximum forward pitch leveling, a maximum operating force of 3,800 lbs., pitch erection time of 1.0 minute, and a brake to prevent jack slippage. Corresponding performance values for the roll actuator jack system were 4.0 in. stroke, maximum operating force of 2,700 lbs., and roll leveling time of 0.5 minutes. The pitch system design utilizes a 6,000 lb. capacity Duff Norton Ball Screw Jactuator with a 24:1 worm gear. The jack is driven with a 1/6 HP DC servo motor manufactured by Torque Systems. A fail safe brake manufactured by the Electroid Company is incorporated in the drive train to fix a selected mast orientation. The roll system design is the same type as for the pitch axis except the jack capacity is 4,000 lbs. Both jacks feature a bellows boot for environmental protection of the jack screw.

Vertical positioning of the antenna is accomplished by actuating the sliding

mast via a ball screw located inside the fixed mast. Mast deployment requirements dictated a 54-inch stroke of the actuator within 1.0 minute. The drive system for the screw consists of a 1.0 HP DC motor, coupled to a 28:1 speed reducer which adapts to the screw. A fail safe brake is mounted on the back of the motor to prevent screw slippage. The screw supports the weight of the entire mast assembly minus the weight of the fixed mast. Maximum compressive load in the screw corresponds to antenna deployment under iced conditions and a 50 knot wind. The calculated maximum operational axial load including friction was approximately 3,700 lbs. The screw is a 1.5 inch diameter Warner Electric ball screw and is supported at top and bottom locations inside the fixed mast. The allowable buckling strength of the screw was calculated as 20,000 lbs. and is 5.4 times the maximum operational load.

**ANTENNA CONTROL:** As specified, total control of the LAADS antenna system is accomplished by a single crew member from within the radar shelter. This required a portion of the antenna control circuits to be housed within the shelter; these included the controller and control display assemblies. Control circuits physically installed on the mast assembly include the elevation upper and lower limit assemblies, pitch and roll boxes, and azimuth stow, pitch lock stow, and pitch aft limit sensors. The controller assembly controls mast erection, antenna leveling, and antenna azimuth drive. Linear and binary sensors plus limit switches located on the pivot box, pitch and roll boxes, pedestal and shelter assemblies provide input data to the controller assembly. Interlocks, backed up by hard mechanical stops, protect the system from self-inflicted damage. Mode selection and antenna position controls for directing the controller circuits are contained in the control display assembly. The display unit contains the necessary switches, meters, and indicators for a single operator to automatically control all mast/antenna functions. Switches for manual control of the mast assembly are also located on the display panel. Functions displayed by the control panel include pitch and roll error, deployed, elevation up and down, azimuth stow, pitch lock, and system stowed indicators.

The elevation upper and lower limit assemblies are located on the upper and lower portions of the fixed mast assembly, respectively. Both assemblies contain two limit switches, one which is the operating limit switch and the second the overtravel limit switch. When the telescoping mast assembly reaches its upper limit, the upper limit switch opens de-energizing the elevation drive motor circuits and

engaging the elevation motor brake. The lower limit switches function in exactly the same manner but in the down or stow mode of operation.

The pitch axis box is located on the pivot box assembly and houses the three pitch limit switches (forward limit, low clear, and high clear) which ride on the pitch actuator cam, and the pitch and roll pendulum potentiometers as shown in Figure 6. The forward limit switch limits

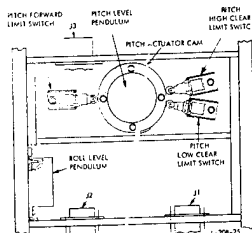


FIGURE 6

travel of the antenna assembly to a maximum of 12° from vertical in the forward direction. The switch, when opened, de-energizes the pitch drive motor circuits. The low clear limit switch switches to its open position when the antenna pitch axis has reached 30° from the horizontal in the forward or erecting direction. The switch action activates both the elevation and roll circuits which are inhibited until this time. The high clear limit switch switches to its open position when the pitch axis reaches 60° from the horizontal in the forward direction. This switch action activates the azimuth drive circuits.

The pitch and roll pendulum potentiometers provide data to the antenna controller circuits which select either forward or aft drive of the pitch actuator and left or right drive of the roll actuator.

The roll axis box shown in Figure 7 is also located on the pivot box assembly

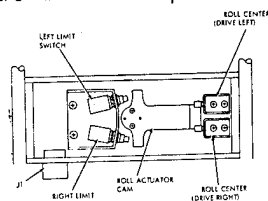


FIGURE 7

and houses the right and left roll limit switches, the roll actuator cam, and two photon-coupled interrupter modules. The right and left limit switches switch to the open position when the antenna assembly approaches a 12° angle to the right or left of the vertical axis. The opening of either switch de-energizes the roll motor circuits and prevents the roll actuator from driving into the mechanical stops. The photon-coupled interrupter modules act as switches

and maintain the roll level axis within 1° of shelter vertical when the antenna assembly is being lowered to its stowed position.

The azimuth stow sensor is mounted on the pedestal housing as shown in Fig. 8. The device is a metal sensing proximity switch and is actuated by a steel target mounted to the rotating antenna base. This circuit is activated when the antenna stow mode is selected and

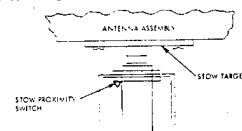


FIGURE 8

correctly orientates and stops the radar antenna for the stow sequence.

The pitch lock stow sensor, Fig. 9, is also a proximity switch. This switch is located on the mast tiedown structure mounted to the shelter roof. When the antenna assembly has reached the desired stow latching position, the sensor is activated and the pitch interlock circuit is opened de-energizing the pitch drive circuits. The pitch aft limit switch, is a back-up to the pitch stow lock sensor.

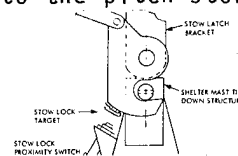


FIGURE 9

**ANTENNA SYSTEM CRITIQUE:** LAADS contractual requirements called for the fabrication of one prototype and twelve preproduction radars. The prototype unit served as a test bed and was subjected to all phases of system testing. Structural verification of the antenna/mast design was dramatically demonstrated by a series of rough road tests, including the "Vehicle Transport Test" of MIL-S-55286. Forty passes, ten each of 5, 10, 15, and 20 MPH were run over a specified course of 4"x8" timbers. In total approximately 1,850 hours of operational time has been logged by the prototype radar. The antenna/mast design has remained unchanged throughout the evaluation program.

At present, the twelve preproduction radars, manned by military crews, have been subjected to approximately nine months of field service, logging in excess of 16,500 hours of operational time. Quality Deficiency Reports submitted from the field have been virtually non-existent. This is the best indication of a successful LAADS design

# EVALUATING COMPUTED DISTORTIONS OF PARABOLIC REFLECTORS<sup>1</sup>

M. SMOOT KATOW

Jet Propulsion Laboratory  
Pasadena, Calif. 91103

## ABSTRACT

Distortion outputs from structural analysis of a 64-m paraboloidal reflector are analyzed by two computer programs for their radio-frequency performance characteristics. The computed and field measured values are compared.

## INTRODUCTION

The Cartesian system of distortion vectors output by a matrix solving structural computing program (i.e., NASTRAN) of a reflector must be evaluated for its radio-frequency (RF) performance characteristics. This paper discusses the evaluation methods and application results of two computer programs, the root-mean-square (RMS) paraboloid best-fitting and the Radiation programs.

## DISCUSSION

The parallel radio waves from afar are reflected to converge at a focus point by the paraboloid with increased amplitude or gain. The reflector's performance is degraded when the converging rays are disturbed by phase differences created by distortions of the reflective surfaces. With the length of the radio wave much greater than the distortions, the change in pathlengths of the rays can be used as a measure of the phase differences.

Ruze (Ref. 1) has shown that the RMS of the weighted (by their corresponding reflective surface areas) half-pathlength errors of the rays associated with the distorted points can be used to describe the degradation of the reflections at the focus point, with

$$\text{Gain loss} = e^{-16\pi^2(\text{RMS}/\lambda)^2} \quad (1)$$

where

RMS = root-mean-square half-pathlength errors

$\lambda$  = RF wavelength

The RMS program (Refs. 2 and 3) with inputs of Cartesian system of distortion vectors best-fits a paraboloid, minimizing in the root-mean-square sense the half-pathlength errors of the radio rays.

The parameters which describe the best-fit paraboloid are shown in Fig. 1 as A, B,  $\rho$ ,

distortion RMS, and the new focal length. The translation of the vertex in the X-direction and the rotation about X, although output from the RMS program, will be assumed to be zero in this discussion, using distortions that are symmetrical about the YZ-plane.

The application of Eq. 1 can now describe the RF performance gain of the reflector when the phase

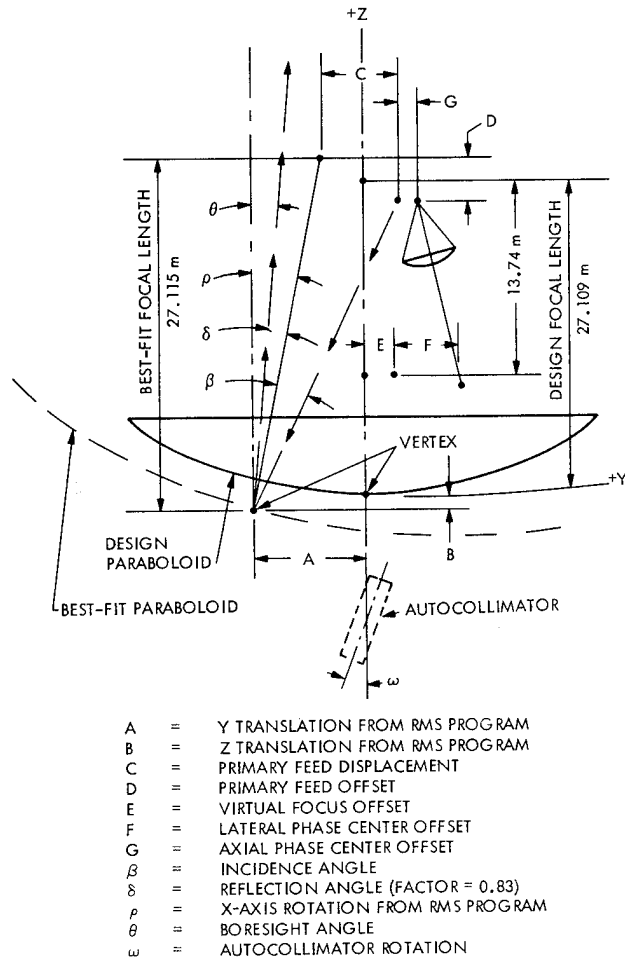


Figure 1. Zenith look with alignment at 45-deg elevation

<sup>1</sup>This paper presents the results of one phase of research carried out at the Jet Propulsion Laboratory, California Institute of Technology, under NASA Contract NAS 7-100, sponsored by the National Aeronautics and Space Administration.

center of the RF feed system is coincident with the focus point of the best-fit paraboloid. However, in practice, there will usually be both axial and lateral offsets between the above two points due to structural deformations, resulting in additional gain losses.

In order to resolve the gain losses due to these offsets, the Radiation program (Ref. 4) is used. This program outputs the RF radiation in the direction  $(\theta, \phi)$  of Fig. 2, with identical distortion inputs as for the RMS program. A complete or full circle of distortion data is required, with sufficient data points to smooth out the integration by the trapezoid rule approximation.

The Radiation program numerically integrates the scalar far-field pattern integral (Ref. 5), with provisions to input the RF feed pattern of amplitudes and phase angles.

Gain losses from axial and lateral offsets are output from the Radiation program by inputs of perfect paraboloids, with all points on the reflector translated in opposite sign directions to the offsets. A series of varied offsets were input and resulted in two straight-line representations, as shown in Fig. 3. The gain loss outputs from the Radiation program were first transposed to equivalent RMS values by Eq. 1.

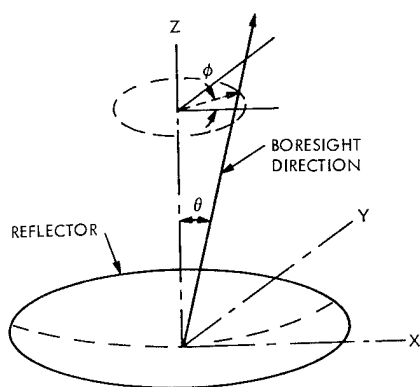


Figure 2. Radiation program output

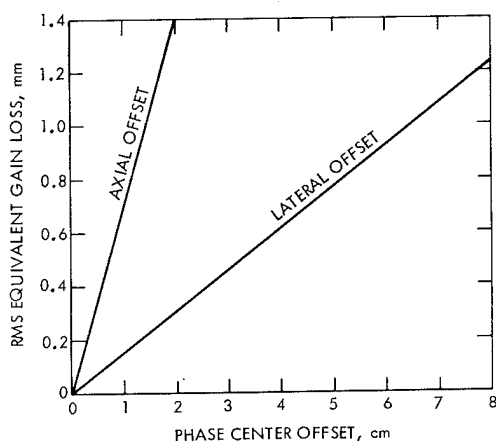


Figure 3. Equivalent gain loss in RMS values, 64-m antenna,  $F/D = 0.42$

It is interesting to note that the slopes of the lines are dependent on the focal-length-to-diameter ( $F/D$ ) ratio of the reflector. The offset gain losses rise dramatically with deeper reflectors for equal offsets. Also, the RMS values of Fig. 3 are independent of RF frequency.

We find that a limitation exists on the accuracy of the rotation angle output by the RMS program. If distortions are from field readings, where there is scatter of the data, it is obvious from the fitting process that a close to circular shape of the paraboloid will result in an uncertain rotational position of the best-fit paraboloid. However, the accuracy of the RMS of the distortions will be only slightly affected.

#### PREDICTING RF BORESIGHT OF THE 64-m ANTENNA

The RF boresight direction was computed for the zenith look configuration for the 64-m antenna with alignment at 45-deg elevation. The direction computed was with respect to the centerline of the servo-system's autocollimator mounted on the center hub of the reflector. This autocollimator aligns with a precision-driven mirror.

Figure 1 describes the computed displacements and rotations for the complete Cassegrain RF system. At zenith look, the computed boresight error ( $\phi - \omega$  of Fig. 1) equaled  $-0.003$  deg for the 64-m antenna at its present structural configuration.

The field data were obtained before a structural change was made, where the computed boresight error was  $-0.009$  deg. At an operational RF frequency of 8.4 GHz (X-band) with a half-power beamwidth of 0.038 deg, the absolute pointing error of 0.010 deg peak to peak was experienced in the test mode, spanning 5- to 40-deg elevation angles during a 5-day test period with low winds ( $<15$  mph) (Ref. 6).

The computed values, in addition to those presented in Table 1, required for the boresight calculations are:  $E = 1.95$  cm,  $F = 2.87$  cm,  $G = 0.58$  cm,  $\theta = -0.000396$  rad, and  $\omega = -0.000446$  rad.

#### PREDICTING RF GAIN LOSS OF THE 64-m ANTENNA

At the alignment elevation angle, the only gain losses are from the manufacturing and field setting distortions of the surface panels. The square root of the sum of the squares (RSS) of the RMS distortion values should be applicable to the above values plus the phase center offset RMS equivalent losses. Our experience supports the assumption that all of these RMS values can be assumed to be of random distribution.

Table 1 delineates the computed phase center offsets for the full range of elevation angles, and Table 2 the equivalent RMS losses. The computed and field data RMS losses are plotted in Fig. 4, with field data from Ref. 7.

At present, a discrepancy exists between the RMS distortion values obtained from RF field tests and the measured distortions of the surface panels at the 45-deg alignment elevation angle because of distortions generated on the subreflector when a mission requirement dictated a solid surface. This was done by field welds, which resulted in warpage of unknown factors on the subreflector's surface. A nominal RMS of the surface of 1.42 mm was

Table 1. Computed offset dimension of Fig. 1 for 64-m antenna

	Elevation angle, deg						
	0	15	30	45	60	75	90
A, cm	5.16	4.57	2.81	0	-3.67	-7.95	-12.55
B, cm	0.26	0.16	0.08	0	-0.06	-0.09	-0.11
$\rho$ , rad	0.001161	0.001021	0.000625	0	-0.000812	-0.001751	-0.002768
C, cm	-3.29	-2.19	-1.89	0	2.33	5.05	7.96
D, cm	2.19	1.41	0.64	0	-0.47	-0.75	-0.81

Table 2. RMS and RSS results for 64-m antenna plotted on Fig. 4

	Elevation angle, deg						
	0	15	30	45	60	75	90
CC, mm	0.51	0.34	0.29	0.0	0.36	0.79	1.24
DD, mm	1.57	1.00	0.45	0.0	0.33	0.53	0.65
L, mm	0.63	0.41	0.20	0.0	0.19	0.35	0.50
M, mm	1.42	1.42	1.42	1.42	1.42	1.42	1.42
N, mm	1.56	1.48	1.44	1.42	1.43	1.46	1.51
O, mm	1.63	1.52	1.46	1.42	1.48	1.66	1.95
P, mm	2.27	1.82	1.53	1.42	1.52	1.75	2.06

CC = equivalent RMS error to C offset of Table 1 (from Fig. 3)

DD = equivalent RMS error to D offset of Table 1 (from Fig. 3)

L = gravity loading RMS distortion

M = total reflective surface RMS distortion (1.06 mm + operational required change  $\approx 1.42$  mm)

N = RSS with lateral and axial focus adjustments

O = RSS with axial focus adjustment only

P = RSS without any focus adjustment

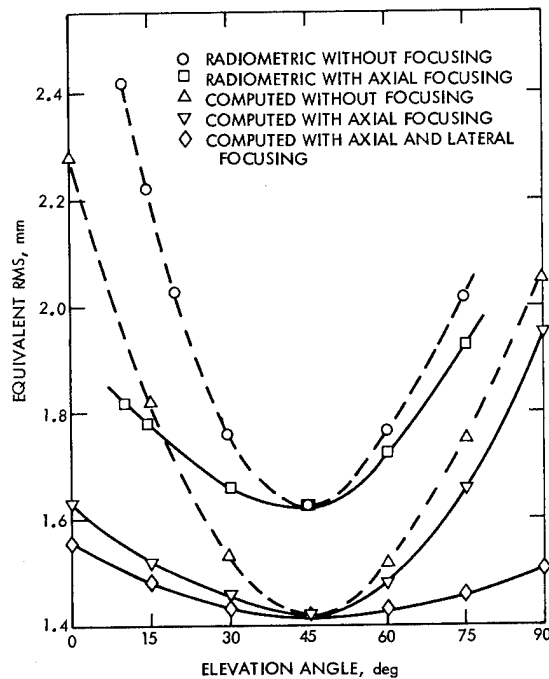


Figure 4. Computed vs. field distortions, 64-m antenna

estimated and used, which should not degrade the computations for offset calculations. Figure 4 shows comparisons of computed and field distortions with and without focusing. In the field data, offsets are eliminated by focusing. There is a close match between the field data and the computed values. Implementation of the lateral focusing should provide increased performance but at the expense of added requirements to compensate for the resulting boresight error.

#### REFERENCES

1. Ruze, J., Physical Limitations on Antenna, Technical Report 248, Research Laboratory of Electronics, Massachusetts Institute of Technology, Cambridge, Mass., Oct. 30, 1952 (ASTIA/AD-62351).
2. Utku, S., and Barondess, S. M., Computation of Weighted Root-Mean-Square of Path Length Changes Caused by the Deformations and Imperfections of Rotational Paraboloidal Antennas, Technical Memorandum 33-118, Jet Propulsion Laboratory, Pasadena, Calif., March 1963.
3. Katow, M. S. and Schmele, L. W., "Antenna Structures: Evaluation Techniques of Reflector Distortions," Space Programs Summary 37-40,
4. Bathker, D. A., "Radiation Pattern Programs," in Computer Programs for Antenna Feed System Design and Analysis, edited by A. Ludwig, Technical Report 32-979, Jet Propulsion Laboratory, Pasadena, Calif., 1967.
5. Silver, S., Microwave Antenna Theory and Design, Radiation Laboratory Series, Vol. 23, p. 173, McGraw-Hill Book Co., New York, N.Y., 1949.
6. Bathker, D. A., Radio Frequency Performance of a 210-ft Ground Antenna: X-band, Technical Report 32-1417, Jet Propulsion Laboratory, Pasadena, Calif., Dec. 15, 1969.
7. Freiley, A. J., Radio Frequency Performance of DSS 14 64-m Antenna at 3.56- and 1.96-cm Wavelengths, in The Deep Space Network Progress Report, Technical Report 32-1526, Vol. XIX, pp. 110-115, Jet Propulsion Laboratory, Pasadena, Calif., Feb. 15, 1974.

# ANTENNA BIAS RIGGING FOR PERFORMANCE OBJECTIVE<sup>1</sup>

R. LEVY

Jet Propulsion Laboratory  
Pasadena, Calif. 91103

## ABSTRACT

An optimum bias rigging for a paraboloidal antenna can be used to minimize the expected average mean-square half-pathlength surface deviations. Statistics of deep space planetary missions are employed to develop weighting factors for antenna elevation angles during these missions. A procedure is shown to compute the optimum rigging angle from these weights.

## INTRODUCTION

Bias rigging is a method of optimizing the performance characteristics of the surface-supporting structure of an altitude/azimuth paraboloidal radio-frequency (RF) transmitting and receiving antenna reflector. The approach is to set the reflecting surface panels to an ideal paraboloid at some particular elevation rigging angle, intermediate between horizon and zenith pointing attitudes. This can provide a built-in bias to improve the accuracy of the reflecting surface with respect to the adverse effects of structural deformations. In particular, loss of accuracy from deformations caused by gravity loading variations over the elevation attitude range can be reduced. Compared to comprehensive procedures that can develop the design of the supporting structure (Ref. 1), bias rigging is a simple procedure that can be readily implemented to help achieve this control.

## ANTENNA SURFACE PERFORMANCE EFFICIENCY

A convenient measure of antenna surface accuracy is given by Ruze's conventional efficiency equation (Ref. 2) that relates surface accuracy to RF wavelength as

$$e = \exp [-(4\pi \text{ rms}/\lambda)^2] \quad (1)$$

in which  $e$  is the efficiency of the surface,  $\lambda$  is the wavelength, and  $\text{rms}$  is the square root of the mean-square half-pathlength deviation of the reflecting surface from a best-fitting ideal paraboloid. The gain-loss can be computed in decibels from Eq. 1 as

$$G = 10 \log_{10} e \quad (2)$$

When the antenna is subjected to gravity loading, the  $\text{rms}$  term to be used in Eq. 1 is a function of the particular elevation angle attitude at which the antenna is pointing. At the rigging attitude, this term is zero. At any other attitude, the loading that produces the  $\text{rms}$  is effectively the change in loading from the loading at the rigging attitude. Typical high-performance antenna structures respond linearly to the operational environmental loading. Therefore, the response to variable gravity loading at any elevation attitude can be conveniently determined by superposition. In Ref. 3, it was shown that the mean-square half-pathlength deviation  $SS_a$  at elevation angle  $\alpha$  can be determined from

$$SS_a = \eta^2 SSY + \zeta^2 SSZ + 2\eta\zeta SYZ \quad (3)$$

and the  $\text{rms}$  half-pathlength deviation is

$$(\text{rms}_a) = (SS_a)^{1/2} \quad (4)$$

In Eq. 3,  $SSY$  and  $SSZ$  are the mean-square half-pathlength deviations for gravity loading applied parallel to the respective  $Y$  and  $Z$  axes shown in the inset of Fig. 1, and  $SYZ$  is the mean inner product of the corresponding half-pathlength deviation vectors. The loading coefficients  $\eta$ ,  $\zeta$  depend upon the elevation angle  $\alpha$  and the rigging angle  $\gamma$  and are given by

$$\begin{aligned} \eta &= \cos \gamma - \cos \alpha \\ \zeta &= \sin \gamma - \sin \alpha \end{aligned} \quad (5)$$

The polar plot in Fig. 1 illustrates a sample pattern of the change in the  $\text{rms}$  half-pathlength deviation over the elevation attitude range. The deviation can be seen to be zero at the rigging attitude ( $\text{rms}_\gamma$ ) and to have extreme values at the horizon ( $\text{rms}_0$ ) and zenith ( $\text{rms}_{90}$ ) attitudes. It can be observed from this figure that choice of rigging angle can have a significant effect on the performance of the antenna.

Relationships were discussed in Refs. 3 and 4 that considered either the minimization of the extreme  $\text{rms}$  pathlength deviations over the elevation range or the minimization of the expected average pathlength deviations for antennas that track targets uniformly distributed within the hemisphere above the horizon. Here we will consider

<sup>1</sup>This paper presents the results of one phase of research carried out at the Jet Propulsion Laboratory, California Institute of Technology, under Contract NAS 7-100, sponsored by the National Aeronautics and Space Administration.

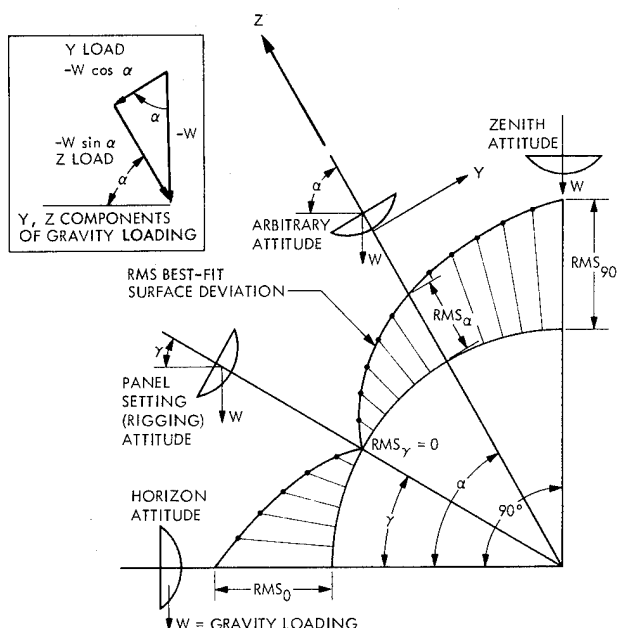


Figure 1. RMS deviation change with elevation angle

bias rigging to minimize the expected average path-length deviations for an antenna that is required to track missions of a collection of planets with known orbits.

#### SELECTION OF RIGGING ANGLE FOR MISSION-WEIGHTED ELEVATION ANGLE USAGE FACTORS

Assume that the projected tracking mission of the antenna is known, so that it is possible to determine the elevation angle time history for the antenna for a particular mission or the average time history for a collection of missions. The elevation angle weighting factor  $W_a$  can be developed to supply the probability of antenna targets occurring at elevation angle  $a$ . A set of weighting factors is developed by dividing the elevation angle range into a set of elevation class marks equally spaced at some constant class interval. Consequently, the weighting factors represent the probability of antenna targets occurring at elevations within the class interval centered on particular class marks. When the class marks are closely spaced, and with appropriate normalization of the weighting factors, the elevation angle probability density function is approximately equal to the weighting factor divided by the class interval. In this case, it follows that

$$\sum W_a = 1.00$$

Optimum performance for a particular antenna with respect to the mission elevation angle weighting is obtained by choosing the rigging angle to minimize the elevation-weighted mean-square half-pathlength deviations. In particular, from Eq. 3, we choose  $\gamma$  to minimize the objective expression

$$OBJ = \sum_a W_a (\eta^2 SSY + \zeta^2 SSZ + 2\eta\zeta SYZ) \quad (7)$$

This objective represents the expected average mean-square half-pathlength deviation. Substituting Eqs. 5 in 7, expanding, using Eq. 6, and simplifying leads to the objective in the following form:

$$OBJ = A^2 SSY + B^2 SSZ + 2C SYZ \quad (8)$$

where

$$A^2 = \cos^2 \gamma + \sum W_a \cos^2 a - 2 \cos \gamma \sum W_a \cos a$$

$$B^2 = \sin^2 \gamma + \sum W_a \sin^2 a - 2 \sin \gamma \sum W_a \sin a$$

$$C = \sin \gamma \cos \gamma + \sum W_a \sin a \cos a - \cos \gamma \sum W_a \sin a - \sin \gamma \sum W_a \cos a$$

The objective in Eq. 8 is a unimodal function of  $\gamma$ , and optimum  $\gamma$  can be conveniently found by a one-dimensional search within the interval of the elevation angle range.

#### COMPUTATION OF ELEVATION ANGLE MISSION WEIGHTS

The weighting factor is computed as proportional to the amount of time in a given period during which the antenna elevation angle is within the particular class interval. For convenience, we consider an annual period of 365 days. The time in hours is  $1/15$  of the difference of hour-angle (in degrees) of the target in passing through the lower and upper elevation class mark boundaries. The hour angle  $H$  is a function of latitude of the site  $\phi$ , the declination angle of the target  $\delta$ , and the elevation angle  $a$ . From spherical trigonometry,

$$H = \cos^{-1} \frac{(\sin a - \sin \phi \sin \delta)}{\cos \phi \cos \delta} \quad (9)$$

Equation 9 can be solved for the maximum elevation  $a_{\max}$  at a particular declination, which occurs at 0-deg hour angle, thus:

$$a_{\max} = \sin^{-1} [\cos (\phi - \delta)] \quad (10)$$

On a given day, assume that the target's declination  $\delta_j$  is approximately constant. The tracking time  $t_j$  on this day is twice the time interval in following the target from the minimum operational elevation angle  $a_{\min}$  to the maximum elevation angle given by Eq. 10. Therefore,

$$t_j = 2/15 H(a_{\min}, \phi, \delta_j) \quad (11)$$

If analysis has been made of the missions to be considered and declination angle weighting factors  $D_j$  have been established to give the probability of target declinations being within declination class marks  $\delta_j$ , the annual hours  $T_j$  at this declination class mark are

$$T_j = 365 D_j t_j \quad (12)$$

At declination class mark  $\delta_j$ , targets will be encountered at elevation class marks between  $a_{\min}$  and  $a_{\max}$ . The daily time  $t_{ij}$  spent in tracking at elevation class mark  $a_i$ , with upper and lower class mark boundaries  $a_i$  and  $b_i$ , respectively, is

$$t_{ij} = 2/15 (H(a_i, \phi, \delta_j) - H(b_i, \phi, \delta_j)) \quad (13)$$



On a 365-day basis, declination class mark  $\delta_j$  contributes the following tracking time hours to elevation class mark  $\alpha_i$ :

$$T_{ij} = 365t_{ij}D_j \quad (14)$$

and the total tracking time  $T_i$  at this elevation class mark is the sum of the contributions from all declination class marks. That is,

$$T_i = \sum_j T_{ij} \quad (15)$$

Finally, the normalized elevation angle mission-weighting factor is

$$W_i = T_i / \sum T_i \quad (16)$$

#### MISSION-WEIGHTED DECLINATION ANGLES

For illustration, analysis has been made of the 16 most significant NASA-JPL deep space planetary mission tracking orbits to determine composite declination angle weighting factors for missions in the time period from 1973 to 1981. Declination angle weighting factors have been developed for declinations spaced at 1-deg class intervals from -50 to +50 deg of declination. For comparison, a solar mission category has been examined. That is, the mission target is the Sun. In this case, the declination is given by

$$\delta = 23.5 \sin (2\pi d/365) \quad (17)$$

in which  $d$  is the number of days from the vernal equinox. In this case, the declination probability density function, which is approximately equivalent to the declination angle weighting factor for a 1-deg class interval declination angle, is given by

$$f(\delta) = \frac{1}{23.5\pi[1 - (\delta/23.5)^2]^{3/2}} \quad (18)$$

for  $|\delta| < 23.5$

#### RESULTS AND DISCUSSION

Figure 2 shows the declination angle probability density functions for the composite and the solar missions. They are similar except for the oscillations exhibited by the composite curve.

The corresponding elevation angle probability density curves are shown in Fig. 3. Again the composite and solar mission curves are reasonably similar.

Table 1 shows the statistics of the elevation weighting factors that are used for computation of antenna rigging angles. Figure 4 is a plot of gain/loss versus antenna elevation angle for the DSN 64-m Mars antenna. The elevation weighting factors used were for the composite missions. One curve is for the optimum rigging angle of 35.4 deg, computed according to the procedure given here, and the other curve is for the same antenna with the current 45-deg rigging angle. Table 2 is a summary of results obtained for this antenna for both mission categories, comparing optimum rigging with the existing 45-deg rigging angle.

It can be noted from the last line in Table 2 that, although the expected average gain loss for this antenna is relatively small for both mission categories, the optimal rigging angle results in

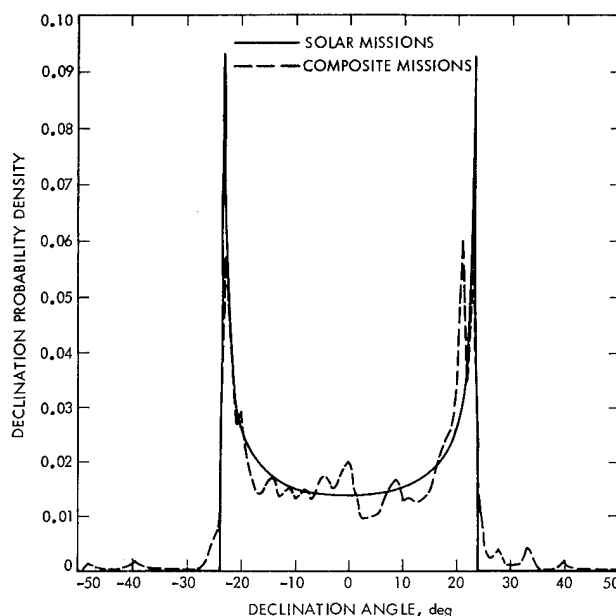


Figure 2. Declination angle probability density

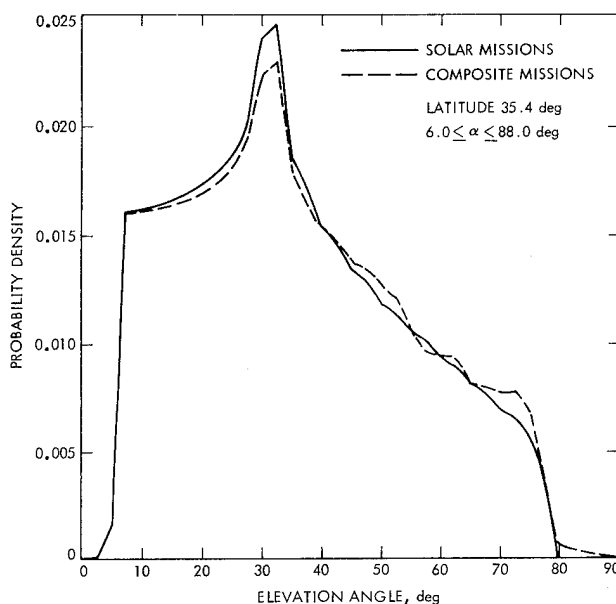


Figure 3. Elevation angle probability density

Table 1. Mission-weighted elevation angle statistics

	Weighting factor	
	Composite missions <sup>1</sup>	Solar missions
$\sum W_a$	1.0000	1.0000
$\sum W_a \sin^2 a$	0.3755	0.3641
$\sum W_a \cos^2 a$	0.6245	0.6358
$\sum W_a \sin a$	0.5610	0.5526
$\sum W_a \cos a$	0.7621	0.7717
$\sum W_a \sin a \cos a$	0.3791	0.3805
Average annual tracking hours		
	4056	3996

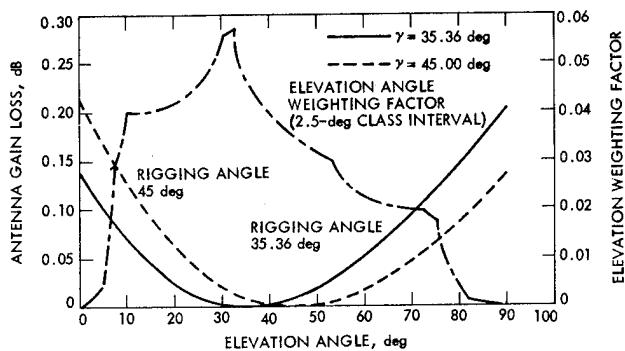


Figure 4. Mars antenna gravity deformation gain loss at 8.45 GHz for composite missions

gain losses about 20 percent less than the gain loss with 45-deg rigging. It can also be observed from Fig. 4 that the relatively higher gain losses with optimal rigging at the elevation angles close to the zenith attitude occur with low probability (weighting factor).

#### REFERENCES

1. Levy, R., "Computer-Aided Design of Antenna Structures and Components," Computers and Structures, Vol. 6, pp. 419-428, Pergamon Press, 1976.
2. Ruze, J., "Antenna Tolerance Theory-A Review," Proc. IEEE, Vol. 54, No. 4, April 1966, pp. 633-640.

Table 2. Comparison for existing Mars antenna

	Composite missions		Solar missions	
	Optimum exist- ing	ing	Optimum exist- ing	ing
Rigging angle, deg	35.4	45.0	34.7	45.0
Expected average gain loss for mission, dB at X-Band (= 8.45 GHz)	0.0337	0.0421	0.0322	0.0420
Relative gain loss, percent	80	100	77	100
SSZ, mm <sup>2</sup> (in. <sup>2</sup> ) = 0.760(0.001176)				
SSY, mm <sup>2</sup> (in. <sup>2</sup> ) = 0.393(0.000610)				
SYZ, mm <sup>2</sup> (in. <sup>2</sup> ) = 0.030(0.000046)				

3. Levy, R., "A Method for Selecting Antenna Rigging Angles to Improve Performance," in The Deep Space Network, Space Programs Summary 37-65, Vol. II, pp. 72-76, Jet Propulsion Laboratory, Pasadena, Calif., Sept. 1970.
4. Levy, R., "Antenna Rigging Angle Optimization Within Structural Member Size Design Optimization," in The Deep Space Network Progress Report, Technical Report 32-1526, Vol. I, pp. 81-87, Jet Propulsion Laboratory, Pasadena, Calif., Feb. 15, 1971.

## DESIGN OF HARDENED RADAR STRUCTURES

RONALD L. MANN

General Electric Company  
Electronic Systems Division  
Court Street Plant  
Syracuse, N. Y. 13221

### ABSTRACT

The structural design of an "edge-supported" phased-array antenna is discussed in some detail. A technique is presented for separately accommodating combined airblast loading and thermal radiation effects. Material strength at elevated temperature is shown to be a major concern in hardened design, along with degradation in surface reflectance for materials exposed to direct thermal radiation. Rock debris studies are being conducted to determine behavior during impact with simply supported beams.

### INTRODUCTION

A structure is considered to be "hardened" in the sense that it can withstand the effects of a nuclear environment, created by the explosion of a given size weapon. Significant advances have been made, during the past decade, in the design of radar structures required to withstand severe external loading.

This paper will present some of the recent "state-of-the-art" structural design approaches to airblast and thermal radiation as well as present research work on debris effects. Exclusion of neutron, gamma, and EMP effects should not suggest that they are of secondary importance. All of these effects are important and must be considered if one is to achieve a satisfactory hardened design.

### DESIGN PHILOSOPHY

Before beginning to design a hardened structure to withstand a nuclear environment, definition of the environment or environments must be complete. It may not be sufficient to design structural systems to survive separate nuclear effects such as thermal radiation and overpressure. The total nuclear environment is comprised of a number of time-dependent parameters. Many of the effects have overlapping time histories, and therefore it is extremely important to consider combined effects.

The initial assumption made in the early design development stage is that the primary, potentially damaging effects are due to thermal radiation and blast overpressure. At this time a review should be made of the time histories of the thermal and overpressure effects to answer the following type of questions:

- 1) What percentage of the total thermal energy has the structure been exposed to upon arrival of the blast wave?
- 2) Are the thermal stress levels in the structure or structural components significant at the time of blast arrival?

- 3) How much of a factor will strength at elevated temperature be?

Only approximate answers to these questions are required to give the design engineer a good baseline with which to start his design.

The design of antenna elements and associated support structure can be effectively developed using the following approach. Addressing first the design of antenna element windows, transparent, opaque, and ablative materials should be considered as candidate materials when acceptable RF transmissibility can be demonstrated. Determine the temperature-time dependent properties "consistent" with the nuclear environment. The important properties include absorptivity, coefficient of expansion, thermal conductivity, yield strength, ultimate strength, and modulus of rupture. Perform thermal tests and analyses on material samples having varying thicknesses. In designing to meet the thermal environment, it is important to consider the time-dependent flux and not just the integrated flux. The degree of nonlinearity of the thermal profile and resultant thermal stress through a given material is very much a function of thermal flux. Materials found to be acceptable are studied to see if they can satisfactorily withstand remaining nuclear effects. Selection of metallic materials for element housings and structural members, which primarily perform a load-carrying function, is approached in a similar manner. An integral part of metallic material studies is consideration of the exposed surface condition. Reflectance behavior is of prime importance in selecting suitable metallic materials and platings.

Incorporation of candidate materials into an antenna element design, as an example, involves a number of considerations. First, consideration is given to the physical configuration which is desirable for electrical performance. A number of conditions regarding window and housing compatibility must be investigated such as relative expansion, method of attachment, and sealing against natural environment. A determination should be made as to whether it is better to use materials that absorb, transmit, or reflect thermal radiation. That is, can ablative or transparent materials be used rather than the normal opaque ceramics?

Many of the aforementioned conditions apply to the design of a support structure. In addition material strength, dynamic response, and maximum deformation are of major concern. The structure stiffness should be optimized if possible to minimize the dynamic response during the airblast impulse loading. A knowledge of behavior of materials subjected to short-time elevated temperatures is required to ensure desired structural integrity. Allowable array surface deforma-

tion based on system performance determines whether the design should be based on a strength or an allowable deformation criterion.

Before a design can be finalized, attention must be focused on combined nuclear effects. In addition to sequence of events and time history effects, consideration must be given to all possible locations of blast relative to the radar array. This is an important consideration, because for a specified weapon size and overpressure the location for the worst thermal effect is not necessarily the same as the location for the most severe overpressure effect.

#### PHASED-ARRAY ANTENNA STRUCTURES

A hardened phased-array antenna can be classified, in a structural sense, as being either a "continuous" or "edge" supported structure. Antennas having surface areas in the range of 200 to 400 sq ft can reasonably be designed as self-supported structures, requiring only the edge support of a hardened bunker. Figure 1 shows the mounting of dipole antenna elements to the front surface of a perforated, edge-supported structure. In addition ground plane plates, which also fasten to the support structure, are shown clamped in place. These plates provide the necessary electrical contact between antenna elements. Furthermore they are designed to facilitate adequate localized thermal expansion, upon exposure to a nuclear weapon environment.

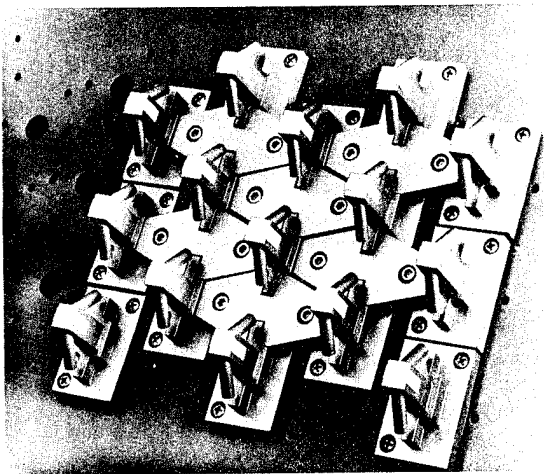


Figure 1. Partial assembly of antenna elements and ground plane plates of the STR (System Technology Radar) system.

A representative section of the array support structure is shown in figure 2. The basic structure consists of front and rear perforated plates separated by continuous horizontal ribs. The air plenum, which provides for cooling of electronic equipment, is not directly attached to the rear surface of the support structure. The clearance space between these major structures accommodates deformation of the array upon being subjected to airblast overpressure loading. Clearance holes are required on the front and rear plate of the support structure to accommodate the coax cables which are connected to each antenna element.

The beauty of this design is its ability to separately accommodate what would appear to be incompatible load conditions imposed by two nuclear weapon combined effects. The elements and ground plane

absorb the thermal radiation and transfer the airblast loading to the support structure, which provides the necessary dynamic load-carrying capacity.

#### SUPPORT STRUCTURE DESIGN

The airblast loading which is experienced by the array face consists of the free-field overpressure, the dynamic pressure, and a reflected overpressure (Ref. 1-3). Large closed rectangular structures having projected areas greater than 100 sq ft are generally taken to be overpressure sensitive, and therefore the maximum structural response should be significantly influenced by the decaying reflected overpressure. The reflected overpressure load-time history is a function of the free-field overpressure, shock front velocity, and a clearance distance which is based on the geometry of the structure. In effect the size of the structure determines how long the reflected pressure contributes to the total loading.

The antenna structure represented in figure 2 can be defined as an anisotropic, perforated plate having an infinite number of degrees-of-freedom (d.o.f.). However, a reasonable assessment of structural dynamic behavior, upon being subjected to a head-on shock wave, can be obtained by modeling the structure as an equivalent 1-d.o.f. system (Ref. 4, 5). This equivalent system can then be subjected to an equivalent dynamic load, consistent with the specified free-field airblast scenario. The response of the system is determined using the "finite difference" computer program given in Ref. 6. An "equivalent static load," or uniform pressure, is subsequently derived from this analysis. Once the maximum "equivalent static load" has been determined, it is possible to perform a detailed stress analysis of the structure. The "SOLID SAP" computer program is one of a number of "finite element" programs well suited for this analysis (Ref. 7). The program output consists of displacement, rotation, normal stress, and shear stress data.

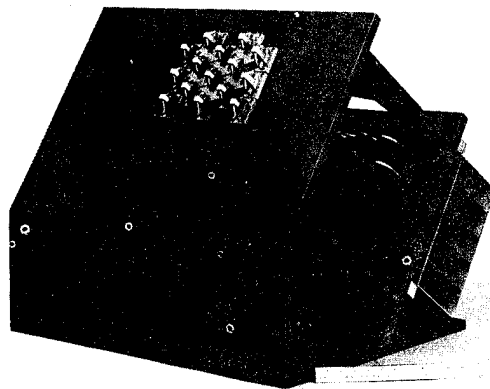


Figure 2. Cutaway section through the STR array support structure and air plenum.

An airblast shock wave approaching the array face from the side will sweep across the array at its free-field velocity. The pressure loading imposed on the array face due to the traveling shock front will result in antisymmetric mode contributions to the dynamic deflection. These modal deflections are extremely important because they may seriously affect radar pointing

error. The "COMET" program (Ref. 6) can be used to determine participation of antisymmetric modes, by modeling the array support structure as a multi-d. o. f. system.

Stress concentration effects, due to penetrations in the front plate of the support structure (figure 2) can be studied experimentally by performing a photoelastic analysis. By cementing an appropriate photoelastic coating to the underside of the front plate of the structure, one can determine the normal stress distribution - i.e., difference in principal stress - due to localized bending between the horizontal ribs. Figure 3 illustrates an isochromatic fringe pattern due to a uniform pressure distribution on the front plate of the structure. The fringe pattern was obtained using a large prism located between ribs, shown at the top and bottom of this figure, and a reflection polariscope. The greatest concentration of fringes can be observed to occur at both left and right edges of holes located midway between the ribs.

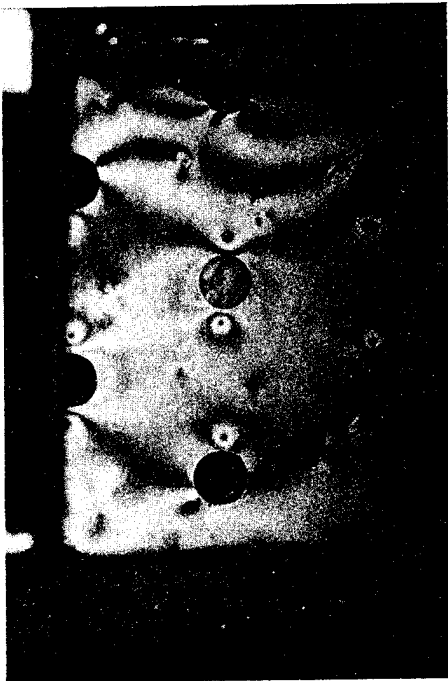


Figure 3. Isochromatic fringe pattern on the underside of the front plate of the support structure.

Material strength at elevated temperature is a major consideration in hardened structural design. Table 1 reveals some rather startling results for the behavior of some metallic materials subject to short-time elevated temperature. A 6061-T6 aluminum test specimen, for example, heated to 800°F and held at temperature for two minutes, will experience a negligible degradation in yield strength. However, this material, after experiencing three 2-min cycles, also at 800°F, will have a yield strength of only 25% of its room temperature strength. A 5456 aluminum alloy will retain 50% of its yield strength when subjected to the same three-cycle test.

Knowledge of material strength behavior, with time and temperature, is extremely important in designing for a single-burst, as well as a multiple-burst threat. In designing structural elements to survive a single event, obviously the luxury of a higher maximum allowable temperature exists. Materials used for

multiple-burst design should be evaluated under variable temperature-time history conditions. These conditions should be consistent with the thermal radiation pulse of each event and the cooling that is experienced between events.

TABLE 1  
MECHANICAL PROPERTIES AT ELEVATED TEMPERATURE

Material	Temperature (°F)	Tensile Strength (ksi)	Yield Strength 0.2% Offset (ksi)
Alum. 6061-T6	70	46.4	43.0
	400 ☆☆	45.6	41.3
	600 ☆	44.1	39.2
	600 ☆☆	33.7	27.2
	800 ☆	41.5	38.3
	800 ☆☆	24.4	10.9
Alum. 5456-H323	70	55.8	40.0
	800 ☆	43.5	38.5
	800 ☆☆	38.3	20.9
Be-Cu Be 0.4-0.7% Co 2.35-2.7% Cu Balance	70	100.0	79.3
	900 ☆☆	82.6	68.5
	1000 ☆☆	81.3	66.2
	700 ☆☆☆	94.5	74.8

(☆) 2-min cycle. (☆☆) three 2-min cycles.

(☆☆☆) 3 hours.

#### THERMAL BEHAVIOR OF ARRAY FACE MATERIALS

Metallic and non-metallic materials used for an antenna array face are particularly vulnerable to thermal radiation. Even the most reflective exterior surfaces of non-transparent materials used in array face design experience severe surface heating upon exposure to a thermal pulse. A typical thermal pulse from a nuclear weapon is shown in dimensionless form in figure 4 (Ref. 1). The pulse is characterized by a rapid rise to a peak flux at time  $t = t_{max}$  and a gradual decay in time,  $t_{max}$  to  $10t_{max}$ . For a pulse which satisfies the Hillendahl equation (Ref. 8), 20% of the energy is emitted in time  $t_{max}$  and 82% in time  $10t_{max}$ .

There are a number of possible modes of material failure associated with the absorption of thermal radiation. Figure 5 shows three temperature variations through a slab of material of thickness  $h$ . The times,  $t_{max}$  and  $10t_{max}$ , correspond to those of figure 4. At a time shortly after  $t_{max}$  a material may fail due to high thermal stress. In time  $2t_{max} < t < 10t_{max}$  materials may have experienced degradation in yield strength and could experience failure due to combined stress upon arrival of the overpressure shock wave. Material surface reflectance may tend to degrade with time at elevated temperature. As a result, materials may experience melting at late time ( $t > 10t_{max}$ ) even though the incident energy level is quite low.

The response of a 0.375-in. polycrystalline glass plate to a thermal pulse is illustrated in figure 6. Results of normal stress variation with time and temperature are shown for one-dimensional heat flow normal to the plate surface (Ref. 9). This figure illustrates a number of interesting results. The rapid rate of energy absorption at the exposed surface is exemplified at time  $t_1$ . At this time the surface temperature is 900°F, while at a depth 0.08 in. below the surface

it is at ambient temperature. For this plate, which is unrestrained at its boundaries, one can observe compressive stresses on both surfaces and tensile stress variation through an interior region. These stress profiles are due to nonlinear temperature variations through the plate thickness.

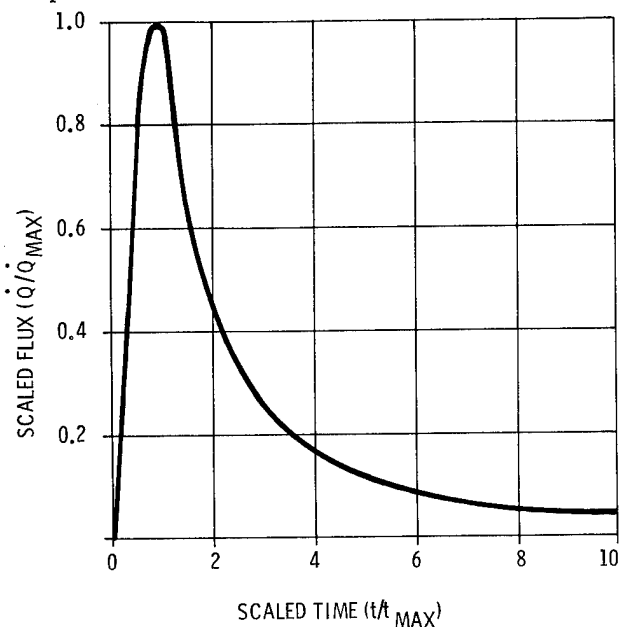


Figure 4. Thermal pulse showing scaled flux vs scaled time for energy emitted from a fireball formed in an air burst.

$Q_{\text{max}}$  is maximum rate of energy emission.

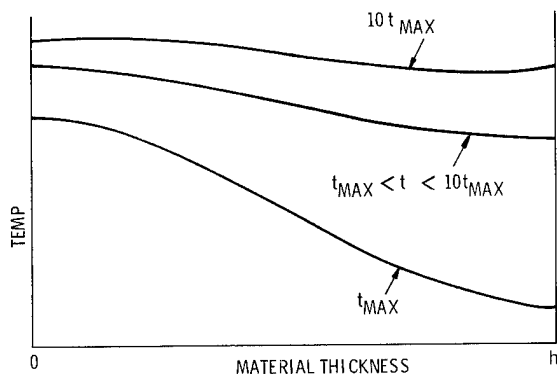


Figure 5. General material response to a thermal radiation pulse.

Thermal radiation testing has proven itself to be an invaluable tool for hardened design. In designing an antenna element, for example, the luxury of using normal factors of safety is not possible. The greatest concern, regarding uncertainty of loading, is with degradation of surface reflectance during exposure to natural as well as nuclear environments. Structural elements which have been weathered in accelerated natural environment tests can readily be tested for behavior upon subsequent exposure to a thermal pulse.

The equipment shown in figure 7 was developed for the purpose of evaluating basic material as well as actual structure behavior, upon exposure to a simulated

thermal pulse. The heat source for this equipment is a solid graphite resistance element. The graphite, shown clamped between water-cooled terminals, is capable of emitting a heat flux of  $440 \text{ Btu}/(\text{ft}^2\text{-sec}) = 120 \text{ cal}/(\text{cm}^2\text{-sec})$ . When the graphite has reached a temperature associated with the desired peak flux level, the water-cooled shutter opens and exposes the test specimen. By this means, it is possible to achieve a rapid rise time at the start of the exposure. The decrease in flux after time  $t_{\text{max}}$  is normally controlled by the natural decay in temperature while the graphite is cooling.

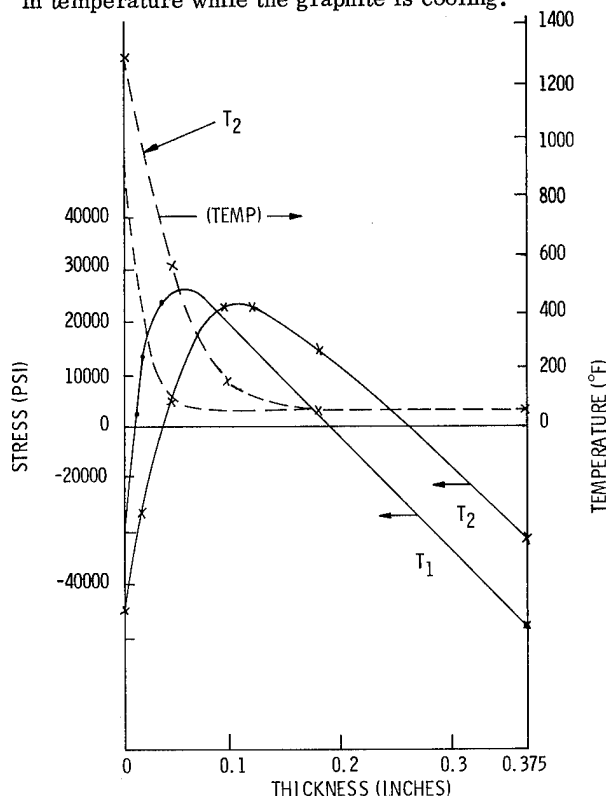


Figure 6. Stress and temperature distribution through a polycrystalline glass plate (Pyrocera-9606) at time  $t_1 < 0.5 \text{ sec}$  and  $t_2 > 1.5 \text{ sec}$ .

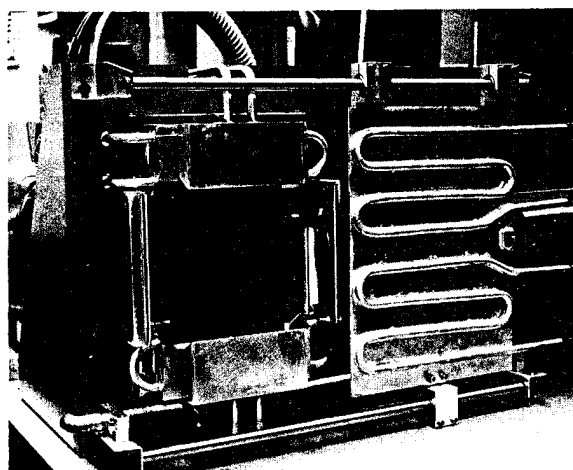


Figure 7. Test equipment for simulating a thermal pulse. Uniform heat flux is  $440 \text{ Btu}/(\text{ft}^2\text{-sec})$  over a test area of  $10 \text{ sq in.}$

## ROCK DEBRIS EXPERIMENTS

Rock debris, which can rain down on radar targets in the vicinity of a nuclear explosion, can significantly influence the design of hardened radar structures. The quantity of rock debris, at a site located in sandstone or granite, is judged to be considerable when it is noted that a 20-MT surface burst in dry soil can produce a crater some 3000 ft in diameter and 300 ft deep (Ref. 1). Recent debris tests in granite have provided valuable information with regard to size, velocity, and radial distribution away from the crater (Ref. 10). Some impact studies have been performed, during the past few years, on antenna element ceramic windows. In addition to antenna element window behavior in a debris environment, one is concerned with permanent deformation as well as penetration of a given structure. Experimental studies are presently being conducted to determine impact behavior of sandstone and granite on simply supported beams. These studies, upon completion, will provide the basic research necessary to develop design criteria. The criteria will provide a means of predicting level of damage imposed on structures subjected to rock debris. The equipment setup illustrated in figure 8 shows a 0.25-in. x 1.0-in. x 18.0-in. aluminum beam supported with thin stainless steel column supports. These supports minimize moment constraint at the boundaries and approximate ideal simple supports (Ref. 11). Strain gages mounted on the back surface of the beam are connected to an oscilloscope and oscillograph for strain data recording. High-speed films are taken using a 16-mm Fastax camera, to study the phenomenological behavior during impact of sandstone and granite with aluminum beams. The camera speed is regulated with a control unit, when operating at speeds above 4000 frames per second (Ref. 12). The control unit regulates voltage to the camera motors and contains timers which independently start the camera and trigger the event. This device allows the film to achieve maximum speed before triggering the air gun. Figure 9 shows three frames, beginning with the start of the impact process, of a sandstone projectile traveling at 112 ft per second. The time duration between frames is 0.174 ms. The second and third frames clearly show the approach between the projectile and beam during sandstone fracturing at the point

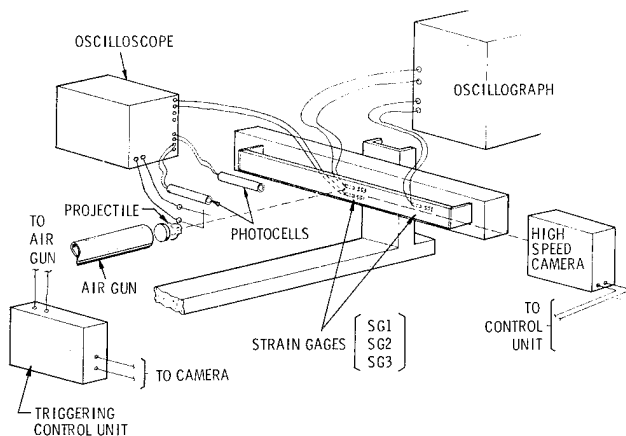


Figure 8. Laboratory equipment used to investigate impact of rock debris on a simply supported aluminum beam.

of contact. These films also provide information on time duration of contact and dynamic deflection at the center of the beam. At a film speed of 5760 frames per second, it is possible to plot 84 data points for one oscillation of the beam at its fundamental frequency. With this many points, good definition of the third mode contribution to the total displacement can be obtained.

Figure 10 shows the indentation in a 6061-T4 aluminum contact plate caused by a 0.036-lb sandstone projectile having an initial velocity of 92 ft per second. The indentation is 0.010 in. deep and has a 0.18-in. average diameter. A conical-shaped mound of sandstone 0.28 in. in diameter and 0.10 in. high remains imbedded in the aluminum. The photomicrograph (figure 10) of the specimen cross-section shows the indentation as having nearly constant curvature. The local

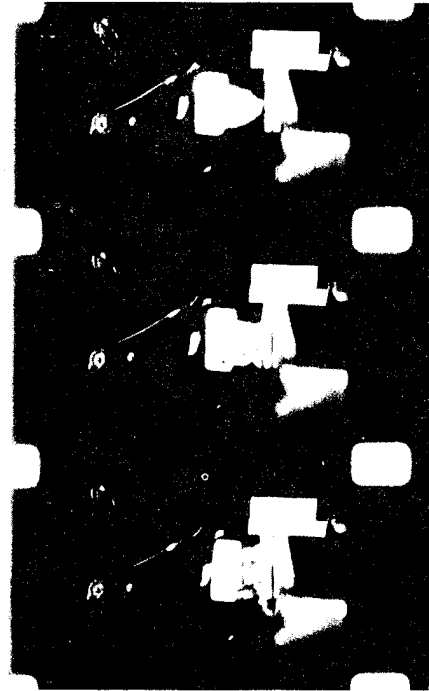


Figure 9. Sandstone projectile impacting an aluminum beam. Projectile velocity = 112 ft per second; film speed = 5760 frames per second.

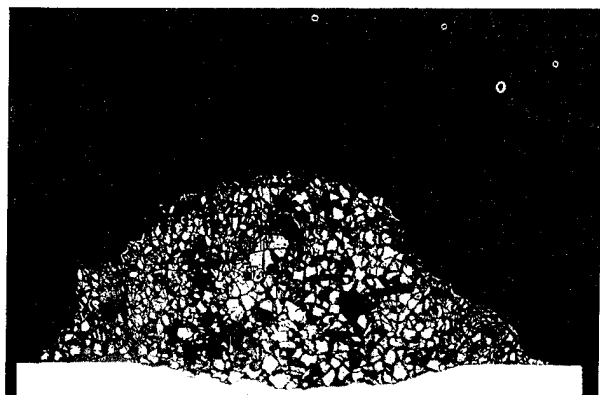


Figure 10. Indentation in an aluminum beam, following impact with a sandstone projectile traveling at 92 ft per second.

variations along the indentation profile are due to deeper penetration of the hard silica grains within the sandstone. At the bottom of each local valley along the profile silica grains can be observed.

#### REFERENCES

1. The Effects of Nuclear Weapons, U.S. Dept. of Defense and U.S. Atomic Energy Commission, U.S. Government Printing Office, Washington, D.C., 1964.
2. Biggs, J. M., Introduction to Structural Dynamics, McGraw-Hill, New York, 1964.
3. Newmark, N. M., et al., Air Force Design Manual - Principles and Practices for Design of Hardened Structures, Report No. AFSWC-TDR-62-138, 1962.
4. Design of Structures to Resist Nuclear Weapon Effects, ASCE Manual No. 42, 1964.
5. Norris, C. H., Hansen, R. J., Holley, M. J., Biggs, J. M., Namyet, S., and Minami, J. K., Structural Design for Dynamic Loads, McGraw-Hill, New York, 1959.
6. Levy, S., Wilkinson, J. P. D., The Component Element Method in Dynamics, McGraw-Hill, New York, 1976, pp. 136-151.
7. Wilson, E. L., SOLID SAP - A Static Analysis Program for Three Dimensional Solid Structures, University of California, Berkeley, Report No. UC SESM71-19, 1971.
8. Hillendahl, R. W., Characteristics of Thermal Radiation from Nuclear Detonations, U.S. Navy Radiation Laboratory Report, USNRDL-TR-383, 1959.
9. Johns, D. J., Thermal Stress Analyses, Pergamon Press, London, 1965, pp. 29-31.
10. Stroberger, D.E., Mineral Rock Ejecta Study, The Boeing Company, Defense Nuclear Agency Report No. 2743P, 1971.
11. Goldsmith, W., Cunningham, D. M., "An Experimental Investigation of the Oblique Impact of Spheres Upon Simply Supported Steel Beams", S.E.S.A. Proceedings, Volume XIV, No. 1, 1955, pp. 171-179.
12. Hyzer, W. G., Engineering and Scientific High Speed Photography, The MacMillan Co., New York, 1962.



# LOW-COST APPROACH TO LARGE SURVEILLANCE ANTENNA PEDESTAL

EDWARD C. HAWKINS

The Bendix Corporation  
Communications Division  
E. Joppa Road, Baltimore, Maryland 21204

## ABSTRACT

A low-cost surveillance radar pedestal, designed for low quantity production, is described. The design maximizes the use of standard commercial components and eliminates special tooling. The unit's adaptability to various drive units, rotary couplers, position data encoders and tower mountings is discussed. Also included in the design is the possibility of incorporating or retrofitting dual drives for additional power and/or low backlash applications. The selection of such features as adjustable gearing backlash, three-point tower mounting, drive-unit slipclutch, leveling shims instead of built-in jacks, turn-of-the-wrench bolt tensioning, and the use of weldments and parallel plane machining is discussed.

## INTRODUCTION

A heavy duty search radar rotator was designed for minimum life-cycle costs using commercially available industrial components and a unique combination of cost-saving design ideas. The resulting pedestal, capable of rotating search radar antennas approximately 10 by 15 meters (30 by 50 feet), with or without a radome, can be fabricated at a competitive piece part price even in quantities of one and two. No special tooling is required. The design and fabrication of one pedestal was found to be less expensive than the building of a pedestal to either of two existing designs created in the 1950's, and the new design has the capability of higher loadings. Alternate features such as dual drive capability, variable rotation rates, low backlash via biased drive torque, and acceptance of various sizes and shapes of RF rotary joints and angle data transducers are available low cost modifications. Features of this pedestal are applicable to almost any antenna rotator. Figure 1 shows the pedestal including antenna mounting/elevation tilting assembly on an assembly test and shipping stand. Figures 2 and 3 indicate the general pedestal arrangement.

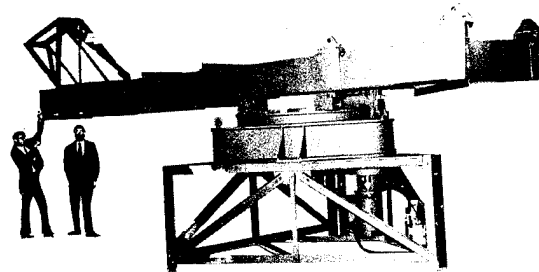


Figure 1. Pedestal on Test Fixture

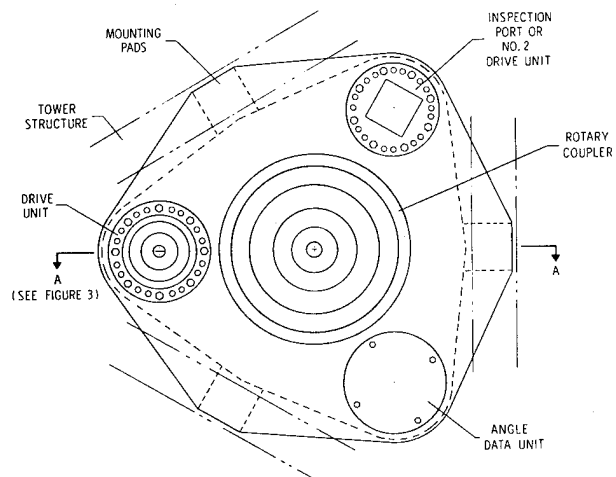


Figure 2. Bottom View of Pedestal

## BEARING/BULL GEAR

This single bearing pedestal design was based upon a commercially available bearing with integral gear teeth that meet the design loads and life requirements. Large diameter bearings of this type with gear teeth cut on one of the races are currently available from at least three manufacturers in the United States as well

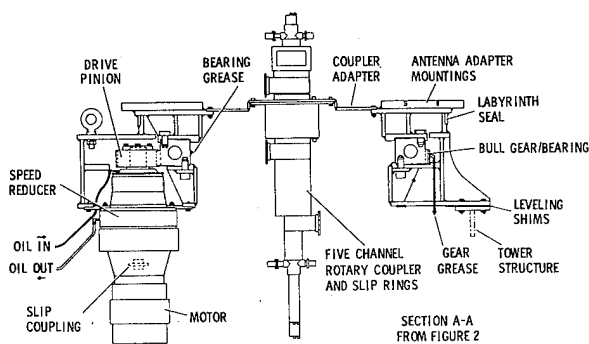


Figure 3. Section AA from Figure 2

as foreign sources. They are usually made-to-order from standard stocked forged rings on approximately three months delivery schedule. This type of bearing has been extensively used in radar pedestals and is currently being used in numerous industrial applications such as turntables, mining and tunnel boring machines, cranes, and machine tools. The bearings are either of the four point contact ball or of the crossed "X" roller type. Bendix Communications Division radar pedestal experience indicates that with proper usage either type will prove equally satisfactory. The particular bearing chosen is in use in a crane application, and spare units are available for direct purchase. This bearing has fifty-one 3-inch diameter balls on a pitch diameter of 53.25 inches. A two diametrical pitch, 122 tooth, 61 inch pitch diameter spur gear is cut on the outer race. The mounting bore is 46.625 inches and the thickness is 6 inches. The bearing is attached directly to the housing via 1-3/8 diameter, 6-thread per inch holes tapped into the races. Figure 4 is an illustration of the bearing.

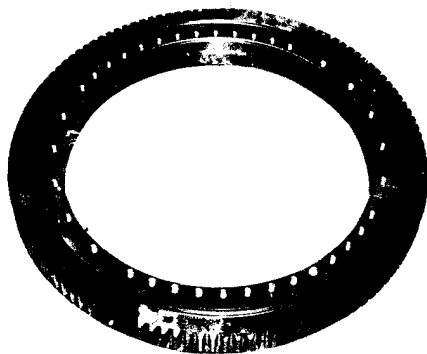


Figure 4. Bearing/Bull Gear

## STRUCTURE

The structure holding the bearing/bull gear and forming the pedestal housing consists of two low carbon steel weldments (approximately 2,500 and 4,000 pounds) fabricated by flame cutting and arc welding. All parts are cut from flat plate. Round sections are press formable as sectors of rings and butt welded at assembly. After welding, the assemblies are vibration stress relieved. The smaller rotating weldment bolts directly to the outer bearing race and bull gear to form the turntable. The other weldment supports the inner fixed bearing race and mounts to the tower structure. It also provides mounting for the drive and angle data units. The design is such that the machining of the weldments is in parallel planes performed primarily on a vertical boring mill. The drive and angle data mounting holes, located off the bore axis to the relatively large tolerance of  $\pm 0.06$  inch, were easily bored on a horizontal mill. This large tolerance is accommodated by the use of eccentric mounting adapters that permit gear backlash adjustment.

All gearing is housed between the two structural weldments. For weather-proofing, the upper outside diameter of the fixed base weldment contains a series of parallel grooves that are overlapped by a collar on the rotating weldment to form a labyrinth seal. This seal, readily machined directly on the weldments, eliminates the need for the usual special separate large diameter contact seal with its lubrication problem. Figure 5 shows the top weldment being lowered into the base weldment. The outer collar of the top weldment will overlap the grooved section of the base. The bolt heads, shown in Figure 5, attached the bearing race directly to the turntable. The bearing is located by pilot diameters in the weldments.

The base weldment includes three mounting feet for direct attachment to the tower. Experience indicates that more than three mounting points should be avoided. Bearing failures are directly traceable to improper race support. If more than three mounting points are used, field leveling and/or tower settling will invariably warp the pedestal, thereby placing unexpected loads on the bearing. This is particularly true of large diameter relatively small cross-section bearings that depend upon the mounting for race rigidity. The three mounting feet can be adapted, via deck beams or trusses, to any tower arrangement, from three-legged to cylindrical.

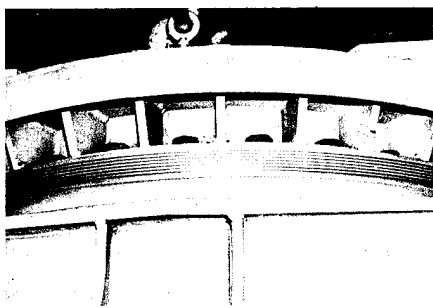


Figure 5. Labyrinth in Process of Assembly

#### DRIVE SYSTEM

The bull gear, previously described, accompanying the bearing is driven by an 18 tooth pinion mounted directly on the output shaft of a commercial speed reduction unit. The speed reduction unit has a ratio of 43:1. This combined with the bull gear to pinion ratio of 122:18 gives an antenna speed of 6 RPM with a 1750 RPM drive motor. Numerous commercial speed reduction units are readily available in sizes and ratios to meet any conceivable radar requirement. The reduction unit is of the flange mounted type, 20 HP, AGMA Class III rated. This unit is installed in the bottom of the pedestal assembly output shaft up on an eccetric adapter flange between the pedestal base and its mounting flange. The backlash between the bull gear and pinion is adjustable by rotating the speed reduction unit on its eccentric mounting. Access ports, closed with pipe plugs, in the pedestal top allow backlash and gear alignment to be measured throughout the mesh.

Although well within the published overhung allowable load for the speed reducer, the effect of deflection of the cantilevered pinion mounting on gear face alignment was of concern during the design. Tests on the unit indicated that the reducer shaft and bearing deflection were of negligible effect. However, increased stiffening of the adaptor plate between reducer and pedestal housing was required. Paper passed through the gear mesh under test loads, as well as the tooth-marking pattern, indicated approximately equal loading across the face. If the machining of the housing and/or reducer mounting flange is not perpendicular to the gear face, the resulting misalignment would cause unequal tooth loading. A pair of matching tapered washers under the reducer mounting flange was considered for a correction to this condition, but probably due to the parallel plane machining of the pedestal and reducer housing, the use of these washers was unnecessary. These shims, if used, could also be set for best alignment under full load conditions.

Rather than using a speed reducer with an integral mounted drive motor, an independent drive motor was used. This allows a slip-type coupling to be used between motor and load. The slip clutch in the coupling prevents overloading of the pedestal mechanism with across-the-line motor starting. In numerous systems, the start-up condition has been an overlooked source of antenna drive mechanism problems. On startup, most motors produce torque in multiples of the maximum rated running torque. Since the antenna and mechanism inertia seen by the motor as the square root of the ratio is several times in excess of the motor rotor inertia, most of the motor torque is transmitted to the pedestal mechanism accelerating the load. (Torque = polar mass moment of inertia times the acceleration.) The clutch in the coupling is set to slip at about 125 percent of the maximum design torque required to rotate the antenna in maximum wind. By slipping the clutch, the motor uses its excess torque to obtain full speed a little ahead of the antenna without overloading the mechanism. This is particularly useful during periods of system testing where the antenna is started and stopped numerous times and often jogged to position. In other systems, motor current limiting devices combined with shear pins were used to protect the gearing. An abundance of shear pins were required during testing. The torque limiting coupling used is a standard catalog item.

The drive motor is a standard 20 HP NEMA flange-mounted four-pole induction motor. The flange mounting assures proper alignment of the coupling. An adaptor for motor mounting is a standard part of the speed reducer. The speed reducer, motor adaptor, clutch side of the slip coupling and the motor are shown in Figure 6. Figure 6 shows the motor being mounted to the speed reducer with the aid of two "comealongs" and a special support cradle. The "comealongs" are used for approximate positioning, and the jack screws at the bottom of the motor give final positioning. A bearing in the plate over the jack screws allows rotating the motor housing. The speed reducer was previously installed in the pedestal base using a similar rig of mostly the same components. This is shown in Figure 7. After the reducer was positioned on the four long studs shown extending from the pedestal base, the rig was removed and the reducer was raised to the final position by nuts on the studs. Upon adding other mounting bolts, the studs were replaced by the remaining mounting bolts. To adjust for backlash between the pinion and bull gear, the reducer is supported by the rig without the antiupset blocks on the eccentric mounting flange bolted to the reducer.

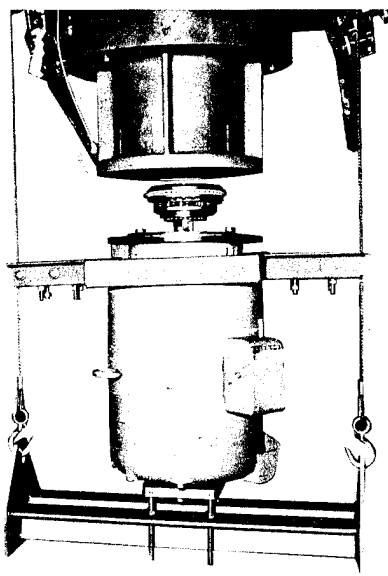


Figure 6. Motor Mounting

Refer to Figure 7. The mounting bolts are then removed and the reducer with mounting flange is rotated about the housing pilot to the set of holes giving the desired backlash, steps of approximately 0.002-inch backlash change are available.

The antenna can be hand positioned by turning the slip clutch coupling. The total reduction being well over 50 percent efficient easily allows the wind to drive the antenna to its minimum torque condition. This prevents gear overloading in survival winds which are above the desired maximum operating wind loads. Standard brakes are available for attachment to a

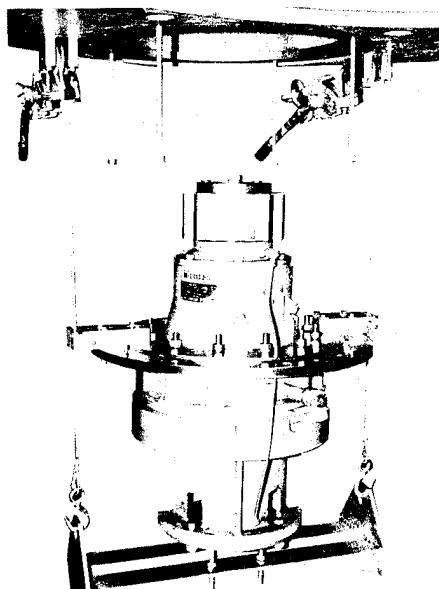


Figure 7. Speed Reducer Mounting

double shaft extension drive motor if desired. The brake, if used, should be released in high wind conditions. A brake is only useful for testing and possibly during antenna maintenance. Since this is used only during a very small percentage of the time, the cost of a brake was not considered effective. The pedestal can be braked in winds that allow testing by holding the clutch coupling or blocking the turntable.

Numerous speed reducer and motor combinations can be selected for almost any pedestal speed and torque combination of future applications. An extra speed reducer mounting pilot is provided in the pedestal housing. This provides an extra port for ease of pedestal assembly and bull gear access, as well as providing for the use of two drive units if ever desired. Two drive units can be used for additional reliability, more power from the same gearing, or torque biasing to remove backlash as various possible applications may dictate.

In this application angle position data is taken from an encoder rotating 1:1 with the antenna. Because of the relative large diameter of the bull gear and the direct connection of this gear to the turntable, the gearing precision was such that data could be taken from part of the face of the bull gear. A spring-loaded gear set shown in Figure 8 drives the encoder. This angle data unit mounts directly into a pilot bore in the base housing. Similar to the drive unit mounting, the mounting bore of the angle data unit is eccentric to its gearing. Thus, rotation of the unit in its housing is used to set the desired fixed backlash with the bull gear. After setting the desired backlash, a pin locking the spring loaded halves of the split pinion is removed. It is possible for a more precise angle data application to mount an encoder to the turntable through a specially built constant velocity universal joint and gearing that would surround the rotary joint. Also, the angle data pilot bore in the pedestal housing is so sized that it will allow the mounting and driving of almost any set of angle transducers.

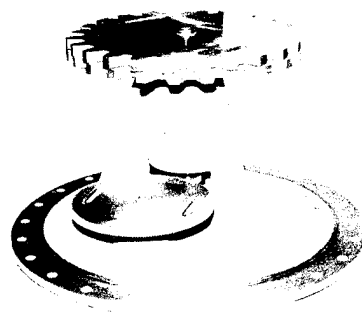


Figure 8. Angle Data Drive

The rotary joint that transfers all electrical data through the pedestal is mounted on the antenna rotation axis in a pilot in the rotating housing. Since the pilot is bored at the same setup as the bearing pilot, runout is low. Flexible waveguide and cables to this joint minimize loading of rotary joint bearings. The 36-inch bore in the pedestal allows various types of rotary joints to be attached with different adaptor plates. This arrangement also allows installing or changing rotary joints from under the pedestal without disturbing the antenna. Figure 9 shows the rotary joint in place.

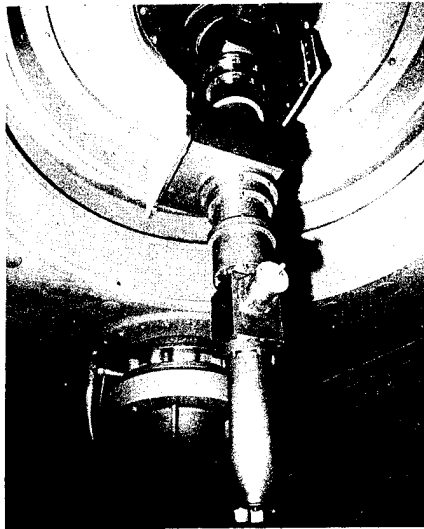


Figure 9. Rotary Joint Mounting

#### LUBRICATION

The lubrication system, using both grease and oil, is serviceable from under the pedestal with the antenna in operation.

Grease fittings on the inner fixed bearing race accept a standard grease gun. These fittings and integral neoprene seals are part of the standard bearing. The bearing seals retain the lubricant and exclude dust and other foreign matter that may be inside the pedestal housing. The housing provides the weather seal. The bull gear mesh is also lubricated by grease through fittings in the bottom of the pedestal base. A 1/8-inch pipe leads from the fittings to the gear face. The bearings and fine gearing in the angle data unit are permanently grease lubricated. The relatively low surface speed of all components grease lubricated was considered well within the capability of commercial greases. Special low temperature greases are required for cold climates, or the bottom portion of the

pedestal below the tower deck can be housed as per the application seen in Figure 10. In this case the tower provides a pedestal maintenance shelter.

Usually with commercial speed reducers of this type, the mechanism is totally enclosed and partially filled with oil. While most reducers are designed for horizontal or vertical mounting, the vertical applications are almost always with the low-speed shaft in the down position. Therefore, in the up-mounted low speed output shaft position, the standard units did not provide adequate lubrication for the bearings on the output shaft. Rather than fabricating a special unit, lubrication of the upper bearing was provided by a standard off-the-shelf industrial type lubrication pump. Since the low-speed bearings could operate for several days without added lubrication, a low-oil-pressure warning system and a spare auxiliary pump were considered adequate from a system reliability standpoint. The pump is replaceable with the antenna in operation.

The drive motor ball bearings are grease lubricated for a life expectancy of 50,000 hours without service. The particular off-the-shelf motor used has pipe plugs for possible grease flushing.

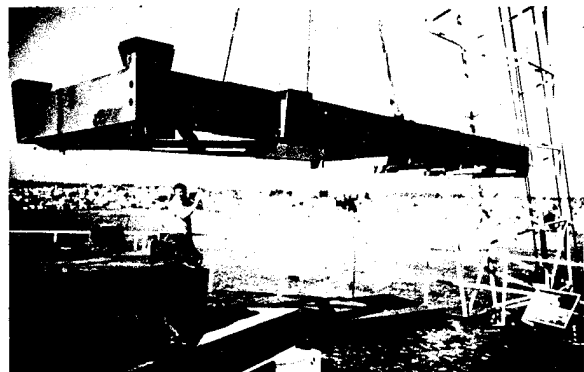


Figure 10. Field Assembly

#### LEVELING

Since permanent leveling jacks for an antenna pedestal must be moment carrying and capable of position changing, they become complex and expensive mechanisms for a seldom used application. In a fixed tower installation they may only be used two or three times over a 10-year period. Usually the last use is hampered by dirt and corrosion. The need for releveling is a rare occurrence. By the use of an assortment of various thickness shims and a portable standard hydraulic jack, this pedestal can be leveled within 1 minute of arc in 1/2 hour. Except for loosening and tightening the nuts on the mounting bolts

located beneath the tower deck, an operation also required if permanent jacks were used, only one technician is required. The holes in the shims for the mounting bolts are slotted to the edge so that it is only necessary to loosen the mounting bolts when adding or subtracting shims.

#### ANTENNA TO PEDESTAL MOUNT AND ELEVATION TILT MECHANISM

The antenna reflector and feed assembly are positioned and mounted to the pedestal by a beam structure commonly called a boom. A high-alloy steel-welded bent-up sheet structure previously designed for this application and used in a great number of systems was of inadequate strength for the wind loading of this application. This member was replaced by a weldment of structural steel channels, angles and plates, heavier and perhaps not as eye appealing, but 50 percent stronger and half of the cost. Again machining was limited to parallel planes. Pads approximately 6 by 12 inches, four on the top and four on the bottom, were milled flat after welding. Pillow block like double shear pin arrangements attached the boom to the pedestal and the reflector to the boom at these pads. The feed was positioned through slotted holes, shims, and threaded support rods. Therefore, the feed required no machining of the boom or the welded structural angle feed support. The boom is shown in Figures 1 and 10.

Adjustment in antenna elevation angle between -2 and +5 degrees is accomplished in steps of 1/4 degree by changing shims between the pedestal and boom at the back pair of pins. The front pair of pins acts as the hinge line. All shims are a permanent part of the assembly and for different settings only change their location along the clamping bolts. These shims eliminate the cost of a heavy duty permanent elevation jack capable of carrying the survival wind loads. They also lighten the boom and pedestal structure by spreading the load. Like the pedestal leveling jacks previously discussed, a permanent elevation jack would seldom be used. Elevation angle change with shims is a short and easy procedure and may be accomplished in winds up to 25 knots. A relatively small turnbuckle-type commercial screw jack is temporarily used to move and hold the reflector during elevation angle changes. Figure 11 shows this jack as well as the tilt hinge pins and shim arrangement. A mechanical jack was chosen in place of a hydraulic jack for personnel safety. It will carry tension and is not accidentally operable.

#### FASTENERS

All components of the pedestal were assembled with high-strength bolts acting

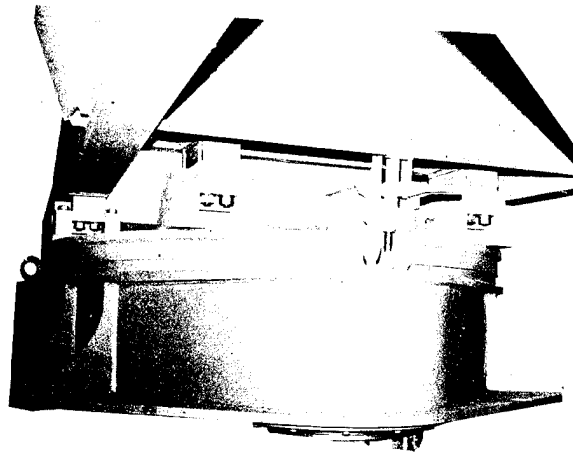


Figure 11. Elevation Angle Mechanism

both in tension and shear. Except for the 1-3/8 inch diameter internal wrenching (Allen) bolts used because of wrench clearances between the base housing and the bearing race, all structural fasteners were ASTM A 490 bolts. Past practice was to depend on bolts for tension only. Shear was assigned to dowel pins driven into reamed holes after assembly. To eliminate pinning, the bolts were assigned to shear by friction. Friction type connections were designed, as recommended by the American Society of Steel Construction, by tensioning the bolts to a minimum of 70 percent of the minimum specified tensile strength of the bolts. Hardened steel flat washers were used under the nuts and bolt heads. With this bolt preload, locking devices were considered unnecessary. For the same reason, most automotive engines no longer use locking devices. Bolt tensioning was obtained by turn-of-the-nut tightening. That is, all bolts were pulled snug tight by one man on a standard wrench. Then, bolts having lengths of less than eight diameters were turned an additional one-half turn and the longer bolts two-thirds of a turn. This preload requires an extension on the wrench.

#### CONCLUSION

A pedestal fabricated as discussed and pictured has been in operation for over two years, and a minimum life of 10 years before overhaul is expected. Cost savings were primarily accumulated by the use of commercially available bearing/bull gear, speed reducer, motor and slip coupling, steel weldments, parallel plane machining, gear backlash adjustment, friction type joints, a labyrinth seal, and shimming instead of permanent leveling and elevation adjustment jacks. Access to all components from the underside of the pedestal provides for easy maintenance with the antenna in operation.

# THERMAL DESIGN OF AIRBORNE RADARS - PRESENT AND FUTURE

F.E. Altoz

Westinghouse Defense and Electronics Systems Center  
Baltimore, Maryland

## Abstract

The significant factors relating to the thermal design of radar equipment is presented along with an identification of potential areas for improvement. The cooling techniques described emphasize the microcircuit packaging area, one which impacts the greatest on radar system reliability. The paper also examines emerging developments most likely to influence the future thermal design of radars.

## Introduction

A new threshold has been reached in the design and production of airborne radar systems. The quality level of soon to be delivered systems must equal or surpass guarantees with respect to MTBF (mean time between failures) and RIW (reliability improvement warranties), both of which entail unknown risks. The thermal factors affecting this risk and the means to reduce them form the subject of this paper. In addition, other subjects treated include the future trends in radar thermal design, particularly with respect to improvements in reliability and hardware.

## Thermal Design - An Overview

Radar reliability is "designed-into" present equipment through implementation of a thermal management plan consisting of these elements.

- Cold plate cooling with complete separation of component and coolant.
- A realistic thermal "derating" plan for components.
- "Thermal placement" of components for optimum location.
- Coolant apportionment to units as a function of reliability sensitivity.
- A validation of thermal interfaces and careful processing of these to ensure accurate and predictable temperature gradients.
- Component "burn-in" and screening procedures.
- Factory environmental in-line testing.

Many of these factors represent a high level of sophistication in thermal analysis techniques which leads to system reliability predictions based on assumed operating missions. Efforts to better define these missions has only recently appeared in radar specifications. These attempts classify missions as composite or extreme types corresponding to expected training and combat missions - frequency of occurrence, flight profiles, etc. The composite mission profile typifies an average flight based on statistical probabilities of average service life and climates encountered. The critical design environment represents corners in the flight envelope both at high and low temperature extremes, and the thermal design then is based on these sets of operating conditions. The process of collecting realistic flight data for establishing these guidelines requires a rather complex system. At one extreme, this is conceivably a black box monitoring key thermal parameters, and at the

other extreme, it is a simple collection of data from selected flights purporting to be typical missions. The more exacting the collection process the more accurate will be the end result. In any event, there is no doubt that more emphasis in this area is needed to improve the assumptions used in the thermal design.

## Reliability

The thermal design begins at the specification level where system flow, pressure drop, and inlet temperature of the coolant is defined to the radar. Figure 1 presents typical flow delivery curves of an aircraft environmental control system (ECS) based on two radar exit air temperatures, 60 and 71°C. The normal delivery air temperature for present ECS ranges from -20 to 30°C and the temperature extremes presently specified correspond to -54 and 49°C ground operation.

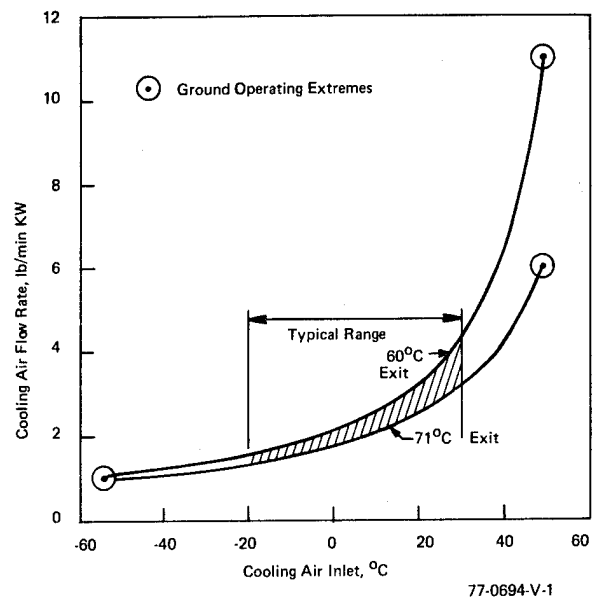


Figure 1. Cooling Air Flow vs Inlet Temperature for 60 and 71°C Exit Air

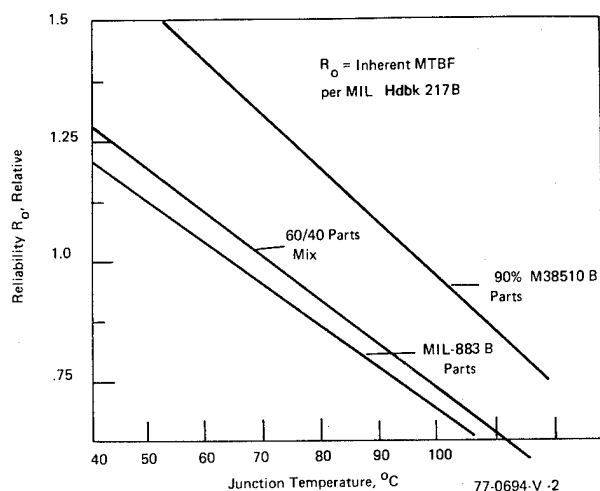
Under these conditions, the cooling air is apportioned to each radar LRA (line replaceable assembly) on the basis of its reliability sensitivity. Those LRA's having a high parts count of temperature-sensitive integrated circuits (IC's) for example, qualify for a higher percentage of total flow which, in turn, lowers their exit temperature, hence average component junction temperature. The overall sensitivity of a typical radar on an LRA basis appears in table 1. For this system consisting of five air cooled assemblies, two units, the digital processor and the low power RF, account for 63 percent of the total system reliability. The processor and computer together account for over 50 percent of system

MTBF. These latter units include a high parts count of IC's which contribute heavily to reliability.

**TABLE 1**  
**RELIABILITY CONTRIBUTION OF LRA'S IN A**  
**TYPICAL AIRBORNE RADAR**

	Percent
Digital Signal Processor	37
Computer	17
Low Power RF	26
Transmitter	13
Antenna	7
	<hr/> 100

It is instructive to note that the quality of an IC package strongly influences the reliability predictions. This is illustrated in figure 2 where  $R_O$ , inherent mean time between failures (MTBF), appears as a function of junction temperature for three types of component mix. There



**Figure 2. Radar MTBF As a Function of Cooling and Mixes of Quality of Parts**

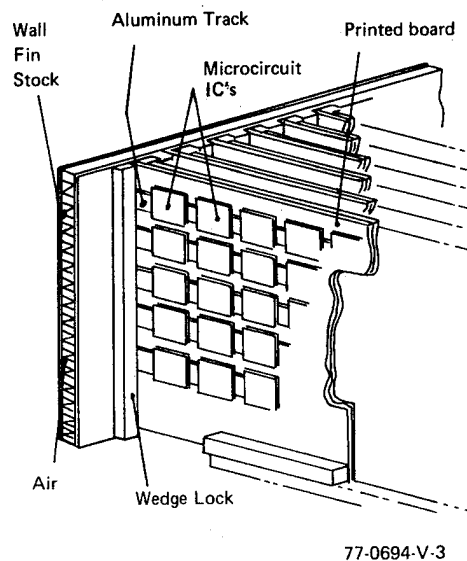
are two main conclusions to be drawn from these curves: (1) higher quality parts (M38510B type) produce significant improvements in MTBF at 50 to 70°C junction temperatures, roughly 40 percent, and (2) for a specific quality part each 10°C change in junction temperature results in only 5 to 12 percent variation in MTBF, a less significant contribution than the parts quality. These data relative to selection of an IC mix for the radar are weighed against cost and delivery. In addition, to increase  $R_O$  in figure 2, flow apportionment is utilized which allocates proportionately more air to the IC units to reduce their absolute junction temperatures.

The next area to be examined is the cooling technique relative to the IC printed board assemblies.

#### Cooling Techniques - Microcircuits

In the design of LRA's, it is essential to minimize the heat path from junction to sink in order to lower junction temperatures. For the high parts count LRA's, there are two basic cooling techniques presently in production on printed wiring assemblies (PWA's): coplanar (C-P) and in-line-conduction (ILC). The in-line-conduction method as defined consists of an aluminum or copper track or runner located beneath the component which serves to conduct heat to a wall surface at one or both ends of the board assembly. The heat from each IC package is

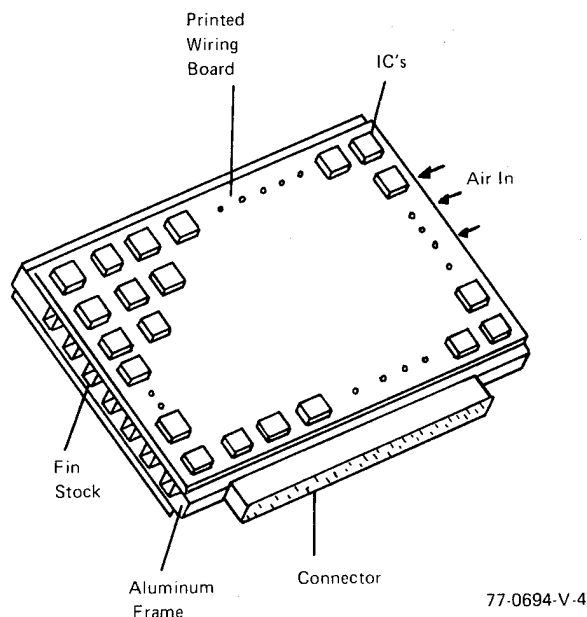
conducted down these tracks into cold plate walls as shown in figure 3. Two contact interfaces impede this flow of heat, one is at the IC level



**Figure 3. In-Line Conduction Single-Sided Printed Wiring Board**

and the other at the wall heat exchanger. The air to fin gradient is still another impedance and it depends on available system pressure drop, the higher the drop the less thermal impedance. This pressure is important because of strict limitations on the aircraft supply, particularly at ground level.

In the coplanar technique, a fin type heat exchanger is sandwiched between two boards as shown in figure 4 and the pressure drop is less critical because all assemblies are in parallel and require less flow per



**Figure 4. Coplanar Flat Pack Dual Board Assembly**

unit area compared to the wall exchanger in the ILC method. The result is lower junction temperatures for the same flow and available pressure. This is apparent from an examination of equations (1) and (2)



which express the contribution to average junction temperatures of various impedances for the two systems.

$$\text{ILC} \quad \bar{T}_j = T_i + \frac{131.6}{\dot{M}} \left( \frac{X}{L} \right)_w + \bar{P}_d (\theta_{jc} + R_c + R_{al} + R_w + R_{hxw}) \quad (1)$$

$$\text{CP} \quad \bar{T}_j = T_i + \frac{131.6}{\dot{M}} \left( \frac{X}{L} \right)_b + \bar{P}_d (\theta_{jc} + R_c + R_b + R_{hx_b}) \quad (2)$$

where:

- $\bar{T}_j$  = average junction temperature, °C
- $T_i$  = air inlet, °C
- $\dot{M}$  = air flow, lb/min kW
- $X$  = effective location of air inlet for reliability predictions;
- $L$  = 0.5 for ILC, 0.66 for C-P
- $\theta_{jc}$  = case to junction impedance, °C/W
- $\bar{P}_d$  = average component dissipation, watts
- $R_{al}$  = aluminum or copper track impedance, °C/W
- $R_w$  = wall interface impedance, °C/W
- $R_c$  = component case to mounting surface impedance, °C/W
- $R_b$  = impedance through board, °C/W
- $R_{hx}$  = heat exchanger impedance, °C/W

and subscripts

- w = wall
- b = printed board assembly

Both equations are plotted in figure 5 for flat pack and dual-in-line packages; the increase in impedance for the ILC technique attributed to the aluminum track, the wall interface, and a slightly higher exchanger impedance results in higher average junction temperatures. Clearly, the

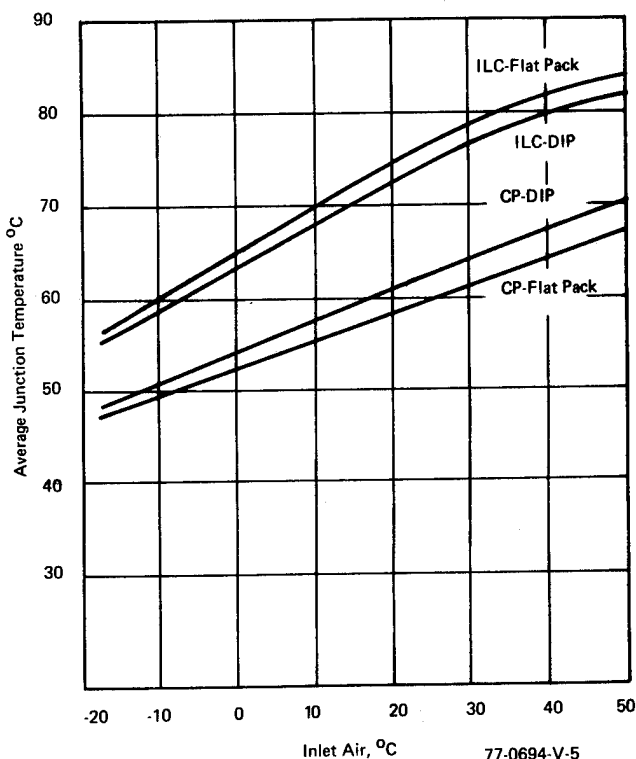


Figure 5. Average Junction Temperature for the Coplanar (C-P) and In-Line-Conduction (ILC) Technique at 60°C Outlet Air Temperatures

coplanar method of cooling is shown to advantage in figure 5; for example at an inlet air temperature of -20°C, the improvement with

coplanar is 8°C, and at 30°C inlet air it is 15°C. It is to be noted, however, that since flat pack components are more applicable to the coplanar technique and dual-in-lines are more compatible to the in-line conduction method, the final selection process must include consideration of weight, component cost, volume, and of course, reliability.

Having chosen the cooling system, the thermal design of the printed boards becomes one of component placement for optimization of temperature and wiring interconnections. Advanced technology to date involves the thermal placement of components by computerization which effectively lowers the average junction of an assembly. This procedure provides temperature data for each component so that hot spots are noted early in the design stage. This technique takes account of component dissipation and conducts a trade between the conflicting requirements of optimum conductor routing within the multilayer board versus temperature. By placing a limit on the number of board layers, the result leads to a board design having a best conductor routing and lowest junction temperature. The predicted temperatures and their derated values under hot extreme operating conditions are compared on a component to component basis and the established criterion for derating junctions; 60 percent of the maximum manufacturer's rating is then applied. This process represents one of the major means of "designing-in" radar reliability. Validation of the predicted temperature takes place during thermal tests on the initial preproduction units.

### Transmitters and Antennas

These represent a lesser impact on reliability than previously described densely packaged LRA's. Traditionally, transmitters have been liquid-cooled because of the high voltage dielectric requirements. More recently, however, the use of sulphur hexafluoride (SF<sub>6</sub>) gas in high voltage enclosures together with ceramic high voltage heat conductors, BeO<sub>2</sub> and Al<sub>2</sub>O<sub>3</sub> provides an additional choice in the trade study process. In addition, higher power air-cooled TWT tubes for the transmitter are available making possible a completely air-cooled radar. Conversely, an entirely liquid-cooled transmitter with flow-through dielectric coolant is also being used in production systems where both air and liquid coolant are available on the aircraft. Both designs are acceptable from a thermal standpoint; the determining parameters in their choice of cooling are weight, volume, cost, and aircraft coolant availability.

Antenna LRA's located in the aircraft nose are mostly ambient cooled. These components include electric drive motors for azimuth and elevation and microwave components mounted on the antenna array structure. The servodrive modules and associated power supplies are cold plate air cooled or, in some cases, are thermally coupled to the antenna pedestal for heat distribution and dissipation to the ambient. Thermal analysis for ambient-cooled components extends from sea level to 60K feet altitude with temperatures varying in accordance with Class 2 requirements of MIL-E-5400.

### Emerging Trends

The factors related to improvements in radar thermal design to be considered in future designs include:

- Mission definition and coolant apportionment
- Circuit design for low heat dissipation
- Advanced ECS
- Thermal hardware.

### Mission Definition and Cooling Apportionment

The structure of thermal management is based on a set of mission requirements specified early in the design stage which represent the best known ground and in-flight conditions. The time use or duty cycle of the radar on a power basis, however, is not considered in design except for warmup and cooldown. It is estimated that approximately 50 percent of the radar heat load is mode dependent, hence, mission dependent. Therefore, the possibility of optimization of cooling air or liquid flow can be accomplished on the basis of more exacting equipment usage. Conceivably, an optimized system of this type will include air

flow monitoring of each LRA with automatic flow adjustments commensurate with dissipation.

Apportionment of coolant is presently made on the basis of the LRU failure rate; i.e., the more sensitive units receive a greater flow of coolant to lower the average component temperature within the LRA. It is anticipated that the incorporation of contract warranties will stimulate better failure data reporting, hence, better apportionment of coolant to the LRA's.

#### **Circuit Design for Low Heat Dissipation**

A promising development in this area is the advanced processor or computer-on-a-chip containing extensive computational capability in a small volume. Some are already in use as programmable processors in place of fixed wire program computers and these offer tremendous savings in volume and power. However, in the area of standard circuit design, there has been virtually no concerted effort to reduce dissipation even though the impact on total system life cycle cost and reliability may be significant. In still another area, power supply improved circuit efficiency translates into direct reductions in dissipation, hence coolant requirements; for example, a 10 percent increase in inverter efficiency from 70 to 80 percent results in 10 percent less system dissipation.

#### **Advanced Aircraft ECS**

Lower ECS delivery temperatures produce improved reliability (reference figure 2) and this is reflected in recent radar specifications which nominally establish air inlet temperatures of 0 to 30°C. Any lower temperatures produce icing conditions which are to be avoided in the ECS. Advanced technology in this area is directed toward air cycle machines as a potential replacement for turbine compressors operating

off bleed air. Since machines of this type operate best in closed cycle loops, the impact on present systems is significant in terms of packaging design. The other consideration more favorable is that since these machines are hydraulic or electric motor driven, there is potential for improved ground cooling of the radar.

#### **Thermal Hardware**

Future radar mechanical design will most likely include extensive use of heat pipes. Their application has been limited to date, but one promising area being explored is the printed circuit board. For in-line-conduction systems, there is a potential reduction of 10°C in junction temperature awaiting the introduction of a cost effective heat pipe. Serious consideration is also being given to TWT heat pipe design, and, in fact, limited applications have already appeared.

Relative to flow control, the emerging radars may conceivably include coolant monitors in each LRA for quality checks and shut off whenever the combined flow/temperature is below a set threshold. These devices have been used at radar inlets and offer excellent protection to equipment on warranty.

Another emerging type of hardware appears to be the heat storage device which is of benefit to high-power, low-duty cycle components. A TWT, for example, in a CW illuminator is a likely candidate where its infrequent heat dissipation can be stored and later released to the supply coolant at average flow, thus conserving on the aircraft supply. This concept is also a possibility for the transmitter proper, although the average and peak power variations are not as great as in the CWI.

These changes as presently envisioned, are presented without the benefit of electrical advances which may necessitate even greater adjustments in the thermal design. Nevertheless, the objective of increased reliability will remain the primary goal of thermal design.

# HEAT PIPE APPLICATIONS TO CONTROL ELECTRONICS TEMPERATURE IN RADARS

Dr. Kal S. Sekhon

Advanced Development and Analysis Section, Environmental Engineering Department  
Engineering Services and Support Division  
Hughes Aircraft Co., Fullerton, Calif. 92634

## ABSTRACT

The advancement of electronics technology and increase in power densities appears to go hand in hand. The trend is to dissipate 10 watts of power in a 5 watt electronics package. This demands new and sophisticated thermal packaging techniques to cope with increasing requirements of heat dissipation. Heat pipe provides a promising technique to achieve high density packaging and still maintain reasonable operating junction temperatures. A number of heat pipe development studies, to reduce overall thermal resistance from junction to ultimate heat sink for electronics, have been conducted at Hughes-Fullerton. These electronics are utilized for surveillance, early warning, fire control, and navigation from both shipboard and airborne platforms. The results of these studies are presented in the proposed technical paper.

## INTRODUCTION

The most important nonelectrical parameter in the prediction of electronic system reliability is the maximum operating junction temperature of the system semiconductor devices. The junction temperature of the device may be computed from equation (1) as follows:

$$T_j = T_a + Q_{\text{chip}} (\theta_{jc} + \theta_{ca}) + Q_{\text{sub}} - Q_{\text{chip}} \theta_{ca} \quad (1)$$

where

- $T_j$  = junction temperature of hottest chip
- $T_a$  = ambient air temperature
- $Q_{\text{chip}}$  = power dissipation in the hottest chip
- $Q_{\text{sub}}$  = total power dissipation on the package
- $\theta_{jc}$  = thermal resistance from junction to case for the hottest chip (internal thermal resistance)
- $\theta_{ca}$  = thermal resistance from case to ambient or ultimate sink (external thermal resistance)

The heat dissipation in the electronics package is a function of the circuit design and is generally fixed by the time it reaches the thermal engineer. The ambient or the ultimate heat sink temperature is a function of radar applications whether it is airborne, shipboard or

land based. It is also specified by the customer by the time it reaches the thermal engineer. It can be seen from equation (1) that the only variables which play an important role in thermal packaging are  $\theta_{jc}$  and  $\theta_{ca}$ . At Hughes-Fullerton, a number of studies have been conducted over the past five years to develop heat pipe to minimize  $\theta_{jc}$  and  $\theta_{ca}$ . This paper summarizes the results of these studies.

## CHARACTERIZATION OF HEAT PIPES

A heat pipe may be defined as any device that transfers heat by evaporation of liquid from heated areas and condensation on cold areas, with continuous return of the condensate to the heated area by capillary action. The simplest form of heat pipe is shown in Figure 1. It consists of a sealed tube lined with a wick which is wet with a suitable volatile liquid. No gas other than the pure vapor of the liquid is present. If

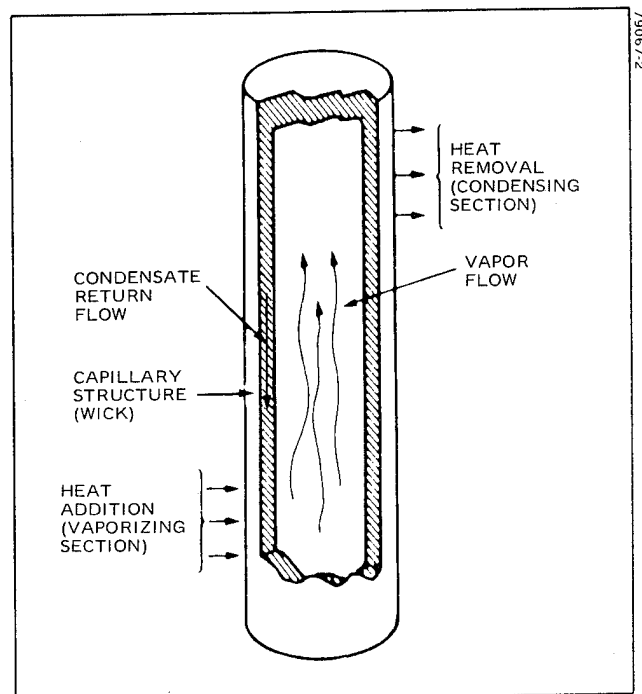


Figure 1. Straight Cylindrical Form of Heat Pipe. Addition of heat causes the liquid in the capillary structure to vaporize and conduct heat to the condensing section.

flow of the vapor through the tube is not at too high a velocity, pressure will be nearly uniform throughout the vapor space. The temperature along the wick surface will then be essentially constant at the equilibrium temperature for the liquid-vapor interface at the given pressure.

Addition of heat at any point along the tube wall will cause the temperature all along the wall to rise through local evaporation and condensation on all cooler areas. Regions of the pipe where heat is introduced into the system are evaporator sections, and those where heat removal takes place are condenser sections. For some applications, portions of the pipe may not perform either of these functions and are approximately designated as adiabatic sections. Several discrete evaporator and/or condenser sections can exist on a single heat pipe. The mechanisms affecting the flow of heat axially along the pipe are all extremely rapid and the adjustment of temperature consequently occurs almost instantaneously. The primary thermal resistance of the pipe is usually caused by the conduction of heat through the tube wall and wick structure.

The thermal performance of a heat pipe cannot be characterized by a single property such as thermal conductivity. Operational limitations are functions of the properties of the entire device. Even with the size, shape, materials and operating temperature specified, the liquid and vapor volume fractions, thermal conductance and maximum heat transfer capability are parameters that must be specified by the designer.

Comparison of a heat pipe with a solid metallic conductor of the same cross section shows that with proper allowance for inherent restrictions, a heat pipe can transport as much as a thousand times more energy

for the same temperature difference. The nearly isothermal operation of heat pipes can provide efficiencies greater than 90 percent. Limitations on the rate of heat transfer in a heat pipe are imposed by the occurrence of sonic flow in the vapor space or by pressure drop in the capillary structure of the wick. The working fluid should have a reasonably high vapor pressure at the operating temperature of the heat pipe. At low vapor pressures, noncondensable gas will cause reduction in heat pipe performance.

The geometry of heat pipes is not limited to the straight cylindrical form shown in Figure 1. A wide variety of configurations are possible, including rectangular sections, bent and branched tubes, loops, etc. A circuit card heat pipe would be in the configuration of a flat circuit card thermal mounting plate.

#### HEAT PIPE DEVELOPMENT TO REDUCE $\theta_{jc}$

Thermal resistance from junction to case for a semiconductor device has been reduced as much as 33 percent by incorporating a heat pipe inside the package. Schematic is shown in Figure 2.

Of the various characteristics of heat pipes, the one of most concern in power transistor cooling applications will be the high limiting values of local heat flux. Heat pipe evaporator power density can exceed the pool boiling limit, the point at which vapor blocks transfer of liquid back to the evaporator, by orders of magnitude. This high power density is possible since, with a heat pipe, pool boiling does not retard the fluid flow within the wick.

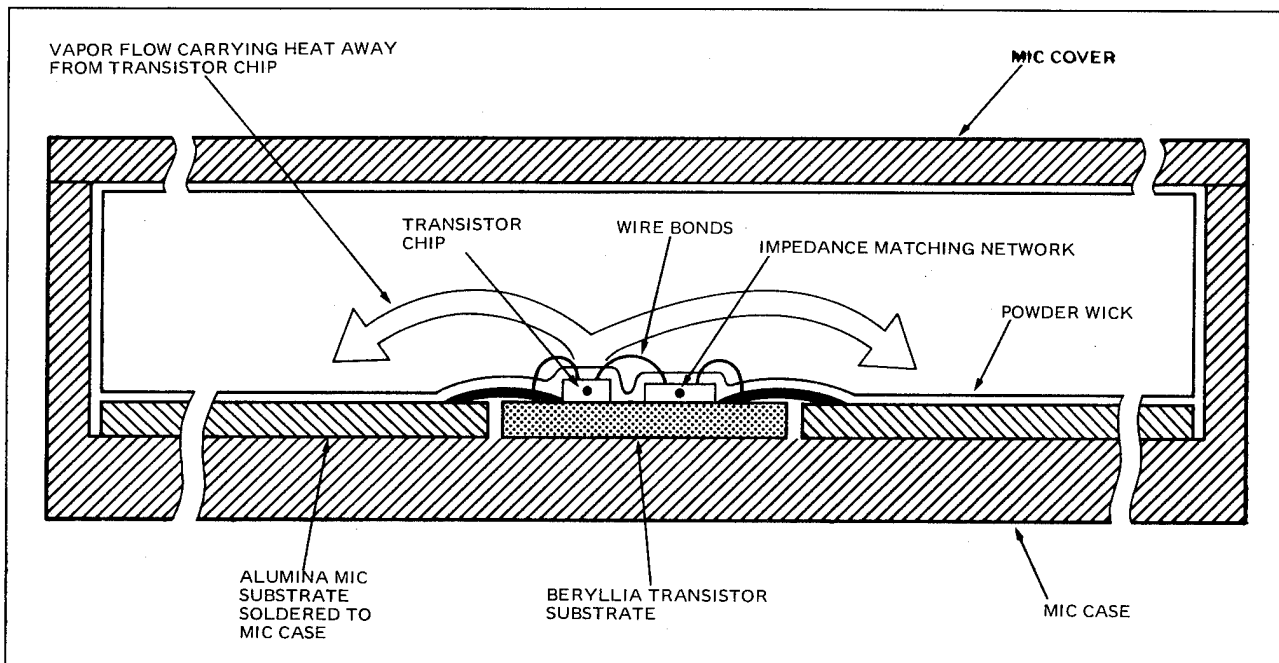


Figure 2. Section of Heat Pipe Cooled MIC RF Transistor. Heat is absorbed by the evaporating heat pipe fluid and carried to the alumina substrate where it is released by the condensing fluid and transferred thru the MIC case to the heat sink. The condensed fluid is returned to the chip by capillary pumping on the powder wick.

High power solid state devices have been effectively cooled by spreading out the junction so the average heat flux density is low enough to provide a low thermal resistance. Solid state devices have been developed for use at high frequency by limiting the device capacitance through minimization of device dimensions. Therefore, the problem in the design of high power, high frequency solid state devices is to overcome the inherent incompatibility between the frequency and thermal power requirements. Hughes has approached this problem through the application of direct heat pipe cooling to increase the power capacity of present transistor designs.

Work to date has demonstrated the feasibility of the Hughes approach by: 1) significantly lowering the junction temperature of RF transistors by heat pipe cooling; 2) demonstrating heat pipe cooling at high junction power density; 3) demonstrating that the electrical performance of the transistors was not affected by the heat pipe fluid and wick materials used; and 4) development of a high performance powder wick concept which can be applied to RF power transistors on a production basis. (See Figures 3 and 4.)

Reduction in thermal excursion during high power applications has two obvious benefits: either (1) increased reliability, or (2) increased power output for the same peak junction temperature and associated reliability. This phenomenon is basically true regardless of the type of solid state power generating device employed or the chosen frequency of operation. Figure 5 demonstrates transistor junction temperature reductions of up to  $60^{\circ}\text{C}$  or (alternatively) 30 percent higher power levels with the same junction temperature with the application of heat pipe cooling. The transistor was eutectically bonded and well heat-sink.

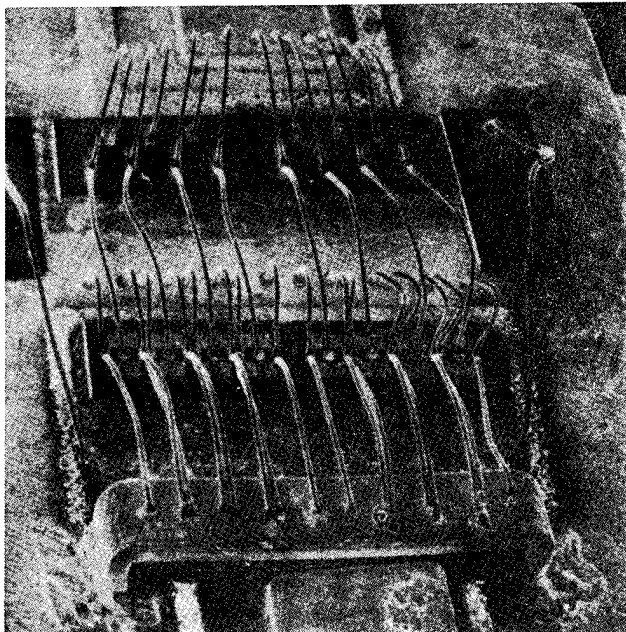


Figure 3. Multicell RF Power Transistor. Typical microwave bipolar power transistors are too complex to incorporate conventional heat pipe wick construction. The Hughes-developed "powder wick" will be utilized to overcome this problem.

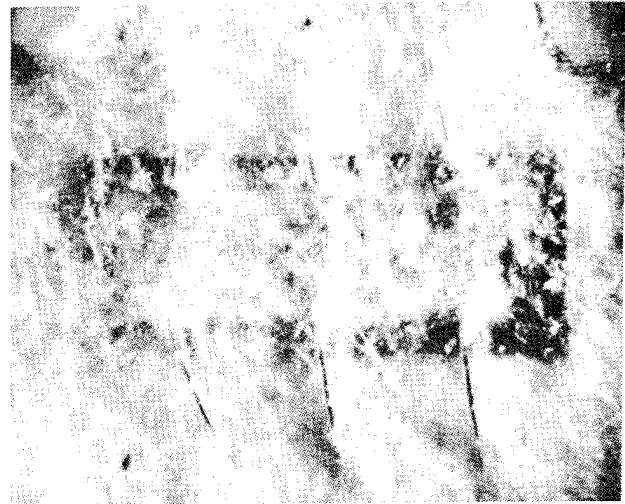


Figure 4. Hughes 'Powder Wick' Applied to a Multicell Transistor. This "powder wick", designed to give high fluid flow and heat transfer performance, is applied without disturbing the transistor bond wires.

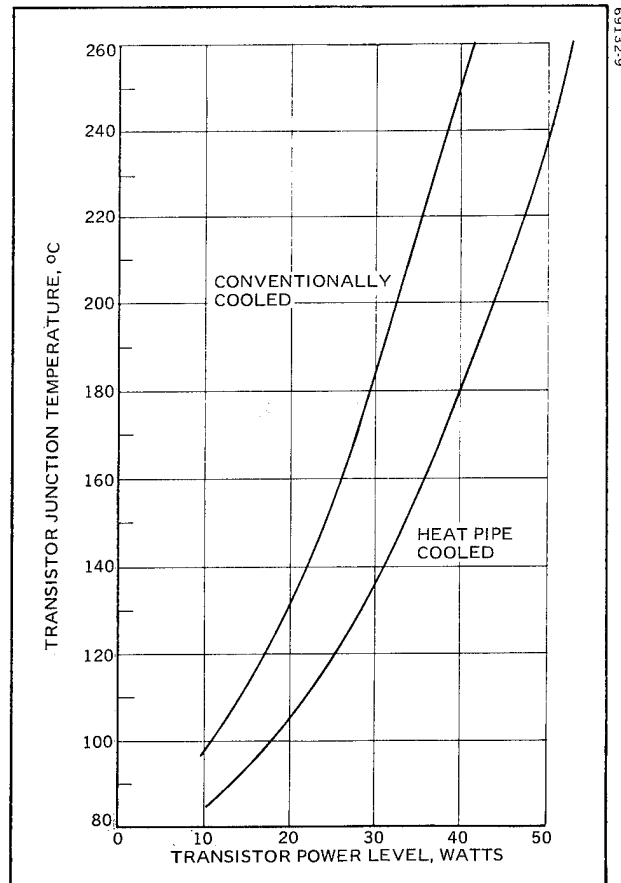


Figure 5. RF Power Transistor Temperature Characteristic. Junction temperatures are compared for a transistor (TRW-2N5071) with and without the application of a heat pipe. The transistor was eutectically bonded and well heat-sunk.

The most fundamental capability offered by heat pipes to the cooling of electronic components is the achievement of extremely high values of thermal conductance. Heat pipes have an additional advantage as thermal conductors in that they may utilize nonmetallic, nonelectrically conductive materials in order to maintain electrical isolation while retaining high thermal conductance.

#### HEAT PIPE DEVELOPMENTS TO REDUCE $\theta_{ca}$

Thermal resistance from case to ambient air (or liquid) has been reduced by mounted microcircuit package on a heat pipe the other side of which is intimate contact with ultimate heat sink. A number of heat pipes have been developed by Hughes-Fullerton but only two will be discussed in this paper because of page limitation.

##### A. Circuit Card Heat Pipe

A typical advanced model of a circuit card heat pipe developed by Hughes is shown in Figure 6. This heat pipe, which accommodates 50 DIP devices was designed to fit into existing Hughes equipments which use aluminum or copper thermal mounting plates for conduction cooling of circuit card components. The circuit card heat pipe shell is made of beryllium copper. This material was selected for its high yield strength, high thermal conductivity and ease of manufacture. It is also corrosion resistant and compatible with the heat pipe fluid. Use of beryllium copper results in a rugged heat pipe not requiring special handling and without sacrifice of thermal conductivity. Beryllium copper is easily fabricated and can be joined by brazing, soldering, or welding.

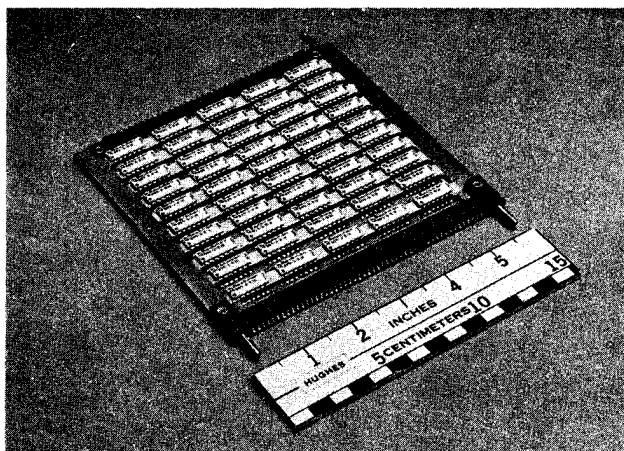


Figure 6. DIP Circuit Card with Heat Pipe Thermal Mounting Plate. The heat pipe is designed to accommodate up to 50 DIPs and has a very high heat transfer capability.

The circuit card heat pipe uses stainless steel screen wicks in the evaporator and condenser in combination with sintered-fiber stainless steel artery wicks. The thin screen wicks provide a short heat transfer path from the shell of the heat pipe to the vapor space, providing a low thermal resistance and resulting in a low temperature drop. Since the thin, tightly woven mesh will have a high resistance to liquid flow, the

artery wick is utilized to provide a low-resistance path for fluid flow. The artery wick is a sintered-fiber metal with an open structure for fluid flow but with a pore size consistent with capillary pumping requirements.

Methanol was selected as the heat pipe fluid for the circuit card heat pipe because it has a high surface tension, high latent heat of vaporization, and low viscosity. In addition, it has a relatively high vapor pressure at the operating temperature, which minimizes problems with sonic velocity, entrainment, or any inert gases in the heat pipe.

Compatibility of heat pipe fluid and materials is essential to reliable heat pipe operation. Incompatibility between the fluid and the wick and shell materials may lead to heat pipe failure from a number of causes. Selection of all materials used was based on experimental life test data developed by Hughes and data from the technical literature on heat pipes.

Analytic studies were made to predict the cooling performance of the heat pipe and metallic thermal mounting plates. Hughes' experience with the metallic thermal mounting plates has shown a high correlation between the test results and the analytic predictions.

The experimental results of testing the heat pipe with a 30 watt load are shown in Figure 7 where a comparison is made with analytical data for similar metallic thermal mounting plates. The data demonstrate the superior performance of the heat pipe in lowering both the maximum component mounting surface temperature and the temperature gradient between components.

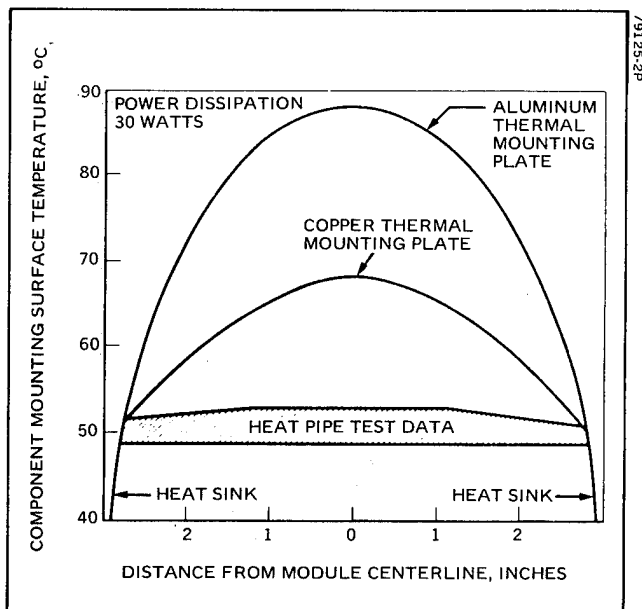


Figure 7. Performance Comparison of Heat Pipe Thermal Mounting Plate with Copper and Aluminum Thermal Mounting Plates. Heat pipe thermal mounting plate shows markedly superior performance.

In addition to thermal testing, the circuit card was qualified for use on jet aircraft by being tested to random vibration per MIL-STD-810C Method 514.2 Procedure 1A Modified, and shock per MIL-STD-810C Method 516.2 Procedure 1. The circuit card was operational during the vibration testing and no degradation of performance was observed. No degradation of performance was noted following the shock testing.

#### B. Standard Electronics Modules (SEM) Heat Pipes

The Navy's conventional SEM circuit cards are designed for low electrical power consumption at the modular level. The maximum power rating is 1.6 watts for SEM-1A circuit cards (approximate size 2.6 x 1.3 inches), and 2.4 watts for SEM-2A circuit cards (approximate size 6.0 x 1.3 inches). A development program at Hughes that applied heat pipe technology to the SEM circuit card has produced a significant increase in power density for circuit cards while also providing uniform component mounting point temperatures.

In the Hughes design, a heat pipe transfers the heat dissipated by the electronic components to the edge of the module where it is transferred to the card cage. Figure 8, illustrates the configuration of the typical SEM heat pipe frame and heat sink.

The heat flow path starts at the interface where the heat dissipating component is bonded to the cooling bar.

The heat flows through the heat pipe shell, and then through the evaporator wick-liquid matrix to the liquid-vapor interface. The heat energy is absorbed in evaporation of the liquid, after which the vapor moves to the condenser where the heat energy is released by the condensing vapor. The heat flows through the condenser wick-liquid matrix and then through the heat pipe shell to the card cage heat sink. The condensed vapor completes the cycle by flowing through the wicks to the evaporator where the cycle started.

As shown in Figure 8 the module consists of the heat pipe module frame, a circuit card, a connector, and the components. The components, DIPs in this illustration, straddle the cooling bars to which they are bonded. The DIP leads are soldered to "through" holes in the circuit card, providing the electrical paths among the components and the connectors. The overall dimensions of the heat pipe modules are those of the original modules (SEM-1A or SEM-2A). Figures 9 and 10 show the completed SEM-1A and 2A heat pipe modules.

The heat pipe cooled modules were found to be several times more efficient in transferring heat dissipated by the components to the side guides than the regular SEM-1A or 2A modules. Tests performed on the Hughes-developed modules proved that heat pipe cooling is very effective in permitting high module power without excessive component temperatures.

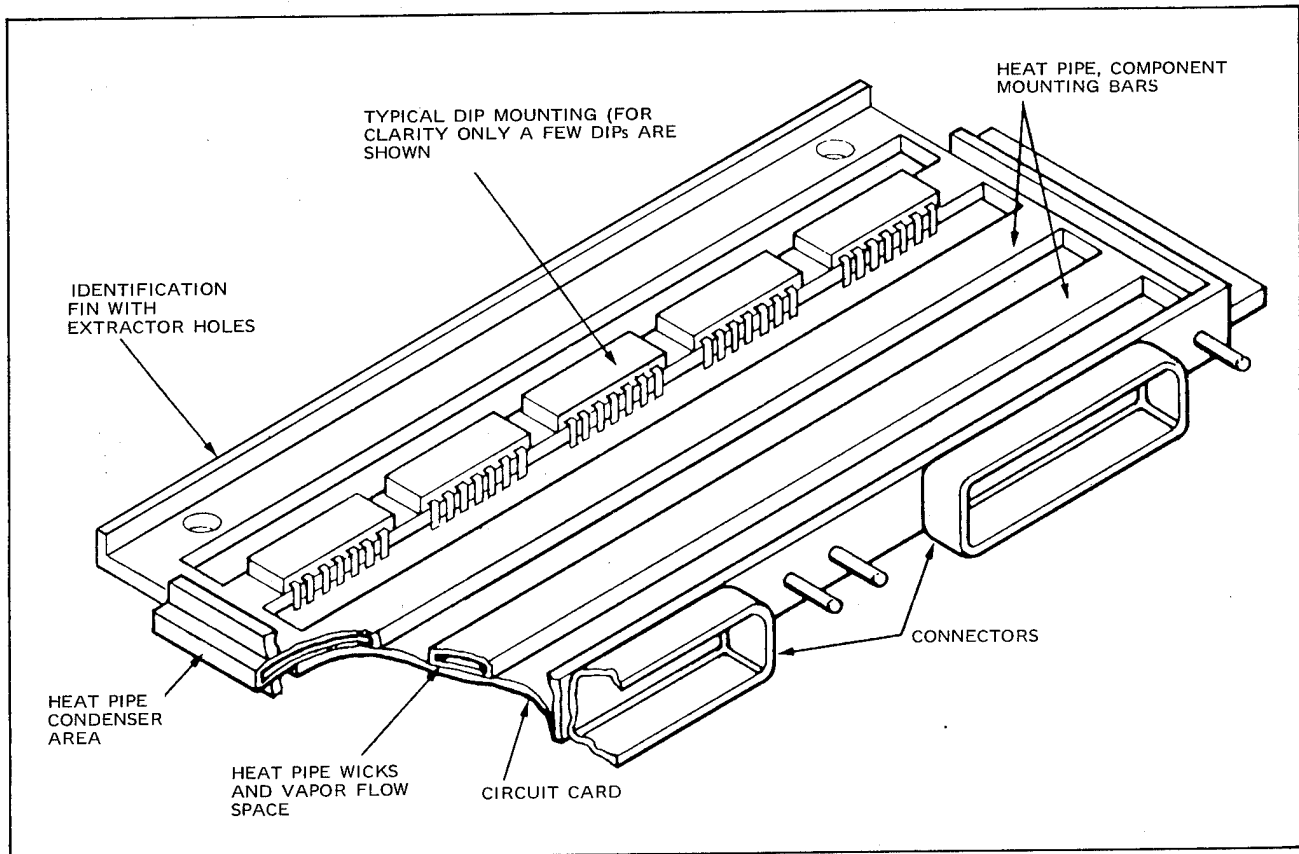


Figure 8. Cutaway View of Heat Pipe Cooled SEM-2A Module. Up to 15 DIPs are mounted on the heat pipe bars, which transmit the heat dissipated by the DIPs to the edges of the module, where it is transferred to the cooled card cage.

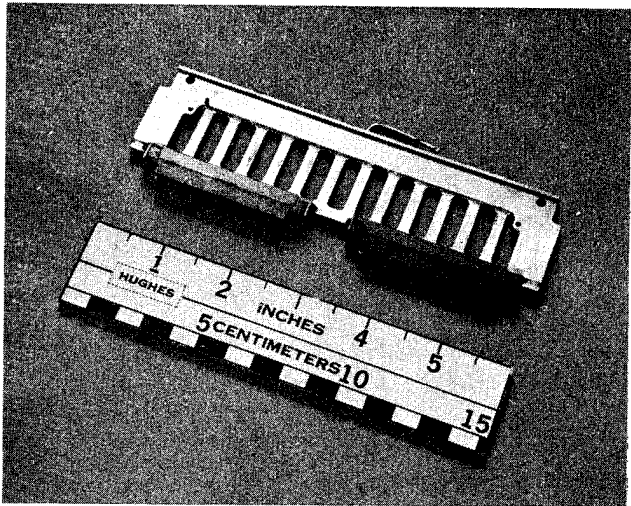


Figure 9. SEM-2A Heat Pipe Module

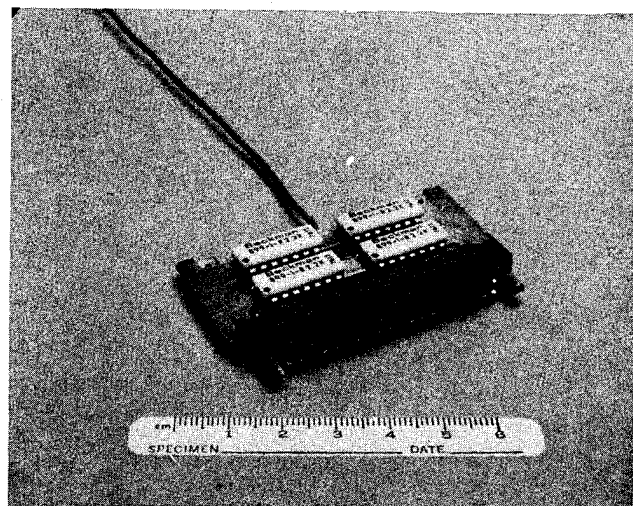


Figure 10. SEM-1A Heat Pipe Module

These Hughes-developed heat pipe cooled modules have the same dimensions as the standard modules they replace while handling approximately 7 times as much power.

The SEM-1A modules have the ability to remove 10 watts from the components at the side guide cooling surface without excessive temperature on the case of the components. The SEM-2A modules are able to remove 20 watts from the components at the side guide cooling surface without excessive temperatures at the case of the components.

#### REFERENCES

1. Cotter, T. P., "Theory of Heat Pipes", LA-3246-ms, March 1965.
2. Sekhon, K.S., Nelson, L.A. and Fritz, J.E., "Improved MIC Performance through Internal Heat Pipe Cooling," National Electronic Packaging and Production Conference, March 1977 and May 1977.
3. Sekhon, K.S. and Basiulis, A., "Heat Pipe in Electronic Component Packaging," National Electronic Packaging and Production Conference, March 1977 and May 1977.
4. Harbough, W. and Eastman, G.Y., "Experimental Operation of Constant Temperature Heat Pipes", Fifth Intersociety Energy Conversion Engineering Conference, Las Vegas, Nevada, September 1970.
5. Dunn, P. and Reay, D.A., "Cooling of Electronic Components", Heat Pipes, Pergamon Press, Ltd., 1976, pp. 235, 241.
6. Collings, J.R. and Harwell, "Rassar Array Comes of Age", Microwaves, August 1972.
7. Nelson, L.A. and Sekhon, K.S., "Development of Heat Pipes for SEM-1A Module", Report No. 0252-1, December 1976.
8. "Thermal Control of Power Supplies with Electronic Packaging Techniques", Final Report MCR-75-389, Martin Marietta, Denver, Colorado, 1975.
9. Ruttner, L.E. and Sekhon, K.S., "Development of Heat Pipe for SEM-2A Module", Report No. 0300-1.
10. Nelson, L.A., "Application of Heat Pipes and Phase Change Devices for Cooling of Electronic Equipment", Nepcon Central, Chicago, Illinois, October 1974.
11. Gianetti, R.J., Merrigan, M.A., and Nelson, L.A., "Thermal Control of Airborne Electronic Equipment", AFFDL-TR-73-12.
12. Merrigan, M.A., "Investigation of Novel Heat Removal Techniques for Power Transistors", Report No. ECOM-0021-F.



## TEMPERATURE CONTROL OF HIGHLY SENSITIVE ELECTRONIC DEVICES

JOHN J. CHINO  
HERMAN ROSSMAN

Westinghouse Electric Corporation  
Defense and Electronic Systems Center  
Baltimore, Maryland 21203

### ABSTRACT

This paper will discuss closed loop, fast response thermal regulator design and operation. This will be accomplished by considering the various elements of the loop and discussing them with regard to stability during constant environmental conditions, stability during abrupt changes in environmental conditions and gain. Further, location of the sensor will be discussed with regard to its dependence on the isothermal pattern of the device. Also included in this paper will be the discussion of a procedure for defining the essential mechanical loop parameters so that a suitable regulator can be designed.

### INTRODUCTION

Radar system performance, during extended periods of airborne operations and over broad temperature excursions, often dictates the need for efficient and highly stable thermal regulators where "sensitive devices" are used. Some examples of these types of devices are voltage controlled crystal oscillators (VCXO's), voltage controlled oscillators (VCO's), low noise assemblies (LNA's) and delay lines. Frequency bandwidth and stability, linearity, gain and pulse attenuation are some of the parameters that often must be closely regulated.

Just as it is important that the regulated device is stabilized at its desired temperature, it is also essential that rapid warm up be achieved from the lowest specified ambient extreme.

Two successful regulator systems will be cited. The first example will be a VCXO design in which approximately 10 in<sup>2</sup> of an oscillator printed wiring board was held to  $\pm 1^\circ\text{C}$  of the tuned value throughout ambient extremes of  $-54^\circ\text{C}$  to  $+71^\circ\text{C}$ . The second example to be cited will be a low noise amplifier assembly. This system was also regulated at the tuned temperature to  $\pm 1^\circ\text{C}$  throughout ambient extremes of  $-40^\circ\text{C}$  to  $+71^\circ\text{C}$ .

### THERMAL CONTROL LOOP

Figure 1 shows a typical temperature control system.

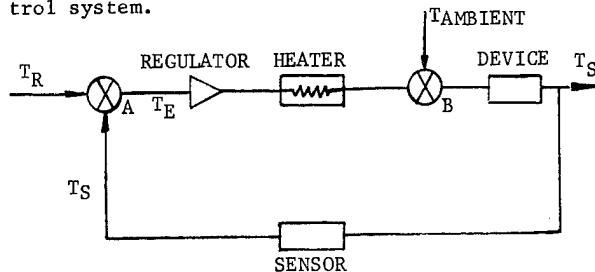


FIGURE 1 Temperature Control System

The sensor senses the temperature,  $T_S$ , at the point of interest and feeds a signal back to summing junction "A" where the signal is compared to the reference temperature,  $T_R$ , thus

$$T_E = T_R \pm T_S \dots \dots (1)$$

The error signal,  $T_E$ , is fed to the regulator which in turn apportions the quantity of heat delivered to the device. Junction "B" is the point at which the device is introduced to the surrounding environment.

### SENSOR LOCATION

Ideally, it is desirable to design an oven in which temperature gradients do not exist between the sensor and the area of interest. While gradients can be minimized by careful design, they cannot be eliminated. Due to the existence of gradients, temperature compensation must often be designed into the electronics. The task of compensating can be measurably simplified if the oven is designed such that locations of interest have repeatable thermal characteristics over the entire ambient excursion. Therefore, it is highly desirable that changes in gradient values between these locations be eliminated. In order to approach this condition, the sensor should be located on

an isotherm which closes on itself (closed contour). In this way the contour can be sensed and controlled so that its temperature remains single valued and independent of the ambient conditions. The geometry, material and thermal impedances of the device determine the location and size of the isotherms. Since the thermal impedances of the device for a given material and geometry are constant, the location and size of the isotherm will remain constant. Now if a sensor is placed on the isotherm, the absolute value of the isotherm will also remain constant. Essentially, the sensed isotherm becomes a controlled boundary within which the temperature at all points are also single valued throughout the specified ambient regime.

When the control sensor is placed on an open contour and the area of interest is somewhat removed from the contour, the thermal gradients (between locations of interest) can experience considerable variation as the oven is subjected to ambient changes. This occurs since suitable boundary control does not exist. However, these variations can be minimized when sensing an open contour providing the sensor is located close to the area of interest. Sensing in this way is perhaps the most logical as well as the most expedient approach since, in general, isothermal patterns for a given device are not readily discernable.

Figure 2 depicts an isothermal pattern for a rectangular shape bounded at the edges by the temperatures  $T_1$ ,  $T_2$ ,  $T_3$  and  $T_4$ . Also shown are several choices of sensor locations with respect to an area to be controlled (shaded area).

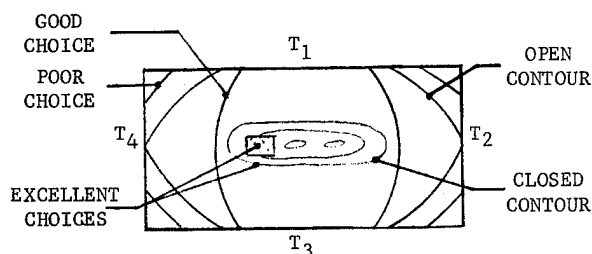


FIGURE 2 Isothermal Pattern and Sensor Locations

#### THERMAL STABILITY

In the design of the regulation loop, two types of potential thermal instability must be considered. The first can result when the quantity of heat selected for rapid warm up from low temperature extremes is too great for warm up at high extremes. At the higher ambients the loop tends to become less stable since the rate of heat exchanged between the device and the surroundings is reduced. As a consequence, more heat is available for heat transfer within the device so that locations within the system tend to overshoot. It is

therefore best to minimize the heater demands by employing dual heater stages for rapid warm up whenever necessary so that warm up at higher ambients is achieved with small quantities of heater power.

The second type of thermal instability results when a device is easily altered thermally, either by losing or gaining heat too rapidly when experiencing an abrupt external disturbance.

Electrical tests were conducted on two VCXO's of similar construction. The difference between the two VCXO's was that one oven frame was made of copper while the other was made of aluminum. The devices were heated in an oven chamber which was held at a constant temperature. The oven maintained its temperature by cyclically blowing quantities of  $CO_2$  vapor into the chamber for temperatures below room temperature, while for temperatures above room temperature, warm air was blown. The cyclic action of the chamber acted as a disturbance to the VCXO system.

Changes in frequency were observed for each device. In the case where the copper frame was used, the change was small due to the higher time constant of the system as compared to the device employing the aluminum frame. However, warm up was faster for the latter system. The ratio of time constants for equal volumes of copper and aluminum is

$$\frac{\tau_{CU}}{\tau_{AL}} = 1.44$$

In this example, it was desirable to minimize the exchange of heat to the environment for the copper frame whereas for the aluminum frame, a greater exchange of heat was desirable.

In a thermal regulation system which requires heating of a device from a low ambient extreme, it is beneficial to minimize the thermal mass. On the other hand, however, once the device is at its regulation temperature, it is desirable to have a large thermal capacitance or mass. This large mass tends to enhance thermal stability, that is, the ability of the mass to maintain its regulation temperature in spite of changing ambient conditions.

The analytical evaluation basically consists of the investigation of the sensor temperature with respect to time while at the same time varying the heater power. This must be done for several ambient conditions including both the minimum and maximum ambients. During this procedure, the temperature variation of the area of interest must be observed to determine if it is within the temperature limits required.

This analytical procedure is illustrated in Figure 3.

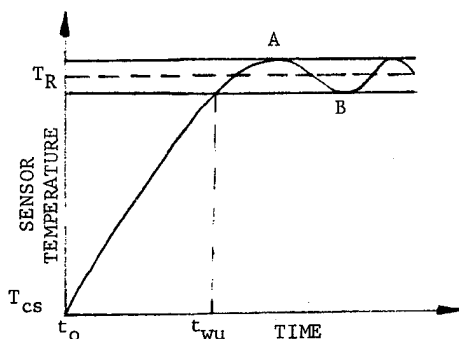


FIGURE 3 Analytical Procedure

In Figure 3,  $T_R$  is the desired regulation temperature bounded by the allowable temperature tolerance ( $\pm$ );

$T_{cs}$  is the initial cold soak temperature;  
 $t_o$  is time zero; and  
 $t_{wu}$  is the warm up time or the time required to heat the mass from the initial cold soak condition to the desired regulation temperature.

The heater power is varied by setting the power  $q = 0$  at point "A" and  $q = q_{max}$  at point "B".

The temperature of the area of interest should now be monitored to insure that the area itself is within the desired regulation temperature bandwidth. Ideally, the area of interest should have a similar temperature time response as that shown for the sensor in Figure 3. It is mandatory that the temperature of the area of interest always falls within the band shown in Figure 3. If it is not, the sensor location and/or the heater power may have to be changed.

#### TYPICAL REGULATION SYSTEMS

A successful regulation system of a voltage controlled crystal oscillator (VCXO) will now be briefly discussed. The VCXO is comprised of the oscillator (resonator) and amplifier sections. Elements such as crystals, varactors, capacitors and inductors which are located in the resonator are all temperature sensitive, although varying in degree.

The configuration shown in Figure 4 was used with excellent success for three VCXO designs employed in several radar systems.

The main design features are:

1. Excellent thermal conduction paths from the heated chassis to the printed circuit board. This is due to the direct clamping action of the upper and lower chassis frames to the board. A surface contact finish of  $\sqrt{63}$  was found suitable to assure good surface contact.

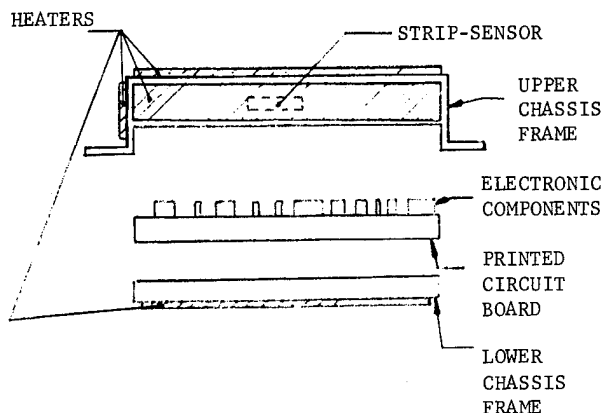


FIGURE 4 VCXO Thermal Design

2. Since the amount of heat required for heating a device to its regulation temperature from the minimum ambient condition (in this case,  $71^\circ\text{C}$  and  $-54^\circ\text{C}$  respectively) is directly dependent on its mass, this mass is kept to a minimum through the use of a thin wall chassis frame construction (.032" thick nominal). The VCXO also utilized low mass heaters (approximately .010" thick). These heaters were bonded directly on the outside of the upper and lower chassis frames.

3. Oven control sensor located on the inside of the upper chassis frame. For this VCXO design, a strip sensor was selected for use primarily because of the peel-away adhesive backing feature which yields a repeatable interface. It is also advantageous in that it senses the temperature over an area rather than a point and the likelihood of the dynamics of a given area changing from unit to unit is considerably less than that of a given point.

The entire VCXO printed circuit board (approximately  $10\text{ in}^2$ ) was held to  $71^\circ\text{C} \pm 1^\circ\text{C}$  throughout the entire ambient extremes of  $-54^\circ\text{C}$  to  $+71^\circ\text{C}$ . The frequency of the design was held to within 40 HZ of the tuned value and over the entire thermal ambient excursion. Warm up to  $+71^\circ\text{C}$  was achieved within the required 5 minute period from the minimum ambient condition of  $-54^\circ\text{C}$ .

The thermal design of the Low Noise Amplifier (LNA) must be handled in a slightly different manner due to the local dissipation of heat present in the amplifier. The thermally critical part of the LNA is the Parametric Amplifier which consists of the varactor mount, circulator and the gunn oscillator pump. The gunn oscillator pump which is intimately attached to the parametric amplifier must be thermally controlled to  $71^\circ\text{C} \pm 1^\circ\text{C}$ . This is done through the sandwiching of the parametric amplifier between two heater plates as shown in Figure 5.

## SUMMARY

This paper dealt with the temperature control of very sensitive electronic devices through the use of highly stable thermal regulation systems. The various elements of the thermal control loop and their relationship to thermal stability were discussed. Location of the sensor and its dependence on the isothermal pattern of a rectangular shaped device were also presented. Finally, two typical successful thermal regulation systems as well as the calculation procedure were cited.

## REFERENCES

1. Milton J. Borgoyne, Supervisory Engineer, Westinghouse Electric Corporation, Personal Correspondence.
2. "Oven Design for a Highly Stable Voltage Controlled Crystal Oscillator" by Herman Rossman.
3. Frank Kreith, "Principles of Heat Transfer" (International Textbook Company).

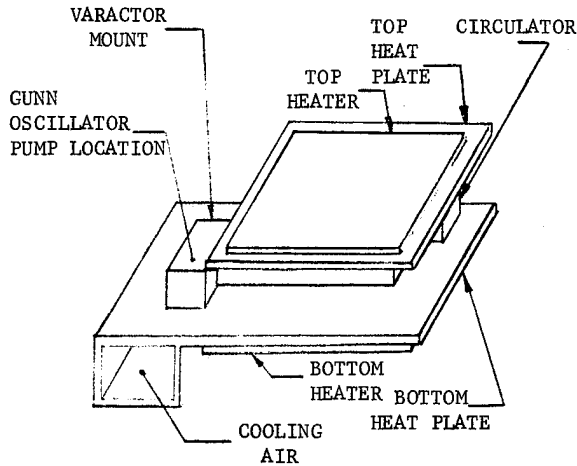


FIGURE 5 Parametric Amplifier Assembly

There is also a heat exchanger designed as part of the plate through which the cooling air will pass. This cooling air is necessary because the pump dissipates a constant four watts of power. Experience shows the need to eliminate thermal "hot spots" if successful regulation is to be achieved. For low ambient operation, there are two heaters - a coarse thermostatically controlled heater and a fine proportionally controlled heater. The thermostatically controlled heater is high powered and is used solely for warm up, while the proportionally controlled heater is low powered and is used to actually maintain the  $71^{\circ}\text{C} \pm 1^{\circ}\text{C}$  temperature.

The thermostat for the high powered heater will open at some time before the required warm up time so as to avoid "overshooting" the upper limit of the regulation temperature. At the same time, the high powered heater should not be turned off too soon as this would cause "undershooting" the lower limit of the regulation temperature. In this way, the pump will gradually or "gently" drift into the regulation bandwidth. This pump temperature versus time characteristic is shown below in Figure 6.

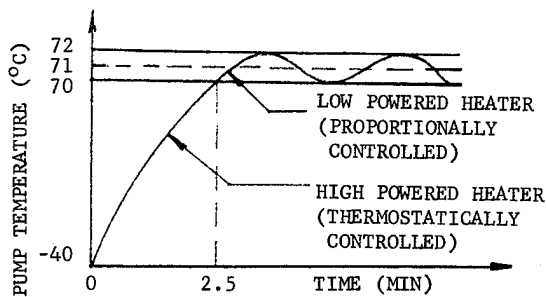


FIGURE 6 Pump Temperature Versus Time

## A HEAT PIPE APPLICATION TO A RADAR TX CABINET

UMBERTO CORSI and GIANDIONIGIO MALAGOLI

Technical Direction - Mechanical Dept.  
SELENIA Industrie Elettroniche Associate S.p.A.  
Rome, Italy, 00131

### ABSTRACT

This paper covers the design efforts and results attained in the application of an heat pipe to a radar TX cabinet to cool and soundproof the system.

At the starting conditions, a blower, located in the TX cabinet, provides to cool the magnetron cavity with high air delivery and head, thus producing a high whistle.

The heat pipe is being applied to transfer the heat from the magnetron tuning to the other edge of the pipe whereto a copper-finining has been welded.

After a thorough examination, the following problems have been solved:

- 1 — the development of a particular type of heat pipe in co-operation with the supplier;
- 2 — a system designed to connect the heat pipe with the magnetron tuning area;
- 3 — an appropriate thermal connection of the magnetron with the heat pipe.

### INTRODUCTION

The application of an heat pipe to a magnetron in a TX cabinet, instead of a local ventilation system, is originated from the necessity of setting up the cabinet in a operational room so as to change the environmental performances and, particularly, to soundproof the cabinet by utilizing the following data specs from the customer:

- 1 — Cooling System: air system with  $\Delta T$  max  $10^{\circ} \text{C}$
- 2 — Noise value: 60 dBA, measured at 1 m distance from the TX and 1.25 m above the floor in different points around the TX cabinet in an environmental room with a reverberation time lower than 1 sec.

### DESIGN

At the starting conditions, the results of the tests performed with the cabinet door closed have been 74 dBA in the 500 ÷ 1000 Hz frequency range and 84 dBA with the door opened.

The most important noise sources have been, as follows:

- Noise produced by the general ventilation system
- Noise produced by the magnetron centrifugal fan
- Air noise in the magnetron.

These two last noise sources are due to the fact that it is necessary to cool a hot spot of a magnetron (the tuning-area of the resonant cavity), wherein the thermal flow per unit surface is very high ( $120 \text{ W}/850 \text{ mm}^2$ ).

The section to be cooled (Fig. 1) consists of a hole ①, being 30 mm deep and with a 11 mm diameter.

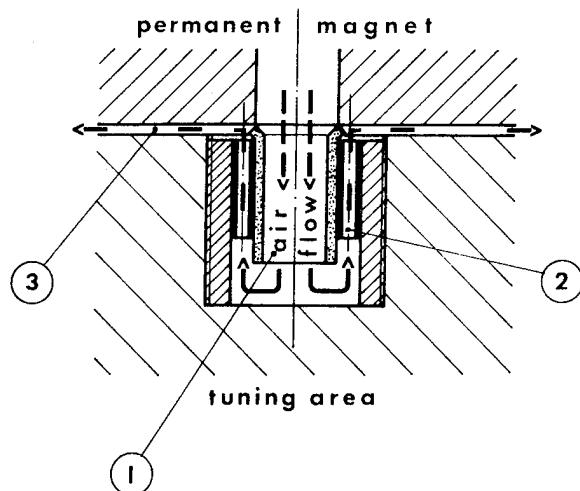


Fig. 1 — Local ventilation system in the tuning area of the magnetron

A set of pipes ②, arranged as a honey-comb, measuring 3 mm diameter and 22 mm depth, are located upon a circular crown near the hole wall.

To cool this section, a  $0.5 \text{ mc}/1'$  air delivery is required with nearly 600 mm  $\text{H}_2\text{O}$  head, which is delivered through a centrifugal compressor, housed within the TX cabinet (1st noise source).

The air, blown into the hole, flows back through the honey-comb and, then, after a sudden  $90^{\circ}$  elbow, slips out of a hollow space ③, thickness 1 mm, and consisting of the

magnetron wall and of the pole shoe of the magnet, parallel to the same.

The high air speed in this area produces a whistle, with a 1000 Hz frequency (2nd noise source).

A reduction of the air delivery to a value being almost the half of the initial one allows to foresee a reduction of the noise power level of about 3 dB, according to the following ratio:

$$PWL = 10 \log_{10} q + C_1 \log_{10} p + C_2$$

where  $q$  = delivery  
 $p$  = head  
 $C_1, C_2$  = constants

This measure may be taken owing to the reduction of the thermal specifications, relative to the max. ambient temperature, but it does not solve at all the noise problem.

We have therefore taken into consideration an heat pipe so as to take off the heat produced in the abovementioned magnetron cavity and transfer the same to the other edge of the heat pipe itself, wherein a set of welded copper-fins is inserted (Fig. 2).

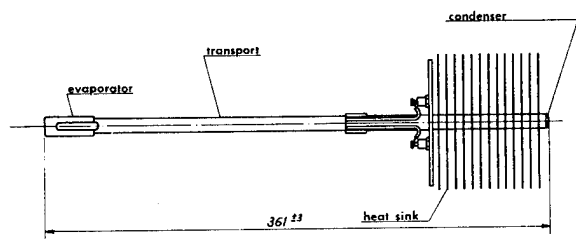


Fig. 2 — Heat pipe system

In this section, being available a large exchange surface, it was possible to take the heat off (120 W) with an air delivery at low speed ( $\sim 2.5$  m/s), thus eliminating both the aforesaid noise sources.

The development of this heat pipe, in co-operation with the supplier, has been particular to some extent, as far as the working conditions are concerned.

The technical characteristics of the heat pipe, supplied by the manufacture concerned:

- thermal resistance  $0.4^\circ \text{C/W}$
- thermal transport capacity 200W (horizontal operation)
- maximum temperature limit  $200^\circ \text{C}$

At the edge of the heat pipe where the heat source is, there is a high-wrought bush, brazed with "Castolin 1802" upon the entire contact surface in order to ensure the thermal contact between the bush and the heat pipe.

The thermal contact between the bush and the internal magnetron cavity cannot be obtained through a mechanical coupling because of the allowance of the magnetron cavity.

We have thereby resorted to the use of a silicon grease type, highly conductive, thoroughly cleaning before the surfaces to be coupled.

The edge bush (1) has a slot where the pipe has a recess so as to form a housing space (2) for a max. temperature thermistor (3) (Fig. 3 detail B).

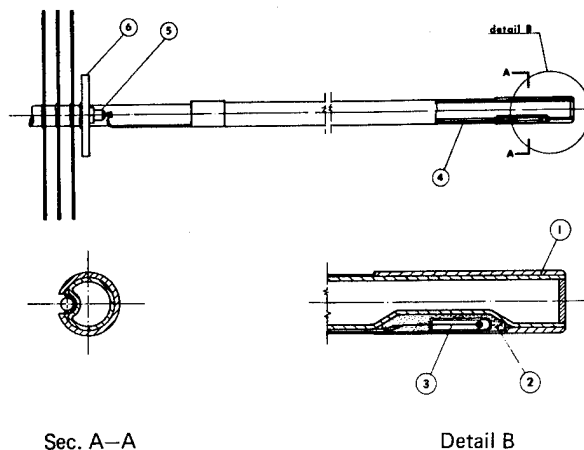


Fig. 3 — Heat pipe section

The thermistor is fastened by a thermal insulating glue (2) to the internal side, thus attaining a thermal insulation and being susceptible to be affected by the only outside temperature, i.e. the magnetron.

It is calibrated at  $180^\circ \text{C}$ . Over this temperature, it trips the overtemperature command of the cabinet. Along a whole pipe generatrix (4) there is a recess to lodge the thermistor signal wire, which terminates by two connection terminals (5) onto a special flange (6), welded at the leading end of the copper finning on the other side.

The finning performances have been checked through the following considerations whereas the cooling fins must be housed in the space allowed by the pre-existent cabinet packaging.

The temperature rise of the cooling fins above the inlet air temperature consists of two parts — the temperature rise of the air as it absorbs heat from the cooling fins ( $\Delta T_{\text{air}}$ ) and the temperature rise of the cooling fins above the air through the fins ( $\Delta T_{\text{fin-air}}$ ).

The first one ( $\Delta T_{\text{air}}$ ) depends on the power  $Q$  that is transferred, and the total air flow rate  $P$ :

$$\Delta T_{\text{AIR}} (^\circ \text{C}) = \frac{Q \text{ (watt)} \times 1.73}{P \text{ (CFM)}} \quad (1)$$

Supposing the total tuning power in the condenser edge and giving 2.5 m/sec., as max. air speed, for the noise reason and  $5^\circ \text{C}$ , as  $\Delta T_{\text{air}}$ , for the customer specs, the minimum size of cross section through the fins is given by the formula:

$$S = \frac{Q \cdot 1.73}{\Delta T \cdot v} = 0.084 \text{ ft}^2$$

$$\Delta T = \frac{Q_w}{n^{0.2} h^{0.2} p^{0.8} l} \quad \cdot 140 \quad (2)$$

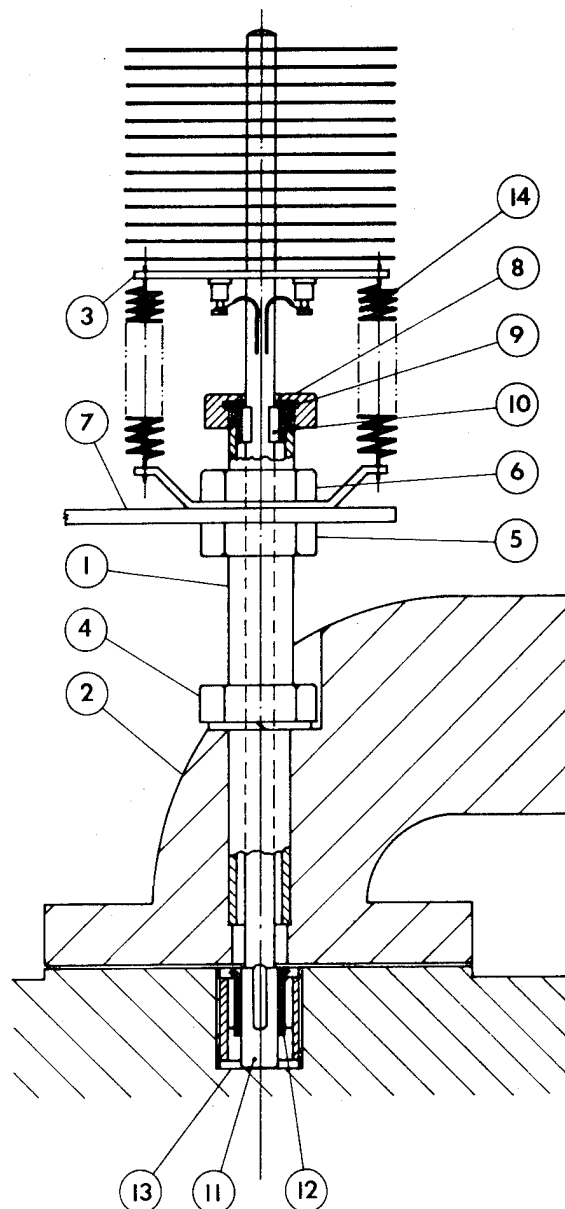
Fixing the fin pitch  $w = 1/4$  inch the pitch number is:

$$n = \frac{S}{h \cdot w} = 12$$

$$\Delta T_{(\text{FIN. AIR})} = \frac{140 \times 0.25 \times 120}{12^{0.2} \times 4^{0.2} \times 41^{0.8} \times 4} = 25^\circ\text{C}$$
$$\Delta T = 32^{\circ} \text{ C}$$

The housing slot of the heat pipe is the tuner cooling air inlet, which consists of a cylinder (1), being externally threaded and fastened upon the permanent magnet (2) by a nut (4) locked with "locktite" in the terminal flange of the pole shoe.

On the top of the threaded cylinder is a blind nut (8), which locks a teflon bush (9), wherein the heat pipe is free to slide forward and backward.



So the heat pipe leans on two points —on the teflon bush and on the tuning bush (12).

In correspondence with this teflon bush, the heat pipe has a welded copper bush (10) to reset the required dimensions.

When the tuning-area moves forward, the heat pipe ⑪, being pushed, must follow the same. When the tuning-area moves in the opposite direction, to insure the thermal contacts two return springs ⑭ have been fixed upon the heat pipe flange ③, where the connection terminals of the thermistor are.

The other end of the springs has been fastened onto the cabinet clamp.

The stiffness  $K$  of the springs is reckoned to overcome the only frictions existing in the motion of the heat pipe within its own housing so as to avoid the magnetron stress.

Thus the magnetron and magnet are not subject to any change.

## EXPERIMENTAL

The technical characteristics of the heat pipe, supplied by the manufacture, have been checked through a test performance, by using an heater in order to have a coupling equal to the magnetron heat pipe :

- the contact area does not exceed  $850 \text{ mm}^2 = 1.33 \text{ sq.in.}$
- the heater must have heat insulation from the environment
- the heat sink should be cooled by natural convection.

Temperature tests have been performed in different heat dissipations and upon several heat pipe samples.

Fig. 5 shows the position of the thermocouples during the test performance and the temperature curve for the different heat dissipations.

The different samples have not produced, indeed, different test results, thus proving the homogeneity of the product as far as technology and manufacture are concerned.

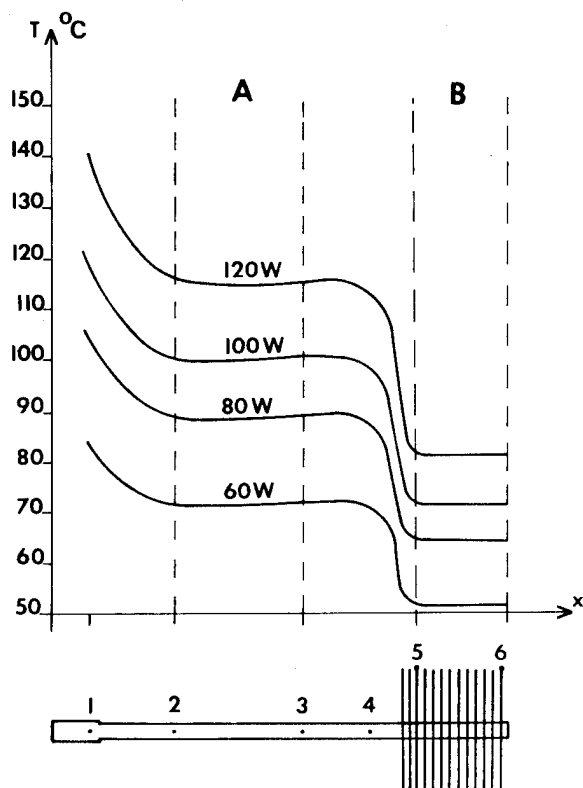


Fig. 5 — Temperature curves

The temperature curves show in the central section A the good performance of the product, in fact, the temperature level keeps constant, along the whole central section of the pipe with an optimum heat transfer coefficient.

Furthermore the constant temperature level of the fins B is indicative of the thermal homogeneity and good performance of the condenser area and fin connection.

The max temperature level attained with 120 W dissipation is  $140^{\circ} \text{C}$  upon the thermistor and  $80^{\circ} \text{C}$  upon the dissipation fins.

Once performed these temperature tests the heat pipe has been installed inside the TX cabinet, and subject to the test controls in view of checking either the tuning temperature or the noise level attained.

The noise levels have been measured in different points around the cabinet according to the design specifications.

The noise has been taped in order to perform an analysis of the tape in a laboratory later on.

The test results showed the noise level of nearly 60 dBA with an unusual quantitative drop.

## CONCLUSION

Many difficulties have arisen in the application of the heat pipe for the installation of this system into the cabinet because of the special technological requirements and of the rough allowances of the magnetron, that could not be worked again.

Anyway, these difficulties have been thoroughly solved by solely acting upon the heat pipe system.

As a consequence the heat pipe system, besides its own heat and soundproof peculiarities above shown, has the advantage to be replaceable by the local ventilation system.

Therefore, the same cabinet may offer both system versions with profitable advantages from the viewpoint of production.

## References :

ALLAN W. SCOTT  
"Cooling of electronic equipment,,



## CONTROLLING TEMPERATURES IN PHASED ARRAY ANTENNAS

RICHARD F. PORTER

Systems Development Division  
Westinghouse Defense and Electronic Systems Center  
Baltimore, Maryland 21203

### ABSTRACT

Phased array antennas are notoriously sensitive to both temperature variations and gradients. At the same time, there is always the desire to operate at as low a temperature as possible. A new and rather novel technique is described which will meet these requirements in an environment ranging from  $-54^{\circ}\text{C}$  to  $+125^{\circ}\text{C}$ . In addition, it maintains the antenna at temperatures lower than the ambient without using any electrical power.

### INTRODUCTION

The application described herein is for the EAR antenna. However, the technique can be scaled for other applications. The antenna is composed of nearly 2000 phase shifters (phasers) which "plug" into an R.F. manifold plate. The manifold plate also serves as the phaser heat sink. In order that the temperature of all the phasers be uniform, the temperature of the manifold plate must be kept very uniform.

In addition, because the phasers are tuned at a specific temperature, it is necessary that the temperature not vary from this "set point" by more than  $\pm 5^{\circ}\text{C}$ .

Most commonly, temperature control is accomplished by installing heaters which maintain a constant temperature. This would require that the antenna be kept at a temperature higher than the ambient. For a larger unit such as the EAR antenna which is approximately 1 meter in diameter, this requires a large amount of power, which is always undesirable.

Other alternatives include the use of a coolant, either air or liquid, which is kept cooler than the ambient. The temperature of this coolant must be maintained at a constant temperature to limit array temperature variations. Controlling gradients is another problem. This is usually accomplished either by very high flow rates or by a counterflow parallel path arrangement which requires a very complicated manifold system.

In the case of the EAR antenna, liquid coolant (Coolanol 25) was available but only minimum flow rates were specified, and these were not high. In addition, coolant temperatures could vary by  $\pm 8.5^{\circ}\text{C}$ . This means that in order to use the above mentioned techniques, both the flow rate and temperature of the coolant would have to be controlled or the antenna might be over-cooled (cooled below its "set point").

It was desired that the manifold plate heat sink be kept below  $70^{\circ}\text{C}$  and that it not vary from this "set point" by more than  $\pm 5^{\circ}\text{C}$ . The ideal gradient was no gradient at all but after extensive analysis, it was decided that a 2 or  $3^{\circ}\text{C}$  gradient could be tolerated.

### SOLUTION

The technique devised incorporates a wickless heat pipe and provides uniform temperature across the antenna. It includes a semi-redundant diverter valve system to control the outlet temperature of the prime coolant. Phaser temperature is maintained within the "set point" independent of prime coolant flow rate and inlet temperature variations.

Figure 1 depicts the antenna manifold. It includes the evaporator portion of a "wickless heat pipe" having the phasers attached conductively to the plate proper. There are 25 embedded tubes within the plate filled with Freon-11 and oriented vertically to provide a gravitational liquid return condensate. These tubes are joined at the top and bottom manifold for pressure and temperature uniformity. The only temperature variations across the plate are caused by variations in local flux density, and these are small because the phaser flux into the plate is less than 5 watts/in<sup>2</sup>.

The vapor which rises in the evaporator cold plate is allowed free access to a condenser. It is here that the prime coolant is supplied, and it acts as the heat sink for the total system. The effectiveness,  $\epsilon$ , for the condenser exchanger which is a measure of its efficiency, is high because the coolant heat exchanger passages are made adjacent to the freon condenser surfaces. Tests on this evaporator/condenser

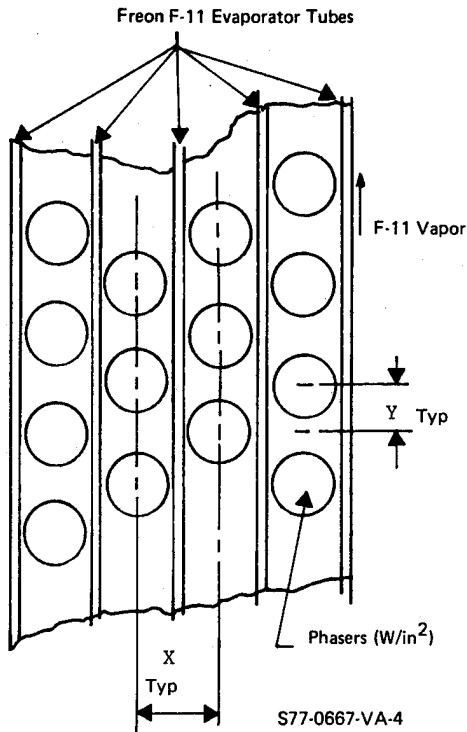


FIGURE 1  
Antenna Evaporator Manifold Configuration

concept reveal exceptionally close temperature control - less than 3°C across the entire antenna surface at a given inlet flow and temperature.

The degree to which the condenser temperature  $T_c$  is maintained for variations in inlet cooling conditions depends on several variables. These are expressed in the following equation which defines the effectiveness  $\mathcal{E}$ ,

$$(1) \quad T_{C_1} = T_1 + \frac{T_{0_1} - T_1}{\mathcal{E}_1}$$

where  $T_{C_1}$  = condensate temperature of Freon-11, °F

$T_1$  = inlet coolanol 25 temperature, °F

$T_{0_1}$  = outlet coolanol 25 temperature, °F

$\mathcal{E}_1$  = effectiveness of exchanger under flow/temperature conditions which result in  $T_{0_1}$

The desired circumstance is for  $T_c$  to be constant for any combination of coolanol flow rate,  $\dot{m}$ , and temperature  $T_1$ . To establish this, equation (1) can be written for a second flow condition as,

$$(2) \quad T_{C_2} = T_2 + \frac{T_{0_2} - T_2}{\mathcal{E}_2}$$

Subtracting (2) from (1),

$$(T_{C_1} - T_{C_2}) \mathcal{E}_1 \mathcal{E}_2 = T_1 \mathcal{E}_1 \mathcal{E}_2 + T_{0_1} \mathcal{E}_2 - T_1 \mathcal{E}_2 - T_2 \mathcal{E}_1 \mathcal{E}_2 - T_{0_2} \mathcal{E}_1 + T_2 \mathcal{E}_1$$

If  $T_{C_1} = T_{C_2}$ , which is what is needed to provide constant temperature,

$$(3) \quad T_{0_2} = T_1 \mathcal{E}_2 + T_{0_1} \frac{\mathcal{E}_2}{\mathcal{E}_1} - T_1 \frac{\mathcal{E}_2}{\mathcal{E}_1} - T_2 \mathcal{E}_2 + T_2$$

This expression says that there is some relationship between the outlet temperatures ( $T_{0_1}$  and  $T_{0_2}$ ) and the heat exchanger effectiveness ( $\mathcal{E}_1$  and  $\mathcal{E}_2$ ) for the two conditions which will cause  $T_{C_1} = T_{C_2}$ .

By examination, if  $\mathcal{E}_1 = \mathcal{E}_2 = 1$ , then  $T_{0_2} = T_{0_1}$ . This means that for a 100% effective heat exchanger, keeping the outlet temperatures equal for different inlet conditions will cause equal condensation temperatures. This means perfect temperature control of the antenna. Obviously, there is no such thing as a 100% effective heat exchanger, but the error can be kept small by making a very efficient heat exchanger - which can be done.

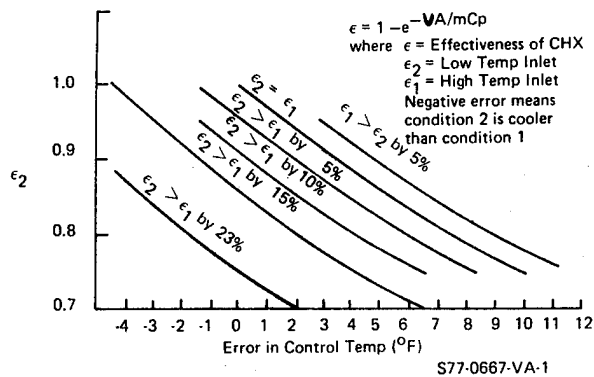


FIGURE 2  
Variations in Freon Condenser Temperature as a Function of Inlet Coolant Temperature and Flow at Constant Outlet Temperature

Figure 2 is a graph showing the error in  $T_c$  caused by the condenser heat exchanger (CHX) having an  $\mathcal{E}$  less than 1 and for variations in  $\mathcal{E}_1$  and  $\mathcal{E}_2$  which occur due to different inlet conditions. Equation (3) was used to generate the  $\mathcal{E}_1 = \mathcal{E}_2$  curve. Equations (1) and (2) were used

to generate the others. Note that these are total errors. Therefore, a 3°F error could be represented as a  $\pm 1.5^\circ\text{F}$  tolerance.

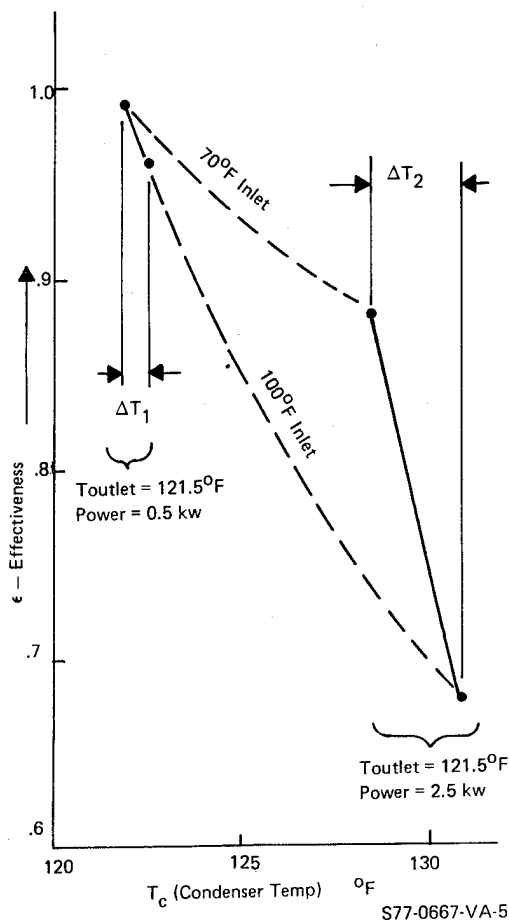


FIGURE 3  
Effectiveness Vs. Condenser Temperature  
at 70 F and 100 F Inlet Condition for  
0.5 KW to 2.5 KW Power Range When the  
Coolant Exit Temperature is Held Constant

Figure 3 illustrates the degree of control possible with the actual CHX system under varying inlet conditions. The data used for this figure is from calculations of the CHX built for the EAR antenna. For the EAR antenna, the inlet coolant temperature variation is 70° to 100°F. The system diverter valve controls the flow in a manner that results in a constant coolant exit temperature. The data plotted in Figure 3 show the temperature control obtained for two different power levels. The freon condensate temperature,  $T_c$ , varies only slightly as a function of coolant inlet temperature at a specific power level as shown. At 0.5 kW the change is only 1.2°F and at 2.5 kW it is 2.5°F. The fact that  $T_c$  is different at the two power levels is due to the change in effectiveness of the CHX over the large flow rate variations required to maintain a constant outlet temperature.

This could be improved substantially by using a larger heat exchanger which would increase the  $\epsilon$  at the 2.5 kW condition (high flow). This is a trade-off against weight and volume for any given design.

The temperature variation at a specific power level in Figure 3 is also due to variations in CHX effectiveness at different coolant inlet conditions. This error can be predicted and is plotted in Figure 2. This figure allows the prediction of freon condensate temperature variations when prime coolant inlet conditions are varied from 70° to 100°F while the exit temperature remains constant. It requires that the effectiveness of the CHX at the bounding flow conditions be calculated.  $\epsilon_1$  is the high temperature inlet condition, and  $\epsilon_2$  represents the low temperature condition. Because of the physical arrangement of virtually all compact heat exchangers,  $\epsilon_2$  is always higher than  $\epsilon_1$ . This is not necessarily true for tubular heat exchangers, and this type of control should be scrutinized very carefully before this technique is used with a tubular heat exchanger. The present EAR design consists of a fin/plate type compact heat exchanger.

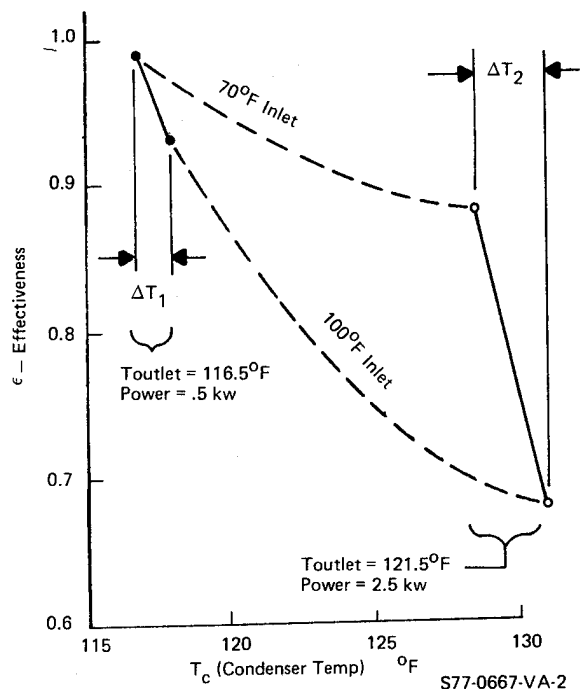


FIGURE 4  
Effectiveness Vs. Condenser Temperature  
at 70°F and 100°F Inlet Conditions and  
for the Power Range of 0.5 to 2.5 KW  
Allowing the Coolant Outlet Temperature  
to Vary from 116.5°F to 121.5°F

Figure 4 illustrates the effect of letting the outlet temperature vary by  $5^{\circ}\text{F}$  ( $2.8^{\circ}\text{C}$ ). This is typical of the actual control system where the coolant sensing device operates over a nominal band of temperature. The control is still quite good since the total variation is only  $14^{\circ}\text{F}$  ( $7.8^{\circ}\text{C}$ ) or  $\pm 3.9^{\circ}\text{C}$ .

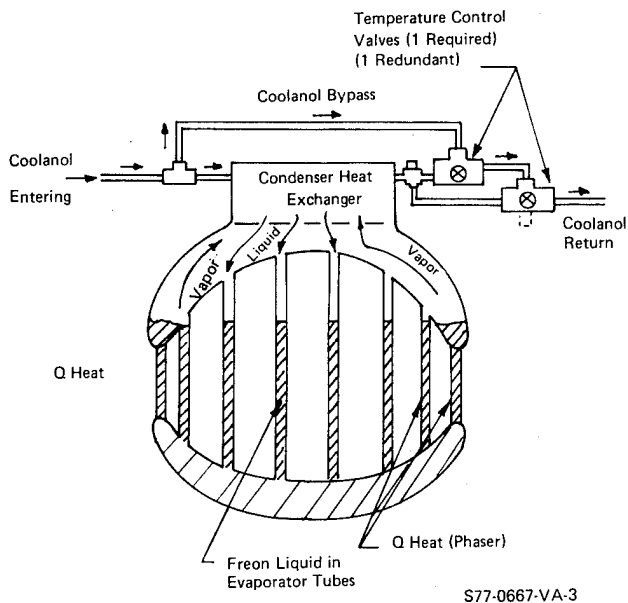


FIGURE 5  
Antenna Temperature Control System

The entire system is shown in Figure 5. The evaporator tubes are filled with Freon-11, the heat entering these tubes via conduction causing the freon to boil, the resulting vapor rises to the cool condenser surfaces, and the condensed liquid falls to complete the cycle. The coolant exiting the CHX is kept at a constant temperature by the valves A and B. Only one valve is necessary, but a second valve is included to give a degree of redundancy and satisfy reliability requirements.

With respect to the valves, it is impossible to implement two valves and achieve complete redundancy. Nevertheless, the arrangement shown gives a degree of redundancy. For example, if either valve A or B fails with the heat exchanger inlet port blocked, the other valve maintains complete control with no degradation. However, if either valve fails with the bypass inlet port blocked, temperature control is lost completely, but the full flow will always pass through the CHX and assure no overheating and subsequent damage can occur. In any intermediate failure position, some degradation will occur.

Although the valves are shown in Figure 5 as two separate units, in actuality they are contained within a single housing. The actuators are located at the valve inlet port which allows

them to sense only the temperature of the coolant leaving the CHX. This also means that a slight leak rate must be built into these ports so that during warm-up they can sense the increasing temperature of the coolant and open when the coolant comes up to the proper temperature.

Figure 6 is a photograph of the CHX installed in the antenna heat sink manifold plate. Three quadrants of the antenna are covered with printed wiring boards used for interconnection of the phasers. The open quadrant shows the evaporator tubes. The CHX is located at the top of the antenna. Tests have been completed on both small scale and full scale models. Test results indicate only minor variations from the data presented herein.

Although the temperature control technique described is used on a large system, the technique itself can be used on a much smaller scale. For example, the controlling of gradients and temperature level on a printed wiring assembly is ideally suited if the circuit is critical, as some are.

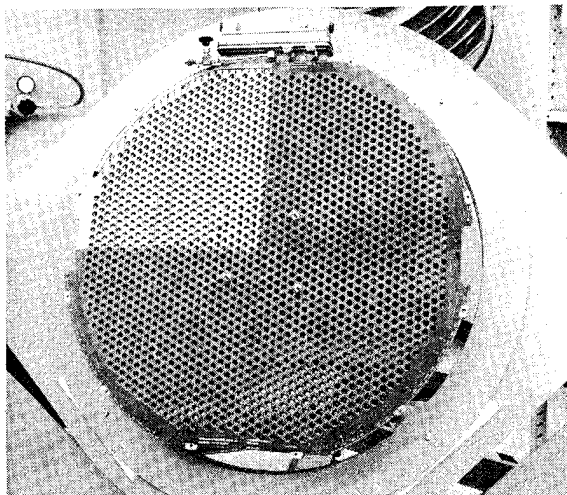


FIGURE 6  
The Evaporator/Condenser Unit  
Installed in the Antenna Manifold Plate

# "OPENCE" (OPTIMUM PERFORMANCE) HEAT SINK DESIGN PROCEDURE

M. Tadmor

H. Frenkel

ELTA Electronics Industries Ltd. P.O.B. 330 Ashdod, Israel

## ABSTRACT

"OPENCE" is a design procedure for heat sinks. The procedure is intended for forced air cooling systems and is presented as a step-by-step design method which is very accurate and easy to follow.

For those interested in pursuing the development of "OPENCE" in depth, a full mathematical analysis is presented at the end of the article.

"OPENCE" was developed as a design tool for wide use. It requires, however, the use of an electronic calculator, preferably having a hyperbolic tangent function capability.

## DESIGN PROCEDURE

Fig. 1 describes a typical heat sink with all pertinent dimensions. Our goal is to design fin dimensions ( $x, y$ ) so that the heat sink shall perform in the best way possible. All other dimensions ( $B, L, W$ ) are fixed and are usually dictated by system packaging considerations. Further,  $\theta_i$ ,  $\theta_w$  and  $Q$  are defined by system requirements.

First step is to select an air fan or blower. This is done considering available voltage and power, space limitations, availability, stock considerations, and most important - the designer's fancy.

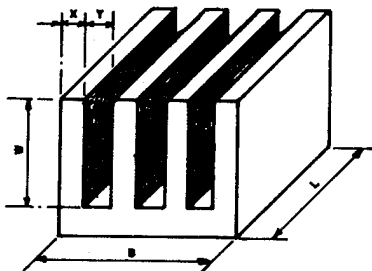


Fig. 1

## WHERE :

- B - Width of heat sink (inches).
- L - Length of heat sink (inches).
- W - Height of heat sink (inches).
- x - Fin thickness (inches).
- y - Fin spacing (inches).
- $\theta_i$  - Inlet air temp. ( $^{\circ}\text{F}$ ).
- $\theta_w$  - Heat sink max. temp. ( $^{\circ}\text{F}$ ).
- Q - Dissipated heat (watts).
- $\dot{m}$  - Air flow (CFM).
- $\Delta p$  - Air pressure drop thru heat sink (inches of water).

Blower characteristics is presented by blower manufacturers in a flow/pressure curve.

Selection of an operating point on the blower characteristic curve is the second step. This provides the final data. Now we have  $\dot{m}$  (air flow) and  $\Delta p$  (air pressure drop).

Step three is to calculate the four "OPENCE" coefficients :

$$E = 0.0446 \frac{W^{0.6} \dot{m}^{0.4}}{L^{0.1} B^{0.4}}$$

$$P = 378 \frac{B W}{\dot{m}} \left( \frac{\Delta p}{L} \right)^{0.555}$$

$$A = 6.7 \frac{W^{0.4}}{L^{0.9} B^{0.6} \dot{m}^{0.4}}$$

$$G = \frac{3.6}{\dot{m}}$$

## NOTE :

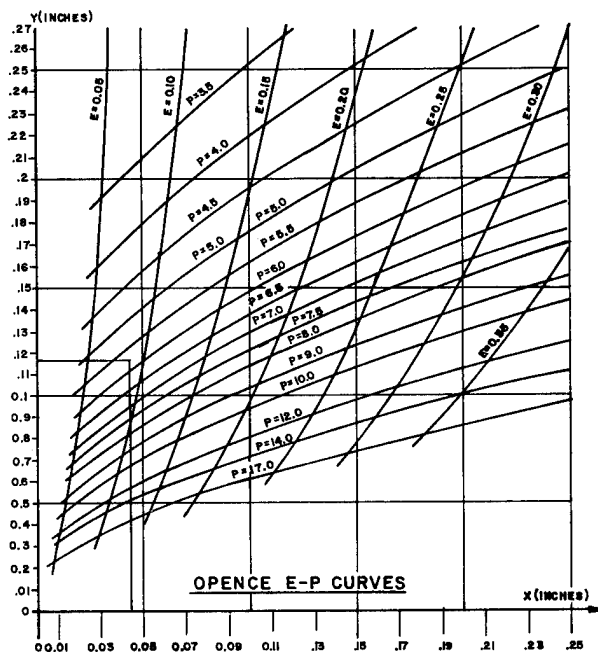
These coefficients are for an aluminum heat sink with air cooling. Refer to general coefficients on page 3 for other materials.

Step four is to locate the values of E and P on the "OPENCE" curves. The intersection of E and P yields values for x and y, fin thickness and spacing. This is the optimum heat sink for the given system.

In step five we check the performance of the heat sink. This is done by calculating  $\Theta_{wv}$ , the maximum temperature the heat sink will attain when operating at design conditions.

$$\Theta_w = \frac{A (x + y)^{0.6} y^{0.4} Q}{X^{0.5} \tanh \frac{E (x+y)^{0.4}}{X^{0.5} y^{0.4}}} + GQ + \Theta_i$$

$\Theta_w$  should be equal to or lower than the maximum allowable heat sink temperature. If this is not so, some design parameters must be changed, such as heat sink dimensions, air flow or blower pressure, heat dissipation, inlet air temperature or allowable final heat sink temperature. The new parameters are then used in the same procedure to arrive at a suitable design.



#### SAMPLE PROBLEM

A heat sink is required to dissipate 500 watts. The dissipating electronic device should not exceed 212 °F (100 °C). Cooling air is supplied at 80 °F (27 °C). Temperature drop between device and heat sink was calculated at 36 °F (20 °C). The available volume for the heat sink is 3.25" width by 0.8" height by 16" length.

Allowable  $\Theta_w$  is calculated from the above data to be 176 °F (212 - 36 = 176).

A Rotron "AXIMAX 2" blower is selected for the job, catalog No. 368YS, having an air flow of 45 cfm at 1.5 inches of water pressure.

The complete design data is then :

$\dot{m} = 45$  cfm  
 $\Delta P = 1.5$  inches of water  
 $B = 3.25$ "  
 $W = 0.8$ "

$L = 16$ "  
 $Q = 500$  Watt.  
 $\Theta_w = 176$  °F  
 $\Theta_i = 80$  °F

Calculating "OPENCE" coefficients :

$$E = 0.0446 \frac{0.8^{0.6} 45^{0.4}}{16^{0.1} 3.25^{0.4}} = 0.0845$$

$$P = 378 \frac{3.25 \times 0.8}{45} \left( \frac{1.5}{16} \right)^{0.555} = 5.87$$

Locating these values on the "OPENCE" curves yields the following :

$$x = 0.047$$

$$y = 0.118$$

In order to check the heat sink performance we calculate the "A" and "G" coefficients and test for  $\Theta_w$  :

$$A = 6.7 \frac{0.8^{0.4}}{16^{0.9} 3.25^{0.6} 45^{0.4}} = 0.054$$

$$G = \frac{3.6}{45} = 0.08$$

$$\Theta_w = \frac{0.054 (0.165)^{0.6} 0.118^{0.4} 500}{0.047^{0.5} \tanh \frac{0.0845 (0.165)^{0.4}}{0.047^{0.5} 0.118^{0.4}}} + (0.08) 500 + 80 = 162.5 \text{ } ^\circ\text{F}$$

Since  $\Theta_w = 162.5$  °F is lower than the design limit of 176 °F the design is successful.

#### MATHEMATICAL ANALYSIS

The "OPENCE" design procedure is based on optimizing the performance of the heat-sink according to three parameters, which are controlled by the designer:

- Fin thickness which is directly related to heat conduction in the fin.
- Fin spacing which is directly proportional to air flow and to heat transfer by convection.
- The number of fins in the heat-sink, which directly effects heat transfer from the metal to the cooling air.

For given heat sink dimensions, air flow and pressure drop, these three parameters contradict each other.

The following is a description of the mathematical analysis used to optimize the heat-sink.

Definition of symbols :

$\theta_o$  - Outlet air temperature  $^{\circ}\text{F}$   
 $h$  - Heat transfer coefficient  $\left[ \frac{\text{watt}}{\text{inch}^2 \text{ } ^{\circ}\text{F}} \right]$   
 $K_L$  - Heat conduction coefficient, Aluminum  $\left[ \frac{\text{watt}}{\text{inch } ^{\circ}\text{F}} \right]$   
 $K_a$  - Heat conduction coefficient, air  $\left[ \frac{\text{watt}}{\text{inch } ^{\circ}\text{F}} \right]$   
 $\rho$  - Air density  $\left[ \frac{\text{Lbm}}{\text{in}^3} \right]$   
 $c$  - Specific heat, air  $\left[ \frac{\text{watt sec.}}{\text{Lbm } ^{\circ}\text{F}} \right]$   
 $\nu$  - Kinematic viscosity, air  $\left[ \frac{\text{in}^2}{\text{sec.}} \right]$   
 $\mu$  - Efficiency of fin  
 $S$  - Surface area of a fin,  $S = 2WL$   $\left[ \text{inch}^2 \right]$

Temperature difference between air at inlet ( $\theta_i$ ) and the heat-sink ( $\theta_w$ ) is calculated using basic heat transfer equations :

$$* \theta_w - \theta_o = \frac{Q}{hS\mu}$$

$$\theta_o - \theta_i = \frac{Q}{\rho c \dot{m}}$$

$$(1) \therefore \theta_w - \theta_i = \frac{Q}{hS\mu} + \frac{Q}{\rho c \dot{m}}$$

\* For the sake of simplification ( $\theta_w - \theta_o$ ) is used here instead of Log Mean Temperature Difference. This introduces a safety factor of up to 10%

Temperature drop ( $\theta_w - \theta_o$ ) for a single fin, considering fin efficiency is taken from ref. 2. Multiplying the equation by the number of fins ( $B/(x+y)$ ) :

$$(2) \quad \theta_w - \theta_o = \frac{Q(x+y) \sqrt{\frac{2hW^2}{xK_L}}}{2hLWB \tanh \sqrt{\frac{2hW^2}{xK_L}}}$$

Heat transfer coefficient  $h$ , for turbulent flow is (Ref. 2):

$$h = \frac{0.033 K_a}{L} (R_L)^{0.8} = \frac{0.033 K_a}{L} \left( \frac{VL}{\nu} \right)^{0.8} \left[ \frac{\text{watt}}{\text{in}^2 \text{ } ^{\circ}\text{F}} \right]$$

$$\text{Flow velocity } V \text{ is : } V = \frac{\dot{m}(x+y)}{WB y}$$

Substituting  $V$  in the above equation :

$$(3) \quad h = \left( \frac{0.033 K_a \dot{m}^{0.8}}{L^{0.2} \nu^{0.8} W^{0.8} B^{0.8}} \right) \left( \frac{x+y}{y} \right)^{0.8}$$

Substituting  $h$  into equation (1) and equation (1) into (2):

$$(4) \quad \theta_w - \theta_i = \frac{AQ(x+y)^{0.6} y^{0.4}}{x^{0.5} \tanh \frac{E(x+y)^{0.4}}{x^{0.5} y^{0.4}}} + GQ$$

Where :

$$A = \sqrt{\frac{\nu^{0.8}}{0.066 K_a K_L}} \left( \frac{W^{0.4}}{L^{0.9} B^{0.6} \dot{m}^{0.4}} \right)$$

$$E = \sqrt{\frac{0.066 K_a}{\nu^{0.8} K_L}} \left( \frac{W^{0.6} \dot{m}^{0.4}}{L^{0.1} B^{0.4}} \right)$$

$$G = \frac{1}{\rho c \dot{m}}$$

In order to find the optimum heat-sink design we will look for a maximum value of  $Q$  as a function of  $x$ . Differentiating equation (4) and equating to zero :

$$\frac{\partial Q}{\partial x} = 0$$

$$(5) \quad \frac{\sinh U}{U} = \frac{5y+x}{5y-x}$$

$$\text{Where } U = \frac{2E(x+y)^{0.4}}{x^{0.5} y^{0.4}}$$

Equation (5) is a function of  $x$  and  $y$ , with  $E$  being a parameter. The function was run on a digital computer for practical values of  $E$ . The results were plotted and form the "OPENCE"  $E$  curve.

The  $E$  curve is the locus of maximum values of  $Q$  as a function of  $x$  and  $y$ . However, this does not include consideration of optimizing the design ( $x$ ,  $y$ , and number of fins) with respect to air pressure drop. This will be done next.

From ref. 2 an expression is developed for pressure drop in a rectangular pipe.

$$f = 0.046 R_d^{-0.2}$$

For rectangular pipe :

$$\Delta p = \frac{\tau 2(W+y)L}{Wy}$$

Since  $W \gg Y$ , and after rearranging :

$$(6) \quad \Delta p \sim \frac{\rho V^2 f L}{y} = \frac{0.046 \rho V^2 L}{y R_d^{0.2}}$$

This is true for a turbulent flow. In practice it is advisable to use spoilers or other means to enhance turbulences if

flow tends to be laminar.

$$R_d = \frac{V d_H}{\nu} ; V = \frac{\dot{m}(x+y)}{yWB} ; d_H = \frac{4Wy}{2(W+y)} \sim 2y$$

Where  $d_H$  is the Hydraulic Diameter, and  $R_d$  is Reynold's Number.

Substituting these into equation (6) :

$$(7) \quad \Delta p = \left( \frac{0.046 \rho \nu^{0.2}}{2^{0.2}} \right) L \left( \frac{\dot{m}}{B W} \right)^{1.8} \frac{(x+y)^{1.8}}{y^3}$$

Extracting x out of equation (7) we get :

$$x = \left[ \left( \frac{2}{y} \right)^{1/9} \frac{1}{(0.046 \rho)^{1/1.8}} \left( \frac{\Delta p}{L} \right)^{1/1.8} \frac{B W}{\dot{m}} \right] \cdot y^{3/1.8} - y$$

Or :

$$(8) \quad x = P y^{3/1.8} - y$$

Where :

$$P = \left( \frac{2}{y} \right)^{1/9} \frac{1}{(0.046 \rho)^{1/1.8}} \left( \frac{\Delta p}{L} \right)^{1/1.8} \frac{B W}{\dot{m}}$$

Equation (8) describes the relationship between x, y, and  $\Delta p$ . Since  $\Delta p$  is a given quantity for a given problem, then for each P there is a definite relationship between x and y. This was plotted on the "OPENCE" P curves. A point of intersection of the P and E curves yields values for x and y which satisfy both pressure drop and heat transfer optimization.

Ref :

- (1) P. J. Schneider, Conduction Heat Transfer, Addison-Wessley Publication Co. 1957.
- (2) A. J. Ede, Heat Transfer Principles and Pergamon Press. 1967.
- (3) C. P. Harper, Hand Book of Electronic Packaging, McGraw-Hill, 1969.



## E-3A ANTENNA PEDESTAL TURNTABLE

C. M. FRITZ

Keystone Engineering Company  
Los Angeles, California 90015

### ABSTRACT

The development of an airborne 4 point contact moment load bearing, employing hollow ring sections is described. The E-3A (AWACS) Antenna Pedestal Turntable transfers the aerodynamic loads from, and provides rotation to the 30 ft. diameter rotodome, mounted on the Boeing E-3A (modified 707) airplane. As an aircraft structure, Boeing engineering support included material selection and stress, fatigue, failsafe and finite element analyses. Keystone Engineering followed a test and extrapolation approach. Turntable moment loads cause ring prying. The resulting ring distortions affect the bearing race geometry, and ball load distribution, hence bearing life. Rotation subjects the rings to fatigue. Concentrated load points affect the limit load race geometry. Bearing performance and stiffness are traded off against weight.

### TURNTABLE DESIGN CONSIDERATIONS

Early AWACS studies by Boeing indicated the feasibility of a modular antenna pedestal turntable, termed Turntable Bearing, made of hollow sections which would fit into the lowermost center section of the rotodome, as shown in Figure (1). Of the aerodynamic and inertia loads exerted on the rotodome, a prevalent pitch moment was the most influential to affect the design.

The design was accomplished by use of extensive stress analysis and tests on the bearing rings and mountings, subject to fatigue due to rotation, and limit load and failsafe criteria.

The proportions of the Turntable Bearing are shown in Figure (2). Its construction is a hollow section outer ring with 4 outrigger leg trusses, supported by a hollow section inner ring with 4 strut support pads, and a number of closely fitted balls as rolling elements along a race periphery.

The use of 4 concentrated load input and output points in the present design satisfies a failsafe principle of

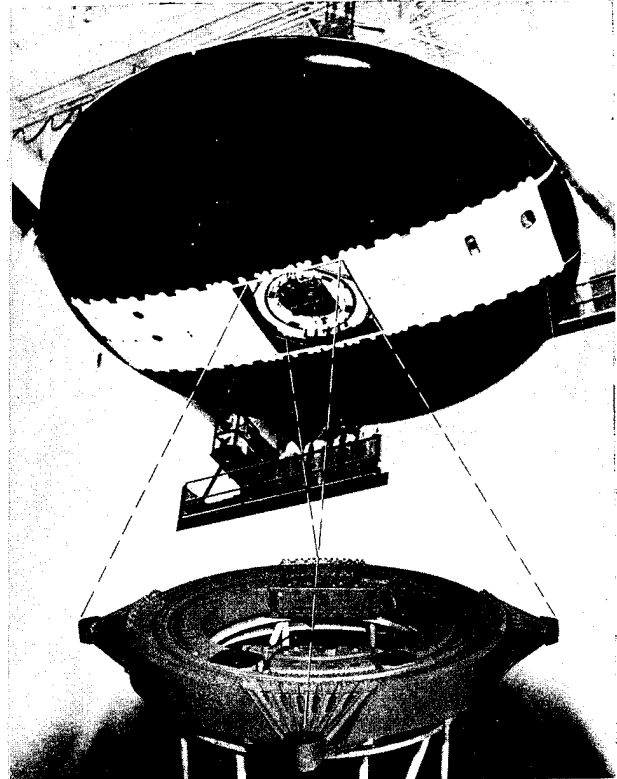


Figure 1. E-3A Antenna Pedestal Turntable with 30 Ft. Diameter Rotodome. Turntable weight is 2300 lbs. Rotation is 1/4 RPM and 6 RPM.

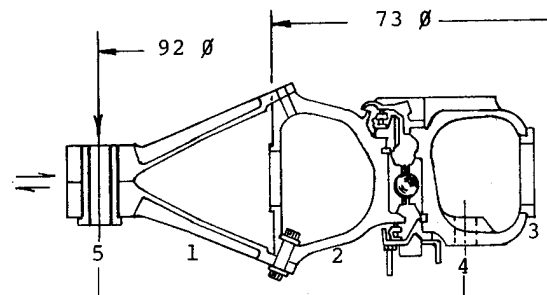


Figure 2. Cross Section of E-3A Turntable Bearing. (1) Leg Truss, (2) Outer Ring, (3) Inner Ring, (4) Strut Support Pad, (5) Shear Bushing

redundant load paths used on aircraft. Should one load path from an outrigger leg to a strut support pad fail, the 3 remaining load paths must be able to carry 92% of each type of limit load.

The Turntable must perform as an aircraft structure by transferring aerodynamic loads. Simultaneously it must provide rotation to the rotodome by means of 2 redundant pinions driving an internal ring gear on the outer ring.

Looking at a more conventional alternate Turntable Bearing, employing, for instance, flanged races with circular bolt patterns, a more homogeneous load path would result. However, the sections and weight required to support such races and a number of other factors affecting integral bearing performance would then be separated from the now modular bearing assembly, and be shifted to the rotodome and strut support structures instead.

The E-3A Turntable may be considered a rolling bearing where the rings act as their own bearing housings.

The manner in which the Turntable is loaded is depicted in Figure (3). Two limit load conditions stand out, a 235 kips eccentric thrust load, and a 8100 inch kips negative pitch moment load combined with thrust.

These two load conditions dictate the structural Turntable design. Required was an ultimate load factor of 1.5 times limit load. For the outrigger legs on the outer ring, a truss design evolved, Figure (2). The pitch moment direction

remains fixed relative to the airplane axis and thus the inner ring. The outer ring continuously rotates under a pitch moment load of fixed direction.

In Figure (4), 2 outer ring azimuth orientations are shown, 2 references used throughout the stress and computer analyses, and the various strain-age, ball load, stiffness, torque and race geometry tests. These 2 positions are termed "leg forward" and "leg at 45°". The latter represents the shortest and most rigid load path through the bearing, from a leg to a strut support.

The pitch moment is the prevailing load in nearly all operating and limit load conditions. It is associated primarily with negative lift, i.e., thrust, while rotodome drag, side load and roll moment play a lesser part. Such bearing moment loads necessitate a different design aspect, because they introduce large ring bending deflections. The ball contact deflection, usually a measure for bearing stiffness, becomes negligible.

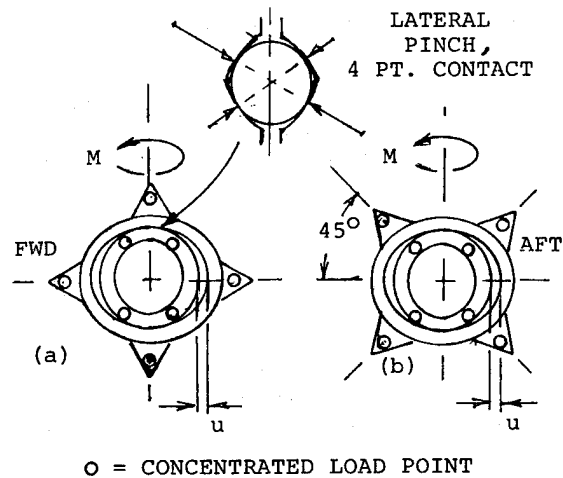


Figure 4. Outer Ring Azimuths. (a) leg forward, (b) leg at 45°.  $u$  = race separation due to pitch moment ( $M$ ). Pinch occurs at lateral center line.

In Figure (5a) the effect of the radial ring deflections is singled out. As a pitch moment, couple ( $P \times C$ ) is applied, the rolling elements, here balls, contained by the race groove curvatures, act like a cam device at the 2 regions of highest ball loads, i.e., forward and aft. A spread ( $u$ ) occurs between the rings, the outer ring being elongated, the inner ring being squeezed elliptically. In Figure (5a) it is assumed that the rings remain plane. The outer ring plane in effect will become tilted as indicated in Steps (v).

The prying on the bearing rings longitudinally results also in pinching action laterally, Figure (4).

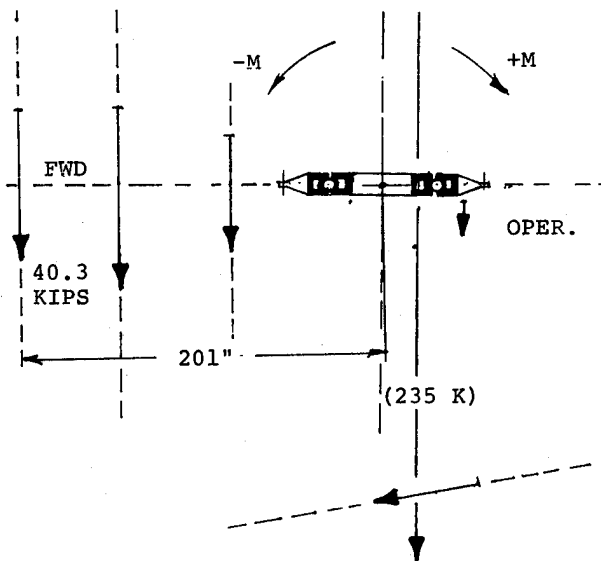


Figure 3. Static Limit Loads. A bearing load combination can be shown by a single load line. Direction, position and size of each load represents a limit load condition. Worst Limit Moment is,  $-40.3 \times 201 = -8100$  inch kips.

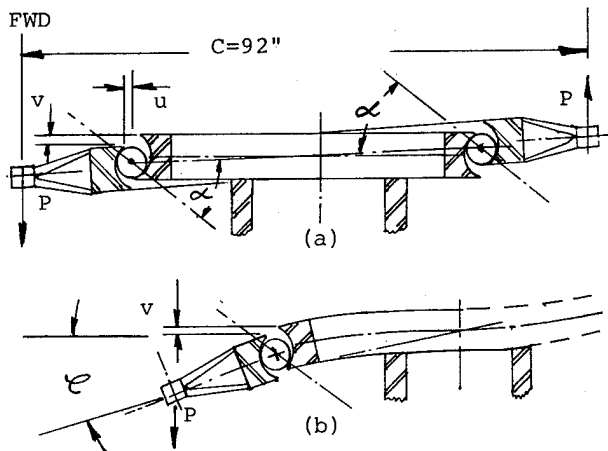


Figure 5. Deflection Effects.  
(a) Radial deflections alone, -tilt occurs of the outer ring plane.  
(b) Out-of-plane ring deflections are superposed.

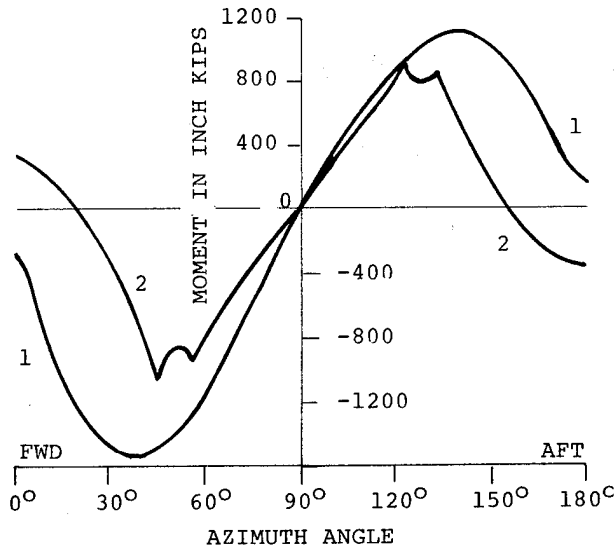


Figure 5c. Ultimate out-of-plane bending moments for lead forward position. (Boeing Finite Element Analysis)  
(1) = Outer Ring, (2) = Inner Ring

Displacements ( $u$ ) and ( $v$ ), Figures (5 to 7), are entirely caused by radial ring deflections. They affect the bearing race geometry, specifically the ball attitudes or contact angles. The contact points of the ball with the races shift with the moment load variations. For limit moment load this shift is critical. The contact ellipse (Figure 7) then extends beyond the race land. This loss of support area is cause for race brinelling.

When the out-of-plane deflections, Figure (5b) of the bearing rings are superposed to the tilt caused by the

radial deflections, a composite line of flexure of the outer ring can be visualized, and a separate inner ring line of flexure, relative to the horizontal plane. ( $\phi$ ) is the angular bearing deflection.

With ring structures of sufficient stiffness the advantage of the four point contact bearing, Figure (6), with self aligning balls, contained between 4 races, is simplicity. Balls and races arranged in this manner can carry the upload as well as the download between the rings, while for instance rollers with inherently larger load capacity would require 2 sets of rollers, and be less suitable with large ring deflections.

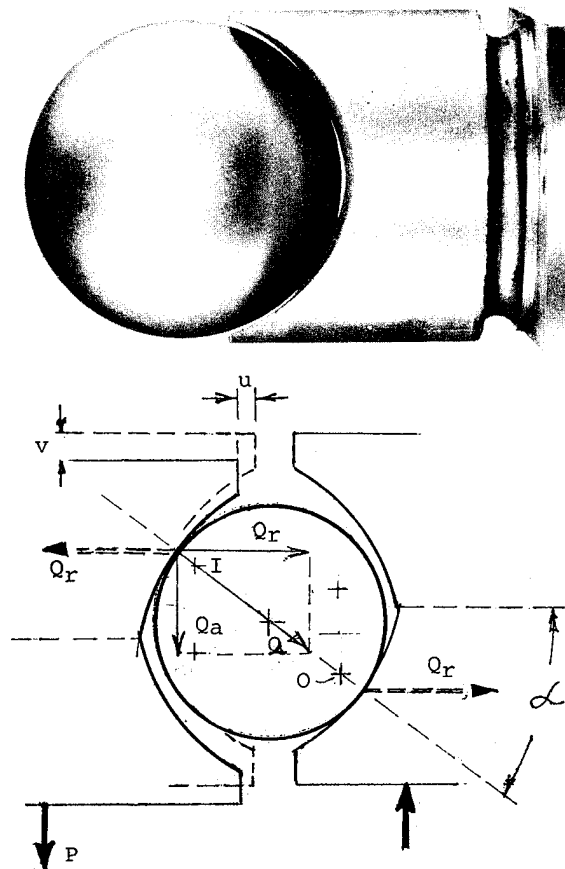


Figure 6. 4 Point Contact Bearing. Deflection ( $u$ ) due to bearing moment load causes 2 point contact. Top photo shows race profiles at inner race loading plug.

For comparison with the lines of flexure indicated in Figure (5), Figure (5c) singles out the interaction of the 2 out-of-plane-ring bending moments for ultimate pitch moment load.

As the outer ring rotates, it progresses through a standing wave of combined stresses derived from out-of-plane

bending, radial bending, torsion and race wall bending of approximately sinusoidal shape. Stressed points of the outer ring and the leg trusses undergo one cyclic stress reversal per bearing revolution.

The definition of uncertainties affecting the design were then:

- Stiffness, and therefore weight required to obtain a satisfactory race geometry for sufficient bearing life capacity, and avoidance of excessive contact ellipse spillover at limit loads, and simultaneously, also to meet the moment stiffness requirement of the Turntable structure.
- A safe fatigue stress level at operating load conditions for the outer ring with appropriate material and heat treatment selection in view of the 9 million fatigue cycles required.
- A ball load distribution which combined with the selected race material, its heat treatment and possible race geometry limitation would give a 30000 hours bearing life at a specified reliability level.

The deflection behaviour of the (2) hollow rings with interacting ball loads and eccentric outer ring leg load is not readily calculated. A test and extrapolation approach was taken.

Keystone Engineering Company had previously designed and built hollow section moment load bearings of approximately 15" diameter for airborne radar. The problem of achieving a satisfactory moment stiffness for a low weight design had been explored. It was also found

that excessively close race groove radii were not compatible with large ring deflections.

For the E-3A, then AWACS, an early engineering test bearing was built employing 1020 steel (35 KSI yield point), solely for the purpose of studying the effects of the moment load deflections of the hollow section rings onto the race geometry and later the ball load distribution. Its structure is shown in Figure (8).



Figure 8. Engineering Test Bearing. Built to study ring deflections and ball load distribution.

Different moment loads combined with thrust were applied with hydraulic cylinders. The resulting ring deflections (u) and (v) at selected points of high ball loads were measured by means of dial indicators. These data were then extrapolated by a method graphically illustrated in Figure (9).

#### RING DEFLECTIONS, RACE GEOMETRY

In diagram of Figure (9) the distance IO was laid out to a convenient scale at the design contact, angle of  $\alpha_o = 35^\circ$ .

$$IO = 2(\text{Race Groove Radius} - \text{Ball Radius}) \\ = D(2f - 1)$$

Points (u) and (v) obtained from test were plotted and a contact angle line drawn (result  $\alpha = 47^\circ$ ). The test true zero point (Z) is found by drawing the best fitting circle with center (I) through the test points. The known test moment ( $M = 1280$ "K") may be plotted on the ordinate through point (I) to a convenient scale.

The moment load for other contact angles after drawing line ( $\alpha = 65^\circ$ ) and measuring the corresponding (u) from zero point (Z), is extrapolated by calculation using the relationship,

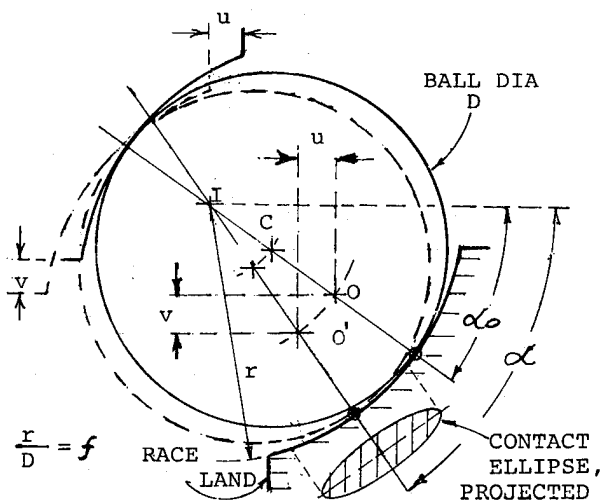


Figure 7. Race Geometry and Contact Angle Change. Race groove radius (r) is exaggerated and is actually only 53% of the Ball Dia (D). - Contact deflections would flatten the ball and increase distance IO'.  $IO = D(2f - 1)$

$$\frac{M_2}{M_1} = \frac{u_2}{u_1} \times \frac{\tan \alpha_2}{\tan \alpha_1}$$

Subscript (1) = test  
(2) = extrapolation

The diagram assumes that for the present Turntable the ball deflections are not significant with respect to the race geometry. Other relationships may be derived from Figures (6) and (7) as was the above, based on proportionality between ( $Q_a$ ) and ( $M$ ), and ( $Q_r$ ) and ( $u$ ).

In the case shown in Figure (9) a 30% increase in ring stiffness was required if the desired race compliance of  $f = .53$ , shown by distance IO, was to be maintained. It meant that the hollow section walls had to be thickened by 30% with corresponding addition in weight, however, with the added advantage of increased Turntable moment stiffness.

Figure (9) also demonstrates the effect of distance IO. With ( $u$ ) remaining equal, ( $\alpha$ ) would change rapidly if distance IO was very short (smaller race groove radius = high compliance), desirable from the bearing capacity point of view, but not desirable from the point of view of contact ellipse spillover.

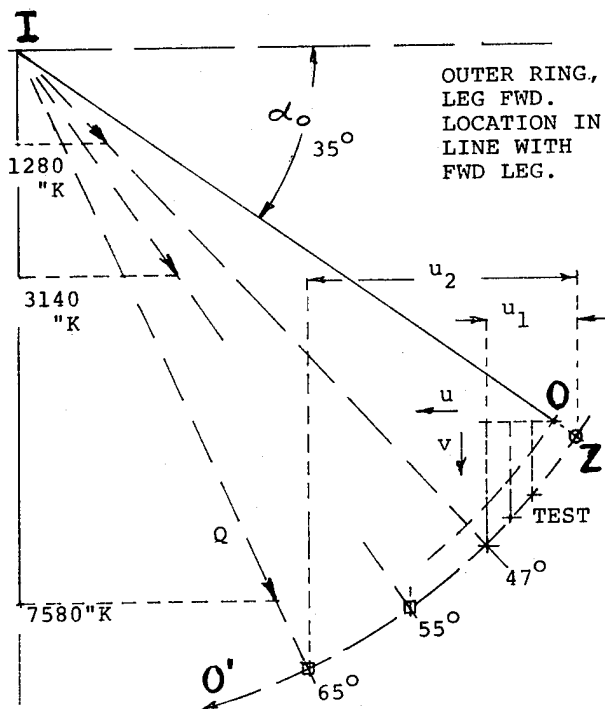


Figure 9. Extrapolation of Moment Load at 65° Contact Angle on Engineering Test Bearing.  
 $\alpha = 47^\circ$ ,  $M = 1280$ "K Test  
 $\alpha = 65^\circ$ ,  $M = 7580$ "K Extrapolated.  
Arrows Indicate Relative Ball Loads.

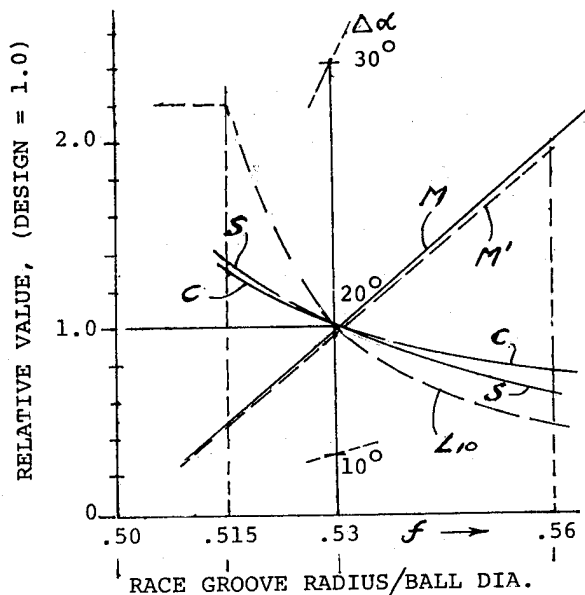


Figure 10. Effect of race groove compliance ( $f$ ) on bearing performance. Design = 1.0.

$M$  = Moment carried at  $20^\circ$  contact angle change,  $1.0 \approx 5000$ " kips  
 $M'$  w/contact defl.  
 $C$  = dynamic cap.,  $1.0 \approx 1800$ " kips  
 $S$  = static cap.,  $1.0 \approx 13000$ " kips  
 $L_{10}$  calc. brg. life,  $1.0 \approx 27$  mill. revs

This trade-off is illustrated in Figure (10).

A convenient criterion for the effect of different race curvatures is the moment load the bearing will carry at  $\Delta\alpha = 20^\circ$  contact angle change at the highest loaded ball.

The present design corresponds to ordinate 1.0 at  $f = .53$ , or race groove radius of 53% of the ball diameter.

The moment load carried increases with the race curvature ( $f$ ). Line ( $M$ ) considers ring deflection only, Line ( $M'$ ) includes ball deflection, both at constant  $\Delta\alpha = 20^\circ$ . Curves ( $C$ ) and ( $S$ ) show the decrease in dynamic and static bearing capacities with increasing race curvature ( $f$ ). Line ( $L_{10}$ ) is the bearing life expectancy, proportional to ( $C$ )<sup>3</sup>.

#### BALL LOAD DISTRIBUTION

To clarify the uncertainties with regard to the ball load distribution, an impact device was used, Figure (11), combined with measurement of the sliding distance of the loaded balls. When several tests were averaged the results indicated that the peak ball load occurred in "Leg at  $45^\circ$ " orientation, in line with the leg truss. The magnitude of the ball loads could be estimated by equating

the sliding distance reciprocals to the known bearing input load. The relation is based on:

$$\text{Energy} = \text{Coeff. of Friction} \times \text{Sliding Dist.} \times \text{Ball Load}$$

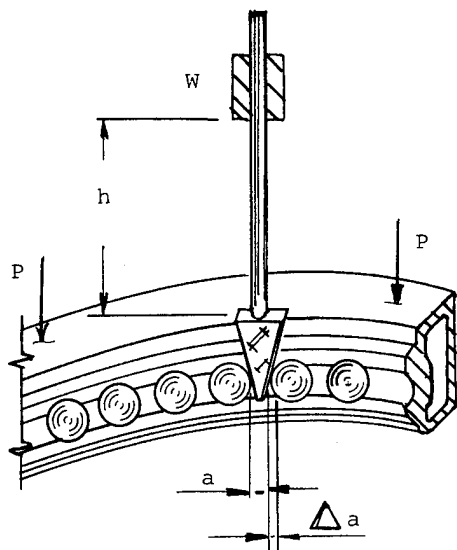


Figure 11. Ball Load Sliding Test. While load (P) is maintained on the bearing, a weight (W) is dropped a fixed height (h). 2 loaded balls slide distance  $\Delta a$ ; its reciprocal is a relative measure of the Ball Load. Several tests must be averaged.

Additional ball load distribution tests were performed during the brass board phase. These tests employed known methods of chemical etching (foot print tests), first by exposing a copper plated inner race while the ball loads were maintained, to gaseous ammonia, leaving the contact ellipse images on the race. A second method employed silver plated balls, exposed to  $\text{SO}_2$  gas.

From the known race groove radius and measured length of the contact ellipses, the apparent ball loads could be calculated and adjusted by equating them to the known input load of the bearing.

Figure (12) is a polar diagram of ball loads, extrapolated for the ultimate pitch moment load condition. It is based on ellipse images at a lower load level.

## FATIGUE

With application of stress coat, later implemented with strain gage readings it could be shown that the outer ring and the leg trusses displayed a safe fatigue stress level for the then required brass board Turntable life. A later

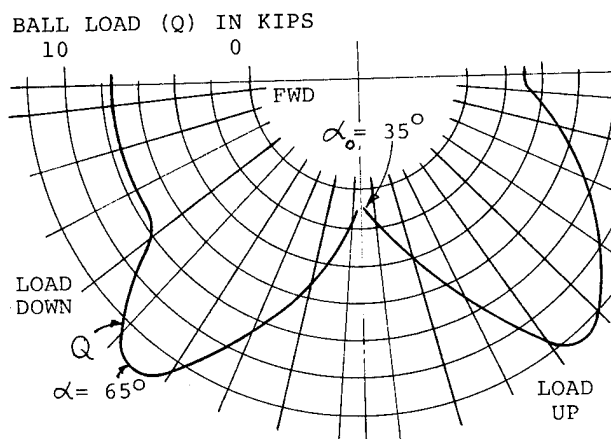


Figure 12. Ultimate Ball Load Distribution (Q) for Leg at  $45^\circ$ .  $\alpha = 65^\circ$ , Ultimate Contact Angle.  $\alpha = 35^\circ$ , at Lateral Pinch.

change in the rotodome angle of attack resulted in reduced operating loads but in higher limit loads.

The selection of the ring material for the brass board Turntable fell on vacuum de-gassed 8620 steel which could be welded, the race sections of which were gas carburized to form an integral race and ring combination. For the DDT&E Turntable the 8620 steel was abandoned for reasons of dimensional control, in favor of a 15-5 precipitation hardening steel for the ring bodies. Each hollow section ring consists of 2 rolled ring forgings. The joining of the forgings, after preliminary profiling and fitting, requires a specialized welding process. The 2 circumferential welds per ring are of x-ray quality to meet the fatigue requirement.

Figure (13), which is primarily a bearing wear damage spectrum, equally reflects the fatigue damage due to the different operating load conditions. The total fatigue damage criterion was based on Miner's Rule, with

$$\sum \frac{4n}{N} < 1.0$$

The fatigue analysis method employed gross area stress comparison with S/N curves, adjusted for the appropriate Boeing fatigue performance indices.

## LEG TRUSSES

The same fatigue criteria were applied to the 4 leg trusses of the outer ring. The material selected here is 4340 steel of electro slag remelt quality. Identical forgings are used for the upper and lower leg truss panel.

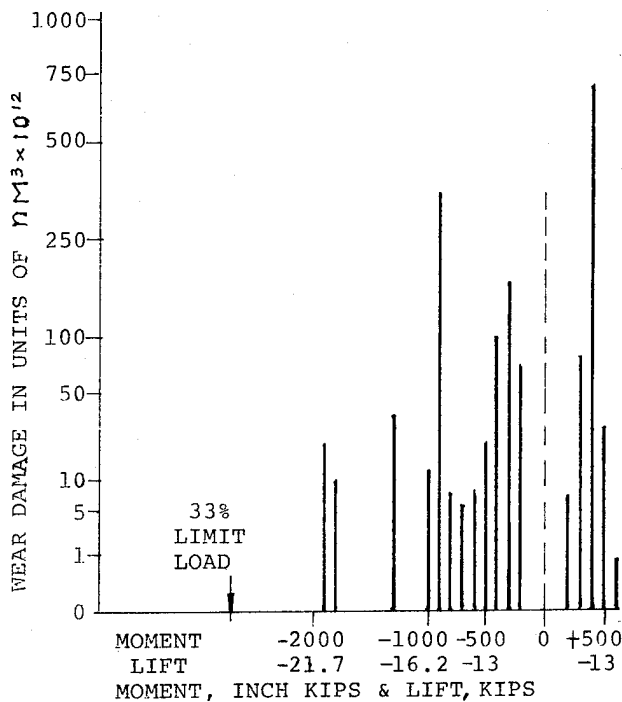


Figure 13. Wear Damage Bar Chart for Individual Operating Loads with Respect to Bearing Life. Chart is also indicative of the structural fatigue damage.

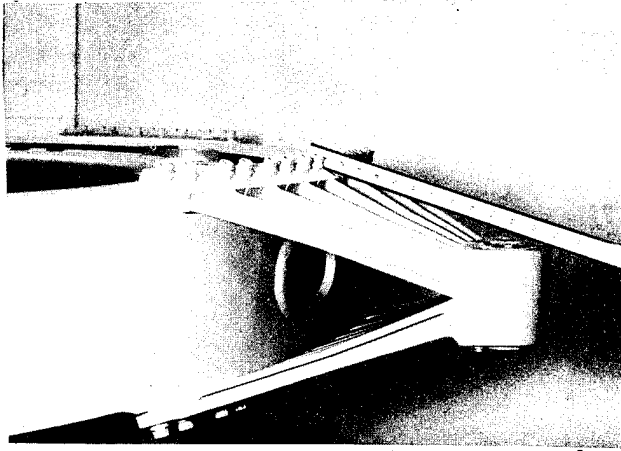


Figure 14. Leg Truss with Access Hole for Bolts.

The leg trusses are influenced by the outer ring deflection as it rotates, to the extent that upper and lower leg panels must be allowed to breathe.

For this reason they were designed as shown in photo, Figure (14), solid around the leg hub but opening up into a fan consisting of 7 different load paths towards the 14 ring attachment bolts. Each member is T-shaped and acts alternately as a column or as a tension member as the ring progresses through one revolution. Near the center of the shrink

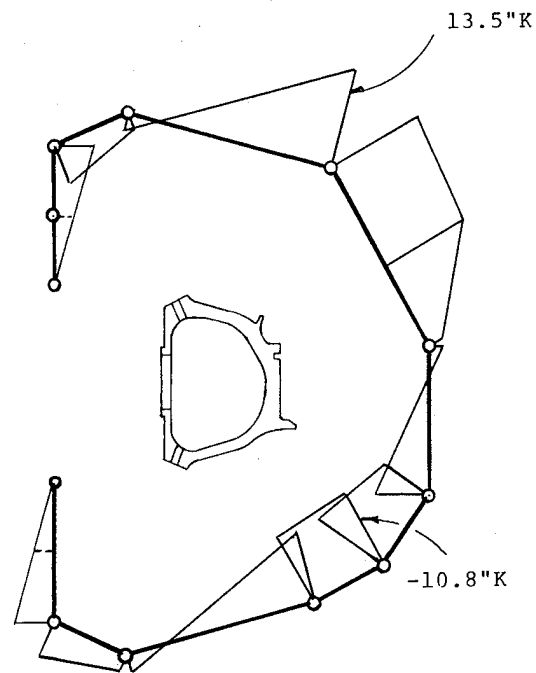


Figure 15. Wall Bending Moments (Ultimate), of Outer Ring Section at Leg Truss Access Hole. (Boeing Finite Element Analysis)

fitted shear bushing, node points must be visualized from where the 7 neutral axes fan out, approximately tangential to the surface of a cone whose vertex is at the bearing rotation axis.

To facilitate the assembly of the 14 bolts of each leg panel, an access hole through the outer ring wall, at each leg truss is provided. The disrupted cross section of the outer ring is cause for maximum wall bending moments as indicated in Figure (15). This wall bending exists at any transverse section of the ring and is caused by shear flow due to torsion.

#### BEARING LIFE

If a ball bearing whose revolution life is

$$L = \frac{C^3}{P^3} \text{ Revs.}$$

is exposed to (n) actual revolutions, then the percentage wear damage is

$$\frac{n}{L} = \frac{nP^3}{C^3}$$

where  $(nP^3)$  is the actual wear damage. The total wear damage for the present individual moment loads  $M_1, M_2, \dots$ , is

$$n_1 M_1^3 + n_2 M_2^3 + \dots = \sum (nM^3)$$

are the individual No's of revolutions.

$M_1$ ,  $M_2$ , are equivalent moments adjusted for lift. They, and the basic dynamic moment capacity ( $M_B$ ), as found in Figure (19) give the bearing life,

$$L = \frac{M_B^3}{\sum (nM^3)} \times \sum (n)$$

Figure (13) illustrates in bar chart form the magnitude of wear damage for each operating condition. The operating loads are below the 1/3 limit load level indicated. Both positive and negative moment loads occur combined with negative lift axial loads. The bar chart ordinates are plotted on a cubic scale for convenience because the No's of revolutions associated with each load vary widely.

Measured with a linear scale the bar heights would represent individual relative loads, all with identical No's of revolutions, which have the same effect as the actual loads. For instance the relatively low nominal moment load condition of +400 inch kps shows the greatest bar height, because of the large number of 4.8 million revolutions at that load level.

The material of the race bands is 440 C corrosion resistant steel. Specially developed heat-treat and stress relieve procedures are used. Figure (17) shows the inner ring race insert at the ball loading plug hole. Because of the hole diameter, there is a loss of cross sectional area of the race insert. The shrink fit tension in the hard race material would be sufficient to cause crack propagation due to stress concentration at the hole. For this reason special fracture toughness tests were performed by Boeing. Consequently, the race hardness which is RC59 minimum was reduced by tempering the race in the vicinity of the hole. The loading plug hole is oriented so that the ball load peaks do not fall into that region.

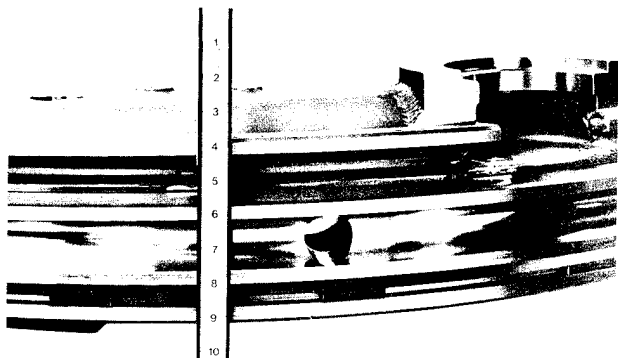


Figure 17. Inner Race Insert Band Showing Loading Plug Hole. To the right is the pinion drive cavity.

## GEARS

The pinion drives interface by means of internal spline shafts with the power input packages supplied by others. The internal gear drive of the Turntable is a relatively low speed drive providing 1/4 RPM or 6 RPM rotation. The pinch at the lateral center lines of the rings, Figure (4), provides 2 regions of negligible torsional and radial movement. These regions are used for mounting the 2 redundant drive pinions into 2 cavities Figure (17) of the inner ring, in 2 neutral zones relative to the pitch moment.

The internal ring gear follows the lines of flexure of the rotating outer ring to which it is mounted. However, its point of mesh with the pinions remains in this neutral zone.

The 10 D.P. gear tooth proportions, the face width and the heat treatments were, besides gear ratio necessity, dictated by the bearing torque and friction of the 2 carbon seals. There are also aerodynamic torque fluctuation in the rotodome. The gear drive also has to meet a maximum yaw moment requirement due to rotodome inertia. The 13,500 and 4,500 hour minimum replacement periods for ring gear and pinion as part of the overall reliability requirement, call for good surface durability. For this reason the pinion teeth are crown shaven to provide a central tooth loading pattern at the ring gear face, should tooth misalignment occur.

The gear set includes an anti-backlash azimuth readout gear, preloaded by means of a torsion bar.

Special flexible carbon seals were developed to contain the MIL-L-7808 gear and bearing lubricant, and to protect the bearing from outside contamination. The lower seal also forms a lightning path through the Turntable.

The aluminum lower seal retainer simultaneously acts as a dry sump for the lubricant. 2 reservoirs are mounted into the inner ring cavity, one for each redundant drive unit and its associated power input package. Figure (1)

## BEARING TORQUE.

In the present bearing the torque is partially due to gross sliding. Two of the reasons are,

- Different Contact Angles of Operation. Of a set of balls of the same diameter, all balls cannot roll at the same speed on a diversity of conical contact surfaces presented by different contact angles. For large ratios of ball pitch diameter to ball size this effect is minimized. Balls tend to retard the ball separator with increasing ball load.
- 4 Point Contact. A ball cannot roll without sliding on (2) surfaces inclined



to each other which belong to the same race. A pure radial load on the 4 point contact bearing is undesirable because of high torque.

Figure (18) depicts the total bearing drive pinion torque as registered by a recorder during an acceptance test.

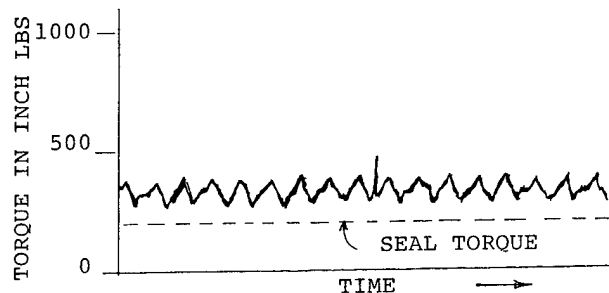


Figure 18. Torque Fluctuations at Drive Pinion, for loads  $M = 400$  Kips, Lift = -13 Kips

#### BASIC DYNAMIC MOMENT CAPACITY ( $M_B$ )

The method of determining ( $M_B$ ) and the equivalent moments ( $M$ ) used in the life formula is indicated in Figure (19).

(a) Shows 3 sinusoidal distributions on rigid rings. (b) Shows 2 actual distributions for the present operating load combinations of moment and lift on flexible rings with varying contact angles. (c) Indicates the 2 angular contact race pairs loaded with radial loads ( $P$ ). Each cubic mean radial load of distribution (b), corresponds to an equivalent radial load of distribution (a), permitting calculation of the race pair lives with standard angular contact bearing formulae. The statistically combined life of the 2 race pairs gives the necessary life or wear damage relation, continuous, if repeated for a sufficient number of moment and lift combinations.

The radial balance between ( $P_1$ ) and ( $P_2$ ) in Figure (19b) is possible with prevalent moment because of the difference in contact angles.

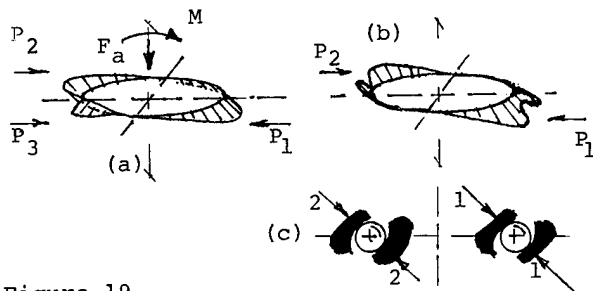


Figure 19.  
(a) Sinusoidal Distribution for Prevalent Moment ( $M$ ) and Thrust ( $F_a$ ).  
(b) Actual Distribution.  
(c) Race Pairs (1 - 1), (2 - 2).  
( $P$ ) = Equivalent Radial Loads

#### STATIC LOAD, FATIGUE LIFE AND BEARING WEAR LIFE TESTS.

The Turntable as part of the over-all rotodome and fuselage strut system underwent ultimate load tests at the Boeing facilities. Aerodynamic and inertia load levels were applied to the surface of the rotodome by means of everner systems.

Accelerated fatigue life tests were performed by Boeing. The Turntable installed in the combined rotodome and fuselage strut assembly was tested for 3 life times (90,000 hours). The rotation was simulated by progressively revolving the loads of the fixed everner system at 80 RPM, by means of computer controlled servos. Cyclic pitch moments were included in the fatigue test program. One lifetime of the program was performed with artificial flaws added to critically stressed points of the Turntable leg trusses and the outer ring. The termination of the test included the application of the limit pitch moment in all directions.

Keystone Engineering Company is running an accelerated test (12 RPM) for wear of one life time duration (30,000 hours). This wear life test, besides the actual bearing life, included the qualification of the pinion and gear drive, and the determination of wear rates of the flexible carbon seals. The Turntable is disassembled every 4500 hours to study the wear progress. Cyclic pitch moments and the loads of Figure (13) are applied by means of computer controlled servos.

The arrangement of the available ring material into hollow sections to obtain maximum moments of inertia and stiffness for the curved ring beams has limitations. The thinner the section walls, the greater is the distortion of the section shape under load. Bulkhead stiffeners are impractical and give rise to stress concentration.

The position of the leg truss load pickup point approximately equalizes the moment and torsion effects on the outer ring.

For the same pitch moment stiffness, an outer ring with a smaller diameter at the section neutral axis would require less weight. Outer and inner ring neutral axis diameters however were dictated by the ball path diameter necessary for the bearing capacity.

# SHOCK MOUNTS FOR SHIPBOARD RADAR PEDESTALS AND STABLE PLATFORMS

LEROY FUSS

Scientific-Atlanta, Incorporated  
3845 Pleasantdale Road  
Atlanta, Georgia 30340

## ABSTRACT

The need for and implementation of shock and vibration isolation of antennas and stable platforms is related to accuracy, the force and motion environment, control system performance and protection of sensitive instruments. It is concluded that an isolator must be stiff rotationally to assure accuracy and performance and must be flexible translationally to accommodate shock and vibration motions. A linkage suspension is proposed which has these characteristics, and its force-displacement and force-velocity relations are derived. Rotational stiffness, weight and snubbing are considered.

## INTRODUCTION

Radars, tracking pedestals and stable platforms for naval ships must accurately point their antennas and execute tracking motions while sustaining wind forces, acceleration torques, ship's vibrations and shocks from nearby explosions.

A representative specification for a stable platform requires that a five-meter reflector be pointed at a stationary satellite within a total error of 0.5 degree in a 70-knot wind during ship's motions. Of this permissible error, the control system static and dynamic error allowance is 0.3 degree, leaving an allowance of 0.2 degree for structural deformation.

Naval ship vibration and shock environments are reflected in and tested for according to Military Standard 167, Mechanical Vibrations of Shipboard Equipment (1) and Military Specification 901, Requirements for Shock Tests, High Impact, Shipboard Machinery, Equipment and Systems (2). Citations from these documents applicable to shipboard radars, other antenna systems and stable platforms are given in the appendix.

With a stable platform using platform-mounted level sensing instruments, shock and vibration isolation is desirable and may be necessary. Remarks on this need are as follows(3):

"To inertially stabilize an antenna to take out pitch, roll and yaw motions, inertial angular motion sensors may be mounted in the antenna frame. These sensors are used as feedback by the antenna drive servo-motors to counter angular motions in inertial space. Sensors used for this application are usually rate gyroscopes, rate

integrating gyroscopes, and/or angular accelerometers. For gyroscopes, construction consists of a spin motor and momentum wheel mounted in bearings designed to operate at speeds of typically up to 12,000 rpm. The effect of linear vibration on these devices is two-fold. First, linear vibration causes radial loading on the precision bearings resulting in accelerated wear and premature degrading of the output signal. The magnitude of the radial loading depends on the displacement, the frequency of vibration, and the mass of the spin motor and momentum wheel. Note that vibrational acceleration amplitude and, therefore, radial loading increases as the square of the vibration frequency assuming constant vibrational displacement amplitude. A second effect is due to dynamic imbalance in the gyroscope. If dynamic imbalance exists, linear vibration when superimposed on angular motion can result in a mixing of the two input signals creating erratic output along with possible bias errors indicating erroneous angular rates. Such erroneous output signals would result in antenna drift about the desired pointing orientation."

"In conjunction with angular motion sensors, a second class of sensor is used to complement the stabilization problem. Level sensors or inclinometers are typically mounted on the pedestal to determine inclination from the horizontal. While inertial rate sensors are used for short term stabilization, inclinometers are used to seek the horizontal and provide for long term stabilization. These sensors are typically constructed as force-balanced linear accelerometers. A pendulously-mounted seismic mass is suspended by needle bearings such that linear acceleration in the appropriate direction results in a deflection torque on the pendulum. A torquer motor and deflection sensor is used to counter the deflection. Output from the device is a signal proportional to the required torque from the motor to completely counter the acceleration-induced torque. This device is susceptible to linear vibration in two ways. First, as with the gyroscope, linear vibration induces radial loading on the suspension, resulting in accelerated wearout of the bearing suspension. Second, vibration in its sensitive direction can result in saturation of the torquer motor and, therefore, the output signal."

"The physical structure of the antenna pedestal makes these sensors not as susceptible to

angular vibration because of the inherent decoupling provided by the antenna pedestal gimbals to rotational motion."

Protection of other sensitive antenna-mounted instruments such as digital angular encoders and indeed the saving in cost of structure may justify the use of isolation.

The accuracy requirement here and in general is rotational; because target distances are great, small translations of the antenna are not critical in the pointing accuracy. In contrast, the shock and vibration environment is translatory; all imposed motions and loadings in the test specifications are linear. The small structural compliance to moment needed to control rotations under load is also necessary to insure a servo control bandwidth sufficient to provide required tracking and slewing performance. This compliance is difficult or impossible to achieve with conventional shock mounts.

A linkage shock and vibration isolation suspension for antennas and stable platforms is proposed which provides both a small compliance to rotation and damped relative translation between the ship and the antenna or platform. Thus, the system is "hard" in rotation to give pointing accuracy and servo bandwidth and "soft" in translation to protect from shock and vibration. Two papers (4,5) which discuss decoupling of translation from rotation appear not to address the need for small rotational compliance.

#### DESCRIPTION OF SUSPENSION

A device which restrains rotation but which permits translation is the double parallelogram linkage (figure 1).

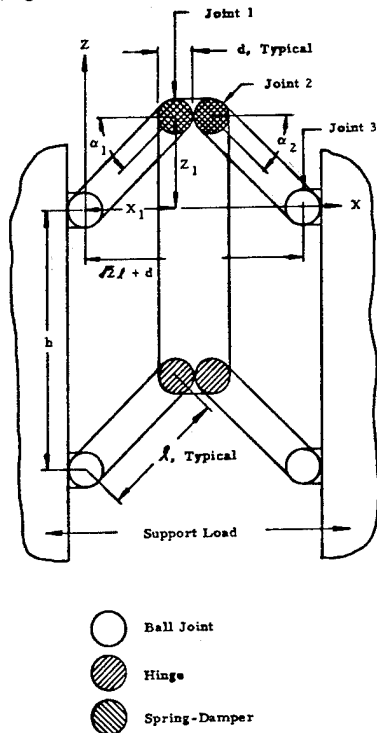


FIGURE 1, LINKAGE

This is a mechanism restraining moments normal to its plane and permitting two degree of freedom motion in its plane. Ball joints at the load and the support permit the linkage to rotate about the Z axis. Each combination hinge, torsion spring and damper passes torque about its Y-parallel axis from link to link while preventing rotations about X- or Z-parallel axes. Load imposed Y-moments are transmitted to the support by axial loads in the members. Thus, the linkage is stiff to Y-moments, but provides a damped compliance to forces in the X Z plane passing from the load to the support.

The parameters are:  $d$ , the allowance for the diameter of the hinge-spring-damper combination or for a hinge or ball joint;  $l$ , the side-link length;  $h$ , the tie-link length; and  $\alpha_1$  and  $\alpha_2$ , the end-link angles. In the static position,  $\alpha_1 = \alpha_2 = \pi/4$ .

The torsion springs might be elastomeric springs which have a linear torque-rotation angle relation in the range of rotations required. The damper might be a rotary viscous damper or a Coulomb damper enclosed for protection from the environment. To stiffly restrain any couple in three-space, three of these linkages are required. Normals to their planes must be non-parallel and are best arranged to be orthogonal in the static position. Such an arrangement is shown in figure 2. The linkage designated X has a normal to its plane in the static position parallel to the X axis and the linkages designated Y and Z have normals parallel to Y and Z correspondingly. Any moment can be resolved into three components parallel to the linkage normals and, since each linkage reacts a component, the moment is reacted with the high degree of stiffness characteristic of the individual linkages. Any

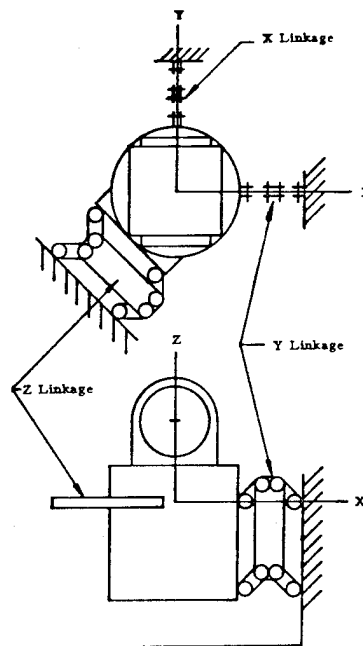


FIGURE 2, SUSPENSION

force can be resolved into three components, each parallel to a linkage plane. By adjustment of the magnitudes of the linkage moments, these forces can be applied to the upper (in figure 1) load-link joint so that this set of three force-moment combinations is statically equivalent to the net force and moment at the load.

Since the compliance to moment at each linkage is small the rotational part of the load displacement can be separated from the translational part for purposes of dynamical analysis. The rotational natural frequencies are at least one order of magnitude higher when compared to the translational ones. This is to say that the two motions can be treated independently with small error. Further, when the force and translation are separated from the moment and rotation in this way, neither the position of the center of gravity nor the size of load affects the force-translation behavior. With rotations suppressed, the elastic center can be said to be at infinity.

#### SUSPENSION KINEMATICS, STIFFNESS AND DAMPING

In the following, geometric nonlinearities are retained while a linear spring moment-rotation law is assumed for the hinge-spring joints. Since there are six link-force components and only three coordinates, the linkage is three times statically redundant. For this reason the force-translation relation is formulated in terms of translation components and yields a stiffness rather than a compliance matrix.

Let the translation of the load be

$$\bar{\delta} = \delta_x \hat{i} + \delta_y \hat{j} + \delta_z \hat{k}$$

in global (figure 2) coordinates. Then the displacements of the load-link joint (joint 3) of each linkage in local (figure 1) coordinates are

$$X_x = \sqrt{\delta_x^2 + (\sqrt{2}l + d - \delta_y)^2}, \quad Y_x = 0, \quad Z_x = \delta_z$$

$$X_y = \sqrt{(\sqrt{2}l + d - \delta_x)^2 + \delta_y^2}, \quad Y_y = 0, \quad Z_y = \delta_z$$

$$X_z = \sqrt{(l + d/\sqrt{2} + \delta_x)^2 + (l + d/\sqrt{2} + \delta_y)^2 + \delta_z^2},$$

$$Y_z = 0, \quad Z_z = \delta_x/\sqrt{2} - \delta_y/\sqrt{2}.$$

Subscripts on local displacements indicate linkage. In each linkage the displaced location of joint 1 (figure 1) in local coordinates is

$$Z_1 = Z/2 + [(X - d)/2] \sqrt{4l^2/[(X - d)^2 + Z^2] - 1}$$

$$X_1 = \sqrt{l^2 - Z_1^2}$$

Joint 2 is located with respect to joint 1.

$$Z_2 = Z_1$$

$$X_2 = X_1 + d$$

Rotations at joints 1 and 2 in terms of  $X$ ,  $Z$ ,  $X_1$ ,  $Z_1$ ,  $X_2$  and  $Z_2$  are

$$\tan \Delta \alpha_1 = \frac{Z_1 - X_1}{Z_1 + X_1}$$

$$\tan \Delta \alpha_2 = \frac{(Z_1 - Z) + [X_1 - (X - d)]}{(Z_1 - Z) - [X_1 - (X - d)]}$$

The springs are assumed to be linear; moments at joints 1 and 2 are

$$M_1 = K \Delta \alpha_1$$

$$M_2 = K \Delta \alpha_2$$

where  $K$  is the torsional spring constant. If Coulomb dampers are also used at these joints, their moments are

$$M_1 = C \operatorname{Sgn} \dot{\alpha}_1$$

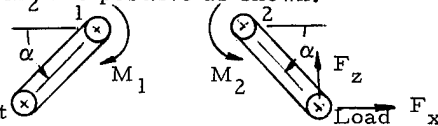
$$M_2 = C \operatorname{Sgn} \dot{\alpha}_2$$

where  $C$  is the constant torque of the damper resisting the change in angle. If rotary viscous dampers are used, they obey the law

$$M_1 = D \dot{\alpha}_1$$

$$M_2 = D \dot{\alpha}_2$$

where  $D$  is the viscous torque constant.  $M_1$  and  $M_2$  are positive as shown.



Support The linkage force components,  $F_x$  and  $F_y$ , at

$$\begin{Bmatrix} F_x \\ F_y \end{Bmatrix} = \frac{1}{Z_1(X - d) - X_1 Z_1} \begin{bmatrix} X_1 - (X - d) - X_1 \\ Z_1 - Z \end{bmatrix} \begin{Bmatrix} M_1 \\ M_2 \end{Bmatrix}$$

These forces for each linkage can be summed to give the force on the load,

$$\bar{\phi} = \phi_x \hat{i} + \phi_y \hat{j} + \phi_z \hat{k}$$

in global coordinates. The components in global coordinates of the forces the linkages exert on the load are, for linkage X

$$\phi_x = \frac{-F_x \delta_x}{\sqrt{\delta_x^2 + (\sqrt{2}l + d - \delta_y)^2}}$$

$$\phi_y = \frac{F_x (\sqrt{2}l - d - \delta_y)}{\sqrt{\delta_x^2 + (\sqrt{2}l + d - \delta_y)^2}}$$

$$\phi_z = -F_z$$

and linkage Y

$$\phi_x = \frac{F_x (\sqrt{2}l - d - \delta_x)}{\sqrt{(\sqrt{2}l + d - \delta_x)^2 + \delta_y^2}}$$

$$\phi_y = \frac{F_x \delta_y}{\sqrt{(\sqrt{2}l + d - \delta_x)^2 + \delta_y^2}}$$

$$\phi_z = -F_z$$

and linkage Z

$$\phi_x = \frac{-F_x \sqrt{(\ell + d/\sqrt{2} + \delta_x)^2 + (\ell + d/\sqrt{2} + \delta_y)^2}}{\sqrt{2} \sqrt{(\ell + d/\sqrt{2} + \delta_x)^2 + (\ell + d/\sqrt{2} + \delta_y)^2 + \delta_z^2}} - \frac{F_z}{\sqrt{2}}$$

$$\phi_y = \frac{-F_x \sqrt{(\ell + d/\sqrt{2} + \delta_x)^2 + (\ell + d/\sqrt{2} + \delta_y)^2}}{\sqrt{2} \sqrt{(\ell + d/\sqrt{2} + \delta_x)^2 + (\ell + d/\sqrt{2} + \delta_y)^2 + \delta_z^2}} + \frac{F_z}{\sqrt{2}}$$

$$\phi_z = \frac{F_x \delta_z}{(\ell + d/\sqrt{2} + \delta_x)^2 + (\ell + d/\sqrt{2} + \delta_y)^2 + \delta_z^2}$$

Substitution of these expressions yields a geometrically nonlinear relation between the force  $\bar{\phi}$  and the translation  $\bar{\delta}$ .

If  $\bar{\delta}$  is small, all the constituents of the  $\bar{\phi}$ ,  $\bar{\delta}$  relation can be linearized to give a stiffness matrix for small displacement in global coordinates. The linearized expressions are, progressively in the order taken above,

$$X_x = \sqrt{2} \ell + d - \delta_y$$

$$Y_x = 0$$

$$Z_x = \delta_z$$

$$X_y = \sqrt{2} \ell + d - \delta_x$$

$$Y_y = 0$$

$$Z_y = \delta_z$$

$$X_z = \sqrt{2} \ell + d + \delta_x/\sqrt{2} + \delta_y/\sqrt{2}$$

$$Y_z = 0$$

$$Z_z = \delta_x/\sqrt{2} - \delta_y/\sqrt{2}$$

For linkage X

$$Z_1 = \ell/\sqrt{2} + (1/2)(\delta_y + \delta_z)$$

$$X_1 = \ell/\sqrt{2} - (1/2)(\delta_y + \delta_z)$$

linkage Y

$$Z_1 = \ell/\sqrt{2} + (1/2)(\delta_x + \delta_z)$$

$$X_2 = \ell/\sqrt{2} - (1/2)(\delta_x + \delta_z)$$

and linkage Z

$$Z_1 = (1/\sqrt{2})(\ell - \delta_y)$$

$$X_1 = (1/\sqrt{2})(\ell + \delta_y)$$

For linkage X

$$M_1 = k \Delta \alpha_1 = (k/\sqrt{2} \ell)(\delta_y + \delta_z)$$

$$M_2 = k \Delta \alpha_2 = (k/\sqrt{2} \ell)(\delta_y - \delta_z)$$

linkage Y

$$M_1 = k \Delta \alpha_1 = (k/\sqrt{2} \ell)(\delta_x + \delta_z)$$

$$M_2 = k \Delta \alpha_2 = (k/\sqrt{2} \ell)(\delta_x - \delta_z)$$

and linkage Z

$$M_1 = k \Delta \alpha_1 = -(k/\ell) \delta_y$$

$$M_2 = k \Delta \alpha_2 = -(k/\ell) \delta_x$$

For any linkage

$$\begin{Bmatrix} F_x \\ F_z \end{Bmatrix} = (1/\sqrt{2} \ell) \begin{bmatrix} -1 & -1 \\ 1 & -1 \end{bmatrix} \begin{Bmatrix} M_1 \\ M_2 \end{Bmatrix}$$

so for linkage X

$$\phi_x = 0$$

$$\phi_y = F_x = -(k/\ell^2) \delta_y$$

$$\phi_z = -F_z = (k/\ell^2) \delta_z$$

linkage y

$$\phi_x = F_x = -(k/\ell^2) \delta_x$$

$$\phi_y = 0$$

$$\phi_z = -F_z = (k/\ell^2) \delta_z$$

and linkage Z

$$\phi_x = -(1/\sqrt{2})(F_x + F_z) = -(k/\ell^2) \delta_x$$

$$\phi_y = -(1/\sqrt{2})(F_x - F_z) = -(k/\ell^2) \delta_y$$

$$\phi_z = 0$$

So, by summing for all linkages,

$$\begin{Bmatrix} \phi_x \\ \phi_y \\ \phi_z \end{Bmatrix} = -\frac{2k}{\ell^2} \begin{Bmatrix} \delta_x \\ \delta_y \\ \delta_z \end{Bmatrix}$$

and the small displacement stiffness matrix is

$$-(2k/\ell^2) [I]$$

Thus the three translational degrees of freedom are uncoupled and exhibit equal spring rates for small displacements.

Expressions for the components of  $\phi$  for Coulomb dampers are not analytically encouraging.

$$\phi_x = -C/\sqrt{2}\ell \{ \text{Sgn}(\dot{\delta}_x + \dot{\delta}_z) + \text{Sgn}(\dot{\delta}_x - \dot{\delta}_z) + \sqrt{2} \text{Sgn} \dot{\delta}_x \}$$

$$\phi_y = -C/\sqrt{2}\ell \{ \text{Sgn}(\dot{\delta}_y + \dot{\delta}_z) - \text{Sgn}(\dot{\delta}_y - \dot{\delta}_z) - \sqrt{2} \text{Sgn} \dot{\delta}_y \}$$

$$\phi_z = -C/\sqrt{2}\ell \{ \text{Sgn}(\dot{\delta}_y + \dot{\delta}_z) - \text{Sgn}(\dot{\delta}_y - \dot{\delta}_z) + \text{Sgn}(\dot{\delta}_x + \dot{\delta}_z) - \text{Sgn}(\dot{\delta}_x - \dot{\delta}_z) \}$$

However, for damping proportional to angular velocity

$$\begin{Bmatrix} \phi_x \\ \phi_y \\ \phi_z \end{Bmatrix} = -\frac{2D}{\ell^2} \begin{Bmatrix} \dot{\delta}_x \\ \dot{\delta}_y \\ \dot{\delta}_z \end{Bmatrix}$$

The damping matrix is

$$-\frac{2D}{\ell^2} [I]$$

The choice of stiffness and damping for an optimum compromise among shock and vibration isolation and resonance suppression is beyond the scope of this paper. However, for those not already familiar with the literature, references are cited (6-8) which provide an introduction to this science.

Because translational compliance is large compared to that for rotation, the center for rotary vibration of the load is near its center of gravity. At zero displacement the compliance to moment of each linkage is

$$\frac{\theta}{M} = \frac{1}{M} \frac{\partial U}{\partial M} = \frac{1}{M} \frac{\partial}{\partial M} \sum_{\text{Bars}} \frac{\ell F^2}{2AE} = \sum_{\text{Bars}} \frac{\ell}{AE} \frac{F}{M} \frac{\partial F}{\partial M}$$

where  $\theta$  = rotation

$M$  = couple

$U$  = strain energy in linkage

$\ell$  = bar length

$F$  = force in bar

$A$  = area of bar

$E$  = Young's modulus

Then the compliance is

$$\theta/M = 8\ell/(A_\ell E h^2) + 4/(A_h E h)$$

where  $A_\ell$  = Area of bar, length  $\ell$

$A_h$  = Area of bar, length  $h$

and the linkage weight is

$$W = \rho (4A_\ell \ell + A_h h)$$

where  $\rho$  = material weight density.

Minimization of  $(\theta/M) W$ , i.e., the weight/stiffness ratio gives  $A_h = \sqrt{2} A_\ell$  and compliance

and weight are, with  $A_\ell = A$

$$\theta/M = (4/AEh) (2\ell/h + 1/\sqrt{2})$$

$$W = A (4\ell + \sqrt{2} h)$$

As an example consider an antenna with a weight of 2,000 pounds and a centroidal inertia of 300 ft-lb-sec<sup>2</sup>. Let the linkage height be  $h = 2$  feet and the end bar length be  $\ell = 1$  foot. Suppose the linkage bars to be made of aluminum with a density of .1 lb/in<sup>3</sup> and Young's modulus of  $10^7$  lb/in<sup>2</sup>. To give a resonant frequency of 20 Hz, the linkage compliance to couple must be  $2 \times 10^{-7}$  rad/ft-lb. The resulting end bar area is 1.7 in<sup>2</sup> and the total bar weight is 42 pounds, or about 2% of the antenna weight.

Lateral (XY plane) motion can be snubbed by the linkages themselves if geometric parameters are chosen to allow full extension without mechanical interference. For example, the force displacement relation for the X direction considering only the Y linkage is

$$F_x = (k/\ell) \left( \frac{\pi/4 - \alpha}{\sin \alpha} \right)$$

$$\text{where } \alpha = \cos^{-1} \left( \frac{\sqrt{2}\ell - \delta_x}{2} \right)$$

$F_x$  grows large as  $\alpha \rightarrow 0$ , i.e., as

$$-\delta_x \rightarrow (2 - \sqrt{2})\ell$$

## SUMMARY

Antennas for ships need small compliance in rotation to meet their pointing accuracy and performance requirements while at the same time their instrumentation needs to be isolated from shock and vibration translations. A linkage suspension satisfying these requirements is composed of three orthogonal, double parallel-gram linkages having torsional springs and dampers at some of their joints. When linearized, the small displacement stiffness and viscous damping matrices are diagonal and isotropic. Rotary stiffness can be supplied with a linkage weight which is a small fraction of the suspended weight. The suspension can be made self-snubbing by suitable selection of geometric parameters.

## REFERENCES

1. : Mechanical Vibrations of Shipboard Equipment, Military-Standard-167-1 (Ships), Department of the Navy, Naval Ship Systems Command, Washington, D.C., 1 May 1974.
2. : Requirements for Shock Tests, H.I. (High-Impact); Shipboard and Machinery, Equipment and Systems, Military-Specification-901C (Navy), Department of the Navy, Naval Ship Systems Command, Washington, D.C., 5 September 1963.
3. Mobley, J. G.: "The Effects of Shipboard-Induced Vibration on Inertial Stabilization Sensing Elements," Unpublished material, Scientific-Atlanta, Inc., Atlanta, Georgia, July 1977.
4. Derby, I. F.: "Decoupling the Three Translational Modes from the Three Rotational Modes of a Rigid Body Supported by Four Corner Located Isolators," U.S. Naval Research Laboratory, Shock and Vibration Bulletin, Vol. 43, Part 4, pp. 91-108, June 1973.
5. Hannibal, A. J.: "Focalization of Semi-Symmetric Systems," U.S. Naval Research Laboratory, Shock and Vibration Bulletin, Vol. 46.
6. Snowdon, J. C.: Vibration and Shock in Damped Mechanical Systems, John Wiley and Sons, Inc., New York, N. Y., 1968.
7. Sevin, E., Pilkey, W. D.: Optimum Shock and Vibration Isolation, Monograph SVM-6, U.S. Naval Research Laboratory, Shock and Vibration Information Center, Washington, D.C., 1971.
8. : U.S. Naval Research Laboratory Shock and Vibration Bulletin, U.S. Naval Research Laboratory, Washington, D.C., 46 Volumes.

## APPENDIX - Citations from Vibration and Shock Test Specifications

MIL-STD-167, Type I

5.1, Type I - Environmental Vibration

5.1.3.3 - Vibration Tests

"Each of the tests specified herein shall be conducted separately in each of the three principal directions of vibration."

5.1.3.3.1 - Exploratory Vibration Test

"...the equipment shall be...vibrated at a table vibratory single amplitude of 0.010 to 0.002 inch."

5.1.3.3.2 - Variable Frequency Test

"...at the amplitudes shown in Table I."

5.1.3.3.3 - Endurance Test

"The amplitudes of vibration shall be in accordance with Table I and figure 1."

Table I gives (single) amplitudes ranging from 0.030 inch down to .003 inch.

5.1.3.3.5 - Endurance Test for Mast-Mounted Equipment

"The amplitudes of vibration shall be in accordance with Table II."

Table II vibrations are between 0.100 inch and 0.010 inch. Figure 1 presents these ranges graphically.

MIL-S-901

3.1.1.1 - Grade A or B

3.1.3.2 - Class II

"...under HI shock, with the use of resilient mountings...allowed or required by the individual equipment specification."

3.1.5.1 - Type A

4.2.4 - Test Procedure

4.2.4.2 - For Medium Weight Equipment

"...six blows...three groups of two each ...height of hammer and the initial up travel of the anvil table shall be as shown in Table I. One blow of each group shall be with the equipment mounted on an inclined orientation."

Table I gives (linear) table travels up to three inches.

6.2.1 m Shock Mounts

A statement on the use of shock mounts and on clearances and connections to accommodate relative motion.

# RADAR AZIMUTH BEARINGS - DESIGN, SELECTION AND APPLICATION

THOMAS A. BUSHAR

Keene Corporation  
Kaydon Bearing Division  
Muskegon, Michigan 49443

## ABSTRACT

A summary of the state of the art is presented. Much useful design and application information is provided to aid the radar structure designer in matching azimuth bearing design to performance requirements. Special emphasis is given to the importance of communication between the engineers of the radar manufacturer and the bearing supplier.

## INTRODUCTION

There are many bearing design types and innumerable configurations which have been used to support radar antennas in the azimuth position. Large, stationary structures such as satellite telecommunications installations use anything from track rollers to hydrostatic pad bearings. Many military shipboard and mobile radars incorporate a single, combination load, rolling element bearing for azimuth support. This preference is due to the advantages of compactness, high stiffness, and low cost for a single bearing system. An example is shown in Figure 1.

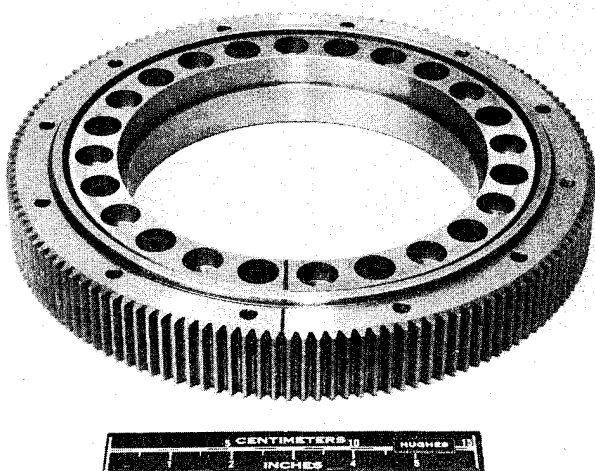


FIGURE 1. Azimuth Bearing for Track Radar Antenna - US ROLAND Mobile Air Defense System.

## SINGLE BEARING DESIGNS

Of the many bearing types available, current design practice usually dictates either a 4-point contact ball bearing, or a biangular roller (crossed roller) bearing in the azimuth position. These bearings are depicted in cross-sectional view in Figures 2 and 3.

The 4-point contact ball bearing incorporates "gothic arch" raceways in order to achieve 4-point or "X" contact with each ball. Raceway geometry can be varied to obtain any contact angle, but most are either 35 or 45 degrees from the bearing radial center line. Osculation or conformity of raceway curvature to ball

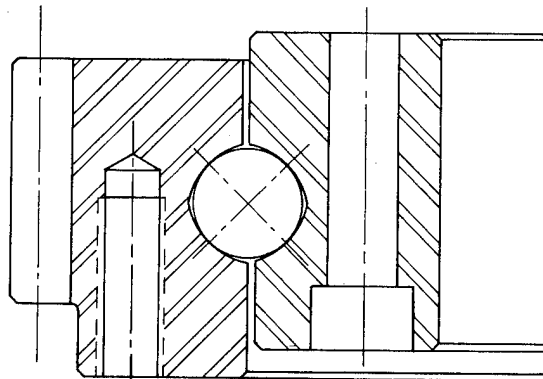


FIGURE 2. 4-Point Contact Ball Bearing.

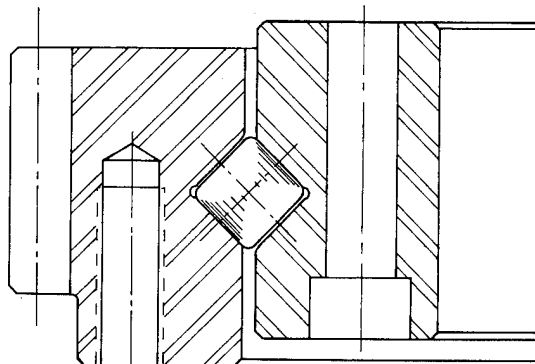


FIGURE 3. Biangular Roller Bearing



diameter is another variable, which is selected to optimize the balance between load carrying capacity and friction. Due to the complex rolling and sliding motion of the balls, it is not recommended that a full complement of balls be employed. Generally, the balls are separated by fiberglass-reinforced nylon spacers. Above 1.0 inch ball diameter, the nylon spacers are surrounded by a steel band for added strength. Although most radar applications are characterized by very slow rotational speed, moderate speed applications do exist, and require the use of segmental separators if a 4-point contact ball bearing is selected. Spacers are acceptable to a speed of roughly 500 FPM at the bearing pitch line, while a segmental separator allows up to 800 RPM. Balls, spacers and cage segments are shown in Figure 4.

Recently, radar manufacturers and users have demonstrated a marked preference for the biangular roller bearing design. This design incorporates cylindrical rollers and conical raceways to provide line contact and smooth rolling motion. The contact angle is 45 degrees, with alternating rollers positioned at 90 degree angles to each other to provide radial, thrust and moment load carrying capacity. The line contact provides high load capacity and smooth rolling at each contact, although the number of load carrying contacts is less than with the ball bearing. It is possible to use a full complement of rollers without greatly impairing bearing performance or fatigue life.

Sintered alloy steel spacers are generally recommended to minimize bearing wear and friction torque. A biangular roller bearing with spacers can achieve speeds up to 800 FPM at the bearing pitch line.

Two developments have improved performance of biangular roller bearings. The first is the generation of a spherical surface on the ends of the rollers. This improvement reduces sliding motion at the roller end contact, while still limiting roller screwing.

Secondly, a TFE coating applied to the cylindrical surfaces of the spacers substantially reduces roller-to-spacer friction. Because the sintered alloy steel spacers are somewhat porous, a residual amount of TFE remains even after the initial transfer of TFE from the surface. It, therefore, provides some degree of operating lubrication as well as facilitating initial assembly and run-in of the bearing. Sphere-end rollers and roller spacers are pictured in Figure 5.

Whether a 4-point ball or biangular roller bearing is specified, raceway material is always bearing quality vacuum degassed steel, of several composition grades, depending on whether races are to

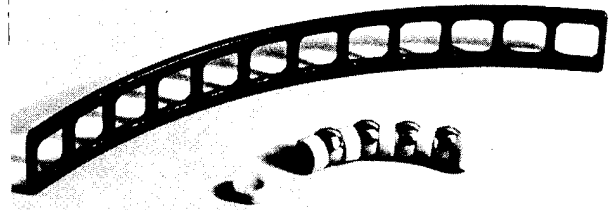


FIGURE 4. Balls, Ball Spacers, Cage Segment.

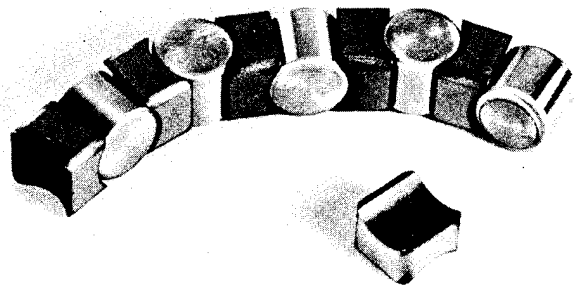


FIGURE 5. Rollers, Roller Spacers.

be through hardened, case hardened, or selectively hardened. Rolling elements are generally through hardened 52100 bearing quality steel.

#### PERFORMANCE COMPARISON

The following comparison of a 4-point ball with a biangular roller bearing is intended as a guideline to the radar manufacturer to aid in bearing selection. Included in the comparison are several performance characteristics, which are tabulated in Table 1, along with deflection curves shown in Figure 6.

It is assumed that both bearings have available the same dimensional envelope, and experience the same operating loads and speeds. Equivalent manufactured preload is assumed for both bearings, providing an initial roller-to-raceway interference intended to improve bearing stiffness. Referring to the table, the ball bearing incorporates slightly larger balls, and each ball takes load in both contact planes, thus providing higher thrust and moment load carrying capacity. Both bearings provide essentially equal radial load capacity. Calculated fatigue life

comparison depends largely on the respective proportions of radial, thrust and moment loading. For the example shown, the ball bearing yields more than twice the calculated life of the roller bearing. Field experience has not supported this prediction, because azimuth bearing failure is usually due to factors other than material fatigue. Ingress of contamination, corrosion, ineffective lubrication and improper mounting or maintenance are more common causes of bearing failure.

Friction torque is lower for a preloaded ball bearing in the free state, but is higher at operating and maximum loading. This phenomenon is explained by the fact that the ball bearing generates much more sliding motion at the internal load contacts than does the roller bearing. The frictional effect of this sliding motion increases non-linearly with increasing load, resulting in a 50% higher friction torque for the ball bearing at maximum loading.

Moment stiffness of the roller bearing is substantially higher under light load conditions, i.e. at loads less than that required to relieve the manufactured preload. This is very often of greater importance than calculated fatigue life.

In many cases, operating loads can exceed preload relief, as with shipboard applications where flank speed creates substantial wind loads. At this point the

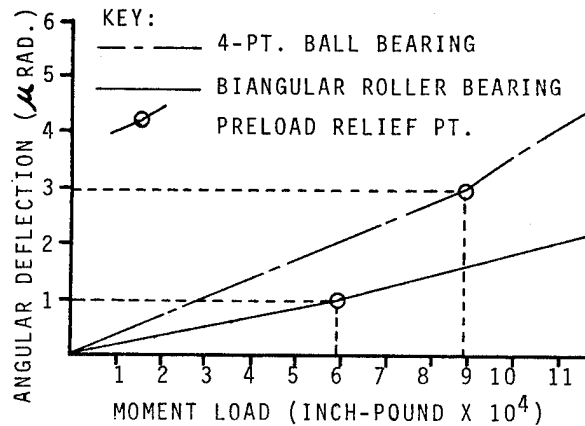


FIGURE 6. Comparison of Deflection Curves

ball bearing stiffness more closely approaches that of the roller bearing. At maximum loads, which are created by near miss shock, earthquake, or hurricane force winds, bearing stiffness is not a critical factor, but is shown in the example merely as a point of reference.

The moment load deflection curve of Figure 6 further illustrates the comparison. The biangular roller bearing graph is shown in solid line, while the 4-point ball is shown in broken line. It should be pointed out that the improvement in stiffness with a biangular roller bearing would be far more dramatic in a comparison of two unpreloaded bearings. In fact, an unpreloaded biangular roller bearing has equal or greater stiffness than a preloaded 4-point contact ball bearing of equal dimensional envelope. It is advisable to require a manufactured bearing preload for applications using biangular roller bearings, and is imperative in those using ball bearings.

#### MOUNTING/INSTALLATION METHODS

Table 1 and Figure 6 are based on the assumption that the bearing races are un-piloted, and are free to uniformly deflect radially without restriction under applied load. Where substantially thick housings with close fitting pilot diameters are employed, a significant improvement in bearing stiffness is possible. Mounting bolts alone will not restrict races from deflecting radially or elliptically under substantial applied loads. Diametral pilot surfaces are recommended whenever possible.

Housing thickness is important to minimize total deflection. The supporting housing should be an essentially uninterrupted surface with section thickness at least 75% of the bearing race section which it supports. In order to approach rigid bearing race conditions, this thickness must be at least equal to race thick-

	Ball	Roller
Static Rating		
Radial (lb)	299,000	302,000
Thrust (lb)	1,060,000	766,000
Moment (in-lb)	9,120,000	6,510,000
L-10 Life (Revs)	4,590,000	2,000,000
Friction Torque (ft-lb)		
@Free State	101	135
Operating Load	438	305
Maximum Load	1631	1101
Stiffness (in-lb/radian)		
@Light Load	$3.2 \times 10^9$	$6.45 \times 10^9$
Operating Load	$2.65 \times 10^9$	$3.35 \times 10^9$
Maximum Load	$3.09 \times 10^9$	$3.45 \times 10^9$
Deflection (radians)		
@Light Load	$1.24 \times 10^{-5}$	$0.65 \times 10^{-5}$
Operating Load	$2.45 \times 10^{-5}$	$1.77 \times 10^{-4}$
Maximum Load	$8.60 \times 10^{-4}$	$7.05 \times 10^{-4}$

TABLE 1. Comparison of Performance 4-Point Ball vs. Biangular Roller Bearing

ness. These are general relationships, which must be modified in cases where extremely thin race bearings are employed.

Pilot diameter fitting practice depends on material employed in the bearing and housing. For steel on steel the pilot diameter should be designed for a nominal tight fit, with maximum looseness of .0005 inches. When steel bearings are used in aluminum housings, a double pilot is recommended - at O.D. and I.D. of each bearing race. This allows thermal expansion and contraction to take place without loss of diametral piloting.

Flatness and roundness of housing surfaces are important to ensure predicted bearing performance, and should generally be equal to required bearing accuracy. It is equally important to conduct installation in a clean, dry area, making sure to clean all mounting surfaces of paint, dirt and other debris. Mounting surfaces should be lightly oiled to ease fitting and minimize scoring. Mounting bolts should be left loose until both mating housings are applied to the bearing, and a centered light thrust load can be applied. Bolts should then be torqued to the level prescribed by the bolt manufacturer.

The bearing should be checked for freedom of rotation and gear center distance and backlash adjusted where applicable. A final check of bearing and gear lubrication is recommended after all other bearing checks.

#### LUBRICATION AND MAINTENANCE

Proper lubricant selection and adequate relubrication are extremely important in radar azimuth bearings. Unlike many rolling bearing applications, this one is often characterized by very slow rotation, partial rotation, reversing direction of rotation, long static periods and extremes of ambient temperature. These factors in combination exclude most commercially available bearing lubricants from consideration. Requirements for military specifications further restrict lubricant selection. In the past, lubricant selection has unfortunately been based in many cases on availability of supply or Mil Spec selection without adequate knowledge about field performance.

Most applications utilize grease lubrication, and this discussion is limited to grease lubricated azimuth bearings. It is generally preferred that the oil within the grease provide at least 70 saybolt universal seconds (SUS) viscosity at the bearing operating temperature.

Due to the slow speed, there can be no dependence on dynamic effects to establish an adequate lubricant film. Therefore, viscosity of the oil takes on great importance. At extremely low temperatures (to -65°F) it is imperative that

the grease remain workable and that oil viscosity does not exceed a usable range. Due to the compact design of 4-point ball and biangular roller bearings, the grease must be capable of lubricating sliding contacts as well as rolling contacts. Field experience shows that relatively few greases have been capable of meeting these disparate requirements.

The most versatile grease is a product meeting MIL-G-81322. This grease has a very high viscosity index, and generally consists of a microgel or clay base with a synthetic hydrocarbon lubricant. Several suppliers have qualified products, including Mobil Oil Co. (Mobilgrease 28) and Shell Oil Co. (Aeroshell Grease 22). Although some applications have experienced relatively high torque values below -40°F, MIL-G-81322 has given the best performance over a broad temperature range. Even at the high temperatures and high instantaneous speeds experienced by aircraft landing wheel bearings, this grease has performed well.

An acceptable grease for many applications is MIL-G-23827. Qualified suppliers include Texaco, Inc. (#2346 low temp. EP) and Chevron Oil Co. (Chevron #55), among others. This grease is formulated for low temperature application, and does not have the moderate to high temperature performance of MIL-G-81322. It has been known in certain cases to become dry after long static periods without rotation. However, the use of MIL-G-23827 has been successful in most azimuth bearing applications.

MIL-G-21164 is not recommended for azimuth bearing lubrication. It has a molybdenum disulfide additive, and works well on pure sliding surfaces. Its performance in azimuth bearings has been less than satisfactory, however. It has usually been selected for the convenience of using the same grease for bearing and gear contact lubrication.

Relubrication after some period of service is important to sustain bearing performance. For azimuth bearings the relubrication cycle should be determined by the most likely cycle to be accomplished regularly in an overall preventive maintenance program, but should not be less frequent than every 100 operating hours or every six months. Relubrication consists of pumping a small amount of grease into the bearing while rotating the bearing, if possible, to achieve maximum distribution. At each bearing relubrication period, the gear should also be relubricated, and all bearing mounting bolts checked for proper torque, if accessible.

## SPECIAL FEATURES

Combination load azimuth bearings such as the 4-point contact ball and biangular roller types can be designed to provide many special features including integral spur gearing, lubrication fittings, integral seals, special markings, and various surface preservation and corrosion protection coatings.

## GEARING

The subject of gearing is very complex. At the risk of oversimplification we will deal here only with the major considerations. Azimuth gears may be required to serve two purposes:

(a) rotation or positioning of the antenna and (b) indication of position. This may be accomplished with one or two gears. If the latter, they are usually referred to as the "drive" and "data" gears.

The AGMA "Gear Handbook" 390.03 is conveniently arranged for specification of the precision by class number. Quite naturally, the higher the class number the greater the cost. But further than this, above Class 8 there is the likelihood that profile grinding will be necessary to meet the tolerances. Above Class 10 grinding is practically certain to be necessary.

Another important factor is gear tooth hardness. Most designs are arranged to permit the use of material in the highest range that is practical for machining, Rc 30-34. Only when sufficient strength or surface durability cannot be provided at this hardness, should higher levels be considered. In such instances, the choice between through hardening and selective hardening of the profiles is one that should be made by someone expert in weighing the various application, cost, and risk factors. Tooth hardness higher than Rc 34 is seldom specified in radar azimuth gears.

## SEALS

Integral seals are often required for several reasons: There is not adequate housing space available for external seals; adjacent parts require different lubricants; or integral seals may be desired to complement external seals or shields. In any case, it is best for the radar structures engineer to indicate the purpose of the seal, but leave design details to the bearing engineer. Different bearing manufacturers have available different seal configurations, as "standard" extruded elastomer shapes. In some cases a face riding seal fits more conveniently into the bearing configuration than a diameter riding seal, and sometimes vice-versa. Decisions regarding seal configuration and design are based on manufacturing feasibility and cost, as

well as seal effectiveness. Therefore, it is best to let the bearing supplier recommend the seal design, based on a full understanding of the seal's function.

## PROTECTIVE COATINGS

Corrosion protection and general preservation methods vary from application to application, depending on severity of the environment. Long and short term storage, protection from direct salt spray, chemical attack or abrasive wear are considerations determining coating selection. Protection is available in many forms with widely varying cost. Simplicity is the best rule to follow.

Coating bearing exterior surfaces with the lubricating grease or preservative oil per MIL-L-3150 provides adequate protection for short or long term storage in original packaging in a protected area.

Black oxide coating per MIL-C-13924 provides limited corrosion protection in mildly corrosive conditions, but is generally used simply to provide a black surface.

At higher cost, electrodeposited zinc plating per QQ-Z-325, Class 2, Type II, or cadmium plating per QQ-P-416, Class 2, Type II are sometimes specified. These platings meet rigorous salt spray test requirements per Federal Test Method Standard No. 151 or ASTM B117. Cadmium plating provides the best corrosion protection and resistance to fungus formation, but also is higher in cost than zinc plating. Both cadmium and zinc plating are somewhat vulnerable to scratching in handling, although scratches are "self healing", and good short term corrosion protection is still provided even in the scratched area.

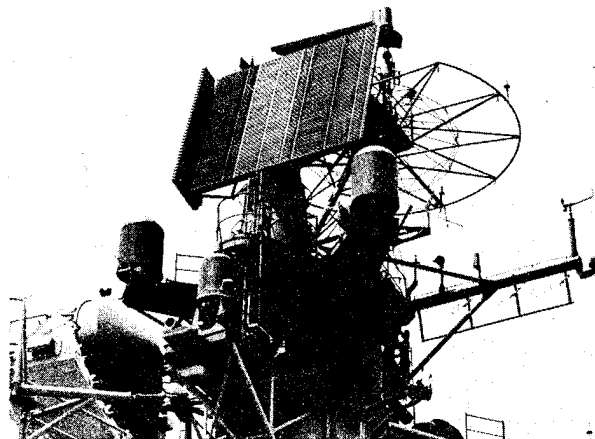


FIGURE 7. U.S. Navy AN/SPS-49 Radar - Aircraft Detection, Air Control and Missile Target Designation.

The most versatile coatings per dollar of cost are phosphate coatings per MIL-P-16232. These are usually less expensive than either cadmium or zinc plating for large parts, and provide good corrosion protection - at least 1½ hours of direct salt spray with no evidence of corrosion. Phosphate coatings are of two types - M for Manganese and Z for Zinc. Manganese phosphate has superior anti-galling properties, and is often required for exterior bearing surfaces including gear teeth. Zinc phosphate provides the best corrosion resistance and is lower in cost. It is the best selection for ungeared races.

Both types of phosphate coatings are available in 4 classifications, but the most common is Class 2 (Supplementary Impregnation with MIL-L-3150 oil). The phosphate coatings are often used as a base for subsequent painting. This combination has been very successful in Navy shipboard applications. It is important to point out that process cost is lower if phosphate coating is applied to all exterior surfaces, rather than specific surfaces.

Solid film lubrication is often applied to gear teeth, and in some cases, to seal riding surfaces. Generally, MIL-L-46010 is called out, requiring a resin bonded heat cured lubricant. This specification includes application of phosphate coating per MIL-P-16232, Class 3 Type M or Z, as a base for the solid film lubricant. A less costly method is sprayed on solid film lubricant per MIL-L-23398 which provides less corrosion protection.

A recent development in corrosion protection is a process called ENDURAKOTE which offers excellent heavy corrosion protection, surface finish, and wear resistance. This method offers the corrosion resistance of 440C stainless steel, yet is available at a lower cost.

#### PRELOAD

Preloading of 4-point contact ball and biangular roller bearings is a feature which makes these bearing types so well suited to radar azimuth applications. Preload is manufactured-in by the bearing supplier, providing an essentially foolproof mounting. The preload value is determined by the bearing designer in order to optimize bearing performance characteristics. This preload remains essentially unchanged throughout the service life of the bearing.

#### CONCLUSION

An attempt has been made to provide usable design and specifications guidelines for radar antenna bearings. It is especially important to avoid overspecification, which can result in needless expense or reduced reliability.

In general, the following parameters should be specified by the radar designer:

1. Dimensional envelope available for bearing.
2. Required bearing life, stiffness, and torque based on stated applied loads and speeds.
3. Gear data including quality classification.
4. Tolerances required on pilot diameters and bearing height.
5. Mounting features, e.g. hole sizes, location, and location tolerances.
6. Lubricant(s) and relubrication feature.
7. Seal locations.
8. Protective coatings.
9. Special requirements.

Areas which should be left to the bearing designer include:

1. Bearing exterior configuration.
2. Bearing internal complement of balls, rollers, and separator design.
3. Preload value.
4. Material and heat treat (hardness) for races, rolling elements and separator.
5. Seal material and design.
6. Exterior surface finishes.
7. Tolerances on race width, chamfers, and other nonfunctional dimensions.
8. Marking methods.

There are, of course, many exceptions to these general recommendations. The purpose of the guidelines is to provide a general reference applicable to most situations. Special requirements should be well communicated to the bearing designer, who has an obligation to take exception or to question any specifications which are beyond his manufacturing capability, which incur unnecessary expense, or which impair or limit the bearing's functional capability.

The radar designer should likewise feel an obligation to invite the comments and questions of the bearing designer. This dialogue is most effective at the inquiry/proposal phase. Once the bearing order is placed, engineering changes incur delays and can even result in costly material scrappage.

Open communication provides an avenue to manufacturing efficiency and optimized bearing design.

## SLIP RING ASSEMBLIES FOR RADAR ANTENNAS

Herbert C. Walker, Stephen R. Cole, Sherwin L. Brady

Poly-Scientific, Litton Systems, Inc.  
1213 N. Main Street  
Blacksburg, Virginia 24060

### ABSTRACT

The design considerations for slip-ring assemblies used in radar antennas are presented. Contact selection and configuration are discussed along with the effects that the environment (e.g. moisture) can have on contact performance. Design concepts for power circuits, low frequency signal circuits and high frequency signal circuits are discussed along with methods of saving space, designing for ease of maintenance and meeting the mechanical requirements of shock and vibration. The importance of the slip ring engineer having the electrical, mechanical and environmental requirements at the early design stages is emphasized.

### INTRODUCTION

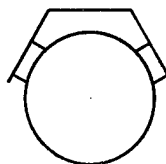
Search and acquisition radar antenna slip ring assemblies typically consist of logic, control, hi-frequency analog, and power circuits to serve devices which are mounted to the rotating portion of the antenna. Hundreds of circuits are generally required consisting of a typical mix of low level signals, hi-frequency coax channels up to 1 gigahertz and power of several hundred amps at 220 and 440 VAC.

With such a variety and quantity of sliding contacts in one package, several prime areas for discussion are evident and discussed. This paper is intended to be an overview for the radar pedestal engineer.

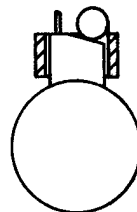
### SELECTION OF SLIDING CONTACT MATERIALS

The choice of contact materials for slip rings used on a radar antenna depends on several factors, including electrical current requirements, operating environment (e.g. earth, space), ring surface speed, ease of maintenance, driving torque, and life requirements. Two types of brushes are commonly used in such assemblies: wire brushes and composite brushes (Figure 1). For conduction of currents in excess of 30A, composite brushes (Figure 1, top) such as those formed from silver and graphite powders, are generally selected. Below 30A gold alloy or gold plated wire brushes (Figure 1, bottom) are often paralleled to obtain the required current

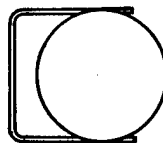
LEAF SPRING



PLUNGER



COMPOSITE BRUSHES ON FLAT RINGS  
FOR POWER CIRCUITS ABOVE 30 AMPS.



WIRE BRUSHES ON VEE-GROOVED RINGS  
FOR SIGNAL CIRCUITS AND LOW POWER  
CIRCUITS (< 30A).

FIGURE 1: POSSIBLE SLIP RING CONTACT  
DESIGNS.

capacity. Although ring surface speeds in excess of 150 ft/min (0.76 m/s) generally dictate the use of composite brushes, wire brushes have the advantage of requiring less space and less driving torque and do not create as much wear debris; however, they must be used where a liquid lubricant can be tolerated. While wire brushes create less total wear debris, slip rings with composite brushes are easier to clean. For a given amount of space and drive torque, wire brush contacts have less electrical noise than composite brushes.

Most radar slip ring assemblies have power rings that require the use of composite metal/graphite brushes. These brushes usually contact flat silver or silver alloy rings. Specifications for metal/graphite brushes and silver rings must be carefully detailed so that materials may be properly controlled to prevent excessive brush wear rates and slivering of the ring surfaces. Wear rates from tests conducted at Poly-Scientific have ranged from  $1 \times 10^{-9}$  in/in (inches of brush wear/inch of ring travel) to  $6 \times 10^{-12}$  in/in. Figure 2 indicates the result

of a Poly-Scientific test of two different grades of 80Ag-20 graphite brushes that were manufactured by the same producer who varied only the graphite from one brush grade to the other.

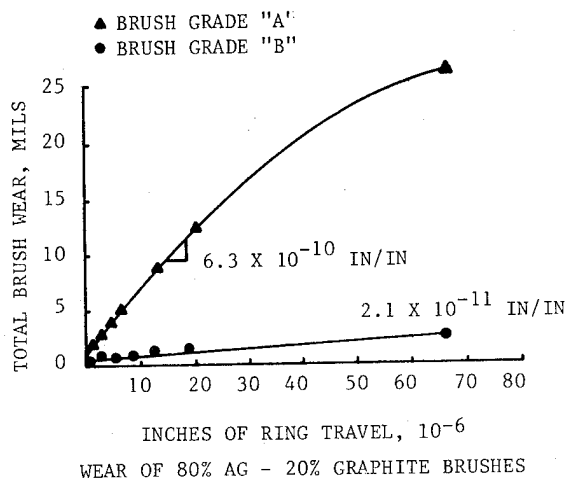
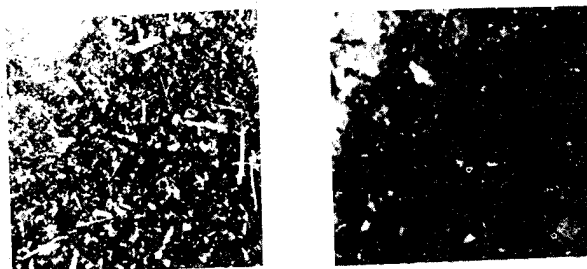


Figure 2: Wear of two different 80Ag-20 graphite brush grades. Both grades were tested at the same time on several different silver and silver alloy rings.

The importance of controlling the ring toughness and type of graphite is indicated by Figure 3. The wear debris shown in the left side of Figure 2 contains many long slivers (some several inches) of ring material.



RING HARDNESS:  
80 HK<sub>100</sub>. LARGE  
PARTICLES OF BRUSH  
ASH.

RING HARDNESS:  
190 HK<sub>100</sub>. SMALL  
PARTICLES OF BRUSH  
ASH.

Figure 3: The wear debris on the left is much more likely to cause electrical shorting due to the long slivers of metal.

This type of wear debris is very dangerous because it can easily cause electrical shorting. The debris at the right is from the same test fixture after the ring material has been changed to a harder silver alloy and brushes installed that did not contain large particles of ash in the graphite. This fine wear debris can be controlled much more easily to prevent shorting between circuits. Silver electrodeposits can vary in hardness from below 70 HK<sub>100</sub> to over

200 HK<sub>100</sub>. Both electrodeposited and wrought silver alloy properties must be controlled by specifications and routine inspections must be made of all lots of brush material to insure the absence of harmful graphitic ash.

The typical radar slip ring assembly also contains many signal and low power circuits (<30A) that are most efficiently accommodated with cantilever gold alloy wire brushes and vee-grooved hard-gold electrodeposited rings. The brushes may be made of a wrought gold alloy (e.g. ASTM B541) or a gold alloy electrodeposited onto a beryllium-copper wire spring. The hard gold electrodeposited ring is usually formed over a nickel encased base of brass or copper. The gold alloy contacts must be lubricated if wear and noise are not to become excessive, although occasionally "unlubricated" gold alloy contacts have been used. These contacts are successful only because of the natural lubricants that are in the atmosphere. Well-lubricated gold alloy contacts manufactured by Poly-Scientific were tested at NASA in a clean nitrogen atmosphere for over 100 million cycles with less than 0.0001 inches of wear. During this time over 38000 electrical noise recordings were below a maximum of 30 mV. Initial acceptance noise was less than 10 mV. Tests showed that this high level of performance was impossible with unlubricated contacts. In order to use liquid lubricated contacts, the surface speed must be below that necessary to cause hydrodynamic lift of the brushes, which is generally not a problem with radar slip ring assemblies. Slip rings with wire brushes have faster ring wear than brush wear, unlike composite brush slip rings which should have negligible ring wear. For design considerations one should consider ring wear of circuits with wire brushes to be 5 X 10<sup>-11</sup> inches per revolution.

Whenever possible wire brushes are used. Wire brushes in contact with vee-grooved rings generate much less wear debris than composite brushes on flat rings. Also, the wire contacts require less space than composite brushes.

#### ENVIRONMENTAL EFFECTS ON SILVER GRAPHITE BRUSHES

The proper amount of atmospheric moisture is very important for the proper functioning of metal/graphite brushes. Water on metal graphite contacts will increase the brush wear rate by more than a factor of 500<sup>2,3</sup>. On the other hand graphite is not an effective lubricant at low humidities, below 3mm Hg partial pressure in air<sup>2</sup>.

If the water vapor partial pressure is below 3mm Hg, graphite is not reliable as a lubricant and in fact becomes abrasive. Humidities at this low level are generally caused by operation of the contacts in space or vacuum, but other factors, such as dry air purging, could cause this condition. When the humidity is too low for graphite lubrication to be effective, Poly-Scientific uses composite brushes with MoS<sub>2</sub> as the principal solid lubricant. MoS<sub>2</sub> is an excellent contact lubricant

in vacuum<sup>4</sup>, but causes high electrical noise and torque if the contacts are exposed to a moist atmosphere (e.g. 40% R.H.). Poly-Scientific MoS<sub>2</sub> lubricated contacts have exhibited 8000 milliohms of noise when tested in laboratory air and then dropped to below 8 milliohms after run-in in vacuum, 10<sup>-6</sup> torr. This demonstrates the importance of the design engineer knowing the environment in which the slip ring will operate.

#### MOISTURE CONTROL - IN NORMAL ENVIRONMENT

##### A. Brush - Ring Materials

The previously described gold-on-gold and silver graphite-on-silver contact materials generally perform well in normal environment with moisture up to 95% RH. However, if an extremely wet condition caused by leakage of rain or wave wash into the area of the silver-graphite brushes occurs, excessive brush wear will result. The graphite cannot deposit a lubricant film on the ring in the presence of water. This film is essential for low wear.

##### B. Insulation Materials

Insulation materials for supporting rings and brushes are frequently mineral filled epoxies. This material has a surface resistivity of about  $2 \times 10^{11}$  ohms per inch. As a rule, creepage between rings and brushes should be sufficient to withstand 95% RH using the above surface resistivity (or the equivalent for other insulation used) and not lower the insulation resistance to less than 100 megohms. In a dried-out condition, e.g. 60% RH, this criteria usually results in an I.R. greater than 50,000 megohms.

Teflon insulation is recommended for lead wire because it will withstand the curing temperature (150 °C) of the plastics that the leads are frequently encapsulated in. By etching the Teflon for the encapsulated length, a moisture resistant bond can be accomplished.

##### C. Sealing

It is apparent from the above that the slip ring and brush block assemblies should be well enclosed and sealed to protect them from high humidity, rain, wave wash, salt spray and other environmental contaminants if the unit is to be exposed to these elements. The sealing normally consists of dynamic shaft "oil" seals outboard of bearings and static o-rings or gaskets under covers and connectors. An illustration of an enclosed slip ring assembly is shown in Figure 4 & 4A.

#### MODULAR DESIGNS - EASE OF MAINTENANCE

The standard design approach for large slip rings involves the stacking and securing of several ring modules to the shaft. Each module contains a given quantity of rings (and leads) encapsulated into mineral filled epoxy or



SLIP RING ASSY FOR  
TPQ-27 RADAR  
Figure 4

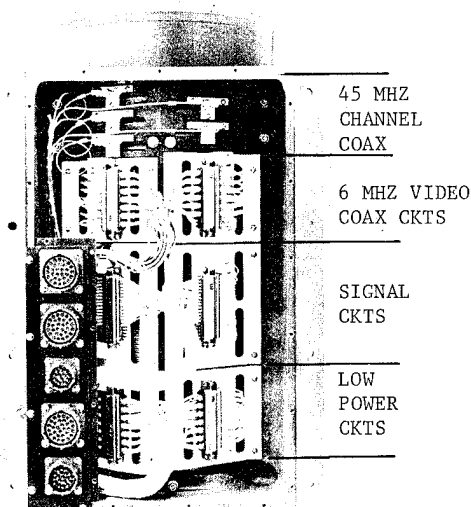


Figure 4A (Cover Removed)

individual components stacked and secured together. These modules are individually replaceable, often at the depot level.

Each ring module is serviced by one or more individually replaceable (at the field level) brush block assemblies. These blocks are readily accessible from the outside of the housing by means of removeable covers.

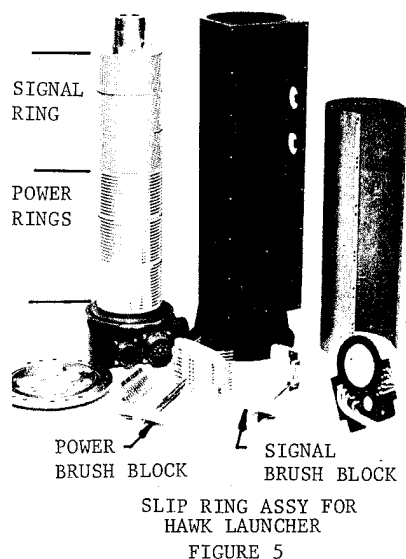
Signal brush block assemblies typically consist of cantilever gold alloy wire brushes and attached leads or terminals encapsulated into mineral filled epoxy. Power brush blocks typically consist of flat cantilever springs



with silver-graphite brushes attached. These power brush-springs are secured with hardware to fabricated or molded plastic blocks. Plunger type power brushes which ride in box holders are generally used above 80 amps. A minimum of two brushes per ring are used.

The insulation barriers between all rings are raised to provide debris control and adequate creepage for the voltages.

Figure 5 illustrates a typical modular construction.



#### A. High Frequency Module Design

Frequencies in the megahertz range and increased ring diameters magnify the problems of intercircuit capacitance and affect on wavelength. As these frequencies become greater, lower dielectric constant insulation and more complete type shielding is necessary to match impedance, control VSWR and insertion loss, and minimize cross-talk. For frequencies in excess of 10 megahertz, it is usually necessary to incorporate a design that consists of channel type shield rings which enclose the center conductor ring on three sides. Dielectric material supports the center ring within the channel. The shield on the coaxial cable is attached to the channel shield ring. The center conductor of the cable is fed through and insulated from the channel shield and attached to the center ring (See Figure 6). The center ring and shield ring are electrically brought out thru brushes which are attached to modified coaxial connectors. To keep the dielectric gap between the center ring and surrounding channel shield to minimum distances and to match as closely as possible the characteristics of the coaxial circuitry, the lowest possible dielectric constant material is desired. Therefore Teflon is frequently used as the dielectric. The assembly illustrated

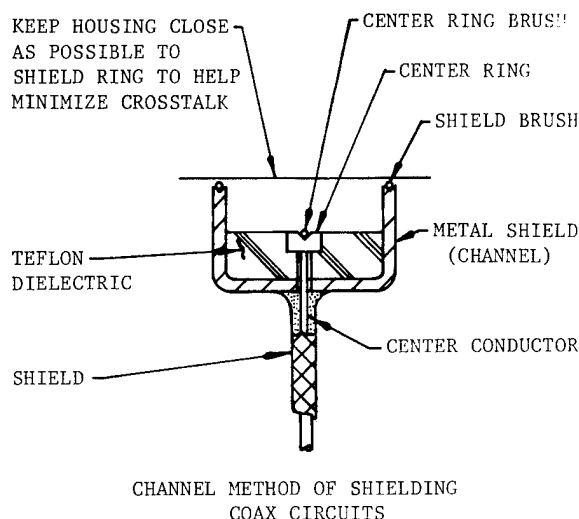
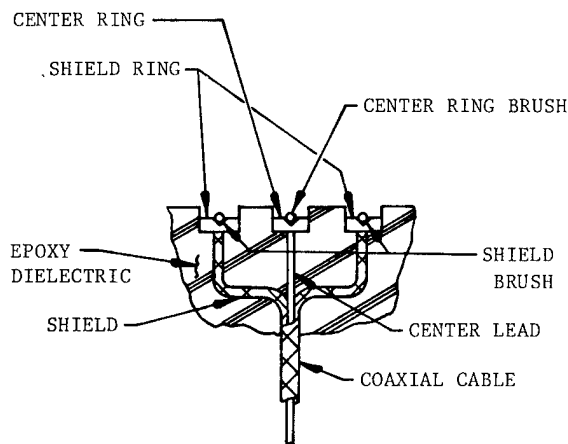


FIGURE 6

in Figure 4A shows this type of coaxial circuit in the top section. Frequencies up to 100 megahertz can be handled in this manner. Cross-talk down greater than -60dB, VSWR < 1.5:1 and insertion loss < .5dB can be expected. Additional tuning to control insertion loss is necessary if ring diameters become too great (above 8"). This greater diameter increases the fractional wave length. However, tuning is only effective over a narrow bandwidth of approximately  $\pm 2$  megahertz.

A less costly conventional type shielding, Figure 7, can be used on frequencies below 10 megahertz because the ring diameters are then a smaller portion of the wavelength. Hence, the VSWR can be held to a reasonable level (1.5:1 or less) without channel shields. Crosstalk is normally down greater than -50dB.



CONVENTIONAL DOUBLE SHIELDING METHOD FOR RF AND VIDEO CIRCUIT

FIGURE 7

Units have been designed and produced for frequencies up to 1 gigahertz. This involves parallel path circuitry to further reduce the fractional wave length. The best VSWR that can be expected is 3:1. Crosstalk can be held to -50dB.

Hard gold plated "V" grooved rings and wire type gold alloy brushes (Figure 1) are used.

#### B. Hi-Power Module Design

Above 30 amps, flat rings of coin silver or hard silver plated copper and composition silver-graphite or copper-graphite brushes are used (See Figure 1). The rings, brushes and leads must be of adequate cross section and conductivity to handle the required power. Above 150 amps, bus bars are frequently used in place of stranded cable. Insulation creepage between rings must be adequate for the voltages and to control wear debris. Power to 600 amps at 440 VAC is not unusual. Units with 600 amps and 35,000 VAC in oil filled chambers have been produced. Figure 5 illustrates typical power rings (lower modules) and brush blocks.

#### C. Signal and Low Power Module Design

Below 30 amps, hard gold plated "V" grooved rings and wire type gold alloy brushes are used (See Figure 1). Multiple brushes are paralleled for circuits above 5 amps to 30 amps. The same criteria applies for cross section of rings, brushes, leads and insulation creepage as noted for hi-power circuits. Low noise is usually critical on these circuits. Normal state-of-the-art acceptance noise is 10 milliohms peak-to-peak maximum. Typical crosstalk is -45dB at 50 KHZ with 1,000 ohm termination. Some circuits are used for multi-plexing digital data. Figure 5 illustrates typical signal rings (upper modules) and brush blocks.

#### SPACE AND WEIGHT SAVING FEATURES

##### A. Composition Versus Wire Brushes

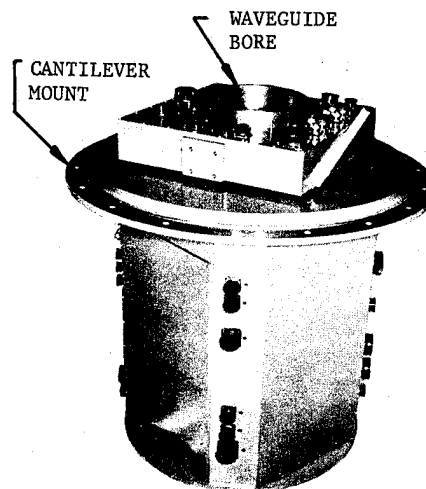
Composition brushes of very small size are limited by the manufacturing techniques. The smallest that can be practically obtained is .040" wide X .060" X .060". Conversely, wire brushes can be obtained as small as .005" diameter. It is apparent from this that the ring width and circumferential space needed for wire type brush circuits can be significantly less than for composition brushes. Hence the envelope size and weight of the total unit can be less.

##### B. Structural Members

There are frequently areas in an enclosed unit where only isolated projections are needed for packaging the brush blocks to mate with the slip rings. By using irregular shaped castings (aluminum) on the housing to conform to these projections, the size and weight can be reduced (See Figure 4).

#### MECHANICAL DESIGN

With very few exceptions, shock and vibration requirements are imposed on slip ring assemblies for radar pedestals. Shipboard shock is usually MIL-S-901 (hi-impact). This can range to 1,000 g's depending upon the mass of the unit. Vibration on slip rings for air-born radar can range to 2,000 HZ. It is essential that the enclosure structures as well as the slip ring and brush block components withstand these stresses. The slip ring assemblies are relatively large by virtue of a bore of some size that is usually required for customer passage of a rotary wave guide (See Figure 8).



SLIP RING ASSY FOR  
TARTER-D FIRE CONTROL  
FIGURE 8

This bore plus the length required for frequently packaging hundreds of circuits results in a significant weight which must be interfaced (mounted) in the pedestal.

This is often cantilever mounted which should be avoided if possible (See Figure 8). An ideal condition is to support the housing on both ends to avoid deflections caused by cantilevering.

The rotor and stator should not be rigidly mounted coincident to each other because bearing failure could occur due to misalignment. If the housing is rigidly mounted, the rotor should be driven with a flexible coupling.

In addition to the structures and electrical components being designed to withstand the stresses, bearings must be selected to handle the loads involved. Bearings frequently used are conrad type four point contact which will withstand both radial and thrust loads.

#### CONCLUSIONS

Properly enclosed slip ring assemblies are a reliable and accepted means of transmitting and receiving coax, signal and power circuits on

continuous or intermittent rotation radar antennas.

Composition brushes on silver rings are recommended only on power circuits over 30A and surface speeds greater than 150 ft per minute. They are sensitive to extremes of moisture and dryness and generate much higher wear debris volume than gold alloy or hard gold plated wire brushes on "V" grooved hard gold plated rings (gold-on-gold). Gold-on-gold is recommended for all other type circuits of 30A or less because of its low wear (with liquid lubrication), non-tarnish, high conductivity properties. This combination also requires much less space than the composition brushes.

Properly enclosed and sealed units are essential to control moisture and other environmental contaminants. Adequate insulation creepage between rings (internally) assures added protection.

Modular design of slip rings and brush blocks provide ease of maintainability and replacement.

Coaxial ring channels up to 100 megahertz are an accepted fact. Frequencies up to 1 gigahertz can be provided with more specialized design and some sacrifice in impedance match. Power circuits of several hundred amperes and up to 440 VAC are not uncommon. Circuits of 600A at 35,000 VAC in oil filled chambers have been produced. Higher current capability can be provided with additional space. Signal circuits including multi-plexing digital with low noise, 10 milliohms maximum, are common to most units.

Size and weight can be minimized by using the gold-on-gold contact combination as much as possible. Irregular shaped housing enclosures also reduce these features.

The enclosure structures and internal electrical components must be designed to withstand the shock and vibration requirements. The radar pedestal engineer should carefully consider the method of mounting the enclosed slip ring assembly to his pedestal. Cantilever mounting imposes higher and more complex stress on the slip ring assembly. It is preferable to support the unit on both ends to avoid this. To prevent bearing failure, the rotor and stator should not be rigidly mounted coincident to each other. If the housing is rigidly mounted, the rotor should have a flexible coupling. Conversely if the rotor is hard-mounted the housing should be allowed to flex. Conrad type four point contact bearings are frequently used to handle both thrust and radial loads.

#### REFERENCES

1. Cole, S. R., E. W. Glossbrenner and J. D. Johnston "Long-Duration Life Test of Slip Ring Capsule Assemblies for Inertial Guidance Platforms." Proceedings of the 7th International Conference on Electrical Contact Phenomena, Paris, France, 1974.
2. Lancaster, J. K. "Dry bearings: A Survey of Materials and Factors Affecting Their Performance", *Tribology*, Vol 6 (1973), p 219.
3. Walker, H. C., S. Cole. "Engineering Laboratory Test Report 293" Poly-Scientific, Blacksburg, Va.
4. Lewis, N. E., S. R. Cole, E. W. Glossbrenner and C. E. Vest "Friction, Wear and Noise of Slip Ring and Brush Contact for synchronous Satellite Use," *Space Tribology*, Proceedings of the First European Space Tribology Symposium, Frascati, Italy April 9-11, 1975.

# RADAR ANTENNA STABILISATION ON NAVAL SHIPS BY A TILTED AXIS CONFIGURATION

W D DELANY  
R WILSON

Mechanical Engineering and Servos Division  
Admiralty Surface Weapons Establishment  
Portsmouth PO6 4AA. UK

## ABSTRACT

A description is given of a novel mechanical configuration for mounting a large surveillance radar antenna on a ship at masthead height so that rotation of the antenna is always maintained about a vertical axis.

The design gives a reduction in weight, and its improved accessibility simplifies maintenance. A mathematical theory is given for the conversion of axes angles. A scale model, fully engineered as regards the servo drives, was constructed and evaluated on a laboratory rolling table. Some results are given of the dynamic tests carried out.

## INTRODUCTION

The purpose of a Naval radar surveillance antenna is to detect targets at long range. It therefore has a narrow main beam which can be rendered ineffective if the ship is subject to much roll motion. Figure 1 illustrates the problem.

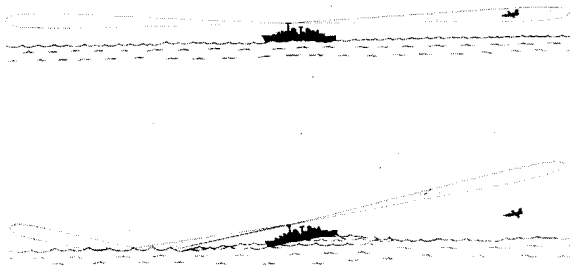


Figure 1. Effect of Pitching of Ship on Unstabilised Radar Antenna.

As the ship rolls the main beam sweeps alternately upwards and into the sea, resulting in the probability of painting the target being reduced.

The problem can be overcome, and the accuracy of information in regard to target height and bearing increased, if the antenna is mounted on a platform that is always maintained horizontal despite the ship's motion.

Figure 1 also illustrates that for the radar to be fully effective, the ship's surveillance antenna must be at the masthead, so that its rf transmission is unobstructed by other structures on the ship.

These constraints set highly challenging problems to the mechanical designer of the antenna and its mounting. Its weight at such a height on the ship constitutes an overturning moment which the ship's architects regard as detrimental to ship stability. Aperture size is dictated by the physical parameters summarised in the radar equation, so that the weight reduction possible is limited if the radar design is to be successful. In addition the antenna must be capable of operation in all the natural environments likely to be encountered, and at least to some limited extent, those of Naval Warfare.

Present designs of mechanisms for such a stable platform frequently weigh several times more than the antenna itself, and appear to offer some scope to mechanical designers in regard to weight reduction.

These considerations have led to the innovation of alternative designs of stable platforms to the conventional roll and pitch gimbal, one of which - the tilted axes gimbal - is described in this paper.

## STABILISATION REQUIREMENTS

The forces acting on an antenna are:

1. Gravity.
2. Wind.
3. Accelerations due to Ship's Motion.
4. Air drag due to rotation about its (vertical) axis.

As a preliminary step towards overall weight reduction the designer will wish to reduce the power requirements on the servo mechanisms stabilising the antenna, so that the weight of the servo drives can be reduced.

This can be done in principle by arranging the configuration such that as far as possible the static members of the structure carry these forces and the servo mechanisms deal only with variations in out-of-balance eg wind load perturbations on the reflector. This leads to the theorem that the stabiliser mechanisms centre of rotation, centre of pressure, and centre of mass, must be coincident if the servo power is to be minimal. Most designers of radar antenna systems set out to achieve this simply by the use of a gimbal ring, as in Figure 2. The antenna is mounted above the ring so that its sight line is unobstructed; the training motor, gearbox, and waveguide rotating joint, are placed below acting in counter-balance. The overturning moment due to the wind force on the antenna is usually only partly balanced as there is generally only limited space below the gimbal ring to allow for the addition of structures to increase the air drag.

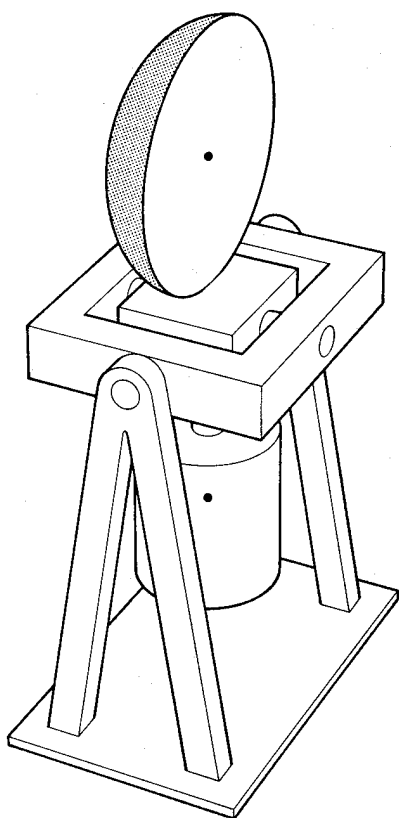


Figure 2. Radar Dish Mounted on a Gimbal Ring.

Figure 2 is a typical arrangement which indicates how the items below the ring limit the angular movement available unless the gimbal is made disproportionately large.

#### TILTED AXIS PRINCIPLE

Figure 3 illustrates the principle.

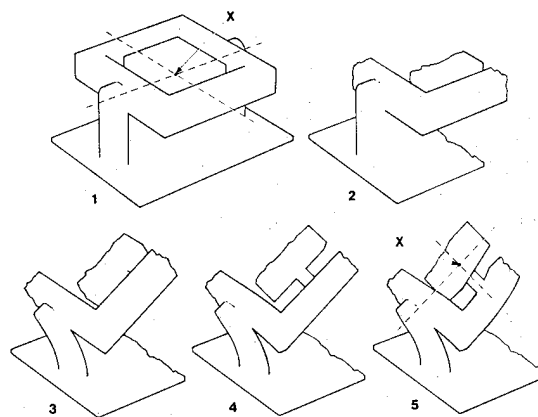


Figure 3. Development of the Tilted Axes Gimbal.

In Diagram 1, X is the centre of the conventional roll and pitch gimbal. In Diagram 2, only the essential parts of the ring are shown. Diagrams 3, 4, 5 show how the axes are "bent" upwards, bringing the centre of rotation above the ring.

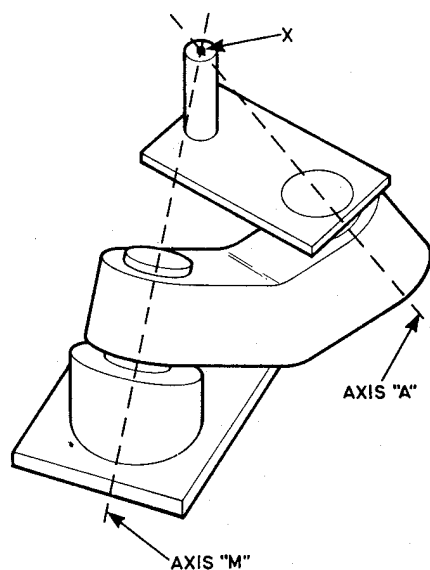


Figure 4. The main elements of the Tilted Axes Gimbal.

In Figure 4 the antenna has been excluded for the sake of simplicity. One servo mechanism drives the "M" axis (mast), as an alternative to the roll servo, and the other servo mechanism drives the "A" axis (antenna), as an alternative to the pitch servo. If the opposing forces can be directed through these axes instead of some distance from them, the potential load on the servos is nullified. Thus mounting the antenna on the rectangular link in a position such that its centre of mass and centre of pressure are

coincident with point X ensures that the forces due to gravity, lateral acceleration due to ships motion, and wind, constitute no load on the servos.

To stabilise the platform so that the antenna can rotate about a vertical axis, the servos will now have to reset to angles different from those of roll and pitch as measured by the ships gyro stabiliser which is used as the vertical reference.

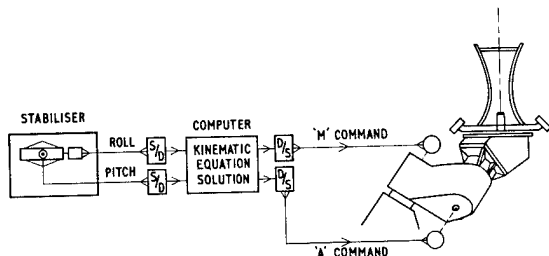


Figure 5. Control scheme for 'A' and 'M' Servos.

Figure 5 shows how the synchro outputs from the stabiliser are converted to digital inputs to the computer, which computes directly from the axes changing equations (9 V). The output is then converted back to synchro data for the servos.

#### ADVANTAGES

These are:

1. No counter-balancing of antenna mass or wind pressure is necessary so that the weight on the stable platform is limited only to items essential to the radar.
2. The centre of mass of the antenna-pedestal structure is lower on the mast, as the stabilising mechanism is located below the antenna.
3. The actual weight of the mechanism is less than that of an equivalently loaded gimbal ring. The two arms weigh less than a complete gimbal ring, and there is no supporting yoke. An implied final gear reduction (approximately three to one compared with direct drive on the roll axis) also gives some weight saving.
4. The servo mechanisms are totally enclosed. The only moving elements that are externally exposed are the two rotating shafts of the tilted axes, and these are protected against dirt ingress by suitable engineering seals.
5. Accessibility is improved.

#### PROBLEMS

##### Azimuth Drive

The torque reaction of a large antenna as it rotates in air creates a particular problem in the case of the tilted axes configuration, as the torque has a component about each of the two axes that the servos have to overcome as a base load.

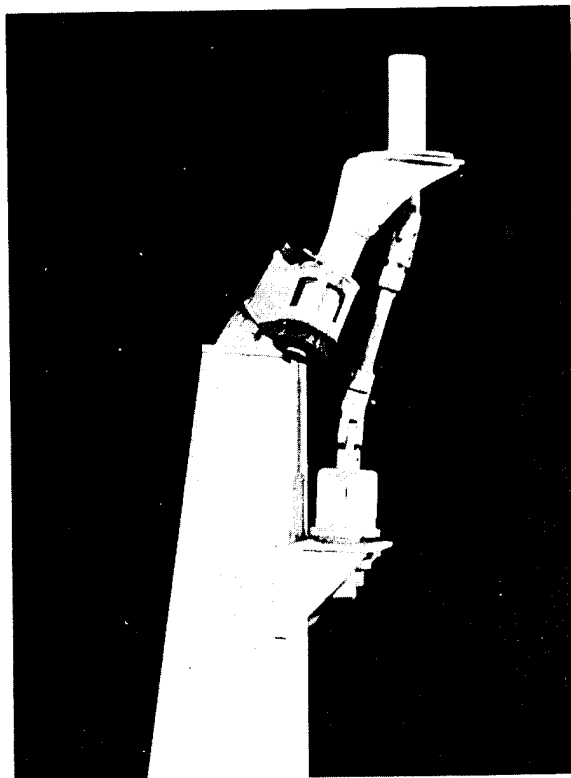


Figure 6. Azimuth Drive Based on Direct Drive from Mast.

There are several ways by which the effect of the azimuth torque can be partly compensated:

1. Figure 6 shows how the drive can be taken from the mast structure through constant velocity joints. This method is suitable for angles of roll and pitch up to  $\pm 25^\circ$  provided that the servos are stabilising properly, as the constant velocity joints can operate at misalignment angles of up to  $40^\circ$ .
2. Alternatively the azimuth motor could be mounted on the A arm, driving against a bearing plate attached via links parallel to the arms and cranks on the tilted axes to the mast structure.
3. A third alternative to the above is by hydraulic cylinders. Each cylinder is suspended on crank arms one of which is attached to the rotating axis, the other to its bearing. If the azimuth drive is by hydraulic motor the cylinders can be supplied in parallel with its hydraulic supply. If they are of the correct diameter, they will compensate for the base load torque that the servos would otherwise have to overcome.

##### Waveguide Feeds

The connection of waveguide feeds from mast to antenna is a problem, due to the movement of the mechanism about its centre of rotation. If the flexibility of the waveguide is utilised, the

change in length must be accommodated either by wrapping it round a drum, or by drooping it from the stable platform to a fixing on the mast. Alternatively, the axes can incorporate waveguide rotary joints as in a conventional gimbal system, in which case the feeds can be made in rigid waveguide throughout.

### AXES CONVERSION

The ship's master vertical reference provides angular measurements of 'absolute' Pitch and 'relative' Roll, which are required to be converted to the appropriate platform commands along the 'A' and 'M' axes.

The kinematic equations are developed by the sequential application of the classical rotation matrices.

The body-fixed axes  $i, j, k$  initially lie along the spatially fixed orthogonal vectors  $I, J, K$  as shown in Figure 7. Let the co-ordinates of a point in the  $I, J, K$  frame be defined as  $X, Y, Z$ . The rotation matrices are applied in sequence and the final co-ordinates of the point  $X, Y, Z$  are determined:

Rotation $\alpha$ about $i$	Rotation $\beta$ about $j$	Rotation $\gamma$ about $k$
$\begin{bmatrix} 1 & 0 & 0 \\ 0 & \cos\alpha & \sin\alpha \\ 0 & -\sin\alpha & \cos\alpha \end{bmatrix}$	$\begin{bmatrix} \cos\beta & 0 & -\sin\beta \\ 0 & 1 & 0 \\ \sin\beta & 0 & \cos\beta \end{bmatrix}$	$\begin{bmatrix} \cos\gamma & \sin\gamma & 0 \\ -\sin\gamma & \cos\gamma & 0 \\ 0 & 0 & 1 \end{bmatrix}$

and the final co-ordinates of a point  $x_f, y_f, z_f$  result from a sequence of rotations:

$$\begin{bmatrix} x_f \\ y_f \\ z_f \end{bmatrix} = [\alpha]_i [\beta]_j [\gamma]_k \dots \dots \begin{bmatrix} X \\ Y \\ Z \end{bmatrix}$$

This procedure is repeated for each of the particular platform angles taken in order and the deck movement. The platform structure angle sequence is shown in Figure 8 and the complete sequence is shown diagrammatically in the 'Pio-gram' Figure 9, (see also Reference 1).

$$\begin{bmatrix} x_f \\ y_f \\ z_f \end{bmatrix} = [C]_i [A]_k [-D]_i [M]_k [F]_i [R]_j [P]_i \begin{bmatrix} X \\ Y \\ Z \end{bmatrix} \dots (1)$$

Equation (1) is the complete co-ordinate transformation equation for the Tilted Axis Stable Platform.

For the ship upright, the co-ordinates of the

deck-normal unit vector are  $\begin{bmatrix} 0 \\ 0 \\ 1 \end{bmatrix}$  and the final

co-ordinates of a unit vector normal to the stabilised

platform are also  $\begin{bmatrix} 0 \\ 0 \\ 1 \end{bmatrix}$ . Equation (1) becomes:

$$\begin{bmatrix} 0 \\ 0 \\ 0 \end{bmatrix} = [C]_i [A]_k [-D]_i [M]_k [F]_i [R]_j [P]_i \begin{bmatrix} 0 \\ 0 \\ 1 \end{bmatrix} \dots (2)$$

Using the property of orthogonal matrices  $[C]^{-1} = [C]^T$  equation (2) becomes:

$$[-D]^T [A]^T [C]^T \begin{bmatrix} 0 \\ 0 \\ 1 \end{bmatrix} = [M] [F] [R] [P] \begin{bmatrix} 0 \\ 0 \\ 1 \end{bmatrix} \dots (3)$$

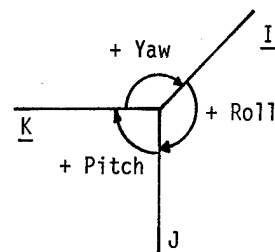


Figure 7. Sign Convention.

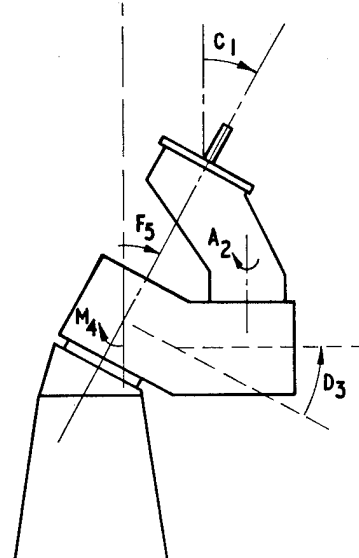


Figure 8. Angles of Structure.

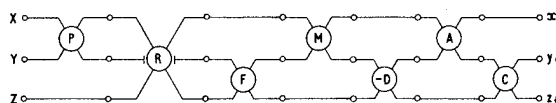


Figure 9. Pio-gram.

For the Tilted Axis Stable Platform, the fixed angles chosen are  $D = F = C = 25^\circ$  to give an acceptable dynamic performance. Solution of equation (3) yields the following expressions for 'A' and 'M' which are used in the axes conversion computer:

$$A = 2 \sin^{-1} \left[ \operatorname{Cosec} C \sqrt{\frac{1}{2} (\cos R \cos P \cos C - \sin P \sin C - 1)} \right] \quad \dots (4)$$

$$M = \tan^{-1} \left[ \frac{\sin A}{\cos C (1 - \cos A)} \right] - \tan^{-1} \left[ \frac{-\sin R \cos P}{\cos C \sin P + \sin C \cos R \cos P} \right] \quad \dots (5)$$

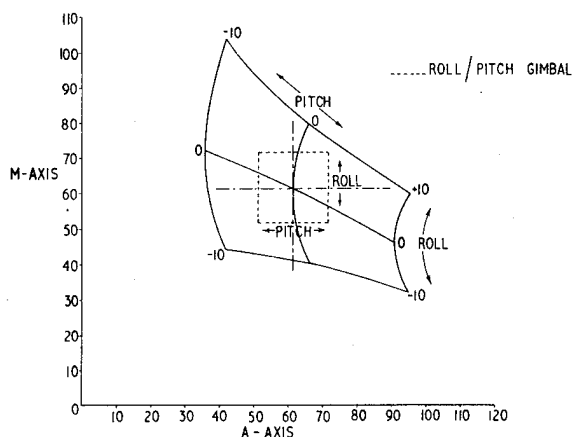


Figure 10. 'A' and 'M' axes angles for combined roll and pitch input.

These equations can be expressed graphically as shown in Figure 10, where the 'A' and 'M' axes angles are given for angles of roll and pitch up to  $10^\circ$  for each.

#### SCALE MODEL

##### Description

Figure 11 shows the scale model used to evaluate the principle. The antenna was simulated by the two metal tubes shown at the top of the photograph which were of equivalent mass and inertia. The servos of the two arms were engineered with coarse only synchros of  $3'$  accuracy. The azimuth drive was taken via constant velocity joints to the motor and gearbox at the base. The entire assembly was mounted on a rolling table.

To provide the angle conversion indicated in Figure 5, a Marconi Locus 16 computer was used, which provided a 16-bit output that minimised interfacing with existing synchros. The programme store was 2 kiloword capacity, which gave a cyclic time of 5 milliseconds for computation. This was adequate for the experimental system.

##### Experiments

The scale model was subjected to various tests on the rolling table, with the objectives of analysing dynamic accuracy, system power requirements, and dynamic effects such as gyroscopic torque interactions. The results obtained were required for data on which the full-scale version could be constructed for eventual trial on a ship in a rough sea environment.

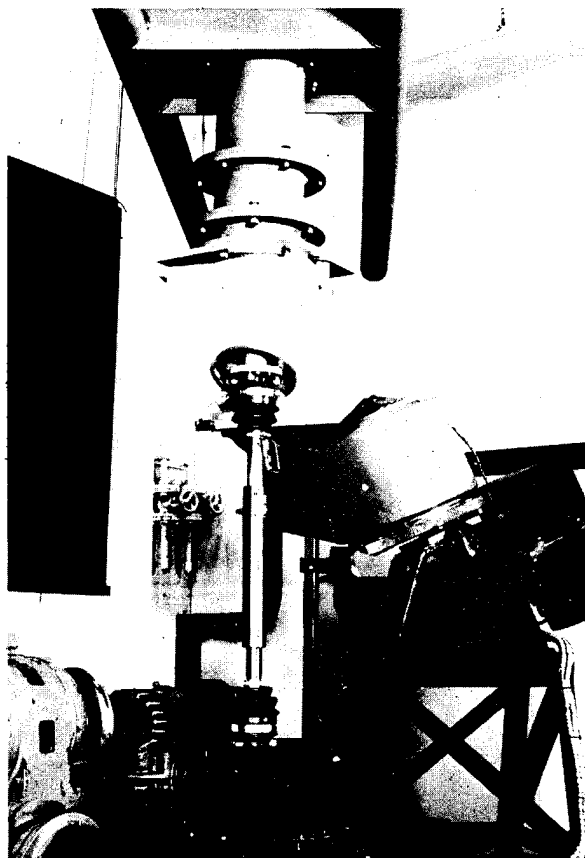


Figure 11. Scale Model.

##### Results

Some results have had to be left out in order to keep this paper within the required confines. Figure 12 shows the static errors for roll. Pitch were of similar magnitude.

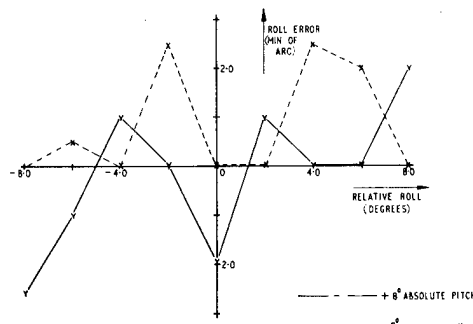


Figure 12. Static Roll Errors.



These servos gave Nichols' charts similar to that of Figure 13.

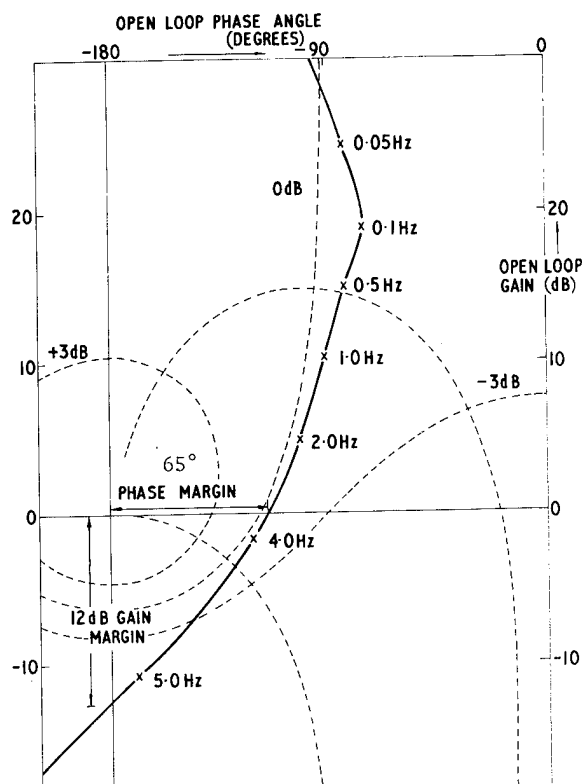


Figure 13. Frequency Response - 'A' Arm.

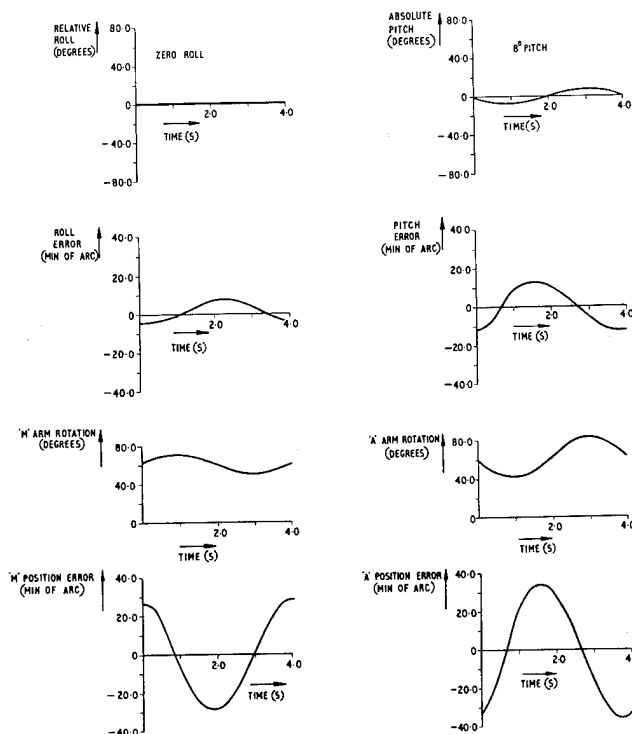


Figure 14. Dynamic Position Errors.

## CONCLUSIONS

1. The tilted axes principle has most advantage when applied to a single antenna of large wind drag.
2. A computer utilising 16-bit logic can perform the angle conversions required adequately.
3. Azimuth drive to the antenna taken directly from the mast requires some type of interlock be provided to ensure that the maximum specified misalignment angle of the constant velocity joints is not exceeded.
4. No problems were encountered in laboratory trials due to peaking of azimuth torque, or gyroscopic effects on the antenna.

## REFERENCE

R.L. Pio "Symbolic representation of co-ordinate transformation" IEEE Transactions Volume ANE-11 pps 128-134, June 1964.

C Controller, Her Majesty's Stationery Office, London. 1977.

## STATIC MASS BALANCING WITH A TORSION SPRING AND FOUR-BAR LINKAGE

Wayne A. Harmening

RCA Government Systems Division  
Missile and Surface Radar  
Moorestown, New Jersey 08057

### ABSTRACT

Two planar four-bar linkages are presented for use with a torsion spring to overcome static mass unbalance typical of steered radars. This arrangement replaces the dead load of a counterweight without increasing the steered mass or inertia.

### INTRODUCTION

A common problem in the design of machinery is the requirement for static mass balance about a rotational axis when an inherent unbalance exists.

Inherent static unbalance may occur in such diverse equipment as cranes, agricultural machinery, machine tools and telescopes. The balancing technique described herein was developed for steered radar antennas for which it is particularly appropriate.

The typical radar antenna consists of a parabolic reflector with an elevation axis offset to the rear of the reflector to prevent obscuration of the antenna aperture. This offset creates a mass unbalance about the elevation axis which can be partially corrected by placing the radar electronic assemblies on the opposite side of the elevation axis. However, when antenna apertures reach approximately six feet in diameter, the reflector tends to predominate, resulting in mass unbalance on the order of 10 to 50 foot-pounds. The unbalance increases as the square (approximately) of the aperture diameter, and may be several thousand foot-pounds as the aperture diameter approaches 100 feet.

The addition of a counterweight is a relatively straightforward and popular solution to the problem. The resulting increase in weight and inertia, however, is almost always undesirable and frequently becomes intolerable. For radars in particular, the drive train components must be sized to overcome either the static unbalance torque or the torque resulting from the increased inertia due to the addition of a counterweight. If large angular acceleration is required, as is the case for many steered radars, neither solution is attractive.

Assuming that the unbalanced mass and the counterweight have no inertia about their own centers of gravity (point masses) then the following weight and inertia relationship applies:

$$\frac{1}{m_R} + \frac{1}{I_R} = 1$$

where  $m_R$  is the ratio of mass after balancing with respect to the initial, unbalanced mass, and  $I_R$  is the ratio of inertia after balancing with respect to the initial unbalanced inertia. Thus, as the mass ratio approaches infinity, the inertia ratio approaches one, and conversely. One typical compromise is to select a counterbalance mass that doubles both the mass ( $m_R = 2$ ) and inertia ( $I_R = 2$ ). Thus, the addition of a counterweight may incur severe penalties.

Springs are often proposed and occasionally used as an alternative means of overcoming static mass unbalance. However, since springs are linear devices and the unbalance varies in a sinusoidal, non-linear manner, the method used to couple the spring to the unbalanced element is crucial to the balancing accuracy achievable.

One of the simplest mechanisms, a four-bar linkage, can approach the relationship required between the spring and the unbalanced element. This becomes an attractive solution since a linkage is simple, reliable, low in cost and generally a lightweight device.

### LINKAGE REQUIREMENTS

Defining the four-bar linkage functional relationship required for overcoming static unbalance is a straightforward procedure ( $\psi = f(\phi)$  in Figure 1). Synthesizing the linkage to satisfy this function, on the other hand, is an extremely difficult task, not previously accomplished. This difficulty is one of the major reasons that the four-bar linkage has not been used for static mass balancing.

But this condition is changing. Linkage synthesis techniques and high-speed computer facilities available today are well suited to the synthesis of the required functional relationships.

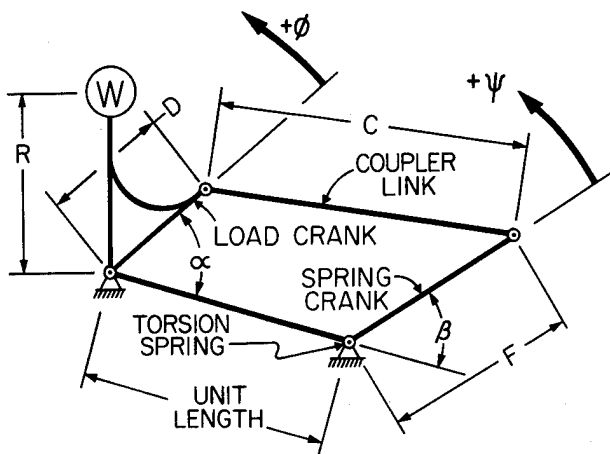


Figure 1. Linkage Nomenclature, shown at  $\phi = 0$  and  $\psi = 0$

It can be shown that any four-bar linkage capable of generating the ideal functional relationship

$$\psi = \lambda \sqrt{1 - \cos \phi}$$

can be coupled to a spring to counteract an unbalanced mass. In this relationship,  $\phi$  is the rotation of the unbalanced mass (rigidly connected to the load crank of the four-bar linkage) with respect to the top dead-center position of the mass as shown in Figure 1. The angle  $\psi$  is the rotation of the four-bar linkage spring crank (rigidly connected to a spring) and  $\lambda$  is an arbitrary constant. The mechanical advantage of the ideal linkage is obtained by differentiating the above expression:

$$\frac{d\psi}{d\phi} = \frac{\lambda}{2} \sqrt{1 + \cos \phi}$$

The stiffness required of the spring is defined as  $K = 2WR/\lambda^2$ , where the product  $WR$  is the unbalanced torque to be counteracted. Then the torque generated at the spring crank is the product  $K\psi$  and the torque generated at the unbalanced mass is:

$$K\psi \frac{d\psi}{d\phi} = WR \sin \phi$$

Thus the unbalanced mass is exactly counteracted by an ideal linkage, and the linkage is independent of the magnitude of the unbalance.

#### LINKAGE DEFINITION

The geometries of two useful, non-ideal linkages are given in Table 1. These linkages were developed using a modified form of the linkage synthesis technique of K. H. Siker as reported in "Analytische Betrachtung des Gelenkviereckes, insbesondere der Burmesterschen Punkte," VDI Berichte, Vol. 5 (1955), pp. 55-60.

TABLE 1

#### USEFUL BALANCING LINKAGES

LINKAGE PARAMETERS	LINKAGE	
	A	B
Spring Rotation for 90° Load Rotation - $\lambda$ (deg)	59.00	59.37
Load Crank Radius - D	0.718536071	0.510538359
Load Crank Initial Angle - $\alpha$ (deg)	69.58391097	55.04888140
Coupler Link Length - C	1.336726849	1.334282867
Spring Crank Radius - F	1.120560460	0.855455651
Spring Crank Initial Angle - $\beta$ (deg)	60.42882477	44.02632057

Linkage A of Table 1 is designed to operate with high accuracy over 90° of load travel ( $\phi$ ) as measured from the top dead-center position of the load. Linkage B of Table 1 is designed to operate over 180° of load travel with high accuracy. The functional error characteristics of the two linkages are shown in Figure 2. These functional errors are the linkage deviations in generation of the ideal product

$$\psi \frac{d\psi}{d\phi} = \frac{\lambda^2}{2} \sin \phi$$

expressed as a percent of the peak unbalance torque  $WR$  as a function of the load crank position  $\phi$  in Figure 1.

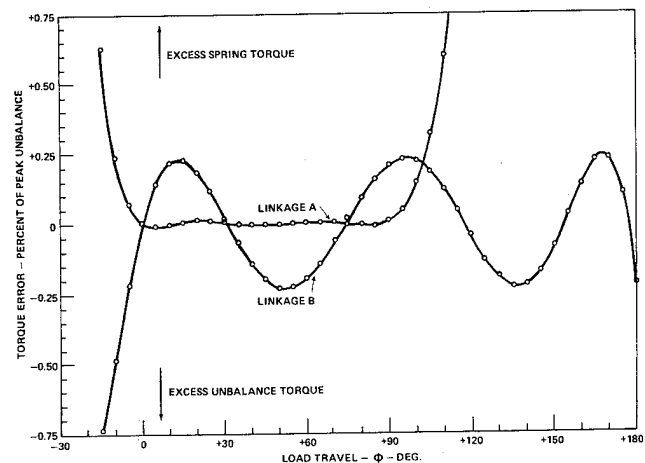


Figure 2. Linkage Functional Errors as Percent of Unbalance Torque  $WR$  vs Load Travel

Linkage A has a peak error (within the 90° design travel region) of -0.012 percent at  $\phi = 5^\circ$ ; linkage B peak error (within the 180° design travel region) of -0.230 percent at  $\phi = 135^\circ$ . It is apparent that for most applications, linkages A and B can both be considered as ideal, within their design travels, because of the low functional errors.

If an unbalance of 100 foot-pounds is to be overcome, the torque error for linkage A will be 0.012 foot-pound in its best accuracy region; the linkage B torque error will be 0.23 foot-pound. Although linkage A can be operated over a travel region larger than 90°, its torque error will greatly exceed the error of linkage B for load travels greater than 105°.

The functional errors shown in Figure 2 exclude numerous additional error sources such as: (1) linkage fabrication tolerances, clearance, friction, compliance and mass; (2) setup of initial linkage angles  $\alpha$  and  $\beta$ ; (3) spring tolerances, elastic modulus uncertainty and zero torque position of the spring; and (4) error in location of the top dead-center position of the unbalanced mass and the magnitude of the unbalance torque.

The linkages may be scaled to accommodate any distance between the crank pivots by multiplying the length ratios listed in Table 1 by the desired distance, while preserving the initial crank angles  $\alpha$  and  $\beta$ . Although rescaling is independent of the unbalance torque, the coupler link and crank loads will change. It is noted that the coupler link is not subject to compressive loads and may therefore be a lightweight tensile member.

#### APPLICATION

A torsion bar spring is ideally suited to application in steered radars. For a solid, circular-section torsion bar with allowable shear stress  $S$ , the bar diameter  $d$  for a given unbalance torque  $WR$  and load rotation  $\phi$  is:

$$d = 2 \left[ \frac{4WR}{\pi S \lambda} \sqrt{2} \sin \frac{\phi}{2} \right]^{1/3}$$

the length  $L$  of the torsion bar of torsional modulus  $G$  is:

$$L = \frac{d \lambda G}{S \sqrt{2}} \sin \frac{\phi}{2}$$

Figure 3 shows the torsion bar diameter  $d$  and length  $L$  required for linkages A and B (for the design travels of 90° and 180°, respectively) as a function of the peak unbalance torque  $WR$ .

The four-bar linkage and torsion spring can be implemented in several ways. Figure 4 shows one method of connecting the linkage to an unbalanced load,

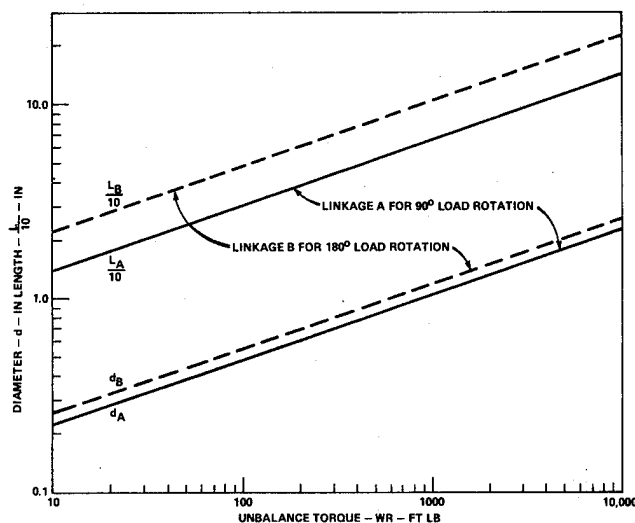


Figure 3. Torsion Spring Diameter  $d$  and Length  $L$  vs Unbalance Torque  $WR$  for a Solid, Circular, Steel Torsion Bar with Shear Stress  $S = 100,000 \text{ lb/in}^2$  and Torsional Modulus  $G = 12 \times 10^6 \text{ lb/in}^2$

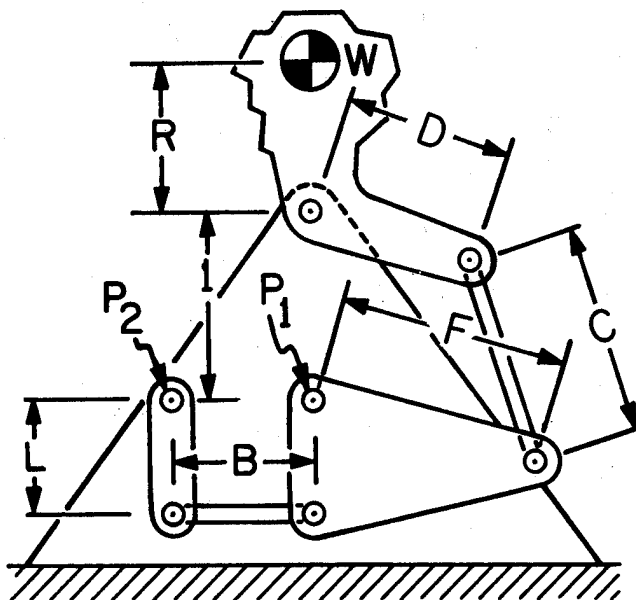


Figure 4. Normal Balancing Linkage Using a Parallel Four-Bar Linkage with Torsion Springs at  $P_1$  and  $P_2$  for Load Sharing

with a torsion spring at  $P_1$ . The addition of a parallel four-bar linkage permits relocation of the spring to  $P_2$ ; by placing springs at  $P_1$  and  $P_2$ , the load can be shared, thereby reducing the torsion spring size. In

For example, assume an unbalance torque of 150 foot-pounds and the use of a single torsion bar spring located at  $P_1$  or  $P_2$  (Figure 4). Using linkage A for  $90^\circ$  load rotation we obtain a torsion bar diameter of 0.563 in. and a length of 34.8 in. (from Figure 3). If torsion springs are placed at  $P_1$  and  $P_2$  and the load is shared at 75 foot-pounds per spring, then  $d = 0.447$  in. and  $L = 27.6$  in.

Figure 6 indicates one technique for utilizing dual linkages with a single torsion bar to achieve mass balancing over a load travel of  $\pm 180^\circ$ . This concept may also be implemented with the torsion spring on the unbalanced element; multiple springs may be used in either form.

One deficiency common to all methods that utilize a spring to counteract mass unbalance is the sensitivity to gravitational orientation. When the frame that supports the unbalanced mass, spring and linkage is tilted,

A schematic diagram of a mechanical system for studying forced oscillations. The system is mounted on a rectangular base. It consists of a horizontal beam pivoted at its left end. An unbalanced mass, represented by a cylinder, is suspended from the center of the beam. A driving crank is attached to the left end of the beam, and a driven crank is attached to the right end. The driven crank is connected to a vertical rod that passes through a spring stop and is attached to a torsion spring. The torsion spring is also connected to a load stop. The diagram is labeled with the following components: UNBALANCED MASS, DRIVING CRANK, LOAD STOP, DRIVEN CRANK, SPRING STOP, TORSION SPRING, and LOAD STOP.

## CONCLUSION

The linkage-spring combination is simple and reliable. However, its application is limited to discontinuously rotating machinery such as steered radars where the weight and/or inertia of a counterweight is unacceptable. For these cases, this technique offers good balancing accuracy at relatively low cost and weight, and can be uniquely arranged and scaled to suit the application.

# IMPACT LOADS ON RADAR DIRECTOR-GEARED SYSTEMS

KENNETH REDMOND

Mechanical Engineering Department  
Lockheed Electronics Company, Inc.  
Plainfield, New Jersey 07061

## ABSTRACT

The design of the Radar Director-Geared System involves a thorough evaluation of gearing loads that result from director dynamics, as well as the general requirements for satisfactory performance under severe environmental loading. Part of this evaluation should include the determination of impact load torques resulting from rapid drive reversals that occur during target acquisition, scanning, and slewing modes of operation. This paper presents a method for calculating peak-transmitted torques under these conditions.

To meet the requirements of tracking high-speed aircraft and missiles, the modern radar tracking system must be capable of high angular accelerations and velocities for target acquisition and must maintain minimum errors during target track. During the performance of a normal tracking mission, the dynamics of antenna motions frequently require sharp reversals in direction, which result in severe impact loads being imposed on the radar director gearing. Frequently, raster-type scanning modes use sharp changes in direction and steps in motion to obtain maximum area coverage in a minimum time, which also result in transmitting high torque loads through the geared system.

In many gearing applications, the drive is unidirectional and large velocity differences do not occur between driven members. Velocity changes that do occur are usually caused by errors in the geometry of the driving elements. Considerable knowledge and treatment of this type of loading which, in the case of gear drives are caused by inaccuracies in gear tooth contour, has been dealt with in the standard gearing equations developed through the research of Earl Buckingham and others in the 1930's. In numerous industrial applications, service data is available from previous applications and a shock or service factor is applied, based upon this experience, to ensure an adequate margin of safety in developing the geared system. In the case of geared drives used on radar directors, information from previous designs is frequently not readily available. Thus, it is necessary for the designer to evaluate shock loading based upon drive element, motor, and load inertia; backlash between the motor and load; and the performance characteristics of the motor. The basic techniques used to evaluate impact

loads involve principles of momentum and energy, and it is the purpose of this paper to apply these principles to determine shock load factors to design antenna system gear trains.

When two bodies collide and move on together, their subsequent motion must be such that the total momentum of the system remains unchanged. The forces on the bodies are equal and opposite and, since they act for the same time, the momentum added to the one must balance the momentum given to the other. Consequently, the total momentum remains unchanged. When two bodies collide and then move on together, a destruction of kinetic energy (KE) is inevitable. Thus, if two bodies of mass  $m_1$  and  $m_2$  moving along the same path with velocities  $v_1$  and  $v_2$ , collide and then move on together, their subsequent common velocity is:

$$\frac{m_1 v_1 + m_2 v_2}{m_1 + m_2},$$

and the loss of KE is:

$$KE \text{ loss} = \frac{1}{2} [m_1 v_1^2 + m_2 v_2^2] - \frac{1}{2} (m_1 + m_2)$$

$$\left[ \frac{m_1 v_1 + m_2 v_2}{m_1 + m_2} \right]^2$$

$$KE \text{ loss} = \frac{1}{2} \frac{m_1 m_2}{m_1 + m_2} (v_1 - v_2)^2. \quad (1)$$

If a spring system is interposed between the two colliding bodies, the loss in KE is stored in the spring as strain energy. If, in addition, the spring is properly designed to absorb the energy, the collision will occur without damage to the bodies. The application to a rotating system is best understood by considering the analogy between the momentum and KE of a body having linear motion and the momentum and KE of a body having rotation. In general, for the case of angular rotation, the  $mv$  term is replaced by  $J\omega$ , the product of the polar mass moment of inertia ( $J$ ), and the angular velocity ( $\omega$ ); and the  $1/2 mv^2$  terms are replaced by  $1/2 J\omega^2$ .

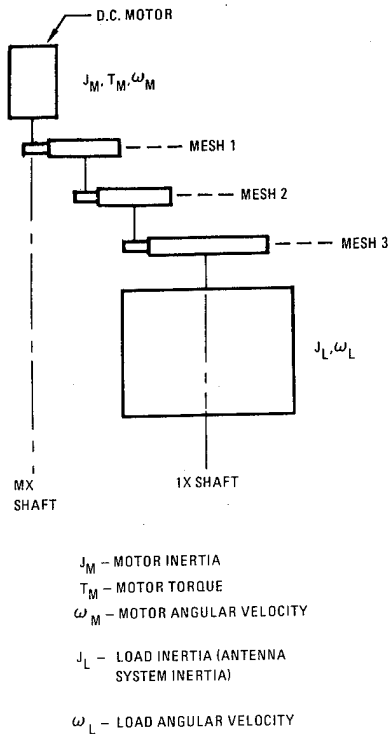


Figure 1. Antenna Drive, Simplified Schematic

A typical radar director drive, illustrated schematically in figure 1, shows a dc servo motor driving through three gear meshes to obtain rotation of the antenna system tracking elements. Inertia and torques can be transferred to the 1x shaft by the following relationships:

$$J_{mix} = J_m (\text{gear ratio})^2, \quad (2)$$

$$T_{mix} = T_m (\text{gear ratio}), \quad (3)$$

$$\omega_{mix} = \omega_m (\text{gear ratio}), \quad (4)$$

where inertias are transferred to one speed by multiplying by the gear ratio squared, and torques and angular velocity are transferred to one speed by multiplying and dividing the gear ratio, respectively, to obtain the equivalent rotating system shown in figure 2. This can then be changed to the dynamic model shown in figure 3 by introducing gear-train backlash ( $\theta_B$ ) and the spring constant ( $K_T$ ) of the gearing and structural elements between the motor and the load, and by considering the relative magnitude of motor, gear train, and load inertia.

The most significant backlash in the gear train is in the last pinion to gear mesh, and the most significant gear-train inertia is contributed by the high-speed end of the train. In establishing the dynamic model, the gear-train inertia has been lumped with the motor inertia. The overall backlash, contributed by each gear mesh, has been lumped in the term  $\theta_B$ . The spring constant ( $K_T$ ) is the spring constant of the gearbox summed with the series spring elements in the load and the motor.

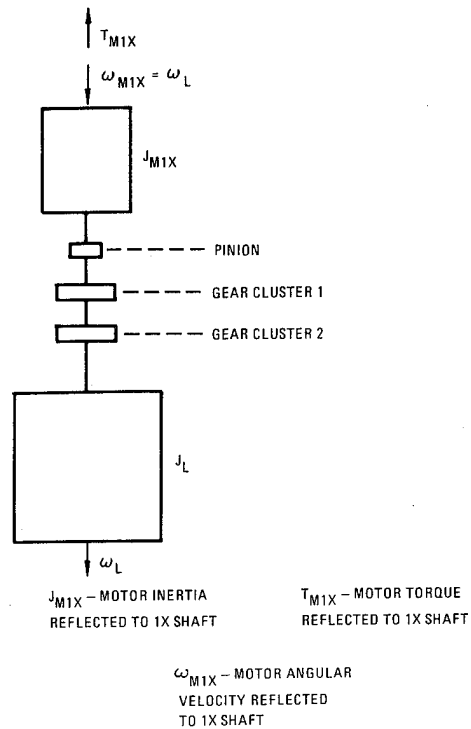


Figure 2. Equivalent Rotating System

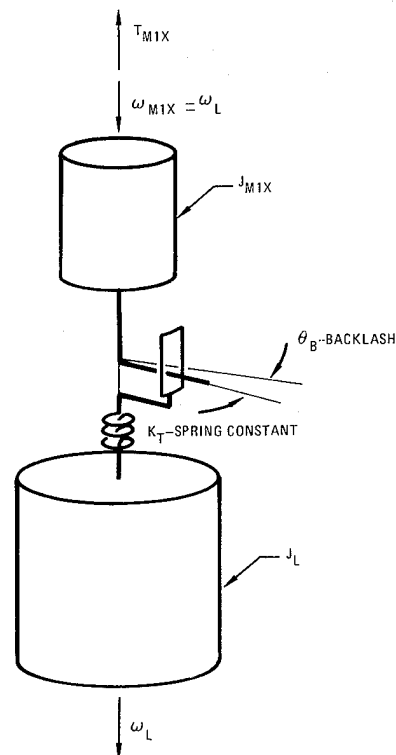


Figure 3. Dynamic Model Drive at Start of Reversal

Referring to figure 3, the drive is shown going clockwise at full speed  $\omega_L$ . The drive is then reversed by instantaneously applying the motor torque ( $T_m$ ) counter-clockwise.\* The motor then slows down relative to the load as the gears disengage due to drive backlash. The difference in angular velocity between the motor and the load ( $\Delta\omega$ ) when gear reengagement occurs is given by the following expression:

$$\Delta\omega = \sqrt{2\alpha\theta_B} : \alpha = \frac{T_m}{J_m} \quad (5)$$

The motor speed ( $\omega_m$ ) at the point that impact begins is:

$$\omega_m = \omega_L - \Delta\omega = \omega_L - \sqrt{2\frac{T_m}{J_m}\theta_B} \quad (6)$$

and the common velocity of the motor and load ( $\omega_c$ ) at maximum gearbox twist is:

$$\omega_c = \frac{J_m\omega_m + J_L\omega_L}{J_m + J_L} \quad (7)$$

The loss of KE due to the impact or the potential energy stored in the gearbox spring is given by:

$$KE \text{ loss} = \frac{1}{2} \frac{J_L J_m}{J_L + J_m} (\omega_m - \omega_L)^2 \quad (8)$$

If no outside torque was acting during the impact, the loss of KE would be equal to  $T_D/2\theta$ , where  $T_D$  is the maximum gearbox torque and  $\theta$  is the angular twist of the gearbox spring. Since the motor torque acts on the drive during impact, the work done by this torque must be considered due to the relative motion ( $\theta$ ) of the motor and load during impact. Therefore:

$$\frac{T_D}{2}\theta = T_m\theta + \frac{1}{2} \frac{J_L J_m}{J_L + J_m} (\omega_m - \omega_L)^2 \quad (9)$$

Substituting  $T_D/K_T$  for  $\theta$ , and solving for  $\omega_m - \omega_L$  from equation 6 and substituting, leads to the following quadratic:

$$T_D^2 - 2T_m T_D - 2K_T \theta_B \frac{J_L}{J_L + J_m} = 0 \quad (10)$$

Solving for  $T_D$ :

$$T_D = T_m + \sqrt{T_m^2 + 2K_T \theta_B T_m \frac{J_L}{J_m + J_L}} \quad (11)$$

The following geared system parameters are taken from an actual design where the overall gear ratio was 175:1. The values given are reflected to the 1x shaft:

$$\begin{aligned} T_m &= 1620 \text{ lb-in} \\ J_L &= 220 \text{ lb-in-sec}^2 \\ J_m &= 38.3 \text{ lb-in-sec}^2 \\ \theta_B &= .001 \text{ rad} \\ K_T &= 5 \times 10^6 \text{ lb-in/rad} \\ \text{Gear ratio} &= 175:1 \end{aligned}$$

Substituting in equation 11, the value for  $T_D$  is 5669 lb-in, which is approximately 3.5 times the maximum-applied motor torque, which is the torque the geared system must be designed to withstand.

In many applications a slip clutch is used, with the torque transmitted through the drive limited by the torque setting of the clutch. The use of a slip clutch is illustrated by example, using the same values for system parameters previously used. The assumption is made that all the energy of impact is dissipated by clutch slip. The clutch setting ( $T_c$ ) has been taken as being 10 percent greater than maximum motor torque. In the equations that follow, the energy dissipated in the clutch, the angle of slip, and the slip time of the clutch are calculated.

The angular velocity of the driver is 2 rad/sec before applying the motor-reversing torque; therefore, the motor velocity at the point of impact is:

$$\begin{aligned} \omega_m &= \omega_L - \sqrt{2\frac{T_m}{J_m}\theta_B} \\ \omega_m &= 1.71 \text{ rad/sec} \end{aligned}$$

The torque acting on the motor and the load is illustrated in figure 4. As before,  $\omega_c$  denotes the common velocity

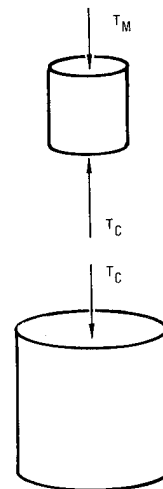


Figure 4. Motor and Clutch Torques

\*The assumption of the instantaneous application of peak motor torque is a close approximation to the actual performance of many modern dc servo and hydraulic motors. If motor dynamics are different for a particular application, appropriate consideration must be given to calculating the change in motor angular velocity.



that occurs the instant that slip ceases. If (t) is the time duration of the impact then, by principles of impulse and momentum, the following expressions can be written for the motor and the load:

The motion of motor is:

$$(T_c - T_m)t = J_m(\omega_c - \omega_m). \quad (12)$$

The motion of load is:

$$T_{ct} = J_L(\omega_L - \omega_c). \quad (13)$$

Combining equations 12 and 13 to eliminate t is:

$$\frac{T_c + T_m}{T_c} = \frac{J_m(\omega_c + \omega_m)}{J_L(\omega_L - \omega_c)}.$$

Substituting:

$$\frac{1782 - 1620}{1782} = \frac{38.3(\omega_c - 1.81)}{220(2.0 - \omega_c)}$$

and:

$$\omega_c = 1.81 \text{ rad/sec.}$$

The time the clutch slips is found by solving equation 13 for t:

$$t = \frac{J_L(\omega_L - \omega_c)}{T_c} = \frac{220(2.0 - 1.81)}{1782} = .0235, \text{ or } 23.5 \text{ ms.}$$

The relative velocity between the motor and the load is  $2.00 - 1.71 = .29$  rad/sec at the start of the impact and, when clutch slips ceases, the relative velocity is zero. As a result, the average velocity is  $.29/2 = .145$  rad/sec, and the clutch angle of slip is  $\theta_s = .145 \times .0235 = .00341$  rad. The angular slip of the clutch at the motor shaft is found by multiplying by the gear ratio:

$$\theta_s = .00341 \times 175 \times \frac{360}{2\pi} = 34 \text{ degrees.}$$

The energy dissipated in the clutch (E) is the product of the clutch torque times the angular slip:

$$E = T \theta_s = 1782 \times .00341 = 6.08 \text{ in-lb}$$

## HIGH ACCURACY HYDRAULIC MOTORS FOR RADAR ANTENNAS

C. EKENBERG, P. STRÖM, B.-O. ÅS

Philips Elektronikindustrier AB  
175 20 Järfälla, Sweden

### ABSTRACT

Philips Elektronikindustrier AB, PEAB, has developed, engineered, and manufactured a line of hydraulic motors for use with radar antennas, in particular in shipborne Weapon Control Systems. Sample designs are presented in some detail along with the rationale for adopting this technique. Special emphasis is given to a design, which in one package contains a number of functions: motor, bearing, angle pick-off, electrical signal transfer through a slipring assembly, oil transfer through "hydraulic sliprings", and the servo valve.

### INTRODUCTION

Most radars, except the very costly phased array types, depend on mechanical means for positioning of the beam. With today's high accuracy monopulse techniques and highly efficient signal processing, the performance of a tracking radar is often limited by the drive mechanisms and bearings of the antenna pedestal. This is especially true in shipboard applications.

The requirements imposed on drives for use in a tracking radar pedestal can be summarized as follows:

- High torque at all speeds
- Freedom from backlash, wear, and other gear defects
- Low effective inertia in order not to add additional load
- Low losses also during stall with high torque applied, e.g. as a result of wind load
- Smooth running at very low speed, which may be experienced when tracking head-on targets
- High speed during acquisition of a target
- Accurate bearings capable of withstanding shocks
- Low weight
- Reasonable cost

The requirement of low speed also implies low overall static friction.

The accuracy requirements are aggravated, if the tracking radar is used for gun laying. Excessive "tracking noise" degrades the gun fire accuracy and causes wear in the gun servo mechanisms. Noise is introduced by various deficiencies, e.g. gear imperfections and friction. The low frequency part of the noise cannot be filtered out and is multiplied by a factor proportional to the time of flight of the projectile. This is so because a future target position is predicted by forming a speed vector through derivatives of a number of position measurements.

### MOTOR SELECTION CONSIDERATIONS

The motor to be described is the result of an effort by PEAB, when the decision had been taken in the end of the 1960:s to develop a tracking radar for shipboard use.

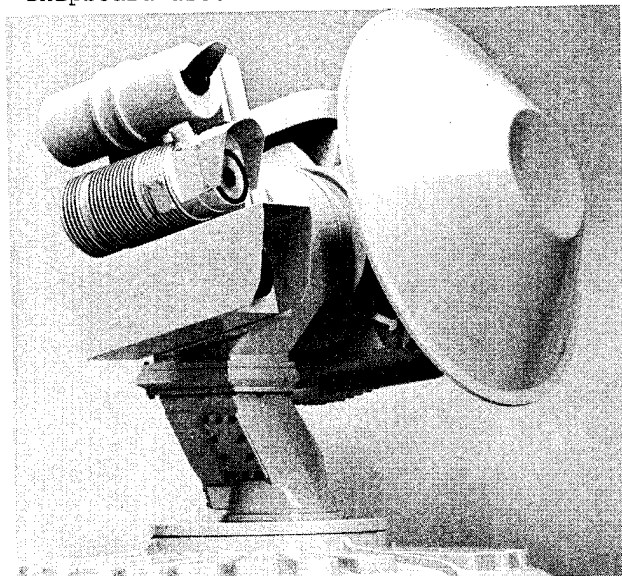


Fig 1. Director with radar, TV, Laser, and IR using hydraulic motors in azimuth and elevation

The radar antenna was to have a diameter of approx 1 m and the pedestal should have the capability of carrying additional optronic sensors; TV-camera, IR-tracker, Laser Rangefinder, cf fig 1. The target was set, that the mechanical components, motor and bearings, should have a performance compatible with that of the radar, which was to be very accurate due to the combination of frequency agility and monopulse.

An analysis of various alternatives

- Electric or Hydraulic motors
- Gears or Direct Drive

was conducted against the requirements on speed, high accuracy, high servo bandwidth etc in the environment of a ship's deck.

The gear solution was ruled out because of the unavoidable defects of gear-boxes and bearings at reasonable cost. Furthermore, gears add moment of inertia and magnifies the motor's moment of inertia.

Electric direct-drive torque motors were found to be capable of giving the desired acceleration performance etc, however at a penalty of high weight and large size. Besides, bearing problems would remain.

The search for a motor accordingly focused on direct-drive hydraulic motors. Various types: radial piston motors, axial piston motors, vane motors, and others were investigated. The vane motor, fig 2, was found to have the combination of high "stiffness" and high torque, specially if a large radius and many chambers were used. This type of motor also permitted easy integration of hydrostatic bearings into the motor itself, thereby solving the bearing problem at the same time within one integrated component.

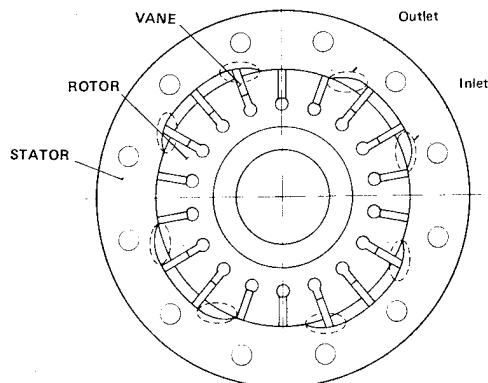


Fig 2. Principle of a vane motor

The main problem of the vane motor principle used to be how to get the vanes to move in and out without introducing excessive friction and wear. Know-how on this type of hydraulic motor was found inside the Philips concern in the Research Laboratories in Eindhoven, Holland. The design was finalized and manufacture undertaken by PEAB. Some hundreds of motors of different sizes have been made to date and the first series has been in operation at sea for close to 5 years. As will be accounted for below, the experience is extremely good.

#### DESIGN DETAILS

A typical design is shown in fig 3. This motor is characterized by a working radius of approx 150 mm, 8 chambers, and 30 vanes. The problem of reducing the friction and tilting forces acting on the vane has been solved by a patented design, which can best be described as miniature hydrostatic bearings between the rotor and the vanes. These bearings have a controlled amount of "leakage", so that the proper amount of oil is automatically fed to the bottom of the vane in order to balance the radial force due to the pressure on the top of the vane. Only weak springs are used between the rotor and the bottom of the vanes to ensure initial contact between the top of the vane and the stator. The leakage around the vanes is small. A typical value for a complete motor is 1.5 liter/min at a stall torque of 250 Nm with an oil viscosity of 90 cSt.

As mentioned above, hydrostatic bearings are an integral part of the motor. There are bearings in both the axial and radial directions. The bearings can be seen in the photograph, fig 3, as "pockets" in the top and bottom end plates. The design of these bearings is fairly conventional.

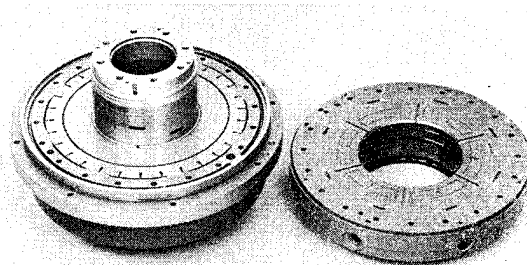


Fig 3. A typical motor and bearing assembly

Sealing inside the motor is by means of gap seals. Sealing to the outside is by means of radial lip seals, one on each side of the motor.

The oil in the hydrostatic bearings gives no static friction and the vane design gives a very low static friction. A typical value of static, and low speed dynamic friction is a torque of 2 - 5 Nm, of which the main part comes from the lip seals around the axis. This figure is to be seen in relation to the maximum torque of 650 Nm.

High stiffness, important for good servo performance, is ensured by a large radius of the rotor and short distance between the chambers and the servo valve in order to give a small enclosed volume of oil. Normally, the servo valve is bolted to the motor assembly, cf fig 4. A typical value of the stiffness is more than  $1 \cdot 10^6$  Nm/rad.

The only source of backlash in this type of motor is the clearance necessary between the rotor slots and the vanes. With a typical clearance of  $5 \mu\text{m}$  and a radius of 150 mm, this gives a "static" play of only 0.03 milliradians. Under dynamic conditions, the backlash will be even smaller because of the oil viscosity.

The motor is further so designed, that a pancake type multispeed synchro or resolver can be easily attached to the stator and rotor, see figs 4 and 5. In this way, gears are avoided altogether, and a compact assembly is formed with mechanical errors in the order of  $1/100$  of one milliradian.

The necessary electrical slipring assembly and/or waveguide rotary joint is easily accommodated by the large hole in the center of the rotor, see figs 4 and 5. Furthermore, the motor has three "hydraulic slippings" which are used to transfer oil from the stationary to the rotary part and on to another motor, or motors, beyond the first one, e.g. the elevation motor above the azimuth motor in the pedestal design of fig 1. In this way, multiple motors are easily cascaded giving a high degree of freedom to the designer of a pedestal. The total assembly thus forms an integrated component with all necessary functions: drive, bearing, angle pick-off, electrical signal transfer, oil transfer, and the servo valve in one compact housing.

The internal clearances and gaps are in the order of  $5 - 20 \mu\text{m}$ . This places requirements on the manufacturing, which can be overcome by proper procedures, and on the purity of the oil. The latter is assured by the use of filters in the normal way and the motor is in fact less critical than the common servo valve.

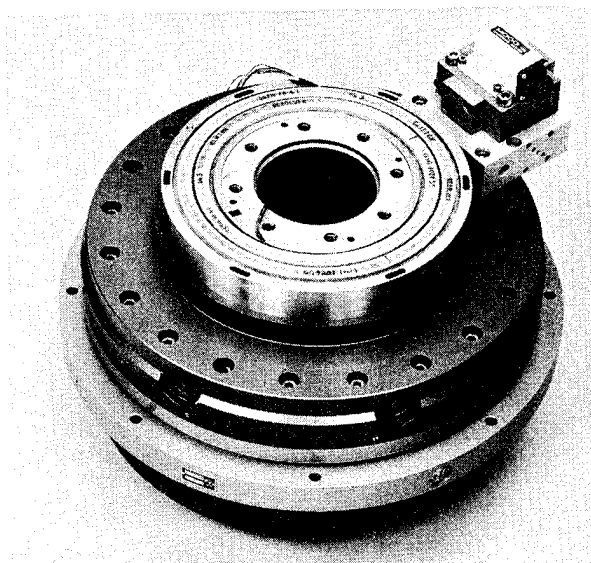


Fig 4. Motor fitted with servo valve and pancake synchro

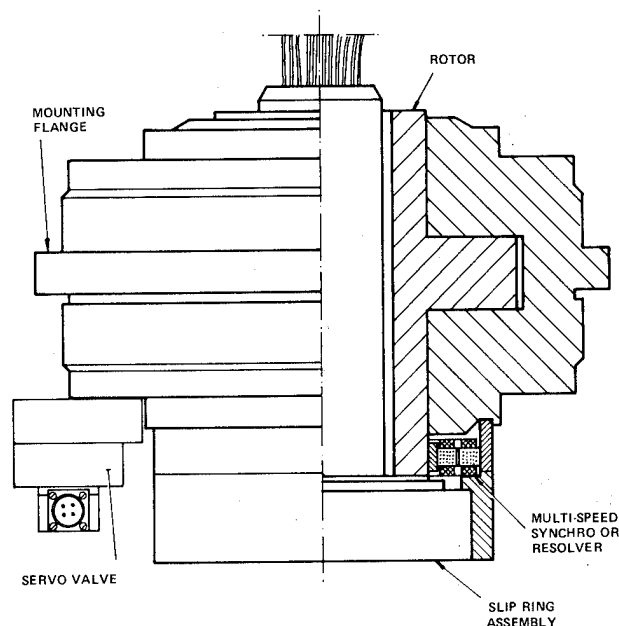


Fig 5. Complete assembly of motor and accessories

### TYPICAL DATA

The data given below apply to a motor-bearing combination currently used in the radar director of the Weapon Control System 9 LV 200 Mk 2, fig 6.

#### Motor

Speed range	0 - 1.5 rad/s
Stall torque	650 Nm
Torque at full speed	350 Nm
Diameter, overall outer	500 mm
Weight	65 kg
Displacement	1.2 liter/rev.
Supply pressure	4 MPa
Resonance frequency, with a load of 20 kg m <sup>2</sup>	>30 Hz

#### Bearing

Axial load, max	25 kN
Radial load, max	13 kN
Bending torque, max	1350 Nm

The figures for permissible load apply under static conditions. Under dynamic conditions, e.g. a shock, the figures are much higher because of the oil viscosity.

### LIFE EXPERIENCE

As mentioned before, a large number of these motors have already been in operation at sea for a long time. By now, a total of about 60,000 hrs have been accumulated without any motor failure.

An early model was bench-tested with full load under simulated dynamic conditions more severe than in actual operation. This early model was tested for approx 12,000 hours.

One of the first motors to be installed on board an FPB has been kept under special surveillance. It was inspected the first time after about 2 years at sea, during which period it had accumulated approx 2000 hrs and a second time, recently, after more than 4 years and close to 4000 hours. Internal dimensions and surface smoothness were checked very carefully. No significant wear could be observed or measured on any of these occasions, and after reassembly, the motor fulfilled the original test specification.

### FIXED VANE MOTORS

Other radar antenna applications, e.g. stabilisation gimbals, fig 7, do not require continuous rotation.

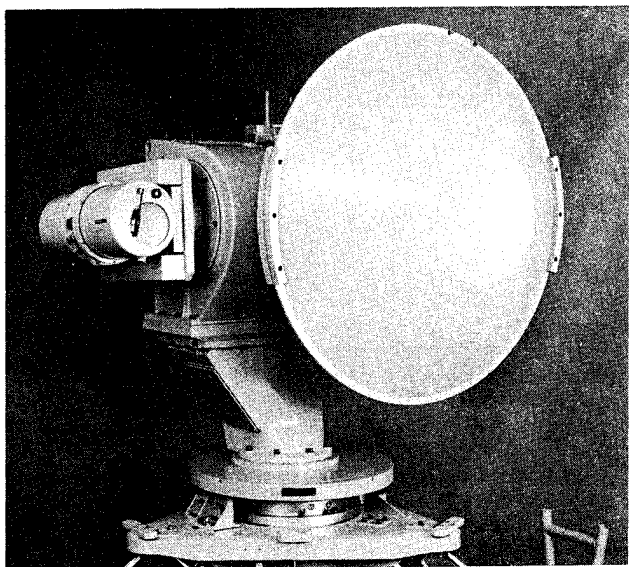


Fig 6. 9 LV 200 Mk 2 Director

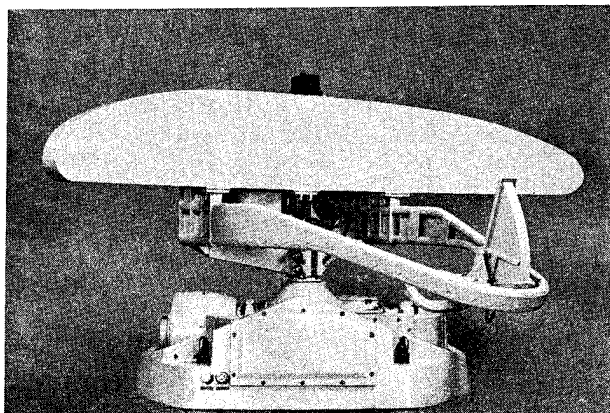


Fig 7. 9 LV 200 Mk 2 fully stabilised Search Antenna

For these applications, another type of motors has been developed, fig 8. This motor has, typically, 4 fixed vanes, which will allow a travel of  $\pm 30^\circ$ . Since the vanes can be made quite heavy, this motor becomes very compact for a given torque.

Special arrangements inside act as automatic, viscous brakes and end stops, if, for some reason, the servo tends to overrun its electrical limits.

Also this type of motor has hydraulic slippers for oil transfer.

Data for a typical motor of this kind are:

Arc of travel	$\pm 30^\circ$
Stall torque, 4 MPa supply	1000 Nm
Diameter	250 mm
Weight	17 kg

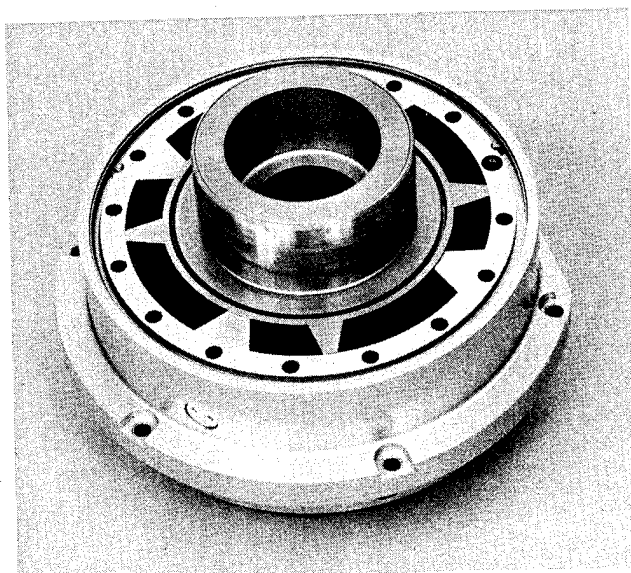
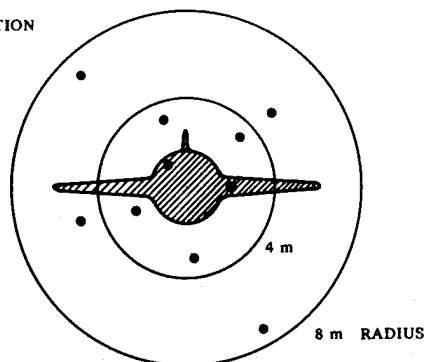


Fig 8. Typical fixed vane motor

## OPERATIONAL RESULTS

Motors of the different types have been incorporated in radars delivered to the navies of many countries. Extensive tests have been carried out by all these navies, each time resulting in meeting the specified accuracy with wide margins. Fig 9 shows an extract of results obtained with the first tracking radar - fire control system using these motors. As can be seen, the overall dispersion of fire, including the gun and ammunition is better than 2 mrad circular rms; indeed a very gratifying result.

ILLUSTRATION  
OF CASE II  
BELOW



CONDITIONS				% HITS WITHIN RADIUS		CIRC. DISPER- SION $\sigma_c$ , m
TARGET SPEED m/s	WIND VEL m/s	SEA STATE	ROUNDS FIRED	< 4 m	< 8 m	
70	3	1	77	80	99	2
150	2	1	10	60	100	3
200	18	4	8	25	67	5

Fig 9. Extract of results obtained from test firings against towed targets with the PEAB 9 LV 200 fire control and the Bofors 57 mm gun on a 145 ton Swedish Navy FPB. Range to target in all cases was 2 - 3 km

# ADVANCED COMPOSITE ANTENNA DEVELOPMENT

John H. Heathman and Robert S. Wilson

General Dynamics Convair Division,  
5001 Kearny Villa Road, San Diego, California 92138

**ABSTRACT** — This paper presents a designed, fabricated, and tested antenna terminal employing advanced composite materials. The antenna demonstrated the advantage these materials have in providing a more compact, lower weight system, while meeting required performance in a cost effective manner. The work was specifically oriented toward the requirements and objectives of the Naval Electronics Command for the development of a lightweight, low-cost, and maintenance-free satellite communications (SATCOM) antenna. The antenna has been identified by NAVELEX as a future requirement for use throughout the fleet. Vibration testing was performed by both Convair and the Naval Electronics Laboratories Center (NELC), San Diego. The antenna structure successfully passed the vibration testing with recorded structural resonant frequencies in all three axes in excess of 45 hertz. The structure also successfully survived shock testing, medium-weight hammer, at NELC.

**INTRODUCTION** — The growing need to place mast-mounted communication antennas on U.S. Navy ships presents unique problems for ships of small displacement. In many instances, the heavy weight of the antenna terminal precludes its installation because of the effect on the ship's stability. This situation is further compounded by a need to locate the antennas at high elevations to prevent signal interference from other deck-mounted structure, and to obtain full hemispherical coverage from a single terminal. Additionally, many present antenna systems have an insufficiently high structural resonant frequency to meet shipboard vibration conditions, resulting in short service life from associated fatigue influences, especially bearings. As a result of the high specific modulus, and strength and tailorability of advanced composite materials (ACM), they offer a potential solution to the problems experienced in the use of all-metal antenna systems. However, limited ACM use by the Navy for shipboard environments (vibration and shock), and cost effectiveness of ACM for such applications, had to be addressed before acceptance by the Navy could be anticipated.

The starting point for this advanced composite antenna development program was the result of a small study contract performed by General Dynamics Convair for NAVAIR. The study indicated an overall 20 percent weight saving was feasible by direct substitution of ACM for metals, in an otherwise conventional design approach. This allowed a four-foot diameter reflector to replace the three-foot diameter metal reflector within the original system target weight. However, it was apparent that taking a different design approach, based on the judicious use of ACM, could produce even greater weight savings and a more favorable production cost for the antenna terminal. The program's objectives were to develop a cost effective antenna configuration and design, and then fabricate and test the antenna structure to validate its cost effectiveness and performance under vibration, shock, and temperature extremes.

**ANTENNA CONFIGURATION** — The antenna has a four-foot dish and a three-axis (elevation, cross-level, and train) gimbal system. Viewing limitations are minimal, being 35 degrees down and 135 degrees up in the elevation axis,  $\pm 60$ -degree viewing in the cross-

level axis, and continuous rotation in the train axis. Analysis of candidate antenna configurations revealed that meeting an overall structural resonant frequency of 50 hertz would be the greatest design challenge in alignment with a least weight, compact, and cost effective antenna structure. The most critical elements of the antenna were determined to be the reflector dish and riser structure, the gimbal-axis bearings and their installation requirements, and the interfacing of these components in a structurally efficient manner. Extensive background and experience with the design and fabrication of composite antenna reflectors that met the program's requirements left the remaining structure to be proven by design, fabrication, and test. The chosen configuration, Figure 1, feasible only by the use of ACM, provided for an antenna height reduction of 10 inches and a weight savings of 32 percent over a metallic baseline configuration.

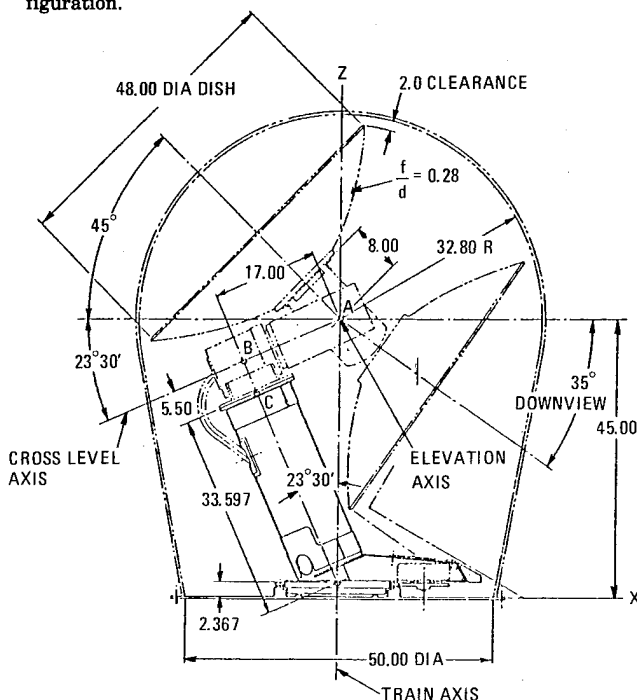


Figure 1. Antenna configurations.

This was achieved by employing a slender, circular cross-section ACM riser structure terminating at the antenna base in a low profile turntable arrangement housing a cross-roller bearing. The diameter of the riser was determined from its ability to efficiently interface with the cross-level structure and train-axis bearing (both sized by shock loading), and ability to provide stiffness sufficient to satisfy natural frequency requirements. The length and inclined angle of the riser and the cross-level cant angle result from the need to satisfy reflector viewing requirements. In all configurations the

elevation axis was maintained directly over the train axis, which produces minimum radome volume and surface area. The length and diameter of the cross-level shaft was arrived at from a balance between providing sufficient shaft stiffness and a space envelope for practical waveguide, and balance weight installations.

**STRUCTURAL DESIGN CRITERIA** — The significant structural design criteria and their implications in the antenna structure design are summarized in Table 1.

Table 1. Structural design criteria.

Phenomenon	Criterion	Design Impact
Shipboard vibration	MIL-STD-167-1 (Mast-mounted equipment)	Implies fundamental frequency should be $> 50$ Hz. Designs riser structure
Shipboard shock	MIL-S-901C (Medium weight shock test machine)	150g vertical load factor, 75g lateral load factor. Designs remaining antenna structure
Nuclear blast	MIL-E-16400 (Modified to $p = 3$ psi, $q = 0.2$ psi, $t + = 3.5$ sec)	Designs radome
Wind	75 knots operational 100 knots survival	Designs radome base
Temperature Environment	Oper -28 to +65C -18 to +149F Non-oper -62 to +71C -80F to +160F	Influences material choices & bearing

By designing the structure to resonate above 50 hertz, ship-induced vibration can be minimized. This is because the maximum excitation frequency specified in MIL-STD-167-1 for mast-mounted equipment is 33 hertz. This results in a ratio of natural frequency to forcing frequency of less than 0.7. The steady-state response of such a system is less than twice the input, even for extremely low damping. Since the specified input at 33 hertz is 1.25g, the response will be less than 2.5g.

Assuming the same test setup (mounting channels, etc.), the natural frequency of the antenna system on the elastic test fixture is 66 hertz. For a two-foot hammer drop, the acceleration imparted to the antenna base is 75g. Using a dynamic factor of 2, the shock design factor is 150g in the vertical direction. MIL-S-901C also requires that the shock table be tilted 30 degrees; this establishes the 75g shock design factor in the lateral direction.

**STRUCTURAL MATERIAL SELECTION** — Criteria in the choice of material for the antenna structure are stiffness and strength-to-weight ratio, corrosive resistance, ductility, and a low cost fabrication. Thermal compatibility with bearings, torquers, synchros, etc., are also important considerations. The major criterion is stiffness rather than strength, especially for a compact antenna configuration with a minimum weight association. Metallics have the same order of specific stiffness ( $E/\rho$ ); except beryllium, but it is expensive, brittle, and difficult to work. However, the graphite/epoxy materials can be tailored to provide up to 6.5 times the specific stiffness of metallics.

At the beginning of the study a survey was conducted to determine the ACM system that best satisfied cost effectiveness requirements. Only material systems with sufficient material property data development and fabrication experience for a production program application were considered.

Weight efficiency of the ACM compared to metallics is illustrated in Figure 2, with a plot of specific tensile strength against specific tensile modulus. The ACM plots are for laminates that at the lower end are pseudoisotropic and at the upper end have unidirectional fiber orientation. Between these two extremes any combination of strength and stiffness can be met by choice of appropriate fiber orientation and layup. The three graphite/epoxy systems shown; T300/5208, HM-S/5208, and GY-70/5209 are representative of the three primary categories of graphite/epoxy material; high-strength, high-modulus, and ultra-high modulus laminates. Relative costs of prepreg material to fabricate laminates varies with quantity

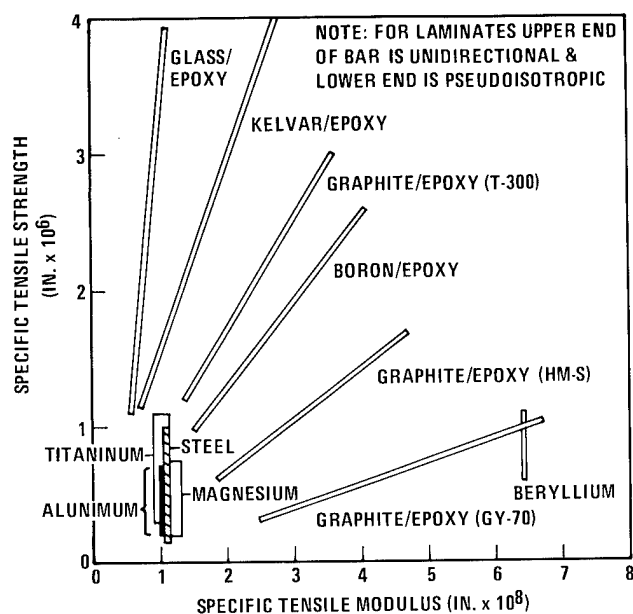


Figure 2. Weight efficiency of structural materials.

requirements, choice of resin system desired, and in some instances fiber diameter employed for the prepreg. Prepreg cost per pound is generally about \$35 for the T300 fiber, \$65 for the HM-S fiber, and \$140 for the GY-70 fiber.

During a later trade study on laminate selection, it was determined that neither the T300/5208 or HM-S/5208 graphite/epoxy systems could be made to meet the natural frequency requirement for the riser. The GY-70/5209 graphite/epoxy system was chosen for the riser design. Although the ultimate tensile strength of the GY-70/5209 material system is the lowest of any of the graphite/epoxy systems, it was sufficiently high for the stiffness critical riser structure.

The Celion GY-70 graphite fiber is a product of Celanese Corporation; the 5209 resin is an epoxy formulation produced by Narmco Materials Inc. The basic material is obtained as a prepreg from Narmco to the requirements of Convair Specification SD75-60130. The prepreg sheets have a cured ply thickness of  $0.0065 \pm 0.0003$  inch.

Materials for other components of the structure include the 2219 aluminum alloy and a corrosive resistant steel, CRES 17-4 PH. The 2219 aluminum alloy provides high strength, weldability, and acceptable corrosive resistance. The CRES 17-4 PH precipitation hardening steel has high strength, weldability, and is sufficiently ductile when used in a H1150 heat treat condition. It requires no special coating other than for cosmetic purposes.

**ANTENNA DESIGN** — The antenna design consists of five major structural assemblies; three moving and two fixed, Figure 3. The three moving assemblies are the elevation, cross-level, and train. The two fixed assemblies are the train-axis base and the radome. Items not included in the fabrication phase were the reflector and antenna feed assembly, waveguide installation, and radome. Both the elevation and cross-level assemblies employ direct drive, d-c torque motors for the rotational capability, synchros for determining angular position, and mechanical stops to prevent exceeding the preset angular ranges together with neoprene bumpers to alleviate shock loading. Balance of both moving elevation and cross-level axes is achieved by counterweights applied to the extended arms of the elevation yoke structure. The train axis, with continuous rotation capability, is driven by a 2.5:1 gear arrangement with the d-c torque motor housed in the train-axis counterbalance arm. This location for the torque motor aids in reducing overall counterbalance weight and provides for good accessibility. The train-axis synchro for determin-



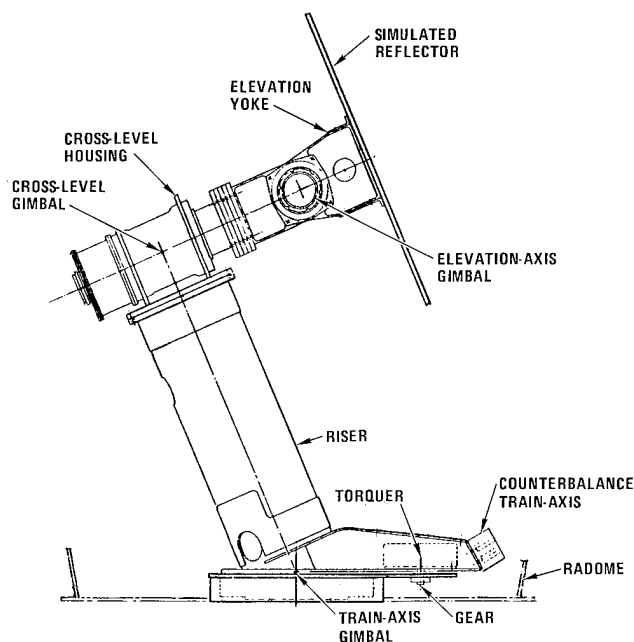


Figure 3. Antenna design.

ing angular position, together with a slipping assembly that allows for electrical transmission between the rotating and fixed parts, are housed in the base of the riser structure.

**ELEVATION AXIS ASSEMBLY** — The elevation axis assembly, Figure 4, consists of a yoke structure pivoted on two bearings mounted on stub shafts cantilevered from the cross-level axis shaft fork fitting. This yoke structure also supports the reflector, feed horn, secondary reflector and its support, inertial sensor module, and counterbalance weights. Balancing the moving and fixed elevation axis assembly and the cross-level moving assembly is accomplished by applying counterbalance weights on the extended arms of the yoke assembly. Angular rotation about the elevation axis is provided by a direct drive d-c torque motor and a synchro to provide angular position sensing. These items are supported from the longer of the two stub shafts and a housing attached to the yoke assembly. Mechanical stops with neoprene snubbers limit the rotational travel to a 135-degree upview and a 35-degree downview and absorb impact

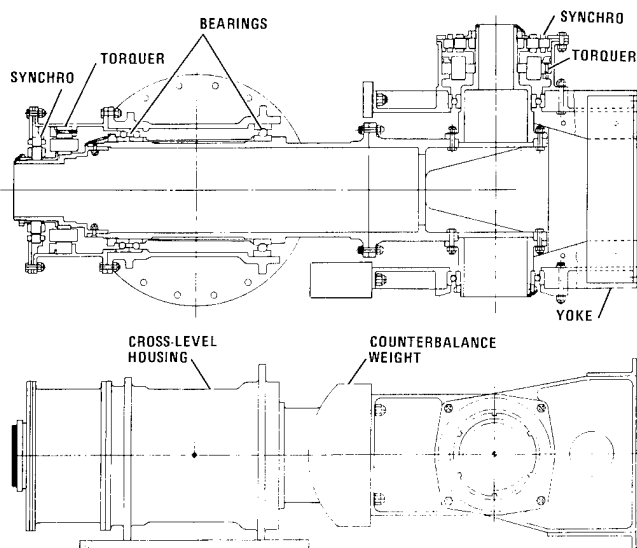


Figure 4. Elevation axis assembly.

loads. Electrical transmission is achieved by flexible, multiconductor flat harnesses. Provision for the waveguide routing, although not installed, was made by providing passage from the back of the reflector down through the yoke assembly, back through the smaller stub shaft, and then through the hollow cross-level shaft. The space envelope is sufficient to allow for waveguide rotary joints and ease of waveguide installation and removal.

The design concept for the elevation axis was determined from trade studies interrelating considerations and constraints of shock loading, stiffness, bearing type and location, efficient balance-weight placement, waveguide routing, and cost effectiveness. Providing a least-weight elevation assembly is of critical importance due to the snowball effect it has on overall antenna weight. The sensitivity of increased weight on obtaining the required structural resonance of 50 hertz is shown in Figure 5.

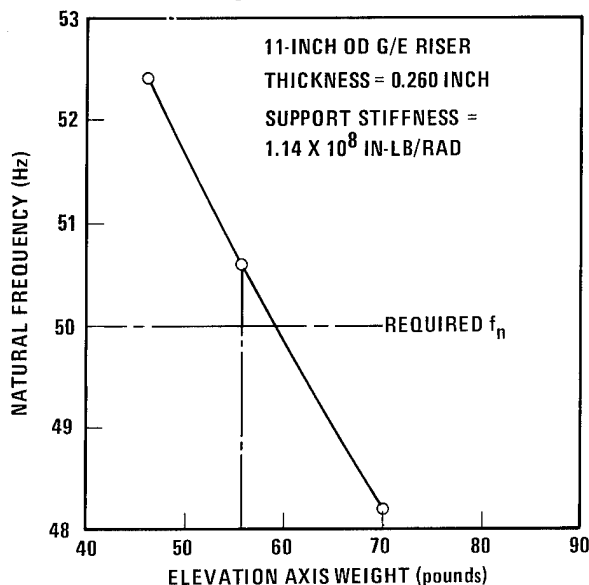


Figure 5. Natural frequency versus elevation axis weight.

**CROSS-LEVEL ASSEMBLY** — The cross-level assembly (Figure 4) consists of a hollow shaft cantilevered from two bearings located in a housing mounted on top of the antenna riser. The shaft cantilevered end transitions from its tubular cross-section to a fork fitting that supports two elevation-axis stub shafts. The opposite end of the shaft, together with an extension of the cross-level housing, supports the torque motor and synchro components. The direct-drive d-c torque motor provides the cross-level driving capability to accomplish the required  $\pm 60$ -degree rotations; the synchro provides angular position sensing. Mechanical stops with neoprene bumpers are incorporated between the shaft and housing structure to limit cross-level rotational travel to the required  $\pm 60$  degrees and absorb any impact loads. Electrical transmission between the rotating (shaft) and fixed (housing) parts of the cross-level structure is accomplished through a flexible multiconductor tape.

The cross-level shaft length-to-diameter relationship was arrived at from iterative trade studies based on cost effectiveness while satisfying shock loading and stiffness requirements. Influences of practical waveguide routing, cross-level cant angles, and elevation balance weight arm sizing were also considered. The shaft has a 17-inch gimbal length and a 5.5-inch outside diameter. It is fabricated in two parts with an intermediate flanged joint. Stiffness considerations and requirements for waveguide routing dictated need for a steel (CRES 17-4 PH) primary shaft; aluminum alloy (2219-T851) provided an acceptable material for the transition from the circular to forked section. The influence of the shaft bending stiffness on overall structural resonance is shown in Figure 6.

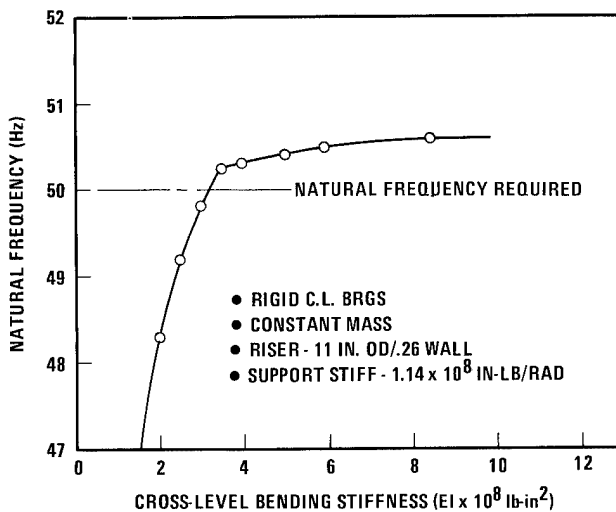


Figure 6. Structural resonant frequency versus cross-level stiffness.

The cross-level housing is a welded 2219-T851 aluminum alloy structural assembly interfacing with the cross-level shaft through a dual bearing installation, and with the antenna riser structure through a bolted flange fitting.

The size, type, location, and installation requirements of the two bearing installations for the cross-level axis were determined through a series of trade studies interrelating considerations of shock loading, stiffness, selective load-carrying abilities, geometry, and location compatibility. This provides efficient structural interfacing with the shaft and housing and antenna riser cross-section. Both forward and aft bearing installations are preloaded and installed with a controlled interference fit at both races. Preloading is required to satisfy bearing installation stiffness in alignment with structural resonance. The controlled interference fit between the inner race, shaft and outer race, and housing ensures rigid installation and provides for relative expansion of steel races and aluminum mating interfaces over the operating temperature range without loss of stiffness. The aft bearing installation employs duplex ball bearings, preloaded by tightening the thrust nut on the shaft, and reacts all reversible thrust loads together with a radial load component. The forward bearing is a single, preloaded, wire race ball bearing that reacts only radial loading.

**RISER STRUCTURE** — The riser structure, Figure 7, is the primary support member for the antenna. The critical design requirement is the 50-hertz minimum natural frequency. Strength requirements are given by the shock loading condition. An 11-inch diameter for the riser in the graphite/epoxy (GY-70/5209) material was arrived at during configuration trade studies, which considered such constraints as suitable train-axis bearing diameters, dish clearances, and efficient structural interfacing with the cross-level housing.

The design variables for the composite material riser were the choice of fiber/matrix materials, ply orientation, layup procedure, and wall thickness. The riser was sized for stiffness and then checked for strength and stability. Sizing of the riser was based on a computerized dynamic analysis. Plots of structural natural frequency versus riser wall thickness are shown in Figure 8 for the graphite/epoxy material system (GY-70/5209) used, a lower cost T300/5208 system, and an aluminum alloy. Neither the alternative graphite/epoxy system nor the aluminum alloy meets the 50-hertz objective. Titanium and steel also produce a curve similar to aluminum since they have the same specific modulus. The fundamental vibration mode for the riser is dependent upon both its bending and torsional stiffness. A trade study employing a family  $0_n/\pm 45_m$  fibers showed 60% unidirectional fibers would best satisfy the requirements with a final laminate of  $(0/45/0/135/0)_4S$  giving a wall thickness of 0.260 inch. The riser is attached by bonded double

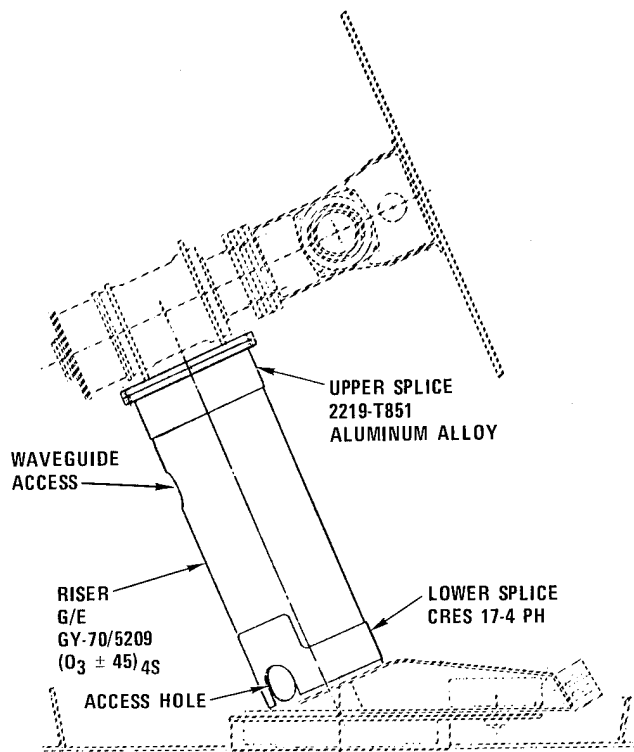


Figure 7. Riser structure.

shear splice joints to an 2219-T851 aluminum alloy flange, which interfaces with the cross-level housing, and to the 17-4 PH steel turntable. There are three cutouts in the riser wall, a 3.5-inch-diameter hole at the top to permit waveguide entry and two diagonally opposed 3.5-inch-diameter holes at the base for access to the slipping assembly. The upper hole requires no reinforcing; the lower holes are reinforced by the same doublers providing for riser attachment.

**TURNTABLE, BEARING, AND BASE** — The canted composite material riser transitions into a welded turntable assembly that, through a bolted flange, attaches to the train-axis bearing through the antenna-radome base. The turntable assembly also supports a

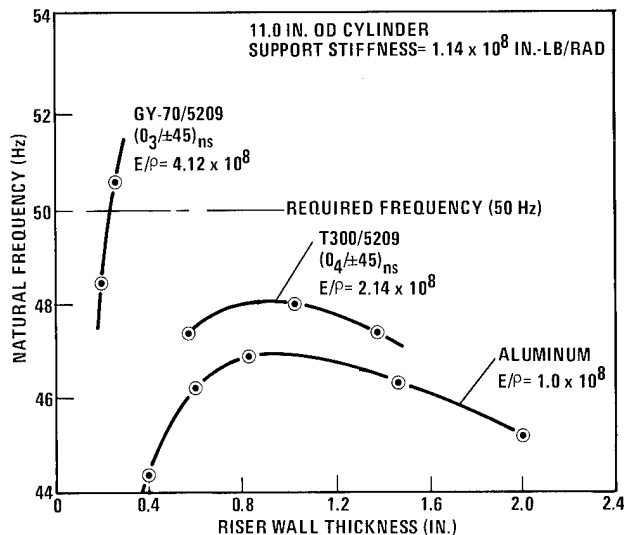


Figure 8. Riser natural frequency versus wall thickness graphite/epoxy and aluminum comparison.

balance arm structure that houses the train-axis torquer. The torquer has a spur gear that drives the antenna pedestal about a gull-gear supported from the antenna base. The interfaces between the train-axis turntable bearing and bearing base are the most critical part of the antenna structure. The structural load path is made as direct as possible to avoid adverse weight and to satisfy the stiffness requirement. The summated stiffness of flange bending, bolts, and bearing under the total range of moment loading is  $1.4 \times 10^8$  inch-pounds per radian minimum.

The slipping assembly, which allows for electrical transmission between the fixed and rotating portions of the train axis structure, is supported by a plate welded into the moving turntable structure. The moving portion of a synchro unit, providing for angular position sensing, is supported from the slipping assembly base; the fixed portion is supported from the inner bearing race.

The material chosen for the turntable assembly structure is CRES 17-4 PH in the H1150 heat treat condition; this steel is weldable, has good strength and ductibility, and is highly noncorrosive and stable when heat treated. This material choice also provides for compatibility with the steel bearing race under temperature changes and provides high stiffness for practical thickness in its flanged connection to the bearing.

Double shear lap splices attaching the graphite/epoxy riser to the turntable assembly are also of this material, and are bonded with a room temperature curing adhesive. A layer of glass cloth is inserted in the bond line to control adhesive thickness and preclude any possibility of galvanic corrosion. The graphite/epoxy-to-steel side of the joint is totally dependent upon the bond for shear strength with local mechanical fasteners to prevent any peel action. The steel-to-steel side of the joint uses mechanical fasteners for all load transfer to accommodate influences of complex stress distribution resulting from the proximity of the balance arm structure.

The train-axis bearing is a 12-inch, solid race, cross-roller bearing with the rollers precisely preloaded to provide the necessary stiffness in the axial, transverse, and overturning moment directions. This type of roller bearing provides the best combination of high stiffness, low operating torque, smooth operation, and low maintenance. The bearing was sized to ensure proper capacity for all required shock, vibration, and operating load combinations. The structural interfaces for the train-axis bearing are designed to prevent excessive deflection or deformation of the bearing raceways, and to ensure long bearing life. The base is fabricated from the 2219 aluminum alloy.

**FABRICATION** — The fabrication of the antenna structure was relatively straightforward and conventional, except for the composite riser and the bearing installations. The completed structural test antenna structure is shown in Figure 9. The structural test antenna used a simulated structure to replace elevation and cross-level assemblies in order that early vibration testing could be carried out on the composite riser.

The riser cylinder was fabricated using graphite tools, which have low thermal expansion characteristics and have proven more cost effective than other tooling materials. Graphite materials low thermal expansion characteristics provide more closely controlled dimensions of the cured part and less chance of thermal crazing. The material used for the riser cylinder fabrication was the ultra-high modulus GY-70/5209 graphite/epoxy prepreg tapes (12 inches wide) purchased to Convair specifications. The fiber orientation and layup was (0/45/0/135/0)<sub>4S</sub>, which is a total of 40 layers with a resulting cured thickness of 0.26 inch. Alternating two and three ply modules, each with one 45-degree fiber layer, were trimmed in the flat and then laid up in the female mold. Subsequent modules were staggered at specified distances. Prebleed precompaction operations were performed at 20-ply intervals. These prebleed operations reduced the resin content of the GY-70/5209 layup to 27-29% by weight, and the thickness to within 106% of that desired after cure. The graphite/epoxy riser cylinder was then cured in an autoclave. The part was removed from the autoclave while hot and disassembled (to

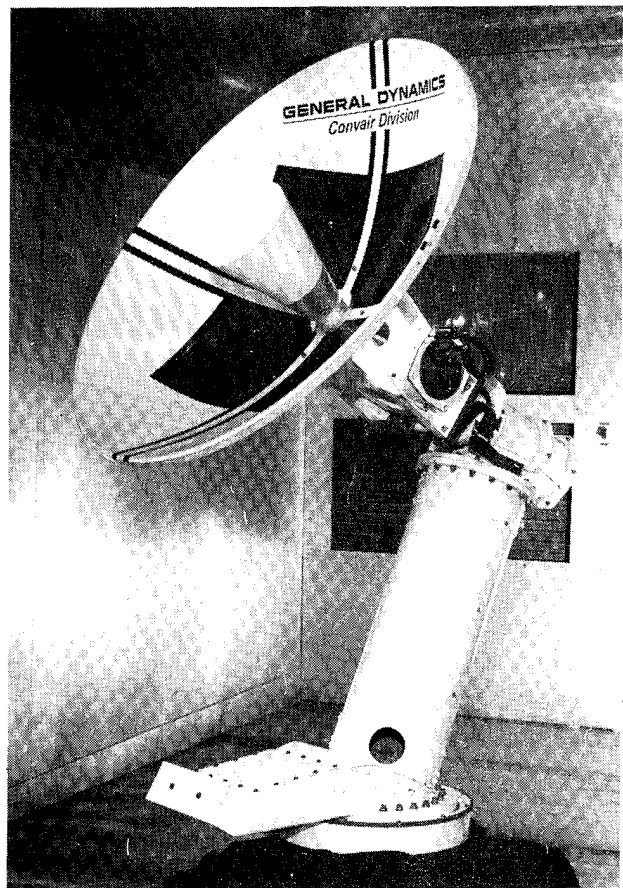


Figure 9. Completed antenna.

remove bagging, rings, etc.) while maintaining a minimum temperature of 200F and a maximum temperature of 270F.

The riser cylinder was machined to provide a required edge trim and hole, and installed in a tooling fixture along with the mating upper aluminum flange fitting and lower steel turntable assembly, Figure 10. Inside and outside doublers were then bonded to both ends of riser cylinder and mating parts using the EA 9309 epoxy paste adhesive. A woven dacron scrim material was used with

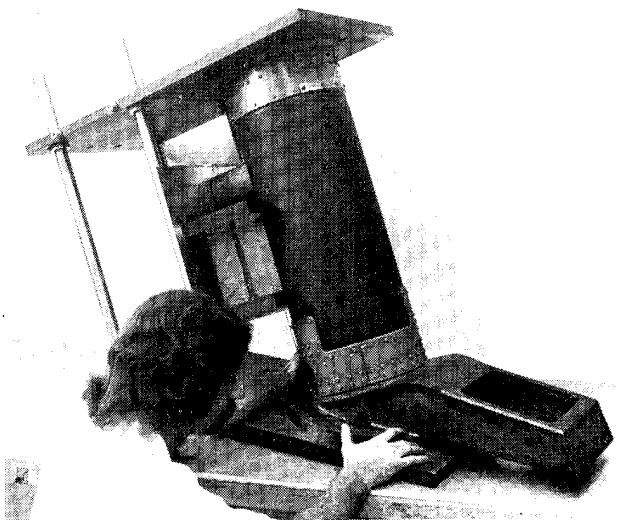


Figure 10. Riser structure tooling fixture.

adhesive to ensure a uniform bondline thickness and prevent any potential galvanic corrosion between the graphite/epoxy and adjacent metallic material. Titanium fasteners were then installed to provide resistance against peel on the composite material side and joint strength on the all-metallic sides.

**TESTING** — Vibration testing of both structural and pointing configurations of the Advanced Composite Antenna were performed. Vibration testing initially followed that specified in MIL-STD-167, but when test facilities available proved inadequate, vibration modal surveys were performed. Successful completion of vibration testing, with all axes having resonant frequencies greater than 50 hertz, was followed by temperature testing. The pointing configuration was installed in a temperature chamber and torque values for all three axes measured at ambient temperature, -18F and +149F.

The structural configuration of the Advanced Composite Antenna was directly mounted to Convair's A-182 vibration exciter, Figure 11, and tested in the Z-axis (vertical) mode to the requirements specified by MIL-STD-167. These requirements are detailed in

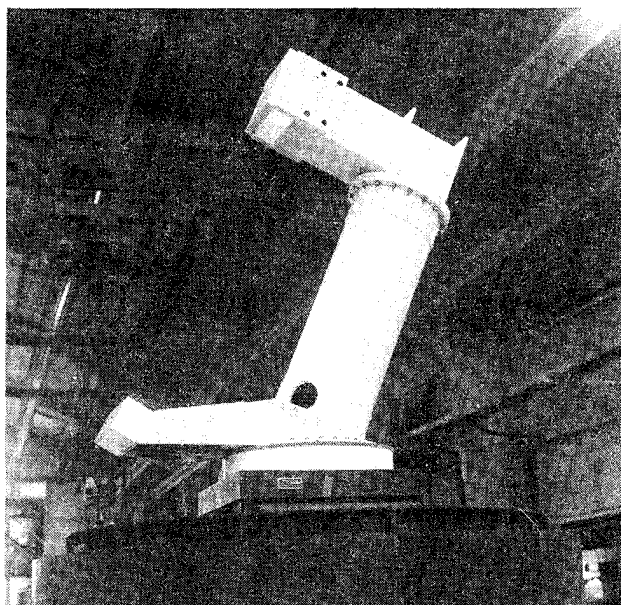


Figure 11. Antenna structure vibration test, Z-axis.

Table 2. The resonance search established the antenna structural resonance frequency in the vertical mode to be in excess of 50 hertz, and the search was continued until the actual value of structural resonance was established, 69 hertz. Both variable frequency and endurance testing ran through smoothly without any resonances being determined or any indication of damage after testing.

The antenna was then installed on a vibration table setup for X- and Y-axis testing, and excited. Testing was terminated when it was determined that the test table was bending and producing a false resonant condition at 33 hertz. Incorporating test table and its support system into the dynamic analysis computer program verified this result.

When an investigation revealed that the test fixtures with existing setups were not adequate, a modal survey testing was initiated.

The antenna was mounted to the modal chamber rigid floor, one-inch steel mounted in four feet of concrete and isolated from adjacent flooring, and modal search testing performed. The testing covered three train-axis bearing preloading conditions in addition to variable input forces to obtain comparison with analytical bearing stiffness structural resonant frequencies. The antenna structure was then shipped to the Naval Electronics Laboratories Center, where vibration and shock testing were performed to MIL-STD-167 and MIL-C-901C respectively. The antenna successfully passed this testing without damage and met all requirements.

Table 2. Shipboard vibration testing, MIL-STD-167.

Test	Procedure
Resonance search	1 Hz steps, 15 seconds duration each
	4 Hz to 33 Hz 0.02 in. DA
	34 Hz to 50 Hz 0.006 in. DA
Variable frequency	1 Hz steps, 5 minutes duration each
	4 Hz to 15 Hz 0.06 in. DA
	16 Hz to 25 Hz 0.04 in. DA
	26 Hz to 33 Hz 0.02 in. DA
	34 Hz to 40 Hz 0.01 in. DA
	41 Hz to 50 Hz 0.006 in. DA
Endurance test	Vibrated for a total period of 2 hours at the resonance frequencies found above. If no resonance frequencies were found, shall be tested at 33 Hz

DA = Double amplitude

## BATTLE DAMAGE SURVIVABILITY FOR CONSIDERATION IN THE DESIGN OF RADARS

M.L. Salive,<sup>\*</sup> H.L. Wolk,<sup>\*</sup> S.L. Wang,<sup>\*</sup> and W.R. Coggins<sup>\*\*</sup>

<sup>\*</sup> David W. Taylor Naval Ship  
Research and Development Center  
Structures Department  
Ship Protection Division (1740)  
Bethesda, MD. 20084

<sup>\*\*</sup> Naval Sea Systems Command  
Surface Warfare Systems Group  
Surveillance Systems Sub Group  
Advanced Systems Division (6522)  
Washington, D.C. 20362

### ABSTRACT

This paper discusses mechanical characteristics of radar systems in a battle environment. The need for Navy radars to survive the threat posed by nearby bursts of warheads makes it imperative that mechanical engineers conscientiously incorporate survivability factors in their design.

The survivability of radar systems depends on (1) the threat characteristics, such as the number of fragments emanating from an exploding warhead, (2) magnitude of the explosive blast, (3) distance from the blast to the radar, and (4) the characteristics of the radar system, such as its location relative to expected burst points or the vulnerability of individual components. Design factors which the mechanical engineer must consider to achieve survivability are:

- |                         |   |
|-------------------------|---|
| (a) Damage Tolerance    | (g) Degradation in performance vs termination of function |
| (b) Blast Resistance    |   |
| (c) Armoring            |   |
| (d) Redundancy          | (h) Presented target areas/configuration                  |
| (e) Repairability       |   |
| (f) Hardening/Shielding | (i) Installation location                                 |

Judicious balancing and tradeoff between these factors<sup>1</sup> can significantly improve the survivability of radar systems. Examples of the design factors contribution to survivability are given and discussed in relation to the mechanical design of radar system components. Methods to evaluate the vulnerability of total systems are briefly outlined.

### INTRODUCTION

Combat survivability of topside ship sensors, electronic/electrical systems is of vital concern to the Navy. Recent battle experience and operational accidents have highlighted the vulnerability of certain types of topside equipment to damage by fragments, shock, blast, and fire. Accordingly, the Chief of Naval Material (CNM) recently requested a study that would provide the basis for an expanded R&D program in ship survivability for both backfit and new construction.

In support of CNM request, a recent Navywide workshop, jointly sponsored by Naval Sea Systems Command (NAVSEA) and Naval Electronic System Command (NAVELEX), was held at Naval Research Lab-

oratory (NRL) on Combat Survivability of Topside Electronic/Electrical Systems Aboard Ship. Reviewed at this workshop were the vulnerability of topside electrical/ electronic systems to nonnuclear threats, and methods of improving the survivability of these systems. Approximately 140 individuals participated in the two-day workshop, representing more than 20 commands from the Fleet, OPNAV, NAVMAT, SYSCOM and Navy laboratories.

It is important to consider the overall aspects of combat survivability in a balanced context in which benefit versus cost must be weighed for a wide spectrum of potential threat effects. Within the scope of the threat to the U.S. Fleet are conventional blast-fragmentation weapons such as cruise and antiradar missiles (ARM) surface-to-air missiles (SAM), and sea skimming missiles; bombs; and projectiles. There are underwater explosion threats of mines and torpedos, and atmospheric threats of electromagnetic pulse (EMP), biological, and chemical warfare. This paper will only concern itself with blast-fragmentation effects of air-delivered warheads.

It cannot be overemphasized that combat systems must be protected as a practical solution to the ship combat-survivability problem. The problem is to clearly identify the vulnerable components and then to assess the effectiveness of any schemes imposed to improve survivability.

### SHIP SYSTEMS VULNERABILITY

Ship evolutions in the last two decades have resulted in limited use of protective armor and location of highly complex, mission-critical equipment in vulnerable superstructure or in exposed topside areas. Additionally, the nature of enemy threats has changed markedly, particularly with the wide deployment of antiship missiles.

Location of the vulnerable superstructure and equipment high above the weather deck and well above the center of gravity of the ship means that additional armor weight in those areas will have a marked effect on the moment, ship stability, and seakeeping ability of the ship, if conventional armor materials are used. Because of the moment problem and the large areas and numbers of system components requiring protection, it is essential that lightweight marine-grade armor materials be identified.

Computerized ship vulnerability analyses are now used by the Navy to evaluate effectiveness of proposed armor schemes for ships in the concept-planning stage and for ships in the fleet. Computer-aided analyses of vulnerability combine a detailed description of the ship structure and its mission-critical systems with a detailed description of the threat warhead. Preselected or randomly generated hits and burst locations are used in combination with the principles of penetration mechanics to predict penetration of projectiles or fragments into the ship structure and its system components like the radar antennas. The number of penetrations into each component is used to predict the probability that the component is damaged to the extent that it is nonfunctional or killed. Blast effects from proximity bursts or internal bursts are considered in predicting structural and electrical component damage. Component kill probabilities (PK) are used to determine probability of prime mission-system functioning. Analyses of the results indicate areas of structural weakness or high vulnerability of compartments and prime mission systems. The vulnerability can be related to specific system components like radars, fire control directors, waveguides, etc.

An analysis of battle-damage reports, computerized ship and system vulnerability assessments, and interviews with ship personnel and equipment-project managers combine to give a clear picture of topside ship vulnerability, its causes, and what steps will have to be taken to improve combat survivability. Lists are prepared of compartments and components that must have their combat survivability improved so that the ship can successfully complete its combat mission.

A weighting system is sometimes used so that some components of a system having greater performance characteristics than others performing a similar function in a parallel path in the inactivation diagram, should be weighed more heavily in figuring total system survivability. For example, if a weapons system can receive targeting information via a radar with a 200-nautical mile (nm) range along one path in the inactivation diagram or via another radar, having a 50-nm range along a parallel path in the inactivation diagram, then the available armor weight should be devoted to protecting the 200-nm radar. In addition, a burst against an unarmored ship that causes inactivation of the 200-mile radar might be weighted more heavily in computing system probabilities of kills (PK) than a burst that kills the 50-mile radar. We compute probabilities of kill not degrees of degradation of system performance. As long as a complete circuit still exists in the inactivation diagram, the system is considered to have survived--regardless of the possible reduction in performance of the remaining circuit. In any case, it is imperative that:

1. The design threat be identified
2. Vulnerable components be identified for strategic topside systems
3. Threat related damage mechanisms and failure modes identified for vulnerable components
4. Tradeoff investigations be made to determine the relative effectiveness of the feasible methods for upgrading the survivability for each component
5. Implementation be made of the most effective method for upgrading survivability for each component in strategic systems
6. Survivable topside structures and systems be introduced into the fleet and into new ships planned or under construction

The payoff from improving survivability of carefully selected areas of ship superstructures and electronics components is the ability to complete combat missions. The complete survivability will be difficult to achieve. Many of the existing electronics components do now lend themselves to armoring in the conventional sense. These electronic components of major ship systems will have to be redesigned completely from a survivability point of view. The Navy will be pursuing a vigorous program to develop a new generation of hardened, damage-tolerant electronic/electrical equipment to improve topside combat survivability of existing and future ships. The new developments will complement ongoing Navy programs for developing blast and shock resistant structures, and for controlling or preventing fire damage to the ship structure and equipment.

#### FRAGMENT PROTECTION METHODS AND TECHNOLOGY APPLICATIONS

In the past, protection designers have frequently confused hardening with armoring. Hardening means increasing damage tolerance or taking other actions to improve survivability, instead of using only armor in order to prevent penetration of fragments. Damage tolerance is the ability to take hits and still function with only a slightly degraded capability; redundant structural supports or electronics circuit paths are a good example.

To improve survivability of topside weapons systems, there are five basic methods of improving weapons systems in general that are overlapping but not mutually exclusive.

The five generally recognized methods for improving survivability are:

- Relocation of components to less vulnerable areas
- Redundancy of components
- Hardening by system reconfiguration
- Armoring
- Repairability after damage

These methods are not independent; various combinations of them can be utilized to provide an "in-depth" concept of subsystem survivability.

#### RELOCATION

Relocation can improve survivability. For example, weather exposed items located high in the superstructure are provided little protection, therefore, if they can be moved to an area away from expected burst or hit locations they will be more likely to survive.

Location is perhaps the single most important factor in considering vulnerability. Obviously a radar that is located far aft is less vulnerable than one located above the main control area of the superstructure at the center of expected hit distributions. Such location is, of course, neither always physically possible nor always operationally desirable for radars. The physical location between radar rooms and antennas, without which a ship would be totally blind, depends on the radar system employed and the degree of transmission-loss acceptable.

Relocation in the sense of pop-up antenna or a folded or retractable antenna mast combination may be considered as opposed to fore and aft relocation. Location of the radar on any ship is best determined through application of analyzed design technology. Operational requirements, mast configuration, ship mission, and various other factors must be considered along with vulnerability. Relocation of components on the radar itself can lead to enhanced survivability. For example if the emitter horn were moved inside the heavy base support, it would be less exposed to attack. A similar relocation of electric motors, hydraulic actuators or hydraulic/cooling lines on fire control directors would improve survivability.

#### REDUNDANCY

The second means of obtaining increased survivability is one of subsystem redundancy in the weapon system on either a circuit or a component level. Parallel, redundant components can be achieved by use of modern technology. Redundancy at the component level is seen in many weapons systems where one radar antenna is backed up by a second, less efficient one.

The concept of damage tolerance through redundancy is one that makes a significant impact. By utilizing widely spaced and parallel paths the impact of localized deactivation would only cause partial loss of capability. Dual side or rear radar signal feeds built into support structures are more survivable than a single exposed emitter horn. Parallel radar antenna elements must be located far enough apart so that a single fragment will not cause simultaneous kills.

Some of the advantages and disadvantages of redundancy as an approach to improving survivability are:

1. Redundancy can be applied to radar antennas that are difficult to armor
2. Weight impact will be much less than for armoring
3. Increased system reliability through peacetime and combat damage tolerance

#### HARDENING BY SYSTEM RECONFIGURATION

Hardening is used in the sense that vulnerability has been reduced by choice of a more damage-resistant or damage-tolerant design such as reduction of component size to reduce areas presented to the threat so that the component will not absorb or collect many fragment hits. If fragments are considered in strikes per square foot of area, and if the size of the component is reduced, fewer fragment hits will be accumulated. Thus the component will be less likely to be hit by a lethal fragment. In addition, reducing the size of the component means having less surface area requiring protection so that it may be possible to armor the component.

Hardening offers an alternative way to improve the survivability of components that cannot be armored or relocated. There is no need to make repairs during combat if hardening is successful, and the weight impact is much less than for armoring. The ingenious use of modern mechanical- and electrical-design methods to achieve damage tolerance constitutes hardening. One of the most promising methods of hardening is the use of stronger or tougher materials to make structures harder to damage. Similarly, selecting penetration-resistant hydraulic actuators and electric drive motors or relocating them inside a heavy antenna base would also harden radars or fire control directors. Finally laminated actuator levers can be designed that will be less likely to fail from a single fragment hit.

#### ARMORING

When discussing improving survivability, the first concept that usually comes to mind is armoring. Armoring to enhance survivability means a strengthening or thickening of structural plates or of equipment chassis to prevent penetration of fragments from bursting warheads. The weight impact of armoring greatly affects ship displacement, ship functions, power requirements, and dead weight to hull loading. Thus, it is necessary to consider less weighty methods or materials for improving survivability or to severely restrict the areas to be armored.

Injudicious application of armoring cause problems such as:

1. Parasitic versus structural load-bearing weight
2. Weight added above center of gravity causes moment problem in heavy seas
3. Weight above center of gravity may require adding an equal or double amount on keel for stability
4. Most weight-efficient materials may not be compatible with marine environment or may not exhibit suitable fire-resistant properties
5. Electromagnetic properties of armor may interfere with electronic requirements of equipment

The amount of aluminum or steel armor required to defeat a fragment can be estimated using the THOR equations which relate initial fragment mass and velocity to armor thickness and striking angle to predict a residual fragment mass and velocity after penetration. Armor thicknesses estimated this way will tend to be slightly heavy and can be reduced by reference to appropriate ballistic tables and handbooks for more effective materials.

#### REPAIRABILITY

Repairability improves station-keeping since it reduces or eliminates need to go to a shipyard for repairs. Instead of returning to base and spending 90 days in port getting 3 miles of cable and numerous antennas replaced damage can be repaired at sea. Perhaps onboard repair kits, spare parts, interchangeable parts, and using the smaller modules will improve repairability.

In a sea battle, it is wise to minimize unnecessary exposure of personnel when repairing topside equipment. In terms of protecting operating personnel, repairability has to be considered as opposed to armoring or relocating critical components on the ship. Some of the problems associated with repairability are:

1. Must store spare parts and kits on ship and have easy access
2. Repair during combat may be difficult and often too late
3. Increased capital investment beyond cost of redesigning more survivable radar types

#### BLAST PROTECTION

To determine the hardening requirements of antenna structure subjected to airblast loading, it is generally possible to uncouple the antenna components and idealize them as simple structural elements such as beams, bars, or plates. They can form a space truss, a disc, or a rectangular box-like structure. These structures can be analyzed by well known techniques, ranging from computerized finite element methods to simple approximate methods using the equivalent static-load concept (Ref.1). The blast loading on these

structures has also been standardized to a large extent (Ref.2). There are a limited number of topside structures on combatant ships composed of cylindrical or spherical segments, such as plastic radomes as ECM antenna covers, support tubes and pedestal of radar antennas, and missile tubes mounted on launchers. A brief discussion of these shell-like structures will be given below.

The targets to be protected against an HE weapon in a near-miss situation could face a spherical shock wave advancing from any source point nearby. The free field blast peak overpressure, positive phase duration and impulse can be estimated from the total explosive charge weight of the warhead, explosive composition, and the distance from the center of the charge to the point of interest (Ref. 3). There are classified handbooks available that allow the designer to compensate for the warhead casing thickness instead of treating the explosive as a bare charge.

There is no systematic treatment available for defining the blast loading over the shell surface with given free-field conditions. For the overall response of a structure, the loading based on a plane shock wave would represent an upper bound, although it would be too conservative for a large structure. The protection problem in that case is mainly concerned with highly localized damages for which the loading variation over the surface in question can be neglected.

A special case of HE blast over the topside of a ship occurs from the firing of its own weapons (Ref. 4). They can generate high intensity pressure close-by, but it rapidly decays with distance and time. The missile blasts are also accompanied by a highly concentrated heat flux from the exhaust gas. Generally, no exposed equipments will be located in the blast-affected zone; the only shell structure in that zone would be shields or barbettes. The loading in these cases would be defined from actual gun and missile blast tests which will not be discussed here.

#### Cylindrical Shells

The detailed loading profile over the cylindrical surface is of interest to the engineer only when he has the resource to perform a rigorous dynamic analysis, or if he wishes to examine the local behavior of a large cylinder. For preliminary vulnerability or design studies, simpler tools of analysis are desired. A useful approach (Ref. 2) is to resolve the loading into two simple components: (1) a compression mode consisting of a uniform radial pressure with an appropriate time-history, and (2) a flexural mode consisting of an antisymmetrical but uniform distributed pressure with a slightly different time-history. For airblast response of these structures, it was shown that good correlation with test results was obtained by using a constant drag coefficient



based on the initial Reynolds Number at the time of blast arrival.

As an approximate analysis, the cylinder may be treated as a complete ring in the circumferential direction and as an uncoupled beam in the longitudinal direction (Ref. 2). Then the peak response of each system is determined from an equivalent static pressure based on a suitable dynamic load factor (DLF). This factor is a function of the period of the predominant response mode and the characteristic time of the loading. It may be necessary to consider the influence of foundation flexibility on the fundamental period. More refined dynamic analysis can be performed by the modal synthesis method for elastic response (Ref. 5), rigid-plastic theory (Ref. 6), and energy method (Ref. 7) for estimating the ultimate load and permanent deformation respectively, or even more powerful computer methods for large-deflection elastic/plastic solution (Ref. 8,9). A useful method to check dynamic buckling is through an approximate peak load-impulse characterization scheme (Ref. 10).

#### Spherical Shells

A parallel situation exists with regard to the question of airblast loading on a spherical shell and its structural response as in the case of a cylindrical shell.

Newmark et al (Ref. 11) gave an example of detailed numerical calculations for a plastic radome using uncoupled modal analyses. Robinson and Blackburn used the modal synthesis method to treat elastic dynamic response of plastic radomes as shells of revolution constructed of layered skins of isotropic or orthotropic material (Ref. 5).

Because of its sensitivity to random initial imperfections (Ref. 12), the actual buckling pressure of a spherical shell could lie anywhere between  $1/4 - 3/4$  of the ideal value. A prediction method restricted to axisymmetrical modes of deformation substantially overestimated the threshold dynamic buckling load (Ref. 13). A numerical method was developed by Liepins (Ref. 14) to calculate the nonlinear dynamic asymmetric response of shallow spherical shells, while Klosner and Longhitano (Ref. 15) made a similar investigation for hemispherical shells. Further work is required to provide general design guide for dome structures of naval interest. The peak load-impulse characterization scheme might be profitably used for this purpose, but so far no detailed analysis has been carried out for blast loaded spherical shells.

#### FRAGMENT PROTECTION

The THOR fragment penetration and residual mass equations (Ref. 16) are used with either actual warhead fragmentation data or a design level compact fragment selected on the basis of

its relationship to the penetrating capability of certain fragments from the design threat. Actual warhead data is given in fragment numbers, masses, and initial velocities in various polar zones around the warhead. Drag coefficients are used to calculate impact velocities at various distances from the warhead. Fragment hits per square foot decrease in proportion to the square of the distance from the warhead to the target and affects such things as the number of redundant antenna elements that will be cut by a single burst.

The THOR equations can be programmed for use with desk top or pocket calculators for giving quick estimates of whether a structure or housing will be penetrated. Coefficients are available for compact fragments penetrating steel or aluminum armor. Methods are given for adapting the equations for use with non-compact (real) fragments and other steel or aluminum alloys. In any case, the THOR equations and tabulated armor/threat data are fairly good estimators for design purposes. However, ballistic tests with fragment simulator projectiles or arena tests with bursting warheads are frequently used to validate the effectiveness of proposed designs and residual operating capability.

The THOR equations are the basic penetration algorithm used in the computerized assessment of overall ship/system vulnerability given a detailed warhead characterization and ship/system description. They are also used in a similar computerized approach to evaluate the vulnerability of large electronic/electrical components. The exterior and interior components are described at the circuit level in appropriate detail, then the effects of various penetration lines assessed in terms of the circuit or reflector grid elements intercepted. Finally, the remaining functional capability is assessed and compared to a previous baseline study on the unprotected or original design. This approach quickly reveals the inadequacy of halfway measures and points out the need for a comprehensive approach that incorporates features of relocation, redundancy, hardening and armoring at the component level.

The authors feel that a comprehensive multifaceted approach to the survivability of radars and fire control directors is possible and will result in urgently needed improvements in ship/ combat system life when under attack.

#### SUMMARY

The Navy has recognized the importance and seriousness of shipboard combat survivability. Of particular concern is the so-called cheap kill produced by a nearby proximity-fuzed warhead burst producing fragments.

The recent 2-day Navy-wide workshop con-

cerning combat survivability of topside electronic/electrical systems showed that we must rethink traditional design and conceptual approaches for these systems, especially relative to the vulnerable, exposed topside antenna and sensors. Combat systems must be designed to survive a nearby burst of a fragmenting warhead and still function in a degradation mode for a specified time so that the ship can maintain station while onboard repairs are being made, or so that the ship may complete its intended mission and return to port for repairs.

Much of the expertise concerning sensitive shipboard combat systems is from private industry; so the Navy needs the strong support of industry in assessing vulnerability and in enhancing the combat survivability of components and equipment employed in these combat systems and in all phases including development, design, production and installation, maintenance and modernization (Ref. 17). New innovative design concepts, employing features such as increased ruggedness, lightweight materials, slow degradation, redundancy, miniaturization, armoring and location must be created to improve the inherent vulnerability of our combat systems.

With the trend in the Navy toward a reduced number of ships, somewhat smaller ships with reduced manning, and the emerging challenges to U.S. sea control missions both from the Soviet Navy and emerging world Navy threats, each ship must be more survivable. The enemy must be denied the capability to inflict lethal damage on our ships with relatively cheap and small weapons; the key to increased combat survivability against these cheap kills depends directly on the ability to incorporate increased survivability in our shipboard combat systems.

Due to the unclassified nature of this paper only unclassified references have been cited. As a result, some of the more comprehensive, application oriented classified reports were deliberately omitted from the reference list.

#### REFERENCES

1. Biggs, J.M., "Introduction to Structural Dynamics," McGraw Hill Book Co., 1964.
2. "Air Force Design Manual: Principles and Practices for Design of Hardened Structures," AFSWC-TDR-62-138, December 1962.
3. "Explosion Effects and Properties, Part I - Explosions in Air," NSWC/WOL/TR-75-116, 6 Oct 75.
4. "Design Criteria Manual for Gun and Missile Blast Protection for DLGN-38," prepared for NAVSEC by Designers and Planners, July 1975.
5. Robinson, A.R. and T.O. Blackburn, "Dynamic Response of Plastic Radomes," University of Illinois, Department of Civil Engineering Report UILU-ENG-75-2003, Feb 1975.
6. Hodge, P.G., Jr., "Ultimate Dynamic Load of a Circular Cylindrical Shell," Proc. Second Midwest Conference on Solid Mechanics, Lafayette, Ind., 1955.
7. Greenspon, J.E., "Post Failure Deflections of Cylindrical Shells under Dynamic Lateral Loads," J.G. Engineering Research Associates Technical Report No. 5, Aug 1964.
8. Almroth, B.O., et al, "Structural Analysis of General Shells, Vol. III - User Instructions for STAGSC," Lockheed Missiles & Space Company, Inc. Sunnyvale, California, Dec 1975.
9. Bathe, K.F., E.L. Wilson, and R.H. Iding, "NONSAP - A Structural Analysis Program for Static and Dynamic Response of Nonlinear Systems," Structural Engineering Laboratory Report No. USCESM 74-5, University of California, Berkeley, California, Feb 1974.
10. Anderson, D.L., and H.E. Lindberg, "Dynamic Pulse Buckling of Cylindrical Shells Under Transient Lateral Pressure," AIAA Journal, Vol. 6, No. 4, Apr 1968.
11. Newmark, N.M. et al, "Blast Resistant Radome Evaluation for Operation Prairie Flat Tests," N.M. Newmark Consulting Engineering Services Report to NSRDC, Apr 1968.
12. Krenzke, M.A., and Kiernan, T.J., "The Effect of Initial Imperfections of the Collapse Strength of Deep Spherical Shells," David Taylor Model Basin Report 1757, Feb 1965.
13. Witmer, E.A., T.H.H. Pian, and H.A. Balmer, "Dynamic Deformation and Buckling of Spherical Shells Under Blast and Impact Loading," NASA Technical Note D-1510, Dec 1962.
14. Liepins, A.A., "Asymmetric Nonlinear Dynamic Response and Buckling of Shallow Spherical Shells," NASA CR-1376, June 1969.
15. Klosner, J.M., and R. Longhitano, "Nonlinear Dynamics of Hemispherical Shells," Polytechnic Institute of Brooklyn, PIBAL Report No. 72-33, Nov 1972.
16. "The Resistance of Various Metallic Materials to Perforation by Steel Fragments: Empirical Relations for Fragment Residual Velocity and Residual Weight," John Hopkins University and BRL, Project THOR Technical Report #47, Apr 1961.
17. Hill, R.T., "Shipboard Radar System Research and Development," IEEE EASCON-77, Sep 26-28, 77.

# CUSTER HORN: A NOVEL APPLICATION OF FIBERGLASS STRUCTURAL COMPOSITES

THOMAS L. RYAN

and

WILLIAM B. HEBENSTREIT

Naval Ship Weapon Systems  
Engineering Station  
Port Hueneme, California 93043

Structofab, Inc.  
334 Godshall Drive  
Harleysville, PA 19438

## ABSTRACT

A method is presented for solving a severe corrosion problem by replacing an aluminum radar horn with one made of fiberglass reinforced plastic. The original horn was made of aluminum and aluminum honeycomb panels screwed together. Key design and manufacturing problems engendered by the conversion from metal to fiberglass and by the requirement for mechanical and electrical interchangeability are presented. Solutions discussed include: achievement of an accurately formed, interior conductive surface; protection of the conductive surface from corrosion and delamination; conductivity-heat dissipation-weight-delamination resistance trade offs in conductive surface design; strength-stiffness-weight-thickness trade offs in side wall design; moisture drainage and pressure limitation; shock resistant anchoring of mounting brackets.

## INTRODUCTION

Each year the cost of corrosion to the American economy can be measured in billions of dollars. In the military, in addition to the measurable costs of damage to equipment and equipment maintenance, there is the potentially catastrophic cost of failure of weapons in combat.

Plastics, although their application to weapon systems is in its infancy, are finding an ever increasing role as replacements for corrosion-prone metals.

This paper describes a novel application of fiberglass reinforced plastics in the construction of the Custer Horn (Figure 1), a high powered, pressurized, horn type antenna used in a Naval fire control system. The fiberglass horn was developed as a replacement for an all-metallic horn, which suffered from corrosion problems.

The geometry of the interior conductive surface, which dictates the beam shape, is illustrated in Figure 2. In operation, the horn is oriented with the long dimension, which is parallel to the electric field, vertical. The transmitted energy, therefore is vertically polarized.

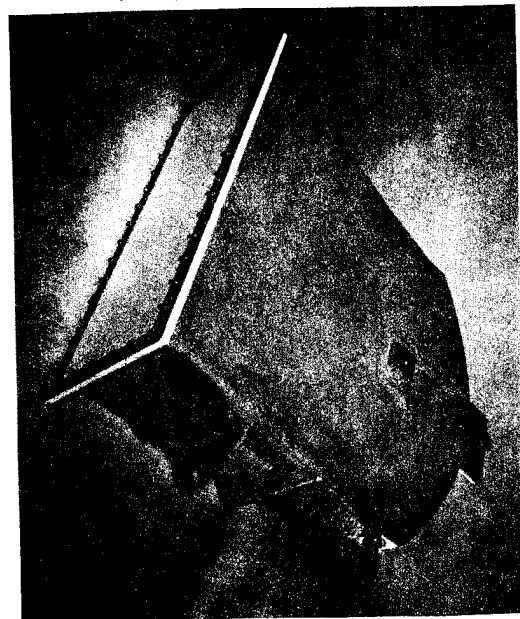


FIGURE 1. Custer Horn

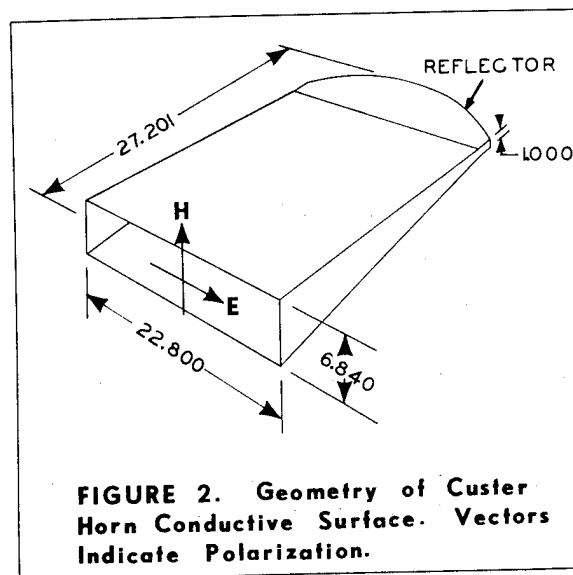


FIGURE 2. Geometry of Custer Horn Conductive Surface. Vectors Indicate Polarization.

The energy is fed into the horn by a  $\frac{1}{2}$ " x 1" waveguide with a 90° H-bend (see Figures 1, 3, and 4). The output end of this feed guide is directed toward the reflector which is an approximately parabolic cylinder one inch high and with a 22.8" aperture (see Figures 1, 2, and 3). The output end of the feed guide is placed at the approximate focus of the reflector, which is shaped to eliminate very deep nulls near the center of the beam in the E-plane pattern.

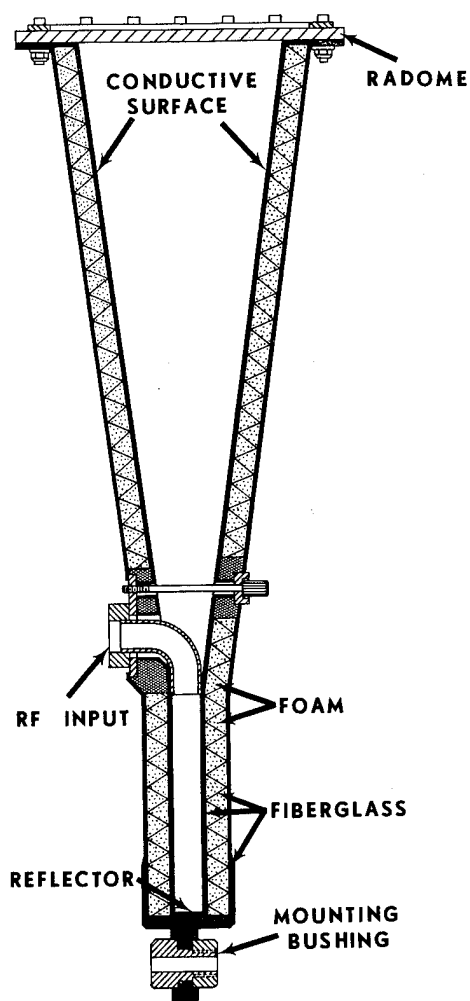


FIGURE 3. H-Plane Section Showing Truss Core Construction.

In the all-metallic predecessor to the fiberglass Custer Horn, the narrow sides and the reflector were machined from solid aluminum. The sides parallel to the electric field were aluminum faced/aluminum honeycomb sandwiches, which were bolted to the narrow sides and to the reflector.

Corrosion attacked the interfaces between the various parts of the assembly

and the interlaminar bond between the honeycomb and the sandwich faces.

#### ADDITIONAL CUSTER HORN REQUIREMENTS

In addition to eliminating the corrosion problem, and duplicating the electrical characteristics of its all-metallic predecessor, the fiberglass Custer Horn had to meet the following, principal requirements:

1. Be mechanically interchangeable with the all-metallic version.
2. Weigh about the same as the all-metallic version.
3. Provide a simple method for draining any moisture which might inadvertently condense inside the horn.
4. Incorporate a means for limiting automatically the internal pressure against variations in system pressurization.
5. Limit the deflection of the horn side-walls in order to maintain the beam pattern within specifications in the range of internal pressure encountered in service.

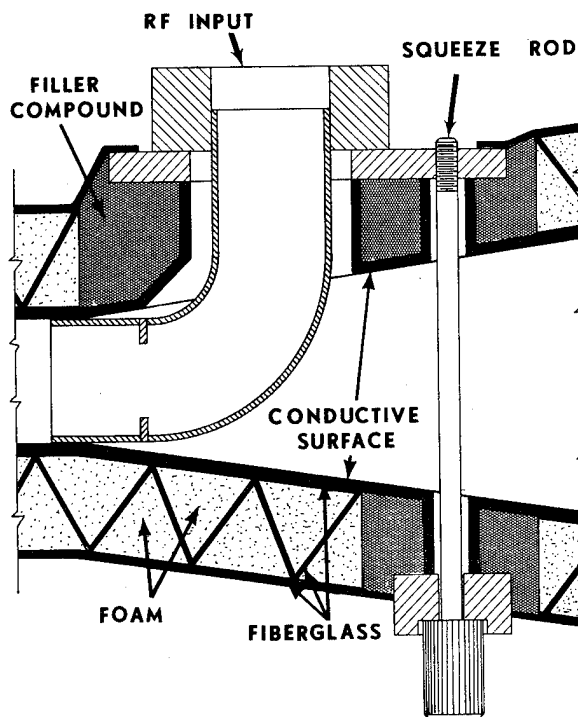


FIGURE 4. Detail View RF Input Section.

Because the fiberglass Custer Horn had to duplicate the electrical perfor-

mance of its all-metallic predecessor, a key problem was to devise a means for making a continuous internal conductive surface which: (a) duplicated accurately the internal geometry of the all-metallic version; (b) was protected from internal moisture; (c) would have minimal susceptibility to delamination from the fiberglass supporting structure.

After considering various alternatives, the method adopted was to start with an accurately machined steel, male mold (see Figure 8) and build from the inside out. In addition to providing the requisite accuracy to the geometry of the internal conducting surface, this method enabled the development of a manufacturing technique and process, which gives lasting protection to the conductive surface and reduces substantially the possibility of its delamination from the support structure.

The process starts with the application of a thin layer of high temperature resin to the tool surface. Before the resin cures, a thin layer (about .005") of aluminum is flame sprayed over it.

This first layer of aluminum is porous, but because the pores are of the order of  $10^{-5}$  to  $10^{-2}$  wavelengths, the layer forms a continuous conductive surface. The inside layer of this surface is smooth. The "outside", this is, the surface away from the tool has a texture about like 200 grit sandpaper - a good tooth for subsequent bonding.

Another thin film of high temperature resin is applied over the outer aluminum surface. This film reaches through the pores of the aluminum and anchors to the first film of resin. Additional aluminum and resin are applied until the specified thickness of aluminum is obtained. Additional layers of aluminum contribute primarily to the dissipation of heat and nothing to the electrical conductivity. (The skin depth is about 30 micro-inches.)

Because of the power handling requirements of the horn, and because the high temperature resin in the interior should be limited to operating temperatures of about 350°F, it was necessary to give careful consideration to both the thermal and structure design. The importance of the thermal design is evident when it is recalled that the two principal materials used in the structure, fiberglass laminate and polyurethane foam, have roughly 1/500th and 1/10,000th, respectively, the thermal conductivity of aluminum.

Basically, the problem was to devise a structure which would satisfy the rigidity and strength requirements and which would also provide the heat flux paths necessary to keep the interior temperature below some safe level, say, 300°F.

In the throat section of the horn, where the section dimensions are 1" x 22.8", the RF dissipation in the conductive surface is about .02 watts/sq. in. The dis-

sipation falls off rapidly toward the aperture. The fall-off is shown in Figure 5, an approximate curve of the dissipation as a function of the distance from the throat toward the aperture. The dissipation falls off so rapidly that one can think of the "hot" throat region and the "cool" aperture region.

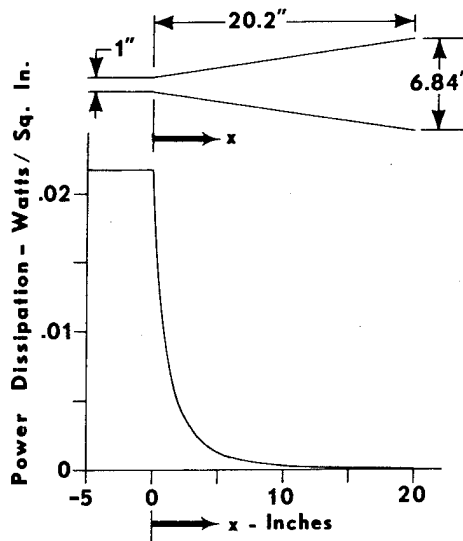


FIGURE 5. Power Dissipated in Sidewalls Parallel to the Electric Field

The heat generated by the dissipation of the RF energy in the throat section can therefore escape in two ways: (a) directly through the adjacent supporting panels; (b) along the interior aluminum surface from the "hot" region to the "cool" region and then out through the panels and the radome. Because neither path is a very good thermal conductor, careful attention needs to be paid to the design of both. In addition to the temperature gradient through the panel, there is another through the surface air film.

#### PANEL DESIGN

It was evident from the outset that the structure for the narrow sidewalls perpendicular to the electric field and for the support backing for the reflector should be a solid laminate and that the principal design criterion is that the laminate have sufficient strength to anchor the steel imbedments (discussed later). The temperature gradient through such a laminate would be only a few degrees F. Through the surface air film it would be about 15°F, assuming no sun heating of the surface.

On the other hand, a solid laminate for the broad sides parallel to the electric field would result in an unacceptable weight penalty. Young's modulus for fiberglass hand lay-up laminates is less

than one-sixth that of aluminum. To meet the stiffness requirement such a laminate would have to weigh over five pounds per square foot.

The stiffness requirement is that the deflection of the sidewalls under the internal pressure is less than 1/32 inches.

Any fiberglass sandwich panel, in which the panel thickness and the face thickness are related by equation A-6 in the Appendix, will satisfy this requirement provided the core material satisfies at least two criteria;

1. Have sufficient shear modulus to make the shear strain small compared to the bending deflection.
2. Be roughly isotropic in the sense that the panel should exhibit about the same bending stiffness in any plane normal to the panel surface.

For other reasons the core should also:

3. Have shear strength high enough to sustain emergency overpressures without damage.
4. Be light in weight.
5. Have a configuration which minimizes the susceptibility to face/core delamination.

Foam core will not satisfy 1 and 3. A honeycomb core will not satisfy 5. Balsa core will not satisfy 4. All five criteria are satisfied by the truss core configuration illustrated in Figures 3, 4, and 6.

The fiberglass is stitched around the polyurethane foam core mandrels which have an equilateral triangle cross section. (Figure 6). In the manufacturing process the fiberglass of the core is impregnated with resin and the webs, foam, and outer skin are all bonded together under pressure. The result is a 100% bond between the foam, the trusses, and the outer faces.

Having selected the basic panel section, the next step was to determine the overall panel thickness and the thickness of the sandwich faces, keeping in mind the factors of cost, weight, and temperature rise of the interior aluminum surface. As noted previously, the stiffness requirement dictates a specific relationship between the face thickness and the overall panel thickness. That is, for each panel thickness, there is a unique face thickness which will provide a minimum weight panel conforming to the stiffness criterion. But for every pair of values of the face and panel thicknesses, there is panel weight and panel thermal conductivity. The temperature gradient through the panel can be computed from the thermal conductivity and the thermal flux.

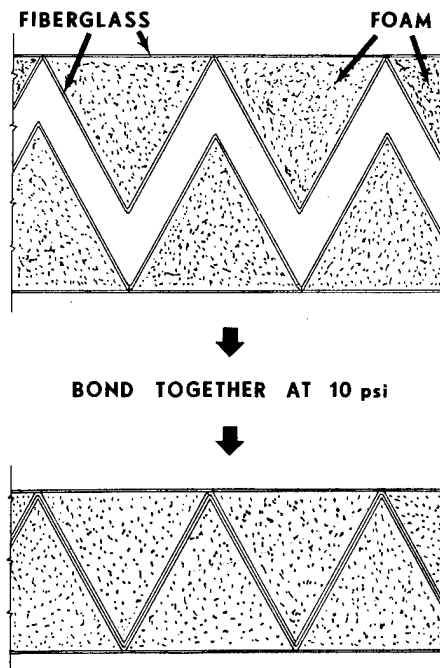


FIGURE 6. Technique for Making Truss Core

These data are combined graphically to provide the design trade-off chart shown in Figure 7. The face thickness, weight, and temperature gradient are all plotted as a function of the panel thickness.

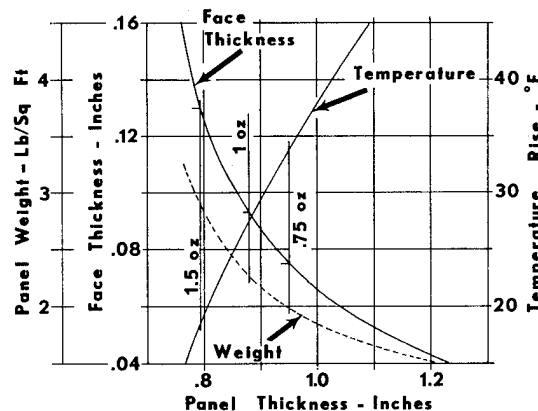


FIGURE 7. Design Tradeoff Chart

Using the data on this chart as guides, final selection of the design, which was committed to production, was made on the basis of manufacturing requirements and cost. To insure good interlaminar bonding, it is necessary to have three plies of fiberglass chopped strand mat between the aluminum surface and the truss core and, for balance, three similar plies on the outside of the truss

core. One ply is bonded to the aluminum and cured; one to the truss core and cured; the third becomes the bond ply when the assembly is vacuum bagged.

The three lightest, normally commercially available mats are  $\frac{3}{4}$ , 1, and  $1\frac{1}{2}$  ounces per square foot. The tentative design lines corresponding to the use of these three candidates are indicated in Figure 7. The mat weighing  $\frac{3}{4}$  ounce per square foot is the least expensive from the standpoint of both material and labor. It also results in the lightest panel. Parenthetically, since there are about eight square feet of sandwich panel in the Custer Horn, it should be noted that the use of the truss core sandwich results in about a 25 pound overall weight saving relative to the use of solid laminate. The Custer Horn now weighs about 50 pounds.

The present design is based on  $\frac{3}{4}$  ounce mat. This results in a panel weight of 2 lbs./sq. ft., a panel thickness of .95" (vs. .57" for the aluminum sandwich), and a temperature gradient of  $30^{\circ}$  -  $35^{\circ}\text{F}$  between the inner and outer surface of the panel in the "hot" region.

Although the use of one of the heavier mats would result in some reduction in the temperature gradient, the modest improvement in this category did not appear to justify the cost and weight penalties.

If the panel is not heated by the sun, the temperature of the interior surface will be about  $40^{\circ}\text{F}$  higher than ambient - the additional  $7^{\circ}$  is due to the thermal resistance of the surface air film.

Generally the most severe condition would occur in direct sunlight in still air. Under the most extreme conditions, the Custer Horn surface temperature will not exceed  $200^{\circ}\text{F}$ . Therefore the interior surface temperature will not exceed  $235^{\circ}$ .

As noted previously, not all the heat generated in the "hot" throat section needs to escape through the adjacent walls as has been assumed tacitly in the immediately preceding discussion. Some of it will leak off toward the "cooler" aperture region. Roughly, for every .010" in thickness in the aluminum coating, the RF energy dissipated in one inch length of the throat section will be "leaked off" toward the "cool" section.

#### CONSTRUCTION TECHNIQUES

The specified minimum thickness of the interior aluminum conductive coating is .010". In practice, the thickness will be greater than this. A flame spray operator generally cannot achieve a perfectly uniform coating. Therefore, in order to insure there is no spot less than the minimum, there is a tendency to overspray. Because .010" of aluminum over the entire conductive surface represents about 25% of the total weight tolerance budget, it is essential to use skilled

operators and good in-process inspection.

After achieving the desired thickness of aluminum coating, the fiberglass lamina, including the solid laminate for the narrow sides and the truss core for the broad sides, are laid up and vacuum bagged.

It should be noted at this point that the aluminum surface is completely encapsulated in a matrix of resin which has permeated the aluminum pores and which, in turn, is firmly bonded over 100% of its surface to the supporting fiberglass laminate structure.

A removable split tool (see Figure 8) provides for molding an opening for insertion of the waveguide feed (see Figure 3 and 4). Removable round rods placed in the tool provide the means for molding in the drain hole (see Figure 9) and the hole for the squeeze rod (see Figures 3 and 4).

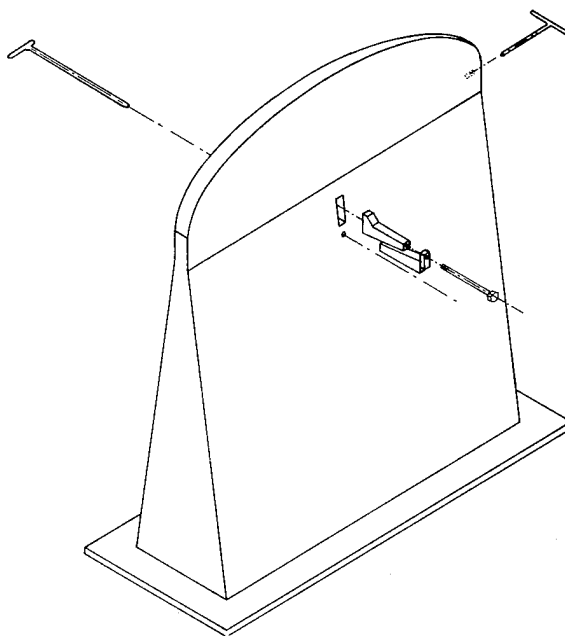
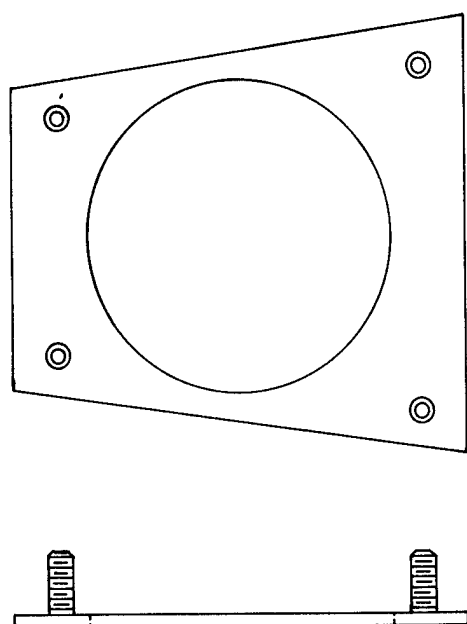
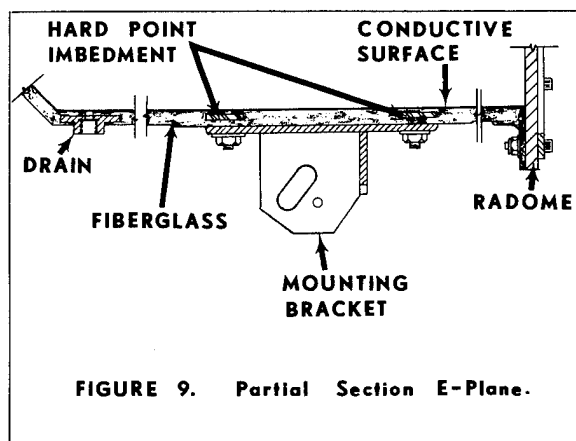


FIGURE 8. Steel Mold

A stainless steel threaded insert with a center hole is imbedded in the laminate under the drain hole. The thread receives a standard Circle Seal relief valve set to open at one PSI (see Figures 1 and 9).

To anchor the top and bottom mounting brackets securely, a stainless steel stud plate (Figure 10) is imbedded as shown in Figure 9. This type of attachment will sustain several thousand pounds of pull and shear. Specifically, these attachments together with the rear mounting shown in Figures 1 and 3, are designed to withstand the shipboard shock and vibration environments.



gain specifications, were originally designed by Mr. John Stangel and Mr. Michael Pallas of Sperry Gyroscope Company.

#### APPENDIX

The following are some of the formulas and physical properties used in the design analyses.

#### ELECTRICAL

In a rectangular waveguide operating in the  $TE_{1,0}$  mode, the average density of the power dissipation in one of the sides parallel to the E-vector, and the average density of the power dissipation in one of the sides perpendicular to the E-vector are, respectively,

$$(A-1) \quad \bar{W}_b = \frac{1}{2} WR \lambda^2 / \left[ \eta_0 b a^3 \sqrt{1 - (\lambda/2a)^2} \right]$$

$$(A-2) \quad \bar{W}_a = WR / \left[ \eta_0 b a \sqrt{1 - (\lambda/2a)^2} \right].$$

a and b are lengths of the waveguide sides perpendicular and parallel, respectively, to the E-vector.

$\lambda$  = wavelength

$\eta_0$  = 377 ohms - resistance of free space.

$\bar{R}$  = intrinsic resistance of the aluminum conductor

$$= 3.34 \times 10^{-7} \sqrt{f}$$

(Note: in the analyses,  $\bar{R}$  was multiplied by a design factor of safety  $\sqrt{2}$ ).

W = transmitted power, watts

The dissipation in the flare of the horn can be computed approximately by substituting

$$(A-3) \quad a = .289x + 1$$

in (A-1) and (A-2), where x is the distance from the throat. (See Figure 5)

#### THERMAL

Thermal conductivities of the various materials, expressed in (watt-in)/(in<sup>2</sup> - °F) are:

Fiberglass laminate:	$4.5 \times 10^{-3}$
2# Polyurethane foam:	$3.1 \times 10^{-4}$
Aluminum:	2.4

Conductance of surface air films, expressed in watts/(in<sup>2</sup> - °F):

Vertical surface:	$3.1 \times 10^{-3}$
Horizontal surface:	$2.2 \times 10^{-3}$

#### ACKNOWLEDGEMENTS

Mr. Luke H. Corzine of the Hallman Corporation contributed the idea for the removable split tool and originated the method and machinery for manufacturing the truss core depicted in Figure 6. Mr. Robert Handler of Structofab, Inc. and Mr. Thomas J. O'Toole, formerly of Structofab, Inc., worked out most of the novel manufacturing techniques including, notably, the method for securely bonding and encapsulating the aluminum conductive surface.

The geometry of the internal conductive surface, including the shape of the reflector and the position of the feed necessary to satisfy the beam pattern and



For operation at full power in the sunlight, the antenna surface temperature ( $T_s$ ) can be calculated from:

$$(A-4) \quad T_s + 1.13 \times 10^{-9} \epsilon (T_s + 460)^4 \\ = T_a + 7 + 232 \alpha$$

$\epsilon$  is the surface emissivity (gray epoxy)

= .85 - .9 (most probable range)

= .6 (extreme condition)

$\alpha$  = surface absorption coefficient

= .75 (most probable)

= .9 (extreme condition)

$T_a$  = ambient temperature

The constants in (A-4) are based on the following assumptions:

RF dissipation inside = .022 watts/in<sup>2</sup>

Sun radiation = .72 watts/in<sup>2</sup>  
(maximum at sea level - normal incidence)

Conductivity of surface air film

$$= 3.1 \times 10^{-3} \\ \text{watt}/(\text{in}^2 \cdot ^\circ\text{F})$$

For maximum sun,  $T_a = 100^\circ\text{F}$ , and using the most probable values of  $\epsilon$  and  $\alpha$ , equation A-4 gives a surface temperature of about  $150^\circ\text{F}$ . Extreme conditions give  $200^\circ\text{F}$ .

#### MECHANICAL AND STRUCTURAL

Material densities in lb/in<sup>3</sup>:

Fiberglass laminate: .056

Polyurethane foam: .0012

Aluminum: .1

Young's Modulus (E) in lb/in<sup>2</sup>:

Fiberglass laminate:  $1.5 \times 10^6$

Aluminum:  $10 \times 10^6$

Foam 500

Flexural rigidity of a solid plate of thickness,  $h$ :

$$(A-4) \quad D = Eh^3/[12(1 - \nu^2)]$$

$\nu$  is Poisson's ratio.

For a sandwich panel of thickness  $h$  and face thickness  $t$ :

$$(A-5) \quad D = \frac{1}{2} E t h^2 (1 - t/h)^2 / (1 - \nu^2)$$

The relationship between  $t$  and  $h$  (in inches) of the truss core panel which will satisfy the minimum weight stiffness criterion is:

$$(A-6) \quad h = t + .24/t^{\frac{1}{2}}$$

## COMPOSITE STRUCTURES FOR NAVAL POINTING SYSTEMS

DAVID C. BRECHT

General Electric Ordnance Systems  
Pittsfield, Mass. 01201

### ABSTRACT

As a step toward the development of lightweight pointing systems for future high speed Naval vessels, General Electric Ordnance Systems developed and fabricated a radar director train yoke structure made from graphite/epoxy composite materials. On an equal stiffness basis, this composite train yoke design is 35 percent lighter than a conventional steel yoke. Introduction of composite structures on shipboard pointing systems should be accomplished on a "selective" reinforcement" approach. A significant problem area is the impact strength of surfaces to falling objects or accidental blows; the use of special outer layer materials show promise as a solution. The use of truss structures instead of monocoque construction may be a more efficient use of composite materials.

Ordnance Systems Department of General Electric has been actively engaged in development activity leading to the use of graphite/epoxy composite materials in Navy shipboard pointing systems such as missile and gun directors and gun mounts. Current interest in the use of graphite/epoxy composite materials is very high in the aviation industry. In particular, there have been numerous technical articles published during the past few years concerning the use of graphite/epoxy composites for aircraft. Advanced aircraft are now being designed with up to 70 percent composite structure with weight savings of 40 percent and costs savings projected by the mid-1980's of 30 percent. Another area of graphite/epoxy composite material use is in sporting goods, and in particular, golf-club shafts and tennis rackets, which constitute a large proportion of sales of this material. The sporting goods usage is significant as such use will enhance the expected price reduction of graphite/epoxy material.

Ordnance Systems engineers foresee the need by the U.S. Navy for lightweight and stiff pointing systems for the lightweight vessels to be commissioned during the next ten years. Hydrofoil ships, already undergoing tests, will require lightweight topside equipment such as gun mounts, missile and gun directors, and missile

launchers. The use of graphite/epoxy materials for such advanced structures would allow high-speed, 50 to 75-knot ships to carry weapons and control systems, that are larger and more accurate. Graphite/epoxy structures also have the advantages of high fatigue resistance and increased internal material damping. (Figure 1)

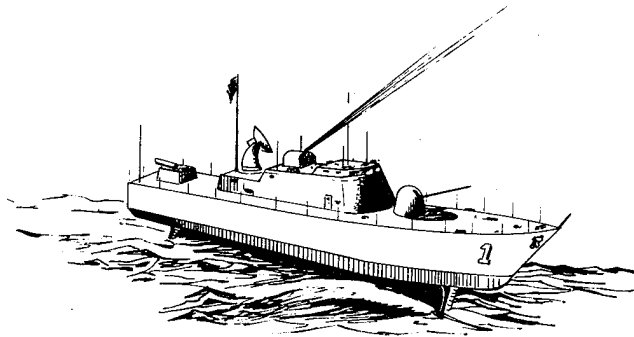


Figure 1. Artist's Conception of Future Hydrofoil Ship

Graphite/epoxy composites have a density just over half that of aluminum. In unidirectional laminates, the modulus of elasticity is comparable to that of steel, ranging from 19 to 42 x 10<sup>6</sup> pounds per square inch, depending on the fibers used. The ratio of modulus of elasticity to density, known as specific modulus, is four times that of steel. The specific tensile strengths (ratio of tensile strength to density) of graphite/epoxy composite materials are almost four times that of steel. To achieve quasi-isotropic properties to resist loads along various directions, composite materials must be laid-up in plies at angles of 0°, 45°, or 90°. Because this construction reduces the specific strength and modulus ratios, design concepts must be judiciously generated to minimize this loss of effectiveness. All metals (except beryllium) have about the same specific strength and modulus ratios, and it is not difficult to achieve ratios for graphite/epoxy materials of upward to two times that of steel or aluminum. Thus, composites have attractive characteristics for structural usage.

A radar director train yoke structure was developed and fabricated at General Electric using high-strength graphite/epoxy composite materials. This yoke structure (Figure 2) interfaces with the train bearing of

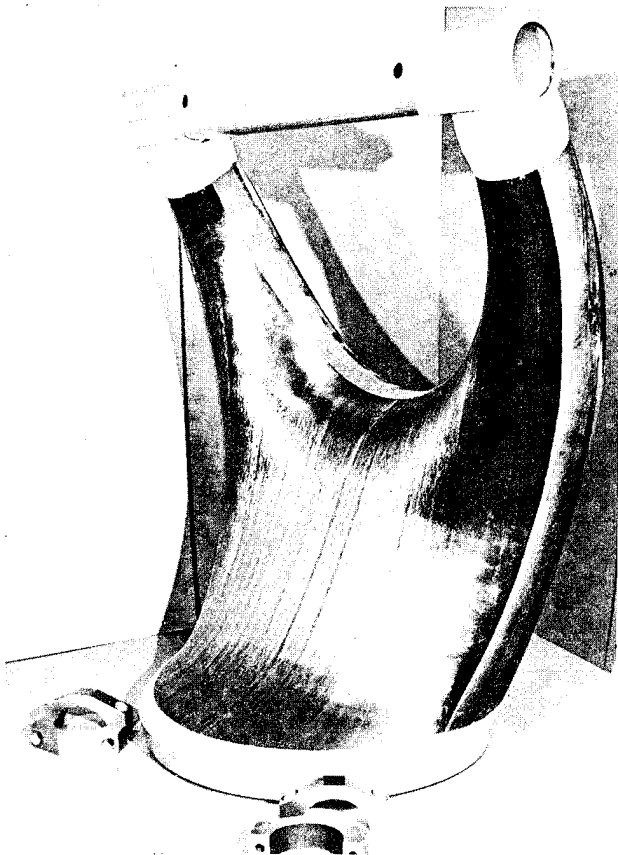


Figure 2. Train Yoke Structure Fabricated of Graphite-Epoxy Materials

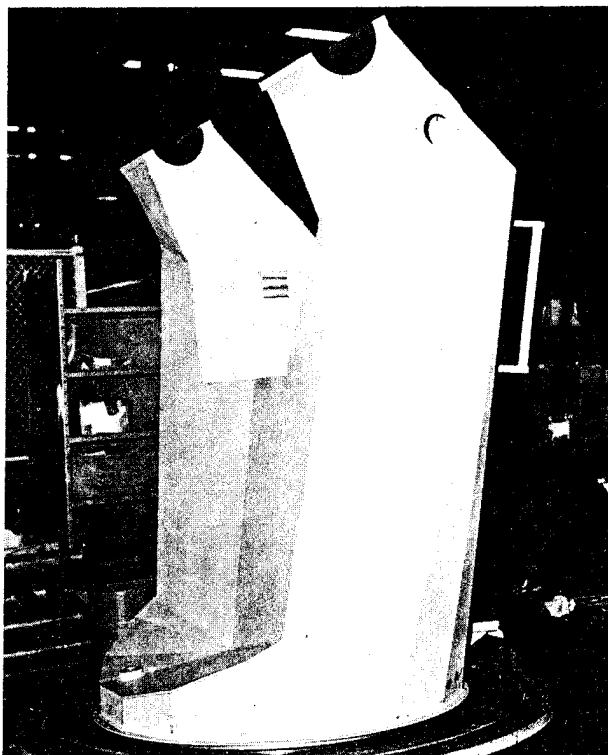


Figure 3. Original Steel Welded Train Yoke Structure

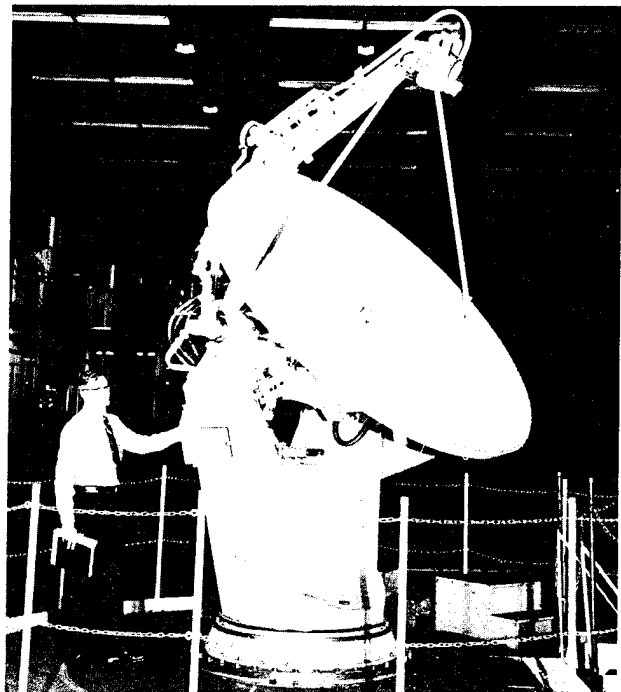


Figure 4. Radar Director

approximately 38 inches in diameter and extends vertically 67 inches to the elevation axis. It could replace the original steel welded structure (Figure 3) and fit into the original director (Figure 4) at the train bearing and at the elevation shaft. Full travel of the elevation structure can be obtained. To reduce development costs, details not needed for the primary development effort such as the step, machined mounting pads, handrails, stops, and cable holes, were omitted. The composite structure was designed to be as strong as the steel one, instead of having the same stiffness, in order to reduce the cost of raw material. The composite yoke design was not copied directly in shape. The ability of the composite material to conform to a mandrel of virtually any shape freed it from the restraints imposed on the metal yoke, allowing curved, streamlined yoke design. The design was basically a monocoque one with internal stiffening members.

The composite structure is now undergoing structure compliance tests. Further testing is planned including shock tests and mode shape/transfer functions/natural frequency tests.

With allowance for the weight of elements omitted, the composite director train yoke structure (Figure 2) with steel interface pieces weighs only 314 pounds, compared to the 655-pound weight of the original steel design (Figure 3) - a 52 percent saving. Although the composite structure is as strong as the steel one, the stiffness of the composite yoke is about one-third that of the steel yoke. By increasing the composite skin thickness, the stiffness of the yoke can be made equal to the steel one. GE calculations indicate that if the skin of the composite structure (Figure 2) was increased

threefold, the stiffness would equal that of the steel structure for a new total weight of 424 pounds, or a weight saving of 35 percent. If a very stiff structure were required, a further doubling of the composite skin thickness would result in a total structure weight of 590 pounds, having twice the stiffness of the steel structure with a 10 percent weight reductions.

At today's \$80/lb. cost of graphite/epoxy composite, the total cost of such structures is high. However, by the early 1980's the price is expected to fall to \$10/lb. Although considerable hand labor is presently required to lay up prototype monocoque composite structures, production-run structures could be fabricated with considerably less labor by utilizing mechanized techniques already in use in the aviation industry. With proper tooling and organization, the lay up could be done by relatively unskilled workers.

Ordnance Systems engineers have tried to avoid the use of the direct substitution technique. Instead, the design utilized the more favorable characteristics of composites while avoiding their less desirable characteristics. First naval applications likely utilize the selective reinforcement approach used on aircraft where small pieces of composite materials are applied at key locations where the increased stiffness may be demonstrated without redesigning the entire structure.

One problem foreseen involves the impact strength of the surface of such structures. Sharp blows by falling objects or accidental blows could pierce the skin and cause local delamination. This problem has been the subject of a number of studies by research organizations. Although this problem appears not to be fully solved, the use of Kevlar composites on the last few outside plies of a graphite/epoxy structure greatly increases the impact strength. The tradeoff, however, is either a weight increase or reduction in structure stiffness.

Graphite/epoxy composites may be configured with a very low thermal coefficient of expansion in a specific direction. The available types of graphite/epoxy composites can be selected and laid up in various ply angles to obtain a low plus or minus thermal coefficient of expansion to suit a specific application. Hence, graphite/epoxy composites may be used in applications where close tolerances are required over an unavoidable temperature range. For example, the mounting and spacing of optical lenses and mirrors on graphite/epoxy structures results in improved performance of such systems.

Preliminary studies have been started at Ordnance Systems of the use of graphite/epoxy composites on Navy gun mounts.

Ordnance Systems engineers are also evaluating the truss-type structure. The monocoque construction used in the yoke shown by Figure 2 requires a buildup of a number of plies to obtain quasi-isotropic characteristics in the plane of the material surface. This construction, however, considerably reduces the effective modulus of elasticity in any one direction and reduces the effective

shear modulus by an even greater amount. The efficiency of graphite/epoxy composite material is greatest when the loading completely along the directions of the graphite fibers. Truss-type structures might be very efficient if designed to take direct and shear loads as either tension or compression members.

Tubes made from graphite/epoxy pre-pregs can be made by techniques already developed, which utilize a high degree of mechanization. Thus, costs would be considerably less than for the ply lay up construction used on the monocoque design. The analysis of truss structures has been well established through the use of computer-aided design techniques. Design costs for truss structures are considerably less than for the finite element techniques used for complex structures. One problem area is the design of joints at the nodal points of the truss tubes, which will be economical to manufacture. Figure 5 depicts a preliminary sketch of a truss structure designed for the same director application as the structures of Figures 2 and 3.

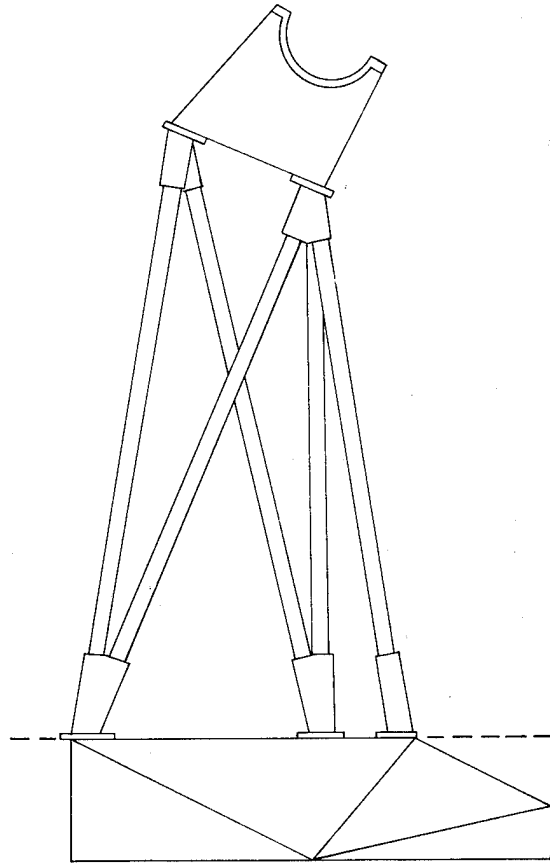


Figure 5. Preliminary Sketch of Truss Structure

Although considerable more effort will be required for the development of shipboard graphite/epoxy structure, General Electric's development work to date indicates that such structures may have important impact on the design of future small, high-speed naval ships.

# DEVELOPMENT OF A FIBER-REINFORCED COMPOSITE DESIGN CONCEPT FOR LARGE, MECHANICALLY-SCANNING, PLANAR SLOT ARRAYS

JOHN W. SMALL

ITT Gilfillan  
Van Nuys, California 91409

## ABSTRACT

Results are presented of the first phase of a study undertaken to investigate the technical and economic feasibility and impact of Advanced Composites on the design of large Radar Antennas for unprotected worldwide shipboard service.

The linear slotted waveguide array element was selected as the critical component for initial development. A current production Radar System is used as the technical and cost base. The design, fabrication, and test of the Composite waveguide are discussed in detail. In addition, cost and weight comparisons between the composite design and the baseline are presented.

## INTRODUCTION

Since their introduction about 15 years ago, the brief history of high performance fibers has been unique among new materials. The extent of their potential benefits was recognized almost immediately and their technology has grown at an extremely rapid rate. This technology, much of it founded on the applications of glass fiber reinforced plastic, has received strong, continuing support from various Governmental agencies and the Aerospace Industry.

Recently, the expansion of Advanced Composites into consumer products such as golf clubs and tennis racquets along with the beginnings of their use for a variety of mass-produced automobile and truck parts has resulted in:

1. Lower cost, improved materials and manufacturing methods
2. Increased design experience and customer acceptance.

To date, the use of these materials in large Radar Antenna Systems has been quite limited, although rewards from their application in this area can be dramatic.

In late 1976, ITT Gilfillan began a study program to determine the feasibility of an all-composite Radar Antenna. At the start of the project we were faced with two main objections to the use of fiber-reinforced composites for this application. The most pronounced was the high cost of the materials; a close second was a lack of confidence in their capabilities for long-term performance within the shipboard environment.

It became apparent that in order to sell the Composite Antenna it would have to be justified by more than the weight savings which could be accomplished with these materials. It would have to equal or surpass the standard metal antenna in both cost factors and survivability in service.

The overall goal that developed for the study program is to generate a technological and cost base for the design and fabrication of the Composite antenna. Furthermore, the design

must be lighter, less expensive, and capable of performing an identical mission at lower life cycle costs than its metal counterpart.

## BASELINE SYSTEM DESCRIPTION

The AN/SPS-48, a large Radar System produced for the Navy by ITT Gilfillan since the early 1960's, was selected as the baseline for the Composite Study Program. This is a high-power, three-coordinate, long-range air search and designation Radar that simultaneously provides aircraft control and target data to shipboard control centers.

The system uses an S-band planar array antenna mechanically rotated 360 degrees in the azimuth plane. The radiating elements are 76 slotted aluminum waveguides with the walls reduced by chemical milling to 0.045 in. Figure 1 shows a typical assembly with one of the eight aluminum mounting clamps. Fiberglass radomes are bonded between these mounting clamps to each length of waveguide.

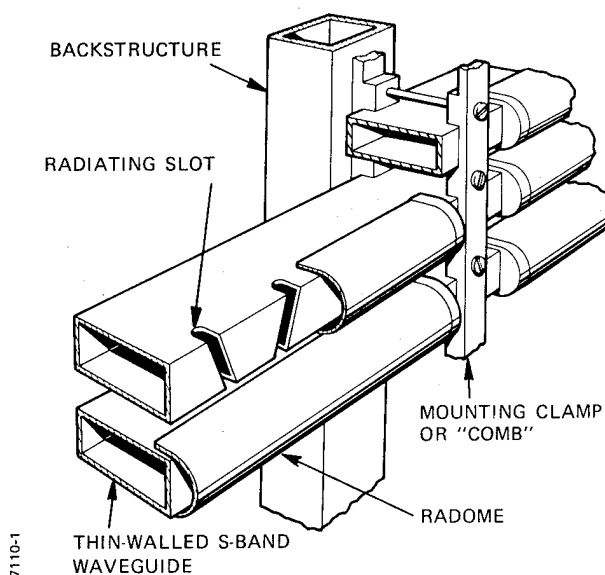


Figure 1. Detailed Section of Baseline Antenna Array Assembly

The baseline antenna, shown in a typical mast installation in Figure 2, has a projected area of 227 square feet, 14.2 feet high by 16.0 feet wide. This planar array surface is inclined at an angle of minus 15 degrees to the rotation axis. A rear view showing the welded aluminum backstructure and the pedestal base is found in Figure 3.

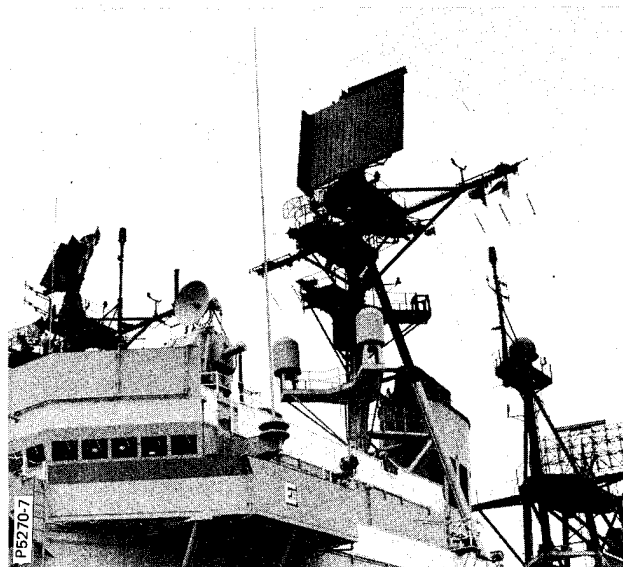


Figure 2. AN/SPS-48 Mast Installation

The weight breakdown of the major Antenna Group components is:

Pedestal	1325 lb	29.4%
Backstructure	1637 lb	36.4%
Array Elements	684 lb	15.2%
Serpentine Feed	342 lb	7.6%
Miscellaneous	512 lb	11.4%
Totals	4500 lb	100.0%

The unprotected mast installation of the baseline Antenna Group exposes it to a wide variety of severe environmental conditions. For example, hot gases from the ship's boiler stack, slightly aft and below the antenna, in combination with salt spray and large temperature changes cause serious corrosion problems. In some instances, small holes have been etched through the waveguide walls. These environmental effects necessitate the removal of the Antenna from its installation every few years for refurbishing.<sup>(1)</sup>

The AN/SPS-48 was chosen as the baseline for the Study Program because of the long operational service of a high quantity of systems, the availability of all types of engineering and cost data, and the opportunities for measurable design improvements by the application of Advanced Composites.

#### DEMONSTRATION COMPONENT SELECTION

During the organization of the study program each of the major components of the Antenna Group was considered for initial development. Since the slotted waveguide array elements are used in large quantities (about 1000 feet per antenna) and are the "payload" of the system, it was decided to devote the primary effort to their development and test.

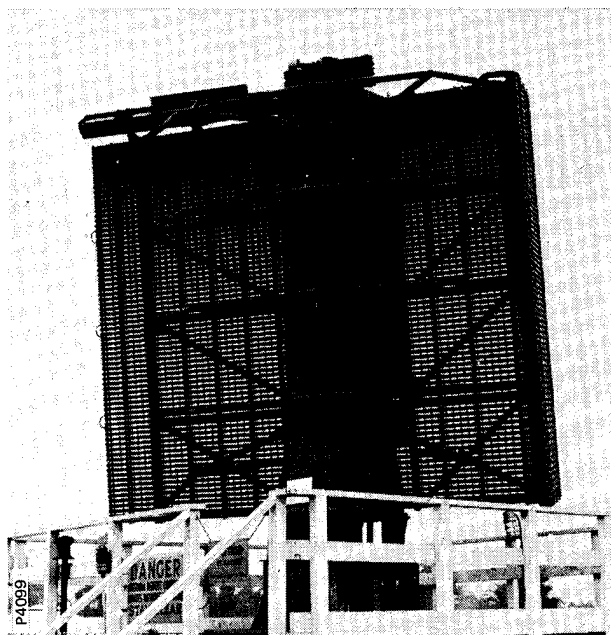


Figure 3. AN/SPS-48 Rear View

In addition to functioning electrically and mechanically with high stability and accuracy, the problems involved with preparing the necessary conductive surfaces presented a challenge.

The choice of the array elements also offered the opportunity to solve several problems of the existing design. One is the high labor costs involved with the set-up and machining of the radiating slots and the assembly of the radomes. Another is signal distortions caused by the eight aluminum mounting clamps which project beyond the radiating surface of the antenna elements. A third is excessive sidelobes due to cross-polarization caused by the horizontal spaces between the elements.

Among other significant advantages, the Composite waveguide concept, discussed in the Component Design section, offers solutions to these problems.

In order to justify proceeding toward an all-composite antenna, the most critical component had to be superior to the present design — not only by a reduction in weight, but in performance and cost.

#### MATERIAL CONSIDERATIONS

A wide variety of composite system components are available with an equally broad range of properties and prices. Although complex, it is exactly this array of materials that offers the nearly unlimited possibilities for adapting composite systems to answer specific design requirements. The engineer can design the material as well as the structure.

Following this principle, the design of the composite waveguide evolved into a "hybrid" concept which makes selective, limited use of the higher cost graphite fibers along with extensive application of the lower cost Dupont fiber, Kevlar 49.

An intermediate strength, general purpose structural graphite fiber, Hercules type AS, was selected for the top and bottom longitudinal stiffening ribs of the waveguide. This fiber has good balance among its properties and a comparatively moderate price. The "S" in its designation indicates that the fibers have been surface-treated to increase the composite shear and transverse tensile strength. The 3501-6 resin system is an amine-cured epoxy rated for 350 degree service.

In general, graphite was chosen for its high specific modulus (per unit weight) to provide high buckling stability, its excellent fatigue resistance, and its high thermal stability. The major unidirectional properties of this GR/EP System include:(2)

Tensile Strength (Ksi)	230
Tensile Modulus (Msi)	20
Compressive Strength (Ksi)	120
Compressive Modulus (Ksi)	8.3
Flexural Strength (Ksi)	260
Flexural Modulus (Msi)	17.5

The choice of Dupont's Kevlar 49, or PRD, for the waveguide walls was governed by its excellent electrical properties that approach those of Quartz fiber, high impact strength, a strength-to-weight ratio about ten times aluminum, moderate cost, and a near zero coefficient of thermal expansion. These properties were important in our application since the laminate has the multiple functions of waveguide structure, radome, and protective sheath for the graphite/epoxy stiffeners. Some of its important electrical properties are:

Dielectric constant (10 GHz)	3.3
Loss Tangent (10 GHz)	0.024
Dielectric strength (volts/mil)	960
Volume Resistivity (ohm/cm)	$5 \times 10^{15}$
Surface Resistivity (ohm)	$5 \times 10^{15}$

The impact strength of Kevlar/epoxy is over eleven times that of graphite, six times that of boron, and is in the range of S-glass and aluminum.(3) This is due to the high ductility and high propagation energy of the fiber which allows it to maintain good load-carrying ability even after fracture initiation. The more brittle materials, such as graphite, tend to fail precipitously with almost no remaining load-carrying capacity.

Kevlar 49/epoxy also has excellent environmental resistance. This is illustrated by a relatively small reduction of 8 percent in interlaminar shear strength after 100-hour exposure to salt water. Similar exposure to both jet fuel and Skydrol oil showed about a 1 percent drop in strength. These results indicate that an excellent resin-to-fiber bond has been maintained.(4)

In summary, the basic concept in the material selection process was to compensate for the weak points of one fiber with the strong points of another; trading-off costs, electrical properties, and other features to achieve the best design balance for the job.

## COMPONENT DESIGN

The array element design selected for development and test is the end product of a variety of early concepts. These evolved from the initial attempt to simply replace metal with composites to the present design making use of the unique properties of the materials to integrate several functions in one assembly as shown in Figure 4.

The "T"-shaped blade stiffener was selected as the most efficient configuration to provide longitudinal rigidity and the necessary strength along the backstructure attachment flanges. This inverted "T" cross-section is more efficient than either a hat-section or a "J" shape, and is simpler to fabricate.

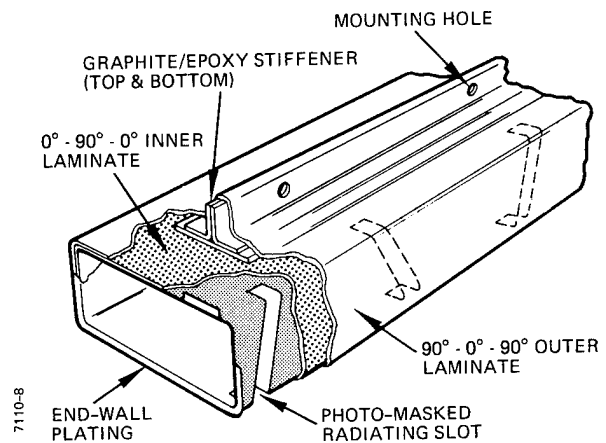


Figure 4. S-Band Composite Array Element Design Concept

Details of the stiffener design are shown in Figure 5. The back-to-back angles and bearing plate are made from the same laminate and cured as a single assembly.

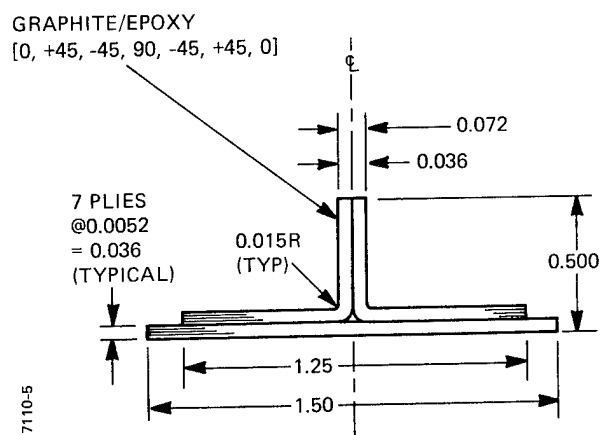


Figure 5. Graphite/Epoxy Blade Stiffener Detail

A graphic example of the penalty for neglecting one of the basic rules of composite design, occurred during an early trial fabrication of this item. The stiffener, made at that time with a lay-up sequence of 0, +45, 90, -45, 0° plies, developed a twist after removal from the mold. This was a good example of the need for both balanced and symmetrical lay-ups. A balanced stack implies that for every +45° ply there is a -45° ply present. Symmetry requires that the stack be a mirror image of ply orientations about the centerline. Following this rule, a second stiffener was made with a 0, +45, -45, 90, -45, +45, 0° lay-up and was absolutely straight after curing.

Since most structures are faced with combined loading situations, it is necessary to orient fibers, or plies, at specific angles to absorb these forces. In actual practice, what could conceivably become an extremely complicated stack of odd

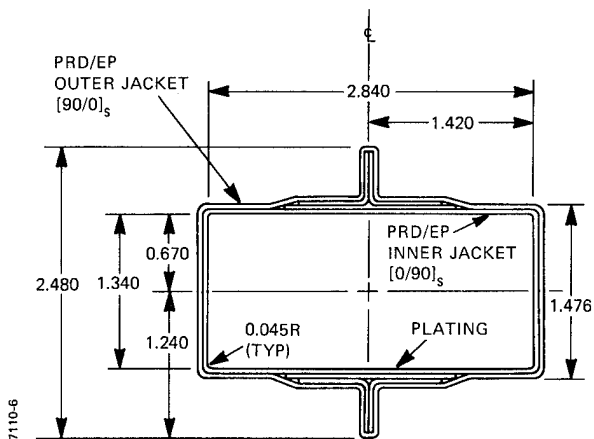
angles, has simplified into a “quasi-isotropic” ply orientation. The idea behind this is that by combining various percentages of 0°, plus and minus 45°, and 90° plies, a lay-up can result which will effectively react all loads and also be reasonably optimum for weight and fabrication.

This principle was followed in the stacking arrangement for the stiffener. Its symmetrical lay-up has 14.3 percent 90°, 28.6 percent 0°, and 57.1 percent 45° fibers. In addition to 1.28 times the column strength of aluminum in the waveguide longitudinal direction, this lay-up develops the following major ultimate strength properties:

Tensile ( $F_x^{tu}$ ) Ksi	70
Compressive ( $F_x^{cu}$ ) Ksi	70
Shear ( $F_{xy}^{su}$ ) Ksi	33

Varying the stack proportions to 40 percent 0°, 40 percent 45°, and 20 percent 90° plies would result in a 17 percent increase in tensile strength, a 12 percent increase in compressive strength, but a reduction in the shear strength of over 24 percent.

The waveguide walls are built up with 0 and 90° fibers since, when mounted to the backstructure, the primary loads occur perpendicular to the waveguide surfaces. This absence of 45° fibers also allows an optimum balance between weight, thickness, and electrical requirements. Figure 6 shows a dimensioned profile of the complete composite waveguide.

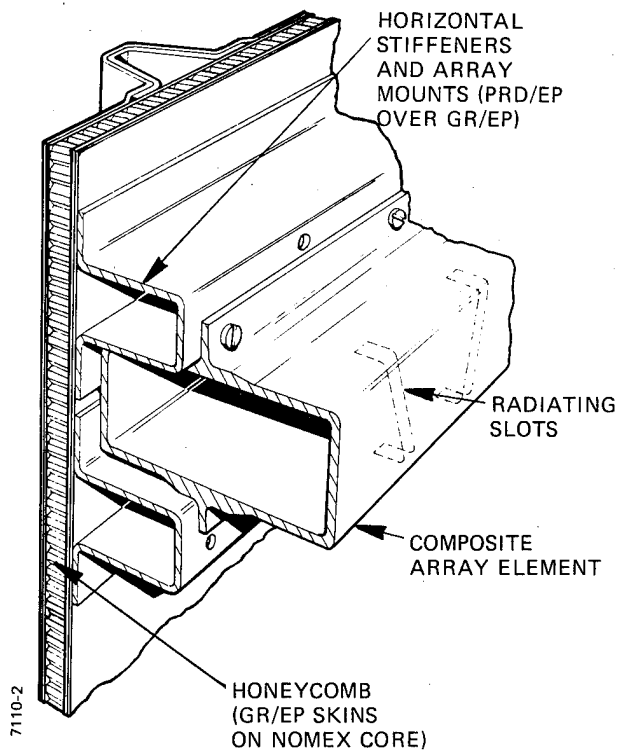


**Figure 6. S-Band Composite Array Element Profile**

The production version will have integral flanges formed from the basic wall laminates. The step in the mandrel, currently high enough to carry the plating across the laminate thickness, will be elevated to plate the complete face of the flange. The flange will be strengthened with an integral Graphite/Epoxy stiffener.

The PRD/Epoxy outer sheath protects the Graphite/Epoxy stiffeners from impact damage and minimizes moisture absorption. The walls of the mounting holes in the top and bottom flanges are sealed with resin to cover the ends of the graphite fibers exposed by the drilling.

The preliminary concept for the continuation of the composite design into the antenna backstructure is shown in Figure 7.



**Figure 7. Composite Backstructure Preliminary Design Concept**

Designed for maximum stiffness and minimum weight, it also combines different fibers to achieve an optimum structure. Built around a Nomex honeycomb core surfaced with graphite epoxy face sheets, a stiffened grid is developed with vertical GR/EP hatsections on the rear and horizontal GR/EP "U"-channels on the front. These also function as the array element mounting rails. As with the array element, Kevlar laminates are used as impact and environmental resistant coatings. Although a 0.375 in. honeycomb was used in the preliminary analysis, a thicker core which moves the face sheets further from the neutral axis will increase the stiffness without adding significantly to the weight.

The increased stiffness developed in this integrated design should raise the natural frequency of the antenna to above the range of the 35 Hz requirement for mast-mounted shipboard equipment.

## FABRICATION

The key to the fabrication of the waveguide array element is in the preparation of the conductive inner surface. This must have a minimum surface roughness, on the order of 10 to 20. Such a surface is almost impossible to attain by plating directly onto the laminate since the metal follows the irregularities in the resin and the fabric weave.

If the usual sequence is reversed, however, and the waveguide is, in effect, built from the inside out, the conductive surface can be controlled by the finish of the core, or mandrel. The problem then is how to extract this core from lengths of straight waveguide up to fifteen or twenty feet.



Several possible solutions to this problem were examined. One method used a collapsing mandrel. This, however, would have parting lines in the core surface and these would be copied by the plating. Another possibility was to shrink the mandrel away from the waveguide by the application of a low temperature solution through the core.

The procedure used is a variation of the old "lost wax" or investment casting process. An accurate steel mold is made to the inner dimensions and surface quality required for the waveguide. This is used to cast a "pattern" or mandrel in a eutectic, or low-melting-point, metal alloy. A rectangular hollow extrusion, as shown in Figure 8, is used to provide rigidity to this form as well as to minimize the amount of alloy required.

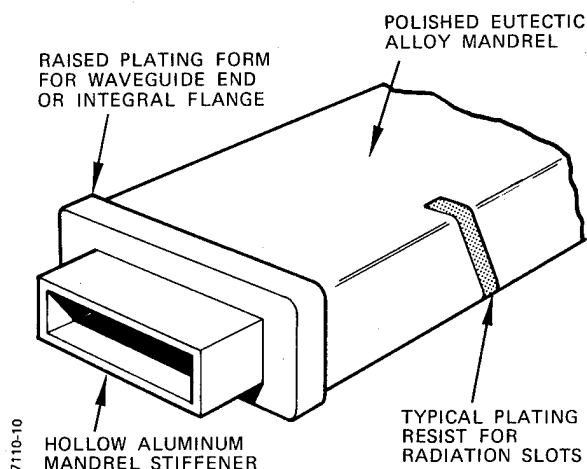


Figure 8. Composite Array Element Core, or Mandrel

The mandrel is then prepared with a thin coat of polyurethane to protect the plating as the core is melted out. The mandrel is plated with a temporary process layer of nickel. The first permanent plating is a 0.0002 gold flash, followed by nickel, and finally copper.

The inner jacket of PRD/EP is laid over the copper plating. The pre-processed stiffeners are positioned above and below and the outer sheath of PRD/EP is wrapped over the whole assembly. The complete unit is vacuum bagged and cured in an autoclave and the mandrel is melted out. The eutectic alloy and the rectangular core stiffener are then salvaged for reuse.

The polyurethane coating is stripped away and the temporary layer of nickel is removed by an acid wash, exposing the gold inner wall of the waveguide.

The radiating slots are incorporated by means of the deposition of a resist material through a mask. This resist prohibits plating where an opening is required.

Several general requirements were established for the fabrication methods to insure that the transition from the prototype stage into production can be readily accomplished:

1. All fabrication conditions, such as time cycles, temperature levels, pressures, etc., must be fully attainable in existing facilities.
2. Procedures must be adaptable to the production of high quantities.

3. Raw material control, quality assurance, scrap rates, repairability, and inspectability must be considered even though they are not specifically part of this stage of the program.

## TESTING

Initial electrical measurements were made using an eighteen-inch length of Composite X-band waveguide which had been fabricated as a reduced-scale trial run of the core-forming and plating processes. This revealed the problem of small flakes of the gold plating being pulled away by the melting-out of the core, or mandrel, and exposing the relatively poor electrically conductive intermediate layer of nickel. The decision to begin the test program with this higher frequency waveguide was made when a series of unanticipated and unavoidable delays slowed completion of the S-band demonstration components.

Another problem encountered with the X-band guide was that the plating, unlike the S-band design, was not continuous over the ends of the walls. This necessitated the removal of about a sixteenth of an inch of the PRD/EP laminate around each end to expose the plating. This provided a space which, when filled with conductive epoxy, formed a back-up for the interface between the aluminum choke flanges and the plating. It was anticipated that both the flanges and the small areas of exposed nickel would cause somewhat degraded performance, particularly since the higher X-band frequency is significantly more intolerant than S-band of surface imperfections.

Both the VSWR and the Insertion Loss of the Composite sample were measured and compared to an equivalent length of standard aluminum waveguide. In Figure 9 the VSWR of the two is plotted against Frequency. A prominent periodic structure modulating the line of the Composite waveguide indicated, as suspected, that the ends of the sample had significant reflections from the mismatches at the flange interfaces. To confirm this hypothesis, a load was inserted partway along the center of the waveguide. This had the effect of suppressing the reflection at that end of the guide. The VSWR was measured again and the result is shown in Figure 10.

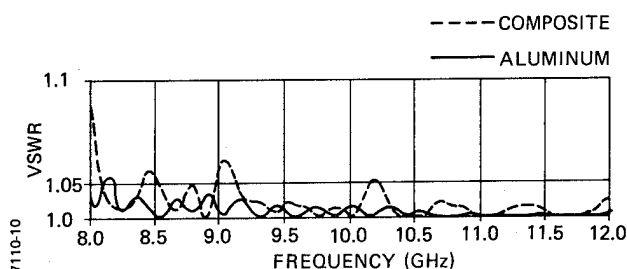


Figure 9. VSWR vs. Frequency of Composite and Aluminum X-Band Waveguide

The insertion loss measurements showed that the average value in dB across the band was 0.25 for the Composite sample compared to 0.05 for the aluminum waveguide. This was in accordance with the problem of exposed nickel plating mentioned above.

These test results were in good agreement with the predictions and underscored the importance of the surface finish, the consistency of the plating, and an effective flange interface. In addition, the test procedures were perfected and are now in use for the Composite S-Band Array Element evaluation.

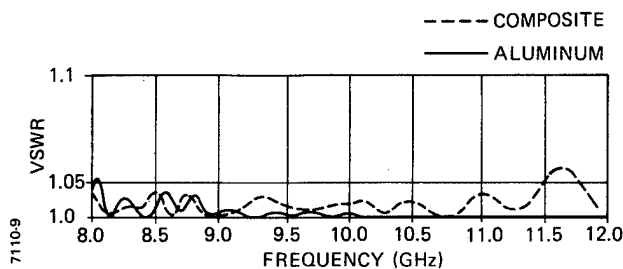


Figure 10. VSWR vs. Frequency of Composite and Aluminum X-Band Waveguides With Inserted Load to Suppress Flange Effect

Various mechanical and environmental tests are scheduled to follow the completion of the electrical measurements of the S-Band Demonstration Components. These tests will be performed using an integrated assembly of the S-Band Array elements and the Composite backstructure shown in Figure 7. A summary of these tests will be included with the presentation of this paper at the Symposium later this year.

#### COST AND WEIGHT COMPARISONS

Based on current data, the array elements represent over 18 percent of the total cost of the AN/SPS-48 Antenna Group. This is more than \$83 a pound compared to just over \$67 per pound average for the rest of the assembly. About 50 percent of the array element cost is fabrication and assembly labor. In general, since their material costs are still high, this is the area where composite designs become competitive with metal. This factor will become increasingly important as the cost of labor continues to escalate. Some of the reasons for this reduction in labor intensity are:

1. Assemblies fabricated closer to their final configuration with reduced numbers of parts, joints, and fasteners.
2. Improved tolerance conditions and fewer assembly problems as a result of the "net molded part" concept.

With its integral radome and mounting provisions, the Composite waveguide array element design is a good example of these qualities. Exclusive of fasteners, it results in a 78 percent reduction in component parts. In addition, the lengthy set-up and machining times for the radiating slots are eliminated since these are simply masked with a plating resistant material before the plating process.

Based on these labor and part savings, anticipated reductions in the cost of materials, and the extension of the fabrication procedures into higher volume methods, a 9 to 12 percent cost reduction could be achieved by the Composite design for a 50 system quantity.

A comparison of weights shows the Composite design at 0.42 pounds per linear foot versus the reduced wall-thickness RG-75U aluminum waveguide assembly at 0.54 pounds per linear foot. This 20 percent reduction represents a saving of 120 pounds on the full antenna.

This decrease in weight for the 76 array elements feeds back through the rest of the Antenna Group, allowing correspondingly lighter backstructure and pedestal designs.

#### CONCLUSIONS

The work to date with the Composite waveguide array element has demonstrated that the concept can be both practical and beneficial. The design has achieved its objectives in the areas of assembly simplification, cost, and weight reduction. Based upon extensions of the measurements derived from the X-band sample to the S-band array element with correct plating, surface finish, and interface design, it will also meet its electrical performance requirements.

The use of Advanced Composites has resulted in a design that effectively combines several discrete parts and functions into one assembly. In addition, it has offered solutions to certain aspects of the baseline antenna design that had caused signal distortion and sidelobe problems.

Although the basic concepts of the Composite array element have been validated, work remains to be done in several areas. The fabrication processes must be developed for quantity production and, in particular, the high cost of gold warrants the study and test of alternative platings.

In addition, the program will continue into the development of Composite designs for the pedestal, serpentine feed, and primary backstructure. While each of these will undoubtedly present new and different challenges, the work accomplished thus far has provided the important first step toward our ultimate goal of an All-Composite Antenna.

#### REFERENCES

1. "Evaluation of Some Organic Coatings for Protection of Equipment in Marine and Stack Gas Environments," by R. E. Barrett, ITT Gilfillan Materials and Processes Engineering Group, April 1967.
2. Hercules Inc. Graphite Materials Product Data, April 1976.
3. Harper, C. A., *Handbook of Plastics and Elastomers*, McGraw-Hill Book Company, Inc., New York, N.Y., 1975.
4. E. I. Du Pont de Nemours Kevlar® Product Data.

## CORROSION PROTECTION FOR SHIPBOARD-MOUNTED ANTENNAS

Alan W. Kline

Mechanical Engineering Supervisor  
Lockheed Electronics Company, Inc.  
Plainfield, New Jersey 07061

### ABSTRACT

This paper presents several methods for protecting shipboard-mounted antennas from the corrosive effects of the operational environment. These methods include a new paint system, corrosive-resistant electrical connectors, and special considerations for waveguide and critical assemblies.

### INTRODUCTION

The modern antenna must be designed to provide a long unattended service life under extreme environmental conditions. The average ship is at sea for extended periods of time and, due to dangerous working conditions, the topside equipment receives minimum maintenance attention. All repairs and maintenance other than those required to keep the antenna on the air are scheduled when the ship is in port.

The shipboard environment plays considerable havoc with the exposed surface of the unattended antenna. The constant wind-driven salt spray erodes the normal paint surface, getting into cracks and crevices to destroy the protective finish and attack the bare metal. In addition, the antenna is usually mounted in areas exposed to stack gasses. The hydrochloric and sulphuric acids formed from the fuel-oil combustion products condense into flange seams and joints between the various gear housings, covers, and other modules attached to the structure, and eventually seep into internal areas of the antenna. The natural ability of metals, such as aluminum to build up oxides as protection against further corrosion, does not offer sufficient protection against the shipboard environment. The constant wind and spray erode the oxides from the surface and expose new metal to the corrosion factors. The common plating materials such as chromium, nickel, zinc, and cadmium have limited life when left unprotected in the corrosive atmosphere. Stainless steel (18-8) and bronze offer good protection against the ship environment, but their use is limited to small hardware items. As in all lightweight structures, aluminum still offers the best all-around choice as the material for shipboard antennas. It is necessary to solve the corrosion problems associated with aluminum by using surface coatings that can withstand the extreme elements with little maintenance.

### CORROSION PROTECTION

In the past, topside structures were painted with vinyl alkyd enamel (MIL-E-15130) over various combinations of zinc chromate primer (MIL-P-8585), wash coat primer (MIL-C-15328), and, in the case of aluminum, iridite (MIL-C-5541). Experience with these coatings has been unsatisfactory and, in extreme cases, refinishing is required in less than one year. In recent years, Navy laboratories and industry have developed finishes that will hold up under the ship environment for more than five years. This increase in the repainting time cycle has meant that repainting topside equipment can be scheduled during major overhaul in the shipyard, and will eventually result in reducing the ship's complement of personnel normally needed to perform these tasks during in-port periods.

A new two-part epoxy paint system is frequently being specified for shipboard equipment. This system requires four separate applications, consisting of three primers and a topcoat of the required color, to provide a total paint thickness of 12 to 20 mils. The epoxy paint system produces an extremely durable, tough, and smooth coat with excellent adhesion that resists the eroding effects of the sea environment. The materials are easily applied with conventional equipment, and suppliers have incorporated a number of features to make the products foolproof. Most have color-mixing control where the mixed product is a different color than either of its components, to easily ensure that the converter has been added to the base portion. The products are also supplied in contrasting colors and are purposely low in hiding power to assist in getting an even, adequately thick film, free from "holidays."

The aircraft industry has developed a number of extremely durable paint systems that could be used for shipboard equipment. One system, which was developed for the undercarriage and wheel wells of aircraft, uses a polyurethane topcoat over an epoxy primer. The polyurethane has slightly greater resistance to abrasion and requires less preparation than the two-part epoxy.

For optimum protection, it is necessary to seal all seams with the finish to prevent the corrosive elements from attacking the underside of the coating. Sealing the exposed seams between the structure and modules mounted

during field installation can be handled effectively by following procedures for properly preparing the joint area and then applying a touch-up coat after completing installation. Procedures must also be developed for removing and replacing external modules for repair. Proper surface preparation, before refinishing with either paint system, involves a thorough cleaning of the area with a solvent and abrading the surface to provide a "tooth" for subsequent topcoats.

The epoxy and polyurethane finishes are not designed to be painted over conventional finishes like vinyl or alkyd coatings. For the best results, these finishes should be stripped completely by sand blasting or with a suitable paint remover. The first coat of the new finish should be applied as quickly as possible after cleaning to prevent corrosion from occurring on the bare metal surface.

To further reduce the maintenance and repair time, the modern antenna is a modular design in which critical parts can be removed as modules so that repair and replacement can be accomplished without a major disassembly of the structure. The modular concept uses connectors for the quick removal of the electrical connections to the individual modules. Cables terminated in connectors not only permit easy removal, but also provide improved electrical shielding over the junction box and stuffing tubes. The shielding requirement makes it essential that the mating connector parts have metal-to-metal contact to provide a good ground path for the cable shields. The connector parts cannot be coated with a corrosion-resisting nonconductive coating, and are subject to considerable deterioration in the shipboard environment.

For most applications, the designer has several options in selecting connectors, for the exposed antenna. The exception is radio frequency connectors where, due to emi considerations, the use of nonferrous (nonmagnetic) material is mandatory. For shielded power and control cables, the options include plated aluminum protected by nonmetallic molded boots and type 316 stainless steel. Aluminum connectors with nickel or cadmium plating have the advantage of lower cost and better availability. Stainless steel connectors are far superior in resisting long-term salt-spray corrosion. Adding plastic boots increases the protection for all connector types, but if assembled incorrectly, these boots can trap moisture.

The effects of the salt atmosphere on the overall antenna depends a great deal on the design of the castings and weldments in the structure. In general, the external surface of the antenna structure should be as smooth and free of pockets and protrusions as possible within the limitations of minimum weight, high stiffness, and ease of maintenance. All surfaces should be sloped to prevent the accumulation of salt water that will eventually destroy any finish.

The internal surfaces of the antenna waveguide, sliprings, and other assemblies are also highly susceptible to damage from the sea environment. The temperature cycling of the internal air during on-and-off periods of operation causes the parts to "breathe" in the salt- and moisture-laden external air. As the warm air cools, the salt is deposited on the critical internal surfaces, which eventually results in the breakdown of the equipment. The life of these items can be increased considerably by pressurizing the internal volume with dry air to prevent this breathing action.

# THE MANUFACTURE OF AIRBORNE CASSEGRAIN ANTENNA

J. SHALIT

ELTA ELECTRONICS INDUSTRIES LTD ASHDOD ISRAEL

## ABSTRACT

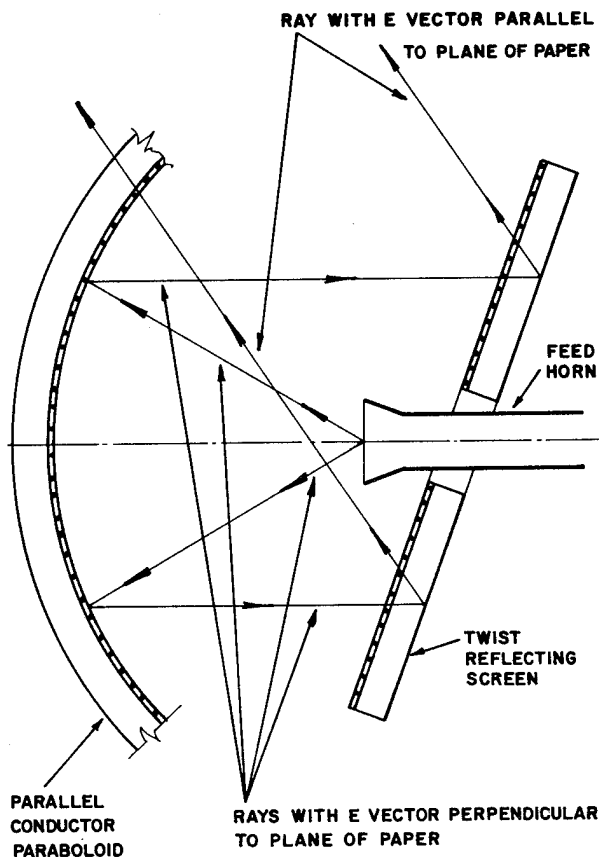
This paper describes the procedure tools and materials used in the production of a cassegrain antenna. The lamination process and the installation of the polarization wires are described precisely. Special attention has been given to the tools involved.

## INTRODUCTION

The cassegrain antenna system is composed of three main components. The horn, the twist reflector and the paraboloid. The only moving part in this system is the twist reflector. The reflector and paraboloid are built from several layers of non-metal materials, with an embedded array of closely spaced metallic conductors.

## PRINCIPLE OF OPERATION

Plane polarized waves from the horn illuminate the paraboloid and are formed into a plane polarized beam. The beam is reflected out by the reflecting surface of the twist reflector and, at the same time, the plane of polarization is rotated through a right angle. The outgoing radar beam can thus pass through the paraboloid. Scanning is achieved by moving the reflector through half the scan angle required.



## PRINCIPLE OF OPERATION.

## DESIGAND PRODUCTION CONSIDERATIONS

1. An accurate paraboloid is required with a maximum over all tolerance of .012 inch at 23 inch diameter.
2. Both the twist reflector and the paraboloid use in their construction hundreds of wires which are set at accurate parallel intervals.

3. Positioning of the reflecting surface relative to the polarizing surface must be set accurately and uniformly over the entire area in order to minimize distortion.
4. Careful evaluation of materials to minimize possible disturbances of electronic function.
5. Structural rigidity since the angle of reflection is doubled any error will also be doubled.
6. Dimensional stability.

#### PRODUCTION

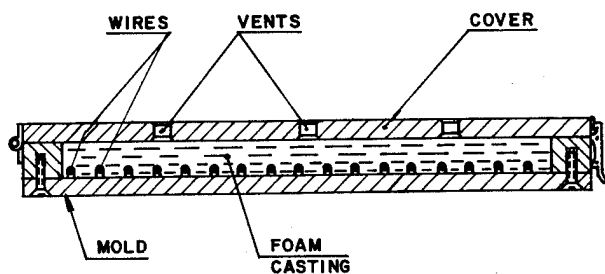
The main problem of production was to find a method of installing hundreds of wires especially in the paraboloid. Simple tools were produced. Electronic development production methods, and progress in tool design advanced together.

#### THE TWIST REFLECTOR

This consists of two parts.

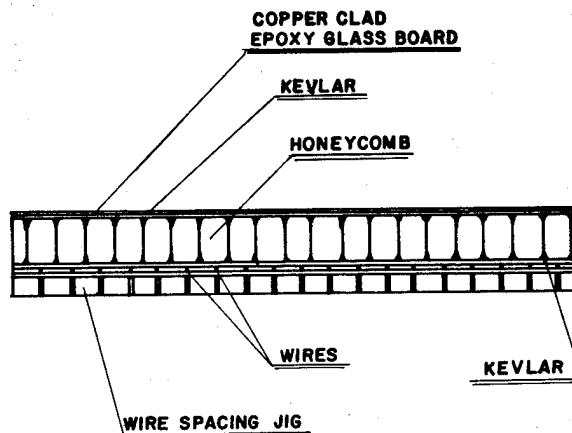
1. The reflecting surface.
2. Polarizing surface.

The reflecting surface is a flat metal surface, while the polarizing surface is an array of metal wires. The wires are positioned very accurately relative to the reflecting surface and to each other. The wires are embedded in kevlar prepreg which maintains the wires in place. The materials used in the mechanical structure of the reflector were selected for the property of minimal disturbance in the electronics function. The first twist reflectors were foam castings. A simple casting tool was used.



#### CASTING TWIST REFLECTOR

The method was first to tie the wires into slots then to pour the foam. The casting was then removed from the tool and cemented to the metal disc which formed the required reflecting surface. This method had a number of drawbacks in particular the wires were displaced during the casting process. The casting process was discarded in favour of a lamination process.



#### LAMINATION METHOD

A copper clad epoxy glass sheet, the material used for printed wiring boards, is used as the reflecting surface. No displacement of the wire occurs since they are held in place while applying the layers of kevlar prepreg. Good performance was achieved by using the lamination process.

#### THE PARABOLOID

This item was more difficult to produce because of its shape. Again the lamination method produced a better product.

The process is as follows :

1. Kevlar layer.
2. Autoclave.
3. Wiring installation cementing.
4. Kevlar layer.
5. Honey comb.
6. Kevlar layer.
7. Autoclave.

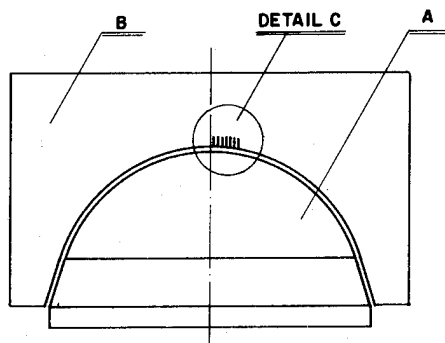
The development of the tools was as follows :

1. First a wooden male tool.
2. A metal male tool.
3. A metal male tool and a wire installation tool.

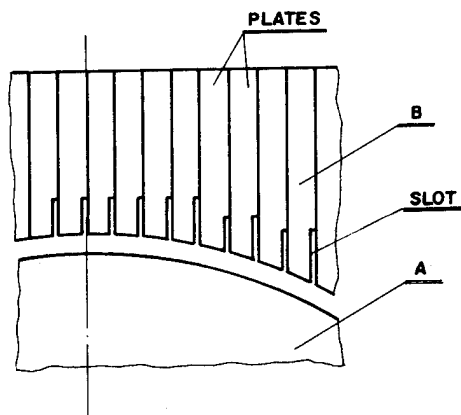
The wiring installation is the longest operation. To mark up, install and glue the several hundreds of wires on a 23 inch diameter paraboloid, takes approximately 300 man hours and a duration of four weeks.

After the completion of the electronic development an effort was made to minimize the production cost. The tool described here is the result of this effort. This tool is composed of two main parts.

1. The male tool - A.
2. The wiring installation tool - B.



WIRE INSTALLATION TOOL

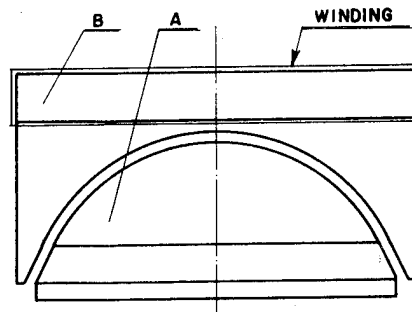


DETAIL C

The tool A is very similar to the male tool mentioned previously, with additional locating holes for tool B. Tool B is an assembly of many plates which form slots at identical and accurate distances. The plates and the slots are held in place and guide the wires through the operation.

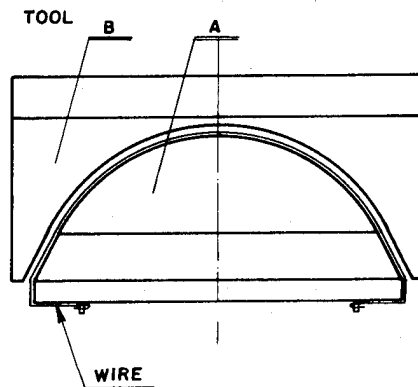
The procedure is as follows :

1. Kevlar layer.
2. Autoclave.
3. Winding the wire on tool B (one continuous wire).



WINDING ON TOOL B

4. Spraying adhesive on the kevlar layer (tool A).
5. Location of tool B to tool A.
6. The winding is cut across one side, the coming hundreds of strands which are tied at the bottom of tool A.



WIRE TRANSFERED TO TOOL A

7. Drying the adhesive. (The wires are now glued to the kavlar layer on tool A).
8. Separation of tool B from tool A.
9. Kavlar layer.
10. Honey comb.
11. Kavlar layer.
12. Autoclave.

Process described here is completed in two days.

## CONCLUSION

This paper described the development of the structure, methods, tools and production of the cassegrain antenna.

Four main principles guided this work :

1. Supporting the electronic development by supplying antennas and other elements for testing.
2. Selecting and testing materials electrically and structurally.
3. Minimal investment cost during development.
4. Design and production of good tools to achieve accuracy and low cost.

All principles were reached as described, and a successful cassegrain antenna had been developed and produced.



## CONCEPTUAL STUDIES FOR UNMANNED HARDENED RADAR FACILITIES

Rene W. Luft, Joseph Antebi, and Howard Simpson

Simpson Gumpertz & Heger Inc.  
Cambridge, Massachusetts 02138

### ABSTRACT

A baseline design concept is developed for a hardened, unmanned, phased-array radar facility. Among the subjects discussed are functional design requirements and constraints, concepts examined, design trade-offs, and special considerations and problems associated with the structural design. The selected configuration is described and a parametric study of the adaptability of the baseline design to varying levels of nuclear threat is discussed. Preliminary cost estimates are presented. While this study is performed for a specific facility, the method of approach is readily adaptable to other hardened facilities.

Of special interest is the reliability analysis which was developed for multimode of operation systems, using Markov processes theory; this is described in some detail.

### DESIGN REQUIREMENTS

**General.** — The facility is for an unmanned, four-face, L-band, solid-state, phased-array radar installation, suitable for a wide range of site conditions. The primary equipment consists of four 35-foot-diameter arrays, three electronic packages (16 x 7 x 8 ft high) and a data processing unit (24 x 7 x 8 ft high).

The facility must provide, in specified modes of operation (including nuclear threat), structural support for the four arrays, a tolerable environment for the radar and data processing equipment, and power and cooling to operate this equipment. The required life of the system is ten years.

The major considerations controlling the design are:

- Configuration, strength, and stiffness requirements for array structural supports.
- Modes of operation of the radar.
- Size and weight of, and power and cooling needed by, the radar electronics and data processor.
- Availability and reliability of subsystems and components.
- Air temperature and humidity, nuclear radiation level, allowable acceleration, and required rattle

space for each piece of equipment.

- Site conditions, including soil, climate, and availability of power and water.
- Nuclear threat, including overpressure, shock, thermal and nuclear radiation level, dust, air temperature, electromagnetic pulse (EMP), and multiple weapons effects.

**Modes of Operation.** — The facility will be unmanned and remotely operated. However, routine periodic maintenance will be scheduled, and in case of malfunctions during nonattack conditions, repair crews can be at the site within a few hours.

Operation is required in various designated modes, defined by the internal and external status of the facility. The internal conditions are dormant (data processor only is functioning); checkout and monitor (data processor and some of the radar electronics are functioning); and full up (data processor, electronics, and arrays all functioning). The external conditions are normal; alert; and attack.

An alert period may occur at any time during the lifetime of the system and may last seven days. An attack by a specified nuclear threat may occur at any time during an alert. The facility must be able to function for two hours after the start of an attack.

**Nuclear Threat.** — The threat for the baseline design is taken as a nominal 15 psi overpressure caused by a weapon in the low megaton range. Multiple bursts may occur during the attack period; however, the time delay between bursts is assumed to be such that blast, radiation, and thermal pulses do not interact. The air temperature and dust cloud density are affected by successive bursts and this is included in selecting their design values.

### STRUCTURAL DESIGN

**Analysis of Alternatives.** — Three important considerations in the structural design of hardened facilities are described below.

(1) Dynamic Characteristics. The structural design of a hardened above-ground building is usually governed by the overpressure, rather than by ground shock or radiation effects. The conventional approach is to design a relatively stiff structure. Since the natural period of this structure ordinarily will be much shorter than the positive phase duration of the applied loads, the resulting dynamic load factor will approximate 2.

Another approach to this problem is to design a structure with a natural period which is large compared to the positive phase duration of the load, so as to obtain a small dynamic load factor, say on the order of 0.2, thus reducing the internal forces very substantially. The disadvantage of such a design is that the resulting deflections are large; hence the probable residual deflec-

\* The work on which this paper is based was performed for M.I.T. Lincoln Laboratory, Lexington, Massachusetts 02173, and was sponsored by the Department of the Air Force.

The views and conclusions contained in this document are those of the authors and should not be interpreted as necessarily representing the official policies, either expressed or implied, of the United States Government.

tions would be large compared to the tolerable pointing error of a few milliradians. Therefore the first approach was selected.

(2) Above-ground vs. below-ground building. The structural design and structural configuration are governed by the need to support the array faces and to provide an enclosure for the radar and support facilities. The number of arrays and their size determine the minimal above-ground structure. Small arrays bias the design toward a mainly buried configuration, while larger arrays favor an above-ground structure. On the other hand, high design overpressures favor a buried configuration with a minimum of structure exposed to reflected overpressures, while low design overpressures favor an above-ground scheme.

The question arises as to whether it is more economical to provide a separate below-ground building to house the radar and support facilities or to provide sufficient space in the array support structure for these facilities. A separate below-ground building is subject to ground shock and to blast overpressure as attenuated by the soil. (In a saturated soil the side walls of a buried structure are subjected to nearly the same overpressure as the roof; it is therefore desirable that a well-drained granular backfill be provided.) The cost savings achieved by reducing the loads on the building by the attenuation in the soil cover must be traded against the increased cost of excavation and the cost of a connecting tunnel.

Equipment not required after attack initiation can be housed in a separate structure which, although unhardened, must be designed not to produce harmful debris.

For the four-faced solid-state L-band radar facility, the design overpressure level and the number and size of arrays led to a solution with two floors above grade and one level of about the same plan dimensions below grade. This results in a compact and economical building that fully utilizes the volume created by the arrays and their supports. The below-grade structure provides resistance to horizontal sliding and usually will extend down to a better bearing soil than would be available nearer grade level, thus reducing foundation costs.

(3) Materials selection. Designs employing reinforced concrete, structural steel, and a combination of both were studied to determine the most appropriate material to meet the strength, deflection, and shielding requirements. Reinforced concrete dimensioned to comply with the structural and radiation shielding requirements was selected; in addition, a 1/8-in.-thick, continuously welded steel sheet, located on the interior surfaces of walls, roof, and foundation slab was used for EMP shielding.

The possibility of using a steel truss or plate structure was considered, but found to be totally inappropriate. A concrete radiation shield would have to be provided; the function of the steel structure would be to carry all loads or the portion of the applied loads which exceed the capacity of the concrete required for shielding. Since the steel structure must be limited to low strains to be compatible with the concrete structure it would be inefficient.

**Structural Concept.** — The structural concept selected is a shear box scheme in the form of a truncated pyramid; this is compatible with the array face configuration and provides an efficient structure with respect to both stiffness and strength. Figures 1 and 2 show the general appearance of the structure and a section through it. In this shear box concept the external pressure applied to a vertical or sloping wall is carried by flexure to the horizontal floors which, in turn, act as

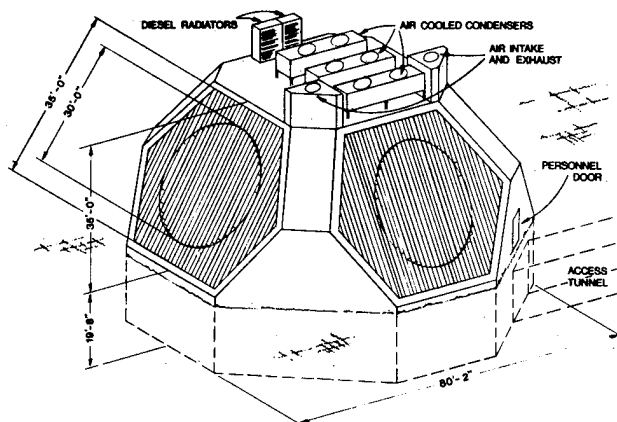


Fig. 1. — Four-Face L-Band Solid-State Radar Facility

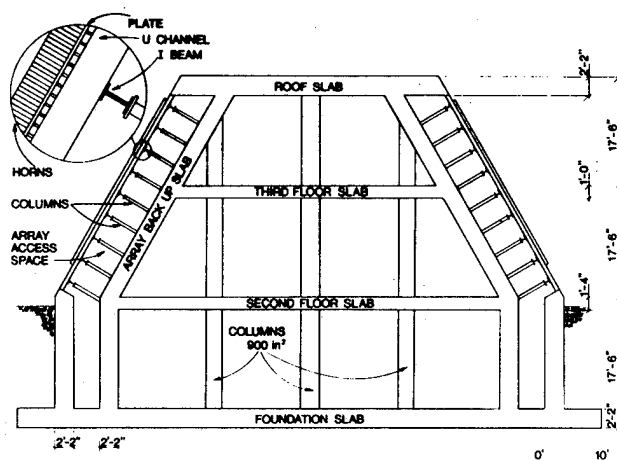


Fig. 2. — Structural Section of Facility

diaphragms. The floors then distribute the shear load to the vertical and inclined walls which are parallel to the direction of the loading; these, acting as shear walls, transfer the load to the foundation.

The array faces are supported by columns which rest on sloping concrete walls parallel to the array face. This arrangement provides access for maintenance of the array elements from the rear.

**Design and Analysis.** — The structure must survive multiple blast loads with stringent requirements on residual deflections; hence the benefits of plastic behavior cannot be utilized. The deflection constraints, both elastic and residual, are that the arrays must be supported so that the rotation of the best fit plane through the deflected array elements not exceed 2 milliradians, the sag of the best fit quadratic not exceed 0.26 in., and the amplitude of higher harmonics not exceed 0.05 in.

Since the facility must be designed to remain in the elastic range, the working stress levels were set below the dynamic yield strengths of the materials. The working stress levels used in the design are 0.9 times the dynamic yield stress for steel, and 0.8 times the dynamic compressive stress for concrete. These values were selected based on the expected scatter of the material properties and the degradation of the structure if the

allowable stresses are exceeded.

High strength reinforcing steel was used in the design to minimize steel areas and enhance placement of both steel and concrete. Note that structures designed for plastic behavior would utilize lower grades of reinforcing steel to provide large plastic deformations.

To compute combined critical stresses, the sum of the peaks was used, since the frequencies associated with different modes of behavior are widely separated — for example, the natural frequencies of the elements in flexure are high compared to the frequencies of the same elements acting in shear.

**Soil Considerations.** — Two types of soil were used in the evaluation of the baseline configuration. The selected upper and lower bounds for soil stiffness were constrained moduli of 200 and 20 ksi, respectively.

The deflection calculations indicate that the facility preferably should not be built on soils whose properties are close to the lower bound of stiffness. If the soil is marginal, backfilling with better soil, increasing the foundation slab area, or using a pile scheme would be required.

**Radiation Shielding.** — The minimum thickness of concrete shielding required was computed based on the incident radiation corresponding to the specified threat and on the allowable radiation levels. These thicknesses are 31 inches for the data processor and 10 inches for the other electronic equipment. As a result of strength requirements, the structure provides a minimum of 26 inches of concrete shielding for equipment on the second level and more for the data processor and other equipment on the first level. The concrete thickness is thus governed by strength and not by shielding requirements.

**Constraints in Equipment Layout.** — In addition to the specified equipment operational constraints, which will be discussed later, other considerations affecting the facility design include the following:

- The data processor, which is highly sensitive to shock and radiation, should be located where shock is near minimum and shielding is near maximum; therefore, it is located on the first level.
- Expendable equipment can be placed in the least protected spaces, or outside the building. The chillers and boiler are located on the third floor; the air-cooled condensers and the diesel radiators are on the roof.
- The number of penetrations into the structure should be minimized to reduce cost of protection from radiation and EMP; however, two personnel exits should be provided for safety reasons.
- Each major piece of equipment, such as electronic package, computer, and diesel generator, should be in a separate room to minimize fire spread and water damage from the fire suppression system.
- Removal and replacement of all equipment and equipment packages should be convenient.
- Minimum support for personnel should be provided at the site; living quarters are provided off-base.
- Spares and parts will be brought to the site as needed; storage space, although desirable, is not required.

A list of the major pieces of equipment and their location is given in Table 1.

## PRIME POWER

**Alternatives and Constraints.** — Selection of the prime power system, which backs up utility power and which provides prime power during alert and attack

TABLE 1. — Major Equipment and Their Location

ITEM	LOCATION
4 Radar Array Faces — 35 ft diameter	Outside
1 Data Processor Unit	Level 1
3 Radar Electronic Packages	2 on Level 1 1 on Level 2
1 Transformer — 1000 KVA	Outside
2 Diesel Generator Sets — 800 KW each	Level 2
2 Diesel Radiators	Roof
1 Switch Gear	Level 2
2 Combustion Air Filters	Level 2
1 Combustion Air Wet Scrubber (Venturi-Centrifugal)	Level 2
3 Chillers — 60 Tons each	Level 3
3 Air Cooled Condensers — 60 Tons each	Roof
1 Cooling Unit for Data Processor including Chiller (water cooled) and Air Handling Units	Level 1
5 Air Handling Units	Distributed
1 Oil Fired Boiler	Level 3
6 Pumps	Level 1
3 Heat Sinks — 10,000 gal. each	Level 1
1 Diesel Heat Sink Tank — 5000 gal.	Level 1
2 Combustion Air Cleaning Water Storage Tanks	Level 1
2 Slurry Tanks — 1 @ 5000 gal., 1 @ 6000 gal.	Level 1
1 Hardened Fire Protection Water Tank — 3000 gal.	Level 1
1 Unhardened Fire Protection Water Tank — 10,000 gal.	Outside
2 Hardened Fuel Tanks — 120 gal. each	Level 2
3 Unhardened Fuel Tanks — 10,000 gal. each	Outside

modes, is a major consideration in the design of the facility. Major considerations affecting the selection of the prime mover are:

- Availability and reliability.
- Continuous, large power level demands by the computer, even in the dormant mode.
- Nuclear effects such as overpressure, thermal pulse, and dust.
- Volume of combustion air required.
- Efficiency of, and heat loads generated by, the prime mover.
- No on-site water for heat rejection.
- Supply problems at a remote location.

These constraints led to the selection of a redundant diesel generator system to provide prime power for the facility; the redundancy is needed to meet the availability and reliability requirements which are discussed later.

Several sources of self-contained power were investigated; namely, diesel, gas turbine, nuclear, fuel cell, and battery.

Although the state of the art is progressing rapidly, fuel cell units of the required size apparently will not be

available in the immediate future.

Nuclear sources are available; however, they are only appropriate for very large and continuous power demands, they are expensive, and they release large amounts of heat. They are not appropriate for the relatively modest power demands and the backup function in the present application. Thus, diesel and gas turbine generators, and batteries are the only serious choices for backup power for the present facilities.

#### **Evaluation of Diesel vs. Gas Turbine Generators.**

Some of the relative merits, drawbacks, and limitations of these two systems are listed below:

- The diesel generator source has the advantages of a multiplicity of manufacturers, high reliability, and reasonable cost per kilowatt. Disadvantages for this application are large physical size, heat release into building, necessity for elaborate filtering of combustion air, and the need for a hardened heat sink during an attack.
- The advantages of a gas turbine generator are low weight, lack of vibration, very high reliability, and some tolerance to dust in combustion air. Disadvantages in this application are high volumes of combustion air required, heat release into building, and the need for a hardened heat sink.
- The volumes of intake air and exhaust gases are significantly less for the diesel than for the gas turbine. Low volumes of intake air and exhaust gas result in decreased requirements for hardened and shielded duct work to and from the diesel, and significantly less equipment for dust elimination and heat-pulse protection.
- The power rating of the diesel is maintained at high altitudes and temperatures, while there is significant decrease in the rating for the gas turbine. Capacity and cost of gas turbine engines would be significantly affected by the temperature-altitude effect in high and/or hot locations.
- Installed costs of units of the same rating appear to be reasonably similar for the diesel and turbine prime movers.
- The probability of startup (i.e., start-up dependability) for gas turbines is marginally less than that for diesels. Mean time between failures (MTBF) is higher for gas turbines than it is for diesels. Reliability requirements for the system (0.997 for two hours) dictate that redundancy is required both for the gas turbines and the diesels. Once redundancy is provided, either the diesel or the turbine satisfies reliability requirements.

In balance, based upon the considerations given above, diesel generators appear to offer more advantages relative to the requirements of the present facility than do gas turbines.

**Evaluation of Batteries vs. Diesels.** — The use of batteries as backup to commercial power and for prime power during the alert period was investigated. Batteries have the advantages of not requiring combustion air, of no heat release to the interior of the building, and of reliability during periods of high overpressure.

However, batteries as the sole power source would be much too costly on an installed basis if used for the entire one-week alert period. Also, batteries would require an unreasonable volume of hardened space within the facility.

The use of batteries as the prime power source during the attack period was also examined. Batteries would reduce or eliminate air cleaning and tempering problems

such as are associated with diesels. Batteries sized only for the attack mode do not occupy an excessive amount of space within the structure; however, some other form of backup power nevertheless is required for the entire alert period. In addition, a battery system needs venting, battery chargers, and motor-generator sets to convert DC to AC power; also it requires maintenance. A cost comparison shows that a diesel plant would cost substantially less initially and requires less maintenance than a battery-diesel system. Although a detailed investigation of the reliability of battery power was not made, it was determined that, to meet the reliability criteria, redundant diesel generators, motor generators, and battery chargers would be required.

#### **HEATING, VENTILATING, AND AIR CONDITIONING**

Most of the power delivered by either commercial utilities or the prime movers is dissipated as heat within the building. Primary considerations are the need for efficient cooling of the building and the tight temperature tolerances required by some of the operational equipment.

Heat sinks are required during all modes of operation to reject heat generated within the facility and heat delivered to the building from external sources. The methods of cooling must take into account the constraints that no outside water is available at the site and that the system must operate after the start of the attack for a period of two hours. For normal and alert conditions, standard radiators were selected for diesel water jacket cooling and air-cooled condensers with exterior freon-to-air heat exchangers for all other cooling. The air-cooled condensers and the water loop to the radiators are expendable during attack; for the remainder of the attack period, a hardened reservoir of chilled water provides a simple, reliable, and economical heat sink.

Cooling towers were considered as an alternative but were rejected because they require significant quantities of make-up water and because of the extent and frequency of the required maintenance.

The system operation utilizes the chilled water storage (sump) as an integral part of the entire building air conditioning system. The chilled water from the chillers is discharged into the sump; the cooling water for the system is drawn from the sump and returned to the sump via the chillers. The sump, which is thus maintained at the design temperature of 44 deg F, is immediately available for use as a heat sink if the attack mode is initiated.

Array face design requires the capability of de-icing by hot fluid for the alert and attack modes. An oil-fired boiler (with a forced hot glycol solution) was selected, since oil must be stored for the diesel engine generators, and because the oil burner requires very little electrical power. The use of electric heat was considered infeasible because of the increased load on the diesel generators.

Since elevated ambient temperatures and very high dust levels may exist during the attack period, the combustion air for the diesel generator requires an effective air cleaning and tempering scheme. A wet scrubber system consisting of a venturi and a centrifugal scrubber is used to clean and cool the air for the attack period; a hardened water reservoir is provided for this equipment. Alternatives evaluated, but rejected for various reasons, included dry inertial collectors and fabric filters.

## PARAMETRIC STUDY

**General.** — The purpose of the parametric study was to evaluate the adaptability and cost of the baseline scheme at several levels of hardness. In addition to the 15 psi baseline design incident overpressure, 5, 30, and 50 psi levels, with associated weapons effects parameters such as radiation and pressure duration, were investigated. Also, the cost of an unhardened facility was estimated.

**Structural Design.** — Table 2 presents the structural member properties determined for the study range. The controlling design criterion for the various structural elements changes with the design overpressure. For example, shear controls in the wall, roof, and third floor slabs for 50 psi overpressure; deflection controls the thickness of the array walls for 5 psi overpressure.

TABLE 2. — Parameter Design Study of Member Properties

Structural Element	5 psi	15 psi	30 psi	50 psi
	t or A p	t or A p	t or A p	t or A p
Foundation Slab	16"	26"	36"	46"
	.020	.020	.020	.020
Second Floor Slab	12"	16"	20"	30"
	.009	.010	.012	.012
Third Floor Slab	12"	12"	24"	53"
	.020	.040	.032	.029
Roof Slab	16"	26"	36"	56"
	.013	.013	.013	.010
Exterior Walls	16"	26"	36"	56"
	.017	.024	.027	.024
Columns	400" <sup>2</sup>	900" <sup>2</sup>	1296" <sup>2</sup>	2304" <sup>2</sup>
	.050	.050	.050	.050

where p = ratio of steel to concrete effective areas  
t = element thickness, in.  
A = column area, sq. in.

Radiation shielding does not govern concrete thickness at any overpressure. To meet the deflection criteria as the overpressure level increases, the required minimum soil stiffness also increases. If the soil is too soft, a different foundation design must be used, or an attitude sensing device may have to be incorporated in the facility.

**Prime Power System.** — The baseline is readily adaptable in the overpressure range from 5 to 50 psi, except for uncertainties concerning the behavior of the diesels at the higher overpressures.

The battery-diesel system discussed earlier will operate at the higher overpressures, but initial costs are substantially more than for a hardened diesel system. In view of the technical uncertainties and of the cost differential, both systems must be considered as possible candidates until the uncertainties are resolved.

**Costs.** — The approximate cost, in July 1971 dollars, of the total facility (excluding data processor and radar equipment) for the baseline design is \$3.0 million for a facility near an urban area and \$3.3 million for one at a remote site. An approximate cost breakdown is shown below.

Item	Urban site (percent)	Remote site (percent)
1. Land acquisition; site work; utilities	18	9
2. Structure	33	40
3. Mechanical	26	26
4. Electrical	13	13
5. Spares and Maintenance	<u>10</u>	<u>12</u>
	100	100

For facilities with a hardened diesel prime power system, only the structural costs vary with overpressure. However, at high overpressure levels it may be necessary to use battery-diesel prime power instead of the hardened diesel system. Fig. 3 shows the relative costs for the structure and for the total facility as a function of the design overpressure.

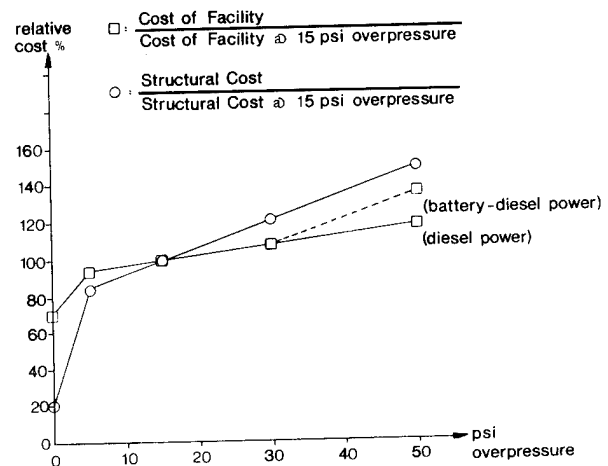


Fig. 3. — Structure and Facility Costs vs. Overpressure

## RELIABILITY OF THE RADAR FACILITY

**Introduction.** — For the evaluation of system reliability, a method of analysis for multimode of operation systems was developed. Because of its general applicability to multimode problems, it is described below.

The facility must have a minimum reliability of 0.997 for the design two-hour attack period and a minimum availability of 0.97 at any time during the ten-year design life. The required probability of mission success is therefore 0.967.

For each type of equipment, the size and number of units were selected to achieve the specified probability of mission success at minimum cost. The type of prime power and of HVAC were selected using the criteria previously described.

The internal and external conditions under which the facility operates have been described. Table 3 shows the feasible modes of operation.

It was determined from the reliability analysis that it is necessary to provide two diesel generators and three chillers that reject heat to the exterior via air-cooled condensers. Only one of the two diesels must function when no outside power is available. Two chillers are required to support the data processing equipment under normal conditions, while all three chillers are needed

TABLE 3. — Modes of Operation of Radar Facility

External Status \ Internal Status	Normal	Alert	Attack
Dormant	Mode 1		
Checkout and Monitor	Mode 1		
Full Up		Mode 2	Mode 3

during alert. At the start of an attack, sufficient chillers must have been operating to maintain the heat sink at its design temperature.

The multimode-of-operation reliability problem with several component groups that include stand-by redundancy can be solved using a method based on the theory of discrete state, continuous time, Markov processes.

**Concepts of Reliability Analysis.** — For the reliability analysis, the totality of the equipment in the radar facility will be referred to as the system, while each major component will be called a subsystem. In each subsystem several states can be defined according to the number of equipment pieces in operation, in stand-by, or in repair. For example, for a nonredundant subsystem three states can be defined, for a once redundant system five states can be defined, and so on. At any time instant the facility is operating in one of its modes.

The probability of the subsystem being in a specific state is a function of time. Let us define  $Q_i(t)$  as the state probability vector for the subsystem operating in mode  $i$ ; an entry  $j$  of this vector is the probability that the subsystem operating in mode  $i$  will be in state  $j$  at time  $t$ . Since the subsystem has to be in one state at time  $t$ , it follows that:

$$\sum_{j=1} Q_{i,j}(t) = 1 \quad (1)$$

While the subsystem is operating in mode  $i$ , the probability vector  $Q_i(t)$  can be computed from:

$$Q_i^T(t) = Q_i^T(0) F_i(t) \quad (2)$$

where  $F_i(t)$  is the transition probability matrix; an entry  $k\ell$  of this matrix is the conditional probability of the subsystem being in state  $\ell$  at time  $t$  given that the subsystem was in state  $k$  at time zero. (The transition matrix governs the changes of state within a mode.) For computational simplicity, time zero is defined as the time when the facility starts to operate in mode  $i$ . The transition matrices  $F_i(t)$  are obtained as solutions to the Chapman-Kolmogorov equations of Markov processes theory when exponential holding times are assumed.

When the subsystem switches modes, say from mode  $i$  to mode  $j$ , the initial probabilities  $Q_j(0)$  can be computed from

$$Q_j^T(0) = Q_i^T(t) T_{ij} \quad (3)$$

where  $Q_i(t)$  is the state probability vector in mode  $i$  at the instant of time  $t$  the switch to mode  $j$  occurs, and where  $T_{ij}$  is the transfer probability matrix; an entry  $k\ell$  of this matrix is the conditional probability of the subsystem starting in state  $\ell$ , in mode  $j$ , given that the

subsystem was in state  $k$ , in mode  $i$ . (The transfer matrix governs the changes of state between modes.)

The probabilistic behavior of the subsystem is therefore completely defined by the transition matrices, the transfer matrices, the initial state probability vector, and a rule defining the starting mode and the times at which mode switches occur. The rule for switching modes can be either deterministic or probabilistic.

The probability of mission success of a subsystem  $m$  of the radar facility is computed from the state probability vector  $Q_3(2)$ , i.e., mode 3 at time  $t = 2$  hours, as

$$P_m = \sum_j Q_{3,j}(2) = \sum_j \sum_i Q_{3,i}(0) F_{3,ij}(2) \quad (4)$$

where the sums are over those states  $i$  and  $j$  for which the subsystem is operational and can therefore accomplish its mission. For a nonredundant subsystem there is only one operational state, for a once redundant subsystem there are two operational states, and so on. (In nonoperational states the equipment has broken down.)

The result of 4 can be interpreted in terms of conventional terminology for a nonredundant subsystem  $m$  since

$$P_m = Q_{3,i}(0) F_{3,ii}(2) = A_i R_i \quad (4a)$$

where  $A_i$  is the availability of the only operational state  $i$  and  $R_i$  is the corresponding reliability. For a redundant subsystem, the concepts of availability and reliability have to be applied to all operational states. For example, in a once redundant subsystem  $m$  with operational states  $i$  and  $j$

$$P_m = Q_{3,i}(F_{3,ii} + F_{3,ij}) + Q_{3,j}(F_{3,ji} + F_{3,jj}) \quad (4b)$$

$$= A_i R_i + A_j R_j$$

where  $A_i, A_j$  are the availabilities of states  $i$  and  $j$  and  $R_i, R_j$  are the corresponding reliabilities.

In general equation 4 can be written as

$$P_m = \sum_i Q_{3,i}(0) \sum_j F_{3,ij}(2) = \sum_i A_i R_i \quad (4c)$$

The probability of mission success for the system is computed from

$$P = \prod_m P_m = \prod_m \left( \sum_i A_i R_i \right) \quad (5)$$

where the product is over all subsystems  $m$ . The series model for subsystems is valid when all subsystems are required for mission success.

In summary, for a given rule for switching between modes, the state probabilities for each subsystem  $m$  are computed as a function of time using equations 2 and 3, with the transfer and transition matrices obtained in explicit form or by numerical integration. Assuming that at any time the facility can go to the attack mode, the probability of mission success for each subsystem as a function of time is computed using equation 4, and for the total facility using equation 5. The probability of mission success for the given rule is then the minimum of the corresponding time function. This process is then repeated for all feasible switching rules and the smallest of all such minima is the design probability of mission success.

Estimates for the probability of mission success can be obtained from the steady state solutions of each mode instead of the time histories. Such estimates can produce useful results because the transition matrices include decaying exponentials.

**Nonredundant Subsystem with Stand-by.** — The concepts described above will be applied first to a subsystem that consists of a single component. For such a subsystem, three states can be defined: State 1, the component is in stand-by, that is in operating condition but not actually functioning; state 2, the component is in repair; and state 3, the component is functioning.

The transition and transfer matrices will be computed on the assumption that the component has an exponential failure rate  $\lambda$  (the inverse of the MTBF), an exponential repair rate  $\mu$  (the inverse of the mean-time-to-repair, MTTR), and a finite probability  $p$  of starting when the component has been in stand-by. The exponential failure law is realistic for components which have no appreciable wear during operation; because of its simplicity, however, it is also used for many other types of components. The exponential repair rate is used primarily because of the analytic simplicity of the model.

A graphic description of the modes of operation is given in Fig. 4. The number next to each arrow is the probability of the path. In mode 1, the equipment is either in stand-by or in repair; if it is in repair, it goes to stand-by once repairs are completed. In mode 2, the equipment is either functioning or in repair; when a breakdown occurs, repairs are started, and when a repair is completed, the equipment functions once again. In mode 3, there is no repair capability: the equipment is either functioning or the mission fails.

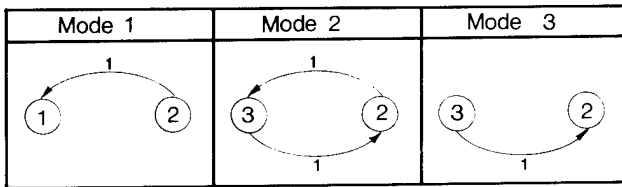


Fig. 4. — Transitions Between States — Nonredundant System

Another graphic description in Fig. 5 shows the transfers between modes that are feasible. A transfer from mode 1 to mode 3 is effectively a transfer from mode 1 to 2 to 3. The arrows are labeled with the probability of the path occurring.

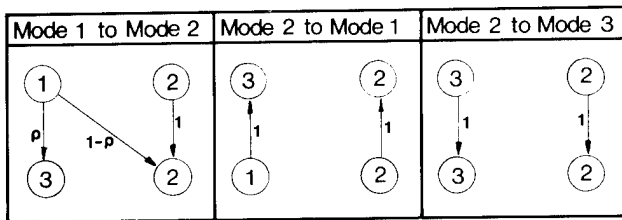


Fig. 5. — Transfers Between Modes — Nonredundant System

The transition matrices and the transfer matrices are given in Fig. 6. The general form of the transition probability matrix is

$$\tilde{F}_i = \tilde{A}_i + e^{-\alpha_i t} \tilde{B}_i \quad (6)$$

where  $\tilde{A}_i$  is a stochastic matrix (i.e., elements in a row add to one) and  $\tilde{B}_i$  is a differential matrix (i.e., elements in a row add to zero). All rows in  $\tilde{A}_i$ , for possible states in that mode, are equal; these are the steady state or limiting probabilities. For mode 2, the availability of the component in steady state is  $\lambda/(\lambda+\mu)$ ; this takes the familiar form  $\lambda r/(1+\lambda r)$  where  $r = 1/\mu = \text{MTTR}$ .

The probability of mission success is given by explicit expressions for the following two limiting cases:

(a) Mode 3 starts after mode 1 reaches steady state,

$$P = A_3 R_3 = p e^{-\lambda t} \quad (7)$$

(b) Mode 3 starts after mode 2 reaches steady state,

$$P = A_3 R_3 = \frac{e^{-\lambda t}}{1+\lambda r} \quad (8)$$

$$\begin{aligned} \tilde{F}_1 &= \begin{bmatrix} 1 & 0 & 0 \\ 1 & 0 & 0 \\ 0 & 0 & 1 \end{bmatrix} + e^{-\mu t} \begin{bmatrix} 0 & 0 & 0 \\ -1 & 1 & 0 \\ 0 & 0 & 0 \end{bmatrix} \\ \tilde{F}_2 &= \begin{bmatrix} 1 & 0 & 0 \\ 0 & \frac{\lambda}{\lambda+\mu} & \frac{\mu}{\lambda+\mu} \\ 0 & \frac{\lambda}{\lambda+\mu} & \frac{\mu}{\lambda+\mu} \end{bmatrix} + e^{-(\lambda+\mu)t} \begin{bmatrix} 0 & 0 & 0 \\ 0 & \frac{\mu}{\lambda+\mu} - \frac{\mu}{\lambda+\mu} \\ 0 & -\frac{\lambda}{\lambda+\mu} & \frac{\lambda}{\lambda+\mu} \end{bmatrix} \\ \tilde{F}_3 &= \begin{bmatrix} 1 & 0 & 0 \\ 0 & 1 & 0 \\ 0 & 1 & 0 \end{bmatrix} + e^{-\lambda t} \begin{bmatrix} 0 & 0 & 0 \\ 0 & 0 & 0 \\ 0 & -1 & 1 \end{bmatrix} \end{aligned}$$

Fig. 6(a) — Transition Matrices for Nonredundant System

$$\begin{aligned} \tilde{R}_{12} &= \begin{bmatrix} 0 & 1-p & p \\ 0 & 1 & 0 \\ 0 & 0 & 0 \end{bmatrix} \\ \tilde{R}_{21} &= \begin{bmatrix} 0 & 0 & 0 \\ 0 & 1 & 0 \\ 1 & 0 & 0 \end{bmatrix} \\ \tilde{R}_{23} &= \begin{bmatrix} 0 & 0 & 0 \\ 0 & 1 & 0 \\ 0 & 0 & 1 \end{bmatrix} \end{aligned}$$

Fig. 6(b). — Transfer Matrices for Nonredundant System

**Once Redundant System.** — The states for a once redundant system are defined in Table 4. At any time either zero or one components are in operation, while the other components are in stand-by or repair. The modes of operation are described in Fig. 7 and the transfers are described in Fig. 8. The transfer matrix is obtained by

TABLE 4. — States for Once Redundant System

State	Number of Components in:		
	Operation	Stand-by	Repair
1	0	2	0
2	0	1	1
3	0	0	2
4	1	0	1
5	1	1	0

inspection of Fig. 8. The general form of the transition matrix is

$$\dot{F}_i = A_i + e^{-\alpha_i t} B_i + e^{-\beta_i t} C_i \quad (9)$$

where  $A_i$  is a stochastic matrix and  $B_i$  and  $C_i$  are differential matrices. (These matrices can be obtained from the authors.) The primary difference between this result and that from the nonredundant system is that now the differential matrices are time dependent.

Explicit expressions for the probability of mission success can be obtained for mode 3 starting after the system reaches steady state in either mode 1 or 2.

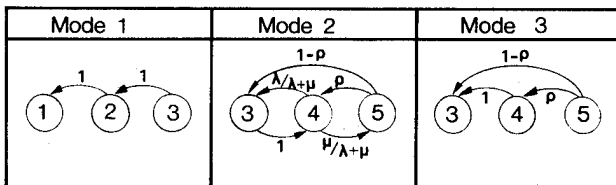


Fig. 7. — Transitions Between States — Once Redundant System

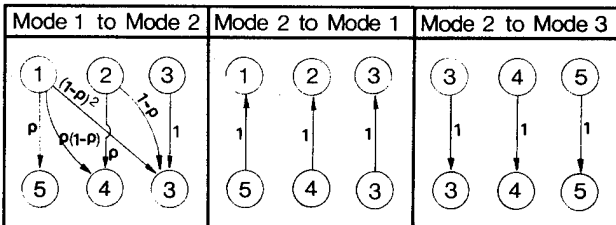


Fig. 8. — Transfers Between Modes — Once Redundant System

**Discussion.** — This formulation can be applied to obtain the reliability of any multimode, multiple subsystem equipment installation with any number of redundancies. It is of interest that the only parameters needed for the solution are the MTBF's, the MTTR's, the probabilities of start up, and the rules for switching between modes.

## CONCLUSIONS

1. The baseline concept developed meets all the design requirements and can realistically be adapted for the range of pressures studied. The size of the structure is governed by the array size; the enclosed space is more than adequate to house all the equipment that must be hardened.

2. The design of the prime power and heating, ventilating, and air-conditioning was controlled by the power requirements of the radar and data processing units. Since this study was performed, advances in electronics have reduced these power requirements. The considerations described herein would still be valid, but would lead to a different design.
3. Reinforced concrete is best suited to meet the strength, stiffness, and shielding requirements. To meet the deflection requirements, the structure had to be designed to behave elastically.

**Acknowledgements.** — This work was performed by Simpson Gumpertz & Heger Inc. for Lincoln Laboratory, Massachusetts Institute of Technology. Jackson and Moreland were retained as consultants in the electrical and mechanical areas, and Charles B. Solomon was consulted for the cost estimates. Personnel at Lincoln Laboratory and representatives of the Office of the Chief of Engineers and Huntsville Division, U.S. Army Corps of Engineers, provided valuable assistance. The authors wish to acknowledge the major contributions to the project by their colleagues Dr. Raymond W. LaTona and Mr. Harold D. Smith.

## APPENDIX. — REFERENCES

1. "DASA EMP Handbook," DASA 2N4-1, DASA Information and Analysis Center, General Electric Company, September, 1969.
2. "Design of Structures to Resist the Effects of Atomic Weapons — Weapons Effects Data," Department of the Army, TM5-856-1, November, 1960.
3. "Nuclear Weapons Effects: Dust and Air Temperature Environment," Technical Manuscript S-2, Construction Engineering Research Laboratory (from report by IIT Research Institute), February, 1971.
4. "Principles and Practices for Design of Hardened Structures," Air Force Design Manual, AFSWG-TDR-62-138, December, 1972.
5. "Study of Shock Isolation for Hardened Structures," prepared for the Office of the Chief of Engineers, Washington, D.C., by Agabian-Jacobson Associates, Los Angeles, California, 1966.
6. "The Effects of High Dust Loads and Elevated Ambient Temperatures on Diesel Engines and Gas Turbines," Arthur D. Little, Inc., 2 January 1969.
7. Bharucha-Reid, A.T., "Elements of the Theory of Markov Processes and Their Applications," McGraw-Hill Book Company, Inc., New York, 1960.
8. Howard, R.A., "Dynamic Probabilistic Systems," John Wiley & Sons, Inc., New York, 1971.
9. Kemeny, J.G., and Snell, J.L., "Finite Markov Chains," D. Van Nostrand Company, Princeton, 1960.



## POINTING BIAS MODEL FOR A 40-FOOT DIAMETER RADAR ANTENNA \*

Joseph Antebi, Rene W. Luft, Howard Simpson,  
Harold D. Smith, and Donald O. Dusenberry

Simpson Gumpertz & Heger Inc.  
Cambridge, Massachusetts 02138

### ABSTRACT

The development of a bias model for upgrading the pointing accuracy of ALCOR, an existing 40-foot diameter radar antenna, is described. The program objective is to achieve a pointing accuracy of 50 microradians. The bias model developed involves the use of real-time measurements, structural analysis, calibration measurements, and regression; the tradeoffs in arriving at the selected combination of methods are discussed.

The structural analyses of the elevation structure and yoke structure were performed separately; the elevation structure was analyzed by substructuring, due to its size and high degree of connectivity.

### INTRODUCTION

The purpose of this study is to develop a bias model for upgrading the pointing accuracy of ALCOR, an existing 40-foot-diameter radome-enclosed Cassegrain monopulse tracking radar antenna. The goal of the upgrading program is to achieve a pointing accuracy of 50 microradians; this is a major improvement over that required of the original design.

The position of a radar target with respect to the local ground axes is defined by its range, azimuth, and elevation. Given the geographic location of the antenna and the local gravitational anomaly, the target position coordinates can be transformed from local to global coordinates. The basic target coordinate output from the antenna system consists of the azimuth and elevation encoder readings, the monopulse signal, and the range. In an ideal system, the encoder readings define the angular position of the main radio frequency (RF) beam and the monopulse signal defines the position of the target with respect to that beam. In an actual system, bias terms must be added to the data readout to account for the effects that cause deviations from the ideal system. These effects, for ALCOR, can be categorized as follows:

- Zero-set biases and deviations in the alignment of the primary and secondary reflectors and of the feed, with respect to each other and to the elevation axis.

\* The work on which this paper is based was performed for M.I.T. Lincoln Laboratory, Lexington, Massachusetts, and was sponsored by the Department of the Army.

The views and conclusions contained in this document are those of the authors and should not be interpreted as necessarily representing the official policies, either expressed or implied, of the United States Government.

- Runout and deviations in alignment of the azimuth and elevation bearings; this includes nonorthogonality of the elevation axis with respect to the azimuth axis and mislevel of the azimuth bearing.
- Distortions of the antenna structure due to gravity, thermal, acceleration, equilibrator, and drive motor loads; these distortions in turn cause displacements of the primary and secondary reflectors, feed, and azimuth and elevation encoders.
- Nonlinearity of the encoders.
- Distortions of the RF beam due to atmospheric refraction, radome diffraction, etc.
- Biases in the monopulse system.

From a study of each of these effects, a bias model can be developed. The model can be expressed as the sum of a set of terms, each of which is a function of variables that can be measured; the coefficients in these functions are evaluated as part of the model development. The appropriate functional forms for these terms depend on the structural configuration, the characteristics of the sources of the bias, and the combination of analytical, measurement, and regression methods used to evaluate the coefficients. Regression in this application involves the tracking of targets with known trajectories, such as GEOS satellites, and the computation of coefficients for the bias terms to minimize the residual bias.

The following describes the development of the bias model and discusses the tradeoffs involved. The terms for the effects of atmospheric refraction, radome diffraction, and monopulse accuracy are not discussed here.

### DESCRIPTION OF THE ANTENNA

#### Geometry and Physical Characteristics

The ALCOR antenna, which is enclosed in an air-conditioned radome, has a 40-foot-diameter parabolic reflector. The reflector configuration is Cassegrain, with a dielguide feed. Some of the principal features of the antenna are shown schematically in Figure 1.

The primary reflector consists of aluminum panels with solid-surface skins over two-inch honeycomb; each panel is supported independently from the backup structure by threaded steel rods. The all aluminum reflector backup, which is symmetrical about a vertical plane through the vertex, consists of a six-pointed-star-shaped central hub, six radial beams, and three ring beams. The central hub consists of six intersecting girder members in a six-pointed-star configuration. The outer, middle, and inner ring beams are straight between radial beams. The beams are made of T-shaped extrusions for the top and bottom flanges, except for the middle ring beam, which has a structural angle for the top flange; solid web plates are riveted between the flanges. The web plates are stiffened by Z-shaped members located along normals to the paraboloid. Torsional bracing is provided in the two

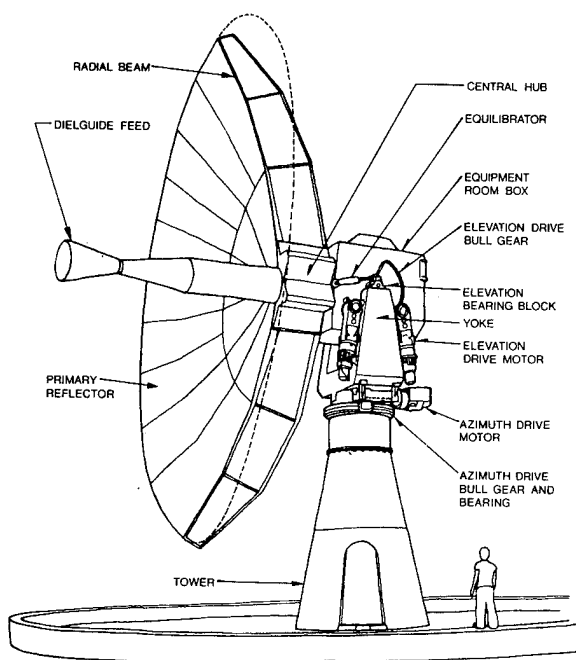


Figure 1. Schematic View of ALCOR Antenna

surfaces formed by the top and bottom beam flanges. Diagonal tubular bracing members are used in the region between the inner and outer ring beam, while continuous skins are used inboard of the inner ring beam towards the hub. The central hub is attached at six places to an equipment room. This room is a double-skinned aluminum box with internal stiffening members. The elevation bearings are attached to two opposite side walls of the equipment room.

The feed and secondary reflector are supported within a tubular structure cantilevering forward from the hub of the primary reflector. This support structure, or feed stick, is aluminum from the hub to the feed; from the feed forward, it is made of fiberglass skins over foam plastic. The feed stick is relatively stiff, but because its attachment to the antenna hub is flexible, it oscillates as a straight line about its root.

Although some ballast weight has been added at the rear wall of the equipment room, the structure above the elevation axis is not balanced. Overturning is prevented by the combined action of a pair of hydraulic equilibrators and the elevation drive motors. These motors are mounted on the left yoke arm and drive against a steel bull gear mounted on the left sidewall of the equipment room.

The equilibrators provide most of the restraint against overturning; they are passive units, consisting of hydraulic jacks with gas accumulators. The righting moment provided by the equilibrators depends on the elevation angle and the pressure in the system. As the elevation angle changes, the piston in the equilibrator moves and the volume of gas in the accumulator changes. The change of pressure depends on the change of the gas volume and on its rate of change. (Slow changes would approach isothermal conditions; fast changes, adiabatic conditions.) The difference between the moment provided by the equilibrators and that required for dynamic equilibrium is applied by the elevation drive through the bull gear. Variations in equilibrator pressure cause

deviations in elevation and azimuth pointing; the azimuth bias occurs because the antenna is driven from the left side only.

The yoke, which is built up of welded steel plates, is in the form of a Y, with two vertical arms, a crossarm, and a cylindrical base. The elevation bearings rotate on stub shafts which are supported by the yoke arms; the elevation encoder is mounted on the left, or drive side; the encoder rotor is attached to the equipment room wall and the stator is mounted on the stub shaft of the elevation bearing. The base of the yoke structure rests on the azimuth bearing. The steel tower structure, or pedestal, below the azimuth bearing consists of a short upper cylindrical portion and a lower conical part. The azimuth encoder is located within the pedestal; the stator is fixed to the foundation and the rotor is connected to the yoke by a vertical shaft. The foundation is a four-foot-thick hexagonal pad of reinforced concrete, 18 feet across.

### Function of the Antenna Structure

The main function of the elevation structure, yoke, and tower is to control the relative positions of the reflectors, feed, and encoders with respect to the ground. This support function can be defined for each structure as follows:

- The elevation structure supports the primary and secondary reflector and the feed with respect to the elevation bearings and the elevation encoder rotor.
- The yoke supports the elevation bearing stub shafts and the elevation encoder stator with respect to the azimuth bearing and the azimuth encoder rotor.
- The tower supports the azimuth bearing with respect to the foundation slab.
- The foundation slab supports the tower and the azimuth encoder stator, which is mounted on an independent pedestal.

### METHOD OF APPROACH

The azimuth and elevation coordinates ( $A^*$ ,  $E^*$ ) of a target can be expressed as

$$(A^*, E^*) = (A, E) \text{ encoder} + (A, E) \text{ monopulse} \\ + (\Delta A, \Delta E) + \text{corrections for atmospheric} \\ \text{refraction, radome diffraction, monopulse} \\ \text{errors, and timing errors.}$$

The pointing direction of the RF beam can be defined by the best-fit-paraboloid through the primary reflector and the positions relative to it of the secondary reflector and feed.

The terms ( $\Delta A$ ,  $\Delta E$ ), which represent the pointing biases with which this study is concerned, can be considered as consisting of the following components:

- Deviations of the RF beam with respect to the direction defined by the encoder rotors.
- Deviations in the position of the encoder stators from fixed reference global axes.
- Nonlinear behavior of the encoders.

To arrive at a bias model, the function and properties of each of the structures described above and the sources of bias related to it must be studied. As an example, we shall examine the tower structure and the azimuth bearing.

The tower structure controls the tilt of the azimuth bearing. This tilt can be resolved in two directions: the component of tilt ( $\alpha_1$ ) about the antenna azimuth

pointing direction, i.e. tilt in the vertical plane that includes the elevation axis, and the component of tilt ( $\alpha_2$ ) about a line parallel to the elevation axis. The bias due to this tilt can be expressed as

$$\begin{aligned}\Delta A &= \alpha_1 \tan E \\ \Delta E &= \alpha_2\end{aligned}$$

The major causes of tilt of the azimuth bearing are:

- Misalignment of the bearing.
- Unevenness of the bearing.
- Thermal gradients across the tower.
- Bending of the tower due to the overturning moment applied by the elevation structure as caused by gravity and acceleration loads.
- Tilt of the foundation slab.

Several methods are possible to evaluate the tilt:

- Real-time measurement: Use a tiltmeter to measure the tilt during actual missions.
- Combined measurement and analysis: Perform calibration tests with the antenna at a fixed elevation and with no thermal gradients, to measure tilt due to misalignment and unevenness of the bearing; use structural analysis to compute the tilt due to unit overturning moments and unit thermal gradients; obtain the overturning moment as a function of elevation angle and acceleration; take real-time measurements of the temperature distribution in the tower; combine the above to compute the tilt at any instant.
- Combined measurement, analysis, and regression: Similar to the previous method, except that regression is used and no calibration tests are performed; structural analysis is used for the effects of gravity and acceleration-induced overturning moments and for thermal gradients in the tower, and regression is used for all the other effects.

Real-time measurement appears to be the simplest method for the evaluation of tilt; however, a tiltmeter with sufficient accuracy and dynamic response to be used during tracking missions must be available.

Real-time measurements cannot be eliminated since, if the tilt is not measured directly, the thermal gradients must be measured. The effects of acceleration and thermal gradients can be evaluated by analysis as indicated above, or by a series of calibration measurements; they cannot be evaluated by regression, since in this instance it is not possible to obtain tracking data in which these variables are adequately represented.

Based on considerations similar to those outlined above for the determination of the tilt of the azimuth bearing, suitable combinations of analytical, measurement, and regression methods were selected for the evaluation of the various bias function coefficients. Each term of the bias model developed is a function of measurable independent variables, with coefficients obtained by analysis, measurement, or regression.

#### BIAS MODEL

The resulting bias model is presented below; the methods selected for the evaluation of coefficients are described and discussed.

#### Methods Selected

**Real-Time Measurements.** These are measurements to be made during tracking.

- Tilt of the azimuth bearing about the antenna azimuth direction ( $\alpha_3$ ).
- Tilt of the elevation encoder stator about the elevation axis ( $\alpha_5$ ).
- Equilibrator pressure (p).
- Traverse and elevation displacements of an x-y diode mounted near the feed with respect to a laser unit mounted on the front wall of the equipment room ( $\delta_L, \delta_E$ ).
- Temperatures in the reflector backup, feed stick, and yoke structures ( $T_i$ ).

**Calibration Measurements.** These are measurements performed under controlled conditions during periods of antenna shutdown.

- Nonlinearity of the azimuth encoder ( $f_{AZ} = f(A)$ ).
- Nonlinearity of the elevation encoder ( $f_{EL} = f(E)$ ).

**Structural Analysis.** - The structures are analyzed to obtain distortions due to gravity, acceleration, and thermal loads, the equilibrator forces, and the elevation drive torques. The elevation structure and the yoke are analyzed separately; an analysis of the tower is not necessary. The analysis of the elevation structure is used to obtain the contribution to pointing bias in traverse ( $\Delta L$ ) and elevation ( $\Delta E$ ) with respect to the elevation bearings and the elevation encoder rotor. The yoke analysis provides the displacements of the elevation bearing stub shafts with respect to the azimuth encoder rotor and the tiltmeter at the azimuth bearing; the displacements are expressed in terms of rotations ( $\theta_Y$  and  $\theta_Z$ ) of the line joining the two stub shafts. (Y is the horizontal parallel to the antenna azimuth direction and Z is vertical.)

The analyses provide values for the bias components  $\Delta L$ ,  $\Delta E$ ,  $\theta_Y$ , and  $\theta_Z$  for various unit load cases. These values are the coefficients in the functions expressing the bias components in terms of the following variables:

$A, \dot{A}, \ddot{A}$	azimuth angular position, velocity, and acceleration
$E, \dot{E}, \ddot{E}$	elevation angular position, velocity, and acceleration
p	equilibrator pressure
$\delta_L, \delta_E$	displacements of the x-y diode in traverse and elevation directions
$T_i$	temperatures at gage locations on the yoke, reflector backup, and feed stick.

**Regression.** - Regression is used to account for the sources of bias listed below.

- Zero-set bias ( $\alpha_0, \beta_0$ ).
- Nonorthogonality of the RF beam with respect to the elevation axis ( $\alpha_1$ ).
- Nonorthogonality of the elevation axis with respect to the azimuth axis ( $\alpha_2$ ).
- Elevation bearing runout.

The total number of terms to be obtained by regression is nine:  $\alpha_0, \beta_0, \alpha_1$ , and  $\alpha_2$  plus five others,  $r_1, \dots, r_5$ . The selection of these five terms is explained in the discussion of the regression terms.

**Bias Equation.** - By superimposing the different effects, the bias equation can be expressed as follows:

$$\begin{aligned}\Delta A &= \Delta L \sec E - \theta_z + \theta_y \tan E \\ &\quad + \alpha_0 + \alpha_1 \sec E + \alpha_2 \tan E \\ &\quad + (\alpha_3 - \alpha_N \sin A + \alpha_E \cos A) \tan E \\ &\quad + f_{AZ} + r_1 \sin E \tan E + r_2 \sin E + r_3 \cos E \\ \Delta E &= \Delta E_0 + \beta_0 + (\alpha_5 + \alpha_N \cos A + \alpha_E \sin A) + f_{EL} \\ &\quad + r_4 \sin E + r_5 \cos E\end{aligned}$$

where:

$\alpha_N, \alpha_E$  north and east components of angle between local gravity and true vertical (gravitational anomaly).

The other terms have been defined earlier; a definition of all terms is given in the appendix.

The functional forms of all the terms in the above equations, except for  $r_1, r_2 \dots r_5$ , are determined by geometry.

## Discussion

**Tiltmeters.** - Instrumentation to measure the position of the elevation bearings with respect to each other and to the azimuth encoder was considered, since it would have eliminated the need to analyze or make other measurements in the yoke, tower, and foundation. Such instrumentation, though possible, involves many practical difficulties and was not pursued. The use of the same approach, but with simpler instrumentation, led to the selection of the two tiltmeters. The reasons for measuring the tilt at the azimuth bearing were presented earlier. The measurement of tilt of the elevation encoder stator refers that encoder directly to ground and eliminates the distortions of the yoke and supporting structure from consideration with respect to elevation bias.

**Equilibrator Pressure and Drive Torque.** - The elevation drive is asymmetric and interacts with the equilibrators, with the result that the biases in elevation and azimuth will depend on the pressure in the equilibrators and the elevation drive torque. Because of the behavior of the gas accumulators, the equilibrator pressure varies in a complex manner; this dictates the need to measure the pressure in real time. The magnitude of the drive torque at the elevation bull gear is obtained by dynamic equilibrium about the elevation axis. The drive torque would have been difficult to measure or evaluate independently, since it depends on the currents in the drive motors, the angular rate of the antenna, and the characteristic of the gear trains.

**Feed Stick Displacements.** - The antenna distortions can be obtained by static analysis if the natural periods of the structure are short compared to the time of application of the loads. This condition prevails except for the first mode of the feed stick, which oscillates approximately as a rigid body about its root with a relatively long period. The displacements of the feed stick due to gravity, acceleration, and thermal loads are computed by quasi-static analysis, and the displacements of one point on the feed stick are measured in real time. The difference in the displacements obtained by measurement and quasi-static analysis for the one point is a measure of the evaluation error accounted for, primarily, by the amplitude of the dynamic displacements. Then, assuming that the difference between the actual and the computed displacements has the straight-line mode

described above, the displacements of the feed and secondary are obtained.

**Thermal Gradients.** - The antenna is enclosed in an air-conditioned radome; however, thermocouples attached to the structure indicate that temperature differences of the order of 2 deg C occur across the depth of the backup structure and that these temperature differences vary with time. The temperature changes are attributed to changes in cloud cover and in antenna position; the time in which the changes occur is of the order of half an hour. Therefore, the temperature distribution within the antenna structure is needed to compute the pointing bias. Thermocouples are located to measure temperature differences in the reflector backup, the feed stick, and the yoke. Where displacements are measured directly, temperature distributions are not needed. For example, temperatures in the tower need not be known, since the azimuth bearing tilt is measured. Yoke thermal gradients are needed, since they enter into the azimuth bias equation; however, they do not enter the elevation bias equation, since the tilt at the elevation encoder stator is measured directly.

**Structural Analysis.** - The elevation and yoke structures were analyzed in considerable detail, because of the level of accuracy required; the analysis is described later. Static, rather than dynamic, analyses are used because, as noted earlier, the time of application of the loads is long compared to the natural periods of the structure, except in the case of the feed stick.

As a consequence of the decision to measure tilts at the azimuth bearing, an analysis of the tower is not required. The analysis of the yoke does not affect the elevation bias terms, since the tilt at the elevation encoder stator is measured; if this tilt were not measured, it could be evaluated by combining the tilt at the azimuth bearing about a line parallel to the elevation axis and the distortions of the yoke.

**Regression.** - The number of coefficients that can be obtained by regression is limited; in practice one, but preferably more than one, satellite pass must be analyzed for each coefficient. Because of the complexity of the antenna behavior, a large number of terms is required to achieve the desired accuracy; it is, therefore, not possible to follow the more direct approach of obtaining all coefficients by regression. Thus, the bias sources to be accounted for by regression are only those which would be extremely difficult, if not impossible, to evaluate otherwise. The functional forms of the terms in  $r_1, \dots, r_5$  are the only ones which are not dictated by the geometry of the structure. The terms in  $r_1, r_2$ , and  $r_3$  are based on an assumed sinusoidal runout of the elevation bearings. In azimuth, sufficient terms of different forms are computed by regression to compensate for inaccuracies in the terms obtained by analysis; to provide similar capabilities in elevation, terms in  $r_4$  and  $r_5$  are included.

## IMPLEMENTATION

The following are the tasks required to obtain the final bias model, with discussions of selected items.

- Install and calibrate the real-time measurement instrumentation.
- Develop a technique for repeatable zeroing of the instruments.
- Calibrate the encoders to evaluate their nonlinearities.
- Perform structural analyses.
- Perform load-deflection tests to verify the structural analysis.

- Collect tracking data and perform regression analysis.
- Collect further tracking data to check the accuracy of the model.
- Use the results to review the adequacy of the model and, if necessary, make changes to improve it.

The repeatable zeroing of instruments is of crucial importance to the model; the following is a possible approach: With the antenna pointing to zenith, rotate the antenna one revolution in azimuth, and record the tilts; then, reset the tiltmeter zeroes to minimize the excursion of the measured tilt. The x-y diode should then be zeroed with the antenna at horizon pointing, and the temperatures throughout the antenna recorded and the values used as the new reference temperatures.

The load-deflection test devised for the elevation structure consists of the application of vertical loads to the ends of two radial beams and the measurement of the vertical deflections at two points on each radial beam. The load test for the yoke involves the recording of the equilibrator pressure, the tilt at each elevation stub shaft, and the tilt at the azimuth bearing, while the antenna scans from zenith to horizon; this test is repeated for successively lower equilibrator pressures.

Once the model has been tested, it can be used during the processing of data after a mission, or, if suitable software is written, it can be used in real time.

## STRUCTURAL ANALYSIS

### Elevation Structure

The model of the reflector dish and equipment box is too large to be solved directly, both because of the large number of degrees of freedom (approximately 4900) and because of the very wide bandwidth of the stiffness matrix typical of a dish structure.

The elevation structure is not symmetric, since it is driven from one side only; however, forward of the equipment box it is symmetric about a vertical plane. Therefore, it was decided to use a substructure approach that would take advantage of symmetry and reduce the bandwidth of the dish. The dish, consisting of the panels, reflector backup, and the feed stick, was treated as one substructure and the equipment box as another. This approach is particularly attractive in that the two substructures are interconnected at six points only.

The dish substructure was analyzed using the six attachment points as supports. One-half of the dish was analyzed, once with symmetric boundary conditions and once with antisymmetric boundary conditions. From these solutions, a six-joint superelement representing the dish was generated. The information obtained for this superelement consists of its stiffness matrix, the equivalent load vectors for all loading conditions, and the backsubstitution data. The analysis of the equipment room with the superelement representing the dish attached to it was then performed. Using the results of this analysis and the backsubstitution data of the superelement, the displacements throughout the elevation structure could be computed. However, only the displacements required for the pointing bias calculations were processed; these include the displacements of the primary reflector surface, the feed, the secondary reflector, and the attachment points of the elevation encoder rotor, the x-y diode, and the associated laser.

Idealization. - Direct representation of the structure was used where possible; a brief description of the model follows.

The central six-pointed hub is modeled with membrane finite elements representing the web plates and the top skin and with axial load members for the flanges and stiffeners. The six radial beams are modeled with membrane elements for the webs and axial load members for the top and bottom flanges; the three hoops of ring beams are modeled similarly, except that space frame members are used for the top and bottom flanges to provide lateral bending stiffness. The outriggers on the inner and outer ring beams which support panel studs are included in the model. Bracing tubes between the ring beams are represented by axial load members. The reflector panels are modeled by an overlay of stretching and bending elements to represent the honeycomb core sandwich construction. The studs that support the panels are represented by space frame members rigidly attached to the panels and pinned at the backup structure connecting point.

The feed stick is modeled as a linear assemblage of beams having structural properties that represent the changing shape and material of the actual structure. Nodes are located at the locations of the feed center of the secondary reflector vertex and the point of attachment of the x-y diode, because the deflections at these points are needed for the pointing bias computation. The attachment to the forward plane of the hub is simulated by a set of radial beams. The proper modelling of this attachment is important because, as noted earlier, it is the most flexible portion of the feed stick assembly.

The double walls of the equipment room structure are modeled by an overlay of bending and stretching elements, plus stringer elements for the stiffeners. The bull gear web is represented by membrane finite elements; frame members are used for the stiffeners and for the connection to the equipment room wall. The structure is supported in a statically determinate manner at the elevation bearings and at the equilibrator attachment points on the equipment room. To force equal loads in the two equilibrators, a dummy seesaw arrangement is used.

Loading Conditions. - The effects to be evaluated by analysis include gravity, acceleration, and thermal loads, and the forces due to the equilibrators and the elevation drive. The load cases selected for analysis are listed below. From these cases all loadings can be obtained by linear combinations.

- Gravity loads corresponding to zenith and to horizon pointing directions.
- Acceleration load cases to account for azimuth and elevation accelerations, and centrifugal and Coriolis accelerations. Nine load cases are sufficient to evaluate by superposition all acceleration components for all elevation angles. The nine load cases are the sum over the antenna of forces  $m_x$ ,  $m_y$ , and  $m_z$ , each applied in turn in the directions  $x$ ,  $y$ , and  $z$ , where  $m$  is the mass at a point whose coordinates are  $(x, y, z)$ .
- Unit loads at the equilibrator attachment points directed towards the elevation bearings.
- Unit torque loads applied to the bull gear at points corresponding to the pinion locations for three different elevation positions. The effects for intermediate positions were obtained by interpolation.

- Two thermal cases: Unit temperature increase on the front and aft portions of one sixth of the reflector backup. Since the reflector structure has six-way symmetry, the effects of thermal gradients across each radial beam were generated by rotation. Calculations for thermal gradients in the feed stick were performed by hand.

**Results.** - The results of analysis for each loading case are the displacements, with respect to the elevation bearings and the elevation encoder rotor, of the best-fit-paraboloid (bfp) through the primary reflector, of the secondary reflector, and of the feed. The displacements are combined to compute the pointing bias contributions to  $\Delta L$  and  $\Delta E$  for each load case. In addition, the displacements of the x-y diode with respect to the laser mount in the equipment room are computed.

It should be noted that the position of the bfp for combinations of loads can be obtained by superposition; however, superposition does not apply for the root mean square of the deviation of the surface from the bfp. Therefore, superposition can be used for pointing bias calculations but not for calculations of loss of gain due to antenna distortions.

#### Yoke Structure

**Idealization.** - The yoke structure is supported at the azimuth bearing and is modeled by an assembly of membrane finite elements. The structural model is a relatively direct representation of the actual plate structure. It includes the cylindrical base, idealized by piecewise flat plates, that merges into the horizontal crossarm, and the two yoke arms.

**Loading Conditions.** - The loading conditions analyzed were:

- Horizontal unit loads at the elevation bearing stub shafts.
- Horizontal and vertical unit loads at the equilibrators attachment points.
- Drive motor loads corresponding to unit torque in the elevation drive.
- Thermal loads, corresponding to a unit temperature rise in the faces of the yoke arms and crossarms, each face taken in turn.

The effects of the acceleration loads due to the inertia of the yoke were found by approximate calculations to be very small, and were neglected.

**Results.** - For each loading case, the displacements of the elevation stub shafts were computed with respect to the tiltmeter at the azimuth bearing and the azimuth encoder rotor. From these displacements the rotations,  $\theta_y$  and  $\theta_z$ , of the line joining the stub shafts were obtained.

#### CONCLUSION

A bias model for upgrading the pointing accuracy of ALCOR was developed. It uses a combination of analytical, measurement, and regression methods to obtain the required coefficients. The functional form of the model represents the characteristics of the antenna and should be a considerable improvement over bias equations based on regression alone.

#### Acknowledgements

This work was performed by Simpson Gumpertz & Heger Inc. for Lincoln Laboratory, Massachusetts Institute of Technology. Personnel at Lincoln Laboratory, both in Lexington and at the antenna site in Kwajalein, provided valuable assistance.

#### APPENDIX

The following symbols are used in this paper:

$A, \dot{A}, \ddot{A}$	azimuth angular position, velocity, and acceleration
$E, \dot{E}, \ddot{E}$	elevation angular position, velocity, and acceleration
$\Delta A, \Delta E$	azimuth and elevation angular biases
$\Delta L, \Delta E_0$	elevation structure contributions to bias in traverse and elevation
$T_i$	temperatures in the yoke, reflector back-up, and feed stick
$X, Y, Z$	yoke axes: X is along elevation axis, Y is horizontal along azimuth direction, and Z is vertical
$\alpha_1$	tilt of azimuth bearing in vertical plane containing elevation axis
$\alpha_2$	tilt of azimuth bearing about line parallel to elevation axis
$f_{AZ}, f_{EL}$	nonlinearities of azimuth and elevation encoders
$m$	mass at a point (x, y, z) in the elevation structure model
$p$	equilibrator pressure
$r_1, r_2 \dots r_5$	coefficients to be obtained by regression
$x, y, z$	elevation structure axes; coincide with yoke axes at zenith pointing
$\alpha_0, \beta_0$	zero-set biases in azimuth and elevation
$\alpha_1$	nonorthogonality of RF beam with respect to elevation axis
$\alpha_2$	nonorthogonality of elevation axis with respect to azimuth axis
$\alpha_3$	tilt of azimuth bearing about azimuth direction
$\alpha_5$	tilt of elevation encoder stator about elevation axis
$\alpha_N, \alpha_E$	north and east components of angle between local gravity and true vertical (gravitational anomaly)
$\delta_L, \delta_E$	displacements of x-y diode with respect to laser as measured in traverse and elevation directions
$\theta_y, \theta_z$	rotation about Y and Z of line joining the elevation stub shafts.

## MECHANICAL DESIGN AND INTEGRATION OF PHASED ARRAYS

R. F. DiFelice  
J. Drenik

RCA Government Systems Division  
Missile and Surface Radar  
Moorestown, New Jersey 08057

### ABSTRACT

A systems approach is presented to mechanically configure and integrate a complex phased array. The phased array described is a major unit of the AN/SPY-1A radar, an element of the U.S. Navy's AEGIS Weapon System MK 7.

Over a period of seven years, two phased array systems have been designed, fabricated, assembled, and tested. One unit, AN/SPY-1, is operational in USS NORTON SOUND; the second unit, AN/SPY-1A, is presently installed in the land-based Combat System Engineering Development site at Moorestown, New Jersey. A comparison of the arrays is made showing the application of the systems approach in configuring the second array for compactness, a reduction in weight of over 30%, and the utilization of materials in combination with manufacturing processes to reduce the weight of the self-supporting structure by 40% without changing the requirements.

### INTRODUCTION

The operation of the AEGIS Weapon System MK 7 begins with search and detection by the phased-array radar. A detected target is automatically placed into track by the radar and passed to the Combat Direction System for evaluation. Once a target is determined to be a threat, orders are furnished to the Weapons Control System for engagement. The phased-array radar then furnishes target-track data for missile launcher pointing.

After launch, the missile is guided by the AN/SPY-1A radar until the homing phase of the flight, at which time a guidance illuminator is slaved to target coordinates supplied by the radar, thereby furnishing the illumination on which the missile can home. Following intercept, the illuminator is available for the next threat. In the meantime, the phased-array radar continuously searches for new targets and simultaneously tracks targets already detected or engaged. The result is virtually instantaneous response to any new threat that appears.

The mechanical design of the AN/SPY-1 phased array is dependent on the functional requirements of the system (search, both active and passive, monopulse angle tracking and ECCM). These requirements impose restrictions in the design to the extent that the mechanical engineer must utilize great ingenuity to integrate the subsystem microwave assemblies, power and logic cabling, and temperature control of critical components within the permissible constraints. In addition, the stringent shipboard environment (including vibration, underwater and nuclear shock, wind velocity up to 70 knots, icing conditions to -20°F, limited weight and volume) must be considered in the design of the phased array to provide a highly reliable operating system.

Although the first array, AN/SPY-1, met or exceeded the established program performance requirements, a re-evaluation of the array configuration was undertaken in an effort to reduce the array weight and cost without sacrificing performance.

This paper will highlight those areas where changes in fabrication techniques or redefinition of component performance specifications assisted in producing a second array, AN/SPY-1A, whose performance met or exceeded that of AN/SPY-1, with lower cost and a 5000-pound weight reduction.

### PHYSICAL DESCRIPTIONS

The significant physical properties of the phased array are:

- Overall Dimensions      160 x 153 inches x 51 inches deep
- Array Weight              11,963 pounds
- Number of Elements
  - Transmit      4096
  - Receive      4352
  - Auxiliary      128

### SUMMARY DESCRIPTION OF ARRAY COMPONENTS

The principal phased-array components include:

- Array Structure
- Radiating Elements
- Array Modules
- Phase Shifters and Drivers
- Beamforming Networks

The following paragraphs in this section of the paper give a brief description of each of the array components. (See Figure 1.) In addition, Figure 2 is a rear view of the AN/SPY-1 array. Figure 3 is the rear view of the AN/SPY-1A array.

#### Array Structure

The components are housed within an aluminum structure having a one piece front plate (160 x 153 x .50 thick) containing 4480 holes precisely located on a .90 x .99 grid spacing. The structure has been designed to protect the array components against damage from all possible dynamic environments as well as nuclear blast and underwater shock. The structure has been designed to have a natural resonant frequency above 25 Hz.

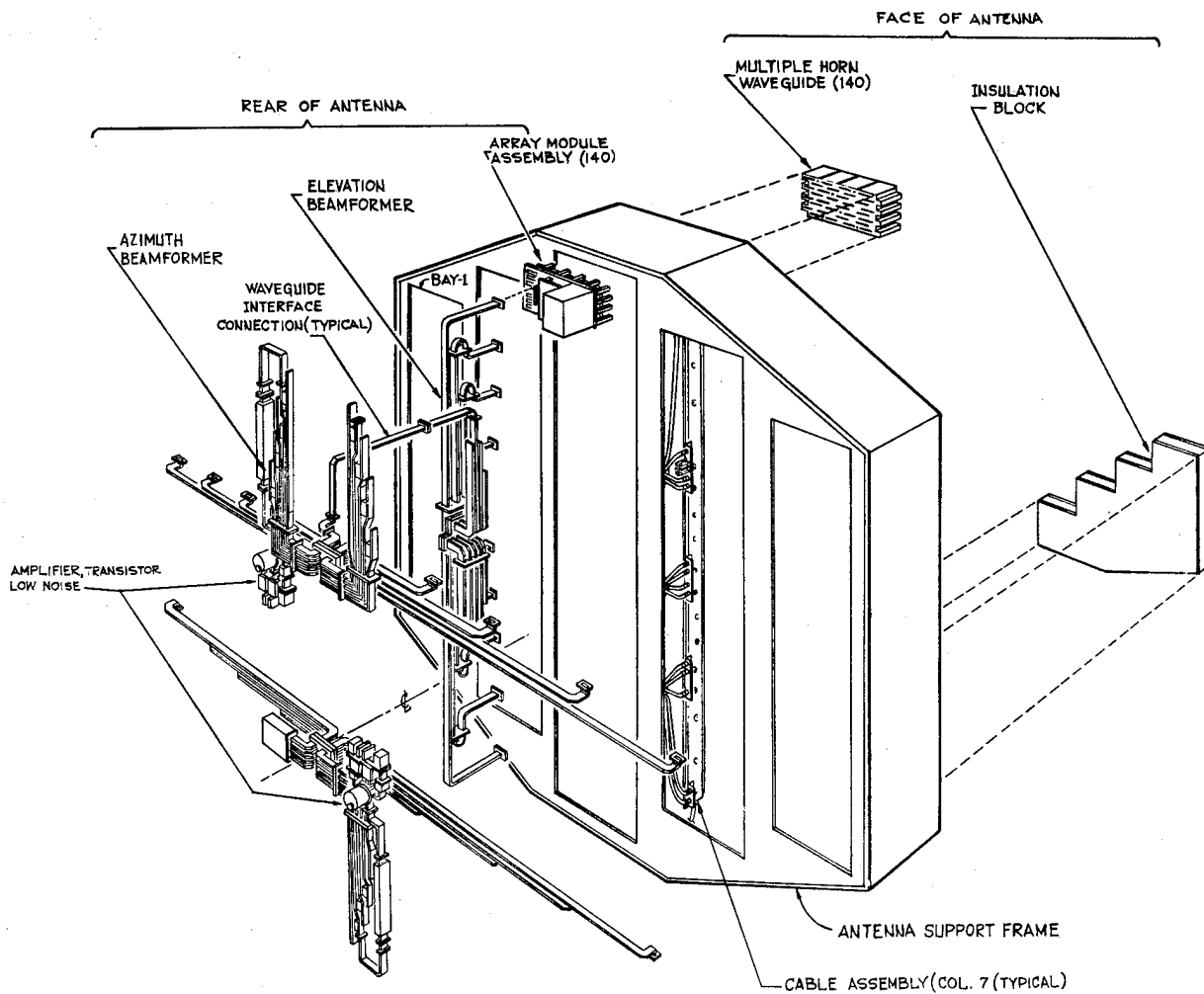


Fig. 1 Phased Array Assembly Exploded View

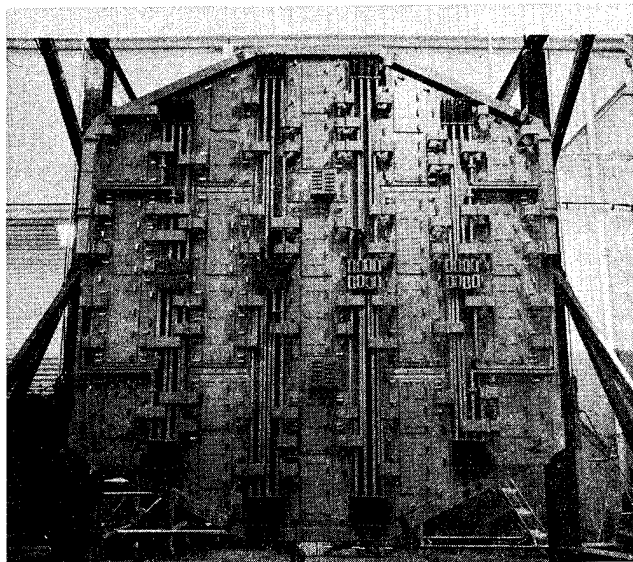


Fig. 2 Rear View, AN/SPY-1 Phased Array

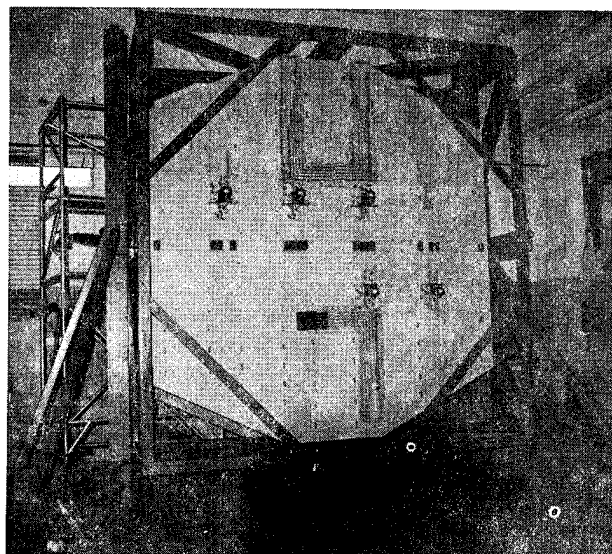


Fig. 3 Rear View, AN/SPY-1A Phased Array



## Radiating Elements

The radiating elements are rectangular horns arranged in a "Brick-Wall" pattern forming a quasi-rectangular module of 32 elements. The spacing has been established on the basis of the required coverage for each array face. This lattice makes allowance for ship motion and provides 360° coverage by the four AEGIS arrays (two forward and two aft).

## Array Module

The array module power divider/combiner is a corporate structure of rectangular coaxial transmission line having cylindrical coaxial interface connections with the 32 antenna phase shifters and a waveguide interface with the self-duplexing waveguide hybrid network. The internal coaxial network of the power divider/combiner utilizes round die-cast inner conductors and rectangular outer conductors fabricated by layers of precision stamped aluminum plates. A reactive 32:1 divider network has been used to gain the advantages of compactness and minimum cost. The coaxial interface between the phase shifters and the power divider network is designed to permit angular flexibility to accommodate initial manufacturing assembly tolerances.

## Phase Shifter/Driver

The array phase shifter consists of a dielectrically loaded rectangular toroid of garnet material mounted in the center of a thin wall rectangular waveguide. RF phase changes for radar beam steering are accomplished by variable current pulses passing through pairs of magnetizing wires embedded in the center of the toroid.

The associated drivers are plug-in printed circuit boards installed within a specially designed nest. Easy access is provided to the nest from the rear of the array for replacement of failed boards. Board replacement is accomplished as part of regularly scheduled maintenance.

## Beamforming Networks

The beamforming networks utilize S-band waveguides of reduced height as a compromise between space/weight considerations and RF loss characteristics. The transmit waveguide height has been reduced from 1.500 inches to 0.670 inch and the receive waveguide height to 0.400 inch. Array modules are combined to form both transmit and receive subarrays each with separate terminals. Waveguide hybrid tee junctions combine pairs of modules where the E arm of the junction is defined as the receive terminal.

## DETAILED DESCRIPTION OF ARRAY COMPONENTS

### Array Structure

Both mechanical and electrical requirements imposed by the radar system for the AEGIS phased array required the fabrication of a large welded aluminum structure (160 x 153 x 32) with critical tolerance control, including flatness, parallelism, element spacing relationships and plane to plane parallelism.

The basic aluminum structure consists of a base plate containing 4480 holes welded to an octagonal outside solid frame with four equally spaced inside "T" beam sections 32 inches deep.

The first system utilized a 1-1/4 inch thick front face, 1/2 inch outside sheets forming the octagonal shape, "T" beams, 1/2 inch web thickness and 1 inch flange thickness. The fabrica-

tion sequences and welding techniques were developed to minimize distortion. The different material thickness required that specific weld joints be designed, and sample tested prior to application to the final structure. Of particular interest was the welding of the 1/2 inch "T" beam webs to the 1-1/4 inch thick face plate. The face plate was machined from raw stock 3 inches thick. After machining the plate to the octagonal shape, 1/2 inch thick upright webs were hogged out of the 3 inch thick plate, resulting in a thick face plate with webs. This permitted the welding of the T section to the face plate with metal of the same thickness.

The welding sequence required that the face plate be mounted in a specially designed holding fixture. The "T" beams were then welded with continuous welds to the face plate starting with the "T" sections on the central part of the face plate and continuing to the outer edges. The welding sequence was carefully addressed to control warpage over the entire face plate. Upon completion of welding the "T" section, the other skirts were welded to complete the enclosure of the structure. Subsequent to welding, the structure was inspected and optically checked for flatness and parallelism prior to drilling the 4480 holes in the face plate.

The drilling of these holes was accomplished by utilizing a 32 hole drill fixture. The tolerance between holes in the cluster was  $\pm .001$  measured to an indexed hole. These critical tolerances and cluster drilling were required to properly interface with an array module assembly containing 32 phase shifters. The array modules are installed from the rear of the array structure so that the phase shifters protrude through the holes in the face plate. A 32-horn module with a radiating horn for each phase shifter is assembled on the array structure face. The 32 hole cluster was drilled in a prescribed pattern across the face of the array to minimize distortion.

Assembly tolerance required that the front surface of the face plate and the mounting surface for the array modules be parallel within .040 and the mounting surface plane for the 140 array modules be in a plane, flat within .020.

The second structure maintained the same configuration and number of holes. However, based on the experience of the first unit, the approach was revised to reduce weight and improve ease of fabrication. The major changes were the thickness of the plates. The face plate was machined from 3/4 raw stock to a 1/2 inch thick plate, the "T" beam web thickness was reduced to 3/8 inch and the T-Beam flange thickness reduced to 1/2 inch. This permitted the welding technique to be simplified by using standard fillet welds. Distortion was minimized by using intermittent welds in all areas except those requiring complete sealing from the environment. Another major change was machining the front face of the structure prior to drilling the 4480 holes. The reduction in material thickness and welds reduced the array structure weight from 5000 lb. to 3000 lb. The weight reduction was achieved within the tolerances needed to permit installation of the microwave subassemblies and with no compromise of the structural integrity (see Figure 4).

### Radiating Element

#### • Design Constraints:

- (a) Fixed Spacing
- (b) RF VSWR Characteristics
- (c) Nuclear Blast
- (d) Ice Inhibition
- (e) Phase Shifter RF Interface
- (f) Environmental Seal

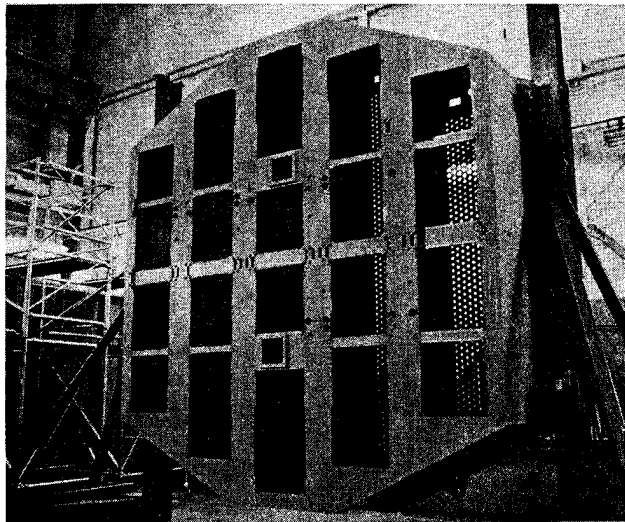
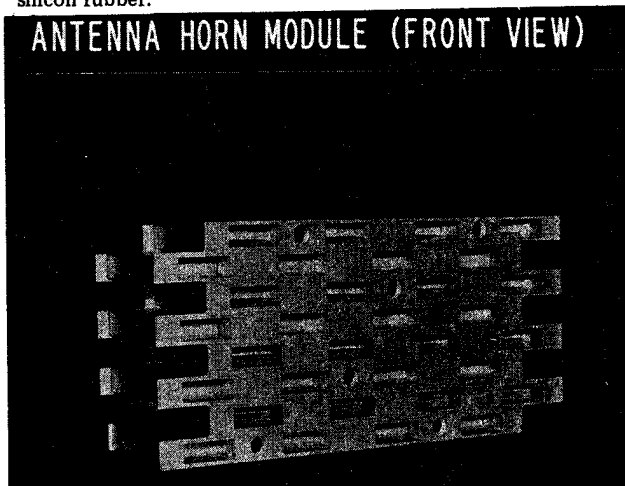


Fig. 4 Array Structure

The basic approach for both systems was a dip-brazed modular assembly containing 32 elements, with each element containing a soldered beryllium oxide window covered with silicon rubber.



What permitted second system costs to drop by 30% without affecting performance?

The first array, AN/SPY-1, required oven brazing for window soldering using a spring loaded fixture to seal all 32 windows and touch-up of solder voids afterwards. The AN/SPY-1A array incorporated a hot plate approach, heating the assembly sufficiently to allow hand soldering, thus eliminating the touchup operation and spring loaded fixture for window sealing.

Both systems apply a layer of  $.012 \pm .003$  thickness of silicon rubber to environmentally seal the front face. AN/SPY-1 required a fast cure cycle by using a humidity chamber for a 24 hour period; AN/SPY-1A permitted the option of allowing the unit to be stored in a humid area for 7 days. Phase shifter insertion on AN/SPY-1 was accomplished by a funnel type casting added to each horn element. This required a larger hole in the structure to accept each casting. In addition, since a flat surface was required, the fabricator had to machine around the 32 funnels. In AN/SPY-1A, the size of the hole was reduced and a lead-in chamber was added in the face plate hole. This permitted utilization of a simple face cut on the horn assembly to achieve the required flatness. The size of the hole in the face plate in AN/SPY-1A was selected after electrical tests to determine optimum hole size for minimum RF leakage (see Figure 5).

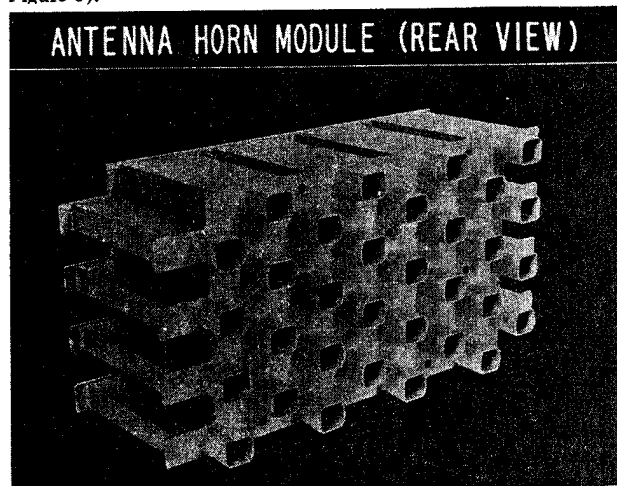
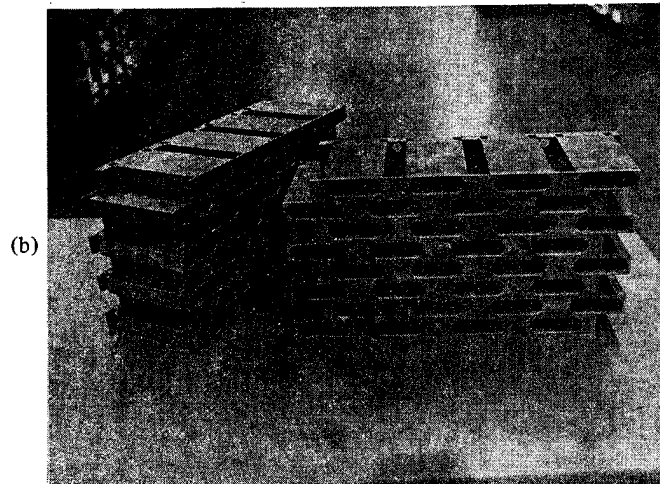
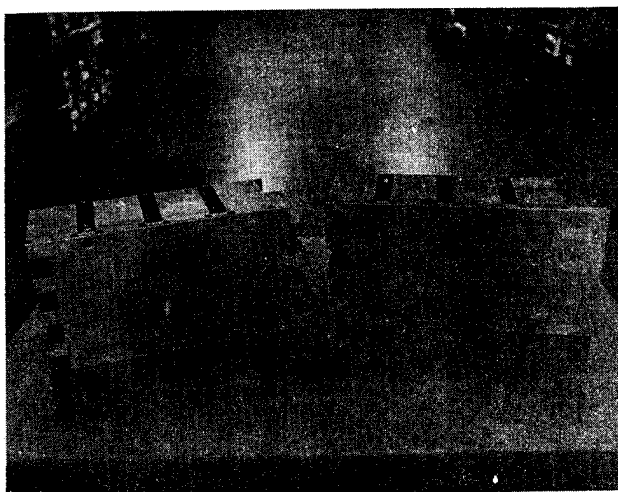


Fig. 5 Radiating Elements (Horn Module)  
a) AN/SPY-1 Design; b) AN/SPY-1A Design



## Array Module

An array module assembly consists of a 32:1 power divider, 32 phase shifters, an electronic nest containing eight driver boards, a line receiver board, and a voltage regulator board with interconnecting wiring and support brackets. The array is composed of 140 array modules. Two of the most critical components in this assembly are the ferrite phase shifters and the 32:1 power divider (see Figure 6).

**Ferrite Phase Shifter** — The phase shifter provides an end-launched coax connector at one end to mate to a coaxial power divider and a blind connection, using spring contacts, at the other end to mate to a radiating horn where no mechanical fasteners are permitted.

For AN/SPY-1, the phase shifter consisted of three (2 inch) hollow rectangular segments of garnet material. These were bonded into an essentially monolithic element with the widths held to within .001 inch through its 6 inch length. With a latching wire threaded through its center and input and output transformers at its ends, the garnet was assembled into its close-fitting waveguide case. For AN/SPY-1A, the garnet construction was changed to a one piece unit 4 inches long. This reduction in length from 6 inches to 4 inches reduced the material cost of the garnet core by 30% and eliminated the labor required to bond three (2 inch) pieces together.

This change in manufacturing technique reduced phase shifter costs and reduced RF losses by 0.2 dB; both of these are a plus for the array. The negative effect was an increase in phase

error when the phase shifter would be required to operate at maximum high temperature (maximum hot day and maximum duty). The achieved results, however, are well within the required electrical tolerances.

The requirement of blindly installing the array module and making 32 blind connections simultaneously was accomplished by mounting the phase shifter to the power divider with a spring clamp that allows up to  $\pm 0.5^\circ$  misalignment from perpendicularity and springs at the horn end of the phase shifter. This permitted self-alignment and self-connection between the array module assembly and the horn assembly (see Figure 7).

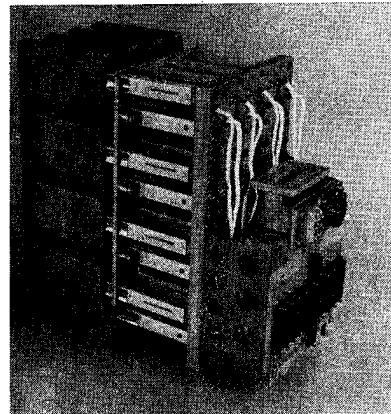


Fig. 7 Array Module and Horn Module Assemblies

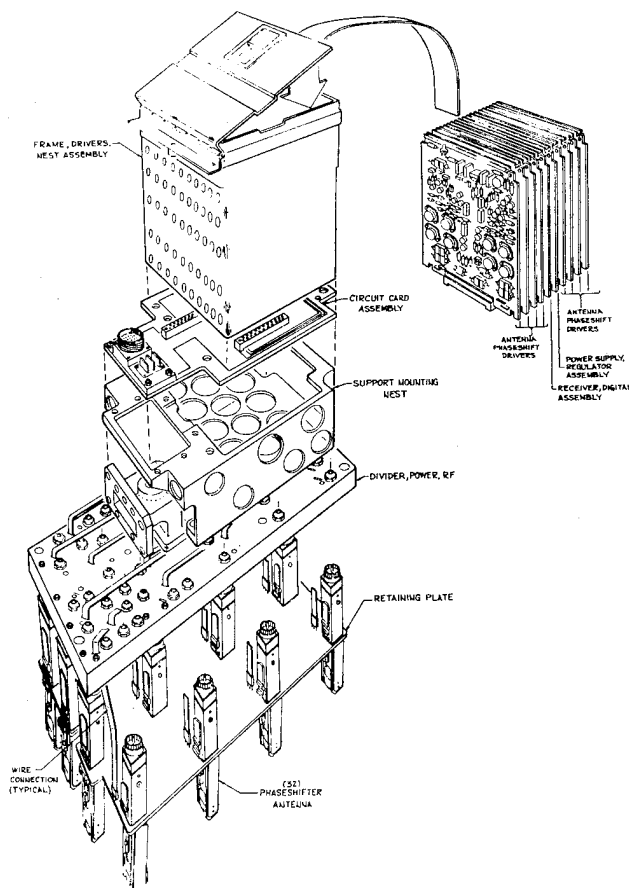


Fig. 6 Array Module Assembly Exploded View

**32:1 Power Divider** — The 32:1 Power Divider is a unique device in that the outer conductor is a square cross section fabricated from punched plates (Fine Press Blanking) with a circular cross section center conductor. The unpressurized power divider is required to handle substantial RF input power, split equally to each of the 32 outputs.

For AN/SPY-1, the center conductor was fabricated from 90 precision pieces fixtured and silver soldered to obtain a total assembly. This fabrication was deemed excessively expensive, and alternative fabrication approaches were considered.

For AN/SPY-1A, the center conductor tolerances on diameters were changed from .001 to .005 allowing the unit to be fabricated from 11 diecast parts with only minimal machining required to fit pieces together. The reduction in cost was 80%. The effect on electrical performance required a change in maximum VSWR specifications from 1.35 to 1.45 over the total operating frequency band. This was analyzed in detail and found to be electrically acceptable.

## Receive Beamformer

AN/SPY-1 required insertion of a fine-steering phase shifter in each of 68 waveguide runs. Each of these runs had to be phased matched to each other within  $4^\circ$  over the total frequency band. The required trimming necessitated a minimum of three 3/8 inch thick spacers per run.

AN/SPY-1A eliminated the fine-steering phase shifter and the spacers. Phase trimming was accomplished by means of thick flanges. By eliminating phase trimming capabilities in the eight longest runs, the net length of waveguide in all paths within the column beamformers was substantially reduced. In addition, the implementation of bench trimming instead of in situ adjustment reduced test and assembly effort by 50% and

allowed AN/SPY-1A to be more closely phase matched than its predecessor (see Figure 8).

#### RF Dummy Load

By specification, the Array must not be damaged by operation into a short circuit. AN/SPY-1 incorporated 32 water-cooled dummy loads located externally on the rear of the array. These loads were rated to carry full system RF power. AN/SPY-1A, on the other hand, incorporated dry load internally within the array, with the dry loads instrumented (with a thermal switch) to disengage the transmitter if the reflected power into the loads indicated a short. The potential for an RF shorted array face is very remote; but, should the face be shorted for some reason, then continued RF radiation would be impractical.

#### CONCLUSION

The systems approach to mechanical integration of a complex phased array described in this paper has been validated in the production of an operating phased array. The close coordination between the AEGIS Project Management, Engineering, and Manufacturing during the design and the production permitted efficient and economical assembly of a most complex equipment.

The assigned subassembly and structure tolerances, error budgets and testing techniques at the subassembly levels prior to completing the array assembly have been validated by integrating the array into a radar system, demonstrating the multi-function capability as a system component.

Manufacturing costs and weight savings of approximately 2-1/2 tons per array have been achieved by a careful study of each step of the design, fabrication and test processes that resulted in reduction shown in this paper.

The design of an efficient, cost effective phased array requires a continuing design effort as advances in microwave make new and better components available. A continuing review of systems requirements permitting relief in certain technical areas can result in improved delivery and lower costs while maintaining performance and reliability.

#### ACKNOWLEDGMENTS

The authors wish to thank their co-workers in RCA's Engineering, Drafting, and Manufacturing, and subcontractors Rockwell International, Industrial Microwave Company, Hazeltine Corporation, and Microwave Associates for their assistance in the design and fabrication of the AN/SPY-1 and AN/SPY-1A arrays.

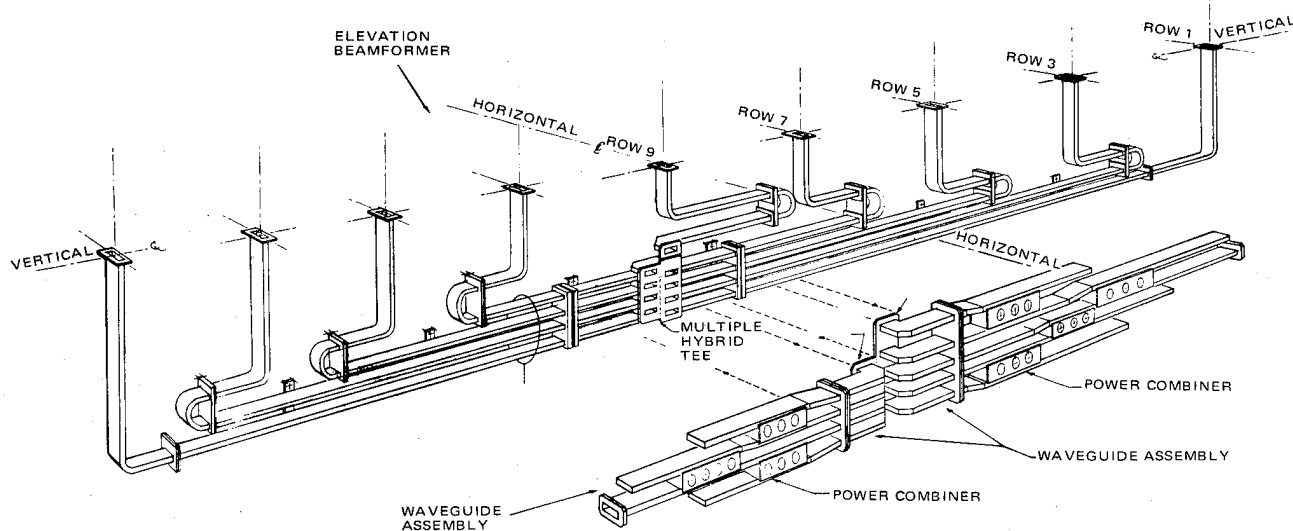


Fig. 8 Beam Forming Network

## THE CONTROL OF TOLERANCES IN AN ARRAY ANTENNA\*

W.R. Fanning, G.N. Tsandoulas and M.A. Nader

M.I.T. Lincoln Laboratory  
Lexington, Massachusetts 02173

### ABSTRACT

An L-band, airborne phased array antenna has been designed, built, tested and flown through a series of airborne experiments. The array works in the Displaced Phase Center Antenna (DPCA) mode in which two beams, each originating from different but overlapping parts of the aperture, are produced and radiated sequentially. The array provides high subclutter visibility of moving targets.

The design was driven by tight mechanical tolerances and a high degree of component similarity as required to achieve excellent identity between the phase and amplitude patterns of the two beams. Considerable design attention was needed in the areas of airframe analysis and control of its thermal distortion during flight, design of the antenna structure and antenna-aircraft interface and tolerance control during fabrication of the array modules. In addition, the development of repeatable measurement techniques that limited the phase and amplitude measurement errors to about  $0.1^\circ$  and 0.01 db, respectively, was accomplished.

### INTRODUCTION

In airborne radar, the effect of platform motion can be either beneficial or deleterious depending on radar function. Synthetic aperture radars make use of the translational property of the antenna in order to produce ground maps of areas of interest. With Airborne Moving Target Indicator (AMTI) radars, the problem is to detect either airborne or surface targets against a strong background of sea or land clutter which appears to move with respect to the airborne antenna, masking the real targets. For the narrower beamwidths obtained at the higher radar frequencies with a given aperture size and for relatively fast moving targets, the doppler shift of the target may be sufficient to place the latter outside the clutter spectrum spread so that

platform motion may not have a significant impact on target detection. However, as the frequency is lowered and/or the target velocity decreases, some form of platform motion compensation usually becomes necessary.

The Displaced Phase Center Antenna (DPCA) concept is a technique whereby the phase center of an antenna is moved along a reference line or plane of the antenna. If the amount of phase center displacement is exactly equal and opposite to the distance  $Vt$  ( $V$  is platform speed and  $t$  is elapsed time) which the platform has moved through space in time  $t$ , then the two antenna beams associated with each phase center are radiated from the same point in space. With the platform motion thus frozen, the clutter returns in the two beams will be identical so that upon subtraction on a pulse to pulse basis the clutter is cancelled but not the target which has moved between pulses.

Figure 1 illustrates the application of the Displaced Phase Center (DPC) concept to a six element linear array. In State 1 the excitation is applied to the four radiators on the left while the two elements on the right are grounded. In State 2 the two elements on the left are grounded and the four on the right excited. The net effect is to move the array phase center parallel to the array axis a distance equal to twice the inter-element separation. The entire feed distribution

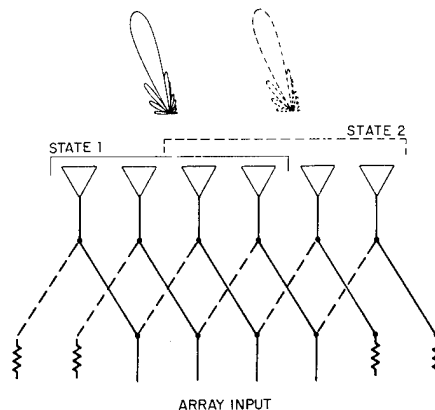


Figure 1. Displaced Phase Center Antenna (DPCA) Concept

\*This work was sponsored by the Department of the Air Force.

The views and conclusions contained in this document are those of the contractor and should not be interpreted as necessarily representing the official policies, either expressed or implied, of the United States Government.

is translated in this way with no truncation at either end. In actual operation, the DPC operation of Figure 1 is accomplished by connecting a single-pole, two-throw switch between the array input and the output radiators. The actual system achieves its final AMTI capability by utilizing additional doppler filtering techniques.

The most challenging technical design problem in the program is the antenna whose two phase center patterns must match in amplitude and phase to a high degree in order to achieve the required clutter cancellation. Significant advances in antenna technology have been achieved in designing, building and measuring the array system which is described in the following sections.

#### ANTENNA DESCRIPTION

The antenna is a phase array operating at L-band; a schematic diagram is shown in Figure 2. From the transmitter, the signal is first passed through a power divider, realized in slab-line and air-stripline, which provides low side-lobe weighting in the horizontal (azimuth) plane. The emerging 32 signals are then phase shifted by 6-bit diode stripline phase shifters for azimuth scan. The displaced phase center switching network that follows excites one or the other of the two phase centers through 32 semi-rigid coaxial cable feeds connected to a set of vertical radiating modules, each of which incorporates a 6:1 air slab-line power divider for realizing -27 dB sidelobes in the vertical plane.

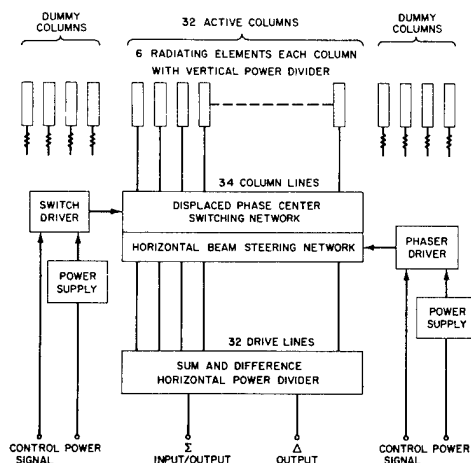


Figure 2. Schematic Diagram of Antenna Architecture

Eight terminated (dummy) radiating modules, four on either side of the antenna, are incorporated in order to stabilize the edge effect so that upon displacing the phase center, the effect of the difference in proximity of each antenna edge is reduced to a level of less than -40 dB from the last excited column as evidenced by mutual coupling measurements. Added edge "smoothness" is obtained through the rather heavy amplitude taper which de-emphasizes the contribution of the outer columns to the composite vector antenna pattern.

The radiating element is horizontally polarized rectangular waveguide excited directly from the stripline power divider through a probe transition. The waveguide module is air-filled and hermetically sealed by mechanically attaching and epoxy-bonding over its radiating face a thin (0.020 inch), low loss dielectric radome (Figure 3).

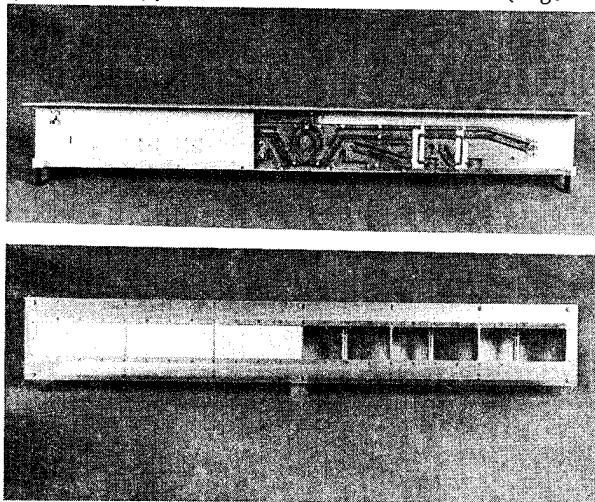


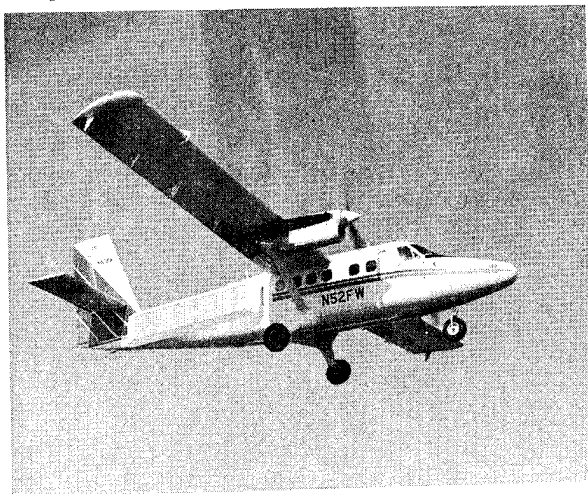
Figure 3. Side View (top) and Front View (bottom) of Radiating Module

The basic mechanical and electrical antenna characteristics are summarized in Table I:

TABLE I  
DPCA CHARACTERISTICS

Frequency	L-band
Bandwidth	~5%
Polarization	Horizontal
Gain	27 dB
Beamwidths	4.2° Az, 19° El
Sidelobe Levels	-32 dB Az, -27 dB El
Phase Center Displacement (at center frequency)	One Wavelength
Antenna Size	15 ft x 2.5 ft x 5.5 in.
Antenna Weight	370 lbs
Radiator	Rectangular Waveguide
Radome	0.020 in. Thick
Phase Shifter	6-Bit Diode Strip- line with fault detection logic
Phase Tolerance (spec.)	0.7 R.M.S.
Amplitude Tolerance (spec.)	0.11 dB R.M.S.
Surface Tolerance (spec.)	0.015 in. R.M.S. 0.050 in. peak first mode bending

There are two phases in the antenna development. In Phase I, which has been completed, there is no scan capability (fixed broadside beam) and no monopulse on receive. Both of these features are being incorporated in the current Phase II antenna. Figure 4 shows the antenna mounted on the side of the experimental Twin Otter aircraft. The antenna face is tilted down  $3^{\circ}$  to optimize the beam pattern in the scan area on the ground.



*Figure 4. DPCA After Final Installation on DeHavilland Two Otter Experimental Aircraft*

The antenna is mounted on the outside of the aircraft fuselage which acts as a basic structural member and provides almost all of the longitudinal stiffness of the array along its 15 foot length. The antenna assembly is mounted on fourteen simple brackets (two rows of seven each) riveted to the circumferential frames of the fuselage at approximately 30 inches on center. This protruding framework is smoothed into the fuselage with a foam and fiberglass fairing. Sections of this fairing around the perimeter of the antenna are removable for access to the attachment points. These removable panels use Eccosorb foam (one wavelength wide) and act as a termination of the array ground plane. The forward and aft ends of the fairing also incorporate inlet and outlet air scoops for thermal control of the antenna and fuselage. Large volumes of ambient air flow between the antenna and fuselage to maintain near iso-thermal conditions and minimize thermal deformation of the antenna and fuselage.

#### ANTENNA REALIZATION

Early in the development program it was realized that if the electrical characteristics and tolerances of Table I were to be met, and in view of the severe environment of the airborne application, the design of the overall antenna and its crucial three forward components (switches, coax cable feed, radiating modules) ought to possess the following characteristics:

1. Simplicity and ruggedness
2. Adjustability (phase)
3. Low Weight
4. Thin Profile

The constraints imposed by these characteristics led to numerous decisions throughout the program. One of the earliest and most obvious was the choice of a DeHavilland of Canada DHC-6 Twin Otter aircraft to fly the proof of concept radar flights. This aircraft has a relatively stiff fuselage of simple construction and is unpressurized. In addition, from a radar reflection point of view, the aircraft has a high wing and tail with small engine nacelles well forward on the wing. This results in minimum reflections from the aircraft itself which could be critical since they would be different in the two DPCA beams. The stiff fuselage allows the antenna itself to be lightweight and relatively thin (3-1/2 inches). The lack of pressurization minimizes fuselage deformations as the pressure altitude of the aircraft changes.

With this concept, the aircraft fuselage becomes the primary structural stiffening element in the antenna system. Mounting brackets are attached directly to the aircraft ribs and skin and interface with a relatively flexible antenna structure. Although the array is 2.5 feet high by 15 feet long, structural components in the antenna are required to span only 2.5 feet in any direction. This results in small structural components, minimal deformation, and very light weight.

In addition, simplicity and low weight were achieved by minimizing the mechanical complexity of the radiating face, integrating the radiating module and its associated vertical power divider into one compact unit and avoiding the use of dielectric materials in order to insure component repeatability.

Ruggedness and thin profile were provided by the integrated design of the waveguide radiating module as a dip-brazed unit (shown in Figure 3). By making the antenna ground plane part of the radiating element package, the shape and mass of the brazed module unit provides vertical support and stiffness to the entire antenna, thereby keeping frame and structural support weight to a minimum.

The waveguide radiating modules, as shown in Figure 3, were developed by a joint effort between Lincoln Laboratory and its subcontractors. The basic unit is 30 inches long, 3.5 inches high, 4.3 inches wide, and weighs 4.5 pounds. It includes six (6) waveguide radiators and exciters, a six way power divider, a ground plane for the radiators, a radome membrane over the waveguide cavities and provisions for structural mounting in the antenna frame such that it provides a significant part of the strength and stiffness of the overall antenna assembly.

The modules were developed as self-jigging, dip-brazed units which are lightweight, low-cost and meet electrical tolerances for the waveguide cavities and power divider section without machining. Some machining of external interface surfaces, such as the ground plane surface and structural mounting pads, was required but this was relatively minor. Other concepts involving



mechanical joining or considerably more machining were evaluated but invariably these added to the overall complexity and cost.

The basic antenna structural frame is aluminum and is composed of a perimeter angle frame, the radiating vertical modules and small T-bars which interconnect the ground planes on the modules. The Horizontal Power Divider (HPD) and phase shifter/switch units are supported by additional T-bars mounted on the back plane of the antenna. Figure 5 shows a view of the rear center section of the Phase II antenna during final assembly. At this time, the switch/phase shifter units were in place and the coax cable to the vertical modules was being trimmed for phase matching. The horizontal power divider will later be mounted to the left of switch units. The HPD to switch coax attach along the lower edges of the switch units. This picture also indicates the compactness of the overall antenna and the complexity and careful design required for the coax cabling.

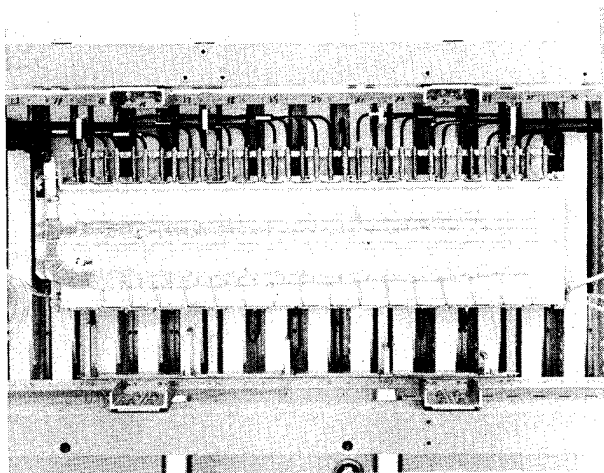


Figure 5. Partial Antenna (Rear Center Section - Phase II)

Dimensional tolerances were chosen such that the modules could be easily assembled into the antenna frame, requiring only simple locating fixtures. Structural mounting interface holes were true position toleranced to match the movement allowed within the floating nut plates and inserts used. Flatness of individual module ground planes was held to 0.015 inches (peak-to-peak) and the module height tolerance was held to 0.010 inches in order to meet the surface tolerance in Table I.

The specified phase tolerance across the array requires phase trimming in several components of the antenna. The phase variation across the six waveguide elements of each radiating module was adjusted by inserting a variable length, screw-type plunger near the exciter probe. Small phase differences were removed with this method without adverse effects on impedance match or on amplitude distribution balance. In addition, all path lengths through the Phase Shifter/Switch and Horizontal Power

Divider were carefully matched internally by tuning. Total path length from power divider input to module output was phase-equalized by the inclusion of variable line length phase trimmers in the 34 semi-rigid coax cables connected to the switch outputs and the 32 cables between the power divider and switch.

The errors associated with path length differences from the input to the horizontal power divider to the switch input (including the phase shifter) are common to both DPC beam positions and as such, they do not contribute to beam decorrelation. However, they do affect antenna pattern quality, sidelobe structure and monopulse performance and so were effectively removed by the second set of trimmers. Thus, it was possible to phase-equalize the entire antenna essentially to the limits of the repeatability of the measuring equipment.

#### ANTENNA SURFACE TOLERANCE

In order to meet the overall R.F. performance goals for the systems, a surface tolerance of 0.015 inches RMS was specified as the design goal, with the further restriction that the first longitudinal bending mode should not exceed 0.05 inches peak (Table I). These values were chosen conservatively as deemed prudent for a proof of concept demonstration. The Phase I experiments and additional theoretical work on signal processing have shown that for a real system in production, these tolerances could be relaxed considerably. However, by paying close attention to details of piece parts, assembly and measurement methods, the specified mechanical tolerances were actually bettered by a factor of approximately two, as will be shown later.

A surface error budget (Table II) was set up early in the program during the basic configuration studies. The R.M.S. shown (0.013 inches) is smaller than allowed by Table I because all of the errors will not truly random and some errors will add algebraically, bringing the total error close to the specified value.

Table II  
Surface Tolerance Budget

		3 $\sigma$ error (inches)
Fuselage Deformation	Bending	.010
	Torsion	.010
	Thermal	.015
Fuselage Frame Tolerance		.010
Antenna Frame Waviness		.015
Module Flatness Tolerance		.015
Height Tolerance		.015
Aeroelastic Deformation	Frame	.010
	Module	.015
Antenna Thermal Deformation		.010
	R.S.S. (3 $\sigma$ )	.039 in.
	R.M.S. (1 $\sigma$ )	.013 in.



During the design phase of the program, each of these areas was evaluated by analysis and/or by tests to verify compliance to these values. For example, the aeroelastic deformations of the fuselage were calculated using data supplied by DeHavilland. Also, a static test using simulated flight loads on a production fuselage was conducted at DeHavilland's plant and an in-flight deflection measurement program was carried out on the airplane under realistic flight conditions. This work indicated that fuselage bending and torsion would not exceed 0.007 inches and 0.005 inches, respectively. In general, each of the budgeted tolerance values in Table II was found to be conservative by a significant amount and the expected surface tolerance during worst in-flight conditions would not exceed 0.010 inches R.M.S.

#### ANTENNA ALIGNMENT AND ASSEMBLY

Assembly of the antenna is carried out on a strackback with mounting brackets which pick up the antenna at the same points as the brackets on the aircraft. This assembly frame is optically aligned in a vertical plane. As a result, the antenna will be essentially stress-free when in position on the aircraft.

The antenna assembly is then carried out sequentially on this frame. Components have been designed to be self-locating with little or no precision measurement required. Only overall squareness of the frame and spacing of the waveguide modules require control during assembly. The squareness was held by measuring and adjusting diagonals of the frame assembly. Module spacing is controlled with simple dowel pin fixtures which leapfrog from unit to unit and index in the ground plane screw holes and the frame edge.

Following assembly, the flatness of the surface was measured optically at approximately two hundred points. The R.M.S. accuracy was 0.004 inches with peak-to-peak errors of 0.020 inches. Three antennas (Flight Dummy Antenna, Phase I Antenna, and Phase II Antenna) have been assembled and measured with very similar results.

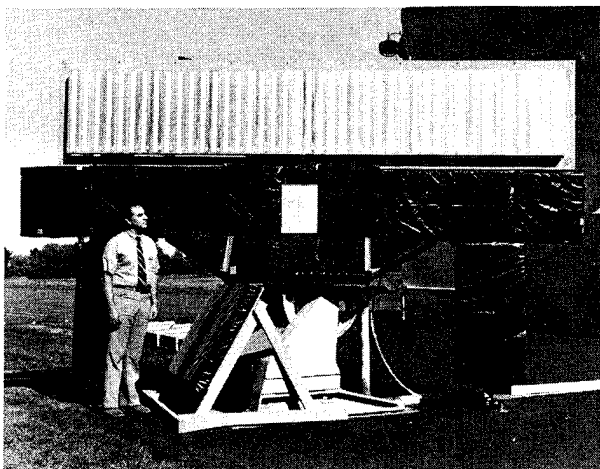


Figure 6. The Full Antenna (front view) Shown Mounted on a Shuttling Fixture for Ground Range Evaluation

After calibration and pattern measurement on the antenna test range, the antenna was mounted in the fairing on the aircraft. Over a period of several months, the flatness of the antenna surface has been measured several times. Since the antenna is tilted  $3^\circ$  down from the vertical and is not parallel to the aircraft centerline, the aircraft was jacked differentially to bring the surface into a vertical plane where it could be most easily measured. This series of measurements on the aircraft have shown consistent results with a surface accuracy of 0.005 inches R.M.S. and peak-to-peak errors of 0.025 inches. Combining this static flatness with the in-flight errors from Table II would lead to an overall surface accuracy of 0.010 inches R.M.S. However, using the final design values for in-flight errors yields surface accuracy of 0.007 inches R.M.S. with peak-to-peak errors of 0.035 inches.

#### PERFORMANCE

The final total error levels for the entire array antenna were measured as  $0.4^\circ$  in phase, 0.10 db in amplitude and 0.005 inches R.M.S. (static) surface tolerance. The amplitude error requirement was met without having to resort to amplitude trimming which would have been rather difficult to carry out effectively. The phase tolerance is the total R.S.S. tolerance of the horizontal and vertical distributions, element positional error and array ground plane flatness. The static flatness of 0.005 inches R.M.S., confirmed by the periodic optical measurements, was achieved over the 15-foot antenna length. Under flight conditions, the flatness is expected to degrade to approximately 0.007 inches R.M.S., well within maximum permissible levels, due to aeroelastic, dynamic and thermal loads.

In Figure 6, the antenna is shown mounted on a translational shuttling fixture which moves it an amount equal to  $(8.60 \pm 0.005)$  inches and opposite the phase center separation that is created by the electronic action of the switch.

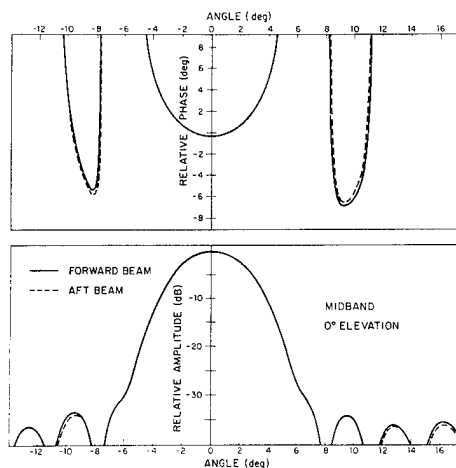


Figure 7. Phase (top) and Amplitude (bottom) Azimuth Patterns of Array

For ground-based antenna range measurements, this allows the two beams to be radiated from the two phase centers as they occupy the same point in space. Therefore, any measured pattern difference may be attributed to the antenna beam decorrelation effects and tolerances.

The excellent degree of identity of the two displaced phase center antenna beams is shown for one case in Figure 7. Patterns for other frequencies and other elevation cuts were of comparable quality.

#### CONCLUSION

With the conclusion of the first phase of the experimental program, the DPCA system has supported the radar measurement effort continuously and reliably and with adequate margin so as to maintain good overall radar performance. The goals of the proof of concept phase have been more than adequately met. The techniques employed in the design, realization and measurement of this antenna have wide applicability and may be used in all cases where tight control of phase and amplitude errors is necessary such as low sidelobe applications and precision multi-beam arrays.

#### ACKNOWLEDGMENT

The contribution of the members of the Airborne Radar and Radar Techniques Groups whose dedication and capability were directly responsible for the success of the entire program is acknowledged. The involvement of the Mechanical Engineering Division was a significant factor in the successful integration of the radar system. The assistance of the antenna ground range personnel is also cited.

#### REFERENCE

"Tolerance Control in an Array Antenna", by G.N. Tsandoulas, M.I.T. Lincoln Laboratory, Microwave Journal, October 1977.

## AN IMPROVED MAINTAINABILITY CONCEPT FOR ADVANCED RADAR SYSTEMS

HARRY W. GARNER

Westinghouse Defense and Electronic Systems Center  
Baltimore, Maryland 21203

### ABSTRACT

An improved maintainability concept is presented for a very dense, complex digital signal/data processor in an airborne radar. The Line Replaceable Module (LRM) design concept, presented herein, results in a lower life cycle cost than is obtainable with conventional Line Replaceable Units (LRU's). This is achieved through fault isolation to the LRM by Built-In-Test (BIT) in the aircraft and replacement of the defective LRM at this level. Tradeoffs of weight, volume, and reliability are discussed to demonstrate the factors which led to the final design. A number of novel features which complement the overall design are discussed.

### INTRODUCTION

The Electronically Agile Radar (EAR, currently under development at Westinghouse for the United States Air Force, provides for air-to-air rendezvous, terrain follow/terrain avoidance, velocity update, and position fixes. The system maintainability concept dictated that all digital electronics, including the Radar Signal Processor (RSP), Radar Data Processor (RDP), and Beam Steering Controller (BSC) be integrated into one unit called the Digital Assembly, shown in Figure 1.

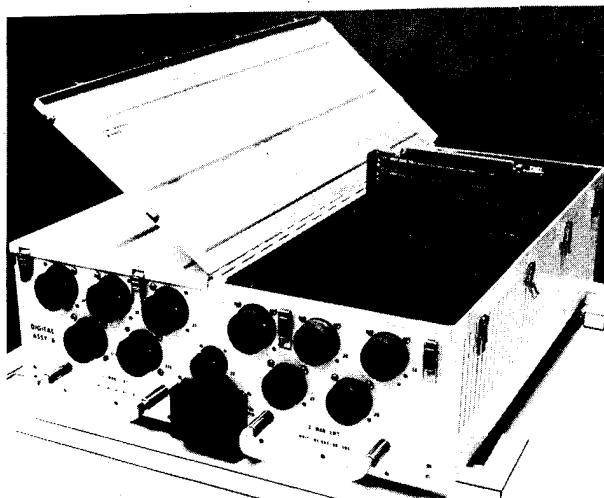


Figure 1. Digital Assembly with Access Cover Open and LRM Partially Inserted

An improvement in system maintainability has been achieved by designing for fault isolation, via built-in-test (BIT) down to the LRM level, rather than to the higher LRU level common in earlier generation radar systems.

### SYSTEM CONSIDERATIONS

Among the system considerations which led to the final design concept, a new maintenance approach emerged as the forcing requirement. The concept of replacing LRM's at the flight line rather than the larger more complex LRU is a new maintenance philosophy requiring that the LRM be a fully ruggedized, easily handled module which can be fault isolated and subsequently replaced at the flight line. Thus, each LRM had to be fully accessible without the use of tools or loose panels and hardware. Access to the LRM's had to be accomplished without removing adjacent LRU's or LRM's. This made it possible for only the individual defective LRM to be removed from the A/C and returned to the depot for repair.

Finally, in order to achieve the reliability goal it was required that the average integrated circuit (IC) junction temperature be maintained at 65°C. This is significantly lower than normally required due to a very high parts count of approximately 10,000 IC's and their associated discretes (approximately 1000 components).

### AIRCRAFT INTEGRATION AND ENCLOSURE DESIGN

The LRM's are grouped into one large Digital Assembly which, along with its associated power supplies, are mounted on slide rails within the aircraft equipment bay. This approach provides maximum utilization of the bay volume by using its full depth, thus minimizing bay surface area. In order to minimize weight and volume, the Digital Assembly enclosure provides cooling air distribution to each LRM in addition to providing integral power and ground distribution, signal distribution, and LRM polarization through a single, large backplane.

The enclosure (6.4 x 19.0 x 21.5) has a central air duct which divides the LRM positions into two rows of 34 each. The LRM's plug into a wire wrap matrix panel which is a 6 layer multi-layer printed wiring board for power (5 voltages) and ground distribution. This panel is lighter and consumes less volume than a metal plate using

discrete bus bars. Four chassis attached levers (2 per module row) are provided for module insertion and extraction. The built-in levers provide a mechanical advantage to overcome the force generated by the 280 LRM contacts. The levers, shown in Figure 2, traverse from front to rear of the enclosure in four guides and index at each module for insertion/extraction. They are captive to the enclosure and stow out of the way when not in use.

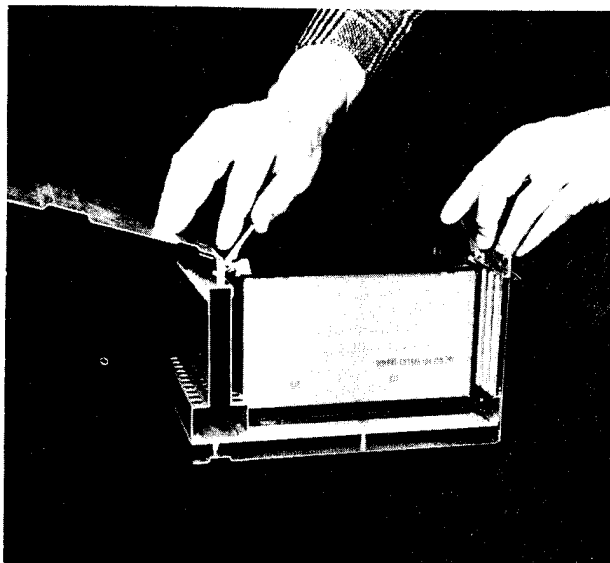


Figure 2.  
Chassis Attached Levers Inserting LRM

Access to the LRM's is through a two section hinged cover which is captivated to the enclosure by a hinge pin running longitudinally along the top surface of the central air duct, and fastened around the enclosure periphery by finger actuated latches. These cover latches and sliding levers for module insertion/extraction eliminate the necessity of tools for unit maintenance at the aircraft.

Bushings are provided on the rear panel to engage shear pins on the aircraft structure. The front panel provides folding handles and high strength hook supports for engaging swing lock clamps. The front panel also contains high current power and ground fittings and MIL-C-38999 connectors which interconnect to the matrix panel through crimp slide-on connectors.

#### LRM Design

With the requirements defined, an LRM design was started by initially investigating whether IC's in Dual-Inline Packages (DIP's) would fit or whether flat packs (FP's) or multichip hybrid packages (MHP's) must be substituted. It was quickly determined that LRM's composed of one printed wiring board (PWB), whether using DIP's, FP's, or MHP's would not give the required packaging density. Since FP's and MHP's have twice

the packaging density and one half the packaging weight as DIP's, it was determined that a concept using FP's must be designed. Flat packs were chosen over MHP's due to lower system cost and slightly lower system weight. An LRM design was developed which reduced the number of modules by 50% of those in similar systems, was light weight (.80#), low volume, provided close module to module spacing, and yielded an average IC junction temperature of 65°C with an average dissipation of 35 watts. This LRM design, shown in Figure 3, is fabricated by bonding and riveting two 4.7 x 8 multilayer printed wiring boards

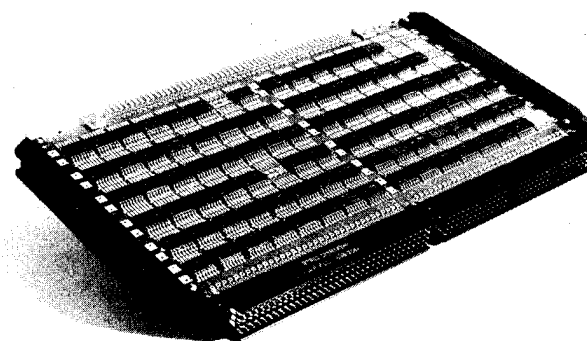


Figure 3. LRM with Covers Removed

of 8-10 layers each, back to back onto a common fin stock heat exchanger. This design yields a very compact light weight and rugged platform for component mounting and handling. Each outer face contains a maximum of 96 planar mounted FP's (with an average of 75) on a standard grid and plated thru hole pattern. Light weight molded plastic air inlet and exhaust fittings are attached which also provide grooves for attaching slide-on protective covers over both module faces. The inlet fitting, shown in Figure 4, has a tapered surface with a molded resilient urethane seal that deflects around the inlet orifice and prevents air leakage as each module is inserted into the enclosure which has a matching tapered fitting at each LRM position. This inlet orifice, which is full module height, creates a very low resistance which maximizes cooling air flow for low component junction temperatures. A molded plastic top cover with captivated hardware is attached to the upper edge of the module and protects the 100 pin test connector on each board, in addition to captivating both face covers. The lower edge of the module contains a one piece 280 contact (140 contacts/board) four row NAFI style skirted connector with polarization keys. These keys prevent LRM's from being plugged into an incorrect position in addition to providing initial alignment for the LRM. The two skirts which extend beyond the row of contacts also provide alignment for the module in addition to elimination of bent contacts during LRM insertion or handling of the LRM while outside the enclosure.

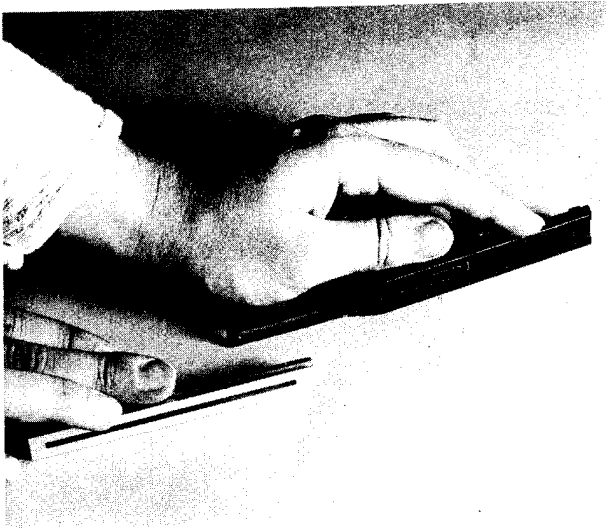


Figure 4. Inlet Fitting and Air Seal

#### SUMMARY

In conclusion, the packaging approach selected for the EAR Digital Assembly, including the LRM and enclosure designs, provided a light weight small volume, and highly reliable unit. A special achievement was the incorporation of a significantly improved maintainability concept. The very compact LRM made it possible to contain all common functional circuits in one unit for fault isolation purposes. By meeting all system requirements, the design resulted in the elimination of the intermediate (base) level maintenance shop and flight line test equipment. As a result of this and the fact that only LRM's need be spared, a significantly lower life cycle cost can be realized.

**JOSEPH ANTEBI** is a Senior Associate with Simpson Gumpertz & Heger Inc. He obtained his BA in Mechanical Sciences and his MA from Cambridge University, England, and his SM and ScD in Civil Engineering from MIT; he is a Registered Professional Engineer. His primary areas of interest are structural mechanics and the design and analysis of unusual structures. He was project manager for the development of the conceptual design of various structures, including a 440-ft. fully steerable radio-radar telescope, a hardened radar facility, and the optical support structure for a multiple mirror telescope which is now under construction. Prior to joining SGH in 1963, Dr. Antebi was Assistant Professor at the University of Hawaii.



**BENGT-OLOF AS** received the degree of Civiling from the Royal Institute of Technology, Stockholm, Sweden, in 1952. Postgraduate studies at the same Institute resulted in the Tekn. Lic. degree in 1958. During the period 1953-58 he was engaged in various research and teaching activities in microwaves and radio. In 1958 he was with Harvard University, Cambridge, Mass. doing research under an exchange scholarship. In 1958 he joined the, at that time, Philips Teleindustri AB, where as Head of Radar Section he pioneered the use of frequency agile radars for various applications. He is currently Manager of System Analysis, Weapon Control at Philips Elektronikindustrier AB.



**ROY C. BERG** has been employed by Lunn Industries for 27 years. He has held various manufacturing, engineering, and management positions, during which time he has developed a broad background in reinforced plastics. He is a graduate of the New York State Maritime College.



**LESLIE L. BERTZ** was the Mechanical Engineer for design, development and test of the AN/TPS-59 EDM. He directed all facets of mechanical design and provided mechanical engineering support during System and US Marine Corps Service Test. He is now involved in the GE592 radar program. Mr. Bertz has a BSME degree from the University of Connecticut and has participated in the design of GE radar and missile borne equipment for 20 years.

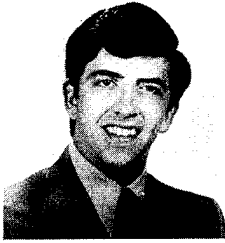


**SHERWIN BRADY** received his B.S.M.E. degree at the University of Maryland in 1960. He worked for the Atlantic Research Corporation of Alexandria, Virginia, after leaving school, designing mechanical components for solid propellant rocket motors. He is presently a product engineer with Litton Poly-Scientific.



**DAVID C. BRECHT** has mechanical design responsibility for pointing systems for shipboard mounts and directors and ground vehicle gun stabilization equipment. Previous assignments within G.E. included development and design of gyroscopes and gyroscopic equipment for directors, stabilizers, antennas, and torpedoes. He graduated from the University of Pittsburgh in 1935 with a BS degree in Mechanical Engineering, joining G.E. the same year.





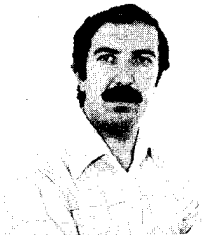
**THOMAS A. BUSHAR** is Chief Engineer—Roller Bearings at Kaydon Bearings Division of Keene Corporation in Muskegon, Michigan. He is responsible for all technical aspects of Kaydon roller bearings including application analysis, bearing design, cost estimating and manufacturing processing. He holds B.S.M.E. (1964) and Master of Engineering Science degrees, both from Pennsylvania State University. Before joining Keene Corporation, he was a senior product engineer with SKF Industries, King of Prussia, Pennsylvania.



**JOHN J. CHINO** received his B.S.M.E. from the Polytechnic Institute of New York in 1971, and his M.S.M.E. from the University of Maryland in 1973. He has been employed for six years by the Westinghouse Electric Corporation in Baltimore, Maryland, and is a member of the faculty staff of the Westinghouse School of Applied Engineering Science.



**STEPHEN COLE** received his B.S. and M.S. in metallurgical engineering, and has done extensive course work in related fields. He is a product engineer at Litton Poly-Scientific, where he is responsible for designing slip ring assemblies for a wide variety of applications. Mr. Cole has worked as a graduate teaching assistant at VPI and at SU, in metals control at Lynchburg Foundry, and was in the army.



**UMBERTO CORSI** joined S.p.A. in 1972 after taking Mechanical Engineering Degree in Rome University. He was employed in Mechanical Department—Technical Direction and worked on mechanical designs and the developments in shipboard and ground radar system and in spatial projects.



**MICHAEL COSTAGLIOLA** has been employed by Sperry Gyroscope Co. since 1949. He has been responsible for mechanical design of numerous military radars, antennas, and other defense equipment. He received the Sc.D. degree in Mechanical Engineering from M.I.T. in 1949.

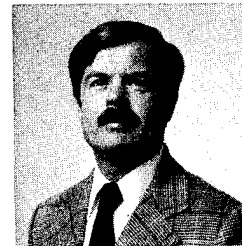


**W. D. DELANY** obtained BSc (Eng) Hons at Imperial College, London in 1948. After a few years in the chemical industry in mechanical engineering research he joined the Ministry of Defence. During his career he has worked on a ship's gyro stabilizer project, and on the mechanical engineering aspects of ships' radar and communications antennas, and radomes. He is at present Head of the Mechanical Engineering and Servo Mechanisms Division of Admiralty Surface Weapons Establishment, Portsmouth UK.

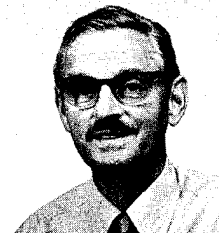
**CHRISTER EKENBERG** received the M.E. degree in mechanical engineering from the Royal Institute of Technology, Stockholm, Sweden, in 1968. Since then he has been with Philips Elektronikindustrier AB working mainly in the area of mechanical and hydraulic system design. He was deeply involved in the design of the hydraulic motors.



**VAUGHN M. FOXWELL, JR.** was born in Brooklyn, New York, N.Y. on 29 April 1938. He received the B.S. degree in Civil Engineering from Virginia Military Institute, Lexington, Va. on 14 June 1960. After serving four and a half years as a Navigator-Radar Intercept Officer in the Air Force, he attended the University of Kansas, Lawrence, Kansas. There he received the M.S. degree in Engineering Mechanics on 6 June 1966. From 1966 until the present, he has been with the Westinghouse Electric Corporation, Systems Development Division, Baltimore, Maryland.



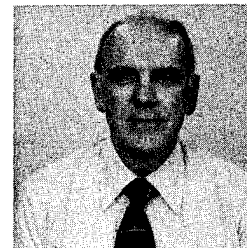
**HARRY FRANKLAND** is a native of Gillingham, Kent, England but he received his basic education and Engineering Training in Newcastle-upon-Tyne, England; obtaining his Electrical Engineering qualification (HNC) at Rutherford College of Technology in that city. After moving to the South Midlands, he qualified in mechanical/aero engineering (HNC) at Luton and S. Bedfordshire College of Technology. He was Chief Draftsman of Hunting Aviation and at Brown and Green Ltd Luton, England. From 1952 to 1957, he was a lecturer at Luton and South Bedfordshire College of Further Education. He emigrated to the United States in 1957 to take a job as a Design Engineer with General Dynamics, Convair. For the past 19 years, he has been with Teledyne Ryan Aeronautical Company on the design of Airborne and Space Radar Systems.



**CONRAD FRITZ** was born in Switzerland in 1916, and educated in Switzerland and England. He has worked for the Keystone Engineering Co. in Los Angeles, California, since 1950, and has been engaged in the design of special machinery and automated equipment.



**LEROY FUSS** earned his Bachelor of Aeronautical Engineering and his Master of Science in Engineering Electronics at Georgia Institute of Technology. At Lockheed Aircraft Company, Marietta, he participated in air frame stress analysis and structural analysis methods preparation. Mr. Fuss is now Staff Mechanical Engineer at Scientific-Atlanta, Inc., Atlanta and is writing his dissertation in elasticity of anisotropic materials also at Georgia Tech.



**WAYNE A. HARMENING** has been involved in the design of mechanical systems and mechanisms since graduation from Iowa State University in 1951. His experience covers fixed and mobile land-based equipment as well as shipboard, airborne, and spacecraft mechanisms. Mr. Harmening's association with static mass unbalance covers the past 15 years at RCA's Missile and Surface Radar business unit. During this time he has been actively engaged in developing high precision rotatable structures for equipments ranging from small, lightweight antennas for deep space probes to pointer-tracker systems for laser applications.



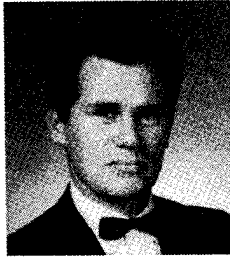




**EDWARD C. HAWKINS** is a Registered Professional Engineer in the State of Maryland. He received the B.S.—Mechanical and Aeronautical Engineering Degree from the University of Maryland in 1941. From 1941 to 1948, he participated in the structural analysis and mechanical design of products in the aircraft industry. In 1948 he joined the Bendix Communications Division where he is presently engaged as a Senior Staff Engineer. Since joining Bendix, Mr. Hawkins has participated, in varying degrees, in the design of most of the major microwave systems produced by Bendix.



**LEONARD J. HAYES** is Manager of Systems Mechanical Engineering in General Electric's Heavy Military Equipment Department. He was the lead mechanical engineer during conceptual design and proposal effort for the AN/TPS-59. He provides management direction and mechanical design consultation for the GE592 and spin-off programs. Mr. Hayes has a B.M.E. degree from the University of Detroit and a M.S.E.A. degree from Syracuse University. He has been involved in GE radar programs for 20 years.



**JOHN H. HEATHMAN** joined Convair in 1957 and now has a total of 25 years of experience in the technical and management aspects of aerospace analysis and design. He has specialized in advanced thermostructural concepts for Aerospaceplane, lifting body re-entry spacecraft, hypersonic cruise vehicles, and the Space Shuttle Orbiter mid-fuselage. He has been associated with all aspects of high-temperature and lightweight structure technology, including both passive and active heat shield systems, advanced fiber composites, development of new fabrication techniques, and thermal and mechanical testing. He has been technical leader on many research and development programs involving advanced composite material use and recently successfully completed the design, fabrication, and shock and vibration testing of a three-axis, four-foot-diameter dish antenna system. Mr. Heathman received his High National Certificate in mechanical engineering degree at Rugby College of Technology, Works, England.



**WILLIAM B. HEBENSTREIT** received his B.S. in Applied Physics from California Institute of Technology in 1941. He has worked at Bell Telephone Laboratories, Hughes Aircraft Company, and TRW, Inc. Since 1965, he has been with Structofab, Inc., where he is now Vice President.

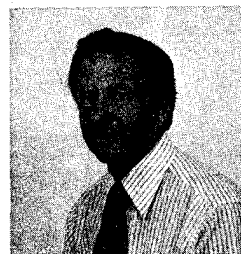


**JAMES A. HENDERSON** has a B.S. in Engineering (US Naval Academy) and M.S. in Mgmt. Science (Johns Hopkins). He has been at Westinghouse for over 12 years, where he is responsible for Interconnection Technologies at the Defense and Electronic Systems Center, including standardization and Research and Development. He teaches on the staff of the Westinghouse School of Applied Engineering Science as well as for special lectures and symposia.



**ARTHUR T. HUMPHREY** has worked on the design and performance evaluation of a range of civil and military radar systems, communication antennas, radio and optical telescopes. Computer programs for stress and vibrational analysis studies are a particular interest and the author has co-written packages in the MARSTRAN suite for usage throughout the GEC-Marconi Group.

**JOHN P. KARPUK** received his B.S.M.E. from the University of Massachusetts; Graduate course in Servo-Mechanics and Advanced Engineering Mathematics, Worcester Polytechnic Institute. He joined Raytheon in 1955. Presently Mechanical Staff Engineer for DATA Acquisition System Directorate. Served as Manager of Mechanical Engineering in the development of radar equipment for commercial, shipboard, land based, airborne and space. Supervised the design of equipment for: TARTAR, HUSTLER, TPN-19, AEGIS, SEA SPARROW, SPS-49, B-52, APOLLO, POLARIS, SPG-51, COBRA DANE, PAVE PAWS, GPN-22, TPQ-31, PATRIOT and MIR. Issued several patents, author of a paper on "The Use of Chemical Milling and Adhesive Bonding in the Design of Air Borne Equipment," and a member of the N.S.P.E.



**YASUO KATOU** was born on July 25, 1938. He graduated from the Metropolitan Technical College in 1959. He joined the Nippon Electric Co., Ltd. in 1959 and is now supervisor of the Production Engineering Department, Radio Application Division. He has been engaged in the mechanical development and design of the various kinds of Radar systems.



**M. SMOOT KATOW** has a B.S. from the University of California at Berkeley (1935) and an M.S. from the California Institute of Technology, Pasadent (1936), both in Mechanical Engineering. He was employed as design engineer in the Caltech Cooperative Wind Tunnel from 1948 to 1961, and has been the MTS cognizant engineer for the 64-meter antenna tipping assembly and has done research on antenna structures at the Jet Propulsion Laboratory since 1961.



**MASARU KAWAI** was born on Oct. 28, 1928. He received the B.E. degree in mechanical engineering from Waseda University in 1952. He joined the Nippon Electric Co., Ltd. in 1952 and is now Manager of the Productions Engineering Department, Radio Application Division. He has been engaged in the mechanical development and design of the various kind of Radar systems, Communication Equipment, Ultra Sonic systems.



**ALAN W. KLINE** is a supervisor in the Mechanical Engineering Section of Lockheed Electronics Company, Plainfield, New Jersey, and has been with the firm for 15 years. He has a B.S.M.E. from Drexel University and a Professional Engineering license in New Jersey. His experience includes the design of antennas and pedestals for the MPQ-4, SPS-12, ASR-4, SPS-17, SPS-29, and SPG-60 Radar Systems.



**CHARLES LEVINE** is a Staff Engineer in the Equipment Division's Mechanical Systems Laboratory at Wayland, Massachusetts. For the past 36 years he has been involved in the electro-mechanical design and development of the numerous radar equipments produced by Raytheon's Equipment Division. His technical specialties include slipring and air pressurization systems design. He is a licensed professional engineer in the state of Massachusetts and is the author of a paper "Slipring Design Considerations" which was presented at the Third International Research Symposium on Electric Contact Phenomena.





**ROY LEVY** received his B.S. from the Cooper Union Institute of Technology in New York and holds an M.S. and Ph.D. in Structural Engineering from the Polytechnic Institute of Brooklyn, New York. He has been working on antenna structures since the late 1950s and has been a member of the Technical Staff at the Jet Propulsion Laboratory since 1968. His current interests are in computerized structural design, and he is the principal developer of the JPL-IDEAS Computer Structure Design Program.



**RENE W. LUFT** is a Senior Staff Engineer with Simpson Gumpertz & Heger Inc. specializing in the areas of structural mechanics, seismic design, and design of unusual structures. Dr. Luft has participated in the conceptual designs of a multiple mirror optical telescope and of a hardened radar facility, as well as in the analysis and design of several radio telescopes. He received the degree of Engineer from the University of Chile and the SM and ScD degrees from the Massachusetts Institute of Technology; he is a Registered Professional Engineer in Alaska, California, Massachusetts, and Rhode Island.



**RONALD L. MANN** is a staff engineer in the Heavy Military Equipment Department, General Electric Company. During the preceding ten years he has been involved in design and vulnerability studies of structures subjected to nuclear weapon environments. Over this period he contributed to the development of a number of large hardened antenna array structures, having primary responsibility for structural design and analysis. Mr. Mann is a Ph.D. candidate in the Department of Mechanical and Aerospace Engineering, Syracuse University.



**LEWIS C. MILLER** was born in LaPorte, Indiana on April 12, 1942. He received the B.S.E.E. and M.S.E.E. degrees from The University of Michigan in 1964 and 1967 respectively. He has worked for Sensor Dynamics Inc. on coherent optical systems, and for Bendix Systems Division on intelligence processing systems. From 1966 through 1970 he was with Conduction Corporation, Ann Arbor, Michigan, where he was involved with digital radar signal processing systems. Since 1971, Mr. Miller has been at the Westinghouse Defense and Electronic Systems Center, Baltimore, Maryland, where he is a Fellow Engineer involved in radar and radar/navigation system definition.



**RICHARD F. PORTER** is a graduate of the Department of Aerospace Engineering at the University of Florida. He obtained a Bachelor of Science Degree in 1965 and Master of Science in 1967. Since graduation, he has worked at Westinghouse Defense and Electronic Systems Center where he has been involved in the thermal and mechanical design of space and airborne electronics systems. He is currently a Senior Engineer in the Thermal Management Group.



**MILTON B. PUNNETT** holds a B.S. degree in Mechanical Engineering from Purdue University and a Masters Degree in Engineering from Cornell University. Mr. Punnett has held engineering positions with Cornell Aeronautical Laboratory, United Aircraft Corporation, and Moog, Inc. He is presently Chief Engineer at Birdair Structures, Inc., Since joining Birdair over 20 years ago, Mr. Punnett has acted as Project Engineer on more than 100 radome programs for both commercial and military applications.

**K. REDMOND** is presently employed as a Staff Engineer in the Mechanical Engineering Department of Lockheed Electronics Company, Inc. He has had considerable experience in developing commercial and military electronics, and is presently involved in developing a radar director used on a Small Ships Gun Fire Control System. His previous director experience has included developing Precision Tracking Systems, Satellite Trackers, and tracking equipment used on the APOLLO program.



**HERMAN ROSSMAN** graduated from the Academy of Aeronautical School of Aircraft Design in 1957; he received his B.S.A.E. in 1965 from the Polytechnic Institute of New York. He has been employed by Westinghouse Electric Corporation in Baltimore, Maryland, since 1965, and is a member of the faculty staff of Westinghouse School of Applied Engineering Science.



**THOMAS L. RYAN** received his B.S.M.E. from the University of Kansas in 1963, and a B.S.Ed. from the same school in 1965. He taught Mathematics in the Albuquerque Public Schools from 1965-1968. Since then, he has been with the U.S. Naval Ship Weapons Systems Engineering Station, TERRIER Department, fire-control radar branch.



**NEVILLE SAWYER** is a graduate of Guildford Technical College and Royal Aircraft Establishment College, Farnborough, England—B.S. (equivalent to A.E. and M.E.). Studied space technology, manufacturing techniques, and management courses at University of California, Los Angeles. Joined A.V. ROE Aircraft, Canada—contributed to CF-100 and 105 Interceptor Programs in controls and instrumentation. Came to the United States in 1956 and joined General Dynamics Convair, San Diego, on the design team as a design engineer in controls, mechanisms and instrumentation in the 880 and F106 programs. In 1960 was co-founder of X-onics Corporation, San Diego—manufacturing microelectronic and ultrasonic equipment for the Atlas, Titan and nuclear programs. Joined Teledyne Ryan Electronics in 1965. Contributed to three generations of interplanetary landing radar systems, Surveyor, Apollo and Viking. Currently is Group Engineer, Product Design, GSDI B-52 Nav System and electro-mechanical packaging.



**HOWARD SIMPSON** obtained his B.C.E. from Cornell University and his S.M. (Building Engineering and Construction) and Sc.D. (Civil Engineering) from MIT. A former associate professor of structural engineering at MIT, on whose faculty he served for 12 years, he has since 1956 been a principal of the firm of Simpson Gumpertz & Heger Inc. His principal professional activities include the development and design of special structures and structural engineering investigations. He is a Vice President of the Boston Society of Civil Engineers Section of the American Society of Civil Engineers and Chairman of its Committee on Seismic Design Criteria and of the Advisory Committee on the seismic provisions of the Massachusetts Building Code. He is a Registered Professional Engineer in Massachusetts and California.



**JOHN W. SMALL** is a member of the Technical Staff at ITT Gilfillan. His current responsibilities include research and development work on a variety of Advanced Composite applications for large radar antennas. Prior to joining ITT, Mr. Small was a Staff Engineer with TRW Defense and Space Systems involved with Mechanical Engineering and design on military and commercial communication satellites and several radar systems for the space shuttle. Before his association with TRW, he was a senior Mechanical Engineer with Raytheon Company.





**PAUL STROM** joined Philips in 1957 after previous positions with SWEDA Cash Register and Printing Equipment. He has been in charge of the mechanical design of a plentiful of radar components, assemblies, equipment, and systems and led the design team engineering the hydraulic motors. He is currently Manager of Mechanical Design in the Defense Electronics division of Philips Elektronikindustrier AB.



**MITSURU SUGIE** was born on July 18, 1934. He received the B.E. degree in electrical engineering from Tokyo Metropolitan University in 1958. He joined the Nippon Electric Co., Ltd. in 1958 and is now Manager of the First Radar Engineering Department, Radio Application Division. He has been engaged in the development of the various kinds of the development of phased array radar systems and design of ATC radar.



**WILLIAM WADE, SR.**, Design Engineer, received his B.S.M.E. in 1966 from Utah State University. He has been at Lockheed since graduation, the past 10 years of which he has been associated with the Antennas and RF Systems Department. He served as design leader, test director and assistant program manager on the ATS-6 reflector program. He is presently coordinating and directing an advanced systems studies on a company funded development program.



**MATSUKICHI WAKABAYASHI** was born on Feb. 19, 1936. He received the B.E. degree in electrical engineering from Chuo University in 1960. He joined the Nippon Electric Co., Ltd. in 1954 and is now Engineering Manager of the Production Engineering Department, Radio Applications Division. He has been engaged in the mechanical design of the various kinds of ATC radar.



**HERBERT C. WALKER** received his education in Mechanical Engineering and Science at Cleveland State University and John Carroll University, Cleveland, Ohio 1939-1948. Since joining Poly-Scientific in 1961. Mr. Walker has served as Project Engineer, Senior Engineer and Manager of Large Product Engineering, his present position.



**PATRICK J. WALSH** has a B.E.S. in Mechanics and an M.S. in Operations Research from Johns Hopkins University. He has worked at the Defense and Electronic Systems Center of the Westinghouse Electric Corporation for three years as an engineer in the Mechanical Design and Materials Engineering Department.

**ARTHUR A. WOODS**, Staff Engineer, received his B.S.M.E. in 1965 from Northeastern University of Santa Clara. He has been at Lockheed since 1965. Since 1970, Mr. Woods has been responsible for the development of large deployable antenna/technology. He is presently responsible for the technical direction of Independent Research and Development programs which are supporting the large aperture antenna design development efforts.



**DONALD J. ZONA** received his B.S. in Mechanical Engineering from New York University and has completed various advanced engineering courses at City College of New York. He has also completed the USAF Communications and Electronics Course. Mr. Zona's current position at Sanders Associates is Section Manager within the Mechanical Engineering Department. In this capacity he has been responsible for the direction and management of mechanical design requirements within the various divisions of the corporations Federal Systems Group. He has served as mechanical program manager on the Lockheed 53A, Navy CAIR I & II Army Hot Brick, and ILAADS programs. He is currently assigned as mechanical program manager of the AN/ALQ-156 program.